Advanced Imaging Techniques in Cerebrovascular Disease

Shalini Ambika AMUKOTUWA
MBBS (Hons), B. Med. Sc, M.Med, FRANZCR

ORCID ID: 0000-0002-1678-3930

UNIVERSITY OF MELBOURNE

submitted in fulfilment of the degree of Doctor of Philosophy - Medicine, Dentistry and Health Sciences

Department of Radiology
Faculty of Medicine, Dentistry and Health Sciences
The University of Melbourne

August 2020

Abstract

This dissertation aims to investigate how advanced imaging techniques can improve diagnosis, prognostication and treatment delivery in patients with cerebrovascular disease. Six original publications are presented in which perfusion imaging and new software algorithms are used to address clinical need in two specific cerebrovascular disease entities: *acute ischemic stroke* (AIS) and *dural arteriovenous fistulas* (DAVFs).

AIS patients with anterior circulation *large vessel occlusions* (LVO) can be successfully treated with mechanical thrombectomy. Patient triage to thrombectomy requires identification of an LVO, the target of therapy, as well as the likelihood of benefit from reperfusion and the potential risk of complication. This assessment must be accurate, fast and efficient since stroke is a time-critical emergency. This poses a challenge for stroke centres because an increasing number of patients are being screened since extension of the thrombectomy window to 24 hours. Additionally, non-tertiary level hospitals are now required to perform acute stroke imaging despite lacking around-the-clock neuroradiology expertise. The first four publications explore how perfusion imaging and automated software algorithms can be used to expedite triage while maintaining high diagnostic accuracy for identifying patients who are likely to benefit from treatment.

The first study introduces and describes a new fully-automated deterministic software algorithm for detecting LVOs on *computed tomography* (CT) angiography, then validates it in a large cohort of 926 AIS patients that was enriched for LVOs. The algorithm had high sensitivity (97%) and moderate specificity (74%) for detecting LVOs. The second study then applied this algorithm to a consecutive cohort of 477 "code stroke" patients presenting to a large regional hospital, with the aim of field testing it in the real world clinical setting where automated LVO detection tools are most likely to be used. The high sensitivity (94%) and negative predictive value (98%), combined with fast

processing times, suggest that it can be used as a screening tool to assist radiologists and expedite diagnosis of LVOs.

Patients with LVOs who have large infarct cores are unlikely to benefit from thrombectomy and have an increased risk of complication. *CT perfusion* (CTP) with fully automated post-processing is widely used to exclude patients with large infarct cores from treatment. Previous studies that validated CTP for this purpose had some key limitations. These were addressed in the third study, which sought to determine whether automated estimation of the infarct core on perfusion, based on reduced *relative cerebral blood flow* (rCBF), is sufficiently accurate for patient triage to thrombectomy. A novel approach was adopted, allowing almost perfectly temporally and volumetrically matched diffusion and perfusion data to be compared in a cohort of 119 prospectively enrolled patients. 94% of patients were correctly triaged using reduced rCBF, suggesting that fully automated perfusion-based measurement of the infarct core can be used for individual patient triage.

Despite widespread use of CT, *magnetic resonance imaging* (MRI) remains the first-line modality for stroke patients in Europe and Asia. One of the most time-consuming sequences is *T2*-weighted gradient recalled echo* (T2*GRE), which is used to detect haemorrhage that contraindicates reperfusion therapies. *Dynamic susceptibility contrast perfusion weighted imaging* (DSC-PWI), which is used primarily to delineate the ischemic penumbra, is also sensitive to haemorrhage. The agreement between DSC-PWI and T2*GRE for detection of haemorrhage was assessed in the fourth study on 393 MRI scans from a cohort of 221 AIS patients. Almost perfect agreement ($\kappa > 0.90$) was shown for detection of acute haemorrhage. This suggests that DSC-PWI is sufficient for haemorrhage screening when it is included in the AIS MRI protocol.

Arterial spin label (ASL) is an entirely non-invasive MR perfusion technique that is an alternative to DSC-PWI. While its use in AIS is limited, it has been serendipitously discovered that ASL signal in venous structures indicates the presence of shunting. Intracranial DAVFs are a type of shunting lesion that can be difficult to detect on structural imaging.

The diagnostic performance and added value of ASL for detection of DAVFs was assessed in the fifth study, in a cohort of 156 patients. Venous ASL signal had a high sensitivity (94%), negative predictive value (98%) and specificity (88%) for the presence a DAVF. Including ASL in the MRI protocol improved diagnostic confidence and performance. The sixth study assessed the accuracy of ASL for

identifying cortical vein drainage, the main risk factor for haemorrhage in DAVF patients. In a cohort of 34 patients, ASL was found to have a sensitivity of 91% and specificity of 96% for the presence of cortical vein drainage. These findings suggest that an MRI protocol augmented with ASL can be used to non-invasively screen for DAVFs and differentiate between high-risk fistulas requiring treatment and low-risk lesions that can be managed with observation.

To conclude, a summary of the findings is presented along with the impact of the work, its limitations and future directions for research.

Declaration

I certify that:

This thesis comprises only my original work towards the Doctor of Philosophy (with thesis by compilation of papers).

Due acknowledgement has been made in the text of all other material which has been used.

This thesis is under 100 000 words in length, exclusive of figures, tables, references, and appendices.

Melbourne, August 2nd, 2020

Shalini Ambika Amukotuwa

Preface

The work towards this thesis was performed in the Department of Radiology, Stanford University and Stanford Hospitals and Clinics, in association with the Departments of Medicine Departments of Medicine and Radiology, Faculty of Medicine, Dentistry and Health Sciences, The University of Melbourne. Data collected though the Stanford Stroke Centre, Stanford University for the following studies and trials has been utilized for this thesis: SENSE 3, DEFUSE 2 and DEFUSE 3. Data collected through the Department of Neurology, Royal Melbourne Hospital, for the EPITHET study has also been used in this thesis. I would like to thank the primary investigators of these studies for permitting me use of their data.

The thesis is my original work without any third-party editorial assistance. It has not been submitted for other qualifications.

The data for the DEFUSE 2 and EPITHET studies was collected prior to enrollment in the degree listed above. Analyses of this data, for the studies presented in this dissertation, were performed by me retrospectively, during enrollment. Data for the SENSE 3 study was collected during enrolment.

All published work (listed below) towards this thesis was completed during enrolment. These studies are my original work. As first author, I was responsible for the conception and $> 80\%$ of the work of each study, including: study design, obtaining ethics approval, data collection (except as listed, for the retrospectively obtained data from the above listed studies) and analysis, literature review, as well as manuscript preparation, editing and finalization. The contributions of my co-authors, whom I would like thank, is also listed below each paper.

Paper 1:

Amukotuwa SA, Straka M, Dehkharghani S, Bammer R. Fast Automatic Detection of Large Vessel Occlusions on CT Angiography. Stroke. 2019 50(12):3431-3438.

Software development and technical advice (RB, MS); image interpretation (SD, second reader of CTAs); data analysis (statistical analyses - RB); manuscript editing and final approval (all authors). Data from the DEFUSE 2 and DEFUSE 3 studies was used for this retrospective study, but constituted $< 50\%$ of the study data.

Paper 2:

Amukotuwa SA, Straka M, Smith H, Chandra RV, Dehkharghani S, Fischbein NJ, Bammer R. Automated Detection of Intracranial Large Vessel Occlusions on Computed Tomography Angiography: A Single Center Experience. Stroke. 2019; 50(10):2790-2798.

Software development and technical advice (RB, MS); data acquisition (collection of clinical patient data - HS); image interpretation (RVC, second reader of CTAs); manuscript editing and final approval (all authors).

Paper 3:

Amukotuwa S, Straka M, Aksoy D, Fischbein N, Desmond P, Albers G, Bammer R. Cerebral Blood Flow Predicts the Infarct Core: New Insights From Contemporaneous Diffusion and Perfusion Imaging. Stroke. 2019;50(10):2783-2789

Software development and technical advice (RB, MS); data acquisition (DA and GA); data analysis (RB); manuscript editing and final approval (all authors).

Paper 4:

Amukotuwa SA, Fischbein NJ, Albers GW, Davis S, Donnan GA, Andre JB, Bammer R. Comparison of T2*GRE and DSC-PWI for hemorrhage detection in acute ischemic stroke patients: Pooled analysis of the EPITHET, DEFUSE 2, and SENSE 3 stroke studies. Int J Stroke. 2020;15(2):216-225.

Data acquisition (GA, RB); image interpretation (JA, second reader); manuscript editing and final approval (all authors). Data from the DEFUSE 2, SENSE 3 and EPITHET studies was used for this retrospective study.

Paper 5:

Amukotuwa SA, Marks MP, Zaharchuk G, Calamante F, Bammer R, Fischbein N. Arterial Spin-Labeling Improves Detection of Intracranial Dural Arteriovenous Fistulas with MRI. AJNR Am J Neuroradiol. 2018;39(4):669-677

Image interpretation (NF, second reader MRI, MM, DSA interpretation); data analysis (RB); manuscript editing and final approval (all authors).

Paper 6:

Amukotuwa SA, Heit J, Marks MP, Bammer R. Detection of Cortical Venous Drainage and Determination of the Borden Type of Dural Arteriovenous Fistula by Means of 3D Pseudocontinuous Arterial Spin-Labeling MRI. AJR Am J Roentgenol. 2016; 207(1):163-9

Image interpretation (JH, second reader MRI and DSA interpretation); manuscript editing and final approval (all authors).

Acknowledgements

I would like to thank my current and previous supervisors, Associated Professor Peter Brotchie, Professor Fernando Calamante, Professor Roland Bammer and Professor Vincent Thijs. Your encouragement and guidance have been invaluable, and you have given me the opportunity and space to grow as a researcher.

Thankyou to Professor Nancy Fischbein for being an amazing mentor and role model. I have learned so much from you, about both neuroradiology and how to be a good human being.

Thankyou also to Professor Patricia Desmond, the chair of my thesis committee, for all her support over the years, and especially for not allowing me to quit radiology.

Most importantly, I would like to recognize the patients whose data have been used in this thesis. Without you, these studies would not have been possible.

The following sources of funding are acknowledged: National Institutes of Health grants R01 EB 2711 and 5R21EB021029.

Thank you from the bottom of my heart to Roland, my husband. You have provided me with so much inspiration, support and knowledge, and encouraged me to be uncompromising in the pursuit of excellence. Thank you for your patience and understanding.

Finally, I would like to thank my parents, Nimal and Dhammika Amukotuwa, for their support and love. Without you, I would not have the luxury of being able to pursue my dreams. You have always encouraged me to value knowledge and learning, and set the best example. I remember those long evenings spent at the law library of Melbourne Uni as a child, which was my first exposure to the trials of a PhD. I would like to dedicate this thesis to you and to Roland, the three people who matter the most to me.

Symbols and Acronyms

This table summarizes the Symbols and Acronyms used in this doctoral thesis.

Symbol	**Full Name**
$\boldsymbol{f}$	Fractional vascular volume
$R(t)$	Tissue residue function
t	Time
$h(t)$	Impulse response function
p	Brain tissue attenuation
CH	Correction factor for lower capillary haematocrit
C_{tissue}	Tissue contrast concentration
C_{artery}	Arterial contrast concentration
M	Magnetization
S	MR signal
T_1	Longitudinal relaxation time
T_2	Transverse relaxation time due to spin-spin interactions
T_2*	Transverse relaxation time due to spin-spin interactions plus magnetic field inhomogeneity
R_2	Transverse relaxation rate due to spin-spin interactions
R_2*	Transverse relaxation rate due to spin-spin interactions plus magnetic field inhomogeneity
R_1	Longitudinal relaxation rate
λ	The brain-blood partition coefficient
δ	Arterial transit time
α	Labelling efficiency in ASL
τ	(in ASL) temporal width of bolus of labelled blood

Acronym	**Full Name**
2D	Two Dimensional
3D	Three dimensional
4D	Four dimensional
ACA	Anterior Cerebral Artery
ACOM	Anterior Communicating Segment
ADC	Apparent Diffusion Coefficient
AIF	Arterial Input Function
AIS	Acute Ischaemic Stroke
AM-CASL	Amplitude-Modulated Continuous Arterial Spin Labelling
ASL	Arterial Spin Labelling
ASPECTS	Alberta Stroke Program Early CT Score
ATA	Arterial Transit Artifact
ATLANTIS	Acute Noninterventional Therapy in Ischemic Stroke
ATP	Adenosine Triphosphate
ATT	Arterial Transit Time
AUC	Area Under the Curve
AVM	Arteriovenous Malformation
BASE	Unprepared Basis and Selective inversion
BBB	Blood-Brain Barrier
bSSFP	balanced Steady-State Free Precession
CASL	Continuous Arterial Spin Labelling
CBF	Cerebral Blood Flow
CBV	Cerebral Blood Volume
CMRO2	Cerebral Oxygen Metabolism
CNN	Convolutional Neural Networks
CNR	Contrast to Noise Ratio
CPP	Cerebral Perfusion Pressure
CSF	Cerebrospinal Fluid
CT	Computed Tomography
CTA	Computed Tomography Angiography
CTDI	Computed Tomography Dose Index
CTP	Computed Tomography perfusion
CVD	Cortical Vein Drainage
CVR	Cerebrovascular Resistance
DAVF	Dural Arteriovenous Fistula

Acronym	**Full Name**
DAWN	DWI or CTP Assessment with Clinical Mismatch in the Triage of Wake-Up and Late Presenting Strokes Undergoing Neurointenvention with Trevo
DCE	Dynamic Contrast-Enhanced
DEFUSE	Diffusion and perfusion imaging evaluation for understanding stroke evolution (for DEFUSE 1 and 2)
DEFUSE 3	Endovascular Therapy Following Imaging Evaluation for Ischemic Stroke 3
DICOM	Digital imaging and Communications in Medicine
DSA	Digital Subtraction Angiography
DSC-PWI	Dynamic Susceptibility Contrast Perfusion-Weighted Imaging
DVO	Distal Vessel Occlusion
DWI	Diffusion-Weighted Imaging
ECASS	European Cooperative Acute Stroke Study
EPI	Echo-Planar Imaging
EPISTAR	Echo-Planar MR Imaging and Signal Targeting with Alternating Radio Frequency
EPITHET	Echoplanar Imaging Thrombolytic Evaluation Trial
ESCAPE	Endovascular Treatment for Small Core and Anterior Circulation Proximal Occlusion with Emphasis on Minimizing CT to Recanalization Times
EXTEND-IA	Extending the Time for Thrombolysis in Emergency Neurological Deficits - Intra-Arterial
FAIR	Flow-sensitive Alternating Inversion Recovery
FAIRER	Flow Alternating Inversion Recovery Extra Radiofrequency pulse
FID	Free Induction Decay
FLAIR	Fluid Attenuated Inversion Recovery
FSE	Fast spin-echo
g	grams
GBCA	Gadolinium-based Contrast Agent
GPU	Graphic Processing Units
GRASE	Gradient and Spin Echo
GRE	Gradient Recalled Echo
HI	Haemorrhagic Infarction
HARM	Hyperintense Acute Reperfusion Marker
ICA	Internal Carotid Artery

Acronym	**Full Name**
ICAD	Intracranial Atherosclerotic Disease
ICH	Intracranial Haemorrhage
IMS	Interventional Management of Stroke
IVT	Intravenous Thrombolysis
Ktrans	trans-endothelial transfer coefficient
kV	kiloVolt
LVO	Large Vessel Occlusion
MCA	Middle Cerebral Artery
MIP	Maximum-Intensity Projection
mL	millilitres
MR CLEAN	Endovascular Treatment for Acute Ischemic Stroke in the Netherlands
MRA	Magnetic Resonance Imaging
MRA	Magnetic Resonance Angiography
mRS	modified Rankin scale
MT	Magnetization Transfer
MTT	Mean Transit Time
NASCET	North American Symptomatic Carotid Endarterectomy Trial
NECT	Non-enhanced Computed Tomography
NIHSS	National Institutes of Health Stroke Scale
NINDS	National Institute of Neurological Disorders
NLP	Natural Language Processing
OEF	Oxygen Extraction Fraction
^{15}O-PET	^{15}Oxygen-Positron Emission Tomography
oSVD	block-circulant Singular Value Decomposition
PACS	Picture Archiving and Retrieval system
PASL	Pulsed Arterial Spin Labelling
PCA	Posterior Cerebral Artery
PCASL	Pseudocontinuous Arterial Spin Labelling
PCOM	Posterior Communicating Segment
PD	Proton Density
PET	Positron Emission Tomography
PH	Parenchymal Haemorrhage
PLD	Post-Label Delay
PROACT	Prolyse in Acute Cerebral Thromboembolism
PS	Permeability Surface area product

Acronym	**Full Name**
Q2TIPS	QUantitative Imaging of Perfusion using a Single Subtraction 2 with thin-slice TI_1 periodic saturation
QUIPSS	QUantitative Imaging of Perfusion using a Single Subtraction
rCBF	relative Cerebral Blood Flow
rCBV	relative Cerebral Blood Volume
REVASCAT	Randomized Trial of Revascularization with Solitaire FR Device versus Best Medical Therapy in the Treatment of Acute Stroke Due to Anterior Circulation Large Vessel Occlusion Presenting within Eight Hours of Symptom Onset
RF	Radiofrequency
RFL	Random Forest Learning
ROC	Receiver Operating Characteristic
rsASL	Region-selective ASL
rt-PA	recombinant tissue-Plasminogen Activator
s	seconds
SAR	Specific Absorption Rate
SE	Spin Echo
SENSE 3	SEnsitivity Encoding for Fast Stroke Imaging 3
SIH	Symptomatic Intracranial Haemorrhage
SNR	Signal to Noise Ratio
SPGR	Spoiled Gradient-Echo
SS-EPI	Single-Shot Echo-Planar Imaging
SVD	Singular Value Decomposition
SWI	Susceptibility Weighted Imaging
SWIFT-PRIME	Solitaire with the Intention for Thrombectomy as Primary Endovascular Treatment
T2*GRE	T2*-weighted Gradient Recalled Echo
TE	Echo Time
TI	Inversion Time
TICI	Thrombolysis In Cerebral Infarction
Tmax	Time to Maximum of tissue residue function
TOF-MRA	Time-of-flight Magnetic Resonance Angiography
TR	Time-resolved
TR	Repetition Time
TR CEMRA	Time-resolved Contrast-Enhanced Magnetic Resonance Angiography

Acronym	**Full Name**
TrueSTAR	true fast imaging with steady-state precession (FISP)-based spin tagging with alternating radiofrequency
UNFAIR	UNinverted Flow-sensitive alternating inversion recovery
VTI	Vessel Territory Imaging
WAKE-UP	Efficacy and Safety of MRI-Based Thrombolysis in Wake-Up Stroke

Table of Contents

Chapter 1

Introduction

Cerebrovascular disease is a leading cause of death and disability, with stroke alone causing approximately 5 million deaths globally each year[1]. This dissertation focuses on two specific cerebrovascular diseases, *acute ischemic stroke* (AIS) and *dural arteriovenous fistulae* (DAVFs). AIS is an acute disease, where the goal of treatment is to resolve acute symptoms, while DAVFs are a chronic condition where treatment is aimed at preventing future complications. The unifying aim of treatment in both entities is to prevent neurological disability. These diseases also have in common the availability of highly effective endovascular treatment that can decrease morbidity and improve outcomes in eligible patients[2, 3]. However, this treatment itself carries a risk of complication, requires access to a centre with interventional neuroradiology expertise and is costly. Accurately identifying patients who require and are likely to benefit from treatment, while excluding those in whom treatment is either futile or unwarranted, is therefore critical. Imaging plays an important role in this task. Unfortunately, standard neuroimaging techniques have some key limitations that need to be addressed in order to improve diagnostic accuracy and efficiency and ensure appropriate and timely patient triage to treatment so that the best outcomes can be achieved.

This dissertation aims to investigate how currently available advanced neuroimaging techniques, specifically perfusion imaging and automated software algorithms, can be used in clinical practice. The overarching hypothesis is that these techniques can improve diagnostic accuracy, workflow efficiency and risk stratification in AIS and DAVF patients. The thesis begins with a review of AIS and DAVFs, and a discussion of the perfusion imaging techniques most often used in patients with these diseases. The investigations performed as a part of this dissertation, that address specific important clinical questions and provide evidence to support the working hypothesis, are then presented.

Endovascular thrombectomy has revolutionized the treatment of AIS. This technique involves mechanical retrieval of the thrombus via an endovascular approach using modern clot-retrieval devices and is therefore also referred to as

"clot retrieval"[4, 5]. It is now the standard-of-care treatment for patients with an anterior circulation *large vessel occlusion* (LVO) up to 6 hours following symptom onset and can be performed in carefully selected patients up to 24 hours from last known well [1, 6]. Patients with intracranial LVOs who have critically hypoperfused but salvageable brain tissue ("ischemic penumbra") are likely to benefit from treatment, while those with large volumes of irreversibly damaged tissue have an increased risk of treatment complication[7, 8]. Appropriate triage of patients to treatment is therefore reliant upon accurate identification of an LVO ("a blocked pipe", which is the target of thrombectomy) and salvageable ischemic penumbra, while a large infarct core and haemorrhage (which contraindicates reperfusion therapies) must be excluded. Fast and efficient diagnosis is also important since AIS is a time-critical emergency, due to the limited window for thrombectomy, the potential for infarct growth with treatment delay, and therefore the better functional outcomes associated with earlier reperfusion[9, 10].

Timely identification of patients with an LVO is particularly important but can be problematic in countries, such as Australia, which have a geographically dispersed population and concentration of interventional neuroradiology services at a few tertiary metropolitan centres ("hubs"). Many peripheral and regional "spoke" hospitals now perform *computed tomography angiography* (CTA) in patients with a suspected ischemic stroke for identification of LVOs, but lack 24/7 expertise in interpretation. These CTAs are often interpreted by general radiologists, neurologists, or trainees, whose diagnostic performance for detection of LVOs can be considerably worse than that of neuroradiologists[11-13]. Further, acute stroke scans may not necessarily receive the highest priority for review, especially at busy times, when there are other time-critical scans such as trauma to be reported. These factors can cause incorrect or substantially delayed diagnosis, and lead to patients missing out on potentially beneficial treatment. Conversely, incorrect diagnosis of an LVO can result in unnecessary patient transfer to a metropolitan stroke hub, wasting valuable resources and inconveniencing the patient. Strategies that improve workflow, diagnostic accuracy and speed of LVO detection are therefore needed. Clinical decision support tools that automate detection of the infarct core and ischemic penumbra are well established and are used routinely to improve workflow and expedite treatment decisions in acute stroke[14, 15].

Automation is now being applied to the task of detecting intracranial LVOs in a clinically acceptable timeframe, however these tools are yet to be validated despite being commercially available. The first study introduced and evaluated a new

automated software algorithm for LVO detection. The aim of this first study was to determine the diagnostic accuracy of the algorithm in a sample of patients with a high prevalence of LVOs and determine the optimal threshold for LVO detection. In the second study, this algorithm was evaluated in the context of a consecutive cohort of patients, applying the threshold determined in the first study. The purpose of this second study was to test the algorithm in a real-world, non-curated patient cohort consisting of all patients presenting with a suspected ischemic stroke, within the thrombectomy window, to a regional "spoke" hospital. Field testing in a "spoke" hospital was considered important, and warranted a separate study, because this is the setting in which automated algorithms are most likely to be useful for improving diagnostic accuracy and efficiency of LVO detection.

In patients with LVOs, the likelihood of benefit from reperfusion decreases and the risk of complication increases with the volume of the infarct core[8, 16]. Accurate and rapid estimation of the size of the infarct core is therefore important. The imaging gold standard for delineation of the infarct core is *diffusion-weighted imaging* (DWI), which has been extensively validated in both human and animal studies[17-21]. Despite this, most centres in Australia and North America use CT rather than *magnetic resonance imaging* (MRI) as the first-line imaging modality in AIS because it is easier to access in the emergent setting and does not require cumbersome safety screening. Unfortunately, *non-enhanced CT* (NECT) has a poor sensitivity and specificity for detection of acute infarction[22]. Interpretation is also highly subjective and dependent upon level of experience. Additionally, NECT measurement of the infarct volume is dependent on crude estimates such as the *Alberta Stroke Program Early CT Score* (ASPECTS)[23]. CT perfusion (CTP) can be used instead to identify the infarct core based on severely reduced cerebral blood flow or blood volume[24-28]. This process can be fully automated, allowing rapid and objective around-the-clock assessment of infarct volume without the need for highly experienced neuroradiologists to interpret the studies.

Fully automated CTP-based infarct core measurement was therefore used in a number of thrombectomy trials for patient selection. In these trials, severely reduced *relative cerebral blood flow* (rCBF) was employed to estimate the infarct volume[29-32]. This has led to widespread adoption of CTP-derived rCBF for infarct core estimation. This approach is not, however, universally accepted as accurate for infarct core measurement in individual patients[33]. Contributing to the persisting doubt, the previous studies that have validated CTP-derived rCBF against the reference standard of DWI for measurement of the infarct core may be inaccurate. The main sources of potential inaccuracy are incomplete brain

coverage on older CTP acquisitions and infarct growth in the interval between CTP and MRI (a time delay necessitated by patient transfer and set up from CT to MRI)[24, 26, 27]. Further validation of automated blood-flow based estimation of the infarct core is therefore required.

The third study therefore aimed to determine whether automated blood-flow-based measurement of the infarct volume is of sufficient accuracy to allow individual patient triage to thrombectomy. To overcome the limitations of prior investigations in this area, more closely volumetrically- and temporally-matched perfusion and diffusion data were used. Treatment decisions based on blood-flow based estimation of the infarct core were compared against the decision based on DWI (the reference standard) in individual patients to determine how frequently they differed.

Given persistent concerns regarding the accuracy of CT perfusion-based infarct core estimation, MRI remains the first-line imaging modality in AIS in Europe, Asia and some centres in North America, particularly for patients with wake-up stroke[34]. The infarct core is estimated using DWI while critically hypoperfused tissue is predicted using *dynamic susceptibility contrast perfusion-weighted imaging* (DSC-PWI), which is the mainstay of MR-based assessment of cerebral haemodynamics. The benefit of thrombectomy has been shown to be related to the presence of a perfusion-diffusion "mismatch", where the volume of critically hypoperfused tissue exceeds the volume of the infarct, indicating the presence of viable ischaemic penumbra[7]. Many (but not all) centres that perform acute stroke MRI therefore include DSC-PWI in the AIS MRI protocol. This does, however, incur a time penalty. Because of the time-critical nature of acute stroke treatment, efforts are made to keep the MR protocol as short as possible while providing adequate diagnostic information[35]. One of the most time-consuming sequences in the AIS MRI protocol is anatomical *T_2*-weighted gradient recalled imaging* (T2*GRE), which is used for haemorrhage detection.

Since DSC-PWI is also T_2*-weighted, hence sensitive to changes in magnetic susceptibility be it gadolinium-based contrast agent or blood product, it can in theory be used for haemorrhage screening. The fourth study assessed whether DSC-PWI can be used for haemorrhage screening in AIS patients. The purpose of this study was to determine whether agreement between DSC-PWI and T2*GRE for the presence of haemorrhage was sufficiently high to allow T2*GRE to be omitted from the acute stroke MR protocol as a time saving measure.

As with AIS, decisions regarding treatment of DAVFs are heavily reliant upon imaging. DAVFs are acquired high flow vascular lesions where there is shunting between dural arteries and either a dural venous sinus or cortical vein[2]. They are therefore characterized by direct flow of arterial blood into the venous system without an intervening capillary bed or resistance arterioles, causing transmission of arterial pressure into the venous system[2]. The resulting venous hypertension can result in cerebral oedema, ischaemia and intracranial hemorrhage[36-39]. Haemorrhage occurs in 15% of patients with DAVFs[36]. The single most important risk factor for haemorrhage and other aggressive neurological presentations, such as cerebral oedema, is the presence of cortical vein drainage, which is associated with an 8.1% annual risk of intracranial haemorrhage and 10.4% annual mortality[37, 40-42]. Cortical vein drainage of a DAVF is therefore a key indication for treatment. Unfortunately, treatment itself has a risk of complication, including stroke and haemorrhage. Therefore, DAVFs without cortical vein drainage are usually managed conservatively, with close clinical and imaging surveillance to detect progression[1-3].

MRI is used to evaluate patients with a suspected DAVF. There are some small studies showing that experienced neuroradiologists have a high sensitivity and specificity for detecting DAVFs on MRI with *time-of-flight* (TOF) MRA[4, 5]. However, these lesions can be difficult to visualize on conventional structural MRI sequences and even MRA. Consequently, in the author's experience, the diagnostic performance for detection of DAVFs on MRI is much poorer in the real-world setting. The imaging gold standard for detection of DAVFs, catheter-based *digital subtraction angiography* (DSA), is therefore performed when there is a strong index of suspicion for a DAVF even if the MRI is deemed negative. DSA is also necessary for accurate detection of cortical vein drainage for risk stratification, to determine whether a DAVF warrants treatment. There are several disadvantages associated with DSA. It is an invasive procedure that exposes patients to ionizing radiation and a risk of complication including ischaemic stroke. It also requires access to an interventional neuroradiology service, which most regional and peripheral hospitals do not have. In countries such as Australia, where the population is dispersed, this can result in patients needing to travel large distances. As such, there is an unmet clinical need for non-invasive imaging strategies that allow accurate and confident diagnosis or exclusion of a DAVF as well as accurate risk stratification.

Preliminary evidence suggests that *arterial spin label* (ASL) perfusion may improve the diagnostic performance of MRI for detection of DAVFs[6]. However, this study was limited by a small sample size. ASL is an entirely non-invasive MR perfusion

technique where water protons in arterial blood water are magnetically labelled and act as a completely diffusible tracer[7]. This magnetically labelled blood water exchanges with tissue water during capillary transit[7, 8]. Because of the large pool of tissue water, the effective mean transit time of labelled water is several minutes, during which time the signal decays due to T_1-relaxation[7, 8]. Therefore, under normal conditions, there is minimal venous outflow of labelled spins, and ASL signal is not seen in venous structures[6, 8, 9]. High signal in venous structures can occur when there is either abnormally rapid capillary transit or arteriovenous shunting of labelled arterial blood. This is referred to as "venous ASL" signal and can alert the radiologist to the presence of a shunting lesion.

The fifth study investigated the diagnostic performance of MRI with and without ASL perfusion for detection of DAVFs. The purpose was to determine the added value of ASL and determine whether the accuracy of MRI with ASL is sufficiently high for it to be used as a reliable screening test for DAVFs. In the sixth study, the question of whether venous ASL signal can be used to detect cortical vein drainage and stratify risk in patients with DAVFs was addressed. The aim of this study was to assess the diagnostic accuracy of ASL against the reference standard DSA, to determine whether it is sufficiently accurate for non-invasive risk stratification.

In the concluding section of this thesis, the clinical implications and limitations the body of work presented are discussed. Potential future directions for use of perfusion and automation in AIS and DAVFs are then outlined.

References

1. Gandhi D, Chen J, Pearl M, Huang J, Gemmete JJ, Kathuria S. Intracranial dural arteriovenous fistulas: Classification, imaging findings, and treatment. *AJNR Am J Neuroradiol*. 2012;33:1007-1013

2. Davies MA, Saleh J, Ter Brugge K, Willinsky R, Wallace MC. The natural history and management of intracranial dural arteriovenous fistulae. Part 1: Benign lesions. *Interv Neuroradiol*. 1997;3:295-302

3. Davies MA, Ter Brugge K, Willinsky R, Wallace MC. The natural history and management of intracranial dural arteriovenous fistulae. Part 2: Aggressive lesions. *Interv Neuroradiol*. 1997;3:303-311

4. Meckel S, Mekle R, Taschner C, Haller S, Scheffler K, Radue EW, et al. Time-resolved 3d contrast-enhanced mra with grappa on a 1.5-t system for imaging of craniocervical vascular disease: Initial experience. *Neuroradiology*. 2006;48:291-299

5. Noguchi K, Melhem ER, Kanazawa T, Kubo M, Kuwayama N, Seto H. Intracranial dural arteriovenous fistulas: Evaluation with combined 3d time-of-flight mr angiography and mr digital subtraction angiography. *AJR Am J Roentgenol*. 2004;182:183-190

6. Le TT, Fischbein NJ, Andre JB, Wijman C, Rosenberg J, Zaharchuk G. Identification of venous signal on arterial spin labeling improves diagnosis of dural arteriovenous fistulas and small arteriovenous malformations. *AJNR Am J Neuroradiol*. 2012;33:61-68

7. Deibler AR, Pollock JM, Kraft RA, Tan H, Burdette JH, Maldjian JA. Arterial spin-labeling in routine clinical practice, part 1: Technique and artifacts. *AJNR Am J Neuroradiol*. 2008;29:1228-1234

8. Zaharchuk G. Theoretical basis of hemodynamic mr imaging techniques to measure cerebral blood volume, cerebral blood flow, and permeability. *AJNR Am J Neuroradiol*. 2007;28:1850-1858

9. Amukotuwa SA, Yu C, Zaharchuk G. 3d pseudocontinuous arterial spin labeling in routine clinical practice: A review of clinically significant artifacts. *J Magn Reson Imaging*. 2016;43:11-27

Chapter 2

Acute Ischaemic Stroke

Stroke is a clinical entity that is characterized by the abrupt onset of neurological dysfunction that is of vascular aetiology. **Acute stroke** is defined as the rapid development of a neurological deficit lasting more than 24 hours resulting from a focal injury to the brain by a vascular cause[1-3]. Approximately 15 million people suffer a stroke each year around the world, of which around 5 million die and another 5 million are left permanently disabled[2]. Stroke is therefore one of the leading causes of death and disability globally, and the third leading cause of death in Australia[2]. The vast majority (approximately 85%) of strokes are *ischemic*, caused by interruption of blood flow to the brain[2, 4]. The remainder are haemorrhagic strokes, caused by rupture or leakage of a cerebral blood vessel[5]. In this chapter, the pathophysiology and treatment of *acute ischemic stroke* (AIS) will be reviewed, followed by detailed discussion of the role of imaging in the management of this condition.

2.1 Pathology and Pathophysiology of Cerebral Ischaemia and Infarction

The brain is a highly metabolically sensitive organ that requires a constant supply of oxygen and glucose, which is the primary energy substrate for neurons[6, 7]. While the brain accounts for only 2% of body weight, its glucose and oxygen consumption is about 20% of that of the entire body[6, 7]. Constant blood flow is required to maintain this high demand. Grey matter, which has a higher metabolic rate than white matter, requires and receives more blood flow; normal blood flow of grey matter is approximately 40 mL per minute per 100 g tissue, while it is around 10-15 mL lower in white matter[8]. Because aerobic metabolism dominates in the brain, oxygen rather than glucose is the limiting substance[6, 7].

Oxygen delivery to brain tissue is impaired when cerebral blood flow is interrupted[6]. Impairment of blood flow to brain tissue, depriving it of oxygen and glucose, is called **cerebral ischaemia**[6]. Global cerebral ischaemia occurs when there is globally reduced cerebral perfusion pressure, as occurs in the setting of

severe hypotension or cardiac arrest[6]. Focal ischaemia typically occurs when there is obstruction or severe narrowing of a cerebral artery, causing reduction or cessation of blood flow to a localized area of the brain (the artery's "territory" of blood supply)[6]. If blood flow remains inadequate, irreversible tissue injury occurs. This is called **infarction**, a term that describes tissue death secondary to insufficient blood flow[9].

The role of cerebral hemodynamic factors in the pathogenesis of ischaemia and infarction has been extensively studied, mostly in the setting of carotid artery stenosis and occlusion[10-17]. Under normal conditions, when *cerebral perfusion pressure* (CPP) remains constant, any changes in regional *cerebral blood flow* (CBF) are caused by a change in regional *cerebrovascular resistance* (CVR), which in turn is controlled by the calibre of arterioles (precapillary resistance vessels)[13]. Dilatation of these vessels causes CBF to increase, while constriction causes it to decrease. Vasodilatation also causes *cerebral blood volume* (CBV) to increase, since more blood enters and pools within tissue capillaries. CBV is proportional to CBF under these normal conditions. CPP can be altered by either decreased arterial inflow pressure or increased venous outflow resistance. CBF is maintained over a wide range of CPP[12, 17]; this is called **autoregulation** and is mediated by CVR through changes in the calibre of resistance arterioles, which constrict when CPP is increased and dilate when CPP decreases[13].

Based on their findings in carotid steno-occlusive disease, *Powers et al* proposed a model of chronic hemodynamic impairment that considers the compensatory responses to reduced CPP in sequential stages (Figure 2-1)[13, 16]. In **Stage I**, as CPP falls, CBF is maintained by autoregulatory vasodilation. This in turn causes CBV and mean capillary transit time (MTT, the ratio of CBV to CBF) to increase[13, 16]. In **Stage II**, the capacity for vasodilatation is exhausted and autoregulation cannot compensate for any further decrease in CPP[13, 16]. This is called autoregulatory failure. CBF starts to decrease as a function of CPP[13]. CBV may decrease as vessels collapse, however MTT remains elevated. *Cerebral oxygen metabolism* ($CMRO_2$) is then maintained by the brain's capacity to increase oxygen extraction from blood, i.e. *oxygen extraction fraction* (OEF)[13, 18]. Therefore, OEF increases and $CMRO_2$ is maintained during this stage, which is also referred to as "misery perfusion"[19]. The effects of decreased CPP on OEF and $CMRO_2$ have been investigated in vivo using haemodynamic *positron emission tomography* (PET) studies that utilize ^{15}O-oxygen and water[8, 11, 14, 20]. These studies have shown that, if CPP continues to fall further, CBF decreases progressively until oxygen extraction is maximal. Any further decrease in CPP (and therefore CBF) causes

ischaemia, since oxygen delivery and extraction are insufficient to meet the metabolic requirements of brain tissue[11]. At this **ischemic threshold**, which depends on the duration and degree of blood flow reduction, energy failure develops, and tissue dysfunction occurs. Although not referred to as such in Power's original paper, ischaemia may be considered **Stage III** in this model[21].

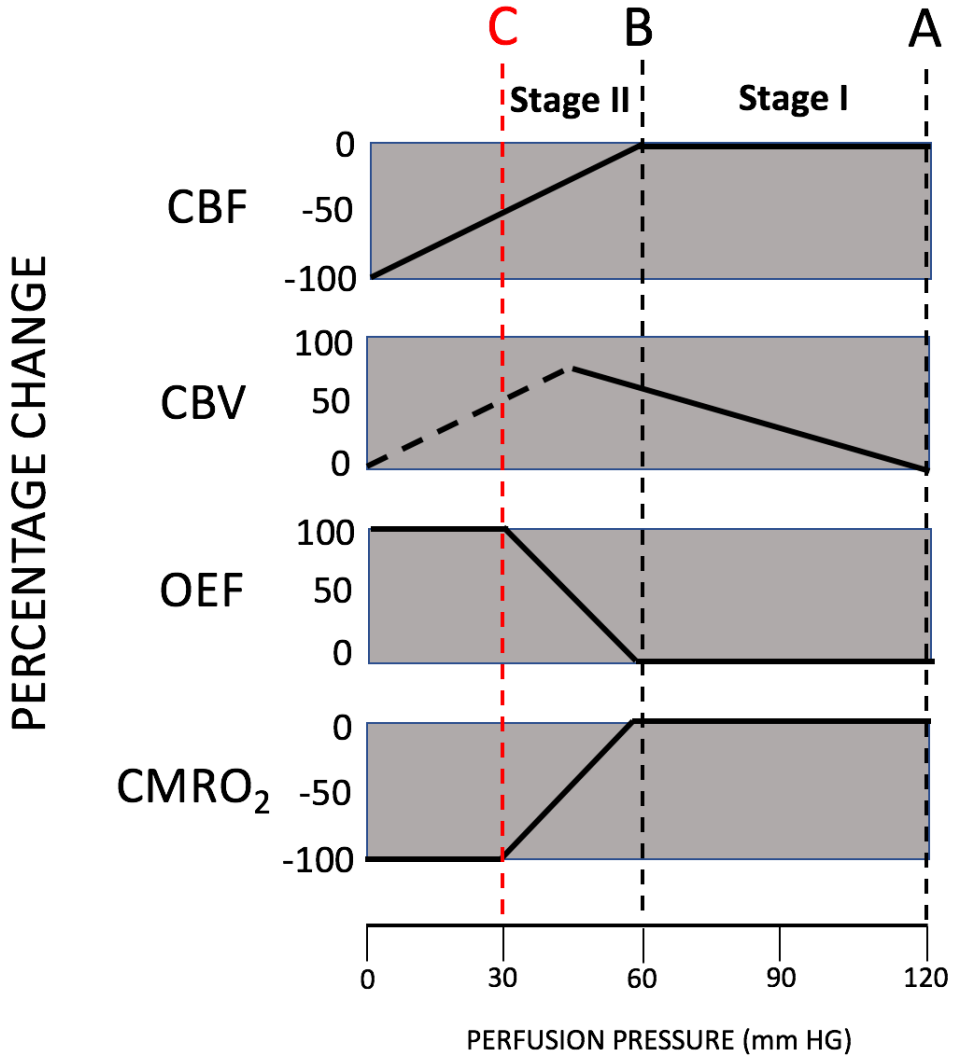

Figure 2-1. *Stages of chronic hemodynamic impairment. In **Stage I**, CPP falls and CBF is maintained by autoregulatory vasodilation (autoregulation occurs between points A and B). CBV increases. OEF and $CMRO_2$ are maintained. Of note, this original description of Stage I is a simplification; there is, in fact, mild decrease in CBF even in the autoregulatory range, therefore OEF starts to increase[11]. In **Stage II** (misery perfusion), autoregulatory capacity is exceeded, therefore CBF decreases with decreasing CPP. CBV initially increases but then may decrease as vessels collapse. OEF increases during this stage to maintain normal oxygen metabolism ($CMRO_2$). At point C, OEF is maximal. Any further decrease in CPP, and therefore CBF, causes ischaemia. Point C is therefore the **ischemic threshold** at which compensatory mechanisms to maintain normal oxygen metabolism are exhausted. This figure has been adapted from Powers[13].*

Experimental animal (including primate) models have demonstrated two different thresholds of CBF reduction for neuronal damage in acute focal ischaemia: penumbral and infarct[22-25]. The **infarct core** consists of tissue that is irreversibly damaged. It is surrounded by the ischemic **penumbra**, which consists of tissue that is severely hypoperfused and functionally impaired (with cessation of electrical activity) but is still viable[22]. The penumbra can regain its function if reperfused. Studies in humans and animals have shown that the infarct core enlarges and expands into the penumbra over time if blood flow is not restored[24, 26, 27]. Therefore, the penumbra represents viable tissue that is at-risk of infarction. In animals, the penumbral threshold, below which neurons become electrically silent due to ischaemia, is 22 mL/minute/100g tissue (40%) in monkeys[22]. Milder reduction of CBF is referred to as "benign oligaemia" since it does not place tissue at-risk of infarction. The CBF threshold for infarction, below which tissue is irreversibly damaged, depends on duration of ischaemia[28]. It is around 10 mL/minute/100g for 1-2 hours in the monkey[28].

Electroencephalographic changes have also been shown when blood flow falls below 20 mL/minute/100g tissue, indicating that this is the penumbral threshold[29]. Studies using O^{15}-PET have confirmed this; the CBF threshold for the penumbra, which is characterized by increased OEF and relatively preserved oxygen consumption ($CMRO_2$) on PET, was found to be 17-22 mL/minute/100g, while the infarct threshold was 7-8 mL/minute/100g in patients who were imaged 5-18 hours after stroke onset[28].

The dependence of the infarct threshold upon duration of ischaemia indicates that infarction is a product of both the severity and duration of CBF reduction[15, 24, 26, 28]. The evolution of penumbra into infarct core is therefore a dynamic process, where the rate of infarct growth is dependent on the severity of CBF reduction; this, in turn, is heavily influenced by the presence and robustness of collateral blood flow[30-34]. Autoregulation results in recruitment of the collateral circulation in an attempt to maintain CBF to downstream brain tissue when arterioles dilate[13, 31]. The collateral circulation varies considerably between individuals[13]. For example, there is up to 50% variation in the anatomy of the Circle of Willis, which is the main source of collateral blood flow in the brain (a complete Circle of Willis is illustrated is shown in Figure 2-2, with the frequency of some common variants indicated)[6, 32]. The internal carotid arteries receive some collateral blood flow from the external carotid artery via anterior and posterior ethmoidal artery-ophthalmic anastomoses [6]. Cortical-leptomeningeal anastomoses of distal branches of the anterior, middle and posterior cerebral arteries are inconstant and highly variable

[6]. Conversely, deep perforating branches of the internal carotid, anterior cerebral, middle cerebral and posterior cerebral arteries, that supply the corpus striatum, internal capsule and thalamus, are effectively end arteries with no/minimal collaterals[6]. Cortical-leptomeningeal anastomoses are the most important source of collateral blood flow in acute ischaemia due to occlusions at or distal to the terminal ICA. The large inter-individual variability in these leptomeningeal collaterals is thought to account for the variability in infarct progression[34].

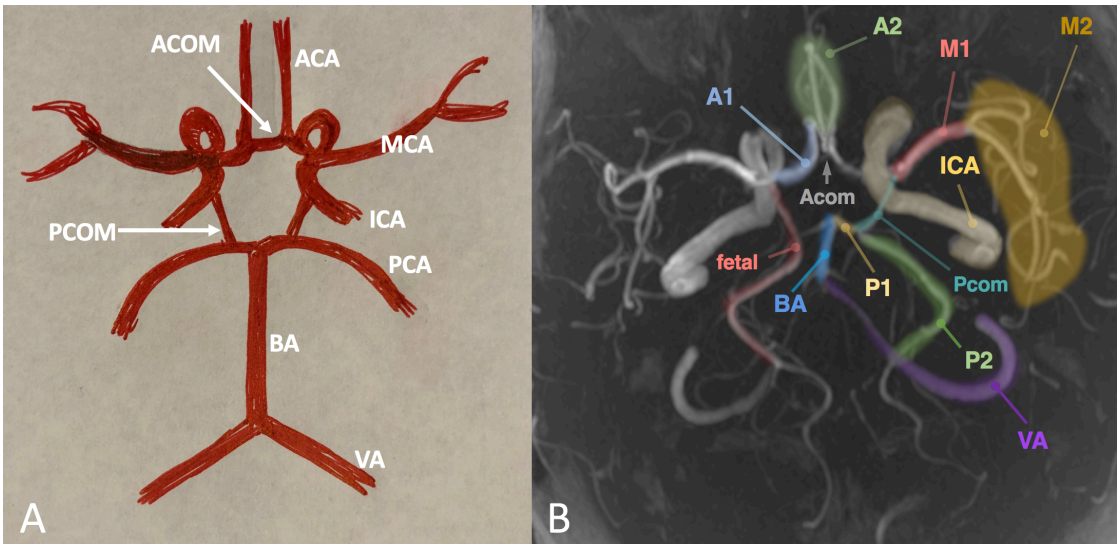

Figure 2-2. *Anatomy of the cerebral circulation.* ***A.*** *Schematic of a complete circle of Willis is shown.* ***ICA*** *= internal carotid artery,* ***MCA*** *= middle cerebral artery,* ***ACA*** *= anterior cerebral artery,* ***VA*** *= vertebral artery,* ***BA*** *= basilar artery,* ***PCA*** *= posterior cerebral artery,* ***PCOM*** *= posterior communicating artery; and* ***ACOM*** *= anterior communicating artery. The ACOM is absent in 5% of the population[35].* ***B.*** *Proximal segments of ACA (A1 and A2), MCA (M1 and M2) and PCA (P1 and P2) shown on an axial time-of-flight MRA maximum intensity projection. The PCOM is the same size or larger than the P1 segment of the PCA on one side in 20% of the population, and bilaterally in 8%. This is referred to as* ***foetal*** *origin of the PCA, because it indicates failure of the embryonic PCA (which originates from the ICA) to regress. The dominant blood supply to the occipital lobes is then from the ICA. The A1-segment of the ACA is absent in 1-2% of the population and hypoplastic in 10%[35]. A bihemispheric A2-segment with hypoplasia of the contralateral A2-segment is present in 2-7%[35]. The definition of the M1-segment of the MCA is variable, but the two main approaches are as follows[36]: functionally as the segment between the bifurcation of the ICA (origin) and the bifurcation/trifurcation of the MCA; or as the proximal horizontal segment of the MCA within the Sylvian cistern (original angiographic definition). The M2-segments can therefore be defined as either the first branches of the MCA, following bifurcation/trifurcation or the vertical segments of the vessel within the Sylvian fissure.*

Patients with good collaterals have slow infarct growth ("slow progressors") and a sustained ischemic penumbra, while those with poor collaterals have fast infarct

growth ("fast progressors") with rapid consumption of the ischemic penumbra[34]. On average, it is estimated that 1.9 million neurons per minute undergo irreversible damage in a typical stroke patient[37]. Acute ischemic stroke is therefore a time-critical emergency, captured by the mantra "*time is brain*".

2.1.1 Neuronal Changes in Ischaemia and Infarction

A cascade of biochemical changes occurs in neurons with ischaemia. In brief, decreased oxygen delivery results in decreased ATP generation, which in turn causes failure of the cell membrane sodium-potassium pump with resultant influx of sodium and water into the cell as well as glycogen loss and decreased protein synthesis[9]. If blood flow is restored, these changes are reversible. With persistent ischaemia, ATP depletion worsens, and acidosis and oxidative stress increase[38]. Release of the excitatory neurotransmitter glutamate from neurons results in neuronal overstimulation, in turn causing massive calcium influx into the cell through specific membrane channels[9]. The increase in intracellular calcium in turn activates intracellular enzyme cascades[38]. These changes, which occur within seconds to minutes of the onset of ischaemia, cause disruption of the cellular cytoskeleton with swelling of cellular organelles including the endoplastic reticulum and mitochondria[6]. Once severe morphological changes such as damage of the cell membrane, severe mitochondrial dilatation and lysosomal swelling develop, the changes are irreversible and cell death occurs[6].

2.1.2 The Blood-Brain Barrier

In addition to neurons, astrocytes (supporting cells of neurons) and the endothelial (lining) cells of the tissue capillaries in infarcted tissue are also damaged[38]. Endothelial cells swell within minutes to hours of the onset of ischaemia, causing the capillary diameter to shrink[38]. Release of enzymes causes degradation of the extracellular matrix[38]. These changes result in increased permeability of the *blood-brain barrier* (BBB) upon reperfusion (when blood flow is restored to the ischemic tissue). The BBB is a specialized diffusion barrier that is composed of the endothelial cells of brain capillaries, supporting cells and extracellular matrix[39]. The BBB, primarily the "tight junctions" between the endothelial cells, tightly regulates and restricts the passage of substances from the blood into brain[38].

Animal models have shown that increased permeability of the BBB may occur in three phases following reperfusion, that depend on the duration of ischaemia and

the degree of reperfusion[38] (Figure 2-3). When reperfusion occurs, reactive hyperaemia and loss of normal cerebral autoregulation due to ischaemia cause an acute increase in CBF. This in turn causes a passive increase in the permeability of the BBB[38]. Following this initial hyperaemia, hypoperfusion of the infarct occurs; referred to as the "no-reflow effect", this is likely mediated by factors including cellular swelling and capillary obstruction[38]. At approximately 3-8 hours following reperfusion, the next phase of increased BBB permeability occurs, and is thought to be mediated by oxidative and inflammatory stress and enzymatic degradation of the extracellular matrix of the BBB[38]. The final phase of increased permeability occurs approximately 18-96 hours following reperfusion, and is again though to be due to inflammatory processes as well as angiogenesis, where there is remodelling of endothelial cell tight junctions[38].

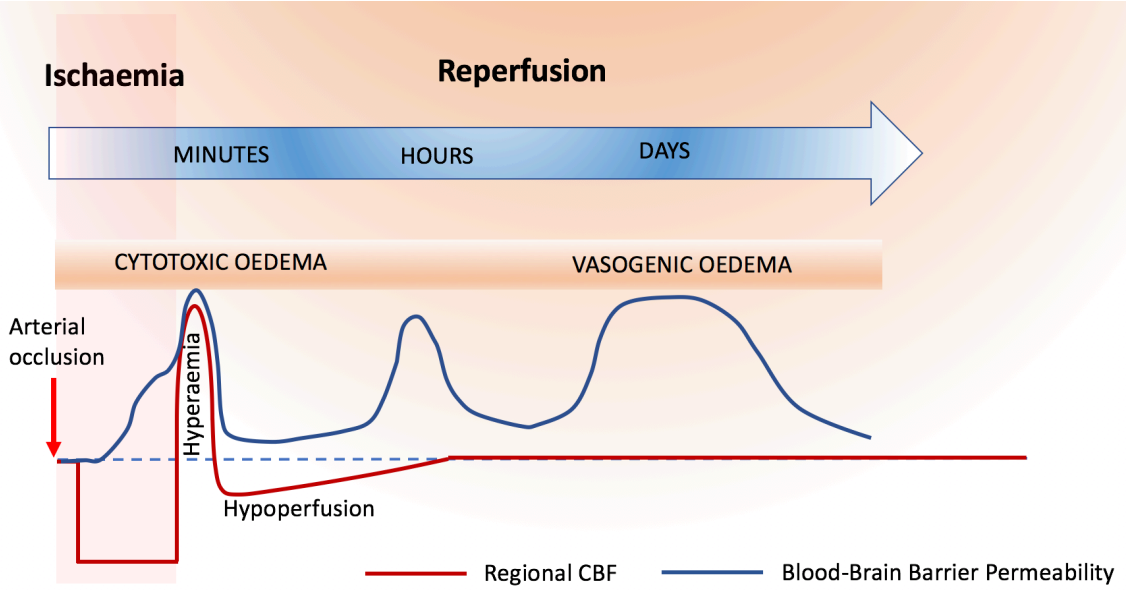

Figure 2-3. *Phasic changes in blood-brain barrier permeability with time from infarct onset. There is an initial increase in permeability when reperfusion occurs, due to hyperaemia. Permeability decreases during a period of hypoperfusion, then increases again at 3-8 hours due to oxidative stress and inflammation. The third phase of increased permeability is associated with the development of vasogenic oedema. This figure has been adapted from Sandoval and Witt[38].*

The increase in BBB permeability is thought to be the underlying cause of haemorrhagic transformation of infarcts[40, 41]. Haemorrhagic transformation refers to bleeding within the area of infarcted tissue; this is characterized by petechiae (1-2 mm bleeds) that can become confluent to form parenchymal hematomas with mass effect[6].

2.1.3 Vasogenic versus Cytotoxic Oedema

Increased BBB permeability to macromolecules also causes **vasogenic oedema**, where fluid moves from the intravascular to the extravascular space. Vasogenic oedema causes a net increase in tissue water and favours white matter. Depending on the severity of ischemia, this net increase in extracellular water can occur within the first 2 hours of infarction, but is relatively mild, becoming more pronounced after 3-4 hours of stroke onset[42]. In keeping with the timing of the third phase of increased BBB permeability, vasogenic oedema typically peaks at 2-5 days following infarction[38]. Vasogenic oedema causes decrease in T2 relaxation, therefore an increase in T2 signal, within affected tissue. It can be detected using T2-weighted MRI sequences[42].

The other type of oedema that occurs in cerebral infarction is **cytotoxic oedema**, which develops within minutes of infarct onset. It occurs due to movement of extracellular (interstitial) water into the intracellular compartment, which in turn is due to the influx of sodium into the cell that occurs with ATP depletion as discussed above[38]. It is also associated with swelling of intracellular organelles, which act as barriers to the diffusion of water; this restricted water diffusion is a widely used biomarker for detecting infarction on MRI that is discussed in section 2.4.3.

2.1.4 Aetiology of Ischemic Stroke

The majority of ischemic strokes are caused by occlusion or stenosis (narrowing) of an artery in the brain or neck that supplies brain tissue (the anatomy of the main cerebral arteries is illustrated in Figure 2-2)[2, 4]. It can also result from globally decreased cerebral perfusion pressure, for example due to severe systemic hypotension or cardiac arrest[5]. Ischemic stroke can, rarely, occur due venous outflow obstruction, which increases regional cerebrovascular resistance and impairs arterial inflow; more commonly, venous occlusion causes vasogenic oedema and haemorrhagic stroke secondary to the congestion[6, 9, 43].

Ischemic stroke is classified aetiologically according to the following mechanisms: embolism, in situ thrombosis and decreased perfusion[5]. Embolus may be of either cardiac or arterial origin, the latter referred to as arterio-arterial embolism[5]. Common causes of embolism from the heart are atrial fibrillation and other sinoatrial disorders, recent myocardial infarction and dilated cardiomyopathy,

which result in intra-cardiac thrombus formation[5]. Valvular heart disease, such as mitral valve prolapse, infective endocarditis and thrombus formation on mechanical heart valves due to inadequate anticoagulation are also commonly recognized sources cardiac embolus. *Patent foramen ovale* also requires consideration as a cardiac source of embolus (although the thrombus forms in the venous system and is shunted into the systemic arterial system via the foramen ovale)[44].

Arterio-arterial embolization of thrombus or cholesterol can occur from complicated atherosclerotic plaques of the aortic arch, extracranial (cervical) carotid arteries and major intracranial arteries[5, 45]. Extracranial carotid plaques and are a frequent cause of arterio-arterial embolic stroke. *Intracranial atherosclerotic disease* (ICAD) is now recognized as one of the commonest causes of ischemic stroke in African, Asian and Hispanic populations[45]. The most frequently affected sites are the M1-segment of the MCA, followed by the basilar artery, intracranial ICA and vertebral arteries[45, 46]. Arterio-arterial embolization typically causes a territorial pattern of infarction, distal to the diseased vessel and confined to its supply territory.

Extracranial carotid atherosclerotic plaques and ICAD can also cause infarcts via arterio-arterial embolism, as well as decreased perfusion when the degree of stenosis is severe[5, 45]. Infarcts secondary to hypoperfusion typically occur in the most distal part of the territory supplied by the vessel, referred to as the "border zone" or "watershed". The hemodynamic changes that occur in the setting of chronic hypoperfusion have already been discussed. The *North American Symptomatic Carotid Endarterectomy Trial* (NASCET) demonstrated that symptomatic patients with extracranial internal carotid artery stenosis of 70-99% benefit from surgery[47].

In-situ thrombosis of intracranial arteries can occur, leading to territorial or perforator territory infarcts. Causes include ICAD and pro-thrombotic states including malignancy and thrombophilias[5, 45]. Dissection and vasculitis are uncommon causes of stroke that can affect extracranial and intracranial arteries, resulting in severe vessel narrowing, in situ thrombosis and/or arterio-arterial embolism[5].

Lacunar infarcts (defined as small infarcts ≤1.5 cm typically involving deep perforating arteries) are classified separately and may occur due to hypoperfusion

due to pathological thickening of the wall of small perforator arteries secondary to chronic hypertension, in situ thrombosis or arterio-arterial embolism[5, 6, 45].

In the clinical setting, subtypes of ischemic stroke are commonly categorized based on aetiology using the TOAST (Trial of Org 10172 in Acute Stroke Treatment) classification system into: large artery atherosclerosis (embolic or due to thrombosis), cardioembolism, small-vessel occlusion (lacunar), stroke of other determine aetiology and stroke of undetermined aetiology[48].

2.2 Clinical Presentation of Acute Ischemic Stroke

Acute ischemic stroke is characterized by the sudden onset of neurological deficit, which can involve motor function, speech, attention, vision and cognition[49]. The specific signs and symptoms depend on the hemisphere and vascular territory involved and can therefore be used to clinically identify the brain region that is likely to be involved. Review of specific clinical stroke syndromes is beyond the scope of this literature review.

Neurological deficit in *acute ischemic stroke* (AIS) patients is quantified clinically pre and post treatment using a standardized stroke severity rating scale, most often the *National Institutes of Health Stroke Scale* (NIHSS)[50]. Here, a number of parameters including the patient's level of consciousness, visual fields, facial and limb motor function, and language are assessed[50]. The use of a standardized scale allows objective assessment and quantification of neurological disability. This, in turn, is important for communication, prognostication, decision making regarding treatment and monitoring of clinical status. Assessment using the NIHSS can be performed rapidly, accurately, and reliably by a broad spectrum of healthcare providers[51, 52]. Baseline and follow-up disability is assessed using the *modified Rankin scale* (mRS) score where 0 and 2 represent no and minimal neurological disability respectively[53]; in stroke trials, a favourable outcome is typically defined as a mRS score of 0-2 at 90 days.

2.3 Treatment of Acute Ischemic Stroke

The goal of treatment in acute ischemic stroke is to restore blood flow to the penumbra, and prevent further infarct growth, by recanalizing the occluded artery.

This is achieved by either dissolving or disrupting/removing the culprit thrombus, using intravenous thrombolytic drugs or direct intra-arterial treatment strategies.

2.3.1 Intravenous Thrombolysis

Intravenous thrombolysis (IVT) with the *recombinant tissue plasminogen activator* (rtPA) alteplase is the standard-of-care treatment for acute stroke patients presenting within 4.5 hours of symptom onset[50]. The American Stroke Association guidelines recommend that alteplase be given to patients presenting within 4.5 hours of symptom onset[50]. It is administered as an infusion over approximately 1 hour.

The *National Institute of Neurological Disorders* (NINDS) rtPA stroke study was the first randomized double-blind trial to evaluate IVT for the treatment of acute ischemic stroke[54]. This study enrolled ischemic stroke patients within 3 hours of onset. It was found that patients treated with rtPA were at least 30% more likely to have minimal or no disability (mRS 0-2) compared to patients given a placebo. The rate of symptomatic intracerebral haemorrhage (defined as severe haemorrhage with mass effect) was 6.4% in the treatment group compared to 0.6% in the placebo group. Three subsequent large trials – the *Alteplase Thrombolysis for Acute Noninterventional Therapy in Ischemic Stroke* (ATLANTIS) study, the *European Cooperative Acute Stroke Study* (ECASS) and ECASS II – failed to demonstrate a clear benefit of rtPA[55-58]. Additionally, high rates of symptomatic intracerebral haemorrhage were observed, for example 11.1 % and 6.5% respectively in the rtPA group and placebo groups in ECASS. These studies enrolled patients up to 6 hours post stroke onset. Sub-analysis of the cohort of patients who were enrolled in the ATLANTIS trial within 3 hours of stroke onset did, however, show benefit[59]. Subsequently, pooled analysis of multiple randomized controlled trials has shown the safety and efficacy of IVT in the first 3 hours after stroke onset[60-62]. Of note, however, the rate of symptomatic intracerebral haemorrhage was 4.8% in patients treated with rtPA in this time window[60].

Published in 2008, approximately a decade after ECASS II, ECASS III evaluated the efficacy of intravenous alteplase versus placebo in the 3 to 4.5 hour window following stroke symptom onset[63]. This time, more patients had a favourable outcome (90 day mRS 0-2) with alteplase than with placebo (52% versus 45%). The rate of symptomatic intracranial haemorrhage was significantly higher with alteplase than placebo (2.4% versus 0.2%), but lower than in previous trials. The

findings of this study and pooled analysis of other studies, therefore, support the use of IVT up to 4.5 hours[50].

Since most stroke patients present outside this narrow treatment window, fewer than 5% of receive IVT[64, 65]. Even when administered in a timely fashion, IVT is often ineffective at recanalizing the occluded artery, particularly in long segment and large vessel occlusions[66, 67]. Successful recanalization is achieved in only 10-15% of internal carotid artery (ICA) occlusions and 25-50% of middle cerebral artery M1 segment occlusions, while IVT is ineffective for clots greater than 8 mm in length[66, 68]. Therefore, only about 25% of AIS patients appear to benefit from IVT[69]. IVT also carries a risk of symptomatic intracranial haemorrhage, which has high morbidity and mortality[63, 70].

2.3.2 Endovascular Therapy

New treatment strategies were therefore sought, in particular for treatment of proximal cerebral artery occlusions involving the intracranial internal carotid artery (ICA), M1-segment of the *middle cerebral artery* (MCA) and the basilar artery, collectively referred to as *large vessel occlusions* (LVOs). While LVOs cause just over a third of acute ischemic strokes, they are responsible for over 90% of mortalities and are associated with severe neurological disability in survivors[71]. Given this significant morbidity and mortality if left untreated, and the poor efficacy of IVT, there was a profound unmet clinical need for a safe and effective treatment strategy.

Endovascular therapy refers to a minimally invasive technique where catheters are used to access the lumen of the occluded artery via a remote site (femoral artery), and either deliver a thrombolytic agent or disrupt the clot (Figure 2-4). Endovascular therapy is an established treatment for basilar thrombosis in clinical practice although there are no randomized controlled trials to date showing its benefit. Studies in the early 1980s described direct intra-arterial delivery of thrombolytic agents using co-axial catheter systems for treatment of vertebral and basilar artery thromboembolic disease[72, 73]. The first study that showed a positive outcome with endovascular therapy in anterior circulation AIS patients was the *Prolyse in Acute Cerebral Thromboembolism* (PROACT) II trial, published in 1999[74]. In this randomized controlled trial, the efficacy of intra-arterial recombinant prourokinase was assessed[74]. Treatment was initiated within 6 hours of stroke onset, and enrolled patients were required to have M1- or M2-segment

MCA occlusion demonstrated on catheter-based cerebral angiography to qualify[74]. The recanalization rate of 66% in the treatment group was significantly higher ($P < 0.001$) than the 18% in the control group. The rate of early symptomatic intracranial haemorrhage was higher, but clinical outcomes were significantly improved as defined by a *modified Rankin score* (mRS) of ≤2 (slight or no neurological disability).

Endovascular devices that could mechanically disrupt or retrieve the thrombus were subsequently developed, with the aim of improving recanalization success and safety. Collectively, these are referred to mechanical thrombectomy devices. The first mechanical thrombectomy device to receive regulatory approval for intracranial use, in 2005, was the MERCI retrieval system (Concentric Medical, Mountain View, California)[75]. This device consisted of a flexible *nitinol* (nickel-titanium alloy) wire delivered using a co-axial micro-catheter system that adopts a corkscrew shape once passed through the catheter tip, in turn used to capture the clot. Recanalization rates of up to 69.5% were achieved with improvements in this device[76]. An early study of 20 patients treated with a subsequent first generation thrombectomy device, the PENUMBRA system (Penumbra, Alameda, California), demonstrated a 100% recanalization rate[77]. PENUMBRA was designed to directly remove thrombus in large intracranial arteries using suction (aspiration) initially, followed by extraction if this failed[77]. Unfortunately, subsequent trials undertaken with the first generation thrombectomy devices and intra-arterial thrombolysis did not show clinical benefit; while recanalization rates (a biomarker of treatment success) of up to 81.6% were achieved, outcomes were poor with overall mortality ranging from 25% to 33%[78-80].

Further analysis revealed that the outcomes of these trials were biased against endovascular therapy due to inclusion of patients without an occluded intracranial artery and those with completed infarcts in whom treatment was likely to be futile[81, 82]. In a sub-study that evaluated outcomes and recanalization in the cohort of patients enrolled in the Interventional Management of Stroke (IMS) III study, a trend favouring endovascular therapy over standard medical management was seen in patients with proximal arterial occlusions, involving the ICA terminus, M1-segment MCA or A1-segment anterior cerebral artery (ACA)[81]. Likewise, in a study that evaluated non-contrast CT findings versus outcome in a cohort of 249 patients who were enrolled in the trials that used the PENUMBRA system, a higher percentage of patients in the group with no/little changes of infarction were found to have a good outcome compared to the group with large established infarcts, with lower mortality[82]. These findings suggested that further trials were

required that: mandated vascular imaging, to prove the presence of a target LVO; and excluded patients with large established infarcts (involving more than a third of the MCA territory) in whom treatment was likely futile and increased the risk of symptomatic intracranial haemorrhage.

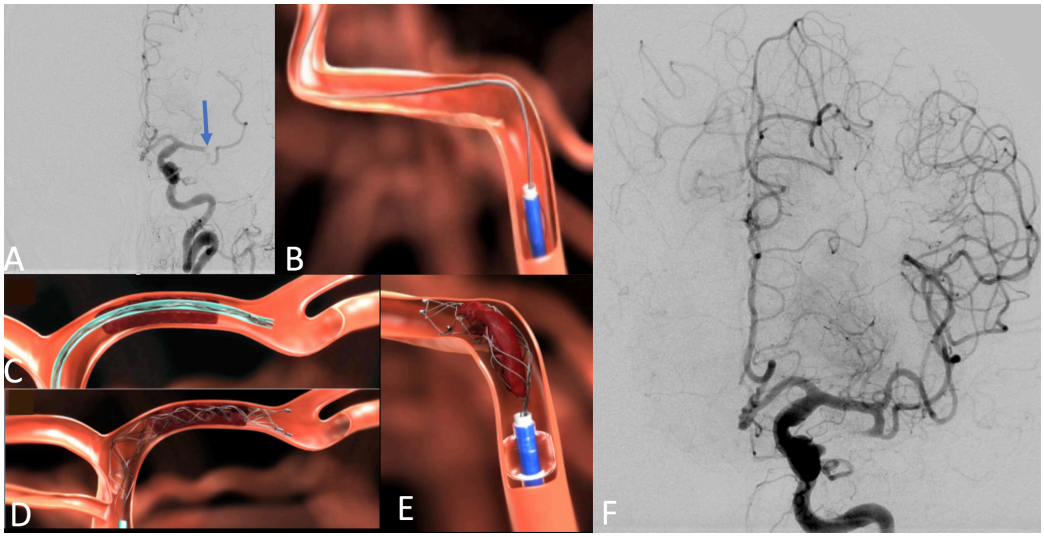

Figure 2-4. *Mechanical thrombectomy using the Solitaire stent-retriever system in a 91 year-old woman who presented with sudden onset right hemiplegia and aphasia.* ***A.*** *Baseline DSA showing occlusion of the distal M1 segment of the left MCA (arrow).* ***B.*** *The microcatheter (blue) is advanced over a guidewire through the occlusion and* ***C.*** *positioned distal to it. The guidewire is retrieved.* ***D.*** *The stent-retriever is unsheathed and expands within the vessel, restoring blood flow.* ***E.*** *the balloon of the device is then inflated. The thrombus ensnared in the stent-retriever is gently retrieved by removing the stent-retriever through the balloon catheter.* ***F.*** *Final DSA image showing complete recanalization of the MCA (TICI grade 3 flow).*

A number of trials were subsequently performed in patients with anterior circulation LVOs, involving the intracranial ICA and/or the M1- or proximal M2-segment of the MCA[83-89]. These trials used self-expanding stent-retriever devices, which had been shown to be superior to the first MERCI device[90, 91]. Recanalization rates of 94% and 92%, respectively, were achieved with the Solitaire (Covidien, Plymouth, Minnesota) and TREVO (Concentric Medical, Mountain View, California) devices, compared to 67% and 77% with the MERCI device in these studies[90, 91]. These devices apply radial force in the centre of the clot and along its length in order to displace the thrombus away from the vessel wall so that it can be incorporated into the struts of the stent (Figure 2-4). This results in immediate restoration of blood flow.

The results of five high-profile trials using these devices were published in 2015:

Endovascular Treatment for Acute Ischemic Stroke in the Netherlands (MR CLEAN); *Endovascular Treatment for Small Core and Anterior Circulation Proximal Occlusion with Emphasis on Minimizing CT to Recanalization Times* (ESCAPE); *Extending the Time for Thrombolysis in Emergency Neurological Deficits - Intra-Arterial* (EXTEND-IA); *Solitaire with the Intention for Thrombectomy as Primary Endovascular Treatment* (SWIFT-PRIME); and the *Randomized Trial of Revascularization with Solitaire FR Device versus Best Medical Therapy in the Treatment of Acute Stroke Due to Anterior Circulation Large Vessel Occlusion Presenting within Eight Hours of Symptom Onset* (REVASCAT)[84-87, 89]. These trials demonstrated that mechanical thrombectomy is safe and effective, decreasing the final infarct volume, and improving functional outcomes in patients with proximal anterior circulation arterial occlusions[84-87, 89]. Patients had significantly less neurological disability when treated with thrombectomy than standard medical management. The key to the success of these trials was careful patient selection using clinical and imaging criteria, including time since stroke onset and proof of an anterior circulation LVO on vascular imaging (mostly CTA). Three of these trials required endovascular therapy to be commenced within 6 hours after stroke onset[84, 85, 89], while the longest treatment window was up to 12 hours of stroke onset[86]. The publication of these trials brought about a paradigm shift in AIS management. Pooled analysis showed the efficacy of endovascular thrombectomy over standard medical management in AIS patients with anterior circulation LVOs[92]. As a consequence, guidelines were altered to recommend endovascular therapy with a stent-retriever in AIS patients aged 18 or older with good baseline neurological function, a causative ICA or M1 segment MCA occlusion, NIHSS score of $\geq$6 and no large established infarct on non-enhanced CT, where treatment could be initiated within 6 hours of onset[93].

Two late window trials were subsequently undertaken to determine whether endovascular thrombectomy can be safely performed in an extended treatment window, and published in 2018[83, 88]. The *DWI or CTP Assessment with Clinical Mismatch in the Triage of Wake-Up and Late Presenting Strokes Undergoing Neurointenvention with Trevo* (DAWN) trial showed benefit of thrombectomy up to 24 hours of symptom onset in patients whose clinical deficit was disproportionately severe in comparison with the size of the infarct core, suggesting viable penumbral tissue[88]. The subsequent *Endovascular Therapy Following Imaging Evaluation for Ischemic Stroke* (DEFUSE 3) trial showed that thrombectomy, in addition to standard medical management, resulted in better functional outcomes than standard medical management alone in patients treated 6 to 16 hours after they were last known to be well[83]. Both trials enrolled only

patients with ICA or proximal MCA occlusions. In DAWN, an infarct volume of ≤50 mL was required for enrolment, measured using either diffusion weighted imaging (DWI) or CT perfusion (CTP)[88]. In DEFUSE 3, enrolled patients were required to have an infarct volume less than 70 mL as well as at least 15 mL of salvageable, at-risk brain tissue (i.e. ischemic penumbra) and a ratio of at-risk to infarcted tissue of at least 1.8[83]. The infarct core and at-risk tissue were measured using either CTP or MRI with both DWI and *perfusion weighted imaging* (PWI)[83]. Given the strict selection criteria, the findings of these studies are applicable to patients with proximal anterior circulation occlusions who have salvageable brain tissue and no large established infarct.

In both late window studies, the rate of functional independence at 90 days was assessed using the modified Rankin scale (a score of 0,1 or 2 indicated functional independence), and this served as the primary end point. Mortality at 90 days and the frequency of symptomatic intracranial haemorrhage were also assessed. In DEFUSE 3, functional independence was achieved in 45% of patients in the endovascular therapy arm, and 17% in the medical management arm which was significantly ($P < 0.001$) lower. Mortality was also lower in the endovascular therapy group (14% versus 26%, $P = 0.05$). In DAWN, the rate of functional independence in the thrombectomy arm was significantly higher at 49%, compared to 13% in the standard medical management arm, with no significant difference between the groups in 90-day mortality[88]. In both trials, there was no significant difference in the frequency of symptomatic intracranial haemorrhage.

The absolute increase in functional independence of 36% with thrombectomy in DAWN is the largest ever reported in an acute stroke treatment trial. This compares with a 19.5% absolute increase in functional independence and 11% reduction in severe disability/mortality in the early window trials on pooled analysis[92]. Therefore, the number of patients who needed to be treated in order to the endpoint of functional independence (3 for DAWN and 4 for DEFUSE 3) was even less than in the early window (<6 hrs of stroke onset) trials. These studies therefore established that endovascular thrombectomy can be safely performed in selected patients up to 24 hours following symptom onset or last seen well in [83, 88]. One explanation that has been put forward to explain the larger treatment benefit in the late-window than in the early window is the "late window paradox"[30]. This theory is based on the strict imaging-based selection criteria used in the late time window trials and our current understanding of the role of collaterals in infarct evolution. As discussed above, the rate of expansion of the infarct core into the ischemic penumbra is dependent upon the status of the individual patient's

collateral blood flow. Patients with large infarct cores were excluded from the late window trials. This, in turn, biased selection in favour of patients with good collaterals and a stable penumbra, who in turn have slower infarct progression and better outcomes. Conversely, patients with poor collaterals, whose infarcts rapidly grow to become large within 2 to 3 hours, were excluded.

In aggregate, the early window and late window trials have provided level 1A evidence for mechanical thrombectomy in selected AIS patients up to 16 hrs and IIa evidence up to 24 hours[50]. Thrombectomy is therefore now the standard-of-care treatment for stroke patients with anterior circulation LVOs up to 6 hours and can be performed in carefully selected patients up to 24 hours following symptom onset[50]. The criteria for patient eligibility as set out by guidelines differ between the early window (< 6 hrs since symptom onset or last seen well) and the late window (6-24 hrs since onset or last seen well) [94]. The major point of distinction is that the guidelines explicitly recommend adherence to the DEFUSE 3 or DAWN selection criteria and therefore avoidance of thrombectomy in patients with large infarcts in the late window.

There is, however, a push to treat patients with large infarct cores, especially if there is still eloquent salvageable brain tissue that is at risk of infarction. In a recent study in patients with large infarct cores, functional independence was achieved in 31% of patients treated with mechanical thrombectomy compared with 14% treated with standard medical management alone, indicating potential benefit[95]. Mechanical thrombectomy was found to be associated with better functional outcomes and less infarct growth. However, the odds of a good outcome with thrombectomy decreased markedly with increasing infarct core volume; there was a 42% reduction in the odds of functional independence for every 10 mL increase in infarct volume; and none of the 10 patients who had an infarct volume exceeding 100 mL had a favourable outcome. Therefore, further work including randomized prospective evaluation is required to determine the benefit of thrombectomy in patients with large infarct cores.

There are no published randomized controlled trials to date on thrombectomy for acute basilar artery occlusion. Early studies of direct intra-arterial thrombolysis were performed in patients with vertebral and basilar artery thromboembolic disease[72, 73]. Basilar artery occlusion is associated with poor outcomes and higher mortality than anterior circulation stroke[96]. The high likelihood of death or severe disability (with patients being “locked-in”) without treatment justified invasive treatment to achieve rapid reperfusion. Endovascular therapy has therefore long

been established for treating basilar thrombosis, initially with direct intra-arterial thrombolysis and subsequently with mechanical thrombectomy when these devices became available. Thrombectomy is now considered standard-of-care for eligible patients with acute basilar occlusion in clinical practice, up to 24 hours of onset at my center[97]. A recent multicentre retrospective observational study of 212 patients showed that mechanical thrombectomy using current generation devices is safe and effective for treating acute basilar occlusion[98]. A randomized trial is difficult to perform due to the low prevalence of this condition. It is also difficult to ethically justify given the availability of an established treatment that has been found to be effective in clinical practice and the poor outcome without treatment.

Another area where the benefit of thrombectomy beyond the initial trial criteria has been explored is the treatment of patients with *distal vessel occlusion* (DVO) - involving the M2- or M3-segments of the MCA, the *anterior cerebral artery* (ACA) and the *posterior cerebral artery* (PCA). Guidelines recommend that endovascular therapy can be performed in carefully selected patients in this group[50]. There is evidence of improved functional outcomes with thrombectomy compared to standard medical management in patients with M2-segment MCA occlusions[99]. Thrombectomy has also been shown to be safe and technically feasible for occlusions distal to the M2 segment and within the ACA and PCA [100]. It may therefore be justified in order to rapidly restore blood flow in patients with occlusion of these vessels who have severe neurological deficits and ischaemia of eloquent brain regions. Further, for patients with DVOs who are ineligible for intravenous thrombolysis (e.g., due to presentation beyond the 4.5-hour window), endovascular therapy may be the only available reperfusion therapy, justifying its use when there is still salvageable brain tissue.

2.3.2.1 Assessment of Recanalization with Endovascular Therapy

Biomarkers of treatment success that have been used in studies include functional outcome (measured using the mRS), final infarct volume, and recanalization rate. The use of recanalization rate as an endpoint is based on the premise that reopening the occluded vessel improves outcome in AIS patients[101]. An objective scale is therefore required to assess the degree of recanalization. In both trials and clinical practice, the modified *thrombolysis in cerebral infarction* (TICI) scale is used to angiographically assess recanalization. This is shown in Table 2-1.

Successful recanalization in trials was defined as TICI grade 2b or 3 recanalization,

which was achieved in 59%, 72%, 86%, 88% and 66% of patients, respectively, in the MR-CLEAN, ESCAPE, EXTEND-IA, SWIFT-PRIME and REVASCAT trials[84-87, 89].

Table 2-1. *Thrombolysis in Cerebral Infarction Scale* [102]

TICI grade	Angiographic definition	Status of target artery
0	No perfusion, vessel remains occluded with no flow distal to it	No recanalization of occluded artery
1	Antegrade blood flow distal to the occlusion however with limited filling of distal branches and slow distal perfusion	Partial recanalization of occluded artery
2a	Antegrade flow distal to the occluded artery with perfusion of less than half of the ischemic territory supplied by the occluded artery	
2b	Antegrade flow distal to the occluded artery with perfusion of more than half of the ischemic territory supplied by the occluded artery	Complete recanalization of the occluded artery with distal flow
3	Complete antegrade perfusion of the occluded artery with flow in all branches	

2.3.3 New Direction in Intravenous Therapy

Following the success of the late window trials, extending the window for intravenous thrombolysis has been revisited, applying the same principles of imaging-based patient selection as in the late window trials[103]. Either CTP or MRI with diffusion- and perfusion-weighted imaging were used to classify brain tissue as infarcted or critically hypoperfused but viable (hence salvageable with reperfusion but at risk of infarction in the absence of reperfusion)[103]. Patients with viable tissue presenting within 4.5 to 9 hours of stroke symptom onset, as well as those with a "wake up stroke" (who have a neurological deficit on waking from sleep) presenting within 9 hours of the midpoint of sleep, were included in this trial. The study authors concluded that IVT compared to placebo resulted in a higher percentage of patients with either no or only mild neurological deficit. A significantly higher rate of symptomatic haemorrhagic transformation (7 patients, 6.2%, versus 1 patient, 0.9%) was observed however[103].

A further new development in IVT is the use of a new thrombolytic agent, tenecteplase[104, 105]. Tenecteplase, a genetically modified variant of rtPA, is a more fibrin-specific agent that also has a longer half-life[106]. It can therefore be given as a bolus rather than infusion. A recent trial compared tenecteplase against rtPA administered within 4.5 hours after symptom onset in a cohort of AIS patients who subsequently underwent thrombectomy for occlusion of the ICA, MCA or basilar artery[104]. Tenecteplase was found to be associated with a higher incidence of reperfusion (22%) than rtPA (10%); reperfusion was defined as restored blood flow to greater than 50% of the involved vascular territory or no retrievable thrombus in the target vessel on angiographic assessment at the start of the thrombectomy procedure. Functional outcome was also better with tenecteplase, with a median mRS score of 2 compared to 3 for rtPA. There was no difference in the rate of symptomatic intracerebral haemorrhage.

2.4 Imaging of AIS

Imaging plays an important role in the diagnosis and management of AIS patients. Its primary purpose, historically, has been to exclude acute haemorrhage, which contraindicates thrombolytic therapies[50]. *Non-enhanced CT* (NECT) is recommended in all patients admitted to hospital with a suspected acute ischemic stroke to exclude hemorrhage[50]. MRI is more sensitive for detection haemorrhage as well as acute infarction[107-109]. However, CT is easier to access in the emergent setting and does not require cumbersome safety screening, which may be difficult in confused or obtunded AIS patients. NECT has also been shown to be cost effective for screening of AIS patients[110]. Therefore, most centres in Australia and North America use CT as the first line imaging modality in AIS, although MRI is more widely used in Europe and Asia.[111]

The paradigm shift in the treatment of AIS that has occurred over the past decade (detailed above) has brought about an increased reliance on imaging to identify the right patients for therapy. We are increasingly moving away from a time-based approach towards a tissue-based paradigm for patient selection. Imaging plays an integral role in this, beyond just haemorrhage screening. In patients being considered for thrombectomy, non-invasive vascular imaging is mandatory to identify the presence and site of an arterial occlusion (the target for reperfusion therapies), as well as the endovascular accessibility of this occlusion[50]. In addition, imaging can also be used to:

1. Detect the presence and quantify the volume of the infarct core of irreversibly injured tissue, which cannot be salvaged with reperfusion;
2. Delineate the penumbra of critically hypoperfused, ischemic but viable tissue that can be salvaged;
3. Assess the robustness of collateral blood flow, which sustains the ischemic penumbra; and
4. Predict the risk of complication, in particular haemorrhage.

These factors determine the likelihood of benefit from reperfusion and the risk of complication and can therefore be used to determine whether treatment is warranted and safe. Each of these will be addressed in detail in the subsections to follow. Briefly, the likelihood of benefit from thrombectomy (or any reperfusion therapy) is related to the presence of salvageable ischemic brain tissue (the ischemic penumbra), while the risk of complication increases with the volume of infarcted brain tissue[112, 113]. Previous MRI-based studies had shown that patients with relatively small regions of infarction and much larger areas of ischemic penumbra are most likely to benefit from reperfusion therapy[27, 114]. Conversely, patients with large established infarct cores (larger than 50-70 mL) are unlikely to benefit and are also at increased risk of complication such as haemorrhagic transformation[27, 112, 113, 115].

Delineation of the size of the infarct core and ischemic penumbra is not mandated by guidelines in the early window (<6 hours from stroke onset)[50]. However, many stroke centres in North America, continental Europe and Australia use either CTP or MRI with DWI and *perfusion-weighted imaging* (PWI) even in the early window to assess for the presence of a large infarct core and an ischemic penumbra, particularly in patients who are eligible for thrombectomy on clinical assessment[50, 111]. This is justified by the finding that the magnitude of benefit was greater in both the thrombectomy and standard medical management arms (Figure 2-5) in the two early window trials that selected patients for enrolment based on perfusion imaging, compared to the three studies that did not[84-87, 89]. In these trials, CTP was used to identify patients with critically hypoperfused but salvageable brain tissue and exclude patients with large completed infarcts[85, 89]. This "penumbral selection" strategy was aimed at ensuring that only patients with viable tissue that could be salvaged by reperfusion were enrolled, while patients with large infarcts in whom treatment was likely to be futile or potentially harmful were excluded. These patients were then randomly assigned to either thrombectomy or standard medical management. The benefit of thrombectomy

was therefore shown in patients with an ischemic penumbra.

In a meta-analysis of the pooled patient-level data from all randomized controlled trials that compared mechanical thrombectomy with standard medical management in patients with anterior circulation ischemic stroke, increasing infarct core volume (measured either using CTP or MRI, which will be explained in section 2.4.3) was associated with a reduced likelihood of functional independence[116]. There was a decrease in odds ratio of 0.77 on CTP and 0.87 on MRI per 10 mL. It is noted that the presence of a large infarct core does not, however, always dissuade treatment in clinical practice, especially in young patients and those with penumbra involving eloquent areas of brain.

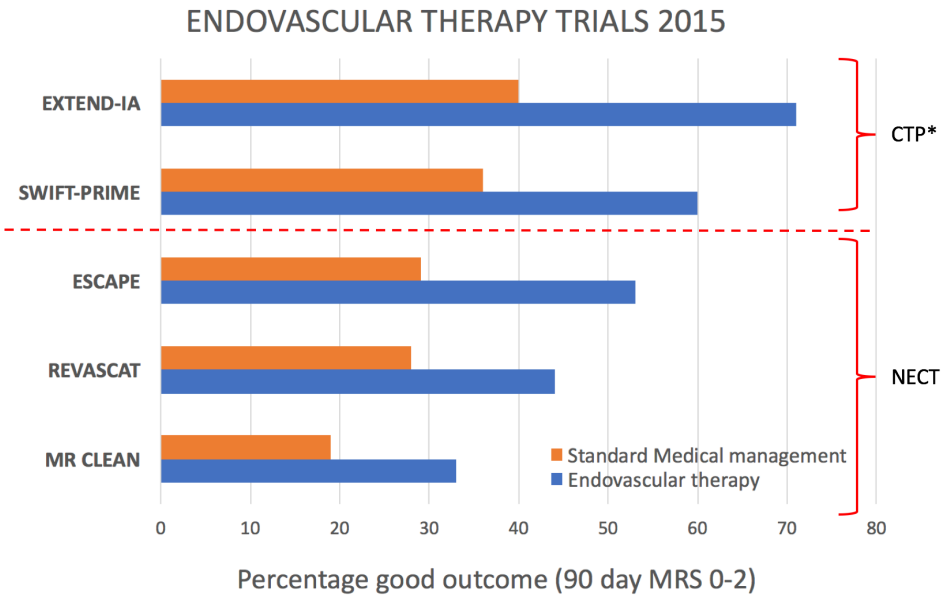

Figure 2-5. *The five early window thrombectomy trials. EXTEND-IA and SWIFT-PRIME (for part of the trial) used CTP-based to select patients who had salvageable penumbra tissue and no large infarct core. The magnitude of benefit with treatment in both the endovascular therapy (thrombectomy) arm and the standard medical management arm was greater in these two trials than in the three trials that did not use perfusion-based patient selection. The infarct core was assessed on NECT in ESCAPE, REVASCAT and MR CLEAN, while the CTA collateral score was used in ESCAPE for penumbral estimation.*

**MRI with DWI and PWI was used instead of CTP for triage in a small number of patients in SWIFT-PRIME*

In the late time-window (6-24 hours), guidelines mandate that either the DAWN or DEFUSE 3 criteria be followed[50]. Patients must therefore undergo emergent DWI or CTP prior to thrombectomy to exclude a large infarct core. In addition,

the DEFUSE 3 criteria necessitate either CTP or DSC-PWI to confirm the presence of salvageable brain tissue that justifies treatment[50]. There is also a move towards using advanced imaging to identify salvageable brain tissue and guide thrombolysis decisions beyond the 4.5-hour window[103]. Therefore, perfusion imaging is being used increasingly to identify patients who are likely to benefit from treatment, especially in extended time windows.

Since acute stroke is a critical emergency, and the benefit of reperfusion is time dependent (with greater proportional benefits seen with earlier treatment), an important caveat when using imaging to select patients for treatment is that it must not cause delay. Therefore, imaging must be performed only as necessary, as rapidly as possible, and interpreted emergently[37, 117]. By helping select the right patients for treatment, perfusion imaging may also expedite treatment and improve workflow. Guidelines recommend that endovascular therapy only be performed at stroke centres with the adequate stroke care infrastructure and expertise, including qualified neurointerventionalists, and an appropriately trained and staffed peri-procedural care team[50]. This has important implications, especially for countries such as Australia with geographically dispersed populations served by many smaller peripheral and regional hospitals that do not have the capability to provide endovascular therapy. Hub-and-spoke models of care, where patients presenting to smaller hospitals can be efficiently transferred to a high-level stroke centre if meeting treatment criteria, had already been developed for thrombolysis and are now being leveraged to improve patient access to thrombectomy[118, 119]. The success of such models is reliant not only on good clinical triage but increasingly on the use of perfusion imaging at regional/peripheral spoke sites to determine which patients are likely to benefit from treatment and should therefore be transferred.

2.4.1 Haemorrhage Exclusion and Prediction

AIS cannot be reliably distinguished from haemorrhagic stroke clinically, on history an examination alone[5]. While the treatment of AIS involves thrombolytic therapies, these agents are contraindicated in intracranial haemorrhage. Exclusion of acute haemorrhage is therefore imperative in AIS patients prior to administering any thrombolytic agents. This is achieved with NECT. If MRI is used as the first-line imaging modality, a sequence that is T_2*-weighted and therefore sensitive to local magnetic field inhomogeneity, such as *T_2*-weighted gradient recalled imaging* (T2*GRE) or *Susceptibility-Weighted Imaging* (SWI), is used for haemorrhage screening[107]. MRI is more sensitive for detection of haemorrhage than

CT[107, 108]. However, as noted above, CT is easier to access and cost effective for haemorrhage screening in AIS patients[110]. Also, while MRI allows detection of chronic microbleeds, these are not a contraindication to thrombolytics[120].

Intracranial haemorrhage can occur due to ischaemic stroke *per se* or as a complication of reperfusion therapies[121]. As discussed in section 2.1.2, ischaemia-induced damage of the vascular endothelium results in increased permeability of the BBB, which can cause of haemorrhagic transformation[40, 41]. This occurs within 2 weeks of ischemic stroke[122]. Conversely, intracranial haemorrhage that occurs within 24 hours of treatment is more likely to be due to reperfusion therapy, given the short half-life of rtPA and the almost immediate reperfusion associated with thrombectomy[121]. Haemorrhage complicating treatment can occur either within or outside the area of infarction; the latter can be parenchymal (remote from the infarct), intraventricular, subarachnoid or subdural[121]. It can be classified anatomically on imaging according to a modification of the ECASS criteria (Table 2-2)[57, 121].

Table 2-2. *Classification of intracerebral haemorrhage in stroke patients after treatment. This table has been modified from von Kummer et al, which in turn incorporates a modification of the original ECASS classification[57, 121].*

Classification	Haemorrhage type
1	**Haemorrhagic transformation of infarct***
	a *Haemorrhagic infarction type 1* (**HI1**): scattered petechiae without mass effect
	b *Haemorrhagic infarction type 2* (**HI2**): confluent petechiae without mass effect
	c *Parenchymal Haemorrhage type 1* (**PH1**): confluent hematoma that occupies < 30%
2	**Parenchymal haemorrhage within infarct extending beyond it** *Parenchymal hematoma type 2* (**PH2**): haemorrhage that occupies at least 30% of the infarcted tissue and may extend beyond its margins; has clear mass effect
3	**Haemorrhage outside infarcted brain tissue:** Parenchymal, remote from infarct (a); intraventricular (b); subarachnoid haemorrhage (c), subdural (d)

*Haemorrhage is confined to the area of infarction

Haemorrhagic transformation that is confined to the infarct and exerts no substantial mass effect is distinguished from parenchymal hematoma which

occupies at least 30% of the infarcted tissue, causes clear mass effect and may extend beyond the margins of the infarct. This distinction is important since only larger haemorrhages and hematoma remote from the infarct are associated with early deterioration and poor outcome[123, 124]. The relevance and prognostic implications of haemorrhage identified on imaging depend upon whether or not it causes neurological deterioration and is therefore "symptomatic". *Symptomatic intracranial haemorrhage* (SIH) is an important safety endpoint in trials that have assessed reperfusion therapies, however its exact definition has varied. It has been proposed that SIH be defined as any new intracranial haemorrhage detected on brain imaging associated with significant clinical deterioration, as evidenced by a decrease of ≥4 NIHSS points (or ≥2 points in one NIHSS category) and for which there is no alternative explanation[121]. NECT is routinely performed at baseline and within 48 hours of treatment to assess for haemorrhage. It is also performed if there is clinical deterioration ≥4 NIHSS points or symptoms that could indicate haemorrhage (e.g., headache or nausea).

Several clinical and imaging-based risk factors for SIH have been identified, including concurrent anticoagulation, stroke severity, advanced patient age, and extensive early changes on non-enhanced CT[112, 125]. Regional markedly reduced CBV and severely delayed arrival of blood in tissue have been found to be associated with a higher risk of SIH[112, 126, 127].

The hyperintense acute reperfusion marker (HARM) refers to high signal in the subarachnoid space on *T_2-weighted Fluid Attenuated Inversion Recovery* (FLAIR) MRI sequences that is caused by to leakage of previously administered gadolinium-based contrast agent [128-130]. It was first described in the setting of ischaemic stroke patients receiving serial MRIs during the acute phase, and is a sign of early blood-brain barrier breakdown (BBB) associated with reperfusion[129, 130]. As noted in section 2.1.2, reperfusion is associated with a passive increase in BBB permeability[38, 129]. Since loss of integrity of the BBB is thought to be the underlying cause of haemorrhagic transformation, it is no surprise that HARM is associated with haemorrhagic transformation[129].

The finding of contrast leakage due to loss of integrity of the blood-brain barrier can be leveraged to assess tissue microvascular permeability (leakage) using more sophisticated methods that promise to allow more direct interrogation of the mechanism underlying SIH[40, 131-133]. This may allow more accurate prediction of this complication. Microvascular permeability is a measure of the integrity of the blood-brain barrier, and can be expressed as the *trans-endothelial transfer*

coefficient (k_{trans}) or *permeability surface-area product* (PS)[40, 134, 135]. PS can be determined using perfusion imaging, by measuring the leakage of an intravascular tracer into the extravascular extracellular compartment[134, 135]. For both iodinated contrast and gadolinium-based contrast agent, the PS in normal brain tissue is approximately 0. A PS larger than 0 indicates loss of integrity and increased permeability of the blood-brain barrier. As discussed and shown in Figure 2-2, there is some evidence that increased permeability may occur early (within 2-4 hours) in AIS[130].

PS can be determined using CTP, DSC-PWI or *dynamic contrast-enhanced* (DCE) MR perfusion. In one study, PS was calculated from standard first-pass CTP using a Patlak model in a cohort of 50 AIS patients imaged within 3 hours of stroke onset[40]. In this study, all 6 patients who developed SIH had elevated PS in the region of haemorrhage. PS was significantly higher in infarcts that developed haemorrhagic transformation on follow up than in infarcts that did not. However focally elevated PS was not specific for predicting haemorrhage (it was seen in 88% of the infarcts). A subsequent study used a prolonged CTP acquisition of 3 minutes; here, the Patlak model was described for the delayed steady-state phase of contrast circulation[132]. In this study, increased permeability on the admission CTP was found to predict SIH with 100% sensitivity and 79% specificity. Limitations of this technique include the longer CTP acquisition, which increases radiation dose to the patient and increases the likelihood of motion, and the requirement for specialized post-processing software.

In one small study of 10 patients, DCE MRI with kinetic modelling of microvascular permeability demonstrated an associated between haemorrhagic transformation and increased permeability[136]. DSC-PWI rather than DCE MRI is the preferred MR perfusion technique, however, since it allows assessment of at-risk tissue. A technique has been described for calculating permeability directly from the source images of DSC-PWI[137]. However, this technique has not been sufficiently validated in AIS patients and has only been applied at one centre. Given the limitations of MR and CT based techniques, permeability mapping is not used widely used, and there is inadequate evidence to support their use in clinical decision-making.

2.4.2 Target Vessel Occlusion

Non-invasive vascular examination, namely CT or MR angiography, is

recommended during the initial imaging evaluation of patients who are otherwise eligible for thrombectomy[50]. The first generation thrombectomy trials, that failed to show benefit, included patients both with *and without* an occluded intracranial artery[81, 82]. The subsequent trials required enrolled patients to have non-invasive imaging proof of an anterior circulation proximal vessel occlusion prior to triage to treatment, to ensure that there was a target for reperfusion therapy[84-87, 89]. *It seems logical that, for thrombectomy to be effective, there must be a target occluded artery!*

Identification of patients with LVOs who present within the treatment window is therefore of critical importance. *CT angiography* (CTA) is the mainstay of non-invasive vascular imaging at most stroke centres around the world[111], and is routinely performed as a part of the standard-of-care multimodal CT protocol in patients who present to the emergency department with a suspected stroke within 24 hours of symptom onset[138]. *Time-of-flight magnetic resonance angiography* (TOF-MRA) is the vascular imaging sequence that is typically included in the AIS MRI protocol.

Identification of DVOs has also become increasingly important. As discussed in the previous section, these patients may be considered for thrombectomy, especially if they present outside the 4.5-hour window for IVT, have an M2-segment occlusion and/or have an area of eloquent brain that is viable but at risk of infarction[99, 100]. The benefit of IVT has also been shown to be greater in patients who have a distal vessel occlusion than those who have no occlusion[139, 140]. Accurate and timely identification of DVOs therefore helps direct therapy towards patients who are likely to benefit. Unfortunately, these distal occlusions are difficult to detect on CTA, with sensitivity as low 33% even for experienced radiologists[139, 141-143]. DVOs may not be included in the TOF-MRA slab, which is typically limited in craniocaudal coverage to save time.

2.4.3 Infarct Core

Magnetic resonance imaging (MRI) with *diffusion-weighted imaging* (DWI) is regarded as the imaging gold standard for detecting cerebral infarction and measuring the infarct core[144-147]. As discussed in section 2.1, brain tissue undergoes infarction when severe energy depletion results in failure of the cell membrane[148]. This in turn results in cell swelling, with shift of water from the extracellular to the intracellular compartment, referred to as **cytotoxic oedema**[149-152].

The Brownian motion of water protons in tissue is dependent upon temperature and barriers to motion such as cell density, membranes and orientation[153]. This diffusion of water protons can be measured on MRI by the application of multidirectional (at least 3, in the x, y and z directions) gradients in diffusion weighted imaging readout[153]. In cytotoxic oedema, there is reduced diffusion of water protons due to cellular and organelle swelling. This **restricted diffusion** can be detected on DWI within minutes of infarction[154-156] (Figure 2-6). The high diagnostic accuracy of DWI for detecting irreversible tissue injury has been shown in both human and animal studies, the latter including histological correlation[149-151, 157]. The degree of restricted diffusion (or "diffusivity") can be quantified by calculation of the *apparent diffusion coefficient* (ADC). DWI allows in vivo measurement of the ADC, and therefore accurate detection and quantification of infarction in AIS patients[147, 152, 157].

A potential limitation of using DWI to measure the infarct core is that ADC values vary between subjects and within an individual patient's brain; different tissue (white versus grey matter and different white matter tracts) having different ADCs[144, 158]. Additionally, early DWI lesion reversal has been described following reperfusion, particularly following early reperfusion and endovascular therapy [144, 159-161]. Approximately a third of patients had early DWI reversal following successful endovascular therapy on analysis of data from the *Diffusion and perfusion imaging evaluation for understanding stroke evolution* (DEFUSE) 2 study[162]. This was related to increase in ADC values following reperfusion, which is likely due to vasogenic oedema caused by increase in the permeability of the BBB that reperfusion (discussed in section 2.1.3)[162, 163]. This ADC increase and DWI reversal following reperfusion have been shown to be transient and not reflective of true tissue salvage[144, 160, 162, 163]. True reversal that was sustained on follow-up imaging was found to be uncommon and limited to a small volume that was not clinically relevant[144, 160, 162].

It was postulated that earlier reports of more extensive reversal were related to methodological limitations where follow up was either performed too early, during the period transient reversal, or too late, where atrophy results in infarct volume underestimation[109, 164]. To avoid these issues, the final infarct volume should be measured using either a T2-weighted or T_2-weighted FLAIR MRI sequences within 3-5 days[109, 164]. ADC maps should not be used at follow up to measure the infarct core since ADC values increase and pseudo-normalize (i.e., become isointense to normal brain tissue) after the first week[165]. This ADC increase occurs earlier with reperfusion as discussed.

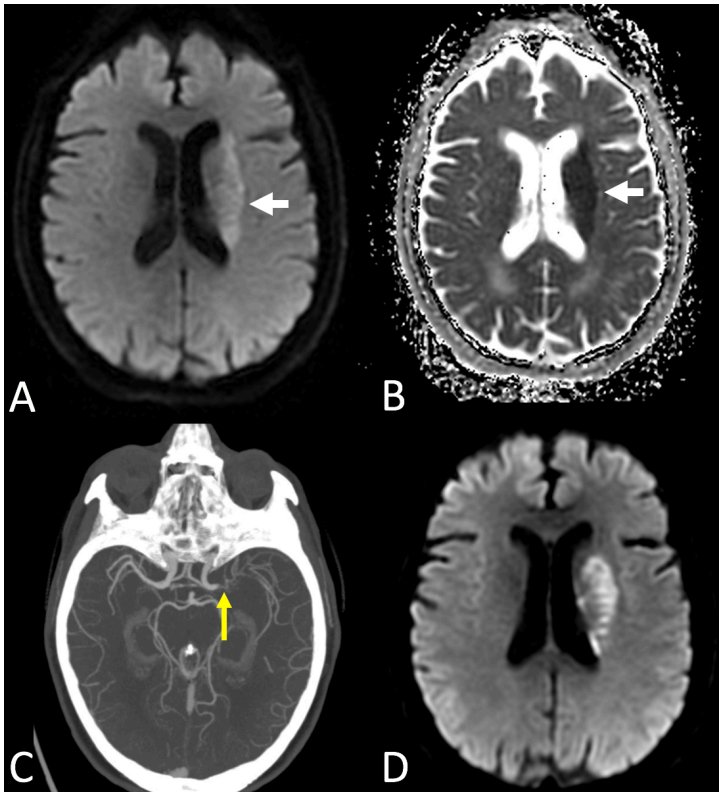

Figure 2-6. *Selected images from an 82 year-old woman who presented 5 hours after last seen well with aphasia and right hemiplegia.* ***A.*** *Diffusion weighted image showing high signal in the left corona radiate and putamen (arrow) with* ***B.*** *corresponding very low ADC (arrow) indicating acute infarction. Infarction of these structures is often seen in patients with proximal M1-segment occlusion, even with early reperfusion. This is due to the lack of collateral blood flow to these structures, which are supplied by end-arteries (the lateral lenticulostriate perforators) which arise from the occluded M1-segment.* ***C.*** *CT angiogram performed 20 minutes earlier shows proximal occlusion of the left middle cerebral artery (blue arrow).* ***D.*** *Much higher signal on the diffusion trace image from DWI at day 3 than the baseline image shown in A is due to T2-shine-through, resulting from vasogenic oedema at this stage.*

Manual outlining of the entire visually apparent DWI lesion has been used to determine infarct volume in the research setting[144, 166]. Given the emergent nature of acute stroke, such time-consuming manual techniques are unsuitable for clinical use. Instead, the infarct core can be segmented in a fully automated fashion by applying an *apparent diffusion coefficient* (ADC) threshold. An ADC of less than 620×10^{-6} mm^2/sec has been found to be the optimal threshold for predicting the infarct core[157]. Although it produces smaller infarct core volumes than manual outlining[166], automated segmentation of the infarct core using an ADC threshold of 620×10^{-6} mm^2/sec allows the volume of the infarct core to be assessed in a rapid

and objective way that is necessary in the clinical setting (Figure 2-7). Accordingly, this approach was used for MRI-based patient triage to endovascular therapy in a number of recent acute stroke trials [27, 83, 88, 89].

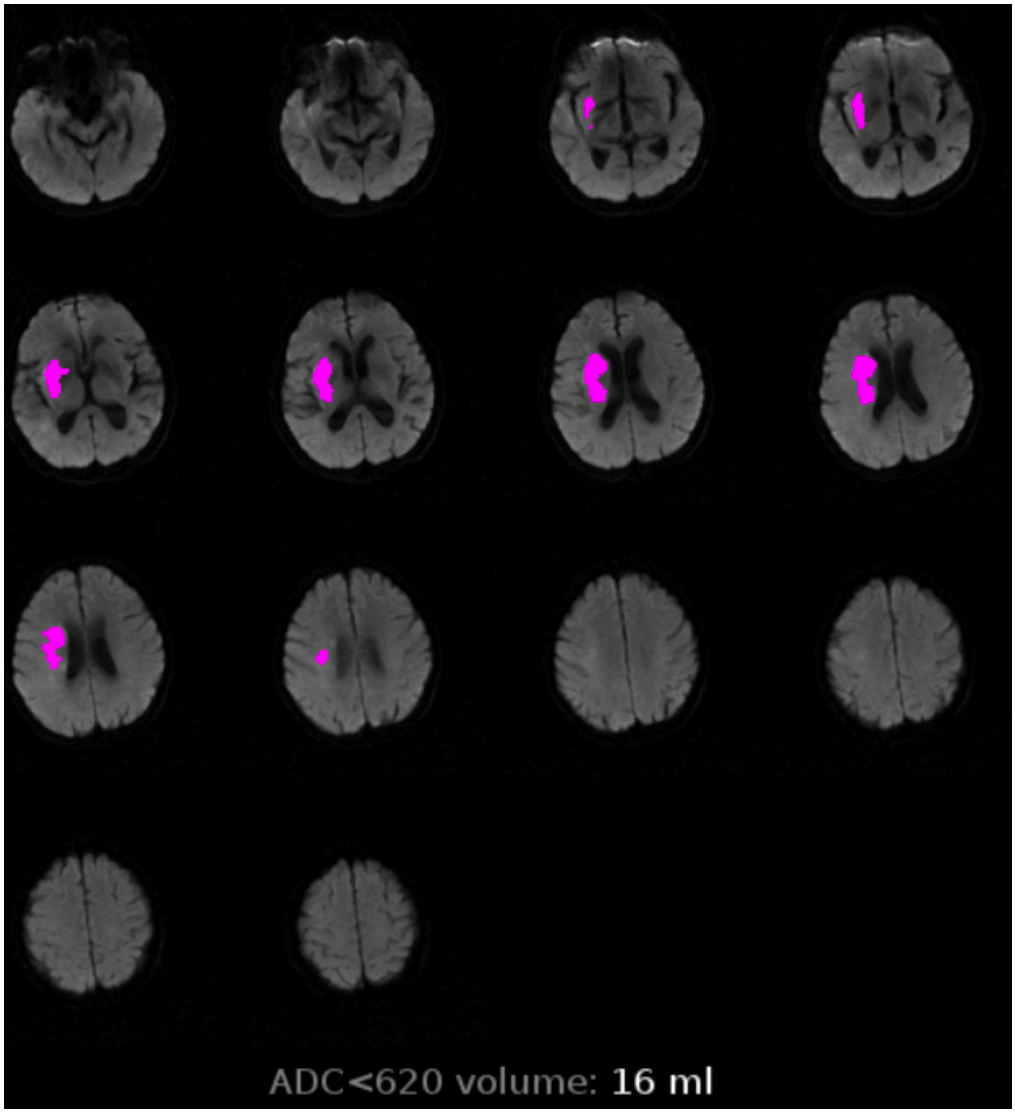

Figure 2-7. *An example of automated segmentation of the infarct core on DWI, using an ADC threshold of 620x10^{-6} mm^2/sec. The area with an ADC value below this threshold is highlighted in pink on the DWI trace images. This 70 year-old woman presented with an acute stroke due to occlusion of the M1 segment of the right MCA.*

Despite extensive validation of MRI, CT is the mainstay of acute stroke imaging since it is easier to access emergently and does not require cumbersome screening for contraindications. The infarct core can be delineated acutely on non-enhanced CT based on early ischemic changes of hypodensity and loss of grey-white matter differentiation. Unfortunately, NECT has low sensitivity and poor inter-rater

agreement for detection of the infarct core based on these criteria[167, 168]. Since NECT hypodensity is caused by vasogenic rather than cytotoxic oedema, it is absent or subtle if the patient is imaged in the first few hours following infarct onset. In one study where NECT was compared against MRI with DWI, CT had a sensitivity of just 26% for the diagnosis of acute stroke[167].

NECT early ischemic changes within the middle cerebral artery territory can be quantified in a standardized fashion using the *Alberta Stroke Program Early CT Score* (ASPECTS)[169]. Here, the MCA territory is divided into 10 segments over two different axial planes: one at the level of the thalamus and basal ganglia, and one rostral to the basal ganglia (i.e. supra-ganglionic). The 10 segments consist of 6 cortical areas supplied by the MCA (the insula and areas M1-M6) plus the internal capsule, caudate and lentiform nuclei and the insula (Figure 2-8). One point is subtracted for each area that shows early ischemic change (hypodensity). Hence a score of 10 indicates no visible ischemic change, a score of 0 indicates infarction of the entire MCA territory and a score of 6 indicates infarction of approximately a third of the MCA territory. It is noted that only one hemisphere is considered for ASPECTS; if the patient has bilateral lesions, one side must be selected. On this initial validation study, baseline ASPECTS was found to be inversely correlated with stroke severity and predictive of functional outcome and SIH[169]. There was, however, no comparison of ASPECTS with a reference standard such as contemporaneous DWI or follow-up imaging. Subsequent studies have shown only moderate inter-rater agreement for NECT ASPECTS[170, 171], indicating the highly subjective nature of early CT signs. Accordingly, despite the increased risk of haemorrhage with any reperfusion therapy in patients with large infarcts, there is currently insufficient evidence to use NECT hypodensity as a contraindication to thrombolysis[50]. Another limitation of ASPECTS is that it is only be applicable to MCA territory infarcts.

CT perfusion (CTP) provides a more objective method of assessment. CT perfusion-derived *cerebral blood flow* (CBF) and *cerebral blood volume* (CBV) have both been investigated for detection of the infarct core, using either DWI or the final infarct volume as the reference standard[172-175]. Absolute CBV reduction, with an optimal threshold of less than 2 mL per 100 g tissue, was identified in an early CTP study as the optimal surrogate for the infarct core[176]. However, CBV may be underestimated when the CTP acquisition does not fully capture the first pass of contrast material through the tissue capillary bed. This can occur with inadequate CTP scan duration, delay in contrast injection, or severely delayed blood flow and tracer arrival in tissue as occurs in ischaemia.

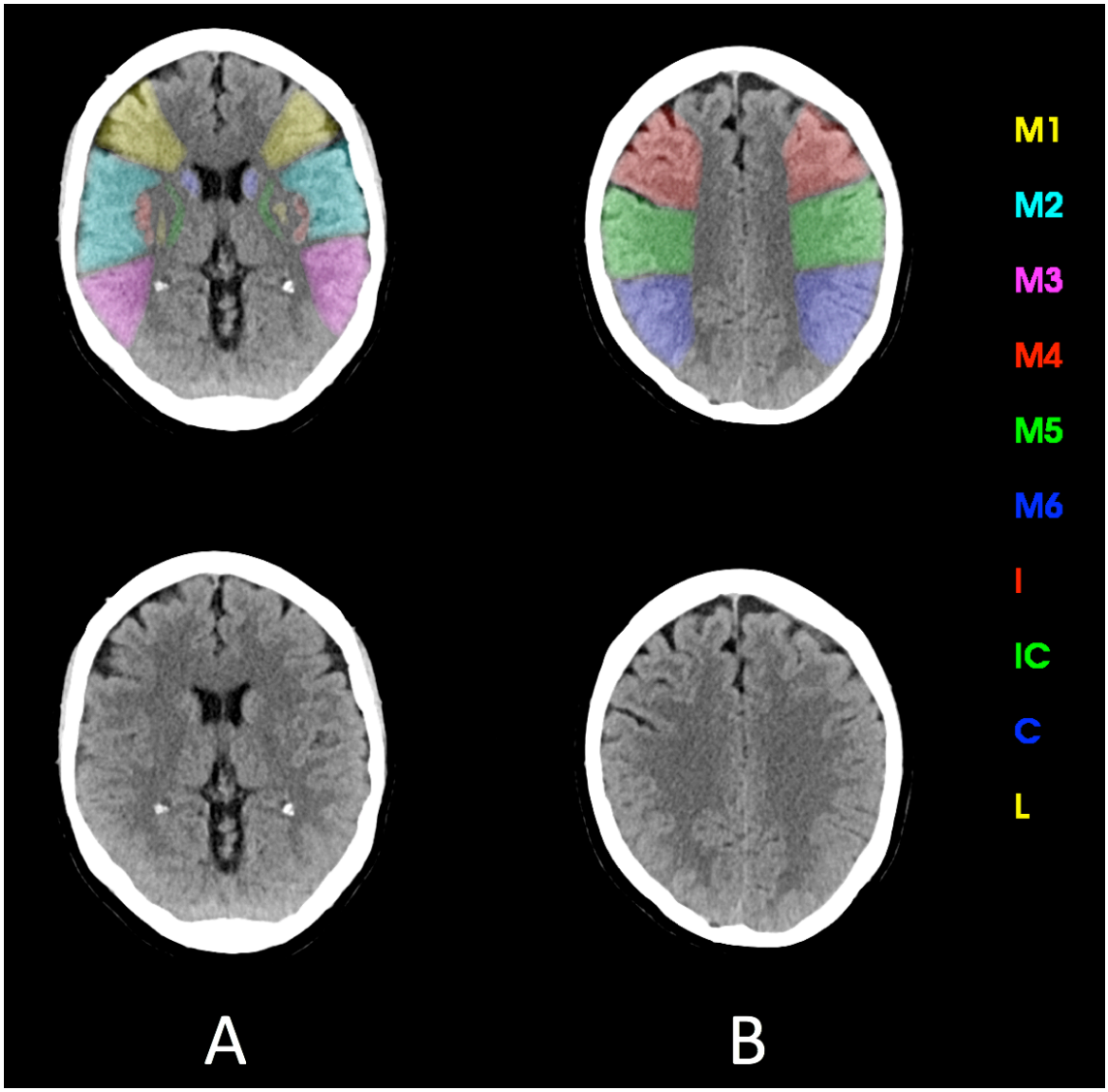

Figure 2-8. *Alberta Stroke Program Early CT Score (ASPECTS). For each hemisphere, the MCA territory is divided into 10 segments over two different axial planes:* ***(A)*** *at the level of the thalamus and basal ganglia, and* ***(B)*** *rostral to the basal ganglia. The 10 segments consist of 6 cortical areas supplied by the MCA (areas* ***M1-M6****), insula,* ***I****, internal capsule (****IC****), caudate nucleus (****C****) and lentiform nucleus (****L****), as shown on the images. A point is deducted for each area that is thought to be hypodense.*

More recent studies, that have used more closely time-matched CTP and DWI acquisitions than previously, have found that severely reduced *relative CBF* (rCBF) to be the most accurate perfusion-derived parameter for defining irreversible infarction[172, 173]. This is unsurprising since persistent severe reduction of cerebral blood flow is the cause of irreversible tissue injury in acute stroke. Relative, rather than absolute, measurements have been found to be better since

they avoid errors related to scaling. The calculation of rCBF is explained in Chapter 4. Briefly, it is obtained by normalizing the CBF in an imaging voxel by the mean CBF in the patients' normally perfused voxels (e.g., in the contralateral hemisphere). Therefore, rCBF measurements are expressed as a value from 0-1 or a percentage. The optimal rCBF threshold for predicting infarction (i.e., the rCBF value below which tissue is likely to be infarcted) depends on the post-processing algorithm that is used; values ranging from ranging from 0.3 to 0.42 (i.e., 30% to 42% of the CBF in the patient's normally perfused tissue) have been reported[172-174]. A threshold of 0.3 (30%), which indicates substantial (70%) CBF reduction, was used to determine the infarct core volume prior to randomization of patients in a number of thrombectomy trials[83, 85, 88, 177]. This rCBF threshold is now widely used to operationally define the infarct core on CTP when the same software is used. An example of infarct core delineation using severely reduced rCBF is shown in Figure 2-9.

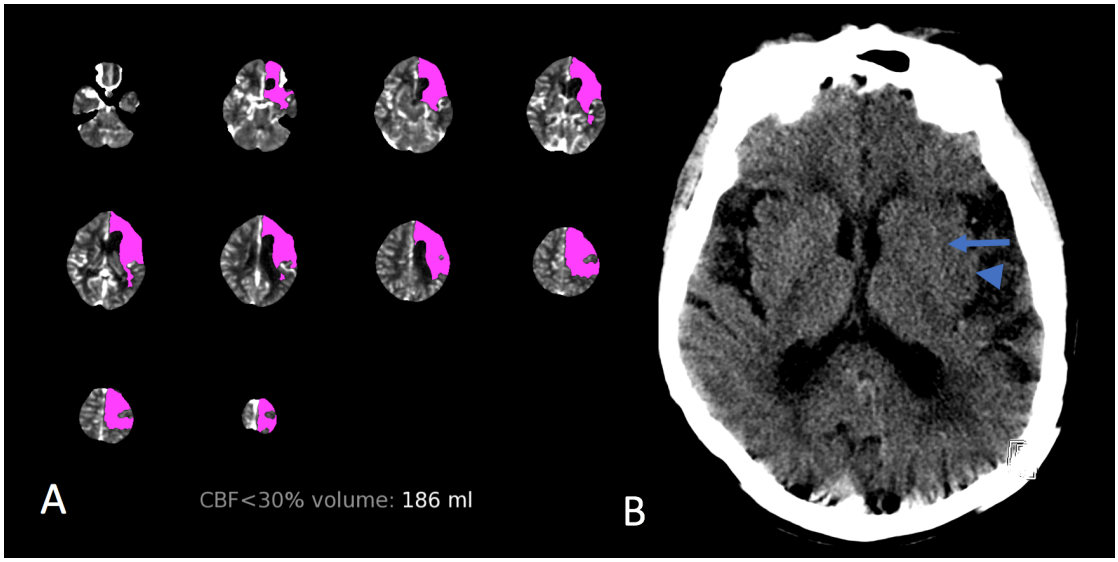

Figure 2-9. *Infarct core delineation on CTP in a patient with occlusion of the terminal left internal carotid artery.* ***A.*** *The infarct, highlighted in pink, has been predicted using rCBF reduction to less than 30% compared to the patient's normally perfused brain tissue (in the right hemisphere and posterior circulation).* ***B.*** *The NECT images are severely motion degraded. There are some signs of early infarction, with subtle loss of density of the insula (arrowhead) and lentiform (arrow) and caudate nuclei however cortical areas M1-M6 were normal. This case highlights how using NECT can result in underestimation of the extent of infarction.*

Diffusion and perfusion imaging therefore offer two different but widely accepted methods of imaging the infarct core. DWI provides unparalleled sensitivity and specificity for detection of irreversible tissue injury. It has been validated in both

human and animal models, and directly interrogates the cellular changes (cytotoxic oedema) that occur with cell death[147, 149-151]. Blood flow imaging attempts to predict tissue fate by measuring the causative agent of tissue damage[145, 178]. Since irreversible tissue injury is a product of both severity and duration of cerebral blood flow reduction, severe CBF reduction at a given time point provides only a "snapshot" which may not be an accurate surrogate of irreversible tissue injury. While the stroke onset time (therefore duration of blood flow reduction) can be determined, it cannot always be assumed that CBF reduction has remained constant over that time. Factors such as fluctuation in systemic blood pressure and distal migration of clot cause changes in regional cerebral perfusion pressure and therefore CBF within the ischemic territory. Therefore, some authors and stroke practitioners have doubt about the accuracy of CTP for accurate delineation of the infarct core in the individual patient and continue to use MRI with DWI in the clinical setting[179].

2.4.4 The Ischemic Penumbra and Mismatch Analysis

The **ischemic penumbra** refers to *critically hypoperfused but viable* brain tissue that is at risk of infarction without timely reperfusion. Salvage of the ischemic penumbra is the objective of any reperfusion therapy. Reperfusion therapies are associated with a risk of haemorrhage and cost to the healthcare system. As such, delineation of the ischemic penumbra is important to ensure that treatment is directed at those patients who have salvageable brain tissue and are therefore likely to benefit. Conversely, showing that there is no salvageable penumbral tissue helps avoid futile and potentially harmful treatment in patients with completed infarcts.

Various methods have been proposed to prove the presence of penumbral tissue and estimate its extent: the perfusion-diffusion mismatch[27, 114, 180-182], magnetic resonance angiography-diffusion mismatch[183], and clinical-diffusion mismatch[184]. These techniques estimate critically hypoperfused tissue based on perfusion parameters, very poor collaterals (MRA), and clinical deficit(s) reflecting neuronal dysfunction, i.e. **functional penumbra**, respectively. A limitation of the functional penumbra is that the extent of ischaemia is underestimated in the non-dominant hemisphere.

The studies that have investigated baseline perfusion imaging for prediction of the ischemic penumbra have used volumetric and voxel-wise techniques to compare perfusion parameters against the final infarct volume (measured on a follow-up

MRI using either DWI or a T2-weighted FSE or FLAIR sequence) in patients who are non-reperfusers[27, 176, 185-187]; these patients have a persistent arterial occlusion hence tissue that is penumbral on baseline imaging has progressed to completed infarction at follow-up. An example is shown in Figure 2-10. A major limitation of this methodology relates to the timing of follow-up imaging: if performed too early, the infarct may still be evolving and incomplete; if too late and in the chronic phase (e.g., at day 30 in the DEFUSE study), atrophy results in underestimation of the infarct size[180]. Follow-up MRI in the late acute/early subacute phase (e.g., at day 5 in the DEFUSE 2 study) is also imperfect since it requires adjustment for mass effect related to vasogenic oedema[27].

Opinion on which perfusion parameter is best for estimating critically hypoperfused tissue has changed over time. Cerebral blood flow reduction below an ischemic threshold of approximately 20 mL/min/100g was shown to cause reversible neurological dysfunction using ^{15}O-PET studies[22-24, 182]. Subsequent clinical stroke studies have, however, used predominantly time-domain perfusion parameters that reflect delayed rather than reduced blood flow. This was because MRI with DSC-PWI, which was in early clinical stroke studies, yields relative rather than absolute CBF measurements[27, 114, 180, 181]. Also, there is less grey-white matter differential for time-domain parameters than CBF and time delay can be measured relatively reliably.

Time domain parameters that have been used to predict critically hypoperfused tissue include tissue *mean transit time* (MTT), *time-to-peak* (TTP) and the *time to maximum of the residue function* (Tmax, obtained by deconvolution, discussed in detail in Chapter 4)[27, 114, 176, 180, 182, 186, 187].

A study of 130 patients with a clinical stroke syndrome who underwent CTP within 12 hours of onset found MTT, normalized to the patient's contralateral normally perfused hemisphere, to be the best predictor of critically hypoperfused tissue[176]. This study initially popularized the use of MTT for prediction of the penumbra. Another group of investigators, who evaluated DSC-PWI data from the first forty patients enrolled in the EPITHET study, found that MTT was more prone to error and advocated the use of Tmax instead to delineate at-risk tissue[182]. Comparison of the baseline Tmax lesion with follow-up MRI in non-reperfusers identified a Tmax threshold of >6 seconds to correlate best with tissue that is at risk of infarction in the absence of reperfusion[187]. It has subsequently shown that Tmax >6 seconds can also be used to delineate tissue at risk on CTP. *Campbell et al* segmented and co-registration of Tmax >6 second derived from DSC-PWI with

CTP-derived Tmax maps, and used receiver-operating characteristic analysis to show that the optimal CTP-derived Tmax threshold was 6 seconds[185]. CTP and MRI mismatch status were found to be concordant in 90% using this threshold.

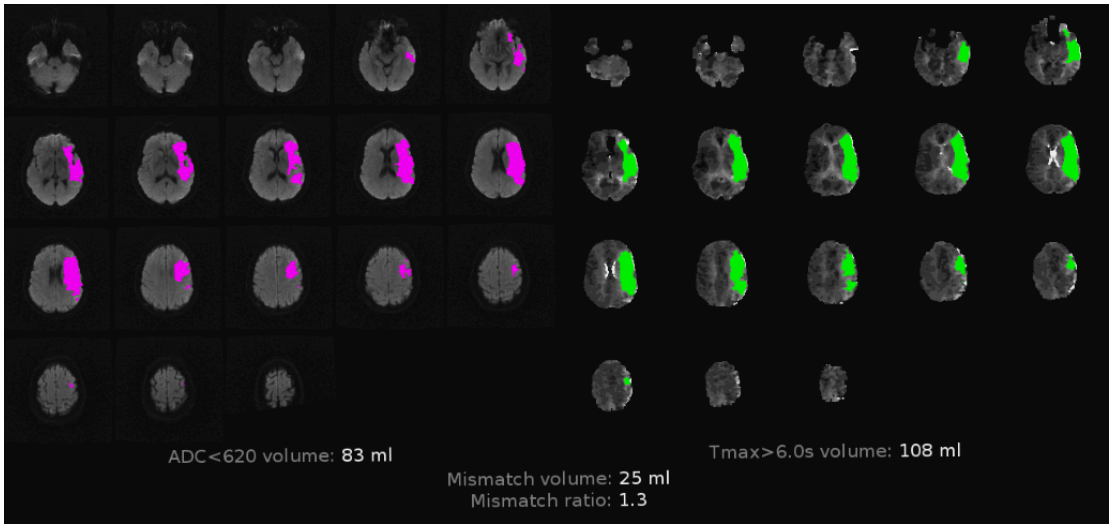

Figure 2-10. *Mismatch analysis performed using MRI in a 71 year-old woman with left MCA M1 segment occlusion. The* ***infarct core*** *(left side panel) has been segmented on DWI using an ADC threshold of 620x10^{-6} mm^2/sec. The segmentation mask is highlighted in pink and the infarct volume is estimated to be 83mL.* ***Critically hypoperfused*** *tissue (right side panel) has been identified using Tmax >6 seconds delay and is segmented in green. The difference in volume between the* ***critically hypoperfused tissue*** *and the* ***infarct core*** *is the* ***mismatch volume*** *(penumbral volume, also called tissue at-risk), while the ratio of these is the* ***mismatch ratio****. Despite a mismatch volume of 25 mL and a large volume of critically hypoperfused tissue (108 ml), the mismatch ratio is only 1.3 due to the large infarct volume. Therefore, this patient does not have a target mismatch according to the DEFUSE 2 criteria.*

Once critically hypoperfused tissue is identified using a perfusion parameter, the infarct core is then subtracted to identify the tissue that is viable but at risk of infarction without timely reperfusion – i.e., the ischemic penumbra, which is also referred to as tissue at-risk. Quantifying the ischemic penumbra using this method is referred to as **mismatch analysis**[27, 114, 180, 187]. The **mismatch volume** is the difference in volume between the critically hypoperfused tissue and infarct core (i.e., penumbral volume). A **mismatch ratio** of these volumes is also calculated.

A few MR-based trials have investigated the effect of reperfusion on tissue salvage and whether a pre-specified perfusion-diffusion mismatch profile, referred to as a **target mismatch**, can be used to identify patients who respond favourably to reperfusion[27, 114, 180]. These studies used Tmax and DWI (ADC <620x10^{-6} mm^2/sec) to predict the volume of critically hypoperfused tissue and infarct core,

respectively[27, 114, 180]; **perfusion-diffusion mismatch analysis** was then performed to determine the mismatch volume (penumbra) and ratio. An example is shown in Figure 2-10. The EPITHET and DEFUSE studies investigated whether a target mismatch profile can predict patients who respond favourably to reperfusion with intravenous thrombolysis 3 to 6 hours after symptom onset[114, 180]. Tmax delay > 2 seconds was used to identify critically hypoperfused tissue in both these studies, and a target mismatch was defined as a PWI-DWI mismatch ratio of > 1.2 mL and mismatch volume > 10 mL. The DEFUSE study had a positive outcome, finding that patients with a target mismatch profile had significantly increased odds of a favourable neurological outcome when early reperfusion was achieved with intravenous thrombolysis[180]. Conversely, patients without a mismatch failed to benefit from early reperfusion. EPITHET, however, was a negative study which failed to demonstrate a significant reduction in infarct growth and increase in reperfusion in patients with a target mismatch[114].

Subsequently, the DEFUSE 2 prospective cohort study found that successful endovascular reperfusion was associated with a favourable outcome in patients with a target mismatch – defined as a ratio of >1.8 and a mismatch volume of >15 mL – while there was no association between a favourable outcome and reperfusion in patients without a target mismatch[27]. A favourable outcome was defined in this study (unlike most randomized controlled stroke trials) as either an NIHSS score of 0-1 on the day 30 follow-up, or an improvement of 8 points compared to baseline.

Mismatch analysis therefore allows identification of patients who are likely to benefit from reperfusion therapies. Triaging patients to endovascular or intravenous reperfusion therapies based on the demonstration of salvageable at-risk tissue on perfusion imaging is referred to as **penumbral selection**.

Several subsequent endovascular therapy stroke studies used penumbral selection, which is to say that perfusion imaging and mismatch analysis were used to identify and enrol patients who were likely to have a favourable response to reperfusion[83, 85, 89]. The target mismatch profile used in these trials was a mismatch volume of 15 mL and a mismatch ratio >1.8, with the exception of EXTEND-IA where a volume of 10 mL and ratio of 1.2 were used. These trials used exclusively or mostly CTP. Examples of mismatch analysis using CTP are shown in Figure 2-11. The rate of favourable outcome in both the endovascular therapy and medical management groups was higher in the trials that used mismatch analysis than those that did not, as was shown in Figure 2-1. Therefore, although not recommended by guidelines in the early window, some tertiary stroke centres in

the United States and many in Australia use CTP to establish the presence of penumbral tissue before proceeding to thrombectomy, even in the early window. For thrombectomy in the late time window, the DEFUSE 3 criteria necessitate perfusion imaging (either CTP or DSC-PWI) to identify salvageable penumbral tissue while the DAWN criteria use a clinical-imaging mismatch[83, 88].

It is noted that strict mismatch criteria are not rigidly adhered to when triaging patients to thrombectomy in routine clinical practice. Stroke topology and the eloquence of penumbral brain tissue, as well as its volume, must be considered in the individual patient; for example, stroke teams are inclined to intervene in patients who present within the thrombectomy window if the motor strip or speech areas are at risk and still viable, even if the mismatch volume is less than 15 mL and the mismatch ratio <1.8. As previously discussed, the image-guided approach to patient selection has more recently been applied to intravenous thrombolysis beyond 4.5 hours in one trial[103]. Mismatch analysis was used to prove the presence of a salvageable penumbra in patients enrolled in this trial, who were shown to have a higher likelihood of functional independence with alteplase than placebo. More evidence from randomized trials is, however, required to show that penumbral selection improves intravenous thrombolysis beyond 4.5 hours.

A "malignant profile", defined as a Tmax >8 second or 10 seconds volume larger than 100 mL, has been used in the past to exclude patients from reperfusion[27, 114, 161, 188]. This was based on evidence of increased risk of reperfusion injury and symptomatic intracranial haemorrhage, with poor outcome, in these patients with reperfusion[188]. None of the patients enrolled in EPITHET who had a malignant profile developed symptomatic intracranial haemorrhage. Excluding patients with a malignant profile from treatment has since fallen out of favour.

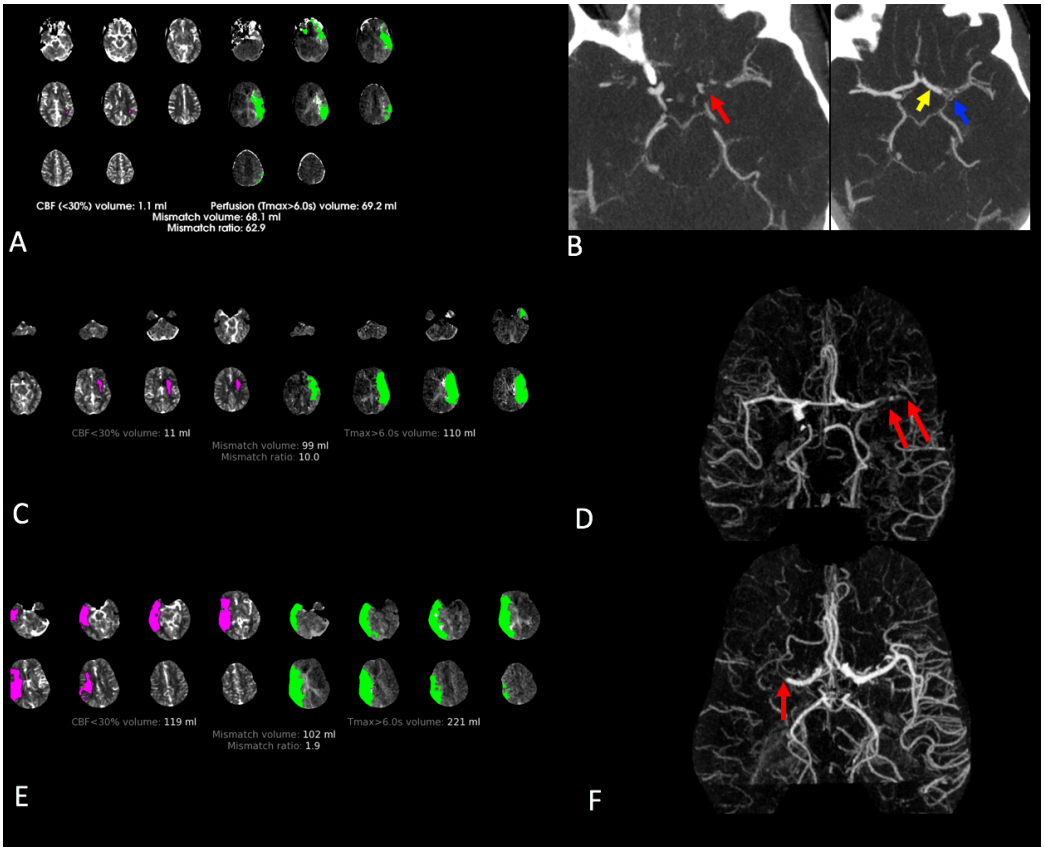

Figure 2-11. *Examples of CTP-based automated mismatch analysis. The infarct core was determined from CTP based on severely reduced rCBF, defined as rCBF reduction to less than 30% of the patient's normally perfused tissue. Critically hypoperfused tissue was determined using a Tmax delay >6 seconds.* ***A.*** *Mismatch analysis in a 63 year-old woman who presented 5 hours after stroke onset, showing a small predicted infarct core (pink, 1 mL) and large area of critical hypoperfusion (green, 69 mL) hence a large ischemic penumbra. This patient has a target mismatch, with a mismatch volume of 68 mL.* ***B.*** *Selected CTA images show occlusion of the left occlusion ICA (red arrow) and non-occlusive clot in the terminal ICA and M1 segment of the left MCA (blue arrow) which have some flow in them due to cross-flow from the right ICA via the ACOM and large left A1 segment (yellow arrow). This is an example of good circle-of Willis collateral flow resulting sustaining a large ischemic penumbra.* ***C.*** *Mismatch analysis in a 60 year-old man who presented 4 hours after stroke onset, showing a large area of critical hypoperfusion (green, 110 ml) and only a small infarct core (pink, 11 mL). Mismatch analysis therefore indicates a large ischemic penumbra of 99 mL.* ***D.*** *CTA bone-masked maximum-intensity projection showing incomplete occlusion of the mid M1 segment and complete occlusion of the distal M1 segment of the left MCA.* ***E.*** *Mismatch analysis in a 61 year-old man who presented 6 hours following stroke onset, showing a large infarct core (pink, 119 mL) and an even larger area of critical hypoperfusion (green, 221 mL). While this patient has a target mismatch according to mismatch criteria alone, he was not considered eligible for thrombectomy because of the large infarct volume.* ***F.*** *CTA bone-masked maximum-intensity projection showing occlusion of the M1 segment of the right MCA.*

2.4.4.3 Imaging the Penumbra using ASL

Arterial spin label (ASL) may be of value in the assessment of the ischemic penumbra [189-191]. It is discussed in detail in Chapter 4. Briefly, ASL is a completely non-invasive perfusion technique that uses magnetically labelled arterial blood water which acts as a freely diffusible tracer[192, 193]. Exogenous contrast administration is therefore not required. ASL may, therefore, be used in patients who cannot be given gadolinium-based contrast agents, for example due to allergy or severe renal impairment. Other advantages of ASL are that it allows quantification of cerebral blood flow and it can be repeated[194].

A few studies that have compared ASL with the reference standard of DSC-PWI for delineation of the ischemic penumbra have shown consistency between these techniques for detecting regions of hypoperfused brain tissue[189-191]. These studies suggest that CBF estimates obtained using ASL agree best with time-based parameters (MTT and Tmax) obtained using DSC-PWI. The optimal threshold for identifying critically hypoperfused tissue was 40% of mean contralateral cerebral blood flow in one study[189]. Another study found 100% agreement between ASL and DSC-PWI for mismatch analysis, using a quantitative CBF threshold of 20 ml/100g per minute on ASL and MTT delay ≥10 seconds on DSC-PWI [195]. The perfusion deficit, and therefore the ischemic penumbra, were however overestimated using ASL[189-191]. This can be explained by the prolonged *arterial transit time* (ATT) in acute ischemic stroke[196]. In ASL, ATT is the time taken for labelled blood to travel from the labelling plane to the brain tissue capillary bed in the imaging plane[197, 198]. In the presence of an arterial occlusion, blood reaches the ischemic penumbra via collateral pathways. The arrival of blood in downstream ischemic tissue is therefore markedly delayed. Under these conditions, the ATT may exceed the standard *post label delay* (PLD) of ASL (the PLD, explained in the Chapter 4, is the delay between magnetic labelling and readout). When this occurs, labelled blood does not have sufficient time to reach the capillary bed via the collateral pathways before image acquisition. The degree and extent of CBF reduction in tissue are therefore overestimated[199]; the reduced signal in tissue is caused by delayed arrival of labelled blood rather than true blood flow reduction. An example is shown in Figure 2-12. Since ASL signal is approximately proportional to cerebral blood flow, this also compromises the SNR of ASL, which is already lower than that of DSC-PWI[194, 200]. These disadvantages of standard-delay ASL limit its clinical utility in AIS.

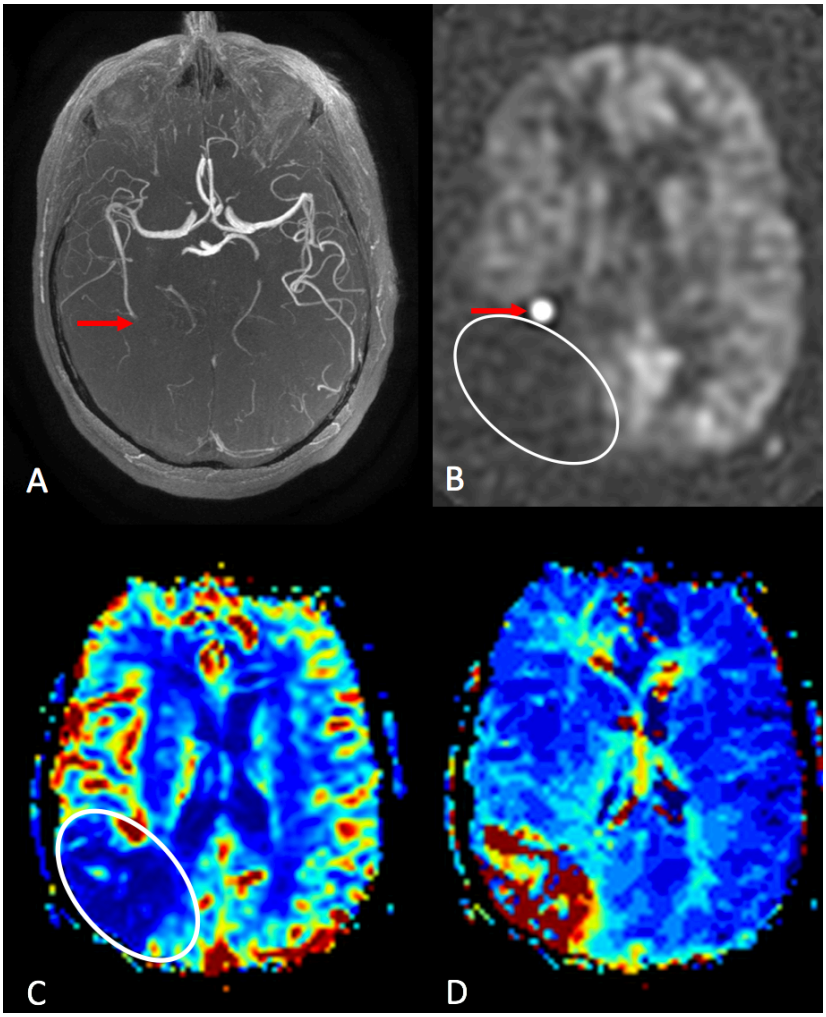

Figure 2-12. *An important limitation as well as the value of ASL in ischemic stroke are shown in an 81 year-old woman with acute occlusion of the inferior M2 division of the right MCA.* ***A.*** *TOF-MRA MIP image showing the occlusion (red arrow).* ***B.*** *ASL image showing an area of very high signal (arrow), which corresponds to labelled blood which is held up in the M2 segment proximal to the occlusion. This is called "arterial transit artifact" and can alert the reader to both the presence and site of occlusion. The tissue downstream from the occlusion has very low signal (circle), suggesting markedly reduced CBF.* ***C.*** *DSC-PWI CBF map at the corresponding level shows that the area of markedly reduced CBF is smaller than the defect seen on ASL. ASL overestimates the area of CBF reduction due to the delayed arrival of labelled blood in tissue via leptomeningeal collateral in the setting of arterial occlusion.* ***D.*** *DSC-PWI Tmax map, showing that the ASL map corresponds better with delayed Tmax (red and yellow areas), since both show delayed arrival of blood in tissue.*

A strategy that may be used to counter CBF underestimation due to delayed arrival of labelled blood is to use a longer PLD that exceeds the prolonged ATT[200]. This would allow sufficient time for blood to reach the ischemic tissue via collateral pathways. However, SNR is reduced because the longer time interval between

labelling and imaging allows greater T_1-decay of ASL signal. The signal of labelled blood decays with the T_1-relaxation time of blood, which is approximately 1.2 to 1.8 seconds at the magnetic field strengths used in clinical practice, in turn resulting in significant signal loss when longer PLDs are used[200]. In order to improve the accuracy of CBF quantification using ASL in patients with delayed ATT, the competing requirements must be satisfied: sufficient SNR on the one hand and a longer PLD to allow labelled blood sufficient time to reach ischemic tissue on the other. Long-label long-delay and multi-delay ASL techniques have been proposed and developed as a solution in both AIS and chronic steno-occlusive disease patients[196, 200-203]. These are discussed in detail in Chapter 4. In one small feasibility study of 24 patients with acute MCA territory stroke, multi-delay ASL was compared against DSC-PWI for measurement of perfusion abnormality within the affected vascular territory and the area of infarction as determined using DWI[196]. This study found significant correlation between multi-delay ASL and DSC-PWI for CBF measurement. Arterial transit time derived from multi-delay ASL was found to correlate best with Tmax derived from DSC-PWI.

2.4.5 Leptomeningeal Collaterals

Penumbral imaging using Tmax offers a snapshot of brain tissue viability[204]. The presence of an ischemic penumbra can be attributed to collateral pathways that enable blood to bypass the acute arterial occlusion and reach the downstream ischemic tissue[205]. For arterial occlusions at or distal to the terminal ICA, cortical-leptomeningeal collaterals are most important. The number and robustness of these leptomeningeal collaterals varies between patients. This, in turn, is thought to account for the variability in the rate of infarct expansion into penumbra[30, 206]; each patient has a different internal "clock", with a different rate of infarct progression that is dependent on their collateral status[30]. While some patients have infarct growth rates of up to 100 mL/hour, slow growth is seen in up to 50% of patients with LVOs[206]. This likely accounts for the "late window paradox", where the treatment effect was higher in the late window than the early window trials[30].

Imaging of collaterals therefore has the potential to allow prediction of the rate of infarct expansion[188, 204, 205, 207-209]. Knowledge of how long the penumbra is likely to survive can potentially improve patient triage and determine whether endovascular therapy is feasible in this treatment window and likely to benefit the patient.

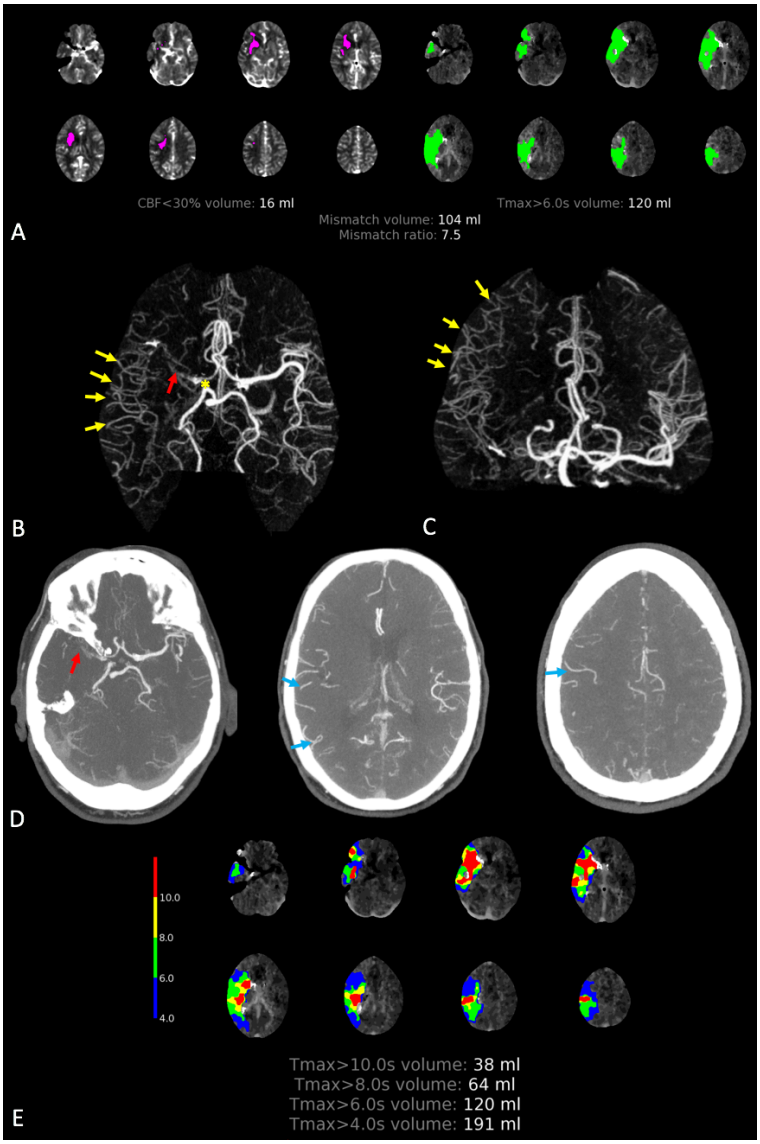

Figure 2-13. *Good collaterals in a 67 year-old woman who presented 5 hours following symptom onset.* ***A.*** *CTP mismatch analysis shows a small infarct core (pink, CBF <30%) of 16 mL and a large area of critical hypoperfusion (green, Tmax >6 seconds) hence a large ischemic penumbra of 104 mL.* ***B.*** *Axial and* ***C.*** *Coronal CTA bone-masked maximum intensity projections (MIPS) show occlusion of the right ICA (yellow asterisk) and M1 segment of the right MCA (red arrow). Prominent leptomeningeal collaterals (yellow arrows). These are greater in extent superiorly than contralateral (left) pial vessels on the coronal projection. This indicates good collateral grade.* ***D.*** *Axial CTA MIPs also show good filling of pial arteries and MCA M4 branches (blue arrows) in the ischemic right MCA territory. Good collaterals are associated with slow infarct progression and likely explain the small size of the infarct in this patient despite the large area of critically hypoperfused tissue.* ***E.*** *Tmax obtained using CTP. There is a large volume of critically hypoperfused tissue with Tmax >6 seconds (120 mL) in the right MCA territory and an even large volume of mild hypoperfusion. There is only a small volume of tissue with severe Tmax delay >10 seconds (38 mL). The hypoperfusion index is therefore <0.4, again an indicator of robust leptomeningeal collaterals. The ACA territory is not hypoperfused due to cross-flow from the left ICA via the ACOM, an example of good collateral flow via the circle of Willis.*

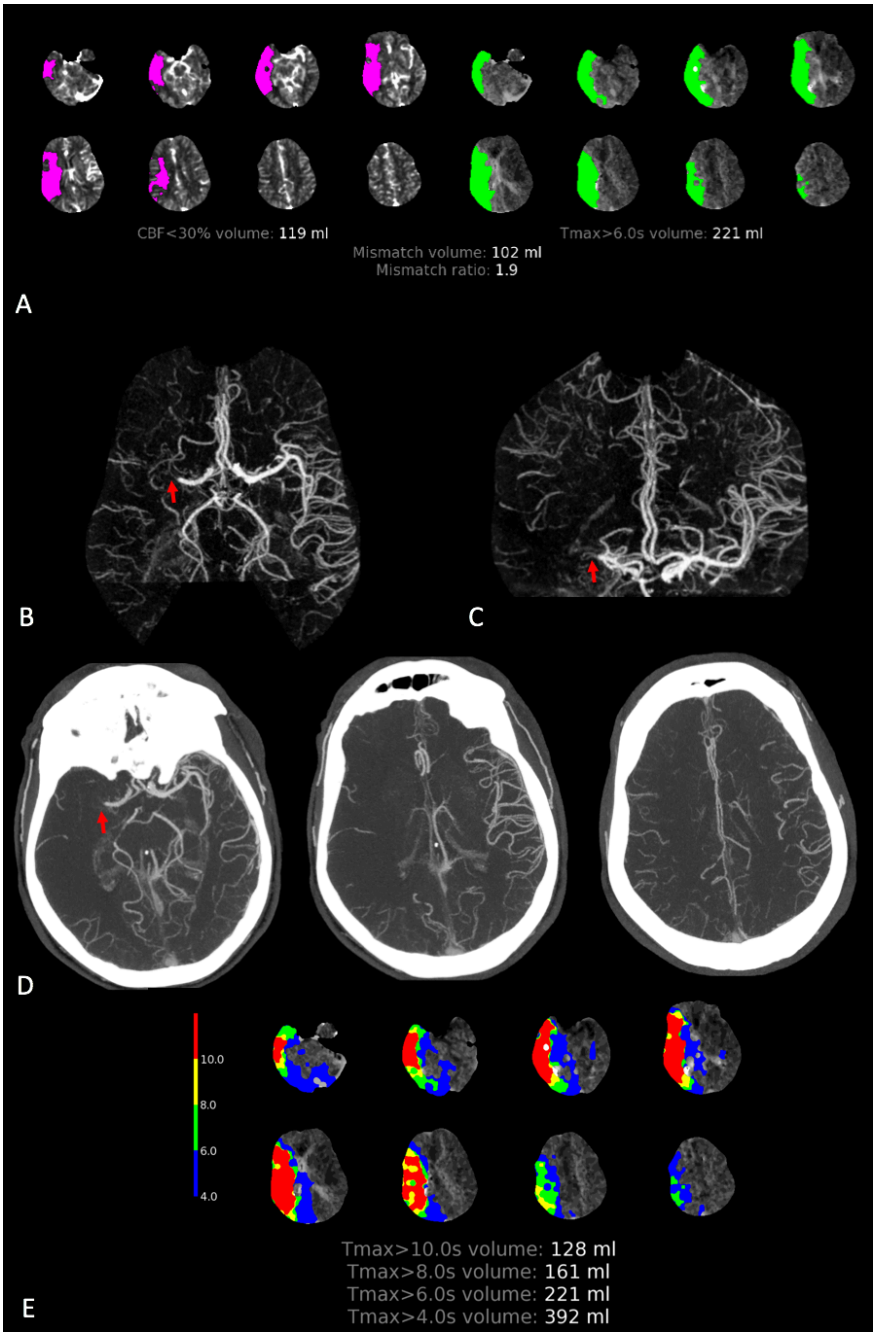

Figure 2-14. *Poor collaterals in a 61 year-old man who presented 6 hours following symptom onset.* ***A.*** *CTP mismatch analysis shows a large infarct core (pink, CBF <30%) of 119 mL and a larger area of critical hypoperfusion (green, Tmax >6seconds).* ***B.*** *Axial and* ***C.*** *Coronal CTA bone-masked maximum intensity projections (MIPS) show occlusion of the right MCA (arrow). There is a paucity of vessels in the ischemic territory, indicating poor leptomeningeal collaterals.* ***D.*** *Axial CTA MIPs also shows a paucity of vessels in the right MCA territory. Poor collaterals are associated with fast infarct progression and likely explain the large infarct in this patient.* ***E.*** *Tmax obtained using CTP. There is a large volume of critically hypoperfused tissue with Tmax >6 seconds (221 mL) in the right MCA territory and also a large volume of tissue with severe Tmax delay >10 seconds (128 mL). The hypoperfusion index is therefore >0.4, in keeping with poor leptomeningeal collaterals.*

A number of investigators have assessed collateral blood flow using CT angiography[188, 204, 207-209]. Single-point (peak arterial phase) CT angiography is now a routine component of the multimodal acute stroke CT protocol. Single-point CTA was used in one investigation to dichotomize collateral status into "good" or "reduced", depending on the degree of visualization of contrast opacification distal to the occlusion[204]. Good collateral status was found to be an independent predictor of a favourable outcome in patients with a mismatch ratio >3. This suggests that collateral status provides additive predictive information regarding tissue fate. This is likely because it indicates the probability and rate of penumbral progression to infarction. The authors concluded that collateral assessment is complementary, rather than an alternative to, CT perfusion since a large mismatch was still prerequisite for a favourable clinical response[204]. Examples of single-phase CTA in patients with good collaterals and poor collaterals are shown in Figures 2-13 and 2-14, respectively.

The ESCAPE trial investigators devised a multi-phase CTA technique with three time points (peak arterial, mid venous and late venous) of contrast-enhanced whole brain images, allowing time-resolved assessment of pial arterial filling using a collateral grading score (Table 2-3)[207].

Table 2-3. *Pial arterial filling (collateral) score using multiphase CT, summarizing the scoring system developed by Menon et al[207].*

Collateral Score	**Pial vessels in ischemic territory in the symptomatic hemisphere (ischemic territory), as compared to contralateral asymptomatic hemisphere**	
	Multi-phase CTA	**Single-phase CTA**
5	Increased or normal prominence and extent	Increased or normal prominence and extent
4	Delay of one phase in filling-in of peripheral vessels, but prominence and extent are the same	Slightly reduced prominence and extent
3	Delay of two phases in filling-in of peripheral vessels; or one-phase delay and significantly reduced number of vessels in the ischemic territory	Moderately reduced prominence and extent
2	Delay of two phases in filling-in of peripheral vessels as well as decreased prominence and extent; or a one-phase delay and some ischemic regions with no visible vessels	Decreased prominence and extent, and regions with no vessels
1	Only a few vessels visible in any phase	Just a few vessels visible
0	No vessels visible in any phase	No visible vessels

Multi-phase CTA collateral grading was compared to CT perfusion mismatch for triage of patients to endovascular therapy. The authors found that the ability to predict clinical outcome using multi-phase CTA was better than for single phase CTA and perfusion CT. Multi-phase CTA was also reported to require a lower radiation dose than CTP. The technique remains to be validated in a broader setting.

Unfortunately, there is no consensus regarding the grading collaterals on CTA, with a wide range of scoring systems in use[209]. While the collateral scoring system devised by the ESCAPE investigators was reported to have a high inter-rater reliability, it is highly subjective and likely to be difficult for inexperienced readers and generalists. It has been suggested that a system that grades the extent and delay of vascular enhancement in the affected territory, rather than the backflow of contrast medium to the occlusion, would be more accurately predictive of tissue fate[209].

ASL is an alternative to angiographic techniques for visualizing and assessing leptomeningeal collaterals, and does not require administration of exogenous contrast agent[210, 211]. As discussed above, arterial transit time is delayed in the presence of an arterial occlusion. Labelled blood is therefore still in transit within proximal arteries and leptomeningeal collaterals at the time that images are acquired using a standard PLD, manifesting as high signal within these structures[210-212]. This intra-arterial high signal, termed *arterial transit artifact* (ATA), is a useful qualitative sign that can alert the radiologist to the presence of a stenosis or occlusion (Figure 2-12) and allow detection of collaterals. It can also enable characterization of collaterals[210, 211]. In one study, ASL collaterals were found to be strongly associated with better neurological outcomes[211]. Multi-delay ASL techniques, acquired using multiple PLDs, allow dynamic assessment of arterial transit artifact at multiple time points and may therefore improve visualization and scoring of leptomeningeal collaterals and allow outcome prediction[196, 203]. The technique showed promise in one study, where leptomeningeal collateral scores were assessed based on visualization of ATA in 55 patients[203]. Patients with moderate or good outcomes following thrombectomy were found to have significantly higher leptomeningeal collateral scores than patients who had poor outcomes[203]. Further investigation is required however, with larger studies, to ascertain the utility of ASL (including multi-delay techniques) for leptomeningeal collateral assessment and outcome prediction.

Collateral status can also be assessed on CTP and DSC-PWI. Tmax is an indirect

measure of the delay of arterial transit time, and arterial transit is more delayed in patients with poor collaterals. It follows that poor collaterals are associated with greater Tmax delay. It has been proposed that collateral status can be quantified based on Tmax, using the hypoperfusion index which is defined as the ratio of the volume of tissue with Tmax greater than 10 seconds to the volume of tissue with Tmax greater than 6 seconds. A hypoperfusion index greater than 0.4 has been shown to be associated with poor collateral status and more rapid infarct progression (Figure 2-14)[213].

2.4.6 The DWI-FLAIR Mismatch

As discussed above, the window for IVT is 4.5 hours. In patients who wake up with a stroke, the exact timing of stroke onset is unknown. In these patients, the time of onset is typically taken as the time last seen well (usually when the patient went to bed) or the midpoint of sleep[83, 103]. MRI shows promise in being able to "time" the onset of stroke in these patients. While ADC reduction due to cytotoxic oedema occurs within minutes of stroke onset, vasogenic oedema, which is manifested as T_2-prolongation, occurs at least 1-4 hours after the onset of infarction[42, 214]. As discussed in section 2.1.3, vasogenic oedema is due to a net increase in extracellular water secondary to BBB leakage, which take longer to develop. Therefore, hyperacute infarcts are not typically visible on T_2-weighted FLAIR sequences[215].

Visualization of the stroke lesion on DWI but not FLAIR, a.k.a. **DWI-FLAIR mismatch**, identified patients within 4.5 hours of stroke onset with a sensitivity of 0.62, specificity of 0.78 and positive predictive value of 0.83[215]. Absence of FLAIR signal can therefore be used as a surrogate for recent stroke onset when the true time of onset is unknown. Limitations of using this technique were the relatively poor sensitivity and only moderate inter-rater agreement for parenchymal FLAIR hyperintensity, which is strongly dependent on windowing. The *Efficacy and Safety of MRI-Based Thrombolysis in Wake-Up Stroke* (WAKE-UP) trial enrolled stroke patients with unknown onset time who had a DWI-FLAIR mismatch[216]. The group who received intravenous alteplase had a significantly better functional outcome than those receiving placebo, however the rate of SIH was also significantly higher (2% versus 0.4% in the placebo arm). Although there is a move towards tissue classification-based patient selection, the time-based information provided by the DWI-FLAIR mismatch may help extend the thrombolysis window for patients with smaller lesions that are difficult to identify

on perfusion imaging.

Table 2-4. *Parameters that are important for AIS treatment decision-making that can be assessed using imaging*

Parameter	Why is it important?	CT	MRI
Arterial occlusion: presence & site	Target for reperfusion therapy. Non-invasive vascular imaging mandatory in workup for thrombectomy	**CTA** (brain & neck - assessment of neck vessel access)	**TOF-MRA**
Intracranial haemorrhage	Contraindicates thrombolysis. Imaging mandated by guidelines to exclude haemorrhage prior to thrombolysis.	**NECT**	**T2*GRE** or SWI, but takes too long in AIS
Infarcted tissue: presence & volume	Increases risk of complication (haemorrhage and malignant oedema); treatment futile if large completed infarct. Imaging recommended to exclude large core prior to thrombectomy in late window.	**NECT:** hypodensity, ASPECTS or **CTP:** reduced CBF (optimal parameter) or CBV	**DWI:** gold standard with unparalleled sensitivity and specificity
Ischaemic penumbra: presence & volume	Purpose of reperfusion is to salvage viable tissue that is critically hypoperfused.	**CTP:** Tmax (optimal), TTP, MTT*	**DSC-PWI:** Tmax (optimal), TTP, MTT **ASL:** CBF, but overestimates penumbra
Collaterals: presence & robustness	Sustain the ischemic penumbra; collateral status determines rate of infarct growth	**CTA:** Single phase or multi-phase **CTP:** hypoperfusion index (Tmax >10s: Tmax >6 s)	**ASL**

*MTT can only be used to predict penumbra if a delay-sensitive deconvolution is used (discussed in chapter 4)

2.4.7 Summary

The introduction of mechanical thrombectomy using stent-retrievers has revolutionized the care of AIS patients. Not only is this treatment highly effective, it has also markedly extended the therapeutic window. Thrombectomy is now the standard-of-care treatment for patients with intracranial LVOs up to 6 hours and can be performed in carefully selected patients up to 24 hours. With this paradigm shift in care has come an increasing reliance on imaging to identify the right patients for treatment (summarized in Table 2-4). In particular, perfusion imaging has played a key role in extending the time window for thrombectomy by allowing tissue-based patient selection; patients with salvageable ischemic penumbra who are likely to benefit from reperfusion can be identified while those with large established infarcts in whom treatment may be harmful or futile can be excluded. As we move increasingly towards tissue-based rather than time-based paradigms for patient selection, work is underway to determine whether the window for IVT can truly be extended and thrombectomy can be performed even beyond 24 hours using perfusion imaging.

2.5. References

1. Sacco RL, Kasner SE, Broderick JP, Caplan LR, Connors JJ, Culebras A, et al. An updated definition of stroke for the 21st century: A statement for healthcare professionals from the american heart association/american stroke association. *Stroke*. 2013;44:2064-2089
2. Grysiewicz RA, Thomas K, Pandey DK. Epidemiology of ischemic and hemorrhagic stroke: Incidence, prevalence, mortality, and risk factors. *Neurol Clin*. 2008;26:871-895, vii
3. The world health organization monica project (monitoring trends and determinants in cardiovascular disease): A major international collaboration. Who monica project principal investigators. *J Clin Epidemiol*. 1988;41:105-114
4. Rosamond W, Flegal K, Furie K, Go A, Greenlund K, Haase N, et al. Heart disease and stroke statistics--2008 update: A report from the american heart association statistics committee and stroke statistics subcommittee. *Circulation*. 2008;117:e25-146
5. Mohr JP, Albers GW, Amarenco P, Babikian VL, Biller J, Brey RL, et al. American heart association prevention conference. Iv. Prevention and rehabilitation of stroke. Etiology of stroke. *Stroke*. 1997;28:1501-1506

6. Frosch MP AD, de Girolami U. The central nervous system. In: Kumar V. AAaFN, ed. *Robbins and cotran: Pathologic basis of disease*. Philadelphia, Pennsylvania: Elsevier; 2005:1347-1420.
7. Jha MK, Morrison BM. Glia-neuron energy metabolism in health and diseases: New insights into the role of nervous system metabolic transporters. *Exp Neurol*. 2018;309:23-31
8. Jones SC, Greenberg JH, Dann R, Robinson GD, Jr., Kushner M, Alavi A, et al. Cerebral blood flow with the continuous infusion of oxygen-15-labeled water. *J Cereb Blood Flow Metab*. 1985;5:566-575
9. Kumar V. AAaFN. *Robbins and cotran: Pathological basis of disease*. Philadelphia, Pennsylvania: Elsevier; 2005.
10. Derdeyn CP, Grubb RL, Jr., Powers WJ. Cerebral hemodynamic impairment: Methods of measurement and association with stroke risk. *Neurology*. 1999;53:251-259
11. Derdeyn CP, Videen TO, Yundt KD, Fritsch SM, Carpenter DA, Grubb RL, et al. Variability of cerebral blood volume and oxygen extraction: Stages of cerebral haemodynamic impairment revisited. *Brain*. 2002;125:595-607
12. Grubb RL, Jr., Derdeyn CP, Fritsch SM, Carpenter DA, Yundt KD, Videen TO, et al. Importance of hemodynamic factors in the prognosis of symptomatic carotid occlusion. *JAMA*. 1998;280:1055-1060
13. Powers WJ. Cerebral hemodynamics in ischemic cerebrovascular disease. *Ann Neurol*. 1991;29:231-240
14. Powers WJ, Grubb RL, Jr., Baker RP, Mintun MA, Raichle ME. Regional cerebral blood flow and metabolism in reversible ischemia due to vasospasm. Determination by positron emission tomography. *J Neurosurg*. 1985;62:539-546
15. Powers WJ, Grubb RL, Jr., Darriet D, Raichle ME. Cerebral blood flow and cerebral metabolic rate of oxygen requirements for cerebral function and viability in humans. *J Cereb Blood Flow Metab*. 1985;5:600-608
16. Powers WJ, Press GA, Grubb RL, Jr., Gado M, Raichle ME. The effect of hemodynamically significant carotid artery disease on the hemodynamic status of the cerebral circulation. *Ann Intern Med*. 1987;106:27-34
17. Rapela CE, Green HD. Autoregulation of canine cerebral blood flow. *Circ Res*. 1964;15:SUPPL:205-212
18. Kety SS, King BD, Horvath SM, Jeffers WS, Hafkenschiel JH. The effects of an acute reduction in blood pressure by means of differential spinal sympathetic block on the cerebral circulation of hypertensive patients. *J Clin Invest*. 1950;29:402-407

19. Baron JC, Bousser MG, Rey A, Guillard A, Comar D, Castaigne P. Reversal of focal "misery-perfusion syndrome" by extra-intracranial arterial bypass in hemodynamic cerebral ischemia. A case study with 15o positron emission tomography. *Stroke*. 1981;12:454-459
20. Sette G, Baron JC, Mazoyer B, Levasseur M, Pappata S, Crouzel C. Local brain haemodynamics and oxygen metabolism in cerebrovascular disease. Positron emission tomography. *Brain*. 1989;112 (Pt 4):931-951
21. Nemoto EM, Yonas H, Chang Y. Stages and thresholds of hemodynamic failure. *Stroke*. 2003;34:2-3
22. Astrup J, Siesjo BK, Symon L. Thresholds in cerebral ischemia - the ischemic penumbra. *Stroke*. 1981;12:723-725
23. Heiss WD, Rosner G. Functional recovery of cortical neurons as related to degree and duration of ischemia. *Ann Neurol*. 1983;14:294-301
24. Jones TH, Morawetz RB, Crowell RM, Marcoux FW, FitzGibbon SJ, DeGirolami U, et al. Thresholds of focal cerebral ischemia in awake monkeys. *J Neurosurg*. 1981;54:773-782
25. Astrup J, Symon L, Branston NM, Lassen NA. Cortical evoked potential and extracellular k+ and h+ at critical levels of brain ischemia. *Stroke*. 1977;8:51-57
26. Bardutzky J, Shen Q, Henninger N, Schwab S, Duong TQ, Fisher M. Characterizing tissue fate after transient cerebral ischemia of varying duration using quantitative diffusion and perfusion imaging. *Stroke*. 2007;38:1336-1344
27. Lansberg MG, Straka M, Kemp S, Mlynash M, Wechsler LR, Jovin TG, et al. Mri profile and response to endovascular reperfusion after stroke (defuse 2): A prospective cohort study. *Lancet Neurol*. 2012;11:860-867
28. Baron JC. Perfusion thresholds in human cerebral ischemia: Historical perspective and therapeutic implications. *Cerebrovasc Dis*. 2001;11 Suppl 1:2-8
29. Leech PJ, Fitch W, Barker J, Miller JD. Proceedings: Operative measurements of cerebral blood-flow (c.B.F.) and internal carotid artery (i.C.A.) pressure during carotid ligation. *Br J Surg*. 1973;60:909-910
30. Albers GW. Late window paradox. *Stroke*. 2018;49:768-771
31. Kluytmans M, van der Grond J, van Everdingen KJ, Klijn CJ, Kappelle LJ, Viergever MA. Cerebral hemodynamics in relation to patterns of collateral flow. *Stroke*. 1999;30:1432-1439
32. Liebeskind DS. Collateral circulation. *Stroke*. 2003;34:2279-2284

33. MacKenzie ET, Farrar JK, Fitch W, Graham DI, Gregory PC, Harper AM. Effects of hemorrhagic hypotension on the cerebral circulation. I. Cerebral blood flow and pial arteriolar caliber. *Stroke*. 1979;10:711-718
34. Rocha M, Jovin TG. Fast versus slow progressors of infarct growth in large vessel occlusion stroke: Clinical and research implications. *Stroke*. 2017;48:2621-2627
35. Dimmick SJ, Faulder KC. Normal variants of the cerebral circulation at multidetector ct angiography. *Radiographics*. 2009;29:1027-1043
36. Goyal M, Menon BK, Krings T, Patil S, Qazi E, McTaggart RA, et al. What constitutes the m1 segment of the middle cerebral artery? *J Neurointerv Surg*. 2016;8:1273-1277
37. Saver JL. Time is brain--quantified. *Stroke*. 2006;37:263-266
38. Sandoval KE, Witt KA. Blood-brain barrier tight junction permeability and ischemic stroke. *Neurobiol Dis*. 2008;32:200-219
39. Daneman R, Prat A. The blood-brain barrier. *Cold Spring Harb Perspect Biol*. 2015;7:a020412
40. Lin K, Kazmi KS, Law M, Babb J, Peccerelli N, Pramanik BK. Measuring elevated microvascular permeability and predicting hemorrhagic transformation in acute ischemic stroke using first-pass dynamic perfusion ct imaging. *AJNR Am J Neuroradiol*. 2007;28:1292-1298
41. Lyden PD, Zivin JA. Hemorrhagic transformation after cerebral ischemia: Mechanisms and incidence. *Cerebrovasc Brain Metab Rev*. 1993;5:1-16
42. Hoehn-Berlage M, Eis M, Back T, Kohno K, Yamashita K. Changes of relaxation times (t1, t2) and apparent diffusion coefficient after permanent middle cerebral artery occlusion in the rat: Temporal evolution, regional extent, and comparison with histology. *Magn Reson Med*. 1995;34:824-834
43. Cognard C, Casasco A, Toevi M, Houdart E, Chiras J, Merland JJ. Dural arteriovenous fistulas as a cause of intracranial hypertension due to impairment of cranial venous outflow. *J Neurol Neurosurg Psychiatry*. 1998;65:308-316
44. Bang OY, Lee MJ, Ryoo S, Kim SJ, Kim JW. Patent foramen ovale and stroke-current status. *J Stroke*. 2015;17:229-237
45. Banerjee C, Chimowitz MI. Stroke caused by atherosclerosis of the major intracranial arteries. *Circ Res*. 2017;120:502-513
46. Chimowitz MI, Lynn MJ, Howlett-Smith H, Stern BJ, Hertzberg VS, Frankel MR, et al. Comparison of warfarin and aspirin for symptomatic intracranial arterial stenosis. *N Engl J Med*. 2005;352:1305-1316
47. North American Symptomatic Carotid Endarterectomy Trial C, Barnett HJM, Taylor DW, Haynes RB, Sackett DL, Peerless SJ, et al. Beneficial

effect of carotid endarterectomy in symptomatic patients with high-grade carotid stenosis. *N Engl J Med*. 1991;325:445-453

48. Adams HP, Jr., Bendixen BH, Kappelle LJ, Biller J, Love BB, Gordon DL, et al. Classification of subtype of acute ischemic stroke. Definitions for use in a multicenter clinical trial. Toast. Trial of org 10172 in acute stroke treatment. *Stroke*. 1993;24:35-41
49. Yew KS, Cheng EM. Diagnosis of acute stroke. *Am Fam Physician*. 2015;91:528-536
50. Powers WJ, Rabinstein AA, Ackerson T, Adeoye OM, Bambakidis NC, Becker K, et al. 2018 guidelines for the early management of patients with acute ischemic stroke: A guideline for healthcare professionals from the american heart association/american stroke association. *Stroke*. 2018;49:e46-e110
51. Lyden P, Raman R, Liu L, Emr M, Warren M, Marler J. National institutes of health stroke scale certification is reliable across multiple venues. *Stroke*. 2009;40:2507-2511
52. Fonarow GC, Saver JL, Smith EE, Broderick JP, Kleindorfer DO, Sacco RL, et al. Relationship of national institutes of health stroke scale to 30-day mortality in medicare beneficiaries with acute ischemic stroke. *J Am Heart Assoc*. 2012;1:42-50
53. Broderick JP, Adeoye O, Elm J. Evolution of the modified rankin scale and its use in future stroke trials. *Stroke*. 2017;48:2007-2012
54. National Institute of Neurological D, Stroke rt PASSG. Tissue plasminogen activator for acute ischemic stroke. *N Engl J Med*. 1995;333:1581-1587
55. Clark WM, Albers GW, Madden KP, Hamilton S. The rtpa (alteplase) 0- to 6-hour acute stroke trial, part a (a0276g) : Results of a double-blind, placebo-controlled, multicenter study. Thromblytic therapy in acute ischemic stroke study investigators. *Stroke*. 2000;31:811-816
56. Clark WM, Wissman S, Albers GW, Jhamandas JH, Madden KP, Hamilton S. Recombinant tissue-type plasminogen activator (alteplase) for ischemic stroke 3 to 5 hours after symptom onset. The atlantis study: A randomized controlled trial. Alteplase thrombolysis for acute noninterventional therapy in ischemic stroke. *JAMA*. 1999;282:2019-2026
57. Hacke W, Kaste M, Fieschi C, Toni D, Lesaffre E, von Kummer R, et al. Intravenous thrombolysis with recombinant tissue plasminogen activator for acute hemispheric stroke. The european cooperative acute stroke study (ecass). *JAMA*. 1995;274:1017-1025
58. Hacke W, Kaste M, Fieschi C, von Kummer R, Davalos A, Meier D, et al. Randomised double-blind placebo-controlled trial of thrombolytic therapy

with intravenous alteplase in acute ischaemic stroke (ecass ii). Second european-australasian acute stroke study investigators. *Lancet*. 1998;352:1245-1251

59. Albers GW, Clark WM, Madden KP, Hamilton SA. Atlantis trial: Results for patients treated within 3 hours of stroke onset. Alteplase thrombolysis for acute noninterventional therapy in ischemic stroke. *Stroke*. 2002;33:493-495
60. Hacke W, Donnan G, Fieschi C, Kaste M, von Kummer R, Broderick JP, et al. Association of outcome with early stroke treatment: Pooled analysis of atlantis, ecass, and ninds rt-pa stroke trials. *Lancet*. 2004;363:768-774
61. Wardlaw JM, Murray V, Berge E, del Zoppo G, Sandercock P, Lindley RL, et al. Recombinant tissue plasminogen activator for acute ischaemic stroke: An updated systematic review and meta-analysis. *Lancet*. 2012;379:2364-2372
62. Wardlaw JM, Murray V, Berge E, del Zoppo GJ. Thrombolysis for acute ischaemic stroke. *Cochrane Database Syst Rev*. 2014:CD000213
63. Hacke W, Kaste M, Bluhmki E, Brozman M, Davalos A, Guidetti D, et al. Thrombolysis with alteplase 3 to 4.5 hours after acute ischemic stroke. *N Engl J Med*. 2008;359:1317-1329
64. Kleindorfer D, Lindsell CJ, Brass L, Koroshetz W, Broderick JP. National us estimates of recombinant tissue plasminogen activator use: Icd-9 codes substantially underestimate. *Stroke*. 2008;39:924-928
65. Qureshi AI, Kirmani JF, Sayed MA, Safdar A, Ahmed S, Ferguson R, et al. Time to hospital arrival, use of thrombolytics, and in-hospital outcomes in ischemic stroke. *Neurology*. 2005;64:2115-2120
66. Riedel CH, Zimmermann P, Jensen-Kondering U, Stingele R, Deuschl G, Jansen O. The importance of size: Successful recanalization by intravenous thrombolysis in acute anterior stroke depends on thrombus length. *Stroke*. 2011;42:1775-1777
67. Saqqur M, Uchino K, Demchuk AM, Molina CA, Garami Z, Calleja S, et al. Site of arterial occlusion identified by transcranial doppler predicts the response to intravenous thrombolysis for stroke. *Stroke*. 2007;38:948-954
68. Bhatia R, Hill MD, Shobha N, Menon B, Bal S, Kochar P, et al. Low rates of acute recanalization with intravenous recombinant tissue plasminogen activator in ischemic stroke: Real-world experience and a call for action. *Stroke*. 2010;41:2254-2258
69. Lansberg MG, Schrooten M, Bluhmki E, Thijs VN, Saver JL. Treatment time-specific number needed to treat estimates for tissue plasminogen

activator therapy in acute stroke based on shifts over the entire range of the modified rankin scale. *Stroke*. 2009;40:2079-2084

70. Intracerebral hemorrhage after intravenous t-pa therapy for ischemic stroke. The ninds t-pa stroke study group. *Stroke*. 1997;28:2109-2118
71. Malhotra K, Gornbein J, Saver JL. Ischemic strokes due to large-vessel occlusions contribute disproportionately to stroke-related dependence and death: A review. *Front Neurol*. 2017;8:651
72. Zeumer H, Hacke W, Ringelstein EB. Local intraarterial thrombolysis in vertebrobasilar thromboembolic disease. *AJNR Am J Neuroradiol*. 1983;4:401-404
73. Nenci GG, Gresele P, Taramelli M, Agnelli G, Signorini E. Thrombolytic therapy for thromboembolism of vertebrobasilar artery. *Angiology*. 1983;34:561-571
74. Furlan A, Higashida R, Wechsler L, Gent M, Rowley H, Kase C, et al. Intra-arterial prourokinase for acute ischemic stroke. The proact ii study: A randomized controlled trial. Prolyse in acute cerebral thromboembolism. *JAMA*. 1999;282:2003-2011
75. Felten RP, Ogden NR, Pena C, Provost MC, Schlosser MJ, Witten CM. The food and drug administration medical device review process: Clearance of a clot retriever for use in ischemic stroke. *Stroke*. 2005;36:404-406
76. Nogueira RG, Liebeskind DS, Sung G, Duckwiler G, Smith WS, Merci, et al. Predictors of good clinical outcomes, mortality, and successful revascularization in patients with acute ischemic stroke undergoing thrombectomy: Pooled analysis of the mechanical embolus removal in cerebral ischemia (merci) and multi merci trials. *Stroke*. 2009;40:3777-3783
77. Bose A, Henkes H, Alfke K, Reith W, Mayer TE, Berlis A, et al. The penumbra system: A mechanical device for the treatment of acute stroke due to thromboembolism. *AJNR Am J Neuroradiol*. 2008;29:1409-1413
78. Broderick JP, Palesch YY, Demchuk AM, Yeatts SD, Khatri P, Hill MD, et al. Endovascular therapy after intravenous t-pa versus t-pa alone for stroke. *N Engl J Med*. 2013;368:893-903
79. Ciccone A, Valvassori L, Nichelatti M, Sgoifo A, Ponzio M, Sterzi R, et al. Endovascular treatment for acute ischemic stroke. *N Engl J Med*. 2013;368:904-913
80. Kidwell CS, Jahan R, Gornbein J, Alger JR, Nenov V, Ajani Z, et al. A trial of imaging selection and endovascular treatment for ischemic stroke. *N Engl J Med*. 2013;368:914-923
81. Demchuk AM, Goyal M, Yeatts SD, Carrozzella J, Foster LD, Qazi E, et al. Recanalization and clinical outcome of occlusion sites at baseline ct

angiography in the interventional management of stroke iii trial. *Radiology*. 2014;273:202-210

82. Yoo AJ, Zaidat OO, Chaudhry ZA, Berkhemer OA, Gonzalez RG, Goyal M, et al. Impact of pretreatment noncontrast ct alberta stroke program early ct score on clinical outcome after intra-arterial stroke therapy. *Stroke*. 2014;45:746-751
83. Albers GW, Marks MP, Kemp S, Christensen S, Tsai JP, Ortega-Gutierrez S, et al. Thrombectomy for stroke at 6 to 16 hours with selection by perfusion imaging. *N Engl J Med*. 2018;378:708-718
84. Berkhemer OA, Fransen PS, Beumer D, van den Berg LA, Lingsma HF, Yoo AJ, et al. A randomized trial of intraarterial treatment for acute ischemic stroke. *N Engl J Med*. 2015;372:11-20
85. Campbell BC, Mitchell PJ, Kleinig TJ, Dewey HM, Churilov L, Yassi N, et al. Endovascular therapy for ischemic stroke with perfusion-imaging selection. *N Engl J Med*. 2015;372:1009-1018
86. Goyal M, Demchuk AM, Menon BK, Eesa M, Rempel JL, Thornton J, et al. Randomized assessment of rapid endovascular treatment of ischemic stroke. *N Engl J Med*. 2015;372:1019-1030
87. Jovin TG, Chamorro A, Cobo E, de Miquel MA, Molina CA, Rovira A, et al. Thrombectomy within 8 hours after symptom onset in ischemic stroke. *N Engl J Med*. 2015;372:2296-2306
88. Nogueira RG, Jadhav AP, Haussen DC, Bonafe A, Budzik RF, Bhuva P, et al. Thrombectomy 6 to 24 hours after stroke with a mismatch between deficit and infarct. *N Engl J Med*. 2018;378:11-21
89. Saver JL, Goyal M, Bonafe A, Diener HC, Levy EI, Pereira VM, et al. Stent-retriever thrombectomy after intravenous t-pa vs. T-pa alone in stroke. *N Engl J Med*. 2015;372:2285-2295
90. Nogueira RG, Lutsep HL, Gupta R, Jovin TG, Albers GW, Walker GA, et al. Trevo versus merci retrievers for thrombectomy revascularisation of large vessel occlusions in acute ischaemic stroke (trevo 2): A randomised trial. *Lancet*. 2012;380:1231-1240
91. Saver JL, Jahan R, Levy EI, Jovin TG, Baxter B, Nogueira RG, et al. Solitaire flow restoration device versus the merci retriever in patients with acute ischaemic stroke (swift): A randomised, parallel-group, non-inferiority trial. *Lancet*. 2012;380:1241-1249
92. Goyal M, Menon BK, van Zwam WH, Dippel DW, Mitchell PJ, Demchuk AM, et al. Endovascular thrombectomy after large-vessel ischaemic stroke: A meta-analysis of individual patient data from five randomised trials. *Lancet*. 2016;387:1723-1731

93. Powers WJ, Derdeyn CP, Biller J, Coffey CS, Hoh BL, Jauch EC, et al. 2015 american heart association/american stroke association focused update of the 2013 guidelines for the early management of patients with acute ischemic stroke regarding endovascular treatment: A guideline for healthcare professionals from the american heart association/american stroke association. *Stroke*. 2015;46:3020-3035
94. Roman LS, Menon BK, Blasco J, Hernandez-Perez M, Davalos A, Majoie C, et al. Imaging features and safety and efficacy of endovascular stroke treatment: A meta-analysis of individual patient-level data. *Lancet Neurol*. 2018;17:895-904
95. Sarraj A, Hassan AE, Savitz S, Sitton C, Grotta J, Chen P, et al. Outcomes of endovascular thrombectomy vs medical management alone in patients with large ischemic cores: A secondary analysis of the optimizing patient's selection for endovascular treatment in acute ischemic stroke (select) study. *JAMA Neurol*. 2019
96. Schonewille WJ, Wijman CA, Michel P, Rueckert CM, Weimar C, Mattle HP, et al. Treatment and outcomes of acute basilar artery occlusion in the basilar artery international cooperation study (basics): A prospective registry study. *Lancet Neurol*. 2009;8:724-730
97. Kang DH, Jung C, Yoon W, Kim SK, Baek BH, Kim JT, et al. Endovascular thrombectomy for acute basilar artery occlusion: A multicenter retrospective observational study. *J Am Heart Assoc*. 2018;7
98. Kuang H, Najm M, Chakraborty D, Maraj N, Sohn SI, Goyal M, et al. Automated aspects on noncontrast ct scans in patients with acute ischemic stroke using machine learning. *AJNR Am J Neuroradiol*. 2019;40:33-38
99. Sarraj A, Sangha N, Hussain MS, Wisco D, Vora N, Elijovich L, et al. Endovascular therapy for acute ischemic stroke with occlusion of the middle cerebral artery m2 segment. *JAMA Neurol*. 2016;73:1291-1296
100. Grossberg JA, Rebello LC, Haussen DC, Bouslama M, Bowen M, Barreira CM, et al. Beyond large vessel occlusion strokes: Distal occlusion thrombectomy. *Stroke*. 2018;49:1662-1668
101. Rha JH, Saver JL. The impact of recanalization on ischemic stroke outcome: A meta-analysis. *Stroke*. 2007;38:967-973
102. Jovin T MM, Bammer R. Acute stroke: Intra-arterial and intravenous treatment options. In: R B, ed. *Mr and ct perfusion and pharmakokinetic imaging*. Philadelphia: Wolters Kluwer; 2016.
103. Ma H, Campbell BCV, Parsons MW, Churilov L, Levi CR, Hsu C, et al. Thrombolysis guided by perfusion imaging up to 9 hours after onset of stroke. *N Engl J Med*. 2019;380:1795-1803

104. Campbell BCV, Mitchell PJ, Churilov L, Yassi N, Kleinig TJ, Dowling RJ, et al. Tenecteplase versus alteplase before thrombectomy for ischemic stroke. *N Engl J Med*. 2018;378:1573-1582
105. Coutts SB, Berge E, Campbell BC, Muir KW, Parsons MW. Tenecteplase for the treatment of acute ischemic stroke: A review of completed and ongoing randomized controlled trials. *Int J Stroke*. 2018;13:885-892
106. Tanswell P, Modi N, Combs D, Danays T. Pharmacokinetics and pharmacodynamics of tenecteplase in fibrinolytic therapy of acute myocardial infarction. *Clin Pharmacokinet*. 2002;41:1229-1245
107. Arnould MC GC, Peeters A, Cosnard G, Duprez TP. Comparison of ct and three mr sequences for detecting and categorizing early (48 hours) hemorrhagic transformation in hyperacute ischemic stroke. *AJNR*. 2004;25:939–944
108. Kidwell CS, Chalela JA, Saver JL, Starkman S, Hill MD, Demchuk AM, et al. Comparison of mri and ct for detection of acute intracerebral hemorrhage. *JAMA*. 2004;292:1823-1830
109. Chalela JA, Kang DW, Luby M, Ezzeddine M, Latour LL, Todd JW, et al. Early magnetic resonance imaging findings in patients receiving tissue plasminogen activator predict outcome: Insights into the pathophysiology of acute stroke in the thrombolysis era. *Ann Neurol*. 2004;55:105-112
110. Wardlaw JM, Seymour J, Cairns J, Keir S, Lewis S, Sandercock P. Immediate computed tomography scanning of acute stroke is cost-effective and improves quality of life. *Stroke*. 2004;35:2477-2483
111. Wintermark M, Luby M, Bornstein NM, Demchuk A, Fiehler J, Kudo K, et al. International survey of acute stroke imaging used to make revascularization treatment decisions. *Int J Stroke*. 2015;10:759-762
112. Lansberg MG, Thijs VN, Bammer R, Kemp S, Wijman CA, Marks MP, et al. Risk factors of symptomatic intracerebral hemorrhage after tpa therapy for acute stroke. *Stroke*. 2007;38:2275-2278
113. Olivot JM, Mosimann PJ, Labreuche J, Inoue M, Meseguer E, Desilles JP, et al. Impact of diffusion-weighted imaging lesion volume on the success of endovascular reperfusion therapy. *Stroke*. 2013;44:2205-2211
114. Davis SM, Donnan GA, Parsons MW, Levi C, Butcher KS, Peeters A, et al. Effects of alteplase beyond 3 h after stroke in the echoplanar imaging thrombolytic evaluation trial (epithet): A placebo-controlled randomised trial. *Lancet Neurol*. 2008;7:299-309
115. Thijs VN, Lansberg MG, Beaulieu C, Marks MP, Moseley ME, Albers GW. Is early ischemic lesion volume on diffusion-weighted imaging an

independent predictor of stroke outcome? A multivariable analysis. *Stroke*. 2000;31:2597-2602

116. Campbell BCV, Majoie C, Albers GW, Menon BK, Yassi N, Sharma G, et al. Penumbral imaging and functional outcome in patients with anterior circulation ischaemic stroke treated with endovascular thrombectomy versus medical therapy: A meta-analysis of individual patient-level data. *Lancet Neurol*. 2019;18:46-55
117. Saver JL, Goyal M, van der Lugt A, Menon BK, Majoie CB, Dippel DW, et al. Time to treatment with endovascular thrombectomy and outcomes from ischemic stroke: A meta-analysis. *JAMA*. 2016;316:1279-1288
118. Bekelis K, Missios S, Coy S, Mayerson B, MacKenzie TA. Emergency medical services for acute ischemic stroke: Hub-and-spoke model versus exclusive care in comprehensive centers. *J Clin Neurosci*. 2019;60:12-16
119. Moynihan B, Davis D, Pereira A, Cloud G, Markus HS. Delivering regional thrombolysis via a hub-and-spoke model. *J R Soc Med*. 2010;103:363-369
120. Fiehler J, Albers GW, Boulanger JM, Derex L, Gass A, Hjort N, et al. Bleeding risk analysis in stroke imaging before thrombolysis (brasil): Pooled analysis of t2*-weighted magnetic resonance imaging data from 570 patients. *Stroke*. 2007;38:2738-2744
121. von Kummer R, Broderick JP, Campbell BC, Demchuk A, Goyal M, Hill MD, et al. The heidelberg bleeding classification: Classification of bleeding events after ischemic stroke and reperfusion therapy. *Stroke*. 2015;46:2981-2986
122. del Zoppo GJ, von Kummer R, Hamann GF. Ischaemic damage of brain microvessels: Inherent risks for thrombolytic treatment in stroke. *J Neurol Neurosurg Psychiatry*. 1998;65:1-9
123. Berger C, Fiorelli M, Steiner T, Schabitz WR, Bozzao L, Bluhmki E, et al. Hemorrhagic transformation of ischemic brain tissue: Asymptomatic or symptomatic? *Stroke*. 2001;32:1330-1335
124. Fiorelli M, Bastianello S, von Kummer R, del Zoppo GJ, Larrue V, Lesaffre E, et al. Hemorrhagic transformation within 36 hours of a cerebral infarct: Relationships with early clinical deterioration and 3-month outcome in the european cooperative acute stroke study i (ecass i) cohort. *Stroke*. 1999;30:2280-2284
125. Derex L, Hermier M, Adeleine P, Pialat JB, Wiart M, Berthezene Y, et al. Clinical and imaging predictors of intracerebral haemorrhage in stroke patients treated with intravenous tissue plasminogen activator. *J Neurol Neurosurg Psychiatry*. 2005;76:70-75

126. Campbell BC, Christensen S, Butcher KS, Gordon I, Parsons MW, Desmond PM, et al. Regional very low cerebral blood volume predicts hemorrhagic transformation better than diffusion-weighted imaging volume and thresholded apparent diffusion coefficient in acute ischemic stroke. *Stroke*. 2010;41:82-88
127. Yassi N, Parsons MW, Christensen S, Sharma G, Bivard A, Donnan GA, et al. Prediction of poststroke hemorrhagic transformation using computed tomography perfusion. *Stroke*. 2013;44:3039-3043
128. Dechambre SD, Duprez T, Grandin CB, Lecouvet FE, Peeters A, Cosnard G. High signal in cerebrospinal fluid mimicking subarachnoid haemorrhage on flair following acute stroke and intravenous contrast medium. *Neuroradiology*. 2000;42:608-611
129. Warach S, Latour LL. Evidence of reperfusion injury, exacerbated by thrombolytic therapy, in human focal brain ischemia using a novel imaging marker of early blood-brain barrier disruption. *Stroke*. 2004;35:2659-2661
130. Latour LL, Kang DW, Ezzeddine MA, Chalela JA, Warach S. Early blood-brain barrier disruption in human focal brain ischemia. *Ann Neurol*. 2004;56:468-477
131. Dankbaar JW, Hom J, Schneider T, Cheng SC, Lau BC, van der Schaaf I, et al. Dynamic perfusion ct assessment of the blood-brain barrier permeability: First pass versus delayed acquisition. *AJNR Am J Neuroradiol*. 2008;29:1671-1676
132. Hom J, Dankbaar JW, Schneider T, Cheng SC, Bredno J, Wintermark M. Optimal duration of acquisition for dynamic perfusion ct assessment of blood-brain barrier permeability using the patlak model. *AJNR Am J Neuroradiol*. 2009;30:1366-1370
133. Thornhill RE, Chen S, Rammo W, Mikulis DJ, Kassner A. Contrast-enhanced mr imaging in acute ischemic stroke: T2* measures of blood-brain barrier permeability and their relationship to t1 estimates and hemorrhagic transformation. *AJNR Am J Neuroradiol*. 2010;31:1015-1022
134. Patlak CS, Blasberg RG, Fenstermacher JD. Graphical evaluation of blood-to-brain transfer constants from multiple-time uptake data. *J Cereb Blood Flow Metab*. 1983;3:1-7
135. Tofts PS, Brix G, Buckley DL, Evelhoch JL, Henderson E, Knopp MV, et al. Estimating kinetic parameters from dynamic contrast-enhanced t(1)-weighted mri of a diffusable tracer: Standardized quantities and symbols. *J Magn Reson Imaging*. 1999;10:223-232

136. Kassner A, Roberts T, Taylor K, Silver F, Mikulis D. Prediction of hemorrhage in acute ischemic stroke using permeability mr imaging. *AJNR Am J Neuroradiol*. 2005;26:2213-2217
137. Leigh R, Jen SS, Hillis AE, Krakauer JW, Barker PB, Stir, et al. Pretreatment blood-brain barrier damage and post-treatment intracranial hemorrhage in patients receiving intravenous tissue-type plasminogen activator. *Stroke*. 2014;45:2030-2035
138. Campbell BC, Yassi N, Ma H, Sharma G, Salinas S, Churilov L, et al. Imaging selection in ischemic stroke: Feasibility of automated ct-perfusion analysis. *Int J Stroke*. 2015;10:51-54
139. Kunz WG, Fabritius MP, Sommer WH, Hohne C, Scheffler P, Rotkopf LT, et al. Effect of stroke thrombolysis predicted by distal vessel occlusion detection. *Neurology*. 2018;90:e1742-e1750
140. Mair G, von Kummer R, Adami A, White PM, Adams ME, Yan B, et al. Arterial obstruction on computed tomographic or magnetic resonance angiography and response to intravenous thrombolytics in ischemic stroke. *Stroke*. 2017;48:353-360
141. Becks MJ, Manniesing R, Vister J, Pegge SAH, Steens SCA, van Dijk EJ, et al. Brain ct perfusion improves intracranial vessel occlusion detection on ct angiography. *J Neuroradiol*. 2018
142. Smit EJ, Vonken EJ, Meijer FJ, Dankbaar JW, Horsch AD, van Ginneken B, et al. Timing-invariant ct angiography derived from ct perfusion imaging in acute stroke: A diagnostic performance study. *AJNR Am J Neuroradiol*. 2015;36:1834-1838
143. Smit EJ, Vonken EJ, van der Schaaf IC, Mendrik AM, Dankbaar JW, Horsch AD, et al. Timing-invariant reconstruction for deriving high-quality ct angiographic data from cerebral ct perfusion data. *Radiology*. 2012;263:216-225
144. Campbell BC, Purushotham A, Christensen S, Desmond PM, Nagakane Y, Parsons MW, et al. The infarct core is well represented by the acute diffusion lesion: Sustained reversal is infrequent. *J Cereb Blood Flow Metab*. 2012;32:50-56
145. Gill R, Sibson NR, Hatfield RH, Burdett NG, Carpenter TA, Hall LD, et al. A comparison of the early development of ischaemic damage following permanent middle cerebral artery occlusion in rats as assessed using magnetic resonance imaging and histology. *J Cereb Blood Flow Metab*. 1995;15:1-11

146. Wheeler HM, Mlynash M, Inoue M, Tipirneni A, Liggins J, Zaharchuk G, et al. Early diffusion-weighted imaging and perfusion-weighted imaging lesion volumes forecast final infarct size in defuse 2. *Stroke*. 2013;44:681-685
147. Gonzalez RG, Schaefer PW, Buonanno FS, Schwamm LH, Budzik RF, Rordorf G, et al. Diffusion-weighted mr imaging: Diagnostic accuracy in patients imaged within 6 hours of stroke symptom onset. *Radiology*. 1999;210:155-162
148. Kumar V. AAaFN. General pathology. In: Kumar V. AAaFN, ed. *Robbins and cotran: Pathological basis of disease* Philadelphia, Pennsylvania: Elsevier; 2005.
149. Back T, Hoehn-Berlage M, Kohno K, Hossmann KA. Diffusion nuclear magnetic resonance imaging in experimental stroke. Correlation with cerebral metabolites. *Stroke*. 1994;25:494-500
150. Dardzinski BJ, Sotak CH, Fisher M, Hasegawa Y, Li L, Minematsu K. Apparent diffusion coefficient mapping of experimental focal cerebral ischemia using diffusion-weighted echo-planar imaging. *Magn Reson Med*. 1993;30:318-325
151. Helpern JA, Dereski MO, Knight RA, Ordidge RJ, Chopp M, Qing ZX. Histopathological correlations of nuclear magnetic resonance imaging parameters in experimental cerebral ischemia. *Magn Reson Imaging*. 1993;11:241-246
152. Li TQ, Chen ZG, Hindmarsh T. Diffusion-weighted mr imaging of acute cerebral ischemia. *Acta Radiol*. 1998;39:460-473
153. Huisman TA. Diffusion-weighted and diffusion tensor imaging of the brain, made easy. *Cancer Imaging*. 2010;10 Spec no A:S163-171
154. Moseley ME, Kucharczyk J, Mintorovitch J, Cohen Y, Kurhanewicz J, Derugin N, et al. Diffusion-weighted mr imaging of acute stroke: Correlation with t2-weighted and magnetic susceptibility-enhanced mr imaging in cats. *AJNR Am J Neuroradiol*. 1990;11:423-429
155. Moseley ME, Cohen Y, Mintorovitch J, Chileuitt L, Shimizu H, Kucharczyk J, et al. Early detection of regional cerebral ischemia in cats: Comparison of diffusion- and t2-weighted mri and spectroscopy. *Magn Reson Med*. 1990;14:330-346
156. Moseley ME, Cohen Y, Kucharczyk J, Mintorovitch J, Asgari HS, Wendland MF, et al. Diffusion-weighted mr imaging of anisotropic water diffusion in cat central nervous system. *Radiology*. 1990;176:439-445
157. Purushotham A, Campbell BC, Straka M, Mlynash M, Olivot JM, Bammer R, et al. Apparent diffusion coefficient threshold for delineation of ischemic core. *Int J Stroke*. 2015;10:348-353

158. Thomas RG, Lymer GK, Armitage PA, Chappell FM, Carpenter T, Karaszewski B, et al. Apparent diffusion coefficient thresholds and diffusion lesion volume in acute stroke. *J Stroke Cerebrovasc Dis*. 2013;22:906-909
159. An H, Ford AL, Vo K, Powers WJ, Lee JM, Lin W. Signal evolution and infarction risk for apparent diffusion coefficient lesions in acute ischemic stroke are both time- and perfusion-dependent. *Stroke*. 2011;42:1276-1281
160. Chemmanam T, Campbell BC, Christensen S, Nagakane Y, Desmond PM, Bladin CF, et al. Ischemic diffusion lesion reversal is uncommon and rarely alters perfusion-diffusion mismatch. *Neurology*. 2010;75:1040-1047
161. Inoue M, Mlynash M, Straka M, Lansberg MG, Zaharchuk G, Bammer R, et al. Patients with the malignant profile within 3 hours of symptom onset have very poor outcomes after intravenous tissue-type plasminogen activator therapy. *Stroke*. 2012;43:2494-2496
162. Inoue M, Mlynash M, Christensen S, Wheeler HM, Straka M, Tipirneni A, et al. Early diffusion-weighted imaging reversal after endovascular reperfusion is typically transient in patients imaged 3 to 6 hours after onset. *Stroke*. 2014;45:1024-1028
163. Marks MP, Tong DC, Beaulieu C, Albers GW, de Crespigny A, Moseley ME. Evaluation of early reperfusion and i.V. Tpa therapy using diffusion- and perfusion-weighted mri. *Neurology*. 1999;52:1792-1798
164. Ritzl A, Meisel S, Wittsack HJ, Fink GR, Siebler M, Modder U, et al. Development of brain infarct volume as assessed by magnetic resonance imaging (mri): Follow-up of diffusion-weighted mri lesions. *J Magn Reson Imaging*. 2004;20:201-207
165. Lansberg MG, Thijs VN, O'Brien MW, Ali JO, de Crespigny AJ, Tong DC, et al. Evolution of apparent diffusion coefficient, diffusion-weighted, and t2-weighted signal intensity of acute stroke. *AJNR Am J Neuroradiol*. 2001;22:637-644
166. Lansberg MG, Lee J, Christensen S, Straka M, De Silva DA, Mlynash M, et al. Rapid automated patient selection for reperfusion therapy: A pooled analysis of the echoplanar imaging thrombolytic evaluation trial (epithet) and the diffusion and perfusion imaging evaluation for understanding stroke evolution (defuse) study. *Stroke*. 2011;42:1608-1614
167. Chalela JA, Kidwell CS, Nentwich LM, Luby M, Butman JA, Demchuk AM, et al. Magnetic resonance imaging and computed tomography in emergency assessment of patients with suspected acute stroke: A prospective comparison. *Lancet*. 2007;369:293-298

168. Farzin B, Fahed R, Guilbert F, Poppe AY, Daneault N, Durocher AP, et al. Early ct changes in patients admitted for thrombectomy: Intrarater and interrater agreement. *Neurology*. 2016;87:249-256
169. Barber PA, Demchuk AM, Zhang J, Buchan AM. Validity and reliability of a quantitative computed tomography score in predicting outcome of hyperacute stroke before thrombolytic therapy. Aspects study group. Alberta stroke programme early ct score. *Lancet*. 2000;355:1670-1674
170. Maegerlein C, Fischer J, Monch S, Berndt M, Wunderlich S, Seifert CL, et al. Automated calculation of the alberta stroke program early ct score: Feasibility and reliability. *Radiology*. 2019;291:141-148
171. McTaggart RA, Jovin TG, Lansberg MG, Mlynash M, Jayaraman MV, Choudhri OA, et al. Alberta stroke program early computed tomographic scoring performance in a series of patients undergoing computed tomography and mri: Reader agreement, modality agreement, and outcome prediction. *Stroke*. 2015;46:407-412
172. Campbell BC, Christensen S, Levi CR, Desmond PM, Donnan GA, Davis SM, et al. Cerebral blood flow is the optimal ct perfusion parameter for assessing infarct core. *Stroke*. 2011;42:3435-3440
173. Cereda CW, Christensen S, Campbell BC, Mishra NK, Mlynash M, Levi C, et al. A benchmarking tool to evaluate computer tomography perfusion infarct core predictions against a dwi standard. *J Cereb Blood Flow Metab*. 2016;36:1780-1789
174. Mokin M, Levy EI, Saver JL, Siddiqui AH, Goyal M, Bonafe A, et al. Predictive value of rapid assessed perfusion thresholds on final infarct volume in swift prime (solitaire with the intention for thrombectomy as primary endovascular treatment). *Stroke*. 2017;48:932-938
175. Schaefer PW, Barak ER, Kamalian S, Gharai LR, Schwamm L, Gonzalez RG, et al. Quantitative assessment of core/penumbra mismatch in acute stroke: Ct and mr perfusion imaging are strongly correlated when sufficient brain volume is imaged. *Stroke*. 2008;39:2986-2992
176. Wintermark M, Flanders AE, Velthuis B, Meuli R, van Leeuwen M, Goldsher D, et al. Perfusion-ct assessment of infarct core and penumbra: Receiver operating characteristic curve analysis in 130 patients suspected of acute hemispheric stroke. *Stroke*. 2006;37:979-985
177. Lansberg MG, Christensen S, Kemp S, Mlynash M, Mishra N, Federau C, et al. Computed tomographic perfusion to predict response to recanalization in ischemic stroke. *Ann Neurol*. 2017;81:849-856
178. Olsen TS. Regional cerebral blood flow after occlusion of the middle cerebral artery. *Acta Neurol Scand*. 1986;73:321-337

179. Schaefer PW, Souza L, Kamalian S, Hirsch JA, Yoo AJ, Kamalian S, et al. Limited reliability of computed tomographic perfusion acute infarct volume measurements compared with diffusion-weighted imaging in anterior circulation stroke. *Stroke*. 2015;46:419-424
180. Albers GW, Thijs VN, Wechsler L, Kemp S, Schlaug G, Skalabrin E, et al. Magnetic resonance imaging profiles predict clinical response to early reperfusion: The diffusion and perfusion imaging evaluation for understanding stroke evolution (defuse) study. *Ann Neurol*. 2006;60:508-517
181. Kakuda W, Lansberg MG, Thijs VN, Kemp SM, Bammer R, Wechsler LR, et al. Optimal definition for pwi/dwi mismatch in acute ischemic stroke patients. *J Cereb Blood Flow Metab*. 2008;28:887-891
182. Butcher KS, Parsons M, MacGregor L, Barber PA, Chalk J, Bladin C, et al. Refining the perfusion-diffusion mismatch hypothesis. *Stroke*. 2005;36:1153-1159
183. Lansberg MG, Thijs VN, Bammer R, Olivot JM, Marks MP, Wechsler LR, et al. The mra-dwi mismatch identifies patients with stroke who are likely to benefit from reperfusion. *Stroke*. 2008;39:2491-2496
184. Lansberg MG, Thijs VN, Hamilton S, Schlaug G, Bammer R, Kemp S, et al. Evaluation of the clinical-diffusion and perfusion-diffusion mismatch models in defuse. *Stroke*. 2007;38:1826-1830
185. Campbell BC, Christensen S, Levi CR, Desmond PM, Donnan GA, Davis SM, et al. Comparison of computed tomography perfusion and magnetic resonance imaging perfusion-diffusion mismatch in ischemic stroke. *Stroke*. 2012;43:2648-2653
186. Christensen S, Mouridsen K, Wu O, Hjort N, Karstoft H, Thomalla G, et al. Comparison of 10 perfusion mri parameters in 97 sub-6-hour stroke patients using voxel-based receiver operating characteristics analysis. *Stroke*. 2009;40:2055-2061
187. Olivot JM, Mlynash M, Thijs VN, Kemp S, Lansberg MG, Wechsler L, et al. Optimal tmax threshold for predicting penumbral tissue in acute stroke. *Stroke*. 2009;40:469-475
188. Mlynash M, Lansberg MG, De Silva DA, Lee J, Christensen S, Straka M, et al. Refining the definition of the malignant profile: Insights from the defuse-epithet pooled data set. *Stroke*. 2011;42:1270-1275
189. Bivard A, Krishnamurthy V, Stanwell P, Levi C, Spratt NJ, Davis S, et al. Arterial spin labeling versus bolus-tracking perfusion in hyperacute stroke. *Stroke*. 2014;45:127-133

190. Bokkers RP, Hernandez DA, Merino JG, Mirasol RV, van Osch MJ, Hendrikse J, et al. Whole-brain arterial spin labeling perfusion mri in patients with acute stroke. *Stroke*. 2012;43:1290-1294
191. Zaharchuk G, El Mogy IS, Fischbein NJ, Albers GW. Comparison of arterial spin labeling and bolus perfusion-weighted imaging for detecting mismatch in acute stroke. *Stroke*. 2012;43:1843-1848
192. Detre JA, Leigh JS, Williams DS, Koretsky AP. Perfusion imaging. *Magn Reson Med*. 1992;23:37-45
193. Williams DS, Detre JA, Leigh JS, Koretsky AP. Magnetic resonance imaging of perfusion using spin inversion of arterial water. *Proc Natl Acad Sci U S A*. 1992;89:212-216
194. Zaharchuk G. Theoretical basis of hemodynamic mr imaging techniques to measure cerebral blood volume, cerebral blood flow, and permeability. *AJNR Am J Neuroradiol*. 2007;28:1850-1858
195. Niibo T, Ohta H, Yonenaga K, Ikushima I, Miyata S, Takeshima H. Arterial spin-labeled perfusion imaging to predict mismatch in acute ischemic stroke. *Stroke*. 2013;44:2601-2603
196. Wang DJ, Alger JR, Qiao JX, Gunther M, Pope WB, Saver JL, et al. Multi-delay multi-parametric arterial spin-labeled perfusion mri in acute ischemic stroke - comparison with dynamic susceptibility contrast enhanced perfusion imaging. *Neuroimage Clin*. 2013;3:1-7
197. van der Thiel M, Rodriguez C, Giannakopoulos P, Burke MX, Lebel RM, Gninenko N, et al. Brain perfusion measurements using multidelay arterial spin-labeling are systematically biased by the number of delays. *AJNR Am J Neuroradiol*. 2018;39:1432-1438
198. Qiu M, Paul Maguire R, Arora J, Planeta-Wilson B, Weinzimmer D, Wang J, et al. Arterial transit time effects in pulsed arterial spin labeling cbf mapping: Insight from a pet and mr study in normal human subjects. *Magn Reson Med*. 2010;63:374-384
199. Deibler AR, Pollock JM, Kraft RA, Tan H, Burdette JH, Maldjian JA. Arterial spin-labeling in routine clinical practice, part 2: Hypoperfusion patterns. *AJNR Am J Neuroradiol*. 2008;29:1235-1241
200. Zaharchuk G. Arterial spin-labeled perfusion imaging in acute ischemic stroke. *Stroke*. 2014;45:1202-1207
201. Fan AP, Guo J, Khalighi MM, Gulaka PK, Shen B, Park JH, et al. Long-delay arterial spin labeling provides more accurate cerebral blood flow measurements in moyamoya patients: A simultaneous positron emission tomography/mri study. *Stroke*. 2017;48:2441-2449

202. Hendrikse J, van Osch MJ, Rutgers DR, Bakker CJ, Kappelle LJ, Golay X, et al. Internal carotid artery occlusion assessed at pulsed arterial spin-labeling perfusion mr imaging at multiple delay times. *Radiology*. 2004;233:899-904
203. Lou X, Yu S, Scalzo F, Starkman S, Ali LK, Kim D, et al. Multi-delay asl can identify leptomeningeal collateral perfusion in endovascular therapy of ischemic stroke. *Oncotarget*. 2017;8:2437-2443
204. Miteff F, Levi CR, Bateman GA, Spratt N, McElduff P, Parsons MW. The independent predictive utility of computed tomography angiographic collateral status in acute ischaemic stroke. *Brain*. 2009;132:2231-2238
205. Calderon-Arnulphi M SP, Liebeskind DS. Collateral flow, luxury perfusion and vasospasm: Clinical applications and theoretical principles. . In: Bammer R, ed. *Mr and ct perfusion and pharmacokinetic imaging.* . Philadelphia: Wolters Kluwer; 2016.
206. Wheeler HM, Mlynash M, Inoue M, Tipirnini A, Liggins J, Bammer R, et al. The growth rate of early dwi lesions is highly variable and associated with penumbral salvage and clinical outcomes following endovascular reperfusion. *Int J Stroke*. 2015;10:723-729
207. Menon BK, d'Esterre CD, Qazi EM, Almekhlafi M, Hahn L, Demchuk AM, et al. Multiphase ct angiography: A new tool for the imaging triage of patients with acute ischemic stroke. *Radiology*. 2015;275:510-520
208. van den Wijngaard IR, Holswilder G, Wermer MJ, Boiten J, Algra A, Dippel DW, et al. Assessment of collateral status by dynamic ct angiography in acute mca stroke: Timing of acquisition and relationship with final infarct volume. *AJNR Am J Neuroradiol*. 2016;37:1231-1236
209. Seker F, Potreck A, Mohlenbruch M, Bendszus M, Pham M. Comparison of four different collateral scores in acute ischemic stroke by ct angiography. *J Neurointerv Surg*. 2016;8:1116-1118
210. Amukotuwa SA, Yu C, Zaharchuk G. 3d pseudocontinuous arterial spin labeling in routine clinical practice: A review of clinically significant artifacts. *J Magn Reson Imaging*. 2016;43:11-27
211. de Havenon A, Haynor DR, Tirschwell DL, Majersik JJ, Smith G, Cohen W, et al. Association of collateral blood vessels detected by arterial spin labeling magnetic resonance imaging with neurological outcome after ischemic stroke. *JAMA Neurol*. 2017;74:453-458
212. Wolf RL, Detre JA. Clinical neuroimaging using arterial spin-labeled perfusion magnetic resonance imaging. *Neurotherapeutics*. 2007;4:346-359

213. Olivot JM, Mlynash M, Inoue M, Marks MP, Wheeler HM, Kemp S, et al. Hypoperfusion intensity ratio predicts infarct progression and functional outcome in the defuse 2 cohort. *Stroke*. 2014;45:1018-1023

214. Venkatesan R, Lin W, Gurleyik K, He YY, Paczynski RP, Powers WJ, et al. Absolute measurements of water content using magnetic resonance imaging: Preliminary findings in an in vivo focal ischemic rat model. *Magn Reson Med*. 2000;43:146-150

215. Thomalla G, Cheng B, Ebinger M, Hao Q, Tourdias T, Wu O, et al. Dwi-flair mismatch for the identification of patients with acute ischaemic stroke within 4.5 h of symptom onset (pre-flair): A multicentre observational study. *Lancet Neurol*. 2011;10:978-986

216. Thomalla G, Simonsen CZ, Boutitie F, Andersen G, Berthezene Y, Cheng B, et al. Mri-guided thrombolysis for stroke with unknown time of onset. *N Engl J Med*. 2018;379:611-622

Chapter 3

Dural Arteriovenous Fistulas

Intracranial *dural arteriovenous fistulas* (DAVFs) account for 10-15% of intracranial arteriovenous lesions and are therefore much less common than *arteriovenous malformations* (AVMs). The age range of those with DAVFs is extremely broad, ranging from neonates to the elderly, with the mean age of presentation 50-60 years[1]. There is no gender predilection, although an increased incidence of haemorrhage has been reported in male patients[1, 2]. DAVFS are being diagnosed with increased frequency due to an increase in the number that are incidentally detected; this is likely attributable to the exponential increase in the utilization of MRI for investigation of a wide range of neurological complaints, in addition to the improved sensitivity of MRI for the detection of vascular lesions[3]. Nonetheless, DAVFS remain a challenge to diagnose on non-invasive imaging.

DAVFs are a heterogeneous group of lesions that are characterized by a common underlying angioarchitecture: arteriovenous shunts within the wall of a dural venous sinus that are supplied by dural arteries (Figure 3-1)[1]. They can be distinguished from *arteriovenous malformations* (AVMs) by the lack a nidus (a tangle of developmentally abnormal shunting vessels). Also unlike AVMs, DAVFs have predominantly meningeal arterial supply; it has been reported that 95% of DAVFs have purely meningeal arterial supply, with only 5% being fed by both by both meningeal and cortical branches[4, 5]. In adults, DAVFs are comprised of a network of tiny "crack-like" vessels in the wall of a dural venous sinus. These lesions can also occur rarely in infants, and typically consist of multiple arteriovenous shunts involving several different dural venous sinuses[6].

The most common location for DAVFs in adults is the posterior fossa, involving the transverse or sigmoid sinuses, or the cavernous sinus[1]. In one series, it was reported that 50% were located in the transverse sinus, 16% in the cavernous sinus, 12 % in the tentorium cerebelli, and 8% in the superior sagittal sinus[4]. Paediatric lesions are typically more complex and involve the torcular herophili, superior sagittal sinus, Vein of Galen or large venous lakes, and characteristically have bilateral arterial feeders[6].

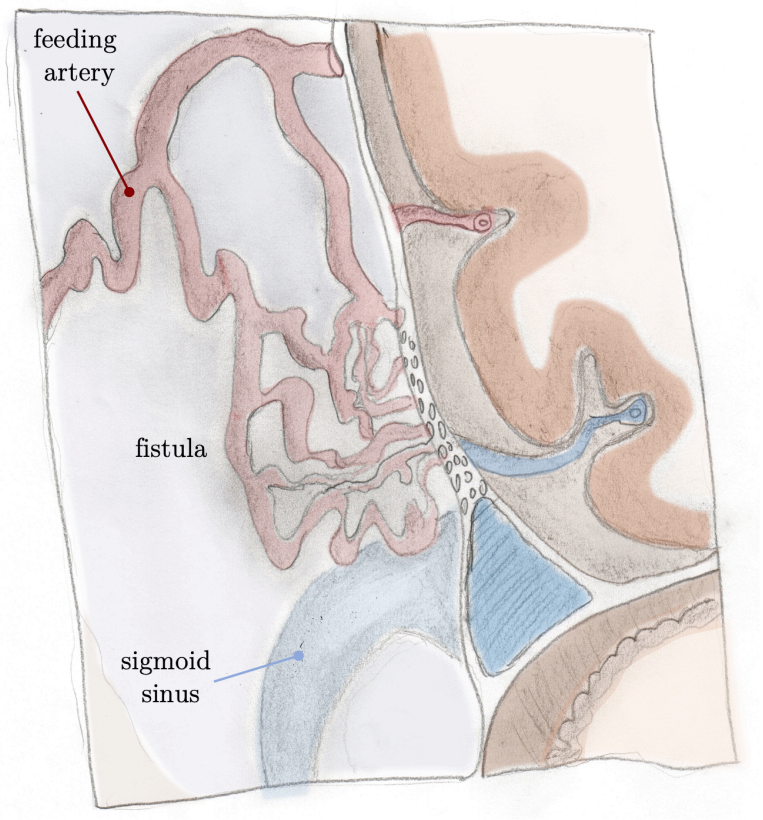

Figure 3-1. *Schematic diagram of a DAVF, showing the extra-axial location in relation to the wall of a dural venous sinus (the sigmoid sinus). A crack-like network of fistulous channels within the wall of a dural venous sinus is supplied by a dural artery. Drainage is into the dural venous sinus or a cortical vein.*

It is noted that cavernous sinus DAVFs are referred to as **indirect carotid-cavernous fistulas**[1] (CCF). **Direct carotid-cavernous sinus fistulas** are characterized by direct communication between the cavernous segment of the *internal carotid artery* (ICA) and the cavernous sinus, resulting from either rupture of a Berry aneurysm or traumatic injury[7]. They are, therefore, angioarchitecturally and aetiologically distinct from cavernous sinus DAVFs.

3.1 Pathophysiology and Aetiology of DAVFs

Unlike AVMs, which are developmental malformations of brain vasculature, DAVFs are acquired lesions[8]. They result from the opening of micro-shunts and/or angiogenesis in the dura mater and are therefore characterized by direct communication between meningeal arteries and veins[1, 8, 9]. The exact pathogenesis of DAVFs is unknown and the majority are classified as idiopathic[1]. There is a reported association with dural venous sinus thrombosis, and DAVFs may develop

as a result of recanalization of a thrombosed sinus[10-12]. It has been postulated that physiologic arteriovenous shunts between meningeal arteries and a dural sinus enlarge as a consequence of elevated local venous pressure in the setting of outflow obstruction due to thrombosis, which in turn leads to pathological shunting[2, 13, 14]. An alternative theory is that venous hypertension in the setting of thrombosis decreases cerebral perfusion and promotes neoangiogenesis[2, 15]. An etiological link between DAVFs and dural venous sinus thrombosis is supported by the association between DAVFs and inherited thrombophilia conditions, such as protein C, antithrombin, and protein S deficiencies[16].

DAVFs are characterized by direct flow of arterial blood into the venous system due to the direct arteriovenous communication[1]. This results in abnormally rapid transit of blood from the arteries into the veins, giving rise to the characteristic finding of early venous filling on dynamic contrast imaging (dynamic contrast-enhanced MRI and catheter-based angiography)[1, 3]. The absence of an intervening capillary bed or resistance arterioles results in transmission of systemic arterial pressure into the draining venous structures, which have markedly increased blood flow. These hemodynamic derangements result in structural changes in the draining veins, such as dilatation, tortuosity and the formation of venous pouches and varices[1, 4, 5]. Elevated venous pressure (venous hypertension) can lead to cerebral oedema and intracranial hemorrhage[1, 3, 5]. Therefore, while extra-axial in location, DAVFs can therefore have similar manifestations to AVMS and affect brain parenchyma by causing venous hypertension.

It is postulated that DAVFs cause intracranial hypertension due to the increased cerebral blood volume and dural sinus pressure, which are directly related to the increased flow rate within the fistula[17]. In turn, the increased pressure in the dural venous sinus pressure causes CSF absorption to be reduced. This leads to increased CSF pressure and venous congestion with increased pressure in cortical veins (Monroe-Kellie rule)[5, 18]. Venous outflow obstruction, due stenosis or thrombosis of the draining dural venous sinus, can further exacerbate this vicious circle[5]. With progressive venous hypertension, venous ischaemia develops; here, severely elevated venous pressure causes disruption of the blood brain barrier, with seepage of intravascular fluid into the extracellular space, manifested as vasogenic oedema, and haemorrhage[19, 20]. With increasing severity, elevated venous pressure can cause reduced cerebral perfusion pressure due to the increased outflow resistance[19-21]. Cytotoxic oedema can also occur if outflow obstruction is severe enough to impair arterial inflow.

3.2 Clinical Presentation

The clinical presentation of DAVFs is dependent upon the pattern of venous drainage as well as location, and is highly variable[3, 4]. They may be clinically silent, and when present, the symptoms are often non-specific[1]. Pulsatile tinnitus is a frequent symptom of posterior fossa DAVFs, particularly those involving the transverse and sigmoid sinus, due to increased blood flow through dural venous sinuses in close proximity to the auditory apparatus[3, 22, 23].

Other non-aggressive neurological presentations include bruit and an isolated headache[4]. More aggressive neurological presentations, secondary to intracranial hypertension, include intractable headaches, nausea and vomiting, visual disturbance or loss, and papilloedema[4, 24]. Seizures, pronounced vertigo, altered mental status, cognitive decline, and focal neurological deficits may result from cerebral oedema, ischaemia and *intracranial haemorrhage* (ICH) with worsening venous hypertension[18, 25-27]. ICH occurs in 15% of patients with DAVFs, and is most often parenchymal or subarachnoid in location[25]. Unexplained ICH therefore warrants consideration of a DAVF in the differential diagnosis. Progressive tumour-like symptoms due to mass effect and mechanical compression of adjacent structures can occur with venous ectasia and pouches[4].

Cavernous sinus DAVFs (**indirect CCFs**) warrant separate mention as an example of how the location of the fistula can result in distinctive clinical manifestations. Patients typically present with signs and symptoms related to cavernous sinus and orbital congestion, namely visual disturbance, retro-orbital pain, ophthalmoplegia, chemosis, and proptosis[1, 2]. Cavernous sinus DAVFs can threaten vision due to ophthalmic vein drainage and congestion[1, 2]. This is clinically important and must be considered in making treatment decisions regarding fistulas in this location.

3.3 Prognosis and Classification

A good understanding of the natural history of DAVFs, hence their prognosis, is vital for decision-making regarding therapy. An early attempt at risk stratification involved comparison of the angiographic features of 100 DAVFs associated with haemorrhage or focal neurological deficits against 277 benign DAVFs[28]. This study found leptomeningeal venous drainage, variceal venous dilatations and Vein of

Galen drainage to be associated with an aggressive clinical course[28]. No DAVF, regardless of location, was found to be definitively benign[28].

This was followed by the seminal work of *Cognard* and colleagues, who performed a detailed analysis of 205 consecutive patients with DAVFs seen at their institution over 18 years[4]. They demonstrated that the natural history of these lesions depends on the degree of venous hypertension and presence of cortical venous drainage[4, 5]. Fistulas that drained into a dural venous sinus with antegrade flow displayed benign behaviour, and no aggressive neurological presentations observed in this group[4]. Retrograde dural venous sinus drainage and cortical vein reflux, which develop with (and indicate) increasing severity of venous hypertension, were associated with aggressive neurological presentations including haemorrhage[4, 17]. The rate of complication was higher still with direct cortical vein drainage, i.e. where an arteriovenous shunt is abruptly established on a mature cortical vein; the frequency of an aggressive neurological presentation in this group was 76%, with haemorrhage observed in 40%. Cortical veins are smaller and less capacious than dural venous sinuses; as such, they have limited ability to adapt structurally to the sudden increase in blood flow and arterial pressure caused by a fistula, which in turn leads to severely elevated venous pressure, predisposing to hemorrhage[4]. Structural changes eventually occur in draining cortical veins, which dilate and may become variceal with formation of venous pouches[1]. This further increases the rate of complication, with an aggressive neurological presentation observed in 97% in this group[4]. It was uncertain as to whether the ectasia *per se* was responsible for the bleeding, or whether it reflected insufficient venous drainage that in turn caused escalating venous hypertension and haemorrhage.

These findings indicate that the risk of haemorrhage is related to presence and severity of venous hypertension, which is in turn related to the pattern of venous drainage. Based on this, a classification system for risk stratification was proposed to guide treatment decisions. The **Cognard classification system**, illustrated in Figure 3-2 and detailed in Table 3-1, categorizes DAVFs into five venous drainage patterns that reflect an increasing risk of haemorrhage and aggressive neurological presentation[4].

Briefly, **Type I** fistulas drain into a dural venous sinus, within which there is normal antegrade flow. **Type II** fistulas also drain into a dural venous sinus, however antegrade flow in the sinus is impaired, resulting in either retrograde flow within the sinus (**Type IIa**), retrograde drainage (reflux) into a cortical vein (**Type IIb**) or both (**Type IIa + b**).

Table 3-1. *The Cognard and Borden classification systems* [4, 24]

Cognard type		Primary drainage structure	Pattern of venous drainage	Frequency†
I		Dural venous sinus	Normal antegrade flow in dural venous sinus	1% (0%)
II	***a***		Retrograde drainage within dural venous sinus	37% (0%)
	b		Retrograde flow (reflux) into cortical vein	30% (20%)
	a + b		Retrograde flow in dural venous sinus *plus* reflux into cortical vein	67% (5%)
III		Cortical vein	Direct drainage into cortical vein	76% (40%)
IV			Direct drainage into cortical vein with venous ectasia*	97% (66%)
V		Spinal perimedullary vein		91% (42%)
Borden type				
I		Dural venous sinus or meningeal vein	Antegrade flow in dural sinus	2%
II			Retrograde flow (reflux) into cortical vein	39%
III		Cortical vein*	Direct drainage into cortical vein‡	79%

* Venous ectasia is defined as venous dilatation > 5 mm diameter and three times larger than the draining vein. A venous varix is an area of focal ectasia.

‡ Drainage into a segment of dural sinus that is isolated by thrombosis on either side, such that cortical vein reflux is the only drainage pathway, is also included in this category.

† Frequency of aggressive neurological presentation, % (frequency of intracranial hemorrhage)

Type II fistulas develop as a result of blood flow within a dural venous sinus exceeding its antegrade drainage capacity. This can occur in the setting of a high flow fistula, where even a normal or enlarged sinus cannot accommodate the increased flow rate and pressure[4, 17]. It can also occur due to downstream stenosis or occlusion of the dural venous sinus, for example due to thrombosis[4, 5, 17]. It is noted that cortical veins normally drain into a dural venous sinus, however this can be reversed, with retrograde flow of blood from the sinus into a cortical vein, in the setting of elevated sinus pressure – resulting in a **Type IIb** or **Type IIa + b** fistula. **Types III** and **IV** fistulas are both characterized by direct cortical vein drainage and are distinguished by the development of venous ectasia.

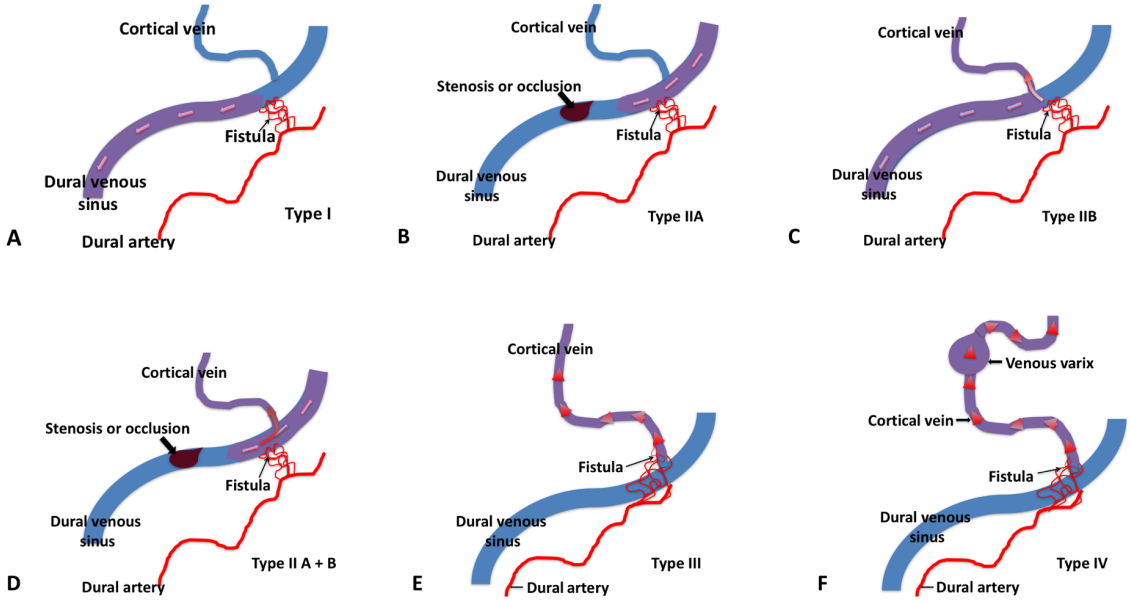

Figure 3-2. *Cognard classification of DAVFs.* ***A.*** *Type I: drainage into dural venous sinus with antegrade flow.* ***B.*** *Type IIA: drainage into dural venous sinus with retrograde flow due to outflow obstruction of the sinus.* ***C.*** *Type IIB: drainage into dural venous sinus with antegrade flow in sinus + reflux of blood into cortical vein. D. Type IIA: drainage into dural venous sinus with retrograde flow due to outflow obstruction of the sinus + reflux of blood into cortical vein.* ***E.*** *Direct cortical vein drainage of fistula* ***F.*** *Direct cortical vein drainage of fistula + venous varix or ectasia >5 mm*

Borden and colleagues also proposed a classification system, again relating the venous drainage pattern to the risk of haemorrhage[24]. This **Borden classification system** (Figure 3-3) consists of three categories differentiated by the site and pattern of venous drainage, described in Table 3-1[24]. The Borden classification scheme further subdivides fistulas on the basis of the number of shunts, into single-hole (a) or multiple-hole (b)[24]. A comparison of the Borden and Cognard classification systems is shown in Table 3-2.

Table 3-2. *Comparison of Cognard and Borden classification systems*

Cognard type	Borden type	Drainage pattern
I	**I**	Dural venous sinus drainage, antegrade flow
IIa		
IIb	**II**	Dural venous sinus drainage with reflux into cortical vein
IIa+b		
III	**III**	Direct cortical vein drainage
IV		

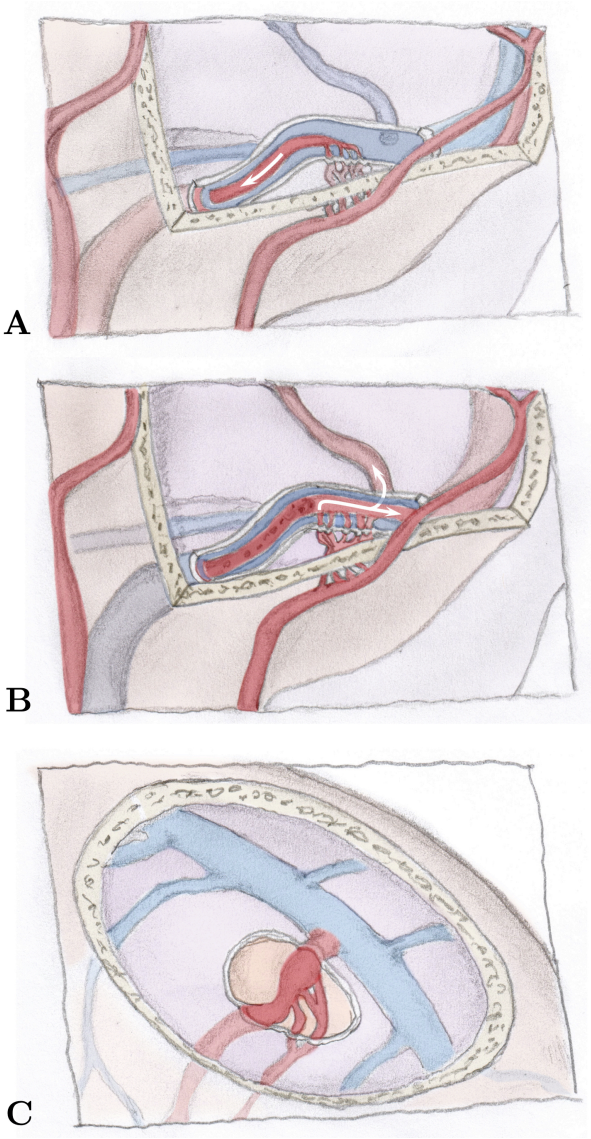

Figure 3-3. *Borden classification of DAVFs.* ***A.*** *Borden type I fistula.* ***B.*** *Borden type II fistula with cortical vein reflux.* ***C.*** *Borden type III parasagittal fistula draining directly into a cortical vein. These are associated with the highest risk of complication.*

Both classification systems reflect the fact that the venous drainage pattern is an important determinant of the natural history of a DAVF and the risk associated with these lesions[4, 23, 24, 26]. The Cognard classification system is more widely used in clinical practice and the literature. It is more granular than the Borden system, considering more venous drainage patterns. However, the distinction between some of these categories is unnecessary for clinical decision making; for example, Cognard **Type I** and **IIa** fistulas are both managed conservatively, while **Type IIb** and **IIa + b** fistulas are both regarded as having an equally high risk of complication, warranting intervention. The simpler Borden system is therefore more practical in the clinical setting, since it categorizes fistulas based on the two

the key factors that increase the risk of complication: **cortical vein reflux** and **direct cortical vein drainage** of the DAVF, which will be collectively referred to as *cortical vein drainage* (CVD) for the remainder of this dissertation. Other terms used in the literature to describe cortical veins are leptomeningeal veins and subarachnoid veins; cortical vein reflux is therefore also referred to as retrograde leptomeningeal venous drainage.

An even simpler approach to risk stratification is to dichotomize patients into those with CVD and those without. This is typically the approach taken in clinical practice when making treatment decisions. CVD is associated with an 8.1% annual risk of intracranial haemorrhage and 10.4% annual mortality[18]. Conversely, as seen from the studies of Borden and Cognard, fistulas without CVD have a benign behaviour and natural history; in this group, Cognard *et al* observed no haemorrhages, while Borden *et al* observed aggressive behaviour in only 2% [4, 24]. These fistulas are usually detected incidentally or present with non-aggressive symptoms related to increased venous drainage, such as pulsatile tinnitus with posterior fossa fistulas[1, 23]. It is noted that haemorrhage can occur, although rarely, even in the absence of cortical vein involvement; tortuous, engorged pial veins have been reported to be an indicator of venous congestion, and an independent risk factor for haemorrhage in these cases[29].

The location of the fistula was also found to be significantly correlated with an aggressive presentation[4]. The incidence of an aggressive presentation was highest at the torcular Herophili (100%), followed by tentorium cerebelli (92%), and anterior base of skull fistulas (88%)[4]. Conversely, cavernous sinus DAVFs were not associated with an aggressive presentation in this series. This was found to be due to differences in the incidence of direct CVD (100% for tentorial and anterior cranial fossa fistulas versus 12 % for cavernous sinus lesions), in turn likely related to anatomical differences in venous drainage at these locations[4]. Once this was taken into account, location was not an independent risk factor for an aggressive neurological presentation. The presence of a cortical arterial supply (5%) also did not alter neurological prognosis[4].

Progression of DAVFs from one type to another is unusual in the absence of treatment, with 2% of low-grade DAVFs reported to progress to a higher-grade[1, 4, 17, 22]. Nonetheless, CVD can develop over time due to progressive venous outflow obstruction (stenosis or thrombosis) or increased arterial flow[17, 22]. Close imaging and clinical surveillance of low-grade fistulas is therefore necessary. Any change in symptomatology (e.g., resolution of pulsatile tinnitus) should also trigger further

investigation, to both exclude complication and the possibility of fistula progression to a higher grade[4]. Of note, spontaneously resolution and thrombosis of a DAVF can occur[30, 31].

3.4. Treatment of DAVFs

Treatment decisions are best made by a multidisciplinary team of neurosurgeons, interventional neuroradiologists, neurologists, and radiation oncologists who have experience in managing patients with DAVFs[1]. Treatment does carry risk, with potential complications including stroke and intracranial hemorrhage[1]. This must be weighed against the risk posed by the DAVF *per se*. Patient factors such as age, co-morbidities and clinical presentation as well as the location and grade of a DAVF are key considerations. CVD is the most common indication for treatment, due to the increased risk of complication associated with this feature. Low-grade fistulas without CVD (**Borden type I** and **Cognard type I** or **IIa**) can be managed conservatively, with close clinical and imaging surveillance to monitor for progression[1, 23, 26]. These low-grade lesions may, however, be treated if the patient has debilitating symptoms, such as severe tinnitus, that impair their quality of life and ability to function[1, 23].

The goal of therapy is complete obliteration of the arteriovenous shunt. Interventional neuroradiologists play an important role in the management of DAVFs since endovascular techniques are now widely used to treat DAVFs[1]. Embolization of the fistula via a trans-arterial, trans-venous or, less often, combined route is the mainstay of treatment[32-36]. Surgery is typically reserved for those patients in whom an endovascular approach is either not feasible or has failed[36, 37]. Stereotactic radiosurgery may also be used in these cases, as well as for the treatment of some low-grade fistulas[36, 38]. Failure to completely obliterate the shunt results in persistence and even progression, due to recruitment of collateral vessels, therefore the risk of haemorrhage is not eliminated[1]. If shunt occlusion is not feasible, or deemed too risky, CVD can be selectively treated by disconnecting the affected cortical vein[39]; this reduces the risk of DAVF complication, with a lower procedural risk, but requires ongoing close surveillance for recurrence[39]. The role of the radiologist, therefore, is to detect a DAVF, localize it, and correctly identify its venous drainage pattern,

3.5 Imaging of DAVs

The signs and symptoms of DAVFs can be non-specific, therefore only a few patients presenting with a clinical picture potentially attributable to a DAVF actually have one[1]. Once a DAVF is detected, thorough evaluation of its angioarchitecture is imperative; in particular, its venous drainage pattern must be determined for risk stratification and treatment planning.

The gold standard for the diagnosis and characterization of a DAVF is catheter-based *digital subtraction angiography* (DSA). DSA is an invasive test that utilizes ionizing radiation and is only performed in hospitals with an interventional neuroradiology service and expertise. It is, therefore, not available at many smaller and peripheral hospitals. It also carries a very small but material risk of stroke and permanent neurological injury[40]. Consequently, there is an urgent clinical need for non-invasive techniques that can confidently exclude a DAVF in those patients with symptoms potentially attributable to this entity, but in whom the index of suspicion on clinical grounds alone is insufficient to justify a DSA. Such non-invasive techniques should also assist treatment planning, so that diagnostic and therapeutic angiography can potentially be performed at the same session, decreasing the risk to the patient as well as health-care costs.

3.5.1 DSA

DSA is the reference standard for detection, characterization and follow-up of DAVFs[41]. Due to its high sensitivity for detecting DAVFs, DSA is routinely performed in patients in whom there is a high index of suspicion for a DAVF, or in whom intracranial haemorrhage cannot be otherwise explained, even when non-invasive imaging studies are negative. DSA has very high spatial resolution (typically 0.2 to 0.25 mm) and also very high temporal resolution of 500 ms to 150 ms (2-7 frames/second)[42, 43]. It is the most sensitive and specific method for detecting DAVFs, allowing delineation of the angioarchitecture and flow dynamics (high flow versus low flow) with high accuracy[44]. Selective or super-selective vessel cannulation can be performed, allowing isolation of individual cerebral arteries so that their contribution to the fistula can be accurately assessed[42]; combined with the high spatial resolution, the arterial feeders of the fistula can be accurately mapped, and even small feeding arteries identified. Importantly, the high temporal resolution allows accurate dynamic evaluation of rapid arteriovenous shunting. This, in turn, enables accurate characterization of venous drainage, including

detection of CVD and differentiation of direct CVD from cortical vein reflux, which is important for risk stratification[4, 24]. Therefore, patients currently routinely undergo diagnostic DSA for definitive characterization of DAVFs, even when the fistula is well visualized on non-invasive imaging (e.g., Figure 3-4).

Standard DSA is a planar 2D technique. Superimposition or overlap of structures on these planar projectional images may impair visualization of feeding arteries and draining veins. To address this, 3D rotational DSA (also referred to as 4D DSA) can be performed on modern bi-plane DSA units that have cone beam CT detectors[45-47]. The C-arm is rotated during image acquisition; an initial rotational scan is obtained (the **mask run**) without contrast injection, followed by a second rotational scan (the **fill run**) during contrast injection[46, 47]. This generates a 3D DSA rotational angiography dataset which can then be post-processed to obtain time-resolved 3D angiographic reconstructions of the cerebral vessels (4D volume rendered reconstructions and maximum-intensity projections). This technique has been shown to allow detailed display of the angioarchitecture of DAVFs, including the fistulous point, in one small study[45]. In another study, the findings on 4D DSA were concordant with 2D DSA with respect to the origin of the main arterial feeders, the location of the fistulous point, and venous drainage in 6 patients with DAVFS[46]. This technique may therefore be of utility for improving the spatial understanding of DAVFs, which in turn can help treatment planning.

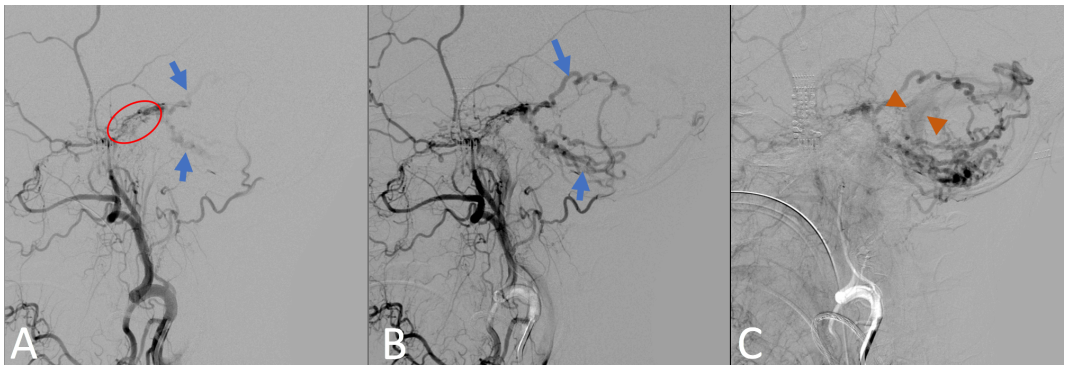

Figure 3-4. *Digital subtraction angiogram in a 79 year-old woman with a Cognard type III DAVF who presented with ataxia. Serial lateral projection DSA images that were obtained following selective cannulation of the left external carotid artery.* ***A.*** *An early arterial phase image shows the left tentorial DAVF (red circle). Early filling of cerebellar leptomeningeal veins (blue arrows) is evident.* ***B.*** *Later arterial phase image shows progressive opacification of the draining cerebellar leptomeningeal veins (blue arrows) which in turn drain into* ***C.*** *the sigmoid sinus (faintly opacified, between orange arrowheads). This temporal information is invaluable - by showing the sequence of filling, direct cortical vein drainage can be differentiated from cortical vein reflux. This DAVF was deemed too difficult to treat via an endovascular approach, and the patient underwent stereotactic radiosurgery instead.*

Table 3-3. *Comparison of different time-resolved angiographic techniques*

Technique	Spatial resolution (mm)	Temporal resolution (ms)	Vessel selective angiography?	Opacification of normal venous structures?	Angiographic contrast mechanism	Ionizing radiation? (effective dose, mSv)
DSA	0.2-0.25	150-500	Yes	Yes	Exogenous, iodinated	Yes, 2-4.5
4D CTA	0.5 (isotropic)	1000	No	Yes	Exogenous, iodinated	Yes, 5-6
TR-CEMRA	0.9-1 isotropic	1200-3000	No	Yes	Exogenous, GBCA	No
PC MRA (4D flow)	0.9 isotropic	167*	Yes	No	Endogenous, flow-induced spin phase accrual	No
TR ASL angiography	0.5 (in-plane; 0.6 through-plane	200-300	Yes	No	Endogenous, magnetically labelled arterial blood water	No
Vessel-selective or vessel-encoded TR ASL angiography	0.9 (in-plane); 1.6 (through-plane)	50-200	No	No	Endogenous, magnetically labelled arterial blood water	No

3.5.2 Computed Tomography (CT)

3.5.2.1 Non-Enhanced CT

Non-enhanced CT (NECT) is typically the initial imaging test performed in patients presenting with ICH or other neurological syndromes, since it is widely available and easy to access. However, due to its limited spatial and contrast resolution, it is confined to the rapid detection of ICH and cerebral oedema. This in turn prompts further diagnostic evaluation to determine the underlying cause of this presentation[1].

3.5.2.2 CT Angiography

Many centres routinely perform CTA in patients presenting with subarachnoid and/or parenchymal haemorrhage to identify an underlying vascular lesion such as an aneurysm, AVM or DAVF. The fistula itself may be visualized on this modality as a cluster of contrast-opacified curvilinear structures adjacent to a dural sinus[1, 48]. Despite its high spatial resolution (0.1 mm to 0.5 mm isotropic voxels typically), which allows delineation of feeding arteries, it has been reported that the sensitivity of CTA for DAVFs is lower than that of MRA (15.5 % in comparison with 50%)[48]. This is likely related to venous opacification, due to poor timing of the CTA acquisition; opacification of venous structures obscures the fistula and precludes assessment of early venous filling and differentiation of feeding arteries from draining pial veins.

More recently, 4D CTA (performed using 320-slice multi-detector CT) was used to delineate the feeding arteries and venous drainage pattern in two patients with DAVFs[49]. In another study, 4D CTA was compared against DSA for detection and characterization of DAVFs[50]. Out of 33 DAVFs, only one was missed on 4D CTA, and there was excellent agreement ($\kappa = 0.92$) between 4D CTA and DSA for the Cognard type of the fistula. Inter-modality agreement for feeding arteries was good ($\kappa = 0.71(\kappa = 0.92)$, with approximately 70% of feeding arteries identified. This technique therefore shows promise for detection, classification, and treatment planning of DAVFs, although its spatial and temporal resolution are inferior to that of DSA. The temporal resolution of 4D CTA is approximately 1s, while the spatial resolution is 0.5 mm (isotropic)[49, 50]. The effective radiation dose reported for 4D CTA is 5-6 mSv, which is higher than the 2-4.5 mSv for DSA[51].

3D reconstructions can be performed for both standard and 4D CTA acquisitions, to improve visualization of the relationship between the fistula, feeding arteries and draining veins[51]. This may assist with treatment planning. Bone subtraction is performed to enable visualization of arteries[51].
Advantages of CTA over MR-based angiographic techniques include that they are easy to access emergently, can be acquired more rapidly (therefore are less motion sensitive) and do not require safety screening. Limitations of CTA are the requirement for patient irradiation and injection of iodinated contrast agent, and the lack of bone and tissue suppression.

3.5.3 Structural MRI

MRI is the mainstay of non-invasive DAVF imaging. A number of studies have evaluated its accuracy and sensitivity for the detection of DAVFs[41, 52-56].

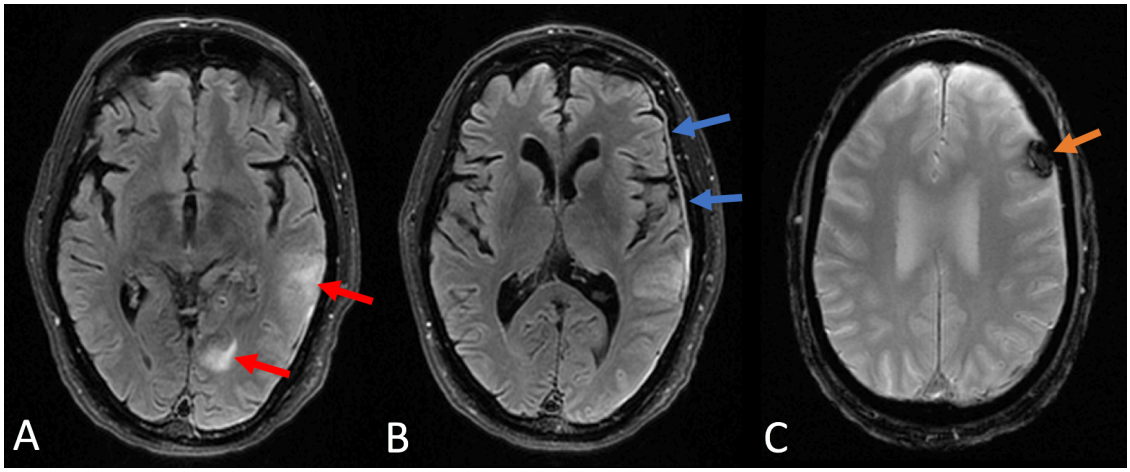

Figure 3-5. **A.** Axial T_2-weighted FLAIR image showing areas of vasogenic oedema (red arrows) in the left occipital and temporal lobes secondary to venous hypertension.
B. Axial T_2-weightedFLAIR image showing a left holohemispheric subdural hematoma (blue arrows) and **C.** axial T_2*GRE image showing a left frontal parenchymal hematoma (orange arrow). This 67 year-old man had an extensive Cognard type II a + b DAVF involving the superior sagittal sinus with cortical vein reflux and had presented with seizures. Despite the extensive DAVF, the diagnosis was missed on the initial MRI which included only conventional structural sequences on which there were no specific signs of a fistula.

Conventional structural sequences allow detection of complications of a DAVF, such as haemorrhage, vasogenic oedema, and infarction[41, 56-58]. MRI protocols typically include T_1-weighted, T_2-weighted and T_2-weighted FLAIR structural sequences as well as a blood sensitive T_2*-weighted sequences such as T_2*GRE. T_2-weighted sequences, including *T_2-weighted Fluid Attenuated Inversion Recovery*

(FLAIR), allow detection of vasogenic oedema related to venous hypertension (Figure 3-5A). The appearance of haemorrhage on structural sequences depends on the location (intra versus extra-axial), age and size of hematoma (Figure 3-5B and 3-5C)[59]. Oedema and haemorrhage are non-specific and can occur due to a wide variety of causes. More specific findings, discussed in the next paragraph, are much less frequent.

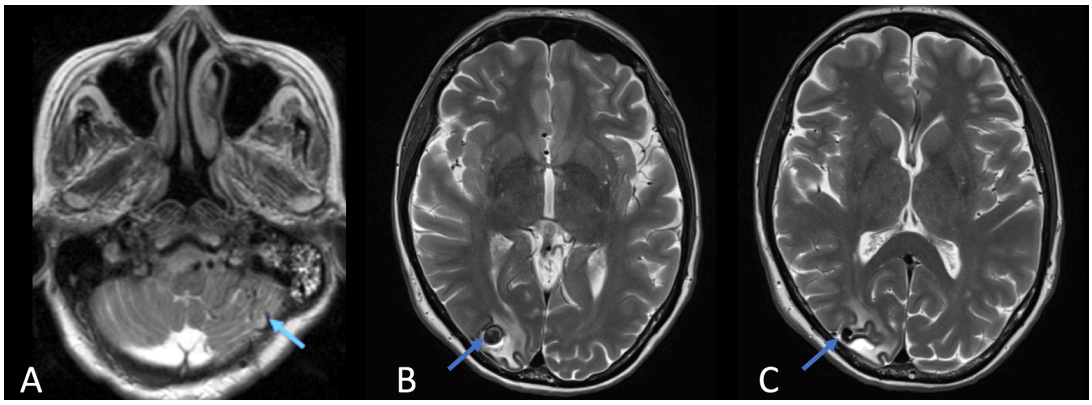

Figure 3-6. *Examples of findings of a DAVF on T_2-weighted imaging in two different patients.* ***A.*** *Axial T_2-weighted image in a 79-year old woman presenting with ataxia. A cluster of flow voids (arrow), consistent with dilated leptomeningeal veins, is seen along the inferior surface of the left cerebellar hemisphere. This patient was subsequently shown to have a left tentorial DAVF Cognard III fistula (DSA shown in Figure 3-4), with direct drainage into these cerebellar leptomeningeal veins.* ***B.*** *Axial T_2-weighted image in a* ***different*** *patient who presented with worsening headaches and visual disturbance. An ovoid flow void (arrow), in keeping with a venous varix, is seen indenting right occipital parenchyma, separated by a CSF cleft indicating that it is located within the subarachnoid space. High signal in subjacent white matter is consistent with vasogenic oedema.* ***C.*** *The ectatic draining vein (arrow) from which the varix arises is seen on a slice above. This patient had a Cognard IV fistula in the superior wall of the right transverse sinus that drainage directly into an adjacent cortical vein.*

Findings on conventional sequences (in particular T_2-weighted imaging) that are more specific and therefore suspicious for a DAVF include: (1) a cluster of dural or leptomeningeal flow voids or regionally increased flow voids (Figure 3-6A); (2) venous ectasia or varix (Figure 3-6B and C); (3) dilated, tortuous and engorged pial/leptomeningeal veins and (4) dilated medullary veins[29, 56-58]. Contrast-enhanced T_1-weighted imaging may also demonstrate enhancement of engorged leptomeningeal or medullary vessels[60] (Figure 3-7A). These findings are infrequent and predominantly associated with cortical vein drainage, therefore are typically absent in low-grade fistulas[41, 60]. They may not be present even in DAVFs with cortical vein drainage, as illustrated in Figure 3-5. Further, the spatial distribution of dilated veins does not necessarily correspond to the fistula location because

extensive collateral flow networks can occur in post-thrombotic conditions[27, 41]. The accuracy of structural MRI for detecting and localizing DAVFs is therefore much lower than that of DSA[41, 55, 56]. The possibility of a DAVF must always be considered in patients with unprovoked intracranial haemorrhage or vasogenic oedema when an underlying cause is not evident, and the diagnosis cannot be excluded on structural MRI alone.

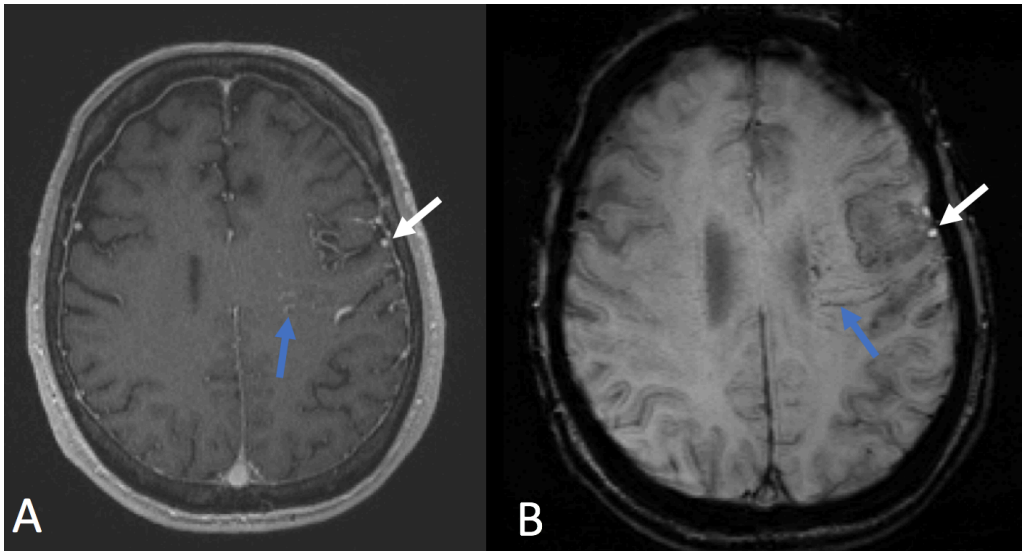

Figure 3-7. *Selected images from 64 year-old man with a Cognard III fistula, draining directly into the superior anastomotic vein of Trolard.* ***A.*** *Axial post-contrast T_1-weighted image shows the dilated medullary veins (blue arrow) in the centrum semiovale and enlarged draining cortical vein (white arrow). The presence of dilated medullary veins reflects venous hypertension.* ***B.*** *Axial SWI image showing corresponding linear low signal intensity structures (blue arrow), again representing the dilated, engorged medullary veins. The low signal intensity in these medullary veins is due to the magnetic susceptibility effect of de-oxyhaemoglobin in venous blood. Conversely, high signal is evident in the lumen of the draining cortical vein (white arrow) due to the shunted fast flowing oxygenated blood.*

Cavernous sinus DAVFs warrant separate mention because they do have more specific findings, related to orbital drainage, which increases the accuracy of structural MRI for detecting these lesions: engorgement of the superior ophthalmic vein, orbital oedema, and proptosis[1, 24].

3.5.4 Susceptibility-Weighted imaging

Susceptibility Weighted Imaging (SWI) may be of value for detecting and characterizing DAVFs[61, 62]. This 3D T_2*-weighted high-resolution sequence is obtained by combining phase and magnitude information obtained from a multi-

echo readout[61, 63]. The short echo time provides time-of-flight information, while the long echo time confers susceptibility weighting[61, 62]. The time-of-flight effect causes fast flowing blood within arteries to appear hyperintense, while magnetic susceptibility effects cause slow flowing deoxygenated blood in veins to appear hypointense. One study evaluated SWI in patients with vascular lesions, including some with arteriovenous shunting (AVMs and DAVFs) demonstrated on DSA[62]. High signal in draining venous structures was found to have a sensitivity of 93% and specificity of 98% for arteriovenous shunting. This was attributed to both the time-of-flight effect and higher fraction of oxygenation blood (diamagnetic effect) within veins draining shunting lesions. Unfortunately, only 5 DAVFs were included in this series. Another report of two cases also suggests that hyperintensity in cortical veins on SWI can be used to detect CVD[61]. An example is shown in Figure 3-7B. Unfortunately, high signal on SWI is a normal finding in the large dural venous sinuses, due to the higher flow in these structures, and can also be seen as a normal variant in normal cortical veins with robust flow.

3.5.5 MR Angiography

Two commonly used *MR angiographic* (MRA) techniques, *three-dimensional time-of-flight MRA* (3D TOF-MRA) and *time-resolved (dynamic) contrast-enhanced MRA* (TR-CEMRA), have high reported sensitivity for detection of DAVFs and localization of the fistula site in a variety of intracranial locations[41, 52, 53, 64]. They provide complementary information in the work-up of DAVFs: 3D TOF-MRA has a high spatial resolution, allowing anatomical delineation of the fistula and feeding arteries while TR-CEMRA provides dynamic information that allows fistula localization and delineation of venous drainage.

3.5.5.1 3D TOF-MRA

3D TOF-MRA is a routine sequence in brain imaging protocols at most centres around the world. It has high spatial resolution, particularly at high field strength, allowing resolution of small feeding arteries. It has been shown to be more sensitive than conventional structural sequences for the detection of DAVFs[52]. There are two key features of a DAVF on TOF-MRA: flow-related hyperintensity (consistent with high flow) within a dural sinus or cortical vein (Figure 3-8A-C); and multiple, nodular or curvilinear hyperintensities located adjacent to a sinus wall (representing the fistula itself)[41, 52] (Figure 3-8D). The latter has been reported to have a 100% sensitivity and specificity for a DAVF[52].

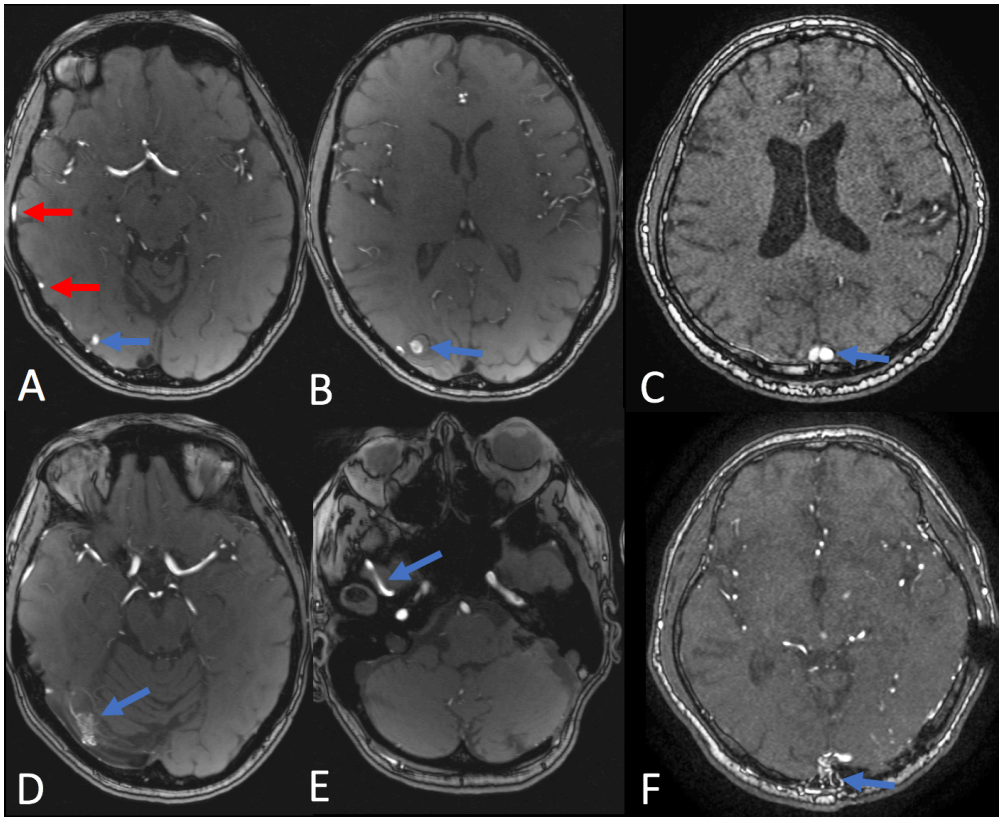

Figure 3-8. *TOF MRA signs of a DAVF. Please note that cases with florid signs have been selected for the purposes of illustration, and the findings of a DAVF on TOF-MRA are often much more subtle.* ***A.*** *High signal in a draining cortical vein (arrow) and a feeding artery (red arrows), an enlarged branch of the middle meningeal artery. Blurriness of the draining vein is due to motion (pulsation due to direct transmission of arterial pressure)* ***B.*** *A venous varix (arrow) is seen in the same patient on a more superior slice. This varix is peripherally thrombosed therefore high signal is only seen in its central part.* ***C.*** *High signal in the superior sagittal sinus (arrow) of a patient with a Cognard I DAVF draining into the superior sagittal sinus. This sinus is normally hypointense on TOF-MRA due to superior inflow saturation* ***D.*** *A cluster of nodular and curvilinear hyperintensities (arrow) within the wall of the right transverse sinus, representing a DAVF.* ***E.*** *An enlarged right middle meningeal artery (arrow) is seen feeding this DAVF.* ***F.*** *Transosseous dural feeding arteries. Note images A, B, D and E are from the same patient with a Cognard IV fistula in the wall of the right transverse sinus, while images C and F are from a different patient with a Cognard I fistula of the superior sagittal sinus.*

The same investigators reported high signal-intensity within venous sinuses to be a less reliable sign, with a sensitivity and specificity of 76% and 86%, respectively[52]. However, others have reported that hyperintensity within venous sinuses or cerebral veins is the most sensitive indicator of a DAVF[41, 60].

An indirect sign of a DAVF on TOF-MRA is enlargement of the meningeal and extracranial arteries that supply the dural feeders, for example the middle meningeal artery (Figure 3-8E)[41, 60]. Focal clusters of transosseous vessels (Figure

3-8F) adjacent to a sinus, best visualized on source images, have also been reported as a frequent TOF MRA sign of a DAVF[41, 52, 60]; these represent small osteodural feeders originating from the extracranial arteries (extracranial branches of the external carotid artery). Trans-osseous dural feeders, which traverse bone, and enlarged meningeal arteries, which lie upon the skull base, are easier to appreciate on TOF-MRA than on CTA. There is a high contrast differential between the low signal of bone and high signal of arteries on TOF-MRA, while both structures are dense on CTA.

Detection of TOF-MRA signs of a DAVF can be aided by using maximum-intensity projections (MIPS). The 3D acquisition also allows 3D renderings; these can be helpful for detection of the DAVF, since asymmetry may be better appreciated on these renderings with give a "bird's-eye" overview of the intracranial arteries. It can also help improve visualization of the angioarchitecture of the DAVF. An advantage of TOF-MRA over CTA is that background tissue (particularly bone) is suppressed, enhancing the conspicuity of arterial signal.

The main limitation of TOF-MRA is the lack of temporal information. High signal in a cortical vein due to reflux cannot therefore be differentiated from direct cortical venous drainage on this static examination[52]. Exact localization of the fistula may also be impossible when there is extensive hyperintensity in the involved venous sinuses and cortical veins. Another disadvantage of TOF MRA relates to its T_1-weighting: intrinsically T_1-hyperintense subacute thrombus in a dural venous sinus following treatment may be interpreted as residual flow. False positives can also result from hyperintense signal caused by in-flow of unsaturated blood[52]. False negatives can occur in low-flow DAVFs, due to signal saturation. In routine clinical practice, the cranio-caudal spatial coverage of the standardized TOF-MRA slab is limited by time constraints. This can result in the fistula being excluded from the imaging slab, leading to false negatives, or feeding arteries being incompletely imaged. Careful protocolling, to ensure whole-brain coverage in patients who may potentially have a fistula, can avoid this pitfall.

3.5.5.2 TR-CEMRA

TR-CEMRA provides temporal information, allowing dynamic visualization of the passage of contrast material through the cerebral vasculature[41]. Dynamic evaluation is imperative for accurate characterization of DAVFs, in order to determine the venous drainage pattern and qualitatively assess fistula flow rate.

TR-CEMRA may be 2D or 3D. Disadvantages of 2D techniques include: the need for repeat injections to acquire images in more than one plane; superimposition of different arterial and venous structures within a slab due to the projective nature of the images, hindering detection and accurate delineation of the DAVF; and signal intensity cancellations along a thick slab[41]. 2D TR-CEMRA has therefore been largely superseded by higher resolution 3D techniques which have been enabled by parallel imaging[41, 53, 64].

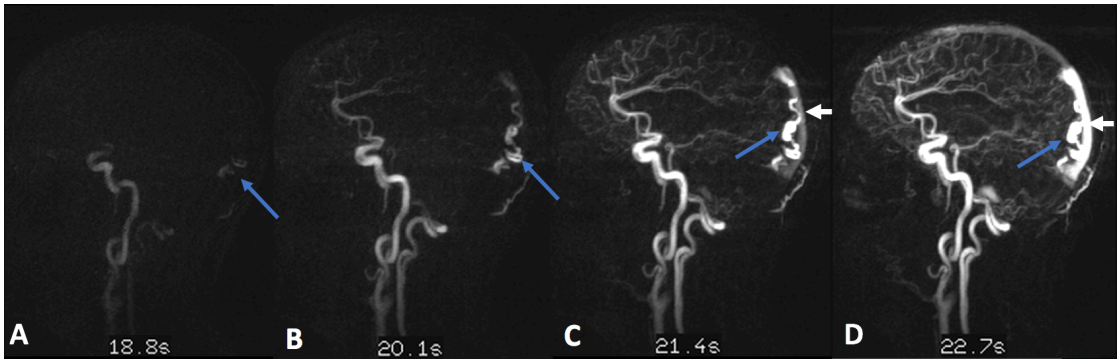

Figure 3-9. *TR-CEMRA with 1.3 second temporal resolution in the same patient with a Cognard IV DAVF whose TOF-MRA images were shown in Figure 3-8. Early venous filling, the hallmark of shunting on dynamic angiography, is shown.* ***A.*** *Early arterial phase opacification of the fistula in the wall of the transverse sinus is evident (arrow). It can be seen that the spatial resolution is inferior to that of the TOF-MRA. However, temporal information is provided.* ***B.*** *Filling of the occipital cortical vein (arrow) precedes opacification of the transverse sinus, indicating that there is direct cortical vein drainage rather than cortical vein reflux.* ***C.*** *and* ***D.*** *Focal variceal dilatation (arrow) of the draining vein is seen. This vein in turn drains into the superior sagittal sinus, which subsequently opacifies (white arrow).*

The key finding of a DAVF on TR-CEMRA is early venous filling, where a cerebral vein or dural venous sinus is opacified in the arterial phase (Figure 3-9); this is pathognomonic of arteriovenous shunting[41, 52]. Early venous opacification has a reported 100% sensitivity for arteriovenous shunting, allowing *de novo* diagnosis as well as detection of residual or recurrent DAVFs following treatment[41]. Since it provides temporal information, 3D TR-CEMRA also allows the Cognard or Borden type to be determined, for example allowing differentiation of direct cortical venous drainage from primarily dural sinus drainage with cortical vein reflux[41, 52]. The multiple phases allow visualization of the cerebral arteries, therefore feeding arteries can also be delineated.

TR-CEMRA has been shown to be superior to 3D TOF-MRA for the confirmation of fistula occlusion post treatment[41]. The major limitations of TR-CEMRA are its spatial and temporal resolution, which are far inferior to those of DSA (a

comparison of the spatial and temporal resolution of different techniques is given in Table 3-3)[41]. A trade-off between spatial and temporal resolution is required, with the user required to choose between "high temporal resolution" and "high spatial resolution". This is problematic since both are required for accurate characterization of a DAVF for treatment planning: high spatial resolution is required to identify small feeding arteries and fistulas, while high temporal resolution is essential for accurate delineate venous drainage, especially of high flow fistulas. The best spatial resolution that can be achieved in a clinically acceptable acquisition time is typically 0.9 to 1 mm isotropic voxels, while the standard spatial resolution of DSA is 0.2 mm[41]. This limited spatial resolution impairs detection of small feeding arteries. *Merkel et al* identified only the dominant feeding arteries using an implementation of TR-CEMRA with a spatial resolution of 2 mm, while DSA identified at least two separate feeding arteries in all cases, and in most cases a network of major and minor feeding vessels[41].

Detection of CVD may also be impaired by the low spatial resolution, particularly given the projectional nature of images where early venous drainage may be obscured by superimposition of normal arterial structures. For example, a short segment of cortical vein reflux may be masked, resulting in the fistula being down-graded to a *Cognard I or IIa* (*Borden I*) fistula, with important therapeutic implications (i.e., treatment indicated but withheld). Accurate assessment of venous drainage is also hindered by the relatively poor temporal resolution of TR-CEMRA. Typical "high temporal resolution" TR-CEMRA scans have a 1.2 to 3 second temporal resolution (compared with 150 to 500 ms for DSA). This can result in a large segment of the venous sinus being opacified in the early arterial phase images, impairing detection of the fistula site and making it impossible to resolve the flow direction within the sinus.

Despite these limitations, all fistulas were correctly graded on TR-CEMRA in one study[53]. Most fistulas were correctly graded according to the Cognard classification (85% and 77% accuracy for the two readers respectively) in the study by Merkel *et al*, and the presence of retrograde cortical venous drainage was detected in all cases by Noguchi *et al*[41, 52].

3.5.5.3 Phase-contrast MRA (4D flow)

Phase-contrast based accelerated four-dimensional flow imaging (**4D flow**) techniques may provide the necessary temporal resolution (see Table 3-3 for

comparison with other time-resolved techniques) required to accurately capture the flow dynamics of a DAVF, allowing differentiation between direct cortical vein drainage and cortical vein reflux[65, 66]. These images are acquired by applying phase-encoding gradients in three directions, gated to the cardiac cycle, to obtain directional, temporal and velocity information regarding blood flow[67, 68]. The velocity data contained in the 4D flow images allows dynamic visualization of blood flow propagation, while the temporal information allows time-resolved images to be reconstructed image reconstruction at a dynamic visualization can be chosen arbitrarily (e.g., 170 ms) to be competitive with DSA[65]. Other advantages 4D are that subacute thrombus does not cause false positives due to high signal, signal saturation does not occur with low velocity flow (theoretically allowing detection of low-flow fistulas). As with CE-MRA, the spatial resolution (typically 0.9 mm isotropic spatial resolution) is inferior to that of DSA, allowing delineation only of major feeding arteries and potentially precluding visualization short segment CVD[65, 66]. A major limitation of this technique, and an obstacle to clinical implementation, is the requirement for complex post-processing, which is time consuming (approximately 1 hour), and requires specialized software[65, 67].

By applying a selective flow-tracking cartographic procedure to vessels feeding and draining DAVFs in 8 patients, *Edjlali et al* showed that 4D flow imaging could be used to accurately characterize these lesions. Excellent agreement was found between DSA and the MR cartographic technique for the main arterial feeders, while there was perfect agreement ($\kappa = 1$) for retrograde dural venous sinus flow and cortical vein reflux. This study had several limitations, including the small sample size of just 8 patients, 5 with CVD.

3.5.6 Perfusion Imaging

Due to the fact that DAVFs are primarily a disease of blood vessels (the "pipes"), there is an emphasis on angiographic imaging in their work-up. However, as has been discussed in sections 3.1 and 3.3, DAVFs can cause venous hypertension, which in turn can lead to parenchymal complications of haemorrhage, vasogenic oedema and ischaemia. As discussed in section 2.1, cerebral perfusion pressure can be decreased due to venous hypertension[69]. This in turn can lead to compensatory haemodynamic changes. Evaluation of the haemodynamic effects of a DAVF on brain parenchyma using perfusion imaging may therefore allow detection of venous hypertension and assessment of its severity. Although MR and CT perfusion may be a valuable adjunct to anatomical imaging for non-invasive risk stratification,

only a few studies that have assessed the effects of shunting and impaired venous drainage on cerebral haemodynamics in DAVFs[70-72].

Perfusion methods can also enhance the diagnostic conspicuity of shunting lesions. While 3D TOF-MRA and TR-CEMRA have shown high sensitivity and specificity for the identification of DAVFs, this has been in the context of studies performed at tertiary centres with experienced neuroradiologists as the readers. The diagnostic performance of the broader community of general radiologists who report brain MRI studies on these standard MRI sequences is likely much poorer. Although improvements in MRA techniques have made the detection of DAVFs easier, the identification of small shunting lesions remains challenging, especially for radiologists outside tertiary referral centres who see these lesions infrequently and do not have neuroradiology expertise. The widespread availability of MRI scanners has led to an increase in the number of MRIs being performed at peripheral, regional, and community centres. There is, therefore, an unmet clinical need for easy to implement and interpret non-invasive techniques that increase the conspicuity of DAVFs.

3.5.6.1 CT Perfusion

While not a routine part of the diagnostic work-up of DAVFs, CTP is now performed at many centres around the world as a part of the diagnostic work-up of stroke patients. Since DAVFs can be a stroke mimic, it is important to be able to recognize the findings on CTP that suggest shunting. There have been no previous specific investigations of the CT perfusion characteristics of DAVFs. The patterns of perfusion abnormalities in patients with brain AVMs has been described, and it is likely (theoretically and based on case studies) that the features related to venous congestion can be extrapolated to DAVFs[73-75]. High flow shunts increase venous pressure and preclude normal venous drainage. This venous congestion and hypertension are manifested as increased *cerebral blood volume* (CBV) and delayed tracer transit time, that is, increased *mean transit time* (MTT) on CTP[74, 75]. An example is shown in Figure 3-10, where CBV and Tmax are increased in the left temporal lobe of a patient with a transverse and sigmoid sinus dAVF.

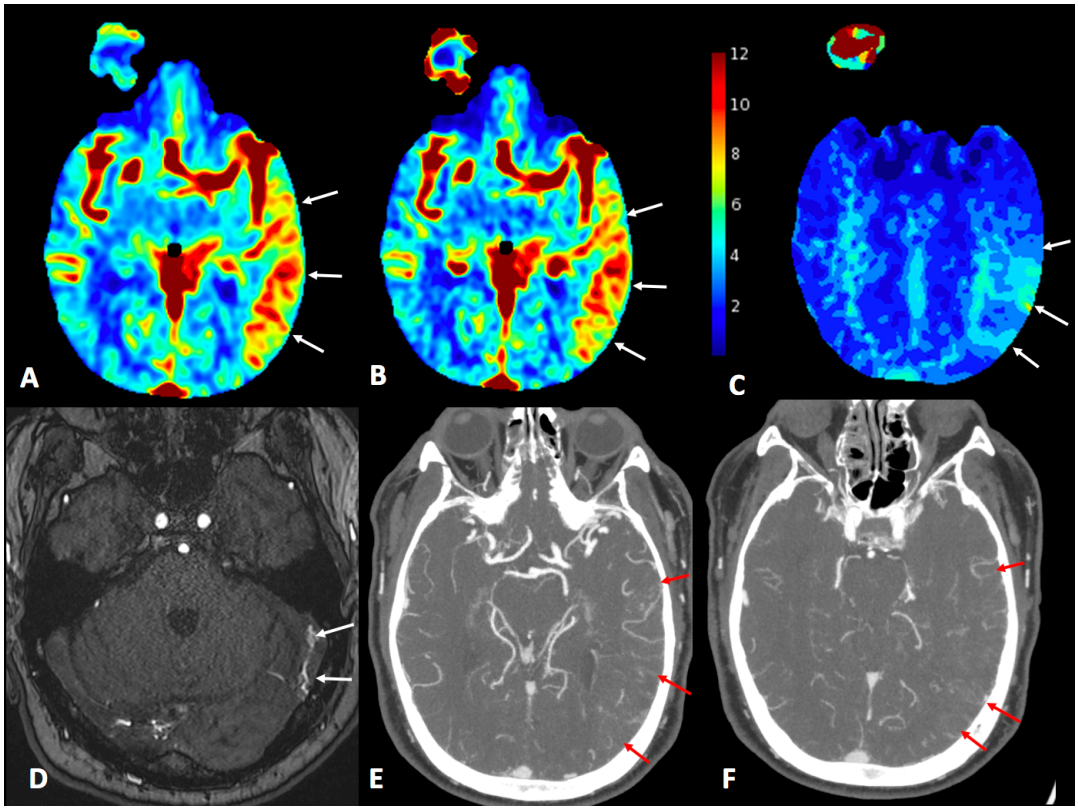

Figure 3-10. *CTP findings in a 62 year-old man who presented with a sudden onset neurological deficit that was thought clinically to be due to a stroke.* ***A.*** *rCBF map showing elevated cerebral blood flow in the left temporal lobe and* ***B.*** *rCBV map showing corresponding elevation of cerebral blood volume in this area. This was initially interpreted as due to seizure activity but the* ***C.*** *Tmax prolongation argued against this.* ***D.*** *TOF-MRA image showing an extensive DAVF with torcula and transverse sinus involvement (arrowed).* ***E.*** *and* ***F.*** *CTA 5 mm maximum intensity projection images showing engorged medullary veins and dilated pial veins. Inclusion of these 100% blood volume structures in the calculation of tissue perfusion explains the elevated rCBF and rCBV.*

3.5.6.2 DSC-PWI

DSC-PWI is the most widely used MR perfusion technique and has already been discussed in the context of stroke. The technical aspects of DSC-PWI will be discussed in detail in the following chapter (section 4.3). Briefly, the first-pass of a bolus of non-diffusible paramagnetic tracer, i.e. *gadolinium-based contrast agent* (GBCA), is tracked dynamically using a high-temporal resolution T_2*-weighted sequence[76]. By analysing the signal intensity changes, perfusion parameters including Tmax, *relative CBV* (rCBV), and *relative CBF* (rCBF) can be determined[76]. Relative values, normalized to a reference point, are obtained rather than absolute measurements due to the non-linear relationship between MR signal and GBCA concentration[76].

Three small studies have examining the hemodynamic findings in DAVFs using DSC PWI[70-72]. To allow inter-patient comparison, the hemodynamic measurements on the side ipsilateral to the DAVF were normalized to measurements obtained in the corresponding location on the contralateral side. One study found that hemodynamic impairment was present in all posterior fossa DAVFs, regardless of venous drainage pattern[70]. Sigmoid and transverse sinus fistulas were associated with elevation of ipsilateral cortical grey matter rCBV, with corresponding decrease in rCBF. These changes were greater in the presence of CVD. The other two studies found that ipsilateral rCBV elevation was a very sensitive indicator of CVD, with significantly increased rCBV only seen in the affected hemisphere[71, 72]. Following treatment that obliterated CVD, rCBV was found to decrease[71]. The small sample size of these studies limits the statistical significance of conclusions that can be drawn regarding DSC-PWI in DAVFs.

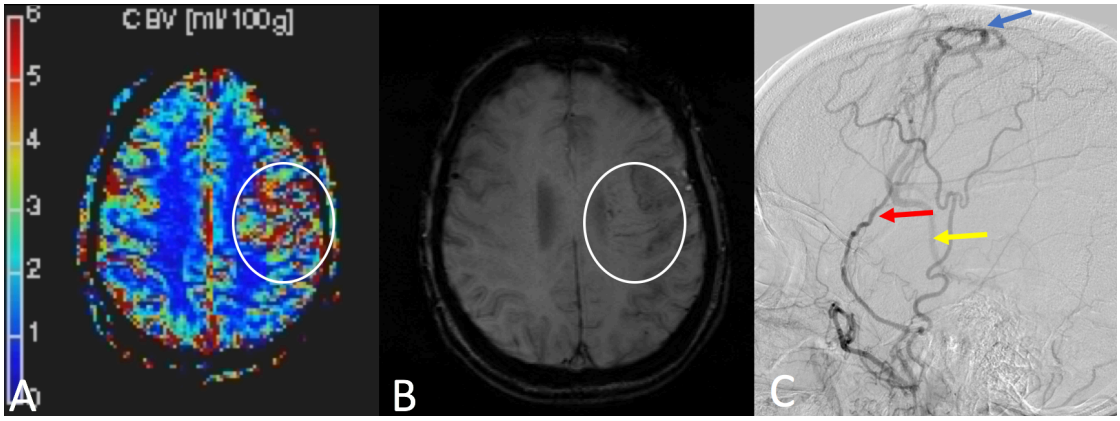

Figures 3-11. *Selected images from a 64 year-old man with man with a Cognard III fistula, draining directly into the superior anastomotic vein of Trolard.* ***A.*** *rCBV map, derived from DSC-PWI, showing markedly elevated rCBV in the posterolateral left frontal lobe (white circle), a highly conspicuous finding which can alert the reporting radiologist to the presence of an abnormality. A gradient echo DSC-PWI acquisition was used here; given the large-vessel sensitivity of this sequence, the apparent increase in rCBV is likely due to spatially exaggerated signal loss resulting from the magnetic susceptibility effects of deoxy-haemoglobin within dilated, engorged medullary veins, rather than true tissue capillary level increase in blood volume.* ***B.*** *Axial SWAN image confirming the presence of dilated medullary veins in the area of elevated rCBV, manifesting as linear very low signal intensity structures (white circle); the low signal intensity on SWAN is again due to the magnetic susceptibility effect of de-oxyhaemoglobin in venous blood.* ***C.*** *Lateral DSA image in the mid arterial phase showing a parasagittal Cognard III fistula (blue arrow) supplied by a branch of the middle meningeal artery (red arrow) and draining into the vein of Trolard and subsequently Labbé (yellow arrow), which is only faintly and partially opacified here.*

Of note, these studies used gradient-echo DSC-PWI implementations, which are more sensitive to large vessels than capillary level perfusion; this is due to the greater susceptibility effects in and around large vessels[76]. The elevated rCBV observed in patients with DAVFs is therefore likely due to the blood pool effect of dilated, engorged medullary and cortical veins rather than true increase in tissue capillary-level blood volume (illustrated in Figure 3-11). In order to calculate true tissue perfusion, either these venous structures should be masked out or a spin-echo DSC-PWI technique should be used. However, accurate measurement of tissue perfusion may not be as important as detecting abnormal veins in this setting. Dilated medullary veins indicate venous hypertension, which is both associated with CVD and an independent risk factor for haemorrhage. The large vessel sensitivity of GRE-based DSC-PWI could therefore be leveraged for risk stratification, allowing differentiation of high grade DAVFs with CVD and/or venous hypertension from low-grade fistulas based on rCBV.

3.5.6.3 Arterial spin labelling

Arterial spin labelling (ASL) is an entirely non-invasive MR perfusion technique that utilizes magnetically labelled water protons in arterial blood as a diffusible tracer[77, 78]. It is discussed in detail in the section 4.5. ASL is associated with a number of artifacts that can be an aide to diagnosis[79-81]. One of these is **venous ASL signal**[79, 82, 83]. Under normal conditions, approximately 90% of labelled arterial blood water is extracted at the capillary level into tissue, giving rise to the parenchymal ASL signal and allowing measurement of tissue blood flow[82, 83]. Further, the T_1-decay of labelled water is much shorter than its mean dwell time within a voxel, therefore most labelled blood water relaxes during capillary transit[81-83]. These two factors result in minimal venous outflow of labelled blood under normal conditions[81, 82]. In shunting lesion, such as DAVFs and AVMs, there is rapid passage of blood from feeding arteries to draining veins. This arteriovenous shunting, with bypass of the tissue capillary bed, results is incomplete T_1 signal decay of the labelled water. Additionally, it precludes normal capillary level extraction of labelled water protons does not occur. The result is ASL signal in venous structures - the **venous ASL sign**[79, 82, 83].

Examples of venous ASL signal in patients with DAVFs are shown in Figures 3-12 and 3-13. It can be seen that venous ASL signal is a highly conspicuous finding, comparable to diffusion restriction in acute stroke. This high conspicuity is due to the high signal and contrast difference between vessels containing labelled blood

(e.g., vein containing shunted, labelled blood) and the adjacent brain parenchyma, which in turn is due to the large volume fraction in vessels in comparison with the low parenchymal capillary volume[78].

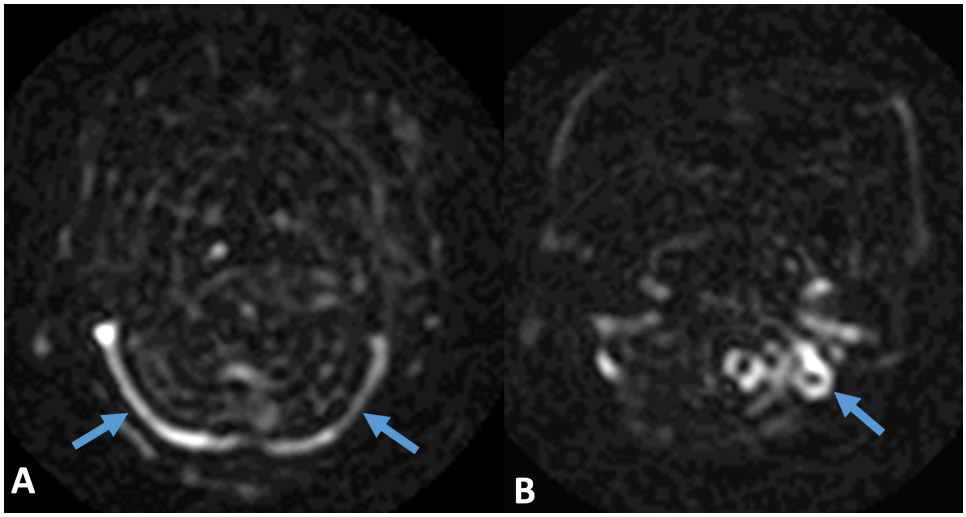

Figure 3-12. *ASL images obtained using pseudocontinuous labelling with a label duration of 1500 ms, a post-label delay of 2000 ms and the labelling plane at the level of the foramen magnum showing* ***venous ASL signal****. The patient was a 79 year-old woman whose DSA and T_2-weighted images have already been shown in Figures 3-4 and 3-5, respectively.* ***A.*** *High signal is seen in the transverse sinuses bilaterally (arrowed).* ***B.*** *High signal is also evident within the draining cortical veins (arrowed) in this Cognard III fistula. Unfortunately, single time-point (single post-label delay) ASL does not provide temporal information that can differentiate between direct and retrograde cortical vein drainage.*

The "light-bulb" conspicuity of venous ASL signal has the potential to be leveraged for non-invasive detection of DAVFs; it can alert the cognizant reader to the presence of arteriovenous shunting, directing them to closer scrutiny of conventional sequences for the structural signs of a DAVF[79, 82, 83]. A preliminary study that included 7 patients with small AVMs and 8 with DAVFs suggested that using the **venous ASL sign** increased sensitivity for detection of shunting lesions, and increased reader confidence in the diagnosis[82]. The authors concluded that including ASL in the MRI protocol improved the detection of shunting lesions, which may otherwise have been occult, by a range of readers[82]. The major limitation of this study is that it included only 8 patients with DAVFs and 11 controls[82]. The control population is important because venous ASL signal is not specific for DAVFs and AVMs; it is also seen in in other conditions where there is arteriovenous shunting, for example some hypervascular tumours and subacute ischaemic stroke with luxury perfusion, as well as in conditions where there is rapid capillary transit such as seizures[81-83]. The clinical context, as well as the findings

on other sequences, are then important to differentiate between these entities. If ASL is to be routinely used for screening purposes in patients with a clinical presentation potentially attributable to a DAVF (e.g., unexplained ICH or pulsatile tinnitus), further validation with a larger number of patients and controls is required to determine whether it is truly a valuable adjunct to more established non-invasive techniques such as 3D TOF MRA. The venous ASL sign may also allow detection of residual or recurrent DAVFs following treatment. One study showed that venous ASL signal had a high specificity and sensitivity for detection of residual shunting after stereotactic radiosurgical treatment of AVMs[84]. Further work is required to determine whether this can be extrapolated to DAVFs.

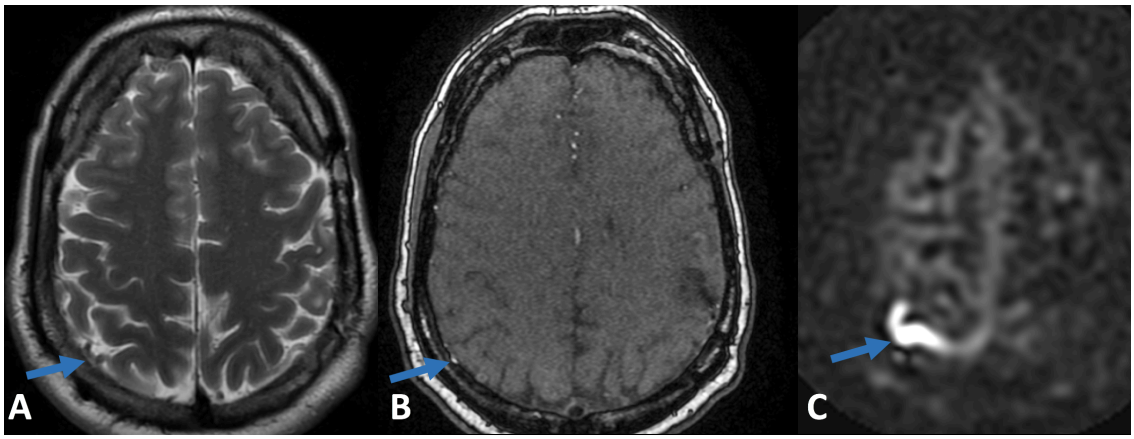

Figure 3-13. Selected images from a 51-year old man with a complex past medical history including previous complete resection of left temporal arteriovenous malformation and an incidental finding of Cognard III DAVF during routine follow-up MRI done to look for AVM recurrence. **A.** A dilated right parietal cortical vein (arrow) is subtle on T2-weighted imaging. **B.** While it is hyperintense on TOF-MRA, this could easily be overlooked and dismissed as a pial artery. **C.** High signal in a cortical vein (***venous ASL signal***) is a much more conspicuous finding, allowing detecting of cortical vein drainage of a DAVF with high sensitivity.

In addition to identifying the presence or absence of a patent DAVF, ASL may also be of value for non-invasive risk stratification. As discussed, the most important prognostic feature, that predicts the risk of haemorrhage with a DAVF, is CVD. The localization of ASL signal may potentially help determine the Cognard or Borden type of the fistula. An example of CVD detected using ASL is shown in Figure 3-13C. A limited study of 9 patients with angiographically-proven DAVFs showed that ASL signal was seen in cortical veins in all 7 patients with CVD but neither of the two patients without CVD[85]. A larger study is required to validate whether venous ASL signal can be used to reliably detect CVD. The perfusion information obtained using ASL may also be of value for risk

stratification, i.e. by allowing assessment of hemodynamic behaviour of the DAVF and detection of venous hypertension[86]. Advantages of ASL over DSC-PWI include that it does not require an extrinsic contrast agent. In a case series of three patients with Cognard **Type IIa+b** DAVFs, elevated CBF was shown around the areas of shunting and was interpreted to be due to a combination of increased CBF within the shunt itself and increased parenchymal CBF[86]. CBF reductions were seen in areas of parenchyma that were drained by cortical veins into which the fistula refluxed in two patients. Further investigation, with a larger patient cohort, is required to determine whether ASL can be used to detect and monitor venous hypertension.

The type of ASL implementation is an important consideration when using this technique for DAVF screening and characterization. The presence, significance and conspicuity of venous ASL signal are dependent upon the ASL technique. Venous ASL signal has been described in association with shunting lesions using all three labelling paradigms: pulsed, pseudo-continuous and continuous[82, 83, 86]. However, signal in the superior sagittal sinus is a normal finding in pulsed implementations where inflow from above the imaging slab causes positive ASL signal[87]. The readout module also impacts upon the ability to visualize venous ASL signal. For example, susceptibility effects related to haemorrhage and embolic material can obscure venous ASL signal when an EPI readout is used[88]. Newer 3D *fast spin echo* (FSE) and combined spin echo-gradient echo (GRASE) techniques have less sensitivity to off-resonance effects[89, 90]. For example, the implementation used by Le *et al* used *pseudo-continuous labelling* (PCASL) with an 3D "stack of spirals" FSE readout[82]; it was reported as "interpretable in all patients, including those with large adjacent hematomas and embolization material", with good inter-reader agreement regarding venous ASL signal[82]. This implementation had a very short echo time, which both decreased sensitivity to off-resonance effects. Importantly, any ASL implementation used for DAVF screening should not use vascular suppression gradients, since these null intravascular signal, including venous ASL signal[89]. The consensus guidelines for clinical ASL implementation recommend the use of PCASL, 3D readouts, background suppression and avoidance of vascular suppression gradients[89]. ASL sequences that adhere to these recommendations optimize the detectability of venous ASL signal. Additionally, scanning at 3T instead of 1.5T should be considered when screening for DAVFs, since higher field strength also increases the conspicuity of venous ASL signal, due to improved SNR and T_1-prolongation (therefore slower ASL signal decay).
The main limitation of ASL that is pertinent to the detection and characterization of DAVFs is the low spatial resolution, which limits the amount of anatomical

information that can be gleaned and necessitates cross referencing with other sequences. The low spatial resolution is necessitated by the inherently low SNR of the technique when it comes to tissue perfusion. However, assessing tissue perfusion is less important than detecting vessel signal in DAVF patients. ASL signal in vessels containing labelled blood is very high due to vessels being 100% blood volume structures. This in turn can be leveraged to increase SNR and obtain angiographic images using ASL.

3.5.6 ASL angiography

Time-resolved ASL angiographic sequences (four-dimensional ASL MR angiography) can provide dynamic information for characterization of DAVFs[91]. These techniques are described in chapter 4 (section 4.5.8). In a series of 9 patients, agreement between DSA and a time-resolved ASL angiographic sequence was found to be excellent ($\kappa = 0.95$) for detection of the fistula site, good ($\kappa = 0.77$) for venous drainage and moderate ($\kappa = 0.53$) for detection of the main arterial feeders. The sequence used had a temporal resolution of 300 ms, which is comparable to DSA, and a spatial resolution that was intermediate between DSA and TR-CEMRA (see Table 3-3), with a voxel size of 0.5 x 0.5 x 0.6 mm[91]. 7 sequential images were obtained with an acquisition time of 8 minutes 20 seconds. This would not be acceptable in the clinical setting if included as part of an MRI protocol; however, one approach would be that patients with findings suspicious or confirmatory of a DAVF on standard MRI sequences can be brought back for timer-resolved ASL angiography to characterize the fistula prior to intervention. The major limitation of this study was the small sample size. Also, only major arterial feeders were delineated. The spatial resolution would likely be inadequate for visualization of small feeding arteries, which may be clinically pertinent if trans-arterial treatment is being contemplated.

Although currently experimental, time-resolved vessel-selective ASL angiographic techniques are likely to be of value for characterizing DAVFs since they provide dynamic vessel-specific information analogous to DSA[92, 93]. These techniques fall under the category of *region-selective ASL* (rsASL), and are discussed in detail in chapter 4 (section 4.5.9)[92-97]. Dynamic imaging can be obtained with high temporal resolution of the order of 50-200 ms using these techniques, which is comparable or superior to that of DSA[92]. The spatial resolution (1.6 mm section thickness and 0.9 mm in-plane resolution) is similar to that of TR CE-MRA, slightly worse than

that of non-selective time-resolved ASL MRA and lower than that of DSA (see Table 3-3).

The diagnostic performance of selective-ASL angiographic techniques for detecting and characterizing DAVFs has not been evaluated. While the lower spatial resolution than that of DSA may hinder detection of small feeding arteries, the technique has a number of advantages over alternative dynamic angiographic techniques that may give it a competitive advantage. First, as with other ASL techniques, there is a large contrast-differential between arteries with labelled blood and background tissue (which is suppressed), which enhances the conspicuity of small feeding arteries and draining cortical veins. Second, venous ASL signal is highly specific for shunting. Therefore, only the draining veins of the DAVF will have high signal. In comparison, normal venous structures opacify and have high signal on both TR-CEMRA and DSA. Identification of the draining veins on DSA and TR CE-MRA is therefore reliant upon detection of early filling, which may be impaired if temporal resolution is inadequate or shunting is slow; in this situation, draining veins may be obscured by normal venous structures. Combined with the higher temporal resolution of the technique, selective ASL angiography is therefore likely to perform better than TR-CEMRA and may even be competitive with DSA for delineating the venous drainage pattern of a DAVF. The other advantage of selective ASL angiography over TR-CEMRA is that it allows selective imaging of individual arteries, which is better for delineating the arterial feeders of a fistula. Single-vessel labelling techniques are likely to be better for selective ASL angiography than multi-vessel techniques that use vessel-encoding (see 4.5.9)[92]; the potential for contamination by labelling of non-target vessels is reduced, which is critical when trying to accurately determine the feeding arteries and their contributions to a DAVF. Using selective labelling, one can be more certain that venous ASL signal occurred as a result of labelling of the selected artery, indicating that it is a feeding artery of the shunt.

Table 3-4. *Summary of imaging techniques used to diagnose and characterize DAVFs*

Modality		**Detection**	**Characterization of DAVF**			**Risk stratification**			**Detection of haemorrhage and oedema**	**Ionizing radiation?**	**Exogenous contrast?**
			Feeding arteries	Fistula location	Venous drainage pattern	CVD	Venous hypertension - altered tissue perfusion	Venous hypertension - structural signs			
DSA	gold standard	+++	+++	+++	+++	+++	-	++	-	Yes	Yes, iodinated
CT	NECT	-	-	-	-	-	-	-	+	Yes	No
	Single-phase CTA	+	++	++	-	-	-	-		Yes	Yes, iodinated
	4D CTA	++	++	++	+	+	+	-	+	Yes	Yes, iodinated
	CTP	+	-	-	-	-	++	-	+	Yes	Yes, iodinated
MRI	Structural sequences*	+	-	-	-	-	-	+	+++	No	No
	SWI	++	-	-	+	+	-	++	+++	No	No
MRA	3D TOF-MRA	++	++	++	+	+	-	-	-	No	Yes, GBCA
	TR-CEMRA	++	+	+	++	+	-	-	-	No	No
	Phase-contrast (4D flow)	++	++	++	++	++	-	-	-	No	No
	Time-resolved ASL angiography	+++	++	++	+++	+++	-	-	-	No	No
Perfusion	DSC-PWI	+	-	-	-		++	-	-	No	Yes, GBCA
	ASL	+++	-	-	++	++	++	-	-	No	No

3.5.7 Summary

A summary of the imaging techniques that can be used to detect and characterize DAVFs is given in Table 3-4. Although uncommon, DAVFs have potentially catastrophic neurological sequelae. Both detection and delineation remain a challenge, due to the non-specific clinical presentation and often-subtle findings on non-invasive imaging modalities. DSA remains the gold standard for diagnosis, characterization, and management planning. Detection of cortical venous drainage and venous hypertension are key to determining the risk of a DAVF, hence this information is vital for decision-making regarding therapy. Preliminary work suggests that ASL perfusion may be a valuable adjunct to conventional structural and angiographic MR sequences, increasing the conspicuity of these lesions and allowing delineation of cortical venous drainage. Larger studies are required to investigate the utility of ASL as a tool that can be used to screen for and accurately characterize DAVFs.

3.6 References

1. Gandhi D, Chen J, Pearl M, Huang J, Gemmete JJ, Kathuria S. Intracranial dural arteriovenous fistulas: Classification, imaging findings, and treatment. *AJNR Am J Neuroradiol*. 2012;33:1007-1013
2. Chung SJ, Kim JS, Kim JC, Lee SK, Kwon SU, Lee MC, et al. Intracranial dural arteriovenous fistulas: Analysis of 60 patients. *Cerebrovasc Dis*. 2002;13:79-88
3. Zipfel GJ, Shah MN, Refai D, Dacey RG, Jr., Derdeyn CP. Cranial dural arteriovenous fistulas: Modification of angiographic classification scales based on new natural history data. *Neurosurg Focus*. 2009;26:E14
4. Cognard C, Gobin YP, Pierot L, Bailly AL, Houdart E, Casasco A, et al. Cerebral dural arteriovenous fistulas: Clinical and angiographic correlation with a revised classification of venous drainage. *Radiology*. 1995;194:671-680
5. Cognard C, Casasco A, Toevi M, Houdart E, Chiras J, Merland JJ. Dural arteriovenous fistulas as a cause of intracranial hypertension due to impairment of cranial venous outflow. *J Neurol Neurosurg Psychiatry*. 1998;65:308-316
6. Morita A, Meyer FB, Nichols DA, Patterson MC. Childhood dural arteriovenous fistulae of the posterior dural sinuses: Three case reports and literature review. *Neurosurgery*. 1995;37:1193-1199; discussion 1199-1200
7. Chi CT, Nguyen D, Duc VT, Chau HH, Son VT. Direct traumatic carotid cavernous fistula: Angiographic classification and treatment strategies. Study of 172 cases. *Interv Neuroradiol*. 2014;20:461-475
8. Chaichana KL, Coon AL, Tamargo RJ, Huang J. Dural arteriovenous fistulas: Epidemiology and clinical presentation. *Neurosurg Clin N Am*. 2012;23:7-13
9. Castaigne P, Bories J, Brunet P, Cassan JL, Meininger V, Merland JJ. [arteriovenous fistulae of the dura mater. Clinical and radiological study of 13 cases]. *Ann Med Interne (Paris)*. 1975;126:813-817
10. Houser OW, Campbell JK, Campbell RJ, Sundt TM, Jr. Arteriovenous malformation affecting the transverse dural venous sinus--an acquired lesion. *Mayo Clin Proc*. 1979;54:651-661
11. Pierot L, Chiras J, Duyckaerts C, Jason M, Martin N. Intracranial dural arteriovenous fistulas and sinus thrombosis. Report of five cases. *J Neuroradiol*. 1993;20:9-18
12. Chaudhary MY, Sachdev VP, Cho SH, Weitzner I, Jr., Puljic S, Huang YP. Dural arteriovenous malformation of the major venous sinuses: An acquired lesion. *AJNR Am J Neuroradiol*. 1982;3:13-19

13. Nabors MW, Azzam CJ, Albanna FJ, Gulya AJ, Davis DO, Kobrine AI. Delayed postoperative dural arteriovenous malformations. Report of two cases. *J Neurosurg*. 1987;66:768-772

14. Kerber CW, Newton TH. The macro and microvasculature of the dura mater. *Neuroradiology*. 1973;6:175-179

15. Kojima T, Miyachi S, Sahara Y, Nakai K, Okamoto T, Hattori K, et al. The relationship between venous hypertension and expression of vascular endothelial growth factor: Hemodynamic and immunohistochemical examinations in a rat venous hypertension model. *Surg Neurol*. 2007;68:277-284; discussion 284

16. Izumi T, Miyachi S, Hattori K, Iizuka H, Nakane Y, Yoshida J. Thrombophilic abnormalities among patients with cranial dural arteriovenous fistulas. *Neurosurgery*. 2007;61:262-268; discussion 268-269

17. Cognard C, Houdart E, Casasco A, Gabrillargues J, Chiras J, Merland JJ. Long-term changes in intracranial dural arteriovenous fistulae leading to worsening in the type of venous drainage. *Neuroradiology*. 1997;39:59-66

18. van Dijk JM, terBrugge KG, Willinsky RA, Wallace MC. Clinical course of cranial dural arteriovenous fistulas with long-term persistent cortical venous reflux. *Stroke*. 2002;33:1233-1236

19. Rother J, Waggie K, van Bruggen N, de Crespigny AJ, Moseley ME. Experimental cerebral venous thrombosis: Evaluation using magnetic resonance imaging. *J Cereb Blood Flow Metab*. 1996;16:1353-1361

20. Villringer A, Mehraein S, Einhaupl KM. Pathophysiological aspects of cerebral sinus venous thrombosis (svt). *J Neuroradiol*. 1994;21:72-80

21. Keller E, Flacke S, Urbach H, Schild HH. Diffusion- and perfusion-weighted magnetic resonance imaging in deep cerebral venous thrombosis. *Stroke*. 1999;30:1144-1146

22. Satomi J, van Dijk JM, Terbrugge KG, Willinsky RA, Wallace MC. Benign cranial dural arteriovenous fistulas: Outcome of conservative management based on the natural history of the lesion. *J Neurosurg*. 2002;97:767-770

23. Davies MA, Saleh J, Ter Brugge K, Willinsky R, Wallace MC. The natural history and management of intracranial dural arteriovenous fistulae. Part 1: Benign lesions. *Interv Neuroradiol*. 1997;3:295-302

24. Borden JA, Wu JK, Shucart WA. A proposed classification for spinal and cranial dural arteriovenous fistulous malformations and implications for treatment. *J Neurosurg*. 1995;82:166-179

25. Lasjaunias P, Chiu M, ter Brugge K, Tolia A, Hurth M, Bernstein M. Neurological manifestations of intracranial dural arteriovenous malformations. *J Neurosurg*. 1986;64:724-730

26. Davies MA, Ter Brugge K, Willinsky R, Wallace MC. The natural history and management of intracranial dural arteriovenous fistulae. Part 2: Aggressive lesions. *Interv Neuroradiol*. 1997;3:303-311

27. Hurst RW, Bagley LJ, Galetta S, Glosser G, Lieberman AP, Trojanowski J, et al. Dementia resulting from dural arteriovenous fistulas: The pathologic findings of venous hypertensive encephalopathy. *AJNR Am J Neuroradiol*. 1998;19:1267-1273

28. Awad IA, Little JR, Akarawi WP, Ahl J. Intracranial dural arteriovenous malformations: Factors predisposing to an aggressive neurological course. *J Neurosurg*. 1990;72:839-850

29. Willinsky R, Goyal M, terBrugge K, Montanera W. Tortuous, engorged pial veins in intracranial dural arteriovenous fistulas: Correlations with presentation, location, and mr findings in 122 patients. *AJNR Am J Neuroradiol*. 1999;20:1031-1036

30. Luciani A, Houdart E, Mounayer C, Saint Maurice JP, Merland JJ. Spontaneous closure of dural arteriovenous fistulas: Report of three cases and review of the literature. *AJNR Am J Neuroradiol*. 2001;22:992-996

31. Saito A, Furuno Y, Nishimura S, Kamiyama H, Nishijima M. Spontaneous closure of transverse sinus dural arteriovenous fistula: Case report. *Neurol Med Chir (Tokyo)*. 2008;48:564-568

32. Cognard C, Januel AC, Silva NA, Jr., Tall P. Endovascular treatment of intracranial dural arteriovenous fistulas with cortical venous drainage: New management using onyx. *AJNR Am J Neuroradiol*. 2008;29:235-241

33. Kiyosue H, Hori Y, Okahara M, Tanoue S, Sagara Y, Matsumoto S, et al. Treatment of intracranial dural arteriovenous fistulas: Current strategies based on location and hemodynamics, and alternative techniques of transcatheter embolization. *Radiographics*. 2004;24:1637-1653

34. Roy D, Raymond J. The role of transvenous embolization in the treatment of intracranial dural arteriovenous fistulas. *Neurosurgery*. 1997;40:1133-1141; discussion 1141-1134

35. Urtasun F, Biondi A, Casaco A, Houdart E, Caputo N, Aymard A, et al. Cerebral dural arteriovenous fistulas: Percutaneous transvenous embolization. *Radiology*. 1996;199:209-217

36. Lucas CP, Zabramski JM, Spetzler RF, Jacobowitz R. Treatment for intracranial dural arteriovenous malformations: A meta-analysis from the english language literature. *Neurosurgery*. 1997;40:1119-1130; discussion 1130-1112

37. Kakarla UK, Deshmukh VR, Zabramski JM, Albuquerque FC, McDougall CG, Spetzler RF. Surgical treatment of high-risk intracranial dural arteriovenous fistulae: Clinical outcomes and avoidance of complications. *Neurosurgery*. 2007;61:447-457; discussion 457-449

38. Guo WY, Pan DH, Wu HM, Chung WY, Shiau CY, Wang LW, et al. Radiosurgery as a treatment alternative for dural arteriovenous fistulas of the cavernous sinus. *AJNR Am J Neuroradiol*. 1998;19:1081-1087

39. Mironov A. Selective transvenous embolization of dural fistulas without occlusion of the dural sinus. *AJNR Am J Neuroradiol*. 1998;19:389-391

40. Cloft HJ, Joseph GJ, Dion JE. Risk of cerebral angiography in patients with subarachnoid hemorrhage, cerebral aneurysm, and arteriovenous malformation: A meta-analysis. *Stroke*. 1999;30:317-320

41. Meckel S, Maier M, Ruiz DS, Yilmaz H, Scheffler K, Radue EW, et al. Mr angiography of dural arteriovenous fistulas: Diagnosis and follow-up after treatment using a time-resolved 3d contrast-enhanced technique. *AJNR Am J Neuroradiol*. 2007;28:877-884

42. Lin A, Rawal S, Agid R, Mandell DM. Cerebrovascular imaging: Which test is best? *Neurosurgery*. 2018;83:5-18

43. Ahn SH, Prince EA, Dubel GJ. Basic neuroangiography: Review of technique and perioperative patient care. *Semin Intervent Radiol*. 2013;30:225-233

44. Brown RD, Jr., Flemming KD, Meyer FB, Cloft HJ, Pollock BE, Link ML. Natural history, evaluation, and management of intracranial vascular malformations. *Mayo Clin Proc*. 2005;80:269-281

45. Lescher S, Gehrisch S, Klein S, Berkefeld J. Time-resolved 3d rotational angiography: Display of detailed neurovascular anatomy in patients with intracranial vascular malformations. *J Neurointerv Surg*. 2017;9:887-894

46. Lang S, Golitz P, Struffert T, Rosch J, Rossler K, Kowarschik M, et al. 4d dsa for dynamic visualization of cerebral vasculature: A single-center experience in 26 cases. *AJNR Am J Neuroradiol*. 2017;38:1169-1176

47. Sandoval-Garcia C, Yang P, Schubert T, Schafer S, Hetzel S, Ahmed A, et al. Comparison of the diagnostic utility of 4d-dsa with conventional 2d- and 3d-dsa in the diagnosis of cerebrovascular abnormalities. *AJNR Am J Neuroradiol*. 2017;38:729-734

48. Cohen SD, Goins JL, Butler SG, Morris PP, Browne JD. Dural arteriovenous fistula: Diagnosis, treatment, and outcomes. *Laryngoscope*. 2009;119:293-297

49. Brouwer PA, Bosman T, van Walderveen MA, Krings T, Leroux AA, Willems PW. Dynamic 320-section ct angiography in cranial arteriovenous shunting lesions. *AJNR Am J Neuroradiol*. 2010;31:767-770

50. Fujiwara H, Momoshima S, Akiyama T, Kuribayashi S. Whole-brain ct digital subtraction angiography of cerebral dural arteriovenous fistula using 320-detector row ct. *Neuroradiology*. 2013;55:837-843

51. Kortman HG, Smit EJ, Oei MT, Manniesing R, Prokop M, Meijer FJ. 4d-cta in neurovascular disease: A review. *AJNR Am J Neuroradiol*. 2015;36:1026-1033

52. Noguchi K, Melhem ER, Kanazawa T, Kubo M, Kuwayama N, Seto H. Intracranial dural arteriovenous fistulas: Evaluation with combined 3d time-of-flight mr angiography and mr digital subtraction angiography. *AJR Am J Roentgenol*. 2004;182:183-190

53. Nishimura S, Hirai T, Sasao A, Kitajima M, Morioka M, Kai Y, et al. Evaluation of dural arteriovenous fistulas with 4d contrast-enhanced mr angiography at 3t. *AJNR Am J Neuroradiol*. 2010;31:80-85

54. Farb RI, Agid R, Willinsky RA, Johnstone DM, Terbrugge KG. Cranial dural arteriovenous fistula: Diagnosis and classification with time-resolved mr angiography at 3t. *AJNR Am J Neuroradiol*. 2009;30:1546-1551

55. Chen JC, Tsuruda JS, Halbach VV. Suspected dural arteriovenous fistula: Results with screening mr angiography in seven patients. *Radiology*. 1992;183:265-271

56. De Marco JK, Dillon WP, Halback VV, Tsuruda JS. Dural arteriovenous fistulas: Evaluation with mr imaging. *Radiology*. 1990;175:193-199

57. Willinsky R, Terbrugge K, Montanera W, Mikulis D, Wallace MC. Venous congestion: An mr finding in dural arteriovenous malformations with cortical venous drainage. *AJNR Am J Neuroradiol*. 1994;15:1501-1507

58. Lee SK, Willinsky RA, Montanera W, terBrugge KG. Mr imaging of dural arteriovenous fistulas draining into cerebellar cortical veins. *AJNR Am J Neuroradiol*. 2003;24:1602-1606

59. Bradley WG, Jr. Mr appearance of hemorrhage in the brain. *Radiology*. 1993;189:15-26

60. Kwon BJ, Han MH, Kang HS, Chang KH. Mr imaging findings of intracranial dural arteriovenous fistulas: Relations with venous drainage patterns. *AJNR Am J Neuroradiol*. 2005;26:2500-2507

61. Hodel J, Gerber S, Zins M, Rodallec M, Leclerc X, Blanc R, et al. Mr imaging findings in intracranial dural arteriovenous fistula shunt with retrograde cortical venous drainage using susceptibility-weighted angiography. *AJNR Am J Neuroradiol*. 2011;32:E196-197

62. Jagadeesan BD, Delgado Almandoz JE, Moran CJ, Benzinger TL. Accuracy of susceptibility-weighted imaging for the detection of arteriovenous shunting in vascular malformations of the brain. *Stroke*. 2011;42:87-92

63. Haacke EM, Xu Y, Cheng YC, Reichenbach JR. Susceptibility weighted imaging (swi). *Magn Reson Med*. 2004;52:612-618

64. Meckel S, Mekle R, Taschner C, Haller S, Scheffler K, Radue EW, et al. Time-resolved 3d contrast-enhanced mra with grappa on a 1.5-t system for imaging of craniocervical vascular disease: Initial experience. *Neuroradiology*. 2006;48:291-299

65. Edjlali M, Roca P, Rabrait C, Trystram D, Rodriguez-Regent C, Johnson KM, et al. Mr selective flow-tracking cartography: A postprocessing procedure applied to four-dimensional flow mr imaging for complete characterization of cranial dural arteriovenous fistulas. *Radiology*. 2014;270:261-268

66. Gu T, Korosec FR, Block WF, Fain SB, Turk Q, Lum D, et al. Pc vipr: A high-speed 3d phase-contrast method for flow quantification and high-resolution angiography. *AJNR Am J Neuroradiol*. 2005;26:743-749

67. Markl M, Frydrychowicz A, Kozerke S, Hope M, Wieben O. 4d flow mri. *J Magn Reson Imaging*. 2012;36:1015-1036

68. Bammer R, Hope TA, Aksoy M, Alley MT. Time-resolved 3d quantitative flow mri of the major intracranial vessels: Initial experience and comparative evaluation at 1.5t and 3.0t in combination with parallel imaging. *Magn Reson Med*. 2007;57:127-140

69. Powers WJ. Cerebral hemodynamics in ischemic cerebrovascular disease. *Ann Neurol*. 1991;29:231-240

70. Fujita A, Nakamura M, Tamaki N, Kohmura E. Haemodynamic assessment in patients with dural arteriovenous fistulae: Dynamic susceptibility contrast-enhanced mri. *Neuroradiology*. 2002;44:806-811

71. Noguchi K, Kubo M, Kuwayama N, Kamisaki Y, Tomizawa G, Kameda K, et al. Intracranial dural arteriovenous fistulas with retrograde cortical venous drainage: Assessment with cerebral blood volume by dynamic susceptibility contrast magnetic resonance imaging. *AJNR Am J Neuroradiol*. 2006;27:1252-1256

72. Noguchi K, Kuwayama N, Kubo M, Kamisaki Y, Kameda K, Tomizawa G, et al. Intracranial dural arteriovenous fistula with retrograde cortical venous drainage:

Use of susceptibility-weighted imaging in combination with dynamic susceptibility contrast imaging. *AJNR Am J Neuroradiol*. 2010;31:1903-1910

73. Lagares A, Millan JM, Ramos A, Alen JA, Gallego JH. Perfusion computed tomography in a dural arteriovenous fistula presenting with focal signs: Vascular congestion as a cause of reversible neurologic dysfunction. *Neurosurgery*. 2010;66:E226-227; discussion E227

74. Kim YW, Kang DH, Hwang YH, Park SP. Unusual mri findings of dural arteriovenous fistula: Isolated perfusion lesions mimicking tia. *BMC Neurol*. 2012;12:77

75. Kim DJ, Krings T. Whole-brain perfusion ct patterns of brain arteriovenous malformations: A pilot study in 18 patients. *AJNR Am J Neuroradiol*. 2011;32:2061-2066

76. Bammer R. Dynamic susceptibility contrast-based pwi. In: Bammer R, ed. *Mr and ct perfusion and pharmacokinet imaging*. Pennsylvania: Wolters-Kluwer; 2016.

77. Williams DS, Detre JA, Leigh JS, Koretsky AP. Magnetic resonance imaging of perfusion using spin inversion of arterial water. *Proc Natl Acad Sci U S A*. 1992;89:212-216

78. Zaharchuk G. Theoretical basis of hemodynamic mr imaging techniques to measure cerebral blood volume, cerebral blood flow, and permeability. *AJNR Am J Neuroradiol*. 2007;28:1850-1858

79. Amukotuwa SA, Yu C, Zaharchuk G. 3d pseudocontinuous arterial spin labeling in routine clinical practice: A review of clinically significant artifacts. *J Magn Reson Imaging*. 2016;43:11-27

80. Deibler AR, Pollock JM, Kraft RA, Tan H, Burdette JH, Maldjian JA. Arterial spin-labeling in routine clinical practice, part 1: Technique and artifacts. *AJNR Am J Neuroradiol*. 2008;29:1228-1234

81. Wolf RL, Detre JA. Clinical neuroimaging using arterial spin-labeled perfusion magnetic resonance imaging. *Neurotherapeutics*. 2007;4:346-359

82. Le TT, Fischbein NJ, Andre JB, Wijman C, Rosenberg J, Zaharchuk G. Identification of venous signal on arterial spin labeling improves diagnosis of dural arteriovenous fistulas and small arteriovenous malformations. *AJNR Am J Neuroradiol*. 2012;33:61-68

83. Wolf RL, Wang J, Detre JA, Zager EL, Hurst RW. Arteriovenous shunt visualization in arteriovenous malformations with arterial spin-labeling mr imaging. *AJNR Am J Neuroradiol*. 2008;29:681-687

84. Heit JJ, Thakur NH, Iv M, Fischbein NJ, Wintermark M, Dodd RL, et al. Arterial-spin labeling mri identifies residual cerebral arteriovenous malformation following stereotactic radiosurgery treatment. *J Neuroradiol*. 2019

85. Noguchi K, Kuwayama N, Kubo M, Kamisaki Y, Kameda K, Tomizawa G, et al. Flow-sensitive alternating inversion recovery (fair) imaging for retrograde cortical venous drainage related to intracranial dural arteriovenous fistula. *Neuroradiology*. 2011;53:153-158

86. Noguchi T, Irie H, Takase Y, Kawashima M, Ootsuka T, Nishihara M, et al. Hemodynamic studies of intracranial dural arteriovenous fistulas using arterial spin-labeling mr imaging. *Interv Neuroradiol*. 2010;16:409-419

87. Kim SG. Quantification of relative cerebral blood flow change by flow-sensitive alternating inversion recovery (fair) technique: Application to functional mapping. *Magn Reson Med*. 1995;34:293-301

88. Kukuk GM, Hadizadeh DR, Bostrom A, Gieseke J, Bergener J, Nelles M, et al. Cerebral arteriovenous malformations at 3.0 t: Intraindividual comparative study of 4d-mra in combination with selective arterial spin labeling and digital subtraction angiography. *Invest Radiol*. 2010;45:126-132

89. Alsop DC, Detre JA, Golay X, Gunther M, Hendrikse J, Hernandez-Garcia L, et al. Recommended implementation of arterial spin-labeled perfusion mri for clinical applications: A consensus of the ismrm perfusion study group and the european consortium for asl in dementia. *Magn Reson Med*. 2015;73:102-116

90. Amukotuwa SA BR. Perfusion in dural arteriovenous fistulas. In: R B, ed. *Mr and ct perfusion and pharmakokinetic imaging*. Philadelphia: Wolters Kluwer; 2016.

91. Iryo Y, Hirai T, Kai Y, Nakamura M, Shigematsu Y, Kitajima M, et al. Intracranial dural arteriovenous fistulas: Evaluation with 3-t four-dimensional mr angiography using arterial spin labeling. *Radiology*. 2014;271:193-199

92. Robson PM, Dai W, Shankaranarayanan A, Rofsky NM, Alsop DC. Time-resolved vessel-selective digital subtraction mr angiography of the cerebral vasculature with arterial spin labeling. *Radiology*. 2010;257:507-515

93. Okell TW, Chappell MA, Woolrich MW, Gunther M, Feinberg DA, Jezzard P. Vessel-encoded dynamic magnetic resonance angiography using arterial spin labeling. *Magn Reson Med*. 2010;64:430-438

94. Wong EC. Vessel-encoded arterial spin-labeling using pseudocontinuous tagging. *Magn Reson Med*. 2007;58:1086-1091

95. van Laar PJ, van der Grond J, Hendrikse J. Brain perfusion territory imaging: Methods and clinical applications of selective arterial spin-labeling mr imaging. *Radiology*. 2008;246:354-364

96. Hendrikse J, van der Grond J, Lu H, van Zijl PC, Golay X. Flow territory mapping of the cerebral arteries with regional perfusion mri. *Stroke*. 2004;35:882-887

97. Gunther M. Efficient visualization of vascular territories in the human brain by cycled arterial spin labeling mri. *Magn Reson Med*. 2006;56:671-675

Chapter 4

Theory of Perfusion and Automation Techniques

The technical aspects of the three perfusion techniques that have been discussed in the previous chapters, CTP, DSC-PWI, and ASL, will be elaborated upon in this chapter. This is followed by a detailed discussion of the current status of automation in AIS.

4.1 Cerebral Perfusion Definitions

Perfusion refers to blood flow at the tissue capillary level. Brain perfusion is usually described using the following physiological parameters: *cerebral blood flow* (CBF), *cerebral blood volume* (CBV), and *mean transit time* (MTT).

CBF is defined as the volume of blood that moves through a given volume of brain tissue per unit time, and is expressed as mL per 100 g brain tissue per minute (mL/100g/minute)[1]. CBV is the total volume of flowing (intravascular) blood in a given volume of brain tissue, and is expressed in mL per 100 g brain tissue (mL/100g)[1]. For an ideal infinitesimally short contrast bolus injected at the arteriolar end, MTT is the time taken for blood to traverse the tissue capillary bed, from arteriolar end to venular end. It is defined as the mean transit time of blood through a given region, for example the brain tissue in the image voxel, and is measured in seconds[1].

4.2 CT Perfusion

CT perfusion is a bolus perfusion technique. It was first proposed by *Axel* in 1980, however it was not until mid 1990s that hardware and post-processing software developments allowed clinical implementation[2, 3]. Further developments over the coming decade resulted in more widespread clinical availability and uptake[4, 5].

4.2.1 CTP Image Acquisition

For a typical CTP acquisition, a 35 to 45 mL bolus of high-concentration iodinated contrast agent is injected at a rate of 4-6 mL/second using a power injector, followed by a 40 mL bolus of saline (**chaser**) at the same flow rate[6]. CT images are then acquired at 80 kV (rather than 120-140 kV which is used for non-enhanced CT and CTA), because it is closer to the k-edge of iodine (~35 kV), therefore increases the conspicuity (i.e., contrast-to-noise ratio, CNR) of intravascular iodinated contrast[6]. This has the added benefit of reducing the radiation dose to the patient.

Image acquisition is performed in the **cine mode**. Both the duration and temporal resolution of the cine acquisition must be adequate to faithfully sample the tissue time-density curve, including in situations where blood flow is markedly delayed as occurs in *acute ischemic stroke* (AIS) but also due to cardiac arrhythmias, poor cardiac output and proximal arterial stenosis or occlusion[7]. The CTP acquisition should therefore be at least 65 seconds long[6]. The need to achieve an adequate temporal resolution must be balanced against the radiation dose. High temporal resolution is used early (e.g., in the first 45 seconds), with a lower temporal resolution for the remainder of the acquisition. With patient radiation dose being the limiting factor, it must also be considered that using sparser sampling places more weight on each point measured (i.e., point estimates need to be more accurate for sparsely sampled datasets). *Wintermark et al* have shown that decreasing temporal resolution and increasing the imaging interval from 1 second to 2-3 seconds does not substantially affect quantification in either normal or ischemic areas[8].

The imaged volume of brain tissue was limited with older generation CT scanners, due to the inherent limitation of CT detector width[7]. A CT scanner with 16 detector rows allowed a 2 cm slab to be imaged, while a 64-detector row scanner could cover a 4 cm slab. This limitation was overcome by either acquiring 2 slabs with two separate contrast injections, or scanning in the **shuttle** (or **jog**) **mode**. Here, the z-direction coverage is increased by moving the scanner table back and forth between two different volumes of brain tissue at reduced temporal resolution[9]. This achieves the same coverage as two separate slabs with a single bolus injection and half the radiation dose. Another alternative is **helical-shuttle mode**, which is based on a dynamic, spiral acquisition and is mainly used for smaller detectors[6]. Newer generation CT scanners have larger detector arrays that allow increased volume coverage. For example, 320 detector-row CT scanners allow 16 cm z-

direction coverage. Whole brain coverage is now possible, ensuring that the entire territory at risk of infarction is covered in stroke patients. These wider detector CT scanners use "cone beam" reconstruction, which is very slow for wide beam collimation.

The typical *volume-normalized CT dose index* ($CTDI_{vol}$) for optimized CTP protocols on contemporary CT scanners is approximately 260 – 350 mGy[6]. Lower radiation doses can be achieved with iterative reconstruction algorithms or machine learning de-noising[6, 10, 11].

4.2.2 Determination of Perfusion Parameters

CTP is a dynamic first-pass bolus perfusion technique. Images of the brain are acquired serially with high temporal resolution to track the initial passage (**first pass**) of an intravenously administered intravascular contrast agent through the brain tissue capillary bed[1]. A key assumption is that the injected tracer (contrast agent) is **non-diffusible**, which is to say that it remains purely intravascular and is not exchanged, absorbed nor metabolized by the brain tissue. This condition is fulfilled with iodinated contrast agents when the blood brain barrier is intact[12].

The passage of iodinated contrast material (typically 350 mg iodine/mol) through the tissue capillary bed results in time-dependent changes in X-ray absorption[6]. Therefore, there is a linear relationship between the density measurement (in Hounsfield units) on CT and the concentration of iodinated contrast agent, i.e. the change in CT attenuation is directly proportional to the concentration of iodinated contrast agent[1]. Density measurements obtained during the first-pass can therefore be converted directly to concentration-time curves[1].

Indicator dilution theory can then be applied to determine perfusion parameters[13, 14]. **Tracer kinetic modelling** describes the passage of a contrast bolus through tissue. According to this theory, the volume of distribution and clearance rate of a non-diffusible tracer can be determined if both the input and output of the contrast agent from a brain tissue voxel can be measured[13, 14]. This model assumes a constant flow rate[13]. The volume of distribution of an intravascular tracer is called the **fractional vascular volume**, and the clearance rate is the **flow per unit tissue volume**.

The *fractional vascular volume* (f) is the fraction of a voxel that is occupied by

blood vessels (the vascular compartment). A voxel within a large vessel is comprised entirely of intravascular blood, hence $f = 1$ (i.e., 100% blood volume). A brain tissue voxel is composed of blood vessels, the interstitial space (extracellular compartment), and cells (neurons and glia):

$$f = \mathrm{V}_{vascular} / (\mathrm{V}_{vascular} + \mathrm{V}_{interstitium} + \mathrm{V}_{cells}) \quad [2\text{-}1]$$

If major blood vessels are excluded, then f represents the tissue blood pool, which is the relative volume fraction of the capillary bed (i.e., the fraction of the voxel that is comprised of capillaries). This is also more commonly known as *relative cerebral blood volume* (rCBV). In a region of brain tissue that is devoid of major blood vessels, the measured change in CT density (hence contrast concentration) will reflect rCBV. The tissue concentration-time curve, $C_{tissue}(t)$, is therefore measured. The concentration-time curve in an artery (100% blood volume structure), $C_{artery}(t)$, is also measured. The integral of $C_{tissue}(t)$ is proportional to the total amount of contrast delivered to tissue, while the integral of the $C_{artery}(t)$ is proportional to the total amount of contrast passing through the artery. For **conservation-of-mass** to be upheld, the total amount of contrast passing through the tissue capillary bed must be equal to the total amount of contrast passing through an artery (100% blood volume structure) multiplied by the tissue blood pool[2, 13]:

$$rCBV = \frac{\int_0^t \mathrm{C}tissue(\tau)d\tau}{\int_0^t \mathrm{C}artery(\tau)d\tau} \quad [2\text{-}2]$$

Absolute CBV can then be determined from the above equation by adjusting $rCBV$ for **brain tissue attenuation**, p, and a correction factor, CH, that reflects the lower **haematocrit** (concentration of red blood cells) in capillaries than in arteries[15-17]:

$$CBV = \left[\frac{CH}{p}\right].f = \frac{CH}{p}.\frac{\int_0^t \mathrm{C}tissue(\tau)d\tau}{\int_0^t \mathrm{C}artery(\tau)d\tau} \quad [2\text{-}3]$$

The importance of having an adequately long enough scan duration, to capture the entire passage of the bolus of contrast agent through the tissue capillary bed, can be seen from equation 2-3: if C_{tissue} is not captured completely, for example because of delayed arrival of contrast or prolonged transit time, its integral and CBV in turn will be underestimated.

In their seminal papers applying indication dilution theory to the measurement of blood volume and blood flow, *Meier* and *Zierler* established the following relationship: volume = flow x mean circulation time[13]. This is termed the **central volume principle**, stated as:

$$CBV = CBF \cdot MTT \quad [2\text{-}4]$$

In addition to the fractional vascular volume, the flow per unit tissue volume, CBF, can also be determined using **indicator dilution theory**[13, 14]. As discussed, indicator dilution theory states that the **volume of distribution** and the **clearance rate** of a non-diffusible tracer can be determined if the input and output of the contrast agent from a brain tissue voxel can be measured[13, 14]. Unfortunately, the voxel output venule cannot be directly measured since it is too small, and large venous structures such as cortical veins and dural venous sinuses cannot be used as a surrogate since they are spatially non-discriminative, draining many voxels. Two parameters that can be measured from the CTP source images are: the density-time curve, which is directly proportional to the concentration of contrast agent over time in brain tissue, C_{tissue}; and the density-time curve, which is directly proportional to the concentration of contrast agent over time in a feeding artery, C_{artery}. **Deconvolution**-based methods are the most widely validated and used approach to calculating perfusion parameters from these measurable inputs and will be the focus of this discussion.

The tissue concentration-time curve, $C_{tissue}(t)$, is produced by the interaction or **convolution** of two functions:

1. The concentration-time curve of the input artery into the tissue voxel, $C_{artery}(t)$; and
2. The tissue residue function, $R(t)$.

$C_{artery}(t)$ is also referred to as the *arterial input function* (AIF), i.e. $AIF(t)$. The residue function, $R(t)$, is the fraction of tracer that remains within the tissue capillary bed of the voxel of interest at time t (i.e., the amount of contrast agent that has entered but not yet left the capillary bed through the venous outlet) following an ideal, infinitesimally short (i.e., *Dirac* impulse) injection of a unit mass of contrast material directly into the inlet of the voxel. The residue function is unit-less, has a value of 1 at time *0* s when all the administered contrast is still in the tissue and has not yet left the capillary bed, and decays over time according to:

$$R(t) = 1 - \int_0^t h(t)dt \qquad [2\text{-}5]$$

In equation 2-5, *h(t)*, is the impulse response function (Figure 4-1). *R(t)* and *h(t)* are intrinsic properties of the tissue and are determined mainly by the distribution of path lengths of the capillaries in the tissue voxel, which in turn determines the distribution of tracer transit times through the tissue capillary bed. For a Dirac-type (infinitesimally short) bolus, *h(t)* is the **probability density function** of the transit time of tracer molecules through the tissue capillary bed (Figure 4-1). The *mean transit time* (MTT) for tracer material to pass through the capillary bed is directly evident from the *h(t)* distribution of tracer transit times, i.e. the 1st moment of *h(t)*. However, for arterial inputs that are not infinitesimally short, this assumption does not hold and *MTT* is defined as the integral of *R(t)* over time.

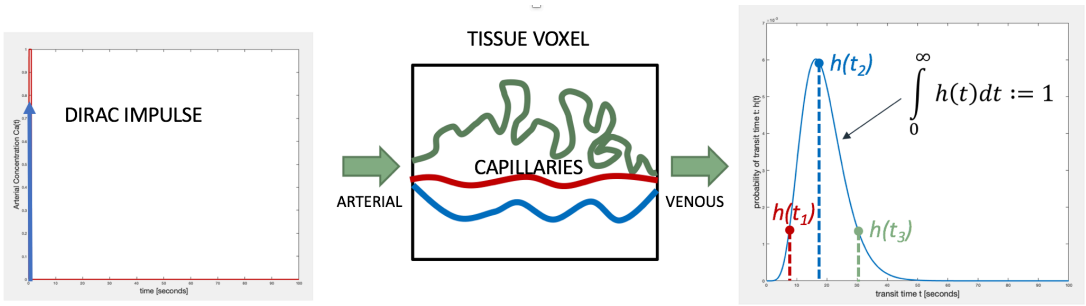

Figure 4-1: *Impulse response function,* ***h(t)****. When a Dirac-type (instantaneous) bolus is applied at the arterial end of the voxel, tracer molecules take different lengths of time to traverse the tissue voxel due to different capillary path lengths (shortest in red, longest in green). This is an intrinsic property of the tissue. The probability density function of this transit time of tracer molecules is* ***h(t)****.*

The area under *h(t)* at time *t* is the total number of tracer molecules that have left the voxel up to time *t*. *R(t)* denotes the residual amount of tracer left in the voxel (equation 2-5). At *t=0*, no tracer molecules have left the voxel yet therefore *R(t)* is maximal and equal to 1. Thus *R(t)* describes the effect of the voxel's capillary bed in response to a given AIF to produce $C_{tissue}(t)$, which can be measured[13]. The mathematical process of convolution describes this effect of *R(t)* on the *AIF(t)* to produce $C_{tissue}(t)$[13]:

$$C_{tissue}(t) = \frac{\rho}{CH} \cdot CBF \cdot [AIF(t) \otimes R(t)] \qquad [2\text{-}6]$$

Using perfusion imaging, we can measure the *AIF(t)* and $C_{tissue}(t)$. *R(t)* can therefore be determined by deconvolution

$$C_{tissue}(t) \otimes^{-1} AIF(t) = \frac{\rho}{CH} \cdot CBF \cdot R(t) \quad [2\text{-}7]$$

Several methods exist to solve this deconvolution equation and obtain CBF and *R(t)*. Model dependent methods assume a particular shape of *R(t)*, but are sensitive to noise and introduce errors since the inherent hemodynamic properties of brain tissue vary and cannot be accurately assumed[18-20]. Model-independent methods, that treat both *R(t)* and CBF as unknowns, are therefore more robust and widely used.

One model-independent solution is to apply the *Fourier transform* (FT) **convolution theorem**, which states that *"multiplying the FTs of two time-domain functions yields the FT of the convolution of these two functions"* [19-21], i.e. convolution in the time domain translates to multiplication in the frequency domain. Therefore, *R(t)* and *CBF* can be determined as follows:

$$R(t) = \frac{1}{CBF} \cdot \Im^{-1}\left\{\frac{\Im[C_{tissue}(t)]}{\Im[AIF(t)]}\right\} \quad [2\text{-}8]$$

This method is very sensitive to noise, since noise in the measured C_{tissue} and *AIF* is amplified by division, particularly in the high-frequency part. Low-pass filters are therefore required to damp these high frequency oscillations[19, 20].

The method that is most widely known and used in perfusion imaging is *singular value decomposition* (SVD). The continuous convolution equation can be **discretized** (i.e., the data are sampled at equally spaced time intervals, Δt, to give $t_0, t_1, t_2, \ldots, t_{n-1}$) and algebraically reformulated as:

$$C_{tissue}(t_j) = \frac{\rho}{CH} \cdot CBF \cdot \Delta t \sum_{i=0}^{j} AIF(t_j) \cdot R(t_j - t_i) \quad [2\text{-}9]$$

Equation 2-9 can be written in matrix notation:

$$\underbrace{\frac{\rho}{CH} \cdot \Delta t \cdot CBF}_{\xi} \cdot \underbrace{\begin{pmatrix} AIF(t_1) & 0 & \cdots & 0 & 0 \\ AIF(t_2) & AIF(t_1) & \cdots & 0 & 0 \\ \vdots & \vdots & \ddots & \vdots & \vdots \\ AIF(t_{N-1}) & AIF(t_{N-2}) & \cdots & AIF(t_1) & 0 \\ AIF(t_N) & AIF(t_{N-1}) & \cdots & AIF(t_2) & AIF(t_1) \end{pmatrix}}_{\mathbf{A}} \cdot \underbrace{\begin{pmatrix} R(t_1) \\ R(t_2) \\ \vdots \\ R(t_{N-1}) \\ R(t_N) \end{pmatrix}}_{\mathbf{r}} = \underbrace{\begin{pmatrix} C_{tissue}(t_1) \\ C_{tissue}(t_2) \\ \vdots \\ C_{tissue}(t_{N-1}) \\ C_{tissue}(t_N) \end{pmatrix}}_{\mathbf{c}} \quad [2\text{-}10]$$

In short-hand matrix-vector notation, this is written as:

$$\xi \cdot \mathrm{CBF} \cdot \mathbf{A}\,\mathbf{r} = \mathbf{c} \qquad [2\text{-}11]$$

Here, **r** is a vector which contains the discretized residue function elements, $R(t_i)$, which are the unknowns. The vector **c** contains the discretized version of $C_{tissue}(t)$ and **A** is the matrix with AIF elements. Close inspection of each row of **A** shows that the AIF time course is mirrored (in time) and then shifted by one time increment before element-wise multiplication with **r**. This is characteristic for the convolution operation. Equation 2-11 is a linear algebra problem and can be solved for the unknown vector **r** using a least-squares approach:

$$min\|\xi \cdot \mathrm{CBF} \cdot \mathbf{A}\,\mathbf{r} - \mathbf{c}\|_2^2 \qquad [2\text{-}12]$$

This can be treated as an *inverse matrix problem*:

$$\xi \cdot \mathrm{CBF} \cdot \mathbf{r} = \mathbf{A}^{\dagger}\mathbf{c} = (\mathbf{A}^{\mathrm{T}}\mathbf{A})^{-1}\mathbf{A}^{\mathrm{T}}\mathbf{c}, \qquad [2\text{-}13]$$

where $\mathbf{A}^{\dagger}$ is the *Moore-Penrose pseudoinverse* of **A**[22]. An alternative way to invert **A**, which will become useful in the next section, is by using *Singular Value Decomposition* (SVD). The SVD decomposes **A** into two matrices, **U** and **V**, that contain the left and right singular vectors, and a diagonal matrix. The latter contains the singular values of **A**[22]. This is not dissimilar to what we see in Fourier transforms, where the sine and cosine are the basis functions which are multiplied by spectral weights for each individual basis function. SVD yields a classical decomposition problem with two sets of orthonormal basis vectors (or basis functions), i.e. the left and right singular vectors stacked into **U** and **V**, such that the matrix becomes diagonal when transformed into these two bases:

$$\mathbf{A} = \mathbf{U}\mathbf{\Sigma}\mathbf{V}^{\mathrm{T}} \in \mathbb{R}^{mxn}, \qquad [2\text{-}14]$$

with

$$\mathbf{\Sigma} = \begin{pmatrix} \sigma_1 & \cdots & 0 \\ \vdots & \ddots & \vdots \\ 0 & \cdots & \sigma_n \end{pmatrix} = diag(\sigma_1, \sigma_2, \ldots \sigma_n) \in \mathbb{R}^{nxn}, \qquad [2\text{-}15]$$

where $\sigma_1 \geq \sigma_2 \geq \sigma_3 \ldots \geq \sigma_n \geq 0$,

and

$$\mathbf{U}=\begin{pmatrix} u_{1,1} & u_{2,1} & \cdots & u_{n-1,1} & u_{n,1} \\ u_{1,2} & u_{2,2} & & u_{n-1,2} & u_{n,2} \\ \vdots & \vdots & \ddots & \vdots & \vdots \\ u_{1,m-1} & u_{2,m-1} & & u_{n-1,m-1} & u_{n,m-1} \\ u_{1,m} & u_{2,m} & \cdots & u_{n-1,m} & u_{n,m} \end{pmatrix} \in \mathbb{R}^{mxn}, \qquad [2\text{-}16]$$

$$\mathbf{V}=\begin{pmatrix} v_{1,1} & v_{2,1} & \cdots & v_{n-1,1} & v_{n,1} \\ v_{1,2} & v_{2,2} & & v_{n-1,2} & v_{n,2} \\ \vdots & \vdots & \ddots & \vdots & \vdots \\ v_{1,n-1} & v_{2,n-1} & & v_{n-1,n-1} & v_{n,n-1} \\ v_{1,n} & v_{2,n} & \cdots & v_{n-1,n} & v_{n,n} \end{pmatrix} \in \mathbb{R}^{nxn}, \qquad [2\text{-}17]$$

where $\mathbf{U}$ and $\mathbf{V}$ are matrices with orthonormal columns, i.e. $\mathbf{U}^{\mathrm{T}}\mathbf{U} = \mathbf{I}_{\mathrm{n}}$ and $\mathbf{V}^{\mathrm{T}}\mathbf{V} = \mathbf{I}_{\mathrm{n}}$, with $\mathbf{I}_{\mathrm{n}}$ being the n x n *identity matrix*. With this decomposition, inverting $\mathbf{A} = \mathbf{U\Sigma V^{T}}$ conveniently becomes:

$$\mathbf{A^{-1}} = \mathbf{V\Sigma^{-1}U^{T}}\,, \qquad [2\text{-}18]$$

where the initial $\mathbf{V}^{\mathrm{T}}$ and $\mathbf{U}$ originating from the SVD are transposed and then switched in position. To achieve the inverse of $\sum$, the diagonal elements of $\sum$ are simply inverted, i.e.

$$\mathbf{\Sigma^{-1}} = \begin{pmatrix} \frac{1}{\sigma_1} & \cdots & 0 \\ \vdots & \ddots & \vdots \\ 0 & \cdots & \frac{1}{\sigma n} \end{pmatrix} = diag\left(\frac{1}{\sigma_1}, \frac{1}{\sigma_2}, \ldots, \frac{1}{\sigma_n}\right) \in \mathbb{R}^{nxn} \qquad [2\text{-}19]$$

Hansen states that "In connection with discrete ill-posed problems, two characteristic features of the SVD are very often found:

- The singular values decay gradually to zero with no particular gap in the spectrum. An increase of the dimensions of $\mathbf{A}$ will increase the number of singular values.

- The left and right singular vectors tend to have more sign changes in their elements as the index i increases, *i*.e. as σ_{i} decreases[23]."

Again, similar features can be seen with FTs.

The problem with inverting *ill-posed problems* is that the solution vector is unstable and dominated by high amplitude oscillations that mask the desired results. These oscillations are exacerbated by measurement noise in the AIF and

C_{tissue}, and typically emanate from high-frequency spectral components in the AIF which have low amplitude and are dominated by noise[23]. A strategy to overcome these oscillations is low-pass filtering, which suppresses high-frequency spectral components. This step, called regularization, can be done either in the frequency domain via Fourier transformation or via an SVD transform (n.b., the analysis is mathematically equivalent to the Fourier transform approach when block-circulant SVD is used)[20, 24].

As the singular values continuously decline as the index i rises, the rate of change (akin to their frequency) of the left and right singular vector (basis functions) also increases[23]. The contributions of the basis-functions therefore diminish in this higher frequency range (i.e., smallest singular values correspond the highest frequencies)[20, 23]. These high-frequency spectral components can therefore be suppressed, and the effects of noise reduced. This can be achieved by removing singular values that fall below a certain percentage relative to the largest singular value (usually σ_1)[20]. This regularization cut-off is often called the SVD threshold and, dependent on application, can range between 5-25% of its maximum value, ϕ. Therefore, when inverting the diagonal elements of $\mathbf{\Sigma}$, all singular values smaller than σ_1 are nulled:

$$\Sigma_{trunc}^{-1} = \begin{cases} 0, & \sigma_i < \phi \cdot \sigma_1 \\ 1/\sigma_i, & \sigma_i \geq \phi \cdot \sigma_1 \end{cases} \qquad [2\text{-}20]$$

This yields an approximated inverse of $\mathbf{A}$:

$$\widetilde{\mathbf{A}}^{-1} = \mathbf{V}\mathbf{\Sigma}_{trunc}^{-1}\mathbf{U}^{\mathrm{T}}\,, \qquad [2\text{-}21]$$

and the regularized residue function is as follows:

$$\xi \cdot \mathrm{CBF} \cdot \mathbf{r} \;\cong\; \xi \cdot \mathrm{CBF} \cdot \tilde{\mathbf{r}} = \widetilde{\mathbf{A}}^{-1}\mathbf{c} = \mathbf{V}\mathbf{\Sigma}_{trunc}^{-1}\mathbf{U}^{\mathbf{T}}\mathbf{c}. \qquad [2\text{-}22]$$

This approximation of the true residue function, $\tilde{\mathbf{r}}$, is used to compute CBF. Since the residue function at $t = 0$ is 1, $\xi \cdot \mathrm{CBF} \cdot \mathbf{r}\,|_{t=0}$ yields $\xi \cdot \mathrm{CBF}$. Removal of the high frequency components results in over-smoothing of $\mathrm{CBF} \cdot \mathbf{r}$ and underestimation of true CBF (Figure 4-2)[20].

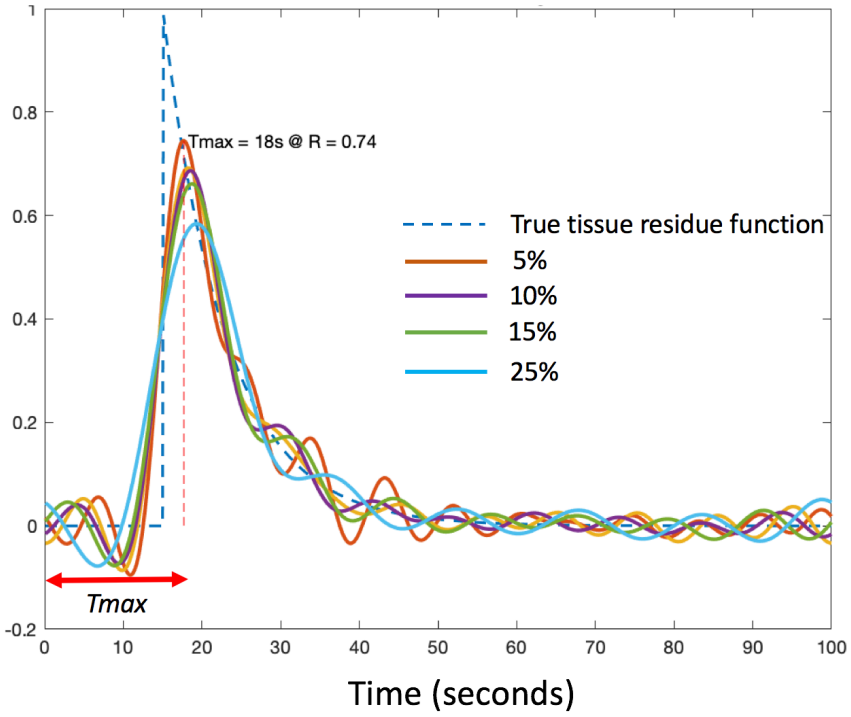

Figure 4-2. *The estimated residue functions, R(t), at different regularization thresholds. R(t) is displaced increasingly to right, with a reduced peak, when stronger regularization is used. CBF is therefore increasingly underestimated with stronger regularization, since CBF is estimated from the peak of R(t) in practice.*

Consequently, data with poor SNR, where stronger regularization is required for stabilization, will result in greater CBF underestimation, underscoring the importance of high SNR in measurement of AIF and C_{tissue}. Conversely, inadequate regularization yields unstable, non-physiological results for $\mathbf{r}$.

Since the true arterial input into each brain tissue voxel cannot be measured directly, due its small size, the AIF is instead estimated from a single large intracranial artery such as the MCA. It is assumed that this measured AIF represents the real input into each tissue voxel. However, non-negligible lag between the measured AIF and the true tissue arterial input occurs in the setting of intracranial arterial occlusion, where blood has to reach the tissue via collateral pathways[7, 25]. This results in **delay** between the measured AIF and C_{tissue}. **Dispersion**, where the contrast bolus shape becomes more spread out due to traversal of multiple collateral paths of different lengths between the measured AIF and true tissue arterial input, also occurs in this setting[7, 25]. This delay and dispersion of the contrast bolus between the reference artery in which the AIF is measured and the true input artery of the voxel results in errors in quantification:

underestimation of CBF and overestimation of MTT[25-27]. Extracranial factors such as poor cardiac output and extracranial carotid stenosis also cause dispersion of the shape of the measured AIF, as well as downstream delay and dispersion between the measured and true arterial input. Using a local AIF, measured in a vessel closer to tissue of interest, can address this delay. Unfortunately, partial volume effects resulting from the small size of these vessels make accurate measurement of a local AIF difficult, and this approach is also impractical in the clinical setting [28, 29]. Therefore, the practical approach of using a global AIF has been widely adopted with several techniques used to minimize the effects of delay and dispersion. The use of a block circulant decomposition matrix with SVD was proposed by Wu et al[27]. Delay between the measured AIF and true tissue arterial input results in the calculated *R(t)* being shifted by a time delay, therefore standard linear deconvolution does not allow *R(t)* to be accurately estimated. By circularly shifting *R(t)* by the time delay, circular deconvolution avoids time aliasing (Figure 4-3). This time shift is simply a phase roll in the spectrum. The *block-circulant deconvolution technique* (oSVD) has been shown to be insensitive to tracer arrival time differences[30]. Other tracer arrival timing-insensitive techniques include incorporation of either an estimated or measured relative time difference between the AIF and C_{tissue} into deconvolution[7]. Of note, Fourier techniques are also insensitive to tracer arrival timing[7].

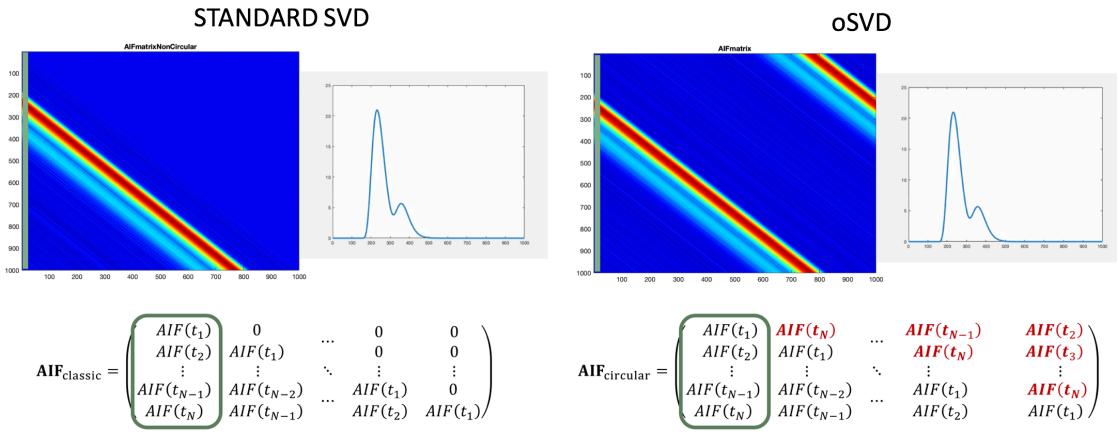

Figure 4-3. *Standard SVD versus block-circulant SVD (oSVD). The AIF matrix for each deconvolution method is shown. The red diagonal is the first pass, whereas the broad cyan diagonal is the recirculation. With oSVD, the time points are circularly shifted (red) – i.e. wrapped around in a circle so that there is no defined start and end.*

Since a global AIF is used, the deconvolved residue function, *R(t)*, is a composite of the true tissue residue function and the transport function of the vasculature (between the input artery where the AIF is measured and the tissue voxel).

Therefore, while the maximum of the true tissue residue function is at $t = 0$, the maximum of $R(t)$ is usually at $t > 0$ [31]. This time point is referred to as *Tmax* – the **time to maximum of the tissue residue function** obtained by deconvolution (Figure 4-4A).

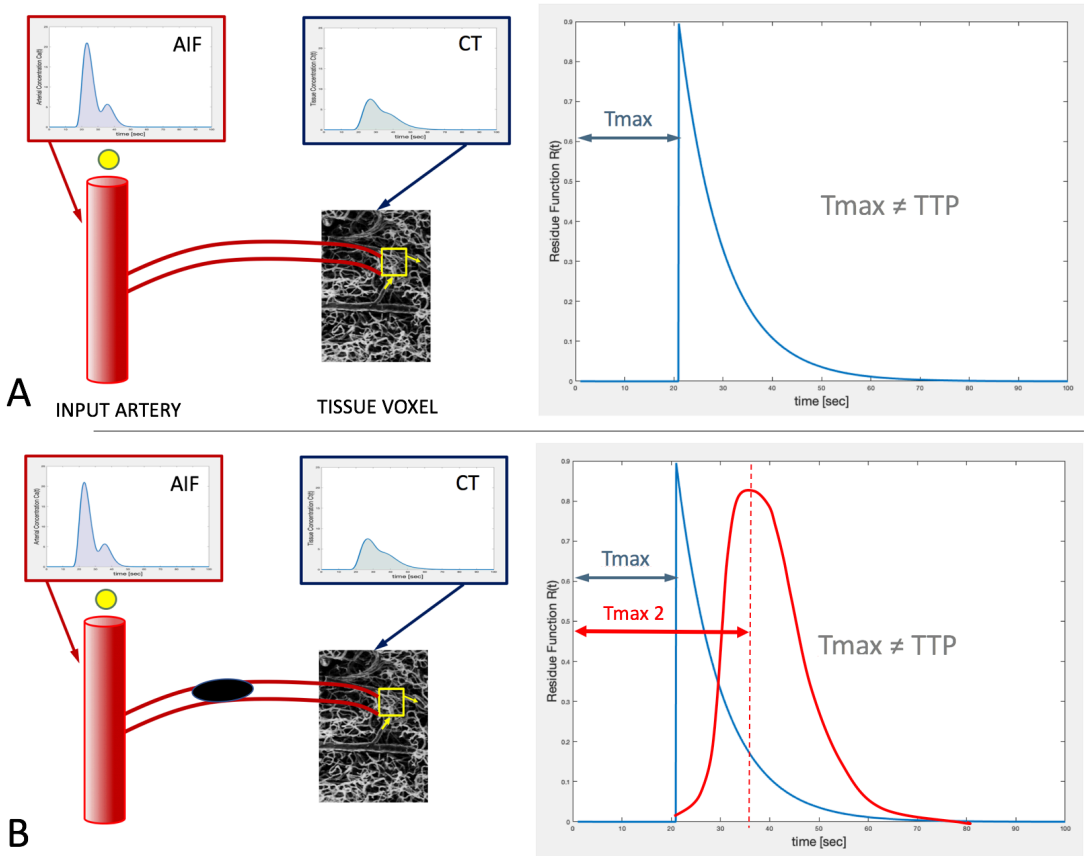

Figure 4-4: *Time to maximum of the tissue residue function, Tmax, obtained by oSVD.* ***A.*** *The tissue residue function, R(t), is shown in blue. Under normal conditions, Tmax is the delay between the measured AIF (at the input artery) and the tissue voxel, corrected for the shape of the AIF.* ***B.*** *When an arterial occlusion (or stenosis) occurs between the input artery (where the AIF is measured) and the tissue voxel, the arrival of tracer in tissue is delayed since blood has to travel collateral pathways to reach the tissue. The tissue residue function (red curve) is therefore delayed (i.e. shifted to the right) and its peak, Tmax, is delayed.*

Theoretically, *Tmax* is the delay between the measured AIF and C_{tissue}, corrected for effect of the shape of the measured AIF[31]. It is therefore a measure of the delay in arrival of contrast in the tissue voxel, and is increased by arterial stenosis or occlusion proximal to the tissue voxel (Figure 4-4B). However, other factors also influence *Tmax*. Arterial stenoses and occlusions proximal to where the AIF is measured, as well as reduced cardiac output, result in bolus temporal dispersion and delay, therefore the AIF is delayed and broadened with a reduced peak[32].

However, due to deconvolution, this delay only causes mild distortion of the shape of *R(t)*. Deconvolution corrects for delay up to where the AIF is measured, but delay between the AIF location and tissue are not corrected for – and manifests as **Tmax delay**. The effect of bolus dispersion on *Tmax*, which becomes more prolonged, is complex[20, 25, 32]. The process of regularization, described above, also distorts *R(t)* and systematically influences the measured *Tmax*[20]; with increasing regularization, hence increased smoothing, *Tmax* is shifted towards later time points (Figure 4-2). For comparability reasons, it is therefore critical to consider the regularization threshold and avoid changes. *MTT* also has a mild effect on *Tmax*[31].

Table 4-1. *Perfusion parameters currently used in AIS.*

Parameter	Calculation	Main confounders
CBV	Area under tissue time-concentration curve divided by area under AIF adjusted for brain tissue density and haematocrit $$CBV = \frac{CH}{p} . \frac{\int_0^t Ctissue(t)d\tau}{\int_0^t AIF(t)d\tau}$$	Too short scan duration: causes truncation of $C_{tissue}(t)$ and underestimation of *CBV*
CBF	Deconvolution of tissue concentration-time curve with AIF $$C_{tissue}(t) \otimes^{-1} AIF(t) = \frac{\rho}{CH} \cdot CBF \cdot R(t)$$ since *R(0)* =1, CBF can be determined	Use of delay-sensitive deconvolution; Strong regularization
MTT	Central volume principle: $$MTT = CBV/CBF$$	*CBV* underestimation; *CBF* underestimation due to strong regularization; Use of delay-sensitive deconvolution
Tmax	*Tmax* = Time to peak of *R(t)*	Same as for *CBF*

As discussed in chapter 2, *Tmax* can be used to predict the ischemic penumbra while both CBF and CBV have been used to determine the infarct core. While CTP allows determination of absolute CBF and CBV, this is dependent on the appropriate selection of a venous output function for scaling. Accurate scaling

requires measurement of density (hence contrast concentration) in a 100% blood volume structure. The reason that a venous output function is used for scaling rather than the AIF is that dural venous sinuses are much larger structures than cerebral arteries, therefore partial volume effects can be avoided. Relative values are therefore favoured in clinical practice and have been established in recent stroke trials[33-37]. Normalization, using contralateral regions of interest, obviates the need for this scaling factor.

Another important step when generating CTP parametric maps is the exclusion of leptomeningeal and perforating blood vessels[7]. These 100% blood volume structures can result in overestimation of blood flow and blood volume, especially in adjacent cortex, due to partial volume effects. Vascular pixel elimination, using either density or CBV thresholds, is one approach which can be used to minimize this effect[38].

A summary of how each perfusion parameter is obtained is given in Table 4-1.

4.3 Dynamic Susceptibility Contrast Perfusion-Weighted Imaging

Dynamic Susceptibility Contrast Perfusion-Weighted Imaging (DSC-PWI) is also a bolus perfusion technique. Here, cine MR images are used instead of CT to track to passage of a non-diffusible contrast agent through the brain vasculature. Gadolinium-chelates are used as the contrast agent and are referred to as *gadolinium-based contrast agents* (GBCAs). It is noted that DSC-PWI is an off-label indication for GBCA.

The dose of GBCA injected for DSC-PWI, 0.1 - 0.2 mmol/kg, must be sufficiently high to produce a measurable drop in MR signal in white matter where CBV is low[39]. However, too high a concentration will cause signal saturation (i.e., signal reaching the noise floor)[20]. Injection is performed using an MR-compatible power injector, to achieve uniformity and ensure a tight bolus width. Rates of 5-6 mL/s are typically used, which are sufficiently high to produce a well-defined arterial bolus that is not dispersed by the injection itself. This is followed by a 20-40 mL saline chaser at the same flow rate to push the small volume of GBCA that is administered (10-30 mL, depending on molarity and body weight) through the injector tubing and arm veins into the central circulation.

Inadequate injection rates can result in underestimation of perfusion parameters[20]. Because of the risk of **nephrogenic systemic fibrosis** or **NSF** in association with GBCAs in patients with *end-stage renal disease*, DSC-PWI is avoided in high-risk patients with estimated glomerular filtration rates below 30 mL/min/1.73m^2 [40, 41].

4.3.1 Image Acquisition

When the blood-brain barrier is intact, GBCAs remain intravascular[42]. The chelated Gd^{3+} ions in the GBCA are strongly paramagnetic[42]. Consequently, the passage of GBCA through the tissue capillaries causes static magnetic field inhomogeneities within these vessels, due to compartmentalization of plasma and red blood cells, as well as in the vicinity of the vessels (since the contrast agent remains intravascular and the position of the vessels in tissue is fixed)[43]. The resulting susceptibility gradients between the capillaries and the tissue cause tissue protons, which are exposed to slightly different local magnetic field strengths, to precess at different frequencies; this results in rapid dephasing of these protons, i.e., **static dephasing**. Additional **dynamic dephasing** occurs due to the *diffusion of water protons through the local magnetic field inhomogeneities*[43]. These local microgradients induced by the GBCA can be much stronger than the external, switched gradients used for diffusion-weighted imaging. Therefore, the passage of GBCAs through the tissue capillary bed causes a transient marked drop in tissue signal (susceptibility contrast) on both T_2*-weighted and T_2-weighted MRI sequences[44, 45].

MRI pulse sequences with a fast readout must be used to capture the bolus as it passes through the tissue capillary bed[20]. *Single-shot echo-planar imaging* (SS-EPI) sequences, which are widely available, are most commonly used for clinical DSC-PWI, allowing whole brain coverage at the required temporal resolution with sufficient SNR[20]. In order to reduce EPI-related artifacts and improve susceptibility contrast as well as spatial and temporal resolution, other implementations such as segmented EPI readouts have been used, but the shorter repetition times result in greater T_1-sensitivity (which is a cause of blood volume underestimation, since T_1-relaxation opposes the signal loss causes by the susceptibility effects of contrast agent)[20].

The magnetization preparation for DSC-PWI sequences can be either *spin-echo* (SE), *gradient-echo* (GRE) or a combination of these in multi-echo

sequences[43, 46, 47]. GRE-based pulse sequences do not refocus the dephasing of the *free induction decay* (FID) caused by the static field inhomogeneities induced by contrast passage. Marked susceptibility-induced signal loss is therefore observed on these T_2*-weighted sequences. Given their sensitivity to susceptibility effects, perfusion maps derived from GRE sequences are dominated by signal from large vessels. Unlike CTP, where large vessels mainly affect the voxels to which they are confined, with GRE-based readouts, the large vessels also affect adjacent voxels. The point-spread function is dependent on T_2*, with shorter T_2* during the peak of bolus passage causing the vessel to be blurred more. This macrovascular sensitivity ("large vessel blooming") can mask true tissue perfusion, which relates to the microvasculature[20, 48].

Conversely, for static spins, dephasing caused by these field inhomogeneities is refocused in SE acquisitions. SE sequences are therefore T_2-weighted; the only signal loss results from the dynamic dephasing of protons that diffuse through the susceptibility gradient field induced by the contrast agent. Since the phase accumulation across the diffusion distance is greatest adjacent to capillaries, the signal loss is largest in the vicinity of capillaries[48, 49]. This confers SE acquisitions sensitivity to the microvasculature[48, 49]. Another advantage of SE acquisitions is that there are fewer distortions related to susceptibility interfaces (e.g., bone-soft tissue and air-bone), especially at high field strength, therefore perfusion abnormalities adjacent to the skull base may be more easily detected[20]. A disadvantages of SE acquisitions is that they take longer to acquire per slice due to the requirement for a longer TE to allow incorporation of the refocussing radio-frequency pulse. Therefore, either volumetric coverage or temporal resolution must be reduced. Also, since the signal drop induced by contrast passage is smaller, a larger dose of contrast agent may be required for SE than GRE acquisitions in order to achieve sufficient CNR[20]. Due to these disadvantages, GRE acquisitions are much more commonly used for DSC-PWI in clinical practice. GRE also allows quantification of the contrast concentration in an input artery, which is important for determining the AIF. For SE, the AIF is usually obtained from tissue near an artery.[39]

Combined SE and GRE sequences confer both microvascular sensitivity (related to the spin echo component) and the ability to measure the arterial contrast concentration[47, 50]. When multiple echoes are acquired as a part of such combined sequences, T_1-effects resulting from contrast leakage can be corrected for[47]. Additionally, multi-echo sequences with more than three echoes allow more accurate determination of the arterial and tissue contrast concentration[46]. Early

echoes (10 -15 ms) can be used to select the AIF (minimize signal saturation due to T_2*-signal loss down to the noise floor) while later echoes can be used to measure tissue signal. The pulse sequence diagram and examples of raw images and CBF maps obtained using a multi-echo sequence are shown in Figure 4-5. This sequence, "SAGE", has three additional gradient echoes and a spin echo.

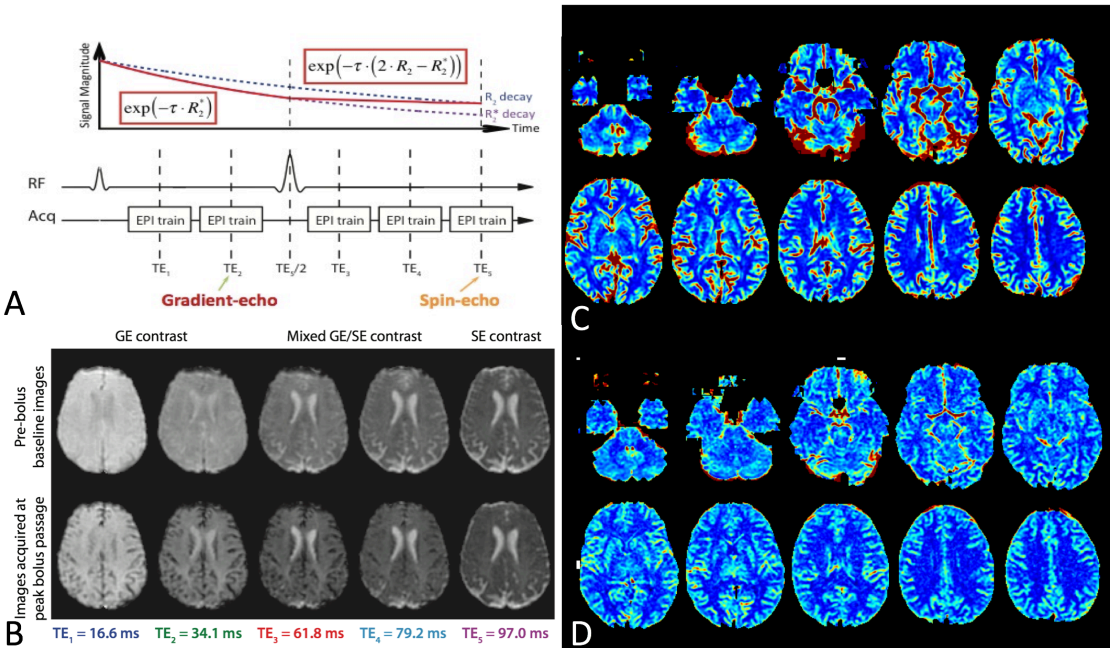

Figure 4-5. *Combined spin-echo and gradient-echo (GRE) multi-echo DSC-PWI sequence.* ***A.*** *Pulse sequence diagram of this sequence, SAGE, which is a 3 times GRAPPA-accelerated sequence with 5 EPI readouts. The spin-echo is produced by a 180º refocusing pulse. Obtaining multiple echoes allows computation of the relaxation rates, $R_2(t)$, $R_2'(t)$, and $R_2^*(t)$ without T_1 contamination. The first gradient echo can be used to measure the arterial input function (AIF) and the venous output function (VOF) without significant signal saturation effects that occur on later echoes (due to the high arterial contrast concentration).* ***B.*** *Examples of the raw data obtained (at a single slice position) at each of the five echo times using this technique. Pre-contrast arrival baseline images shown in the top row, and the images obtained at the peak of contrast passage in the bottom row.* ***C.*** *rCBF maps from the second gradient-echo, showing the large vessel sensitivity of GRE, with prominent curvilinear areas of elevated CBF in the basal cisterns and Sylvian fissures corresponding to blood vessels.* ***D.*** *rCBF maps obtained using the spin echo show reduced large vessel blooming (SE images are more capillary weighted) and reduced susceptibility distortions at the skull base.*

Similar to CTP, the sampling duration must be selected to ensure that the first pass of contrast bolus through the tissue capillary bed is captured in its entirety, without truncation. Truncation, which is particularly likely to occur in the setting of stroke where arterial occlusion results in delay and dispersion of the contrast bolus, results in CBF and CBV errors of up to 50%[25, 51, 52]. As with CTP, accurate

calculation of these perfusion parameters requires the tissue concentration-time curve to be captured completely, therefore the MR signal intensity must return to baseline during the scan acquisition. Scan duration of 90-120 seconds is therefore recommended[53]. For accurate quantification, the baseline component of the acquisition, prior to contrast arrival, must also be of sufficient duration to achieve steady state in tissue magnetization (approximately 10 - 15 seconds)[20].

The optimal TE for GRE-EPI DSC-PWI sequences is set to approximate the T_2* of tissue, in order to optimize tissue contrast and capture the maximum signal drop[54, 55]. This must be balanced against the higher SNR at shorter TEs. At 1.5 Tesla, a TE of 40-60 ms is typically used. A shorter TE of 20 - 35 ms is required at 3 Tesla, due to the shorter T_2* of tissue at high field strength; for example, in one study, a TE of 21 ms was found to provide a good balance between sufficient signal drop in tissue and prevention of signal saturation in the input artery for AIF measurement[55]. The repetition time must be selected to ensure that the sampling rate (temporal resolution) is sufficiently high to allow faithful characterization of the transient first-pass signal drop. A typical TR used in clinical practice is 1800 ms, with values between 1700 ms and 2000 ms recommended. As the TR is reduced, confounding T_1-sensitivity increases[20]. The recommended flip angle for GRE DSC-PWI is 60 - 90° at 1.5 Tesla and 60° at 3 Tesla[53]. Increasing the flip angle improves SNR, and therefore the accuracy of calculated perfusion parameters. For a given TR and T_1-relaxation time of tissue, the **Ernst Angle**, $\arccos\{\exp(-TR/T_1)\}$, will provide the strongest DSC-PWI signal and can be used if contrast leakage is not expected to occur. However, increased flip angle also increases the sequence's sensitivity to T_1-changes (see section 4.3.3), particularly contrast leakage during bolus passage that temporarily alters T_1 of tissue and thus affects quantitation of hemodynamic parameters[20, 56]. Therefore, if extravasation of contrast is anticipated (e.g., subacute stroke), pre-loading with 1 - 2 mL GBCA, and lowering the flip angle to 60° at 1.5 T is suggested to limit confounding T_1-effects.

4.3.2 Determining the Tissue and Arterial Concentration Time Curves

Once the DSC-PWI images are acquired, MR signal in each tissue voxel can be measured and converted to a concentration-time curve. The MR signal in a reference artery is also measured, and again this must be converted into an arterial concentration-time curve (the AIF). The same principles of indicator dilution theory and processes of deconvolution as for CTP set out in section 4.2.2 can then be applied to determine perfusion parameters.

Unlike with CTP, the MR signal on DSC-PWI sequences is not linearly related to the concentration of GBCA. For a SS-EPI GRE DSC-PWI sequence, the relationship between signal, *S*, and contrast concentration (*C*) can be approximated as follows:

$$S(C) = M_0 \frac{\sin\alpha\left[1-e^{(TR\cdot R_1(C)}\right]}{1-\cos\alpha e^{-TR\cdot R_1(C)}} e^{\left(-TE\cdot R_2^*(C)\right)} \quad [3\text{-}1]$$

This equation takes into consideration both T_1 (longitudinal) and T_2* (transverse) relaxation time. R_1 is the contrast-concentration dependent longitudinal relaxation rate. It is inversely related to T_1, which is the time constant for recovery of longitudinal magnetization back to its initial state. Therefore,

$$R_1 = \frac{1}{T_1} \quad [3\text{-}2]$$

R_2* is the transverse relaxation rate, which is inversely proportional to the time constant T_2*. Therefore,

$$R_2^* = \frac{1}{T_2^*} = R_2 + R_2', \quad [3\text{-}3]$$

where R_2 is the transverse relaxation rate due to spin-spin interaction and R_2' is the contribution to the relaxation rate caused field inhomogeneities, which are induced by local magnetic susceptibility gradients. The α term is the flip angle and M_0 is the equilibrium (initially available) magnetization[20]. The T_1-effects (see next section) are negligible in comparison with the stronger T_2*-effects, provided the blood brain barrier is intact and TR >> T_1 and are therefore ignored[20]. The gradient echo signal therefore can be taken as:

$$S(t) = S_0(t) \cdot e^{\left(-TE\cdot(R_2^*(0)+\Delta R_2^*(t))\right)}, \quad [3\text{-}4]$$

Where ΔR_2* is the change in the transverse relaxation rate induced by contrast, R_2*(0) is the pre-bolus arrival R_2* value in a given tissue and S_0 is the transverse MR signal that is initially available. In the absence of any T_1-shortening caused by contrast extravasation, $S_0(t)$ remains constant during the acquisition and if TR < 4*T_1 $S_0(t) < M_0$. Therefore, equation 3-4 can be solved for the time-dependent component of R_2*:

$$\Delta R_2^*(t) = R_2^*(C) - R_2^*(0) = -\frac{1}{TE} \cdot log\left(\frac{S(t)}{S_{baseline}}\right), \quad [3\text{-}5]$$

where

$$S_{baseline} = S_0 e^{-TE \cdot R_2^*(0)} \quad [3\text{-}6]$$

A linear relationship between contrast concentration and R_2* is assumed. The latter is based on a theoretical model developed by *Kjolby et al* to describe the effect of contrast agent within a vascular network on tissue transverse relaxation[57]:

$$\Delta R_2^*(t) = r_2^* \cdot C_{Tissue}(t) \quad [3\text{-}7]$$

Here, $C_{tissue}(t)$ is the contrast concentration in tissue over time. The proportionality constant, r_2*, is the T_2*-relaxivity of the contrast agent, which depends on blood flow velocity, magnetic field strength, the acquisition sequence, capillary topography and the GBCA[49, 58]. It is assumed to be the same in grey and white matter[57]. The concentration-time curve in tissue can therefore be calculated from the measured MR signal as follows:

$$C_{Tissue}(t) = -\frac{1}{r_2^* \cdot TE} \log\left(\frac{S(t)}{S_{baseline}}\right) \quad [3\text{-}8]$$

Since, for many applications, absolute concentrations are not relevant, r_2* can be set to 1 or ignored.

4.3.3 T_1-Effects

T_1-effects require special mention. As mentioned in the previous section, if TR<4*T_1, even T_2- and T_2*-weighted DSC-PWI acquisitions have some degree of T_1-weighting. GBCAs cause T_1-shortening (i.e., faster longitudinal signal recovery towards equilibrium M_0) that competes with the desired effect of signal loss resulting from T_2*-relaxation[44, 45]. This opposing T_1-effect can result in net signal increase relative to pre-bolus values, confounding the calculation of ΔR_2*. Since the blood volume (related to capillaries) in brain tissue is around 4-5%, the signal increase from T_1 shortening related to intravascular contrast is small. The T_1-effects are therefore minimal and can be ignored in the setting of an intact *blood-brain barrier* (BBB)[20]. When the BBB is disrupted, for example in brain tumours and late acute stroke (Figure 4-6), leakage of contrast agent into the extravascular-extracellular compartment can cause T_1-shortening of tissue[56]. In this setting, significant T_1-effects may confound or even dominate the signal profile[56].

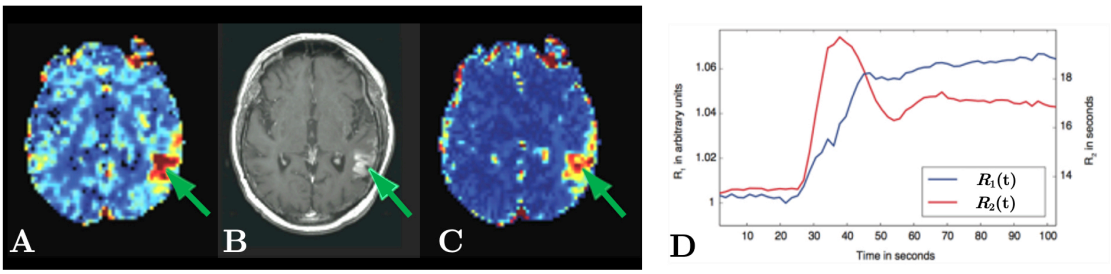

Figure 4-6. *BBB breakdown in a stroke patient.* ***A.*** *CBV map;* ***B.*** *contrast-enhanced T_1-weighted MRI; and* ***C.*** *k_{trans} map demonstrate an area of BBB breakdown (green arrow) with subsequent increased permeability as demonstrated by the contrast agent uptake.* ***D.*** *Corresponding $R_1(t)$ and $R_2(t)$ curves in that region that were obtained simultaneously with SAGE confirm that contrast material leaks into the tissue during the first pass of the bolus (see $R_1(t)$ uptake slope starting at t=25 seconds) and that CBV will be overestimated as contrast material is retained in the extra-vascular extra-cellular space (see $R_2(t)$ does not return to baseline after first pass – elevated shoulder comprises contrast material in capillary pool and interstitial space).*

The DSC-PWI acquisition parameters can be selected to minimize these T_1-effects, for example by use of a smaller flip angle and longer TR [20, 56]. However, these strategies incur an SNR penalty. Alternatively, multi-echo DSC PWI techniques can be used (Figure 4-5A). These allow T_1-shortening effects to be eliminated from the estimation of ΔR_2*[20, 47]. Here, the MR signal equation can be formulated for the readout obtained with each echo:

$$S(t,\tau) = S_0(t) \cdot e^{-(\tau \cdot R_2^*(t))}, \qquad [3\text{-}9]$$

with τ = TE_1, TE_2, TE_3, … being the different echo times of a multi-echo GRE sequence and then fitted with a least squares algorithm to determine R_2* and S_0 for each DSC time point. Most importantly, however, by directly measuring R_2*(t)* via a parameter fit for each time point, the multi-echo DSC sequence can be decoupled from contaminations due to T_1-shortening. Only S_0 is affected by T_1-shortening, which allows computation of DCE-type contrast uptake curves (Figure 4-6D). The SAGE sequence combines multiple gradient- and spin-echoes and has a slightly more complex signal equation as seen in Figure 4-5 and described in detail elsewhere.[47]

With use of single-echo sequences, changes in T_1-relaxation during the first-pass can also be minimized by administering a loading dose of contrast agent prior to DSC PWI acquisition[59]. Post-processing methods, that involve application of mathematical correction algorithms, such as gamma variate fitting and integration after a post-bolus baseline correction, can also be employed but are very limited[56].

Post-processing correction has been shown to improve accuracy of blood volume estimation beyond preload alone[59]. T_1-effects can be counteracted by using a longer TR at the expense of temporal resolution (and are therefore rarely used).

4.3.4 Determining the Arterial Input Function

As with CTP, the AIF is typically measured in the middle cerebral artery contralateral to an occlusion. There are a number of potential sources of error in determining the arterial contrast concentration-time curve from the measured MR signal. One of the major obstacles to accurate AIF determination is the spatial resolution of DSC-PWI sequences, which is lower than that of CTP. Typical slice thickness for a clinical DSC-PWI scan is 5-6 mm while the image acquisition matrix is usually 92*92 or 128*128 over a field-of-view of 22-26 cm. This yields in-plane resolution of 1.7-1.8 mm. Since the voxels are larger than the input artery, e.g., the MCA, where the AIF is measured, partial volume effects occur; signal contributions from adjacent brain tissue or CSF to the AIF can result in inaccuracy in calculated perfusion parameters[26]. Faster imaging enabled by parallel imaging techniques reduces spatial blurring related to the EPI readout and allows higher spatial resolution, therefore reducing partial volume effects[46].

Unlike in tissue, the relationship between contrast concentration and changes in $R_2{*}$ in bulk blood has been found to be quadratic due to the higher intravascular contrast concentration[60]. Assuming a linear relationship between signal and arterial contrast concentration can therefore result in substantial errors in CBF quantification[61]. Nonetheless, a linear relationship is often assumed to calculate the AIF in clinical practice. It has been found that the AIF can be estimated from voxels adjacent to but outside the MCA, where there is a linear relationship between arterial contrast concentration and $\Delta R_2{*}$[62]. The signal profile adjacent to the MCA can therefore be used to determine the AIF, however this method provides only relative perfusion measurements as it allows estimation AIF profile but not its magnitude. The orientation of the vessel in which the AIF is measured relative to the main magnetic field is also important. Maximal signal change is observed in and adjacent to vessels that are oriented perpendicular to the main magnetic field, such as the middle cerebral artery[20]. Saturation of signal at peak arterial concentrations and position shift of vessels (due to the GBCA-induced change in resonance frequency) can also have considerable effects on the measured signal change, therefore the computed tracer concentration[63, 64].

4.3.5 Determining Perfusion Parameters

Once MR signal is converted into C_{tissue} and the AIF, the same process of deconvolution as used in CTP can be used to determine perfusion parameters. As discussed above, there are numerous factors that introduce error and bias in quantification. The proportionality constants used in calculation, for example relating the signal to concentration in tissue and the input artery, are assumed; they are not accurately known and are likely to vary between individuals[20]. Therefore, unlike with CTP, absolute values cannot be simply determined by scaling to a venous output function. Instead, relative values are derived. This is achieved through normalization to the patient's normal-appearing tissue[20]. It has been found that such normalized parametric maps more accurately predict the final infarct volume than non-normalized maps[65].

As with CTP, macrovessel artifacts must be addressed to prevent overestimation of CBF due to partial volume effects. The large vessel sensitivity of GRE-based DSC-PWI means that macrovascular signal can bloom into adjacent brain tissue, resulting in overestimation of CBV and CBF in these tissue voxels[20]. This is particularly problematic with cortical grey matter adjacent to pial blood vessels. Methods such as principle component analysis can be used to minimize macrovascular signal, and this process can be fully automated[66, 67]. Use of spin echo DSC-PWI sequence is another strategy for minimizing CBF and CBV overestimation related to macrovascular blooming[47].

4.4 Effect of Post-Processing Algorithm on Perfusion Quantification

A variety of software programs are available for CT and MR perfusion post-processing. There is marked variability in the post-processing algorithms used by these programs, for example in the definition of the arterial input function and whether or not deconvolution is used, as well as the specific implementation of deconvolution[68-70]. This variability results in substantial differences in the derived perfusion parameters and quantification, causing variability in the calculated infarct core and penumbral volumes[68-70].

The variability in perfusion parameters derived from different CTP algorithms, using deconvolution and non-deconvolution based methods, was assessed by *Kudo et al* using identical source data[70]. There were significant differences between these

algorithms in the areas of MTT and CBF abnormality as well as quantitative MTT and CBF values. The algorithms could be divided into those with tracer-delay sensitivity and those that were delay-insensitive. Delay-sensitivity resulted in overestimation of the infarcted area based on CBF reduction, hence the delay-insensitive algorithms predicted the final infarct region and size more reliably[70]. MTT was also overestimated using delay-sensitive techniques. These findings were concordant with those of an earlier study, which found that delay-sensitivity resulted in erroneous CBF decrease and MTT increase in areas of tracer arrival delay that do not have true CBF reduction or MTT delay[69]. In a subsequent study, the accuracy and reliability of a wide range of CT and MR perfusion post-processing algorithms were assessed using a digital phantom dataset in which the true CBF, CBV and MTT values as well as tracer arrival delay were known[68]. It was found that only the algorithms that used oSVD produced accurate results without tracer arrival-delay induced errors. This phantom analysis also suggested that the increase in MTT observed on delay-sensitive algorithms is erroneous[68]. While oSVD yields true MTT maps, the "MTT" derived using SVD is also influenced by delay between the artery in which the AIF is measured and the tissue; it is therefore is a composite of MTT and Tmax, which is what we observe clinically (Figure 4-7). *This error in MTT, in turn, is related to errors in estimation of the tissue residue function, R(t), that occur when delay sensitive-deconvolution is used* (Figure 4-7). This, in turn, leads to incorrect CBF estimation. Since MTT is determined either using the central volume principle (from CBF and CBV) or by integration of R(t), it follows that this parameter is also calculated incorrectly. An example of the differences in CBF, CBV, MTT, and Tmax determined using delay-sensitive versus delay-insensitive deconvolution is shown in Figure 4-7.

These studies by *Kudo et al* support the use of delay-insensitive algorithms for computation of perfusion parameters in AIS. Their findings also explain why an early stroke study, that used delay-sensitive deconvolution, found MTT to be the optimal parameter for predicting critically hypoperfused tissue, while more recent studies, that use delay-insensitive deconvolution, have found that MTT is more prone to error and *Tmax* is therefore better for this task[65, 71-73].

Therefore, MTT can be used to predict critically hypoperfused tissue when a delay sensitive algorithm is used, because the "MTT" obtained using this technique also contains *Tmax*. When delay-insensitive deconvolution is used, MTT more closely approximates the true mean tissue capillary transit time; *Tmax*, rather than MTT, should then be used to predict critically hypoperfused tissue. It is noted that

perfusion parameters vary even between different delay-insensitive algorithms. This is because there are factors other than tracer-delay that affect CBF and MTT, including regularization, density, time signal, interpolation and curve fitting (Figure 4-2) [70].

Given the variability between different post-processing software, it is not surprising that CBF and CBV thresholds for predicting infarction vary, even between different algorithms that use oSVD[74-76]. Since perfusion imaging is used to triage AIS patients to treatment, accurate and consistent estimation of the size of the ischemic penumbra and infarct size is critical. It is therefore important to apply the particular parameter and threshold that is optimal for a particular software. Even when this is done, there remains considerable variability. In one study, the accuracy of three different perfusion post-processing software packages for predicting final infarct volume was compared in a cohort of 118 patients who underwent mechanical thrombectomy with successful recanalization[77]. The type of deconvolution algorithm used and the parameters and thresholds used to predict infarction and critical hypoperfusion are given in Table 4-2. Software package C was found to be most accurate for predicting the final infarct volume, with less measurement variability. There were statistically significant differences between the three software packages when it came to overestimating and underestimating the final infarct volume; both underestimation and overestimation was significantly less with package C.

Standardization of perfusion analysis has therefore been identified as an issue of paramount importance in advanced AIS imaging and may help address this variability[53]. In the trials setting, standardization allows uniform perfusion criteria to be applied, and ensures comparability between study sites using different algorithms. In reality, multicentre trials have achieved this by adhering to a single software package across different sites[33, 34, 36, 37, 78]. However, not all hospitals that treat stroke patients have access to the software used in these trials. Standardization is therefore important for clinical translation of the perfusion criteria developed in trials, allowing reliable extrapolation to other post-processing software. Such standardization strategies include the use of data phantoms, which allow validation of post-processing algorithms and standardized quality control, as well as the use of calibration datasets[68, 76]. It is likely that even with such strategies, the results obtained using different post-processing software packages will differ.

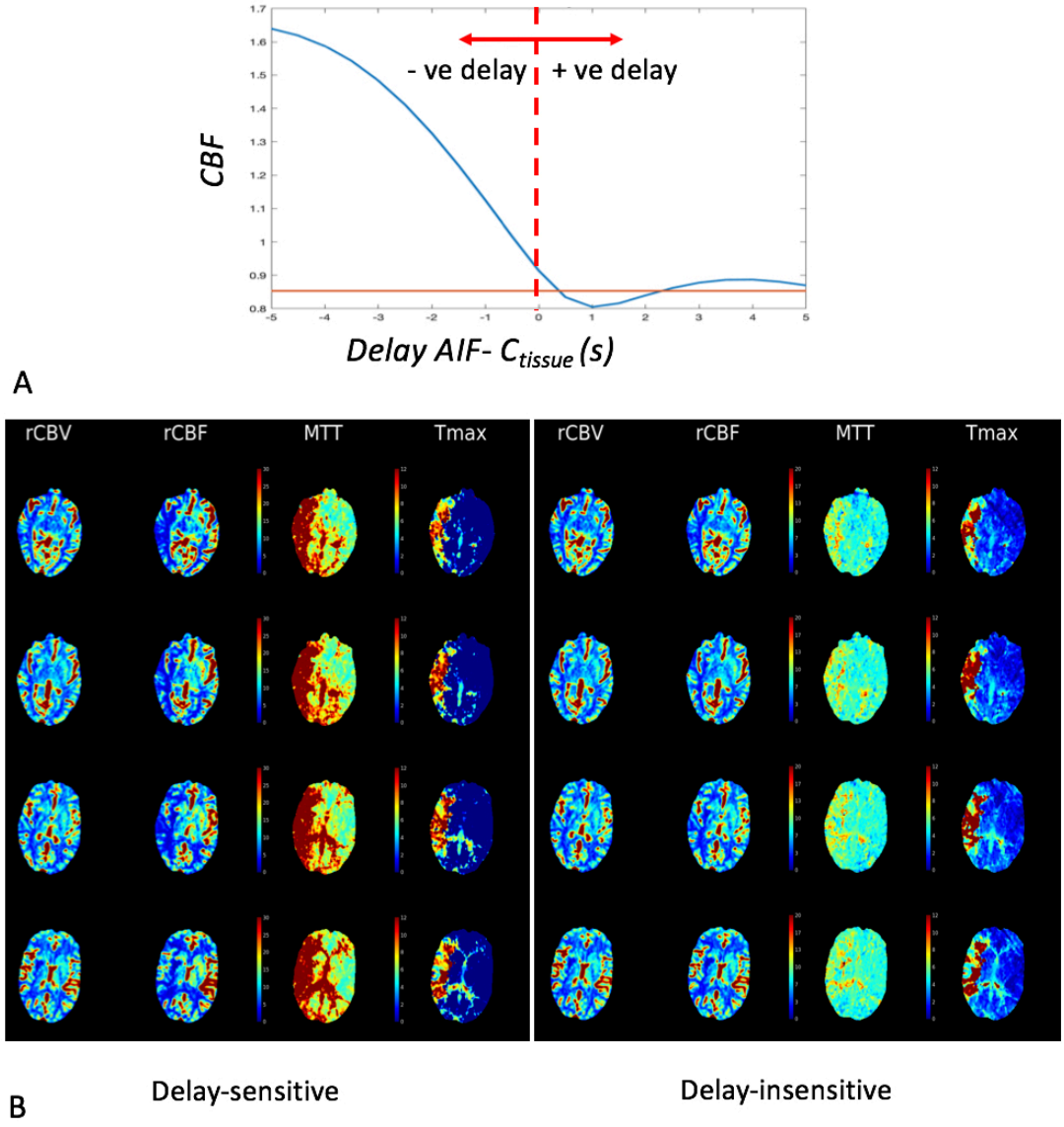

Figure 4-7. ***A.*** *CBF versus true delay between the measured AIF and measured C_{tissue}. The accuracy of CBF estimation depends on the type of deconvolution. With delay-insensitive deconvolution (orange line), R(t) does not change with the delay between the AIF and C_{tissue}. Therefore, while CBF is underestimated (due to regularization), the degree of underestimation remains fixed. With delay-sensitive deconvolution (blue line), the estimated R(t) changes with the delay between AIF and C_{tissue}, resulting in substantial error and variability in CBF estimation (since CBF is estimated at the peak of R(t)).* ***B.*** *Perfusion maps obtained using delay-sensitive and delay-insensitive deconvolution in a patient with acute ischemic stroke due to right MCA occlusion. With delay-sensitive deconvolution, MTT (which is either determined using the central volume principle from CBF and CBV, or by integration of R(t)), is incorrectly estimated and is a composite of true MTT and the delay between the measured AIF and the peak of the tissue residue function (Tmax). rCBF is underestimated in the right MCA territory. Delay-insensitive deconvolution removes this dependence of R(t) on the true delay between the AIF and C_{tissue}. Therefore, the Tmax information is shifted out of MTT, which is "cleaner" and reflective of tissue capillary transit time. CBF is more accurately estimated.*

Table 4-2. *Optimal perfusion parameters and thresholds for three different post-processing software packages*[77]

Software	(A) Brain CT Perfusion Package†	(B) Syngo Perfusion CT Neuro‡	(C) iSV RAPID§
Deconvolution	Delay-sensitive	Delay-insensitive	Delay-insensitive
Infarct (core)			
Parameter	Absolute CBV	Absolute CBV	Relative CBF *normalized to mean CBF in areas with Tmax <4 sec*
Threshold	< 2.0 mL/100 g	< 1.2 mL/100 g	< 30%
Critical hypoperfusion			
Parameter	Relative MTT *compared to contralateral hemisphere*	Absolute CBF	Tmax
Threshold	145%	< 35.1 mL/100 g/min	>6 seconds

† Philips Healthcare, The Netherlands; ‡ Siemens Healthcare, Erlangen, Germany; § iSchemaView Inc, Menlo Park, CA

4.5 Arterial Spin Labelling Perfusion

Arterial spin labelling (ASL) is a completely non-invasive MR perfusion technique that utilizes inflowing magnetically labelled arterial blood water to qualitatively assess cerebral perfusion and quantitatively measure cerebral blood flow[79-83]. It is an alternative to DSC-PWI that does not require exogenous contrast agent. Instead, the labelled protons in arterial blood serves as an endogenous tracer[81-83]. It is therefore repeatable and can be used in patients with severe renal impairment in whom concerns regarding gadolinium deposition and nephrogenic systemic fibrosis contraindicate the use of GBCAs[79, 84, 85]. Since intravenous cannulation and GBCA are not required, it is also an attractive alternative to DSC-PWI in children.

The concept of ASL was first developed in the early 1990[82, 83, 86]. However, it remained largely a research tool for over a decade. Since then, several factors which

had previously hindered the clinical implementation of ASL have been overcome. Although ASL can be performed at 1.5 Tesla, the inherently low SNR of the technique necessitates long acquisition times and results in poor image quality at this field strength. The more widespread availability of 3T MRI scanners has been a major factor in promoting translation of ASL into the clinical domain; this is due to the longer T_1 of blood, hence longer lifetime of label, and the inherently high SNR at 3T[87]. Multichannel array receiver coils, which allow faster scanning using parallel imaging, have reduced scan times to a clinically acceptable range. Advances in ASL sequences, including the development of pseudo-continuous labelling and background suppression, the streamlining and automation of post-processing, and resolution of licensing issues have allowed the major vendors to implement ASL on clinical MR scanners. These factors have made ASL feasible in clinical practice. In addition, consensus guidelines have been developed to address the lack of standardization; this had, in the past resulted in a wide variety of ASL implementations and been an obstacle to clinical utilization of ASL[88].

4.5.1 ASL technique overview

Inflowing arterial blood water protons ("spins") are magnetically labelled ("tagged") in a plane proximal to the brain, which is called the labelling plane or slab (Figure 4-8A and B)[80-83, 86]. This is achieved by *selective radiofrequency* (RF) pulses that invert the longitudinal magnetization of blood water protons[81, 83, 89]. Imaging is then performed following a short time delay that allows labelled blood to reach the brain tissue. The MR signal in these labelled images arises from both inflowing labelled arterial blood water and static tissue water. When the magnetically labelled arterial blood water reaches the tissue capillary bed, it leaves the intravascular compartment and acts as a freely diffusible tracer that completely exchanges and mixes with tissue water[89]. Mixing of the negatively magnetized inflowing labelled water protons with positively magnetized static tissue water protons produces a small signal intensity decrease of 1-2% in the images acquired after labelling[89].

In addition to the flow-sensitized labelled images, a separate set of *control* images are always obtained. The **control acquisition** (control condition) is identical to the **labelled acquisition** (labelling condition) with the exception that arterial blood water is not labelled prior to imaging. **Pairwise subtraction** of the *labelled* images from the *control* images (to reduce likelihood of misregistration between label and control) theoretically removes static tissue signal, yielding *difference*

images that are proportional to the amount of blood that was magnetically labelled and delivered to tissue by perfusion (Figure 4-8C) [79, 88]. If all labelled blood has reached the tissue by the time of image acquisition, the signal difference is proportional to cerebral blood flow[79].

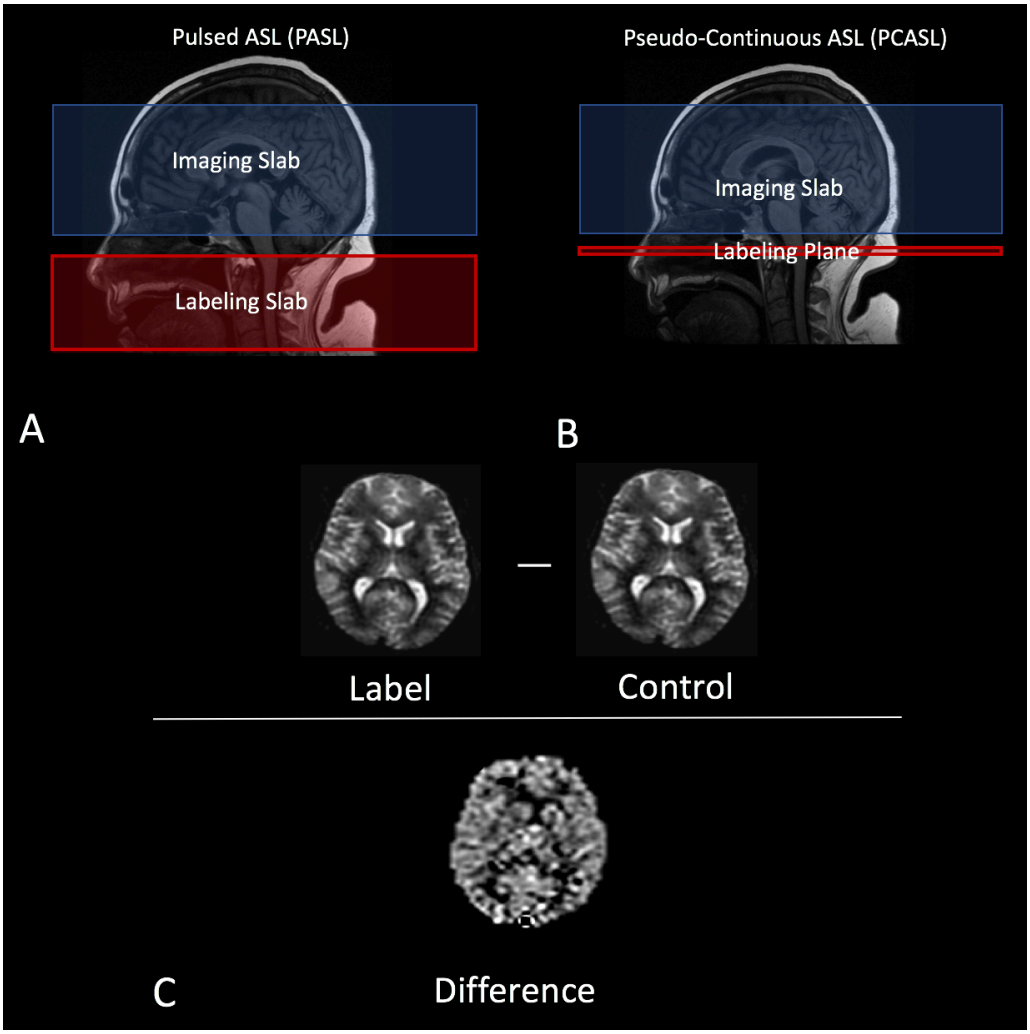

Figure 4-8. *Positioning of the labelling slab/plane and imaging slab.* ***A.*** *The labelling paradigm for the Echo-Planar MR Imaging and Signal Targeting with Alternating Radio Frequency" (EPISTAR) implementation of pulsed ASL is shown. Here, a short RF pulse is applied to a thick slab in the upper neck extending to the skull base. This produces a segment of labelled blood that flows into the imaging plane or volume. Images are acquired after a short time interval, called the inversion time (TI).* ***B.*** *With pseudo-continuous labelling, RF is applied as a long series of short pulses at the labelling plane, which is positioned at the skull base or neck. Images are acquired following a time delay, which is called the post-label delay (PLD). Note that the "imaging slab" can be either a stack of 2D slices or a true 3D volume acquisition.* ***C.*** *For both labelling schemes, images are acquired both with and without magnetic labelling, to yield label and control images. The difference in signal between these images is proportional to the amount of blood that is magnetically labelled and delivered to tissue by perfusion. The signal difference in ASL images can be used to quantify cerebral blood flow.*

Much of the signal in both the label and control images arises from static brain tissue, and the difference between label and control images is approximately 1%[88]. This is due to the small volume fraction occupied by capillaries in a tissue voxel (approximately 4% as discussed previously), and the fact that only a small fraction of labelled water exchanges with the extracellular compartment[89]. It is noted that, since labelled spins are freely diffusible, the **tracer distribution volume fraction** is 100% (unlike DSC-PWI, where GBCA remains intravascular and is hence confined to the plasma compartment as long as the BBB is intact). Inflowing labelled water replaces ~1% of tissue water in grey matter every second; therefore only 2% of the magnetization in a typical brain voxel will be perturbed by a 2 second bolus of labelled blood produced by ASL[88, 89]. Additionally, the lifetime of the tracer (magnetically labelled blood water protons) during arterial transit is dependent upon the longitudinal (T_1) relaxation time of blood, which at clinical field strengths (1.5 - 3.0 T) ranges from 1300 to 1750 ms[90]; labelled spins gradually lose signal during their passage by T_1-relaxation. ASL therefore has inherently low SNR[89].

Once in tissue, relaxation is accelerated due to the shorter tissue T_1-relaxation time. Therefore, in order to achieve sufficient SNR, it is necessary to obtain multiple averages of control-label images. Proton density images are also obtained as a part of the ASL acquisition, based on which a global scaling factor can be applied to the ASL difference images to determine absolute CBF[89].

The ASL sequence can be decomposed into 2 components: **1. labelling** (magnetization preparation) and **2. image acquisition** (readout), which are discussed below in greater depth.

4.5.2 Labelling

The magnetization preparation in ASL is produced by labelling pulses. Three major labelling techniques are used: continuous, pulsed and pseudocontinuous[79, 89]. Velocity-selective labelling is an experimental variant that has not been clinically validated and is therefore not discussed further in this review[91]. The labelling plane for *continuous ASL* (CASL) and *pseudo-continuous ASL* (PCASL) is usually in the skull base, near the spino-medullary junction, while for the PASL the more cranio-caudally extensive labelling slab is used (Figure 4-8A and B).

4.5.2.1 Continuous Arterial Spin Labelling

In *Continuous Arterial Spin Labelling* (CASL) arterial blood is continuously labelled as it passes through the labelling plane in CASL, which is the original ASL method that was proposed by *Williams el at* in 1992[82, 83, 86]. Here, labelling is performed in CASL by applying a continuous RF pulse to a single labelling plane over a long duration, typically 1-3 seconds[88]. A magnetic gradient is applied simultaneously in the direction of arterial blood flow[86, 92]. Blood flowing through the labelling plane therefore has its magnetization inverted by continuous RF energy. As the blood flows along the magnetic field gradient, the spins *slowly change their resonance frequency while being exposed to continuous RF energy*, which is the condition for adiabatic RF pulses. This process is therefore called **flow-driven adiabatic inversion**. Here, the magnitude of the RF field (B_1) is kept constant but its frequency is gradually increased from below the resonance frequency of spins in the imaging plane to above this resonance frequency. Since the RF field is off-resonance, magnetization aligns with an *effective field* (B_{eff}) that is at an angle to both the main magnetic field, B_0, and B_1. During this slow frequency sweep, the net magnetization gradually becomes inverted. In CASL, the flow of arterial blood water protons through the labelling plane produces this frequency sweep, resulting in inversion of their magnetization.

The **labelling efficiency** (also called inversion efficiency, α) refers to the percentage of arterial blood water protons that are inverted. CASL has the highest labelling efficiency, in the range of 80-95%, and produces the highest SNR of all labelling strategies [83, 93]. An important limitation of CASL when a single coil is used for both labelling and image acquisition is that the labelling pulse acts as an off-resonance pulse on the imaging slice. This causes *magnetization transfer* (MT) effects on the imaging slice, resulting in reduced signal from the free water pool in the labelled (but not the control) acquisition[93, 94]. Since tissue perfusion is calculated by subtracting control from label images, CBF is overestimated.

MT effects can be mitigated by using a localized surface coil for labelling or, more commonly, by applying an RF inversion pulse *above* the imaging slice, at the same distance offset as the labelling plane below for the control condition[83]; this *control* inversion plane must be parallel to the labelling plane and equidistant from the imaging slice. Unfortunately, this can only be used for single slice acquisitions. For multi-slice acquisitions, MT effects can be addressed using *amplitude-modulated CASL* (AM-CASL)[80]. Amplitude modulation is produced by multiplying the RF inversion pulse of frequency f_0 used for labelling condition by

a sinusoidal wave of frequency f_1 for the control condition[80]. This is equivalent to applying two successive inversion pulses, of amplitude f_0 - f_1 and f_0 + f_1, during the control condition; the magnetization of arterial blood water is inverted as it traverses the first plane and is theoretically restored to its original state during passage through the second plane, while the MT effects of the labelling condition are matched because the same RF power is used [80]. A disadvantage of this technique, although it allows multi-slice acquisition, is that there is approximately 32% loss of inversion efficiency. Yet another solution to avoid MT effects is to use a small dedicated coil for labelling the carotid arteries; here, the extent of the applied RF field is limited and does not result in saturation effects on the imaging volume[95-97]. This has the additional advantage of allowing selective labelling of each carotid artery so that the vascular territories can be mapped individually (discussed in section 4.4.10)[96, 97].

Disadvantages of CASL include that it is *specific absorption rate* (SAR) intensive. The continuous RF energy deposition related to continuous labelling can be very high[98]. CASL is also very hardware intensive, beyond the performance limits of the RF amplifiers in most clinical MR units.

4.5.2.2 Pulsed Arterial Spin Labelling

Pulsed Arterial Spin Labelling (PASL) is a less SAR and hardware intensive labelling strategy than CASL which can therefore be implemented on clinical MRI scanners[99]. Multiple PASL sequences exist. In-depth discussion of each of these sequences is not undertaken since they have largely been superseded by 3D PCASL, which is the focus of this dissertation. The two main variants of PASL, *Echo-Planar MR Imaging and Signal Targeting with Alternating Radio Frequency* (EPISTAR) and *Flow-sensitive Alternating Inversion Recovery* (FAIR), will each be discussed[99, 100].

Pulsed ASL methods differ fundamentally from CASL with regard to both the duration and spatial extent of labelling[88]. A single short RF pulse or limited number of pulses is applied over 10 - 20 ms to invert the magnetization of arterial blood water in a thick labelling slab (Figure 4-8A); this slab is typically 10 - 20 cm thick and limited by the spatial coverage of the RF coil used for trasmission[99-101]. For efficient inversion, adiabatic hyperbolic secant inversion pulses are used since these are insensitive to B_1-inhomogeneity and therefore produce efficient labelling as well as sharper edges of the slice profiles.

EPISTAR was the prototype PASL implementation, first introduced in 1994[99]. Labelling is performed by an RF inversion pulse applied to a thick slab below the imaging region. Subsequent flow of labelled arterial blood water into the imaging slice produces negative perfusion contrast. In order to balance the MT effects caused by the labelling inversion pulse (which are less than for CASL), an inversion pulse is applied *above* the imaging plane for the control condition. Since arterial blood only flows into the imaging plane from below, this cranial inversion pulse produces no perfusion contrast. It does, however, result in venous labelling. Assuming that this produces symmetrical MT effects on the imaging plane, subtraction of control from label images causes the MT effects to cancel out. Similar to CASL, this only mitigates MT effects for a single slice[93]. To allow compensation for a multi-slice acquisition, the same strategy as for amplitude-modulated CASL is used[93, 102]. It also avoids venous labelling.

In FAIR, the other main type of PASL implementation, two sets of interleaved inversion recovery images are obtained by applying slice-selective and non-selective inversion pulses[100, 103]. The main difference to EPISTAR is that *both control and label conditions invert magnetization in the imaged volume.* For the label condition, images are obtained by applying an inversion pulse concomitant with a slice-selective gradient to the imaging region, which inverts the local tissue magnetization *only* within the imaging slice. Inflowing arterial blood water spins, which originate *outside* this slice, remain fully magnetized; they move into the imaging slice and exchange with tissue water, resulting in an increase in net tissue magnetization, producing *positive* perfusion contrast. For the control condition, the same inversion pulse is used without a slice selective gradient to invert *both tissue and blood* spins (i.e., global inversion within the whole volume of the coil). The **signal difference between the label and control image is therefore positive** and directly related to tissue blood flow. This is the opposite of conventional ASL where labelled blood causes *negative* perfusion contrast. Another important point of distinction, which has relevance for interpretation of FAIR ASL images, is that it is sensitive to blood flow from both below and above. Since the inversion RF pulse is applied to the imaging slab or slice, all tissue outside this imaging slab is effectively labelled; therefore, venous blood flowing into the imaging slab from above, as well as arterial blood flowing in from below, have high signal. Venous ASL signal is therefore a normal finding with FAIR, but this does not affect tissue signal. An advantage of the RF pulse being applied to the imaging plane is that asymmetrical MT effects between labelling and control are avoided. Several variants of FAIR have been developed. They are aimed at improving the accuracy of CBF measurement. These are not discussed in detail, but include

UNinverted Flow-sensitive alternating inversion recovery (UNFAIR)[104], *Flow Alternating Inversion Recovery Extra Radiofrequency Pulse* (FAIRER)[105], and Unprepared Basis and Selective Inversion (BASE)[106].

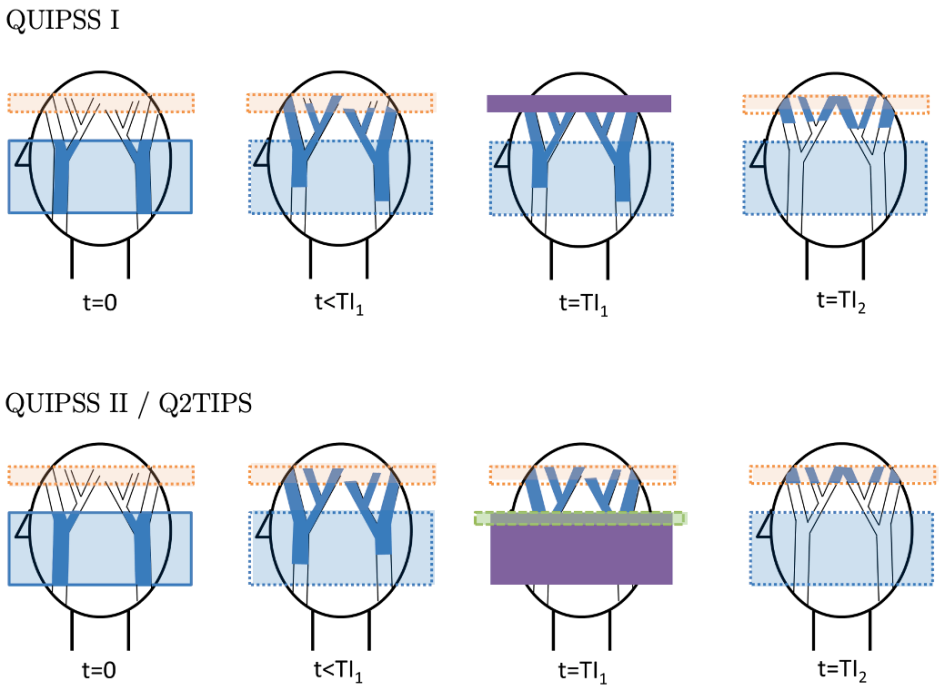

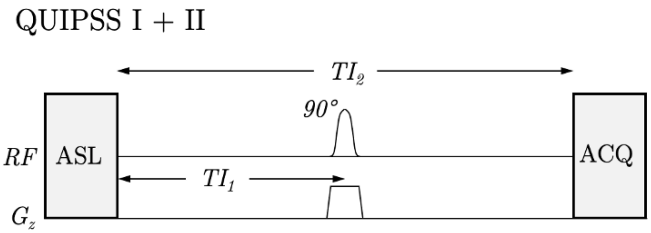

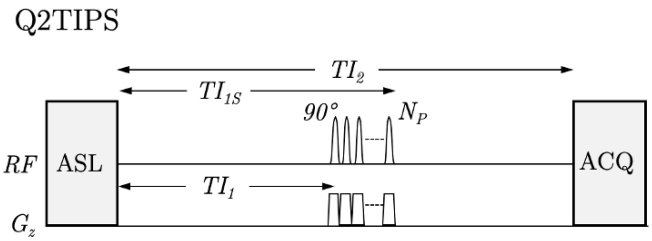

Figure 4-9. *Schematic (top two rows) and pulse sequence (bottom two rows) diagrams of QUIPSS I and QUIPSS II with Q2TIPS. TI is the inversion time. The blue boxes and orange boxes represent the inversion and imaging regions, respectively. The saturation band is applied at the purple box. The thin saturation band used in Q2TIPS is applied at the position of the green box. QUIPSS II and Q2TIPS saturate the trailing edge of the label bolus while in QUIPSS I the leading edge of the bolus is saturated.*

A major source of error when quantifying perfusion using PASL relates to interaction of the slice profiles of the RF pulses. Due to the finite duration of the RF pulses, the edges of the inversion and imaging regions are ramped rather than straight-edged. If the imaging slice and labelling slab are not adequately separated, these ramps will cause subtraction errors that may affect the accuracy of CBF estimation. To address this, inversion RF pulses producing a sharper edge profile are used. This can be achieved by modulating the gradient and RF amplitude at the edges of the pulse, which is called *frequency-offset corrected inversion* (FOCI)[107]. Additionally, a 1-2 cm gap between the labelling slab and imaging slices is used to avoid slice crosstalk.

A limitation of PASL is that the temporal width of the bolus of labelled blood, created by the inversion pulse applied to the labelling slab, is short and unknown. The label bolus length must be known for accurate quantification of CBF using PASL with a single delay time. To address this, the width of the labelled bolus can be controlled by *QUantitative Imaging of Perfusion using a Single Subtraction* (QUIPSS)[108]. In the QUIPSS II technique (Figure 4-9), a saturation pulse is applied to the labelling slab at time TI_1, which is shorter than the inversion bolus length and therefore truncates the trailing end of the labelling bolus. This create a well-defined bolus of known duration. Imaging is subsequently acquired at TI_2, which must be sufficiently long for the entire bolus of labelled blood to reach the imaging slice ie $TI_2 > TI_1 +$ arterial transit time. QUIPSS 2 can be used for multi-slice acquisitions since it does not affect the labelled blood destined for slices downstream, provided that slices are acquired in a proximal to distal (ascending) order. This slice acquisition order also ensures that TI_2 is sufficiently long for all slices. *QUIPSS 2 with thin-slice TI_1 Periodic Saturation* (Q2TIPS) is a modification where a thin-slice (2 cm) saturation pulse is applied to the top edge of the labelling slab repeatedly between TI_1 and TI_2[109]. This thin saturation band has a sharper edge, therefore less slice profile interactions, compared to the thick saturation band applied with QUIPSS2.

4.5.2.3 Pseudo-continuous Arterial Spin Labelling

Pseudo-continuous Arterial Spin Labelling (PCASL) represents a modification of the CASL approach in which a long train of 1,000 or more short (approximately 1 ms) RF pulses is used to simulate a long labelling period of 1 - 2 s[110]. This train of RF pulses is applied at the labelling plane, together with a train of pulsed gradients. This results in flow-driven adiabatic inversion of the magnetization of

arterial blood protons flowing through this plane[110]. For the control condition, a 180° phase shift is introduced into every second RF pulse; the magnetization of the flowing blood water protons is not perturbed during these alternate pulses (i.e. no labelling is produced). The pulse sequence diagram of a PCASL sequence is shown in Figure 4-10.

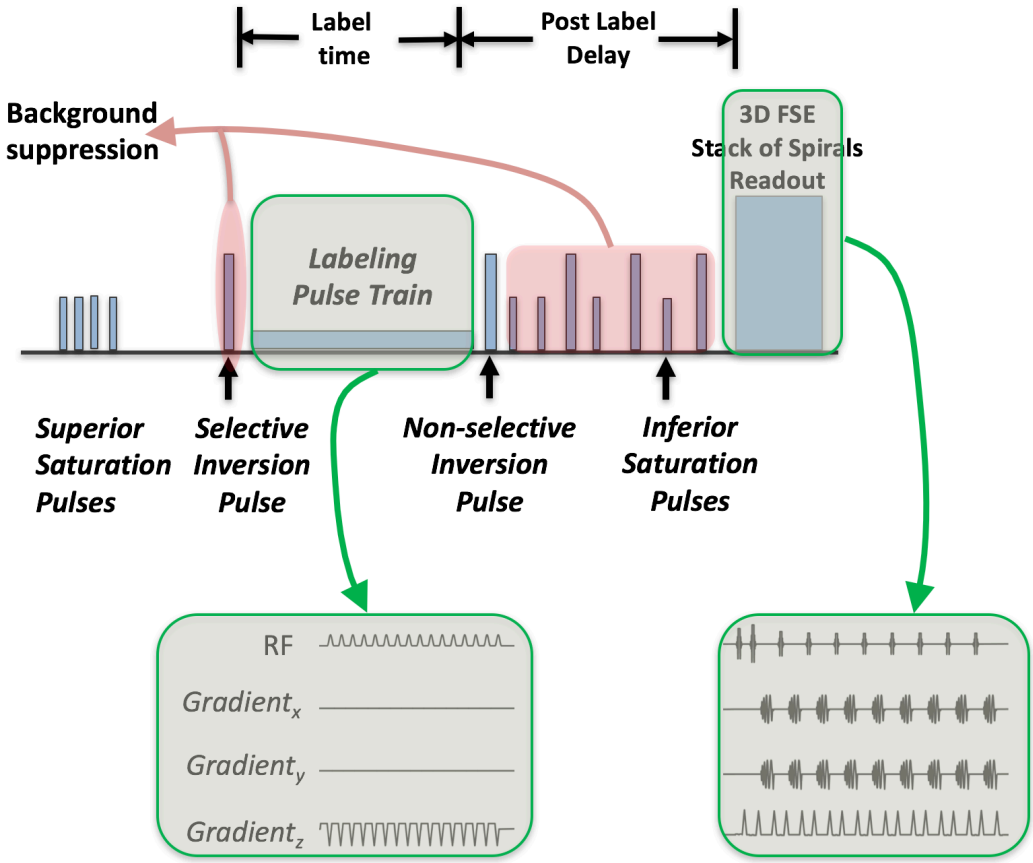

Figure 4-10. *Schematic of a typical 3D PCASL pulse sequence. The ASL perfusion images in this dissertation are obtained using this sequence. The labelling part of the pulse sequence diagram is shown in the left-hand green box; the pseudo-continuous labelling condition is produced by a long train of ≥1000 very short RF pulses together with a train of gradient pulses) that simulate a long labelling period of 1-2 s. The pulse diagram for the 3D fast spin echo (FSE) stack-of-spirals readout module is shown in the green box on the right.*

An advantage of PCASL over CASL is that larger gradients are present during the RF pulses, which increases the resonant offset of pulses relative to brain tissue[88]. This decreases MT effects, which can be substantial with the CASL approach, and increases labelling efficiency. Additionally, PCASL is less hardware and SAR intensive than CASL due to the pulsed versus continuous RF delivery. The continuous application of RF power required for CASL is beyond the capabilities of the typical RF amplifiers used on clinical MRI units. Conversely, PCASL can

be implemented using existing RF amplifiers and modern body coil RF transmission hardware on clinical MRI scanners[88].

PCASL also has advantages over PASL, the most important being higher SNR[99-101]. The first reason for this is that the volume of labelled blood delivered to tissue is proportional to the duration of the labelled bolus, which is longer in PCASL than PASL. In EPISTAR PASL, the labelling slab is 10 - 20 cm thick; the duration of the bolus of labelled blood generated by this approach is therefore 1 s or less[99-101]. Also, the labelled magnetization delivered to tissue by PCASL is higher than with PASL. The entire bolus of blood in the labelling plane is labelled by a single short RF pulse in PASL, and T_1-decay of this bolus occurs between labelling and imaging. The labelling plane used for PCASL is typically in the same location as the distal end of the PASL labelling slab. Therefore, since blood is inverted as it passes through the labelling plane, the bolus is on average inverted later in time than in PASL. The duration between labelling and imaging is therefore shorter, leading to less T_1-decay and more signal with PCASL and PASL.

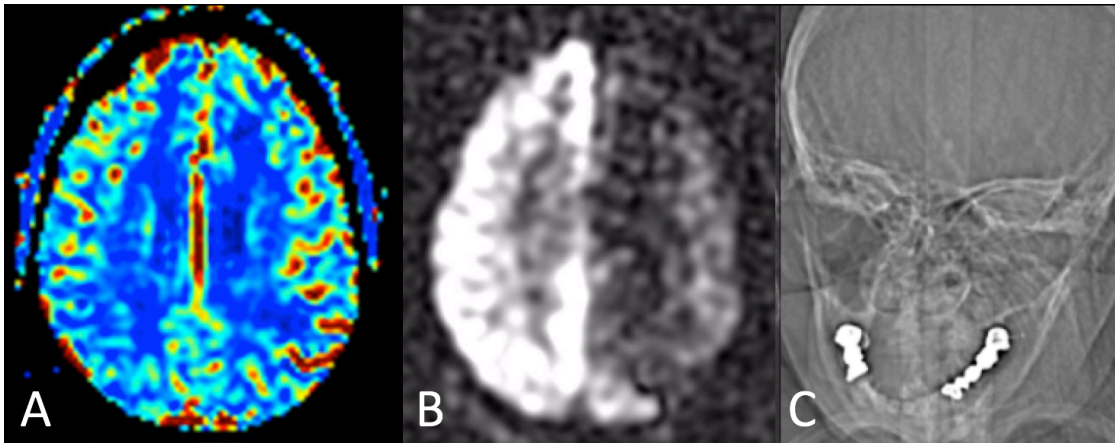

Figure 4-11. *Reduced labelling efficiency due to off-resonance effects from dental enamel.* ***A.*** *Single representative slice of the rCBF map obtained using DSC-PWI shows normal blood flow in the left ICA territory.* ***B.*** *PCASL shows reduced blood flow within this vascular territory, which is an artifact.* ***C.*** *The cause of this artifact was thought to be paramagnetic dental enamel on the left (the enamel on the right presumably has a different with different magnetic properties*

Given these advantages, PCASL is the labelling method of choice for clinical ASL and is recommended for clinical applications[88, 99-101]. The label duration recommended by the consensus guidelines is 1800 ms[111]. The optimal label duration is determined by the longitudinal (T_1) relaxation time of blood (1650 ms at 3 Tesla) [88, 112]. Although ASL signal increases with label duration, this must be balanced against the disadvantages of using a longer label duration: increased TR, increased

signal dependence on tissue rather than blood $T_{1,}$ (since "exchanged" labelled spins accumulate in tissue) and greater RF power deposition (increased SAR).

A limitation of PCASL is the sensitivity of the labelling train to off-resonance effects[88]. The PCASL label train is, in essence, like a *balanced steady-state free precession* (bSSFP) train and, as such, demonstrate signal stop band/pass band behaviour for spins that are off-resonant over a TR cycle. Air-bone interfaces, metallic surgical hardware and paramagnetic dental enamel at the labelling plane can cause the RF inversion pulse to be off-resonance, resulting in inefficient labelling. This is uncommon but should be considered when there is uniformly low signal throughout a vascular territory (Figure 4-11).

4.5.3 Delay Between Labelling and Imaging

A time delay is necessary between application of the labelling inversion pulse and image acquisition to allow the labelled blood to reach the tissue compartment in the imaging plane. The terms used to describe this delay differ between PCASL and PASL.

For PASL, the labelling pulse is almost instantaneous (of the order of 10 ms) and is therefore characterized by a single time point. The delay between the time point of the labelling pulse and the image acquisition is referred to as the *inversion time* (*TI*).

For PCASL, the time between the beginning and the end of the labelling pulse train is called the labelling duration and is typically 1500 - 2000 ms. The time between the end of the labelling pulse train and the image acquisition is called the *post-label delay* (PLD) and is typically 1800 to 3000 ms. Since the PLD commences when the end of the labelled bolus leaves the labelling plane, the analogous time in PASL is when the tail end of the labelled bolus passes through the distal edge of the labelling slab. This time point is estimated (slab width/blood flow velocity) when the QUIPSS 2 modification is applied (TI_1, the time when the saturation pulse is applied to the labelling plane to truncate the trailing edge of the labelled bolus) and the interval $TI\text{-}TI_1$ is then analogous to the PLD.

The choice of PLD with PCASL must take into consideration the *arterial transit time* (ATT). The ATT, which is also called *arterial arrival time* and *transit delay*, is the transport time of labelled blood to travel from the labelling plane to the

tissue compartment in the imaging plane[88, 89, 113, 114]. If the PLD is shorter than the ATT, image acquisition is commenced prematurely. The bolus of labelled blood will not have sufficient time to reach the tissue capillary bed. Instead, it will be in transit in arteries at the time that images are acquired. Since there will be incomplete delivery of labelled blood water to tissue, perfusion is underestimated (Figure 4-12B and C). Additionally, high signal is seen in arteries (**arterial transit artifact**) (Figure 4-12D), which may be mistaken for cortical hyperperfusion. Regional differences in signal will be related to differences in arterial transit time rather than true perfusion.

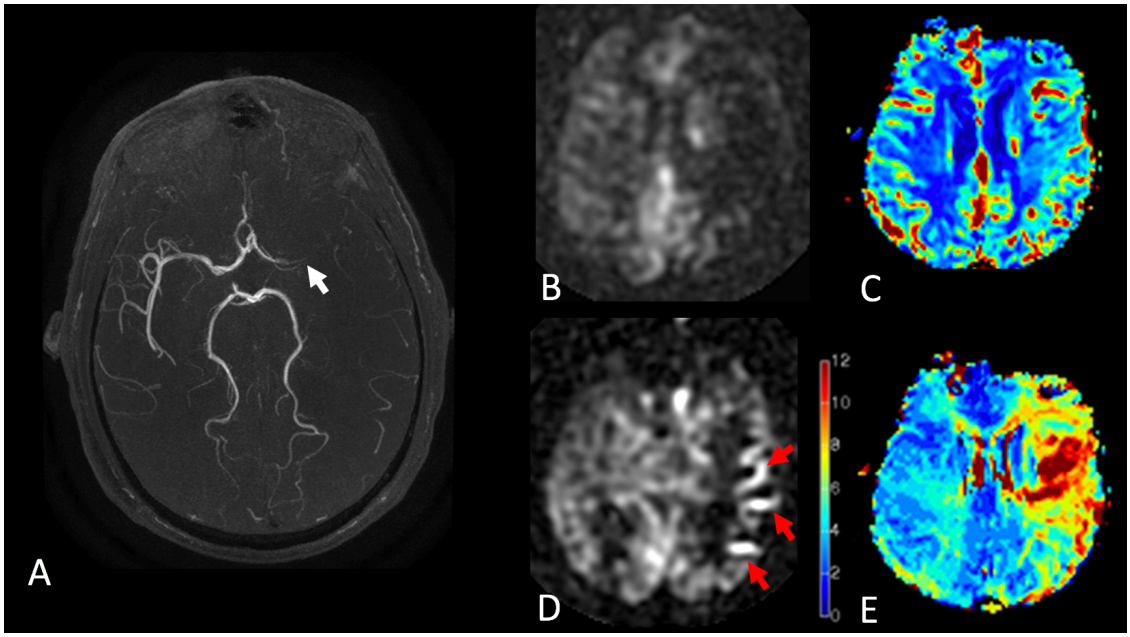

Figure 4-12. *Both ASL and DSC-PWI perfusion sequences were performed in a 69 year-old man who presented with an acute ischemic stroke due to thromboembolic occlusion of the of the M1 segment of the left MCA.* ***A.*** *TOF MRA showing MCA occlusion (arrow).* ***B.*** *PCASL performed with a PLD of 2000 ms, showing apparently reduced CBF in the left MCA territory compared to the right.* ***C.*** *No reduction in rCBF is evident on DSC-PWI, instead with mild elevation seen due to autoregulatory compensation. The apparent CBF reduction on ASL perfusion is therefore spurious, caused by delayed arrival of labelled blood in tissue (ie delayed arterial transit time) due to the proximal occlusion. The labelled blood must travel via indirect collateral pathways to reach the tissue, which takes longer.* ***D.*** *Imaging at a more inferior slice demonstrates curvilinear high signal (red arrows) overlying the left MCA territory, which is due to the presence of labelled blood in transit within M3 and M4 branches of the left MCA as well as leptomeningeal collaterals that supply these (bypassing the occlusion). This is referred to as arterial transit artifact.* ***E.*** *Tmax map at the same level as A. The area of CBF reduction on ASL corresponds to the area severely delayed Tmax, which confirms severe prolongation of arterial transit.*

Selecting the optimal PLD would be simple if the ATT were exactly known and uniform. However, **ATT varies considerably between different brain**

regions due to differences in vessel geometry. It is typically of the order of 300 to 2000 ms, with the longer times occurring in **vascular borderzones** and **white matter**[101]. ATT can vary between 500 and 1500 ms in healthy grey matter, depending on the location of the labelling plane as well as tissue location[88]. A PLD that is just longer than the longest ATT present in the patient would allow the entire bolus of labelled blood to be delivered to the tissue capillaries by the time of imaging, and reduce the contribution of arterial signal to the perfusion image[88]. Unfortunately, this choice of PLD would incur too high a penalty in terms of SNR. Since the signal of labelled blood decays with the T_1-relaxation time of blood (1650 ms at 3T), which in turn is similar to the ATTs observed even in healthy subjects, using a PLD that exceeds the longest ATT would incur substantial signal loss. In Figure 13, the effect of different PLDs is shown. The choice of PLD is therefore a trade-off between achieving sufficient SNR (shorter PLDs) and achieving complete delivery of labelled blood to tissue (longer PLDs). The recommended PLD for paediatric imaging is 1500 ms[88]. A PLD of 1800 ms is recommended in healthy adult subjects aged less than 70 years while a 2000 ms is recommended in adult clinical patients and healthy adults aged over 70 years[88]. This takes into account the increase in ATT with ageing due to steno-occlusive disease, increased vessel tortuosity and reduced cardiac output[88, 112].

It is noted that the PLD may therefore be shorter than the ATT in some brain regions/tissues, especially white matter and vascular borderzones. It is therefore important to be cognizant of the fact that low ASL signal does not always reflect low CBF and may instead be due to the ATT exceeding the PLD. This problem is further exacerbated in patients with abnormally prolonged ATT, for example due to poor cardiac output and steno-occlusive disease (Figures 4-12 and 4-13). Prolonged ATT can be recognized in many cases by the presence of arterial transit artifact in the vascular territory where CBF appears decreased.

ATT, which is correlated with *Tmax*, is delayed when there is arterial stenosis or occlusion[115]. This delay can be substantial in acute stroke, as evidenced by *Tmax* prolongation of 6 seconds or greater in critically hypoperfused ischemic tissue. In these conditions, a longer PLD is required to allow sufficient time for labelled blood to reach the tissue capillary bed, to avoid underestimating tissue perfusion. Given that ASL signal decay during arterial transit is governed by the T_1-relaxation time of blood (approximately 1650 ms at 3T with normal haematocrit), there can be substantial decay of label between the labelling plane and tissue[90, 112, 115]. This, in turn, leads to severe underestimation of CBF even if a longer PLD is used. Techniques to address these limitations are discussed in section 4.5.7.

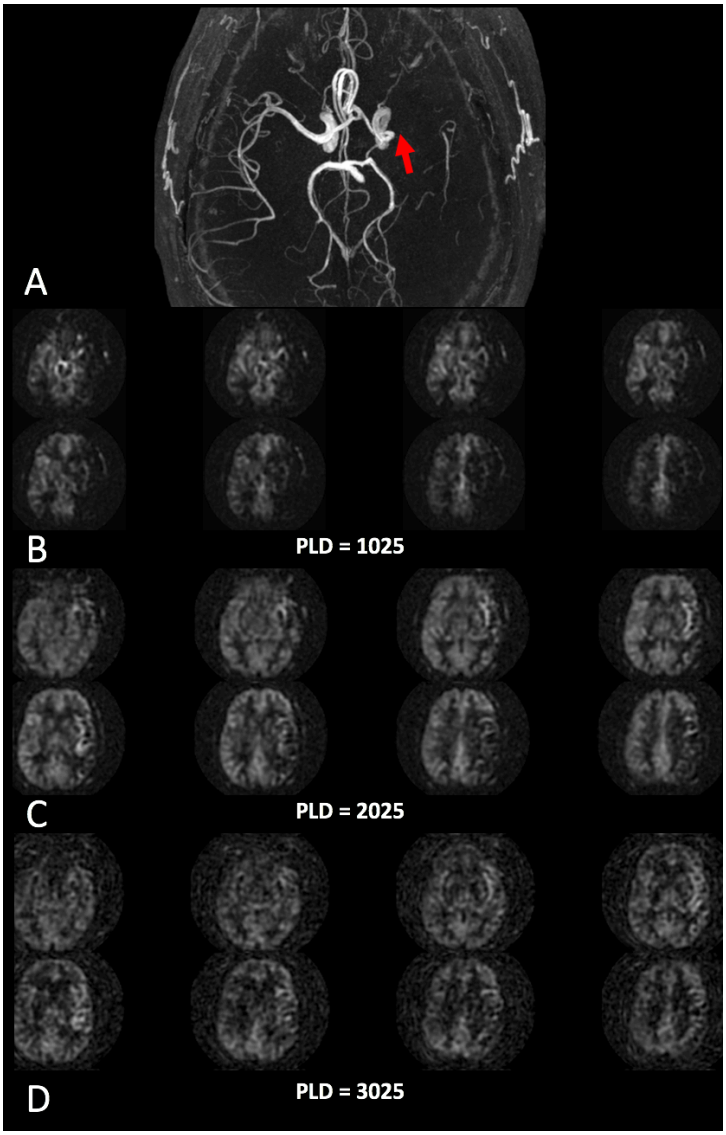

Figure 4-13. *The effect on PLD on tissue and arterial signal in a 51 year old man.* ***A.*** *Chronic occlusion of left MCA (arrow) is shown on TOF MRA. Arterial transit time will therefore be delayed in the left MCA territory compared to the rest of the cerebral circulation.* ***B.*** *Images obtained at a short PLD show high signal in the basal cisterns, interhemispheric fissure, and right Sylvian cistern as well as the proximal part of the left Sylvian fissures bilaterally, due to labelled blood within the proximal cerebral arteries. CBF appears markedly reduced in the left MCA territory.* ***C.*** *A standard PLD allows labelled blood to reach the tissue in the normal vascular territories (right MCA and posterior circulation). Labelled blood is still seen in transit in left MCA branches, manifested as arterial transit artifact on the left Sylvain fissure that has now progressed more distally. CBF appears reduced in the left MCA territory.* ***D.*** *A long delay allows the labelled blood to reach the tissue in the MCA territory via collateral pathways, although there is still some mild arterial transit artifact. The CBF in the left MCA territory now only appears slightly reduced on the two most superior slices, while it appears slightly increased compared to the right in more inferior slices; tis can be explained by a combination of arterial transit artifact in maximally dilated leptomeningeal collaterals (compensatory) and tissue perfusion. It can be seen that, as the PLD is increased, signal and SNR decrease due to T_1-decay of label.*

4.5.4 Image Acquisition

Rapid acquisition techniques are required to obtain the sufficient number of control and label images. Older ASL implementations used 2D *echo-planar imaging* (EPI) readouts. A disadvantage of 2D acquisitions is that each slice has a different *TI* (the delay between the nearly instantaneous labelling pulse and image acquisition). The slices which are acquired earlier (typically the proximal slices) have the shortest *TI*. If this *TI* is too short (i.e., $TI <$ ATT), there will be incomplete delivery of labelled blood to the tissue compartment in the imaging slice; the images will therefore be more vessel-weighted than tissue perfusion-weighted and arterial transit artifact will be seen. Conversely, the longer PLD of the most distal slices leads to more T1-decay of labelled blood. These slices will therefore have reduced SNR. This is compounded by loss of signal resulting from the RF pulses used to image the more proximal slices, which decreases the label delivered to the tissue in the more superior slices.

3D techniques can be made more SNR efficient and are less sensitive to off-resonance effects and transit time variability than 2D EPI readouts. Segmented 3D sequences are therefore the preferred readout method, and are recommended by guidelines[88]. Most new ASL implementations therefore use 3D image acquisition techniques. These include single-shot 3D *gradient- and spin-echo imaging* (GRASE) and 3D multi-echo (RARE)/*fast spin-echo* (FSE) readouts. The latter is implemented with a stack-of-spirals k-space trajectory[116, 117]. These readout methods are optimal for detecting the signal produced by labelling, having the dual advantages of insensitivity to T_2*-effects that RARE methods offer and the time efficiency of EPI and spiral acquisitions. Another solution to mitigate motion is adaptive, real-time motion correction[118, 119].

Another advantage of 3D techniques over 2D is that they use a single excitation per TR, which is better for implementing background suppression since the timing of the tissue null point is more exactly defined[88]. With 2D techniques, background suppression is only optimal for a few slices at best. Since the time required for image acquisition within each TR is less for 3D readouts than multiple 2D slices, this also allows more efficient use of time (longer labelling time per TR or a shorter TR). A disadvantage of 3D readouts is that they are more sensitive to motion than single-shot 2D readouts since they are multi-shot techniques[88]. This motion sensitivity is mitigated by effective background suppression[88]. Additionally, oversampling of the centre of k-space decreases the motion sensitivity when a stack-of-spirals trajectory is used.

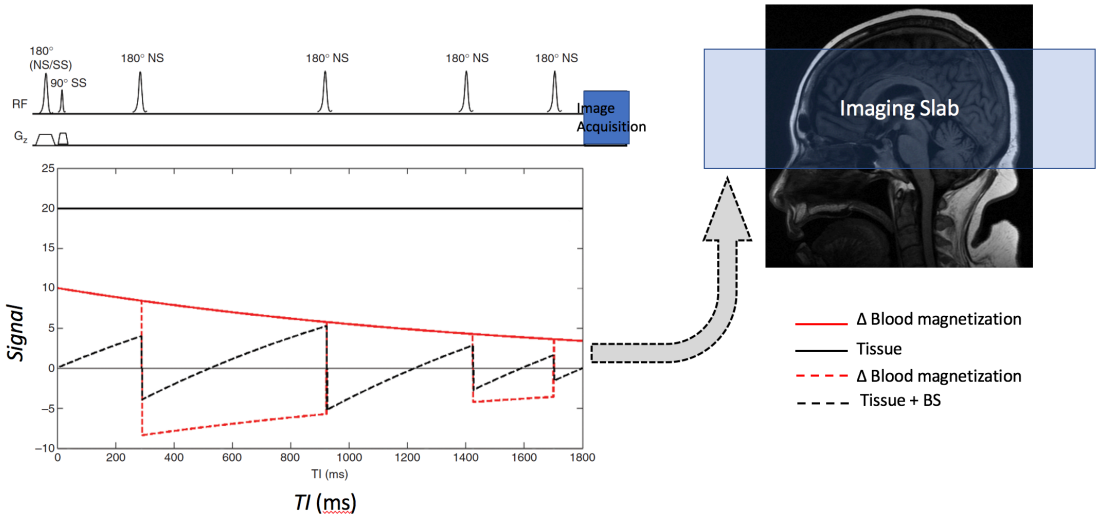

Figure 4-14. *Background suppression. An initial 90º slab saturation (SS) pulse is applied to the imaging region immediately after the PCASL labelling pulse. This is followed by non-selective 180º (inversion) pulses that are timed so that the longitudinal magnetization of static brain tissue is ~0 (dashed black line) at the time of image acquisition, while inflowing blood is unaffected since it has not encountered the initial 90º pulse.*

Background suppression refers to the use of additional RF pulses image slice/volume to **null the static signal** from grey and white matter, and CSF. It is important because of the small (typically ~ 1%) signal change in tissue produced by ASL[88]. Patient motion, which is the main source of noise in ASL, causes fluctuations in signal that are proportional to the signal in unsubtracted images. The purpose of background suppression is to decrease the signal intensity of label and control images without a proportional decrease in the ASL difference signal, in turn improving the SNR of ASL[88, 120]. This is achieved using a combination of saturation and inversion pulses[110, 121, 122]. An initial 90º slice or slab saturation pulse is applied to the imaging region immediately after the labelling pulse. This is followed by non-selective inversion pulses that are carefully timed so that the longitudinal magnetization of static brain tissue is zero or close to zero at the time of image acquisition (Figure 4-14). The use of background suppression markedly improves the temporal SNR of ASL and decreases motion sensitivity[88]. This is important for clinical implementation of ASL because acquisition times need to be shorter than in the research setting, and the perfusion data from a single scan influences clinical decisions[88]. Additionally, significant motion is more likely in the clinical setting where unwell patients rather than healthy volunteers are scanned. Background suppression is therefore recommended by guidelines[88].

Vascular suppressor gradients should be avoided since they null the signal within arteries and veins; this intravascular signal can be a valuable clue to underlying pathology as will be shown in this disseration[123].

4.5.5 Quantification in ASL

The equations for calculating CBF from ASL can be derived from the Bloch equation, which describes the decay of longitudinal magnetization of tissue, M_t, by the time constant T_1:

$$\frac{dM_t(t)}{dt} = \frac{M_t^0 - M_t}{T_{1,t}} \quad [4\text{-}1]$$

Here, M_t^0 is the equilibrium magnetization of tissue and $T_{1,t}$ is the T_1 (longitudinal) relaxation time of tissue at the field strength at which the scan is performed. The effects of labelled blood are incorporated into the Bloch equation by two additional terms to describe the *inflow* and *outflow of magnetization into the voxel*[83]:

$$\frac{dM_t(t)}{dt} = \frac{M_t^0 - M_t}{T_{1,t}} + fM_a(t) - fM_v(t) \quad [4\text{-}2]$$

where M_t is the magnetization in the tissue voxel of the labelled image; f is CBF in mL of blood per minute per second per mg tissue; M_a is the arterial blood magnetization; and M_v is venous magnetization. A single compartment model is applied, where it is assumed that intravascular labelled water rapidly exchanges and equilibrates with the much larger pool of tissue water instantaneously[124]; the magnetization of blood leaving the voxel at the venous end, M_v, is therefore proportional to the average magnetization of the whole voxel, M_t. The volume of water in tissue is lower than that in blood; the constant λ (the brain-blood partition coefficient) is therefore used to scale the signal intensity of tissue to that of blood:

$$M_v(t) = M_t(t)/\lambda \quad [4\text{-}3]$$

Substituting this into equation *4-3* yields:

$$\frac{dM_t(t)}{dt} = \frac{M_t^0 - M_t(t)}{T_{1,t}} + fM_a(t) - \frac{f}{\lambda}M_t(t) \quad [4\text{-}4]$$

The signal in the labelled image decays with the relaxation time $T_{1,app}$ which is shortened in comparison with the T_1 of tissue ($T_{1,t}$) due to the presence of labelled blood:

$$\frac{1}{T_{1,app}} = \frac{1}{T_{1,t}} + \frac{f}{\lambda} \qquad [4\text{-}5]$$

Therefore,

$$\frac{dM_t(t)}{dt} = \frac{M_t^0}{T_{1,t}} - \frac{M_t(t)}{T_{1,app}} + fM_a(t) \qquad [4\text{-}6]$$

Instead of treating the control and label images separately, the magnetization in the ASL difference image, ΔM, can be considered directly. The equilibrium magnetization in this difference image is 0 in the absence of labelling, therefore equation *4-8* becomes:

$$\frac{d\Delta M_t(t)}{dt} = -\frac{\Delta M_t(t)}{T_{1,app}} + f\Delta M_a(t) \qquad [4\text{-}7]$$

The difference in arterial magnetization between the control and label conditions, ΔM_a, is therefore given by:

$$\Delta M_a = 2\alpha M_a^0 e^{-t/T_{1,a}} \qquad \textit{(for PASL)} \qquad [4\text{-}8]$$

and

$$\Delta M_a = 2\alpha M_a^0 e^{-\delta/T_{1,a}} \qquad \textit{(for PCASL)} \qquad [4\text{-}9]$$

where M_a^0 is the equilibrium magnetization of arterial blood, α is the labelling efficiency, δ is the arterial transit time, which (as defined earlier) is the time that labelled blood takes to travel from the labelling plane to tissue in the imaging plane, and $T_{1,a}$ is the longitudinal relaxation of time of arterial blood. These equations hold true for time points between the arrival of label in the tissue (i.e., labelling plane) and the trailing edge of the bolus (i.e., $\delta < t < \delta + \tau$, where τ is the temporal width of the bolus). $M_a = 0$ for time points outside this range (i.e. $t < \delta$ or $t > \delta + \tau$). For PASL, equation 4-8 assumes that there is no gap between the labelling slab and imaging plane, and M_a arrives at the imaging plane instantaneously. The magnetization of labelled arterial blood decays exponentially

with the T_1-relaxation time of blood during its transit from the labelling plane to the imaging plane. For PCASL, it is assumed that all labelled blood takes the same length of time, δ, to reach the tissue compartment in the imaging plane, therefore the amplitude of label remains constant over the imaging period.

In PASL, the labelling pulse is applied to a slab (therefore a volume) of tissue rather than a plane; a bolus of finite width is therefore generated, the trailing edge of which takes longer to reach the tissue voxel, and will consequently have decayed more than the leading edge. This leads to decay in arterial magnetization with time from labelling. The time after labelling must therefore be taken into consideration specifically when calculating arterial magnetization.

Substituting equation *4-9* into equation *4-7*:

$$\frac{d\Delta M_t(t)}{dt} = -\frac{\Delta M_t(t)}{T_{1,app}} + 2\alpha f M_a^0 e^{-\delta/T_{1,a}} \qquad [4\text{-}10]$$

and rearranging equation 4-10 yields

$$\frac{d\Delta M_t(t)}{dt} + \frac{\Delta M_t(t)}{T_{1,app}} = 2\alpha f M_a^0 e^{-\delta/T_{1,a}} \qquad [4\text{-}10b]$$

By multiplying equation 4-10b with $e^{t/T_{1,app}}$:

$$\frac{d\Delta M_t(t)}{dt} \cdot e^{t/T_{1,app}} + \frac{\Delta M_t(t)}{T_{1,app}} \cdot e^{t/T_{1,app}} = 2\alpha f M_a^0 e^{-\delta/T_{1,a}} \cdot e^{t/T_{1,app}} \qquad [4\text{-}10c]$$

and applying left side of equation 4-10c is product rule of differentiation:

$$\frac{d(u \cdot v)}{dt} = \frac{du}{dt} \cdot v + u \cdot \frac{dv}{dt}\ , \qquad [4\text{-}11]$$

with $u = \Delta M_t$ and $v = e^{t/T_{1,app}}$, we recognize:

$$\frac{d(\Delta M_t(t) \cdot e^{t/T_{1,app}})}{dt} = 2\alpha f M_a^0 e^{-\delta/T_{1,a}} \cdot e^{t/T_{1,app}} \qquad [4\text{-}12]$$

By integration of both sides of equation 4-12:

$$\int \frac{d(\Delta M_t(t) \cdot e^{t/T_{1,app}})}{dt} dt = 2\alpha f M_a^0 e^{-\delta/T_{1,a}} \cdot \int e^{t/T_{1,app}}\, dt\ , \qquad [4\text{-}13]$$

we get:

$$\Delta M_t(t) \cdot e^{t/T_{1,app}} = 2\alpha f M_a^0 e^{-\delta/T_{1,a}} \cdot T_{1,app} \cdot e^{t/T_{1,app}} \ , \qquad [4\text{-}14]$$

which can be further simplified to:

$$\Delta M_t(t) = 2\alpha f M_a^0 e^{-\delta/T_{1,a}} \cdot T_{1,app} \qquad [4\text{-}15]$$

Since M_a^0 is difficult to measure, it can be approximated using M_t^0/λ. This equation is not time dependent, which holds true as long as a sufficiently long labelling duration is used to allow tissue magnetization to reach the steady state.

An alternative and perhaps more intuitive approach to quantification with PCASL is **Buxton's general kinetic model**[125]. This model is based on a finite label duration, producing a square bolus of labelled blood with width, τ, which is assumed to arrive at the arterial transit time, i.e. $t = \delta$. The following three functions are combined to define the relationship between the change in tissue magnetization and blood flow:

1. The delivery function, *c(t)*, defines the bolus of width τ arriving at time t $= \delta$, which is the arterial transit time as previously defined:

$$c(t) = \begin{cases} 0 & 0 < t < \delta \\ \alpha e^{-\delta/T_{1,a}} & \delta < t < \tau + \delta \\ 0 & \tau + \delta < t \end{cases} \qquad [4\text{-}16]$$

   This takes into account labelling efficiency, α, and the T_1-relaxation of labelled arterial blood during transit, $T_{1,a}$.

2. The residue function, *R(t)*, reflecting the exchange of labelled spins between blood and tissue:

$$r(t) = e^{-ft/\lambda} = e^{-t/MTT} \qquad [4\text{-}17]$$

3. Magnetization relaxation function, *m(t)*, resulting from the continued relaxation of labelled blood water after exchange into tissue:

$$m(t) = e^{-t/T_{1,t}} \qquad [4\text{-}18]$$

Combining these functions yields:

$$\Delta M_t = 2M_a^0 f \int_0^t c(t')r(t-t')m(t-t')dt' \qquad [4\text{-}19]$$

$$\Delta M_t = 2M_a^0 f c(t) * [r(t)m(t)] \quad [4\text{-}20]$$

Therefore,

$$\Delta M_t(t) = \begin{cases} 0 & 0 < t < \delta \\ 2\alpha f M_a^0 T_{1,app} \cdot e^{-\frac{\delta}{T_{1,a}}}\left(1 - e^{-(t-\delta)/T_{1,app}}\right) & \delta < t < \tau + \delta \\ 2\alpha f M_a^0 T_{1,app} \cdot e^{-\frac{\delta}{T_{1,a}}} \cdot e^{-(t-\tau-\delta)/T_{1,app}}\left(1 - e^{-\tau/T_{1,app}}\right) & \tau + \delta < t \end{cases} \quad [4\text{-}21]$$

The distal edge of the labelled bolus arrives in tissue at $t = \delta + \tau$. τ is the temporal width of the bolus (label duration for PCASL). If τ is sufficiently long to allow brain tissue to reach a steady-state signal, then these equations will reduce to equation *4-15*.

The Buxton model can also be applied to PASL, with modification of the delivery function to account for the different arrival times of the leading and trailing edges of the bolus of labelled blood.

The signal intensity on proton density images (where the blood water protons are fully relaxed) is used as the scaling factor to obtain absolute CBF from the signal intensity of the subtracted ASL images[88]. Greater accuracy is achieved by using separately acquired proton density images to obtain the scaling factor for each voxel, instead of estimating the scaling factor. This corrects for signal variation caused by inhomogeneity in RF coil sensitivity and differences in T_2/T_2*-relaxation[88]. The PD images should be acquired with the same readout module as the ASL images, with a long TR to provide true proton density weighting. Although λ should ideally be obtained from an image, since the tissue water density differs between different tissue types, it is recommended that a brain average value of 0.9 mL/g is used[88, 126].

Guidelines recommend using the following values for inversion efficiency, α, which is the signal difference of blood between the control and tag conditions expressed as a percentage of the maximum possible signal difference: 0.85 for PCASL and 0.98 for PASL[88, 110]. It can be measured for more accurate quantification of CBF. This m can be achieved by obtaining control and label images of blood vessels downstream from the labelling plane, using a flow-compensated gradient-echo sequence.

4.5.5.1 Influence of ATT on Quantification

As discussed above, the ATT (noted mathematically as δ) is the time taken for labelled blood to travel from the labelling plane to the tissue compartment in the imaging plane. T_1-relaxation of labelled blood occurs during this time. Since ATT is of the order of the T_1-relaxation time of labelled blood, considerable underestimation of CBF can occur if this is not corrected for[89].

In the models for CBF quantification described above, the arterial blood magnetization is corrected for the T_1-relaxation during arterial transit based on the assumption of "plug flow" of arterial blood from the labelling plane to the imaging plane without dispersion. Under this assumption, the ATT is uniform for all labelled spins. The effect of signal decay during the ATT can then be corrected for, provided that the bolus of labelled blood has a well-defined temporal width. With PASL, a temporally defined bolus is achieved using the QUIPSSS and Q2TIPS modifications (discussed above), which truncate the trailing end of the bolus of labelled blood. Provided that the *TI* is long enough to allow the entire bolus to reach the imaging slice, the effect of variability of ATT on CBF quantification is minimized. For PCASL and CASL, the temporal width of the bolus of labelled blood is controlled by the use of a PLD[111]. This reduces the sensitivity of CBF quantification to variations in ATT since, in theory, it allows the entire bolus of labelled blood to reach the tissue. Hence labelled spins with a longer ATT are given time to catch up with those that have arrived earlier in the imaging plane. Provided that the PLD is sufficiently long, exact knowledge of the ATT is no longer required under these assumptions, and the δ term can be replaced with the PLD for CBF calculation.

As discussed above, different brain regions and tissue (white matter versus grey matter) have different ATTs. Although the PLD reduces the sensitivity to this variability in transit times, it does not entirely eliminate it. This is due to the fact that it is not feasible to use a PLD that is longer than the ATT of all tissue under all conditions, since it would result in insufficient SNR due to T_1-decay of signal. It must therefore be remembered that the techniques and models for quantification of CBF described above may be inaccurate for white matter and vascular border-zones, which have longer ATTs. Quantification using these models can also lead to considerable error in CBF measurements when there is delayed arterial transit, as occurs in AIS and chronic steno-occlusive disease. In these conditions, a standard PLD does not allow sufficient time for the entire bolus of labelled blood to reach tissue at the time of imaging, and there is also increased variability in the

ATT. A solution is to perform multi-delay ASL, which will be discussed in the next section where ASL images are acquired at different PLDs. This allows direct measurement of ATT, and correction of CBF for more accurate quantification.

4.5.6 Summary of the Recommended Clinical Implementation of ASL Perfusion

A summary of the recommendations for clinical implementation are given in Table 4-3. The main limitation of ASL perfusion is poor SNR, which has been discussed above. Consequently, anatomical detail is poorly delineated on ASL perfusion images. Additional limitations are variability in ATT, which affects image quality and quantification. In patients with prolonged ATT, the use of a standard PLD results in arterial transit artifact and underestimation of tissue perfusion due to incomplete delivery of labelled blood to the tissue at the time of imaging. Because ASL images are obtained by subtraction of control from label images, the technique is sensitive to motion[88]. Additional motion sensitivity is incurred by the use of segmented 3D image acquisition techniques. This is partially mitigated by the use of background suppression and adaptive motion correction.

Table 4-3. *Recommendations for clinical implementation of ASL[88]*

ASL Parameter	**Recommendation**
Labelling strategy	Pseudo-continuous labelling
Labelling duration	1800 ms
PLD	Single, 1800 ms (children and healthy adult subjects < 70 years old) 2000 ms for adult patients & healthy adult subjects > 70 yrs
Readout technique	segmented 3D sequences: 3D FSE stack of spirals or 3D GRASE
Background suppression	Yes
Spatial resolution	3-4 mm in-plane 4-8 mm through-plane (slice thickness)
Acquisition time	Approximately 4 minutes
Vascular crusher gradients	No

4.5.7 Long-Label Long-Delay and Multi-Delay PCASL

Long-label long-delay and multi-delay ASL implementations may address the limitations of single-delay PCASL in patients with AIS and chronic steno-occlusive disease.

Long-label long-delay PCASL was developed to improve the accuracy of cerebral blood flow in chronic steno-occlusive conditions such *Moyamoya disease*[115]. As with standard-delay techniques, a 3D readout (e.g., FSE with stack of spirals readout trajectory) is used. A longer PLD, for example 4000 ms, allows blood to reach tissue downstream from chronic occlusion via collaterals[115]. The use of a longer PLD causes SNR to decrease, due to T_1-decay of labelled blood. A longer labelling time of 3.0 seconds is therefore implemented to counter this and boost SNR. A long-label long-delay PCASL scan can be acquired in approximately 5 minutes. An example of long-label long-delay ASL is shown in Figure 4-15.

A number of strategies can be used to obtain multi-delay ASL. The most straightforward technique is the acquisition of multiple separate sets of label and control images with different PLDs. Typically, 4 to 7 PLDs are obtained ranging from 0.5 to 3.5 seconds[113, 115, 127]. Imaging can be performed in a clinically acceptable time, under 5 minutes, using a 3D GRASE or FSE readout and background suppression[115, 127]. A slightly longer labelling duration is used than for standard PCASL (e.g., 2 seconds versus 1.5 seconds), to improve SNR. By acquiring images at multiple PLDs, the ASL uptake and decay curve is sampled at several time points. A kinetic model (e.g., Buxton, as described in the previous section) can be applied to this data to determine the ATT; for example, ATT can be quantified using a weighted delay approach and look up table[128]. ATT values obtained using multi-delay ASL have been shown to be correlated with Tmax derived from DSC-PWI, and may therefore be of diagnostic utility for delineating the ischemic penumbra (Figure 4-15E and F) [127]. This seems intuitive, since Tmax is also a measure of delay in arrival of contrast agent in tissue (compared to the reference artery where the AIF is measured, instead of the labelling plane), and is therefore reflective of delayed arterial transit. Measurement of ATT also allows correction of blood flow, improving the accuracy of CBF quantification[127]. This multi-delay technique also allows assessment of the dynamics of blood flow and visualization of leptomeningeal collaterals at multiple time points. This, in turn, may allow more accurate collateral scoring[129]. A limitation of multi-delay ASL is the poor SNR at longer PLDs. Because of the longer overall scan time, echo averaging, and spatial resolution are also limited.

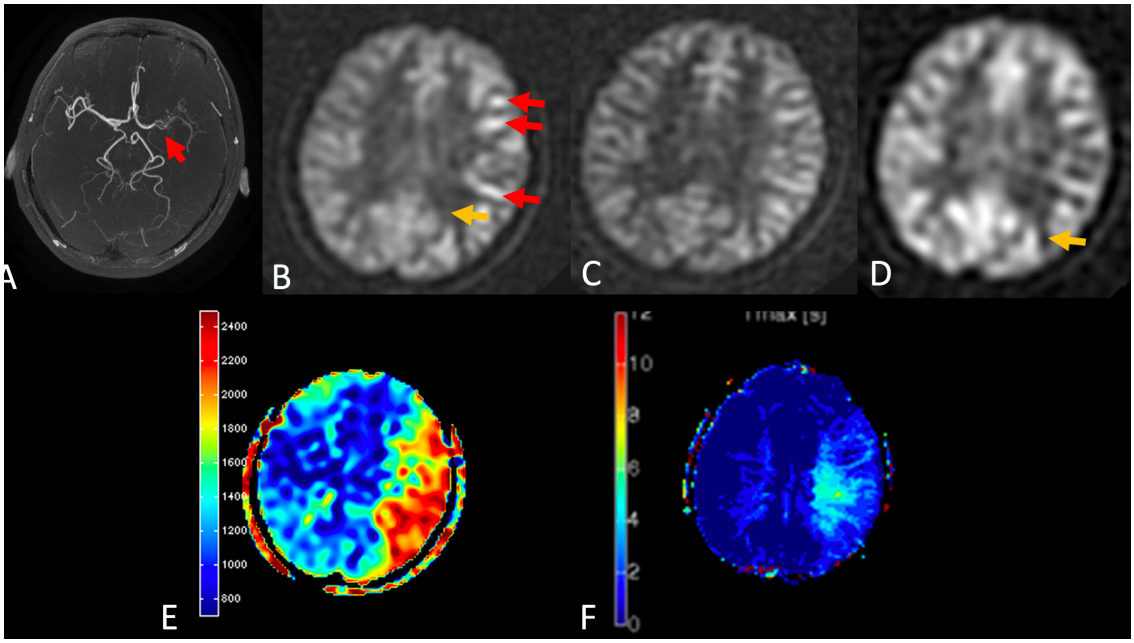

Figure 4-15. *Long-label long-delay and multi-delay ASL in a 49 year-old woman with a unilateral chronic MCA occlusion.* ***A.*** *TOF MRA showing occlusion of the proximal M1 segment of the left MCA and reconstitution of a narrow calibre vessel via a leash of collaterals (arrow).* ***B.*** *Representative slice of the CBF maps obtained using standard delay ASL (PLD of 2025 ms). Curvilinear high signal (red arrows) is seen in the left MCA territory due to arterial transit artifact. CBF appears reduced in posterior frontal and parietal (yellow arrow) white matter.* ***C.*** *Long-label long-delay ASL image acquired with a labelling duration of 3000 ms and PLD of 4000 ms shows that CBF in these areas is in fact normal, with low signal on the previous image due to delayed arrival of labelled blood. The signal overall can be seen to be lower than with standard delay ASL.* ***D.*** *Multi-delay ASL image at the same level has higher signal and SNR. The CBF in white matter appears lower (arrow) despite correction.* ***E.*** *Colour arterial transit time map, which quantifies the delay in arterial transit time. The area in red is the left MCA territory, which has markedly prolonged arterial transit time due to the MCA occlusion. ATT maps are analogous to, and correlated with, Tmax, shown in* ***G****. This is unsurprising, since Tmax is also therefore reflective of delayed arterial transit.*

Another approach to multi-delay ASL is to use a Look-Locker readout scheme to obtain images at multiple different time points[98]; these images will have different effective PLDs. Look-Locker schemes consist of multiple image acquisitions following a single (labelling) inversion pulse[130]. This technique is also associated with reduced SNR related to the reduced readout module flip angle.

A solution which has been proposed to improve SNR in multi-delay acquisitions is the use of a **Hadamard-encoding** scheme[131-133]. This technique involves splitting the labelling period into a series of blocks which are alternated between label and control conditions in different combinations, using a Hadamard encoding matrix, across a series of imaging cycles (Figure 4-16)[133]. Post-processing (matrix

inversion) is used to calculate the signal from each block. The images obtained from each block have a different effective PLD due to the encoding strategy. Fewer measurements are required than for the multi-delay techniques discussed above. The increased data averaging, resulting from the use of multiple imaging cycles, yields higher SNR and reduced physiologic background noise.

Multi-delay techniques are expected to improve the accuracy of CBF quantification. The optimal number of delays for accurate estimation of ATT and precise quantification of CBF is unclear[113, 127]. Incorporating more PLDs into the sequence improves estimation of ATT, allowing more accurate correction of CBF. However, SNR efficiency is sacrificed due to use of shorter label durations[113].

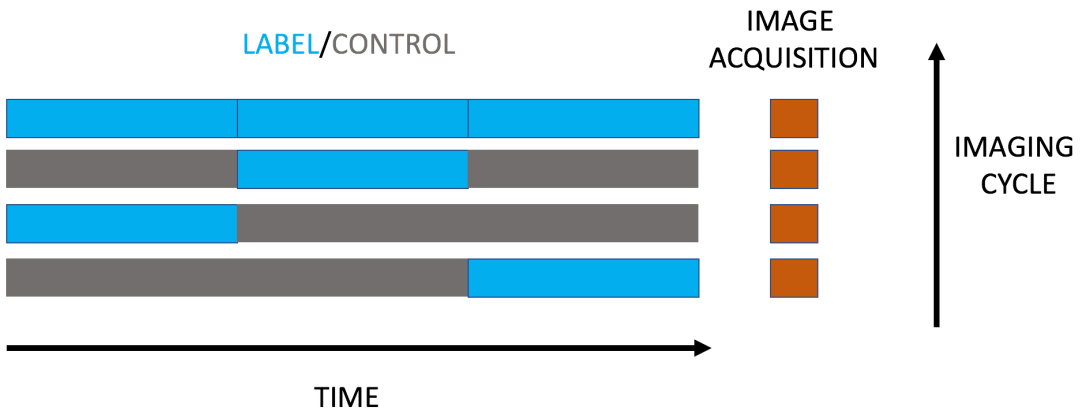

Figure 4-16. *Hadamard-encoded ASL. The labelling period is split into a series of blocks which are alternated between label and control conditions in different combinations (according to a Hadamard encoding matrix) across a series of imaging cycles.*

4.5.8 ASL angiography

The high signal produced by intravascular label on ASL images can be leveraged for angiography[92, 134-138]. Here, the images are acquired soon after labelling (i.e., with a shorter post label delay) to capture labelled blood within arteries, yielding angiographic contrast. ASL angiographic techniques were first described in the 1980s[92, 134]. Higher spatial resolution can be achieved with ASL angiography than ASL perfusion, which is important if this technique is to be used for cerebral angiography since the intracranial arteries are of small calibre. The poor spatial resolution of ASL perfusion images arises from the necessity to use relatively large voxels to improve SNR (due to the paucity of label, hence poor signal, in tissue). Arteries, on the other hand, are 100% blood volume structures. They therefore have a high concentration of labelled blood in them when imaged after labelling.

The short time delay between labelling and image acquisition also means that there is less T_1-decay of label. Arteries with labelled blood therefore have high signal. Consequently, the SNR of ASL angiography is considerably higher than that of ASL perfusion. This allows the voxel size to be reduced and spatial resolution increased. Another advantage of ASL angiography is that, as with all ASL techniques, static tissue signal is nulled through pairwise subtraction of label and control data. This leads to a large signal differential between the arteries and background tissue, and mitigates against partial volume effects. This high angiographic contrast allows smaller calibre and lower contrast arteries to be visualized. Also, as discussed in Chapter 3, **signal is not seen in normal cerebral veins under normal conditions**, preventing these structures from obscuring small arteries. The high specificity of venous ASL signal for shunting also allows detection of shunting lesions and delineation of their venous drainage pattern on ASL angiography, without obscuration by overlying tissue signal or normal venous structures.

Any of the three labelling strategies discussed above can be used for ASL angiography[92, 134, 136, 139]. In addition, vessel-selective labelling or vessel-encoded labelling schemes can be used to obtain selective angiographic images of individual arteries, similar to DSA (these techniques will be discussed in section 4.4.9)[135, 137, 140].

Static angiographic images can be obtained using PASL techniques where the inversion time is selected to capture labelled blood within arteries in the imaging plane[134]. With PCASL, a longer labelling duration is required than for angiography than perfusion, in order to fill the arterial tree with labelled blood[139].

ASL can also be used for dynamic angiography, which is referred to by variable terms including time-resolved ASL-based dynamic MRA and 4D ASL MRA[135, 138-142]. These time-resolved ASL angiographic sequences use *Look-Locker cine readouts*, which allow visualization of the passage of labelled blood within arteries at very high temporal resolution. Unlike other angiographic methods, the temporal resolution is virtually only limited by the *repetition time* (TR) of acquiring one cine frame (5 - 10 ms)[138]. This would make acquisition time prohibitively long if a conventional Look-Locker readout is used (where a single line of k-space is acquired after each excitation pulse in the cine readout). Instead, a *segmented Look-Locker* readout is used, where TRs are binned together to resemble one time sample (dwell time) during which several lines of k-space are acquired before advancing to the next time point of the angiogram[138]. Low flip angles are used with Look-Locker

sampling to ensure that images are PD-weighted, to minimize any added contrast from the cine readout.

Fast gradient-echo sequences, including *balanced steady-state free precession* (bSSFP) and 3D *spoiled gradient-echo* (SPGR), are used for Look-Locker readouts[135, 136, 139, 141, 142]. A limitation is that the low flip angle and saturation effects result in reduced SNR. Higher SNR can be achieved by using bSSFP techniques, which are also suited to angiography because they are inherently flow-compensated and associated with high signal intensity of blood. A dynamic ASL angiographic sequence that uses a bSSFP sequence is *true fast imaging with steady-state precession (FISP)-based spin tagging with alternating radiofrequency* (TrueSTAR)[142]. In a study that compared TrueStar against a standard Look-Locker EPI sequence, found that its SNR and CNR were 29% and 39% higher respectively. The TrueSTAR implementation in this study had a temporal resolution of 83 ms, which was only slightly lower than that of the Look-Locker EPI sequence[142]. Its in-plane spatial resolution of 1 mm^2 is, however, inferior to that of DSA and the through-plane resolution of 2 to 3 mm is inferior to even that of time-resolved CE-MRA. A limitation of bSSFP sequences is that they are sensitive to *off-resonance effects* with signal loss in regions of magnetic field inhomogeneity.

As with static ASL angiographic techniques, an advantage of time-resolved ASL angiography over alternative dynamic angiographic techniques (4D CTA, DSA, and TR CEMRA) is the **high specificity of venous ASL signal for arteriovenous shunting**[143, 144]. High signal is therefore only seen in venous structures into which labelled arterial blood is either directly shunted or flows subsequently. The absence of high signal in normal veins prevents these structures from obscuring feeding arteries and small draining veins.

Therefore, combined with the very high temporal resolution and higher spatial resolution (compared to ASL perfusion and TR CE-MRA), time-resolved ASL angiography has the potential to allow the arterial feeders and venous drainage pattern of AVMs and DAVFs to be delineated with high accuracy. One small study has evaluated a dynamic ASL angiographic sequence for characterization of DAVFs[141]. The temporal resolution of the sequence was 300ms, which is comparable to DSA, however its spatial resolution (0.5 x 0.5 x 0.6 mm^3) was lower. The fistula site and draining veins were accurately delineated. The major limitation of this sequences was the long acquisition time of 8 minutes 20 seconds.

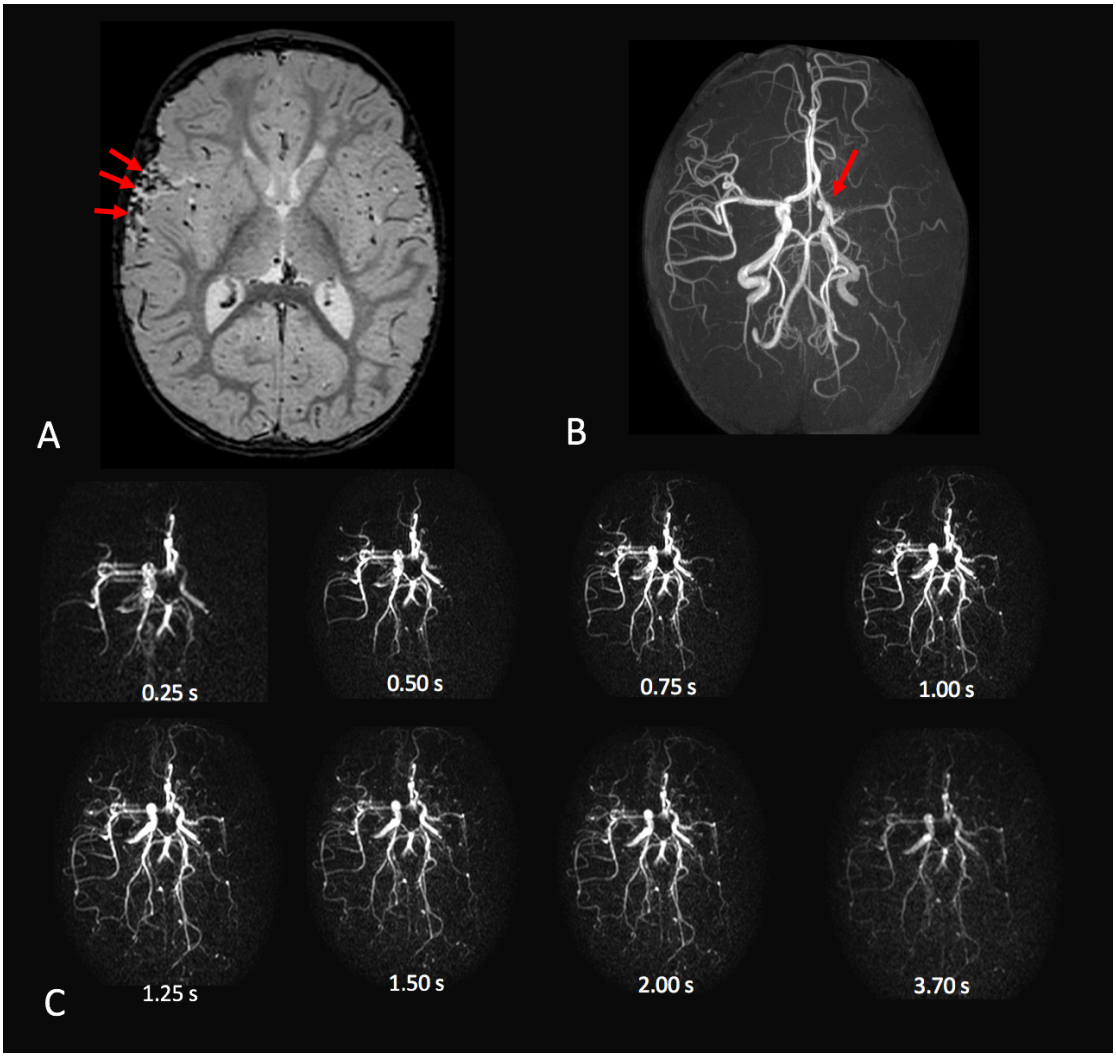

Figure 4-17. *Images from an 18 month-old with developmental delay.* ***A.*** *axial T_2-weighted image showing prominent flow voids due to dilated leptomeningeal vessels in the right Sylvian fissure, which raised suspicion for a shunting lesion such a DAVF.* ***B.*** *TOF MRA maximum-intensity projection shows no evidence of a high-flow vascular lesion, however there is chronic occlusion of the left ICA (arrow).* ***C.*** *Dynamic ASL MRA, using a FAIR inversion technique (pulsed labelling) with look-Locker sampling. High temporal resolution (250 ms) was achieved with this sequence, allowing visualization of progressive flow of labelled blood into the more distal arterial branches. No venous ASL signal is seen to indicate shunting. Left LCA occlusion is confirmed. Labelled blood is not seen within the abnormal leptomeningeal vessels to indicate that these are dilated leptomeningeal collateral arteries. They are therefore suspected to be abnormal veins resulting from either chronic hypoxia or a proliferative vasculopathy. The value of ASL angiography is shown in this example. Although spatial resolution is considerably lower than that of DSA, the lack of venous ASL signal allows exclusion of a high-flow shunting lesion without the requirement for a DSA. Since it is still possible that the patient has a low-flow shunt, a definitive DSA will be performed. Contrast-enhanced MRA (and therefore the need for cannulation of this child) was avoided.*

Nonetheless, it is now available on clinical MR units (including at my institution) and combines *flow-sensitive alternative inversion-recovery* (FAIR) ASL with a 3D segmented T_1-weighted *turbo field-echo Look-Locker* readout[141]. By using Look-Locker sampling with multiple inversion times after each 180° pulse, time resolved angiographic images are obtained. An example of time-resolved angiographic images obtained using this technique is shown in Figure 4-17. Spatial resolution and long acquisition times are the main limitation of dynamic ASL angiography.

4.5.9 Region-Selective ASL

Region-selective ASL (rsASL), also known as *region-specific* and *flow-territory mapping ASL*, is a technique that enables mapping of individual brain vascular territories[145-150]. Selective angiographic images can be obtained using this technique, analogous to DSA, where an individual artery and its branches can be visualized and assessed individually[135, 140, 148]; this has been variably termed vessel-encoded magnetic resonance angiography, vessel-encoded ASL angiography and vessel-selective digital subtraction MR angiography. The tissue supplied can also be visualized, allowing delineation of the perfusion territory of an individual artery (vascular territory mapping)[145, 147, 149, 150]. The perfusion within a vascular territory can be quantified, and the borders of this territory can be assessed at tissue level using rsASL unlike with DSA[145].

The ability to non-invasively visualize the perfusion territory of individual arteries can be of clinical utility. Population averaged templates of the vascular territories are used in clinical practice. However, there is large inter-individual variability in the perfusion territory of each major brain artery[151]. Mapping of the territory supplied by a given artery in the individual patients can be useful for identifying the aetiology of AIS. For example, in a patient with recurrent embolic events, it may be uncertain as to whether these events are within a single vascular territory therefore likely related to arterio-arterial embolization from a particular artery. By imaging the territory perfused by this artery, the likelihood that it is the culprit can be determined. Flow territory mapping has also been shown to be valuable for classification of cortical and borderzone infarcts[152]. In conjunction with MRA, selective ASL provides temporal information on collaterals that is comparable to DSA in patients with steno-occlusive disease[153]. rsASL angiographic and perfusion techniques may also be used to characterize AVMs and DAVFs for the purposes of treatment planning and guiding endovascular therapy, as discussed previously.

There are two different approaches to implementing rsASL: **1. single-vessel rsASL** and **2. multi-vessel rsASL**. These are considered separately.

4.5.9.1 Single-Vessel rsASL

Also called *vascular territory imaging* (VTI), labelling is limited to a single artery or group of arteries with single-vessel rsASL; subsequent imaging allows visualization of the vascular territory of this individual artery[146, 150, 154]. Single vessel rsASL can be performed sequentially for two or more vascular territories to obtain a complete map of cerebral perfusion or the arterial supply of a target lesion. Early rsASL methods were difficult to implement in clinical practice due to the advanced hardware requirement and the need for cumbersome planning to limit the labelling to a single artery[149, 150].

Labelling of a single artery or group of arteries can be achieved using one of three types of strategies: 1. by limiting the spatial RF distribution of the transmit coils; 2. using spatially selective RF pulses; or 3. applying rotating gradients. Spatially restricted labelling can be achieved using a separate local transmit coil positioned over the artery in the neck[155]. This strategy is confined to the research arena due to the requirement for specialist hardware and cumbersome set-up procedure that prevents adoption in the busy clinical setting.

A dedicated MR pulse sequence design can be used instead of hardware to limit or control the spatial distribution of RF to a particular region. The simplest approach is to perform pulsed ASL with the labelling slab angled and translated spatially, such that only a single artery is labelled. This technique has been described for selective labelling in the circle of Willis[150]. It can be adapted from a regular PASL sequence by changing the direction of the slice-selection gradient of the labelling slab and the frequency of the RF pulse. However, the positioning of the labelling plane to limit inversion to a single artery can be challenging. It requires careful planning, taking into consideration the anatomy of the target artery as well as neighbouring vessels. This is due to the fact that the labelling plane is only really spatially restricted in one direction, with coverage in the other two directions governed by the spatial extent of the transmit coil. Limitations of this technique include intersection of the labelling plane with the imaging plane, and difference in MT effects between the label and control conditions. It is also inefficient for mapping more than one vascular territory, since the sequence (including the control condition) has to be repeated for each vessel.

Efficiency can be improved by using a cycling scheme for labelling using spatially-selective RF pulses[156]. Although multiple vessels are labelled simultaneously, this is not classified as a multi-vessel rsASL technique, since the labelling efficiency is not spatially varied. Here, the bilateral ICAs are labelled in one acquisition, followed by a second acquisition where the left ICA and posterior circulation are labelled, a third acquisition where the right ICA and posterior circulation are labelled, and a fourth acquisition which is the global control condition (Figure 4-18). This process is repeated for signal averaging to improve SNR. Post-processing of the acquisitions, where the four phases are combined (further improving SNR) according to a decoding scheme, allows the perfusion territory of each individual vessel to be resolved. Unfortunately, labelling precisely the same part of a particular vessel for each acquisition can be difficult with the spatial cycling, and can lead to subtraction errors that can be mistaken for collateral flow.

The third strategy for achieving selective vessel labelling is the use of rotating gradients to restrict flow-driven adiabatic inversion over time to a single location. This can be implemented with continuous or pseudo-continuous labelling strategies. Gradient rotation is achieved by changing the gradient strength over time in the x and y directions. These added in-plane gradients rotate around the vessel of interest[146]. The magnetization added by these gradients is zero at the target vessel, but changes in other locations, throughout the labelling duration. The result is that a small 3D volume cantered upon the target vessel is labelled[146]. Modulating the amplitude of the rotating gradient helps prevent labelling outside the target region[146]. This technique does not require careful planning, and knowledge of vascular anatomy is only required over the short segment in the labelling plane. SNR is also higher because of the longer labelling duration achieved with PCASL. Labelling of arteries distal to the circle of Willis is possible using this technique. A limitation that arises from labelling a small volume is motion sensitivity; even mild motion can decrease labelling efficiency. Dynamic vessel-selective ASL angiographic images can also be obtained using rotating gradients for vessel-selective labelling[140]. This technique, which has been referred to as ASL digital-subtraction MR angiography, yields time-resolved vessel-specific information, analogous to DSA. Pseudo-continuous labelling is used, with vessel-selective labelling achieved by rotating the directions of added amplitude modulated in-plane gradients as described above. A balanced steady-state free precession sequence was used for readout. Background suppression was maintained using hard 180^{o} flip angle refocusing pulses. Whole-brain coverage is achieved with a temporal resolution of 200 ms, which is comparable to that of DSA, albeit with lower spatial resolution.

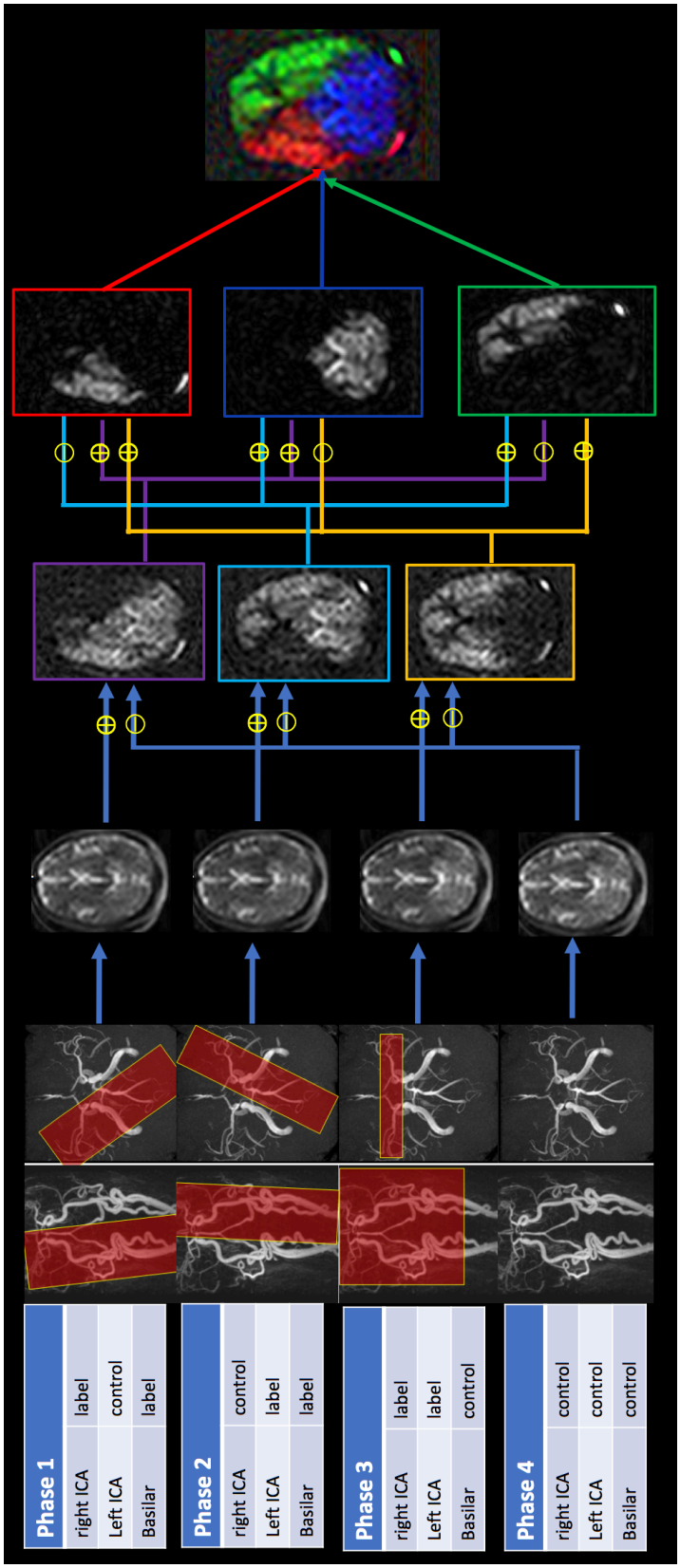

Figure 4-18. *Region-selective ASL performed using a cycling scheme for pulsed labelling. Spatially-selective RF pulses are used to label two vessels simultaneously at a time. The labelling slab is varied in four phases, which vary the label and control condition of the three main cerebral arteries: the right ICA, left ICA and the basilar artery. The four phases are then combined according to a decoding scheme to determine the flow territories of the right ICA (red), left ICA (green) and basilar artery (blue).*

4.5.9.2 Multi-vessel rsASL

Multi-vessel rsASL, also called vessel-encoded ASL, is more time-efficient since it allows simultaneous mapping of multiple vascular territories. Here, combinations of vessels are labelled using encoding schemes where the labelling efficiency is varied in different spatial patterns and frequencies[147, 149, 157]. This is achieved by spatially varying gradient strength and additional phase changes to the RF pulses of a PCASL sequence. Post-processing is then used, specifically *clustering algorithms* (an image processing technique), to decode the contribution of individual vessels to signal[149, 157]. The underpinning concept is that all voxels that are supplied by the same artery will behave similarly with the different labelling configurations. This allows generation of individual vascular territory maps. Multiple, sufficiently different, spatially variant labelling configurations must be used to allow separation of the flow territories of vessels that are located close to each other. Through the use of clustering algorithms, the requirement for time-consuming planning to select an appropriate labelling plane is eliminated; the term **planning free flow territory mapping** is therefore used to describe this method. Perfusion of all major vascular territories of the brain can be mapped in under 5 minutes, and this technique has been shown to be reproducible, making it suitable for clinical use[147]. Unfortunately, erroneous results may be produced, for example when arteries are inadequately spatially separated within the labelling area.

A similar method can be implemented with supervision, to separately encode the contribution of multiple vessels to the MR signal[147]. Again, differential encoding is achieved by spatially varying the labelling efficiency in different patterns according to an encoding schedule. Instead of using a clustering algorithm, the operator plans the multiple configurations of spatial variations in labelling efficiency. As with the unsupervised approach, the PCASL sequence is modified: a single labelling gradient waveform is applied in the flow direction, with a non-zero mean for both the control and label conditions; additional gradients are applied perpendicular to this labelling gradient to generate phase shifts between the target vessels; and RF phase modulation across pulses is used to place the target vessels in control and labelling conditions according to the encoding scheme[147]. Individual vascular perfusion territory maps can then be generated by pseudoinversion of the encoding matrix. This vessel-encoded ASL method allows simultaneous imaging of the perfusion of two or more vascular territories, with SNR close to that of conventional PCASL images[147].

The same vessel encoding PCASL technique can also be used for dynamic vessel selective ASL angiography[135]. In one implementation, a 2D thick-slab flow-compensated fast low angle shot readout module was combined with a Look-locker sampling strategy[135]. A Bayesian inference method was used to reconstruct the selective angiograms of individual vessels. High temporal resolution (55 ms) was achieved. Selective dynamic angiograms of each internal carotid artery and vertebral artery reconstructed using this technique were found to match well with TOF-MRA[135]. Limitations include the long acquisition time (approximately 10 minutes), which is an impediment to clinical implementation, poor spatial resolution (thick 5-10 cm slabs were used), motion sensitivity and incomplete suppression of static tissue signal. Poor signal due to significant T_1-decay in the presence of steno-occlusive disease causing delayed arterial transit is a limitation inherent to ASL (as discussed previously).

4.6 Automation

Fast analysis of imaging is crucial for clinical decision making, especially in the setting of time-critical conditions such as acute ischemic stroke[158]. Automated tools can be used to rapidly process and analyse complex imaging data and produce output images and quantitative data that can be used for diagnosis and treatment decision-making. They can also be used to identify and quantify abnormalities and aide interpretation, potentially improving diagnostic performance and confidence. Additionally, automation can improve workflow related to imaging. As such, these automated tools can expedite diagnosis and treatment.

4.6.1 Post-Processing of CT and DSC Perfusion Data in AIS

It can be seen from the discussion in sections 2.4.2 and 2.4.3 of this chapter that analysis of bolus perfusion data is complex. Specialist software is used to perform the complex computation that is required to obtain the perfusion parameters from raw perfusion data. Many of these software programs require some manual input, for example the sending of raw data to a processing unit for computation and selection of appropriate arterial input and venous output functions. While these tasks may appear simple, they can potentially introduce delay, error, and variability. They also require the operator to be trained and experienced. This, in turn, is an obstacle to clinical implementation of these perfusion techniques, especially in smaller hospitals that lack the resources, appropriately trained staff, and training opportunities.

Fully automated perfusion post-processing is therefore now widely used in AIS. Here, all steps between the acquisition of perfusion data and image interpretation are automated. This enables standardized and reproducible computation of perfusion parameters from raw perfusion data for objective quantification. The likelihood of errors, delay, and variability related to manual post-processing are reduced. By eliminating the requirement for specially trained staff, automation also facilitates the clinical implementation of CTP and DSC-PWI outside research centres. Further, it improves workflow efficiency by eliminating operator input for steps, such as the sending of raw perfusion data to a processing unit and AIF selection. This saves time and expedites the availability of perfusion maps for diagnosis.

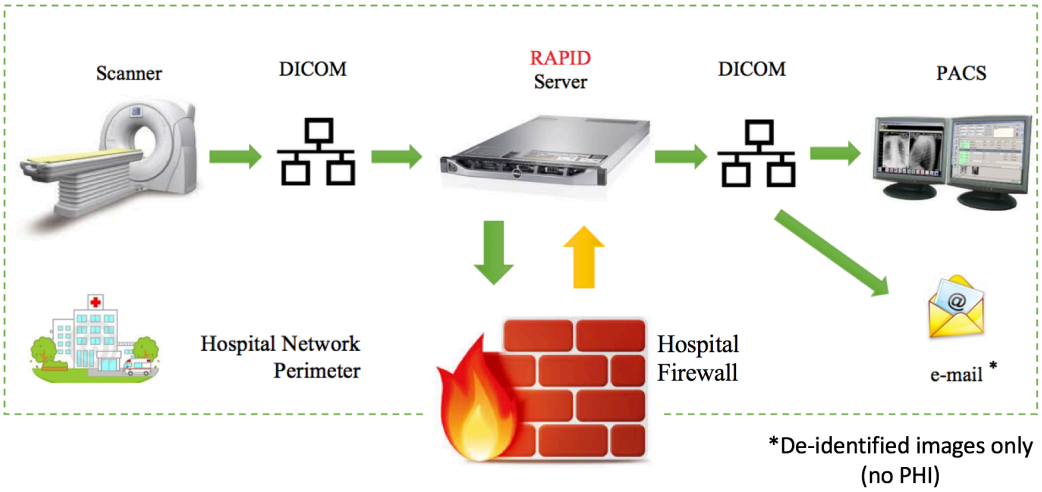

Figure 4-19. Example of a fully automated perfusion post-processing pipeline that is designed for use in stroke patients. PHI = Protected Health Information; DICOM = Digital imaging and Communications in Medicine and PACS = Picture Archiving and Communication System.

An example of a fully automated, operator independent perfusion processing pipeline is shown in Figure 4-19. This software algorithm, details of which have been previously published, can be used to process both CTP and DSC-PWI data[159]. Raw perfusion data are sent automatically from the scanner to a processing unit or server; for MRI, DWI data are also sent. The data are 3D motion-corrected by the algorithm. DWI and DSC-PWI data are then co-registered in the case of MRI. For CT, bone subtraction is performed using the averaged unenhanced baseline CTP frames. CTP and DSC-PWI data are then processed using a delay-insensitive deconvolution algorithm[159]. The AIF selection is automated based on criteria, such as an early rise, narrow width and large area under the curve[20, 159]. Perfusion

parameters (CBF, Tmax, MTT, and CBV) are calculated for each voxel. Normalization is performed by dividing the CBF within the voxel by the median CBF of the patient's normally perfused brain tissue, as defined by voxels with Tmax ≤4 seconds. Normalization of CBV is performed similarly. The parametric maps (rCBF, rCBV, Tmax, and MTT) are generated in grey-scale and colour. They are automatically sent to the picture archiving and retrieval system (PACS) as well as via email, ready for clinical use. Although these steps are fully automated, a user interface is available for any manual adjustments (such as removal of severely motion degraded data) that are deemed to be necessary by the operator.

4.6.1.1 Segmentation of the Infarct Core and Tissue At-Risk

In addition to post-processing of raw perfusion data to obtain perfusion maps, most automated software platforms used in AIS also automate segmentation of the infarct core and tissue-at risk as well as mismatch analysis. The volume of the infarct core, tissue at-risk and ischemic penumbra of potentially salvageable tissue are therefore objectively quantified.

Automated segmentation of the infarct core on MRI is achieved by applying an ADC threshold to DWI data. The software platform discussed above and shown in Figure 4-19 segments the infarct core using an ADC threshold of $620x10^{-6}$ mm^2/sec, with all voxels with an ADC below this value included in the infarct core segmentation mask. Automated segmentation of the infarct core on CTP is typically performed using CBF, CBV, rCBF, or rCBV, since these parameters have been found to be best for predicting infarcted tissue as previously discussed. The optimal perfusion parameter and threshold depend on the specific post-processing algorithm. For the algorithm discussed above, rCBF is used, with a threshold of 0.30 applied; all voxels falling below this threshold are segmented as the infarct core. Given that reduced rCBF is not specific for infarction and can occur in areas of chronic white matter ischemia, segmentation of the infarct core is constrained to voxels within the area of severe hypoperfusion (with Tmax >5.5 seconds), where tissue is at risk of undergoing infarction.

Detection and quantification of the ischemic penumbra of tissue that can be salvaged by reperfusion is also automated. First, the area of tissue that is critically hypoperfused, therefore at risk of infarction, is segmented using time-based parameters (MTT, Tmax, or TTP). *MTT can only be used to predict tissue at-*

risk tissue when a delay-sensitive deconvolution algorithm is used. As discussed in section 4.4, the "MTT" obtained using delay-sensitive SVD reflects both true MTT and Tmax (Figure 4-20A and B). The software platform discussed above uses a delay-insensitive deconvolution method. Therefore, Tmax is used to segment tissue at risk. A threshold of Tmax >6 seconds is applied to both CTP and DSC-PWI, since this has been established as optimal for predicting tissue that is destined to undergo infarction without reperfusion using this particular software[160]. The segmentation masks for the infarct core and tissue at-risk are then either superimposed upon each other or displayed or next to each other (the output of two different software platforms is shown in Figure 4-20C and D). The penumbral volume is displayed as a **mismatch volume** (difference between volume of infarct core and at-risk tissue) and quantified as a **mismatch ratio**. Objective information about the presence/absence and volume of salvageable brain tissue, and therefore the likelihood of benefit from reperfusion, is therefore provided. As such, tools which automate mismatch analysis serve as decision support tools to aide diagnosis and guide treatment.

Some of the high-profile thrombectomy trials used the fully automated perfusion post-processing software described above to determine the infarct core and penumbral volumes and to perform mismatch analysis[33, 34, 36, 37]. Triage decisions were then made based on the software's results. Automation is also of value in clinical practice[161]. It allows objective quantification. In the absence of fully automated software, infarct core and penumbra estimates are based on subjective, qualitative assessment. The *Alberta Stroke Program Early CT Score* (ASPECTS), which was developed for estimation of the size of the infarct core on *non-enhanced CT* (NECT), has been extrapolated to CTP[162, 163]. This approach is only semi-quantitative and remains subjective. One study compared a qualitative approach (using NECT-ASPECTS, CBF-ASPECTS, CTA collateral score, and a CTA clot burden score) against infarct core and penumbral volume obtained using a fully automated post-processing tool[161]. Diagnostic performance of the automated tool was found to be superior to that of the qualitative approach for prediction of a favourable clinical outcome, as well as estimation of final infarct volume.

In addition to improving diagnostic performance, automation is also faster, less operator dependent and improves workflow efficiency. Some of the automated software platforms used in AIS have additional in-built functions, such as direct notification via email. The latter can be utilized to expedite the availability of images and perfusion information for diagnosis and clinical decision making for many years.

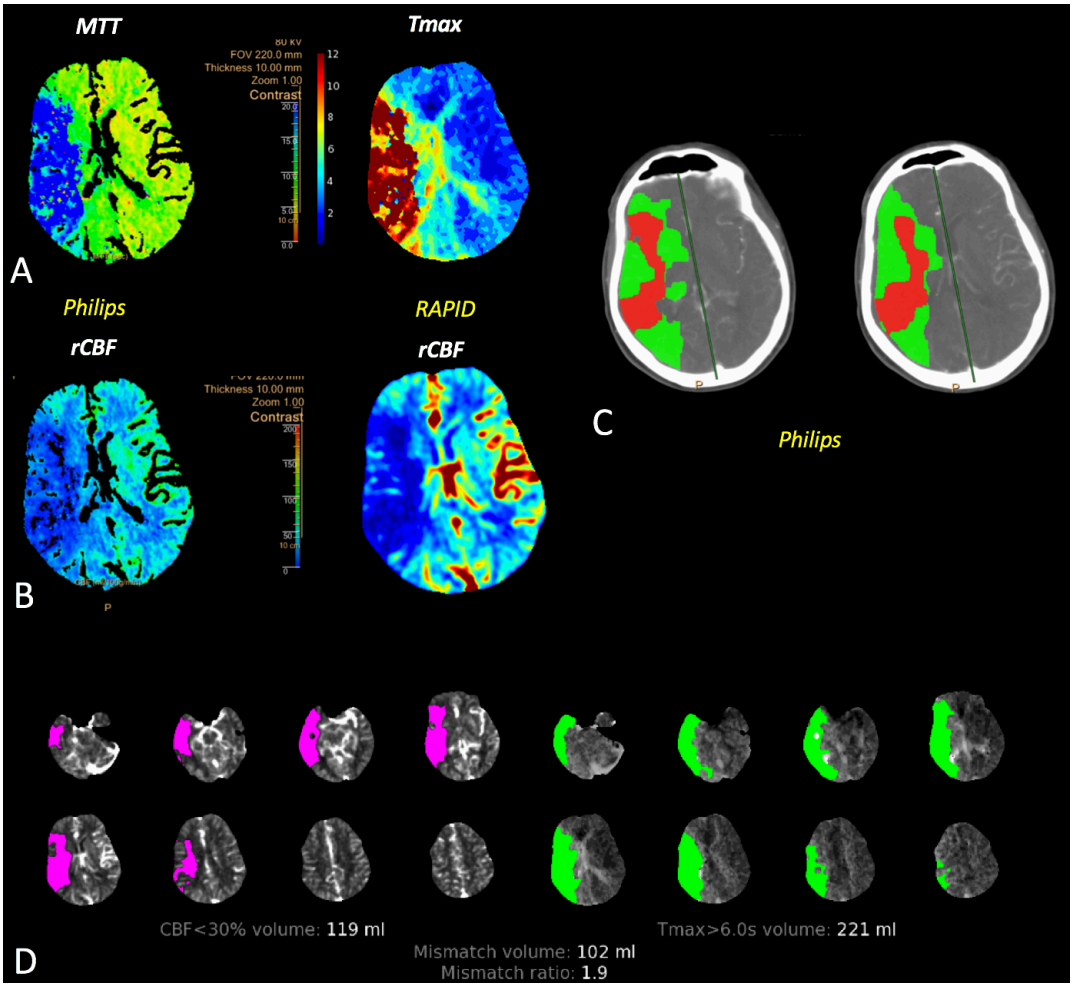

Figure 4-20. *CTP in a 60 year-old man with an acute right MCA occlusion. Perfusion post-processing, tissue segmentation, and mismatch analysis were performed using two different software packages: Philips Brain CT Perfusion Package (Philips Healthcare, the Netherlands) and RAPID 4.6.1 (iSchemaView Inc, Menlo Park, CA).* ***A.*** *The MTT obtained using the Philips software, which uses a delay-sensitive deconvolution algorithm, shows the same area of critical hypoperfusion as the Tmax map obtained using RAPID, which uses delay-insensitive deconvolution. The MTT obtained using delay-sensitive deconvolution is not true tissue capillary transit time, but a composite of capillary transit and Tmax.* ***B.*** *The rCBF maps obtained using the two different algorithms.* ***C.*** *Two representative images of mismatch analysis performed using the Philips software, where the infarct core (red) is overlaid on the area if critical hypoperfusion. The Philips software segmented the infarct core based on absolute CBV reduction to <2.0 mL/100 mL, while critical hypoperfusion was segmented using MTT >145% of contralateral MTT. Volumes are not computed.* ***D.*** *Mismatch analysis performed using RAPID. The infarct core is segmented using rCBF <30% of that in normal tissue, while critical hypoperfusion is segmented using Tmax >6 seconds.*

These tools can also be used to notify and mobilize the stroke team and interventional neuroradiologist, which may in turn lead to faster reperfusion; although there are no specific studies that have evaluated the impact of automation

on workflow efficiency to determine whether these tools truly improve patient outcomes, it is likely that their use leads to more rapid patient triage and treatment.

Automated software tools are particularly valuable in the setting of primary stroke centres and smaller metropolitan and regional hospitals. The technologist staff at such small volume centres may have limited experience with CTP processing, therefore automation of steps, such as AIF selection, decreases the potential for error. These centres also often lack around-the clock-expertise in CTP interpretation, and automation can be a valuable diagnostic aide to radiologists and general neurologists who have limited experience with this test.

Automated perfusion post-processing does, however, have limitations and pitfalls. An important limitation, that has been discussed in section 4.4 of this chapter, is that there is considerable variability between different post-processing algorithms. It is important that radiologists and stroke physicians are cognizant of this, and know the optimal parameter and corresponding threshold for predicting infarction and tissue at-risk that is specific to the particular software algorithm that they are using.

Other pitfalls of automation include incorrect calculation of perfusion parameters, resulting in either spurious perfusion abnormalities or the masking of true pathology. The major culprit is patient motion, which can result in spatial misregistration of perfusion data obtained at different time-points and incorrect AIF selection (for example, in bone with through-plane motion). Although automated software has built-in motion correction mechanisms, including exclusion of severely motion degraded time points in an acquisition, these do not always work perfectly. Other sources of error in segmentation of the infarct core on CTP include reperfusion, old infarcts and leukoaraiosis[75]. Some automated software platforms automatically mask out chronic infarcts, based on the low density of tissue voxels on the baseline pre-contrast images of the CT acquisition. The effects of leukoaraiosis are partially mitigated by constraining infarct core segmentation to the critically hypoperfused region. Reperfusion results in underestimation of the infarct core; reperfused tissue no longer has reduced rCBF, which is the criterion for automated detection (Figure 4-21). Errors in segmentation of tissue at-risk can also occur, due to old infarcts and chronic steno-occlusive disease, which result in prolonged Tmax. It is therefore important that radiologists and neurologists interpreting perfusion studies are cognizant of these sources of error. They must be able to recognize the manifestations of significant motion on

perfusion maps, and exercise caution in interpreting motion degraded studies and question perfusion abnormalities that do not conform to the vascular territory expected based on clinical presentation. To avoid missing areas of infarction that are reperfused, NECT images should always be carefully scrutinized for signs of early infarction (Figure 4-21B). Hyperperfusion on rCBV and rCBF maps is also a clue that can indicate reperfusion (Figure 4-21C). It is also important that we acquire and maintain the skills, knowledge, and preparedness to trouble-shoot and re-process the CTP raw data if required.

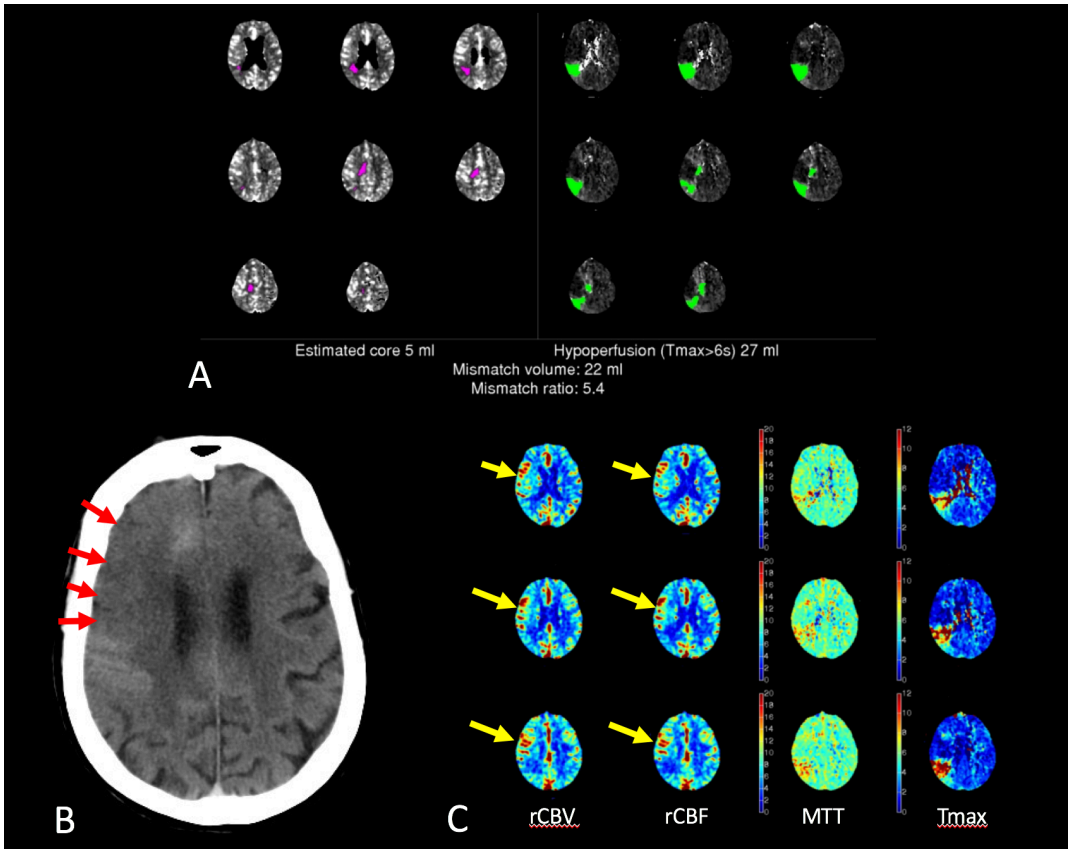

Figure 4-21. *Multimodal stroke CT, including CTP in a 62 year-old man transferred to a hub hospital post thrombolysis at spoke hospital to hub.* ***A.*** *Only a small infarct core is estimated, based on severely reduced rCBF with two areas of critical hypoperfusion corresponding to right MCA M3 segment and right ACA A4 segment occlusions. This patient had a right terminal ICA occlusion on imaging previously performed at the spoke hospital. The findings on the repeat imaging indicating recanalization of the right ICA fragmentation and distal embolization of this clot following thrombolysis. If automated segmentation of the infarct core on CTP using reduced rCBF were relied upon, the infarct would be underestimated due to reperfusion.* ***B.*** *NECT shows established infarction with cortical hypodensity and loss of grey-white matter differentiation in a reperfused area (arrows). The subtle high density posterior to this and in the medial right frontal lobe is due to contrast staining of infarcted tissue, indicating blood-brain barrier breakdown.* ***C.*** *Scrutiny of the rCBF and rCBV maps also reveal hyperperfusion (arrows) in the reperfused infarct, due to luxury perfusion.*

4.6.2 Automated Post-Processing of ASL Perfusion

Obtaining CBF maps from ASL perfusion is also complex. Fully automated post-processing is therefore used in order to facilitate clinical implementation of the technique[84]. This post-processing involves several steps, including motion correction, subtraction of label from control images (to obtain perfusion-weighted signal intensity images), segmentation of the anatomic *proton-density-weighted* (PDw) image and voxel-wise computation of absolute CBF. The calculation of absolute CBF requires the signal in ASL difference images to be scaled by the mean signal intensity, M_0, of arterial blood. Since this value is difficult to determine, the mean signal intensity of white matter is used instead. This is obtained from the PDw images, which are segmented by the automated software. Typically, the output of ASL post-processing software consists of grey-scale and colour absolute CBF maps. ASL multi-delay techniques require more complex post-processing. Again, this can be automated for generation of both CBF and ATT maps.

4.6.3 Machine Learning and Deep Learning

Artificial intelligence refers to a computer method that is used to perform tasks that would otherwise require human intelligence. These methods can be **deterministic**, where a certain *set of rules or logic is applied*, akin to a flow-chart. Alternatively, they may involve **machine learning**, which involves the development of *algorithms that allow the computer to learn (without programming input)* from existing data[164]. Classification algorithms such as *clustering*, *logistic regression*, *random forest*, and *support vector machines (a.k.a. SVMs)* are all examples of machine learning[164]. These machine learning approaches can be further subdivided into **supervised** and **unsupervised learning**[164]. *Supervised learning* is characterized by the *use of a reference standard to train algorithms.* Conversely, *no such ground truth exists with unsupervised learning*, where the computer determines the classes on its own[164]. Clustering, where images are categorized based on similarity metrics without a priori knowledge, is an example of unsupervised learning which is used to decode the signal in single vessels with multi-vessel rsASL[165].

Deep learning is a form of machine learning that uses neural networks[166]. It shows promise for imaging applications and is being increasingly adapted to medical imaging. The application of deep learning to imaging data has been

recently galvanized by convergence of advances in computer hardware (the development of *graphic processing units* (GPUs) with sufficient computational power), theoretical advances in the organization of the algorithm, and software companies making network training algorithms freely available[167]. The strength of deep learning techniques is that they can automatically extract relevant features. Therefore, an image classifier for example can be created from a labelled dataset in days. Combined with the widespread use of PACS systems in radiology departments, natural language processing of radiologist and medical records and an increasing availability of large-scale datasets in a format that can be used to train these networks, there is enormous potential for applying deep learning to medical imaging. Acute stroke imaging, with the high volume and rich multimodal imaging information, lends itself well to deep learning.

The neural networks used for deep learning are inspired by, and loosely modelled on the structure of neurons in the brain, mimicking axons and dendritic interconnections[166]. They consist of input and output layers, with intervening hidden layers that represent interneurons. The network architecture refers to how deep (i.e., how many layers the network has) and wide (number of neurons per layer) it is, and varies depending upon the application[164]. Each connection between individual neurons represents a weight, which reflects the strength of connection. Even a shallow network may have the order of 100,000 weights to learn, hence the necessity for large sets of data to determine these weights. The desired outcomes, or labelled states, are encoded in the final layer; therefore, if there are two potential outcomes, for example "LVO" or "no LVO", there will be two neurons in the final layer, and the value stored by each neuron is the probability that the image corresponds to a specific class. The purpose of training the network is to optimize the weights that connect the neurons in different layers for the specific task, so that when a new image is entered at the input, the probabilities measured at the output are heavily skewed to the correct class; for example, if the input into the network is an image with an MCA occlusion, the model output should be a high probability of an LVO.

Different data, although with similar features in group, is used for training, validation and testing of the network. Here, the largest fraction of data (50-60%) used for training and the smallest for validation (10-20%). Training data is placed through the network repeatedly and the output is compared against the ground truth via a **cost function**, which is a single function that quantifies divergence or goodness of fit. Common cost functions that are used for image prediction tasks are measures of similarity (e.g., structural similarity index metric) and the root

mean square of the difference between the reference and predicted images[164, 168]. The **weights** (strength of connection between neurons) are then adjusted based on the cost function in a process known as **back-propagation**. The procedure is repeated with multiple training data (**batches**) and iterations (**epochs**). Subsequently, a test dataset, that has not been used for training, is used to assess the accuracy of the model. The error rate here is similar to or higher than with the training data.

For imaging tasks, input into a deep learning algorithm can consist of an individual image or entire series of images, including from different modalities. Because a very large number of weights is required for images of typical matrix size, *fully connected neural networks (where every voxel is connected with the entire network) are computationally intensive.* More computationally effective *convolutional neural networks* (CNNs) are therefore used for imaging applications; instead of fully connecting layers, a *small "kernel" of weights is applied at each image position.* This kernel is then rastered across the image to obtain the next layer. This process is akin to convolution filter in image processing (hence convolutional neural network). Multiple different kernels can be trained for each layer, enabling the network to learn multiple different features, such as textures and edge. These representations of the image data are location invariant. The CNN can pool adjacent voxels or slide the kernel across the images at spaced intervals to incorporate larger features into the hidden layers. Finally, for classification, at least one fully connected layer is added to reach the final output layer.

For supervised machine learning, annotated input data is required to serve as the reference standard. Annotation of data can involve either flagging the image as abnormal/containing a specific lesion, or manual outlining of the lesion. Radiology reports can also be used for annotation, since they can be searched for key findings encapsulated as free text; this task can be readily automated, since *natural language processing* (NLP) is an area where deep learning is already advanced. Manual lesion outlining is tedious and time-consuming task (the author of this dissertation has first-hand experience of this) and is often a rate limiting step for training algorithms. Effort is therefore being put into automating this task, by training a neural network to take input images and produce an output of lesions outlined as segmented masks[164]. Obtaining access to enough data is another obstacle. There is, therefore, great interest in synthetic data generation, such as with *general adversarial networks* (GANs).

4.6.3.1 Machine Learning in AIS

Machine learning, in particular deep learning, can be applied to a wide range of tasks in diagnostic imaging. These include image acquisition and optimization, workflow, lesion/pathology detection and segmentation, and differential diagnosis. Broadly, these tasks fall into the categories of image reconstruction, image classification and segmentation. These will be discussed in the context of AIS.

An application of deep learning that is potentially of high value in AIS is the automated triage and prioritization of scans for review. It has been shown that a network can be trained to identify critical findings that require urgent treatment, such as intracranial haemorrhage and positive mass effect, with excellent diagnostic performance (AUC of ROC curve >0.90)[169]. This, in turn, can potentially be leveraged to optimize workflow and expedite review of scans with these findings, by flagging them or moving them to the top of the reporting worklist. This is especially valuable in cases where the findings were not anticipated clinically, therefore the scan may not be read as a priority. One study specifically evaluated the impact on radiology workflow of a convolutional neural network that was trained to detect intracranial haemorrhage. The algorithm was implemented to re-prioritize routine outpatient CT scans on the radiology worklist in real time[170]. It was found that the algorithm had an AUC of 0.846 on ROC analysis for haemorrhage detection, and significantly reduced the median time to diagnosis of new intracranial haemorrhage (from 512 minutes to 19 minutes). It was also able to identify subtle haemorrhage that was overlooked by the radiologist.

Another application of relevance to AIS is image acquisition and improvement. For example, it can be used to reduce the radiation dose of multimodal stroke CTs by improving the quality of NECT and CTA acquired with reduced radiation dose; an algorithm can be trained with both high quality normal dose and simulated reduced dose images, allowing the network to "learn" the optimal non-linear transform between them and reduce noise in the low-dose scan[11, 164]. Deep learning can also be used to expedite MR image acquisition by transforming sequences acquired with reduced *k-space* sampling and shorter acquisition time into diagnostic quality images. For example, a deep network was able to increase the SNR of ASL CBF images acquired in 2 minutes and 30 seconds, which is approximately two minutes shorter than a standard ASL acquisition[164].

Importantly, deep learning and machine learning can be used for lesion detection and segmentation, to assist radiologists and stroke physicians interpret diagnostic

images accurately. Images can be classified according to whether or not a particular abnormality (e.g. an LVO or acute infarct) is present or absent; this is called a **classification task**. Alternatively, the algorithm can mark the abnormality or delineate the region containing the abnormality, which is referred to as an **image segmentation task**.

A classification task that is of high clinical relevance is haemorrhage detection; in AIS patients, haemorrhage exclusion prior to thrombolysis, and monitoring for development of haemorrhagic transformation are important. This is a two-part classification task, where haemorrhage is deemed either present or absent. Given the inherently poor soft tissue contrast of CT and the high incidence of artifacts, detection of small volume haemorrhage with high sensitivity and specificity on NECT is challenging, especially for less experienced readers. This is exacerbated by the push for radiation dose reduction, which reduces the SNR of images, making identification of subtle abnormalities even more difficult. Given that even highly trained experts can miss subtle life-threating haemorrhage, particularly subarachnoid haemorrhage, and lesion detection is a strength of deep learning, much effort has been invested in developing haemorrhage detection algorithms.

A number of studies have found that deep learning algorithms have excellent diagnostic performance for detecting intracranial haemorrhage on NECT[169-173]. In these studies, the interpretation of one or more experienced radiologists or neuroradiologists served as the reference standard. Some of these studies have also reported on diagnostic performance for detecting haemorrhage in specific intracranial compartments (a multi-part classification task)[169, 171, 172]. In the largest study, where 21,095 CT scans were used for training and 491 for validation, the algorithm achieved an AUC of 0.94 on ROC analysis for haemorrhage detection, with AUC >0.90 for detection of haemorrhage in each individual compartment, in the validation cohort[169]. In another study, 10,159 NECTs (12% of these had haemorrhage) were used for training and 862 for testing; a sensitivity, specificity and AUC of 0.97, 0.98, and 0.98, respectively, were found in the validation cohort and 0.95, 0.97, and 0.98, respectively, in the prospective test cohort[172]. Sensitivity was greater than 0.90 for detection of haemorrhage in each individual compartment, and poorest for subarachnoid haemorrhage (0.91 in the test cohort). Overall, accuracy was lowest for detecting small punctate haemorrhages < 0.01 mL (accuracy 0.87 to 0.88 across validation and test cohorts).

Some studies have compared the performance of deep learning algorithms with that of radiologists for haemorrhage detection. In one study, the diagnostic

performance of an algorithm trained to detect intracranial haemorrhage was found to be only slightly worse than that of an experienced radiologist (who had 100% accuracy), and better than that of junior trainees[171]. Its performance for detecting haemorrhage of different subtypes was also better than that of the average performance of the trainees, although inferior to that of the senior radiologist. Of note, the performance of the algorithm was markedly inferior to that of the senior radiologist for detecting subarachnoid haemorrhage (95% versus 69% sensitivity). In a more recent study, a deep learning algorithm, which had an AUC of 0.99 for detecting haemorrhage with a sensitivity of 100% and specificity of 90%, was found to perform better than 2 out of 4 radiologists[173]. These findings suggest that deep learning algorithms can be trained to achieve comparable accuracy to that of radiologists for haemorrhage detection, although there remain some abnormalities where the highly trained human eye performed better. Therefore, instead of replacing the experienced human, they can serve as screening and diagnostic support tools, especially for more junior readers and in contexts where resources are limited. Combined with the fast processing times, they can also improve workflow and expedite diagnosis.

The performance of deep learning algorithms is affected by the amount of data used for training, the particular architecture of the neural network as well as the degree of supervision. Strong supervision decreases the data volume required for training. For example, the haemorrhage detection algorithm that has the highest classification accuracy to date was trained with a relatively small dataset of 4396 CTs, of which 1131 had haemorrhage[173]. A strongly supervised approach, with pixel-level supervision, was adopted to train the fully convolutional neural network in this study. This approach, where each pixel is associated with a class label, is called semantic labelling or semantic segmentation. In comparison, previous studies had relied on weaker supervision, using either examination or imaging level labels or automated segmentation masks[169-172]. The optimal supervision approach depends on the classification task.

In addition to detecting the presence of a particular pathology, deep learning can also be used to localize and segment abnormalities. Examples of haemorrhage segmentation using a deep learning algorithm, for which I annotated the training data, are shown in Figure 4-22. The lesion can either be outlined or a coarse localization map can be generated with important regions in the image highlighted to produce heat-maps of the probability of abnormality; a probability threshold (e.g. 80%) is selected, such that only regions where the probability of the lesion being present exceeds this threshold are highlighted.

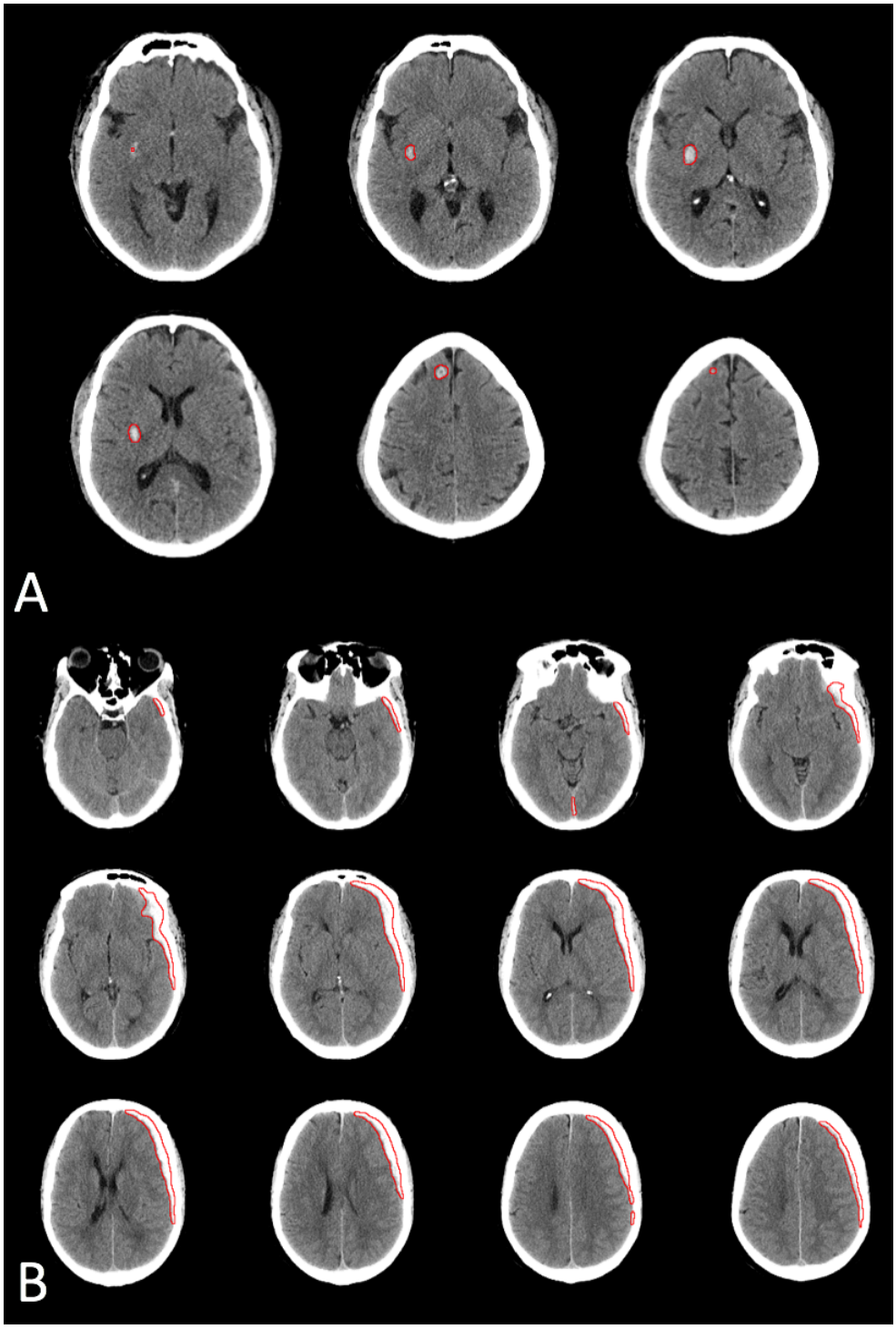

Figure 4-22. *Examples of the automated segmentation of acute haemorrhage using a deep learning algorithm.* ***A.*** *Intraparenchymal haemorrhages in the right frontal lobe and right putamen.* ***B****. Subdural haemorrhage in a different patient.*

This lesion localization can be used as a diagnostic aide for radiologists. Localization maps can also be used to try and understand how an algorithm arrives at a decision, by highlighting the areas in the image(s) that led the algorithm to

make a particular decision in a classification task[171]. The accuracy of localization and segmentation are assessed using a **dice score**, which measures the similarity between the output of the algorithm and ground truth (typically manual) segmentation; it is determined by the size of the overlap between the two segmentation masks divided by their total size. A dice score of 1 indicates complete overlap, therefore perfect agreement, while 0 indicates no overlap. In one study that evaluated quantification of intracranial haemorrhage in different compartments using a hybrid 3D/2D CNN, dice scores of 0.93, 0.86, and 0.77 were obtained for segmentation of intra-parenchymal haemorrhage, extradural/subdural haemorrhage and subarachnoid haemorrhage, respectively, compared with manual segmentation[172]. In another study, a dice score of 0.75 was achieved for localization accuracy[173]. Segmentation can also allow more accurate quantification. Quantification is important for prognostication, risk stratification and treatment planning. For example, the decision to perform decompressive craniectomy in AIS patients is dependent upon the size of the infarct or volume of haemorrhage (in cases of haemorrhagic transformation), as well as mass effect[174]. This is currently reliant upon crude estimates. More accurate quantification using deep learning algorithms may, in the future, allow better risk stratification and refinement of criteria for patient selection for decompression.

Another task that machine learning has been applied to in AIS is the detection and quantification of infarction on NECT. This is motivated by the poor sensitivity of radiologists for detecting infarcts on NECT[175]; due to the poor soft tissue contrast of CT, there is only a small difference in density between normal and infarcted tissue in the hyperacute and early acute time windows, which makes it difficult for the human eye to identify the early signs of infarction. Machine learning tools have been developed for determining the extent of acute infarction on NECT to predict ASPECT[176-181]. The technical details available on most commercial algorithms is scant. One implementation, where this information is available, uses *random forest learning* (*RFL*) instead of neural networks. RFL, a machine learning but not a deep learning method, ranks features for a classification problem, where the predictions of multiple decision trees that process feature vectors - extracted from the image input - are aggregated[182]. Strong agreement between the output of these tools and interpretation by experienced radiologists and neurologists has been shown in a number of studies[177-179, 181, 183, 184]. One study showed that an automated algorithm had substantially better agreement (κ=0.90) than two individual neuroradiologists ((κ=0.56 and κ=0.57) with the reference standard of consensus neuroradiologist interpretation[184]. The algorithm showed substantial agreement with the reference standard (κ=0.78) for detection of

infarcts in the 60 to 120 minutes time window, in which the human readers' interpretation had poor agreement ((κ=0.27 and κ = 0.36). Figure 4-23 shows an example of the automated ASPECTS output of this algorithm for which I outlined the ASPECTS regions to train the algorithm. In another study, the sensitivity of ASPECTS determined with a different machine learning algorithm was found to be 98% when compared to the reference standard of DWI[181]. The use of machine learning may, therefore, improve accuracy for detecting early infarction on NECT. These tools are also likely to improve diagnostic efficiency given the fast processing times. The next logical step after using machine learning for ASPECTS, which is known to be a poor predictor of outcome, is to determine core volume on NECT.

Other applications of machine learning in AIS include the detection of LVOs, infarct core segmentation, and prediction of final infarct volume based on baseline CTP, early DWI and DSC-PWI data[164, 185-188]. Deep learning offers an alternative to the use of ADC thresholds for segmenting the infarct core on DWI. A dice score of 0.67 was obtained using one such algorithm[186]; this performance is inferior to that of threshold-based segmentation. A deep learning algorithm for LVO detection has been described, with sensitivity greater than 90% reported in abstracts, however there is no published study to date validating this tool[187, 188]. Another recent study showed the ability to detect infarct core from CTA using deep learning[189].

Tools for predicting the final infarct volume are likely to be of value in research, aiding understanding of stroke evolution, and the assessment of the impact of different therapies.

Limitations of deep learning include its lack of transparency (exactly how a deep network arrives at a particular decision cannot be explained), the large amounts of data required, and the need for labour-intensive annotation for strongly supervised techniques[171]. The quality of training data is of importance, and obtaining large volumes of high-quality, well-annotated data can be challenging. Deep learning itself can provide the solution to some of these limitations. For example, annotation can be achieved using deep learning algorithms.

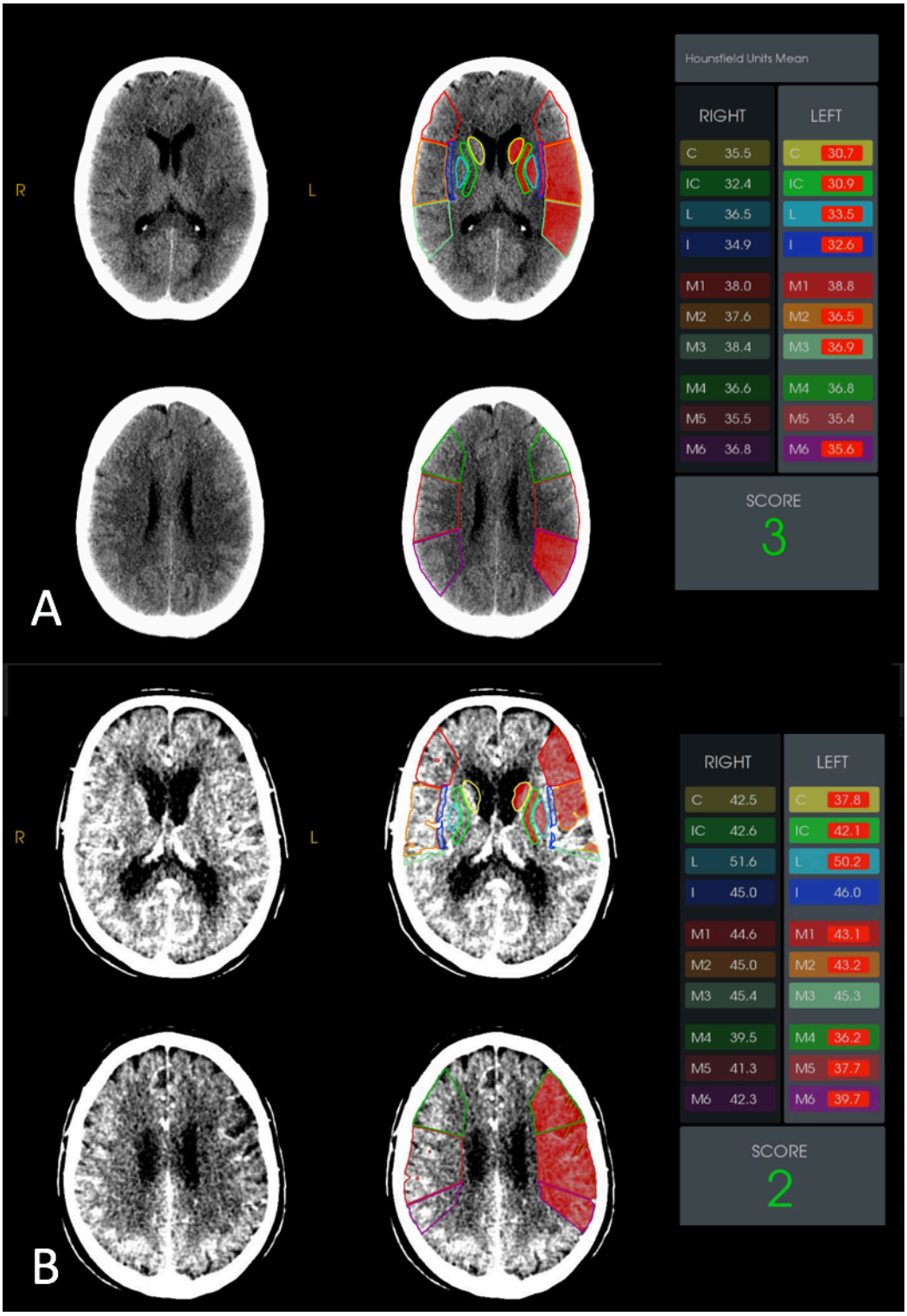

Figure 4-22 *Examples of the automated ASPECTS output of a machine learning algorithm.* ***A****. Hypodensity is identified and segmented in the caudate and lentiform nuclei, internal capsule, the insula and 3 cortical areas of the left MCA territory, leading to ASPECTS of 3.* ***B****. More subtle hypodensity is seen in these areas in a different patient with ASPECTS of 2, also with acute left MCA territory infarction. While the findings in A are easy to detect, the findings in B may be overlooked, especially by less experienced readers.*

4.7 References

1. Konstas AA, Goldmakher GV, Lee TY, Lev MH. Theoretic basis and technical implementations of ct perfusion in acute ischemic stroke, part 1: Theoretic basis. *AJNR Am J Neuroradiol*. 2009;30:662-668
2. Axel L. Cerebral blood flow determination by rapid-sequence computed tomography: Theoretical analysis. *Radiology*. 1980;137:679-686
3. Hamberg LM, Hunter GJ, Halpern EF, Hoop B, Gazelle GS, Wolf GL. Quantitative high-resolution measurement of cerebrovascular physiology with slip-ring ct. *AJNR Am J Neuroradiol*. 1996;17:639-650
4. Heit JJ, Wintermark M. Perfusion computed tomography for the evaluation of acute ischemic stroke: Strengths and pitfalls. *Stroke*. 2016;47:1153-1158
5. Wintermark M, Luby M, Bornstein NM, Demchuk A, Fiehler J, Kudo K, et al. International survey of acute stroke imaging used to make revascularization treatment decisions. *Int J Stroke*. 2015;10:759-762
6. Bammer R. Acquisition schemes for computed tomography perfusion. In: Bammer R, ed. *Mr and ct perfusion and pharmakokinetic imaging*. Philadelphia: Wolters Kluwer; 2016.
7. Konstas AA, Goldmakher GV, Lee TY, Lev MH. Theoretic basis and technical implementations of ct perfusion in acute ischemic stroke, part 2: Technical implementations. *AJNR Am J Neuroradiol*. 2009;30:885-892
8. Wintermark M, Smith WS, Ko NU, Quist M, Schnyder P, Dillon WP. Dynamic perfusion ct: Optimizing the temporal resolution and contrast volume for calculation of perfusion ct parameters in stroke patients. *AJNR Am J Neuroradiol*. 2004;25:720-729
9. Roberts HC, Roberts TP, Smith WS, Lee TJ, Fischbein NJ, Dillon WP. Multisection dynamic ct perfusion for acute cerebral ischemia: The "toggling-table" technique. *AJNR Am J Neuroradiol*. 2001;22:1077-1080
10. Yu S, Zhang L, Zheng J, Xu Y, Chen Y, Song Z. A comparison of adaptive iterative dose reduction 3d and filtered back projection in craniocervical ct angiography. *Clin Radiol*. 2017;72:96 e91-96 e96
11. Chen H, Zhang Y, Kalra MK, Lin F, Chen Y, Liao P, et al. Low-dose ct with a residual encoder-decoder convolutional neural network. *IEEE Trans Med Imaging*. 2017;36:2524-2535

12. Lin K, Kazmi KS, Law M, Babb J, Peccerelli N, Pramanik BK. Measuring elevated microvascular permeability and predicting hemorrhagic transformation in acute ischemic stroke using first-pass dynamic perfusion ct imaging. *AJNR Am J Neuroradiol*. 2007;28:1292-1298

13. Meier P, Zierler KL. On the theory of the indicator-dilution method for measurement of blood flow and volume. *J Appl Physiol*. 1954;6:731-744

14. Zierler KL. Equations for measuring blood flow by external monitoring of radioisotopes. *Circ Res*. 1965;16:309-321

15. Hamberg LM, Hunter GJ, Kierstead D, Lo EH, Gilberto Gonzalez R, Wolf GL. Measurement of cerebral blood volume with subtraction three-dimensional functional ct. *AJNR Am J Neuroradiol*. 1996;17:1861-1869

16. Lipowsky HH, Kovalcheck S, Zweifach BW. The distribution of blood rheological parameters in the microvasculature of cat mesentery. *Circ Res*. 1978;43:738-749

17. Klitzman B, Duling BR. Microvascular hematocrit and red cell flow in resting and contracting striated muscle. *Am J Physiol*. 1979;237:H481-490

18. Ostergaard L, Sorensen AG, Kwong KK, Weisskoff RM, Gyldensted C, Rosen BR. High resolution measurement of cerebral blood flow using intravascular tracer bolus passages. Part ii: Experimental comparison and preliminary results. *Magn Reson Med*. 1996;36:726-736

19. Ostergaard L, Weisskoff RM, Chesler DA, Gyldensted C, Rosen BR. High resolution measurement of cerebral blood flow using intravascular tracer bolus passages. Part i: Mathematical approach and statistical analysis. *Magn Reson Med*. 1996;36:715-725

20. Willats L, Calamante F. The 39 steps: Evading error and deciphering the secrets for accurate dynamic susceptibility contrast mri. *NMR Biomed*. 2013;26:913-931

21. Gobbel GT, Fike JR. A deconvolution method for evaluating indicator-dilution curves. *Phys Med Biol*. 1994;39:1833-1854

22. Calamante FSFW, L. Practical aspects of deconvolution. In: Bammer R, ed. *Mr and ct perfusion and pharmacokinetic imaging*. Philadelphia: Wolters-Kluwer; 2016.

23. Hansen AK.

24. Gall P, Emerich P, Kjolby BF, Kellner E, Mader I, Kiselev VG. On the design of filters for fourier and osvd-based deconvolution in bolus tracking perfusion mri. *MAGMA*. 2010;23:187-195

25. Calamante F, Gadian DG, Connelly A. Delay and dispersion effects in dynamic susceptibility contrast mri: Simulations using singular value decomposition. *Magn Reson Med*. 2000;44:466-473

26. Calamante F, Gadian DG, Connelly A. Quantification of perfusion using bolus tracking magnetic resonance imaging in stroke: Assumptions, limitations, and potential implications for clinical use. *Stroke*. 2002;33:1146-1151

27. Wu O, Ostergaard L, Weisskoff RM, Benner T, Rosen BR, Sorensen AG. Tracer arrival timing-insensitive technique for estimating flow in mr perfusion-weighted imaging using singular value decomposition with a block-circulant deconvolution matrix. *Magn Reson Med*. 2003;50:164-174

28. van Osch MJ, Vonken EJ, Bakker CJ, Viergever MA. Correcting partial volume artifacts of the arterial input function in quantitative cerebral perfusion mri. *Magn Reson Med*. 2001;45:477-485

29. Calamante F, Morup M, Hansen LK. Defining a local arterial input function for perfusion mri using independent component analysis. *Magn Reson Med*. 2004;52:789-797

30. Wittsack HJ, Wohlschlager AM, Ritzl EK, Kleiser R, Cohnen M, Seitz RJ, et al. Ct-perfusion imaging of the human brain: Advanced deconvolution analysis using circulant singular value decomposition. *Comput Med Imaging Graph*. 2008;32:67-77

31. Calamante F, Christensen S, Desmond PM, Ostergaard L, Davis SM, Connelly A. The physiological significance of the time-to-maximum (tmax) parameter in perfusion mri. *Stroke*. 2010;41:1169-1174

32. Calamante F, Willats L, Gadian DG, Connelly A. Bolus delay and dispersion in perfusion mri: Implications for tissue predictor models in stroke. *Magn Reson Med*. 2006;55:1180-1185

33. Albers GW, Marks MP, Kemp S, Christensen S, Tsai JP, Ortega-Gutierrez S, et al. Thrombectomy for stroke at 6 to 16 hours with selection by perfusion imaging. *N Engl J Med*. 2018;378:708-718

34. Campbell BC, Mitchell PJ, Kleinig TJ, Dewey HM, Churilov L, Yassi N, et al. Endovascular therapy for ischemic stroke with perfusion-imaging selection. *N Engl J Med*. 2015;372:1009-1018

35. Mokin M, Levy EI, Saver JL, Siddiqui AH, Goyal M, Bonafe A, et al. Predictive value of rapid assessed perfusion thresholds on final infarct volume in swift prime (solitaire with the intention for thrombectomy as primary endovascular treatment). *Stroke*. 2017;48:932-938

36. Nogueira RG, Jadhav AP, Haussen DC, Bonafe A, Budzik RF, Bhuva P, et al. Thrombectomy 6 to 24 hours after stroke with a mismatch between deficit and infarct. *N Engl J Med*. 2018;378:11-21

37. Saver JL, Goyal M, Bonafe A, Diener HC, Levy EI, Pereira VM, et al. Stent-retriever thrombectomy after intravenous t-pa vs. T-pa alone in stroke. *N Engl J Med*. 2015;372:2285-2295

38. Kudo K, Terae S, Katoh C, Oka M, Shiga T, Tamaki N, et al. Quantitative cerebral blood flow measurement with dynamic perfusion ct using the vascular-pixel elimination method: Comparison with h2(15)o positron emission tomography. *AJNR Am J Neuroradiol*. 2003;24:419-426

39. Bammer R. Dynamic susceptibility contrast-based pwi. In: Bammer R, ed. *Mr and ct perfusion and pharmacokinet imaging*. Pennsylvania: Wolters-Kluwer; 2016.

40. Leiner T, Kucharczyk W. Nsf prevention in clinical practice: Summary of recommendations and guidelines in the united states, canada, and europe. *J Magn Reson Imaging*. 2009;30:1357-1363

41. Prince MR, Zhang HL, Roditi GH, Leiner T, Kucharczyk W. Risk factors for nsf: A literature review. *J Magn Reson Imaging*. 2009;30:1298-1308

42. Garbow JR AJ. Mr relaxation theory and exchange processes in the presence of contrast agents. In: Bammer R, ed. *Mr and ct perfusion and pharmakokinetic imaging*. Philadelphia: Wolters Kluwer; 2016.

43. Boxerman JL vOM, Schmainda K. Susceptibility contrast in tissues: Gradient echo versus spin echo. In: Bammer R, ed. *Mr and ct perfusion and pharmakokinetic imaging*. Philadephia: Wolters Kluwer; 2016.

44. Carr DH, Brown J, Bydder GM, Steiner RE, Weinmann HJ, Speck U, et al. Gadolinium-dtpa as a contrast agent in mri: Initial clinical experience in 20 patients. *AJR Am J Roentgenol*. 1984;143:215-224

45. Rosen BR, Belliveau JW, Vevea JM, Brady TJ. Perfusion imaging with nmr contrast agents. *Magn Reson Med*. 1990;14:249-265

46. Newbould RD, Skare ST, Jochimsen TH, Alley MT, Moseley ME, Albers GW, et al. Perfusion mapping with multiecho multishot parallel imaging epi. *Magn Reson Med*. 2007;58:70-81

47. Schmiedeskamp H, Straka M, Newbould RD, Zaharchuk G, Andre JB, Olivot JM, et al. Combined spin- and gradient-echo perfusion-weighted imaging. *Magn Reson Med*. 2012;68:30-40

48. Weisskoff RM, Zuo CS, Boxerman JL, Rosen BR. Microscopic susceptibility variation and transverse relaxation: Theory and experiment. *Magn Reson Med*. 1994;31:601-610

49. Boxerman JL, Hamberg LM, Rosen BR, Weisskoff RM. Mr contrast due to intravascular magnetic susceptibility perturbations. *Magn Reson Med*. 1995;34:555-566

50. Donahue KM, Krouwer HG, Rand SD, Pathak AP, Marszalkowski CS, Censky SC, et al. Utility of simultaneously acquired gradient-echo and spin-echo cerebral blood volume and morphology maps in brain tumor patients. *Magn Reson Med*. 2000;43:845-853

51. Calamante F. Bolus dispersion issues related to the quantification of perfusion mri data. *J Magn Reson Imaging*. 2005;22:718-722

52. Kosior JC, Frayne R. Perfusion parameters derived from bolus-tracking perfusion imaging are immune to tracer recirculation. *J Magn Reson Imaging*. 2010;31:753-756

53. Wintermark M, Albers GW, Alexandrov AV, Alger JR, Bammer R, Baron JC, et al. Acute stroke imaging research roadmap. *Stroke*. 2008;39:1621-1628

54. Boxerman JL, Rosen BR, Weisskoff RM. Signal-to-noise analysis of cerebral blood volume maps from dynamic nmr imaging studies. *J Magn Reson Imaging*. 1997;7:528-537

55. Thilmann O, Larsson EM, Bjorkman-Burtscher IM, Stahlberg F, Wirestam R. Effects of echo time variation on perfusion assessment using dynamic susceptibility contrast mr imaging at 3 tesla. *Magn Reson Imaging*. 2004;22:929-935

56. Paulson ES, Schmainda KM. Comparison of dynamic susceptibility-weighted contrast-enhanced mr methods: Recommendations for measuring relative cerebral blood volume in brain tumors. *Radiology*. 2008;249:601-613

57. Kjolby BF, Ostergaard L, Kiselev VG. Theoretical model of intravascular paramagnetic tracers effect on tissue relaxation. *Magn Reson Med*. 2006;56:187-197

58. Newman GC, Hospod FE, Patlak CS, Fain SE, Pulfer KA, Cook TD, et al. Experimental estimates of the constants relating signal change to contrast concentration for cerebral blood volume by t2* mri. *J Cereb Blood Flow Metab*. 2006;26:760-770

59. Boxerman JL, Prah DE, Paulson ES, Machan JT, Bedekar D, Schmainda KM. The role of preload and leakage correction in gadolinium-based cerebral blood volume estimation determined by comparison with mion as a criterion standard. *AJNR Am J Neuroradiol*. 2012;33:1081-1087

60. van Osch MJ, Vonken EJ, Viergever MA, van der Grond J, Bakker CJ. Measuring the arterial input function with gradient echo sequences. *Magn Reson Med*. 2003;49:1067-1076

61. Calamante F, Connelly A, van Osch MJ. Nonlinear deltar*2 effects in perfusion quantification using bolus-tracking mri. *Magn Reson Med*. 2009;61:486-492

62. Bleeker EJ, van Buchem MA, van Osch MJ. Optimal location for arterial input function measurements near the middle cerebral artery in first-pass perfusion mri. *J Cereb Blood Flow Metab*. 2009;29:840-852

63. Bleeker EJ, van Buchem MA, Webb AG, van Osch MJ. Phase-based arterial input function measurements for dynamic susceptibility contrast mri. *Magn Reson Med*. 2010;64:358-368

64. Conturo TE, Barker PB, Mathews VP, Monsein LH, Bryan RN. Mr imaging of cerebral perfusion by phase-angle reconstruction of bolus paramagnetic-induced frequency shifts. *Magn Reson Med*. 1992;27:375-390

65. Christensen S, Mouridsen K, Wu O, Hjort N, Karstoft H, Thomalla G, et al. Comparison of 10 perfusion mri parameters in 97 sub-6-hour stroke patients using voxel-based receiver operating characteristics analysis. *Stroke*. 2009;40:2055-2061

66. Reishofer G, Fazekas F, Keeling S, Enzinger C, Payer F, Simbrunner J, et al. Minimizing macrovessel signal in cerebral perfusion imaging using independent component analysis. *Magn Reson Med*. 2007;57:278-288

67. Reishofer G, Koschutnig K, Enzinger C, Ischebeck A, Keeling S, Stollberger R, et al. Automated macrovessel artifact correction in dynamic

susceptibility contrast magnetic resonance imaging using independent component analysis. *Magn Reson Med*. 2011;65:848-857

68. Kudo K, Christensen S, Sasaki M, Ostergaard L, Shirato H, Ogasawara K, et al. Accuracy and reliability assessment of ct and mr perfusion analysis software using a digital phantom. *Radiology*. 2013;267:201-211

69. Kudo K, Sasaki M, Ogasawara K, Terae S, Ehara S, Shirato H. Difference in tracer delay-induced effect among deconvolution algorithms in ct perfusion analysis: Quantitative evaluation with digital phantoms. *Radiology*. 2009;251:241-249

70. Kudo K, Sasaki M, Yamada K, Momoshima S, Utsunomiya H, Shirato H, et al. Differences in ct perfusion maps generated by different commercial software: Quantitative analysis by using identical source data of acute stroke patients. *Radiology*. 2010;254:200-209

71. Lansberg MG, Straka M, Kemp S, Mlynash M, Wechsler LR, Jovin TG, et al. Mri profile and response to endovascular reperfusion after stroke (defuse 2): A prospective cohort study. *Lancet Neurol*. 2012;11:860-867

72. Wintermark M, Flanders AE, Velthuis B, Meuli R, van Leeuwen M, Goldsher D, et al. Perfusion-ct assessment of infarct core and penumbra: Receiver operating characteristic curve analysis in 130 patients suspected of acute hemispheric stroke. *Stroke*. 2006;37:979-985

73. Butcher KS, Parsons M, MacGregor L, Barber PA, Chalk J, Bladin C, et al. Refining the perfusion-diffusion mismatch hypothesis. *Stroke*. 2005;36:1153-1159

74. Bivard A, McElduff P, Spratt N, Levi C, Parsons M. Defining the extent of irreversible brain ischemia using perfusion computed tomography. *Cerebrovasc Dis*. 2011;31:238-245

75. Campbell BC, Christensen S, Levi CR, Desmond PM, Donnan GA, Davis SM, et al. Cerebral blood flow is the optimal ct perfusion parameter for assessing infarct core. *Stroke*. 2011;42:3435-3440

76. Cereda CW, Christensen S, Campbell BC, Mishra NK, Mlynash M, Levi C, et al. A benchmarking tool to evaluate computer tomography perfusion infarct core predictions against a dwi standard. *J Cereb Blood Flow Metab*. 2016;36:1780-1789

77. Austein F, Riedel C, Kerby T, Meyne J, Binder A, Lindner T, et al. Comparison of perfusion ct software to predict the final infarct volume after thrombectomy. *Stroke*. 2016;47:2311-2317

78. Goyal M, Demchuk AM, Menon BK, Eesa M, Rempel JL, Thornton J, et al. Randomized assessment of rapid endovascular treatment of ischemic stroke. *N Engl J Med*. 2015;372:1019-1030

79. Haller S, Zaharchuk G, Thomas DL, Lovblad KO, Barkhof F, Golay X. Arterial spin labeling perfusion of the brain: Emerging clinical applications. *Radiology*. 2016;281:337-356

80. Alsop DC, Detre JA. Multisection cerebral blood flow mr imaging with continuous arterial spin labeling. *Radiology*. 1998;208:410-416

81. Detre JA, Alsop DC, Vives LR, Maccotta L, Teener JW, Raps EC. Noninvasive mri evaluation of cerebral blood flow in cerebrovascular disease. *Neurology*. 1998;50:633-641

82. Detre JA, Leigh JS, Williams DS, Koretsky AP. Perfusion imaging. *Magn Reson Med*. 1992;23:37-45

83. Williams DS, Detre JA, Leigh JS, Koretsky AP. Magnetic resonance imaging of perfusion using spin inversion of arterial water. *Proc Natl Acad Sci U S A*. 1992;89:212-216

84. Deibler AR, Pollock JM, Kraft RA, Tan H, Burdette JH, Maldjian JA. Arterial spin-labeling in routine clinical practice, part 1: Technique and artifacts. *AJNR Am J Neuroradiol*. 2008;29:1228-1234

85. Sadowski EA, Bennett LK, Chan MR, Wentland AL, Garrett AL, Garrett RW, et al. Nephrogenic systemic fibrosis: Risk factors and incidence estimation. *Radiology*. 2007;243:148-157

86. Roberts DA, Detre JA, Bolinger L, Insko EK, Leigh JS, Jr. Quantitative magnetic resonance imaging of human brain perfusion at 1.5 t using steady-state inversion of arterial water. *Proc Natl Acad Sci U S A*. 1994;91:33-37

87. Golay X, Petersen ET. Arterial spin labeling: Benefits and pitfalls of high magnetic field. *Neuroimaging Clin N Am*. 2006;16:259-268, x

88. Alsop DC, Detre JA, Golay X, Gunther M, Hendrikse J, Hernandez-Garcia L, et al. Recommended implementation of arterial spin-labeled perfusion mri for clinical applications: A consensus of the ismrm perfusion study group and the european consortium for asl in dementia. *Magn Reson Med*. 2015;73:102-116

89. Zaharchuk G. Theoretical basis of hemodynamic mr imaging techniques to measure cerebral blood volume, cerebral blood flow, and permeability. *AJNR Am J Neuroradiol*. 2007;28:1850-1858

90. Zhang X, Petersen ET, Ghariq E, De Vis JB, Webb AG, Teeuwisse WM, et al. In vivo blood t(1) measurements at 1.5 t, 3 t, and 7 t. *Magn Reson Med*. 2013;70:1082-1086

91. Wong EC, Cronin M, Wu WC, Inglis B, Frank LR, Liu TT. Velocity-selective arterial spin labeling. *Magn Reson Med*. 2006;55:1334-1341

92. Dixon WT, Du LN, Faul DD, Gado M, Rossnick S. Projection angiograms of blood labeled by adiabatic fast passage. *Magn Reson Med*. 1986;3:454-462

93. Petersen ET, Zimine I, Ho YC, Golay X. Non-invasive measurement of perfusion: A critical review of arterial spin labelling techniques. *Br J Radiol*. 2006;79:688-701

94. Wolff SD, Balaban RS. Magnetization transfer contrast (mtc) and tissue water proton relaxation in vivo. *Magn Reson Med*. 1989;10:135-144

95. Zhang W, Silva AC, Williams DS, Koretsky AP. Nmr measurement of perfusion using arterial spin labeling without saturation of macromolecular spins. *Magn Reson Med*. 1995;33:370-376

96. Mildner T, Trampel R, Moller HE, Schafer A, Wiggins CJ, Norris DG. Functional perfusion imaging using continuous arterial spin labeling with separate labeling and imaging coils at 3 t. *Magn Reson Med*. 2003;49:791-795

97. Floyd TF, Ratcliffe SJ, Wang J, Resch B, Detre JA. Precision of the casl-perfusion mri technique for the measurement of cerebral blood flow in whole brain and vascular territories. *J Magn Reson Imaging*. 2003;18:649-655

98. Petersen ET, Lim T, Golay X. Model-free arterial spin labeling quantification approach for perfusion mri. *Magn Reson Med*. 2006;55:219-232

99. Edelman RR, Siewert B, Darby DG, Thangaraj V, Nobre AC, Mesulam MM, et al. Qualitative mapping of cerebral blood flow and functional localization with echo-planar mr imaging and signal targeting with alternating radio frequency. *Radiology*. 1994;192:513-520

100. Kim SG. Quantification of relative cerebral blood flow change by flow-sensitive alternating inversion recovery (fair) technique: Application to functional mapping. *Magn Reson Med*. 1995;34:293-301

101. Wong EC, Buxton RB, Frank LR. Implementation of quantitative perfusion imaging techniques for functional brain mapping using pulsed arterial spin labeling. *NMR Biomed*. 1997;10:237-249

102. Golay X, Petersen ET, Hui F. Pulsed star labeling of arterial regions (pulsar): A robust regional perfusion technique for high field imaging. *Magn Reson Med*. 2005;53:15-21

103. Kwong KK, Chesler DA, Weisskoff RM, Donahue KM, Davis TL, Ostergaard L, et al. Mr perfusion studies with t1-weighted echo planar imaging. *Magn Reson Med*. 1995;34:878-887

104. Tanabe JL, Yongbi M, Branch C, Hrabe J, Johnson G, Helpern JA. Mr perfusion imaging in human brain using the unfair technique. Un-inverted flow-sensitive alternating inversion recovery. *J Magn Reson Imaging*. 1999;9:761-767

105. Mai VM, Berr SS. Mr perfusion imaging of pulmonary parenchyma using pulsed arterial spin labeling techniques: Fairer and fair. *J Magn Reson Imaging*. 1999;9:483-487

106. Schwarzbauer C, Heinke W. Base imaging: A new spin labeling technique for measuring absolute perfusion changes. *Magn Reson Med*. 1998;39:717-722

107. Yongbi MN, Yang Y, Frank JA, Duyn JH. Multislice perfusion imaging in human brain using the c-foci inversion pulse: Comparison with hyperbolic secant. *Magn Reson Med*. 1999;42:1098-1105

108. Wong EC, Buxton RB, Frank LR. Quantitative imaging of perfusion using a single subtraction (quipss and quipss ii). *Magn Reson Med*. 1998;39:702-708

109. Luh WM, Wong EC, Bandettini PA, Hyde JS. Quipss ii with thin-slice ti1 periodic saturation: A method for improving accuracy of quantitative perfusion imaging using pulsed arterial spin labeling. *Magn Reson Med*. 1999;41:1246-1254

110. Dai W, Garcia D, de Bazelaire C, Alsop DC. Continuous flow-driven inversion for arterial spin labeling using pulsed radio frequency and gradient fields. *Magn Reson Med*. 2008;60:1488-1497

111. Alsop DC, Detre JA. Reduced transit-time sensitivity in noninvasive magnetic resonance imaging of human cerebral blood flow. *J Cereb Blood Flow Metab*. 1996;16:1236-1249

112. Lu H, Clingman C, Golay X, van Zijl PC. Determining the longitudinal relaxation time (t1) of blood at 3.0 tesla. *Magn Reson Med*. 2004;52:679-682

113. van der Thiel M, Rodriguez C, Giannakopoulos P, Burke MX, Lebel RM, Gninenko N, et al. Brain perfusion measurements using multidelay arterial spin-labeling are systematically biased by the number of delays. *AJNR Am J Neuroradiol*. 2018;39:1432-1438

114. Qiu M, Paul Maguire R, Arora J, Planeta-Wilson B, Weinzimmer D, Wang J, et al. Arterial transit time effects in pulsed arterial spin labeling cbf mapping: Insight from a pet and mr study in normal human subjects. *Magn Reson Med*. 2010;63:374-384

115. Fan AP, Guo J, Khalighi MM, Gulaka PK, Shen B, Park JH, et al. Long-delay arterial spin labeling provides more accurate cerebral blood flow measurements in moyamoya patients: A simultaneous positron emission tomography/mri study. *Stroke*. 2017;48:2441-2449

116. Vidorreta M, Balteau E, Wang Z, De Vita E, Pastor MA, Thomas DL, et al. Evaluation of segmented 3d acquisition schemes for whole-brain high-resolution arterial spin labeling at 3 t. *NMR Biomed*. 2014;27:1387-1396

117. Vidorreta M, Wang Z, Rodriguez I, Pastor MA, Detre JA, Fernandez-Seara MA. Comparison of 2d and 3d single-shot asl perfusion fmri sequences. *Neuroimage*. 2013;66:662-671

118. Aksoy M, Maclaren J, Bammer R. Prospective motion correction for 3d pseudo-continuous arterial spin labeling using an external optical tracking system. *Magn Reson Imaging*. 2017;39:44-52

119. Zun Z, Shankaranarayanan A, Zaharchuk G. Pseudocontinuous arterial spin labeling with prospective motion correction (pcasl-promo). *Magn Reson Med*. 2014;72:1049-1056

120. Ye FQ, Frank JA, Weinberger DR, McLaughlin AC. Noise reduction in 3d perfusion imaging by attenuating the static signal in arterial spin tagging (assist). *Magn Reson Med*. 2000;44:92-100

121. Garcia DM, Duhamel G, Alsop DC. Efficiency of inversion pulses for background suppressed arterial spin labeling. *Magn Reson Med*. 2005;54:366-372

122. Maleki N, Dai W, Alsop DC. Optimization of background suppression for arterial spin labeling perfusion imaging. *MAGMA*. 2012;25:127-133

123. Amukotuwa SA, Yu C, Zaharchuk G. 3d pseudocontinuous arterial spin labeling in routine clinical practice: A review of clinically significant artifacts. *J Magn Reson Imaging*. 2016;43:11-27

124. Zhou J, Wilson DA, Ulatowski JA, Traystman RJ, van Zijl PC. Two-compartment exchange model for perfusion quantification using arterial spin tagging. *J Cereb Blood Flow Metab*. 2001;21:440-455

125. Buxton RB, Frank LR, Wong EC, Siewert B, Warach S, Edelman RR. A general kinetic model for quantitative perfusion imaging with arterial spin labeling. *Magn Reson Med*. 1998;40:383-396

126. Herscovitch P, Raichle ME. What is the correct value for the brain--blood partition coefficient for water? *J Cereb Blood Flow Metab*. 1985;5:65-69

127. Wang DJ, Alger JR, Qiao JX, Gunther M, Pope WB, Saver JL, et al. Multi-delay multi-parametric arterial spin-labeled perfusion mri in acute ischemic stroke - comparison with dynamic susceptibility contrast enhanced perfusion imaging. *Neuroimage Clin*. 2013;3:1-7

128. Dai W, Robson PM, Shankaranarayanan A, Alsop DC. Reduced resolution transit delay prescan for quantitative continuous arterial spin labeling perfusion imaging. *Magn Reson Med*. 2012;67:1252-1265

129. Lou X, Yu S, Scalzo F, Starkman S, Ali LK, Kim D, et al. Multi-delay asl can identify leptomeningeal collateral perfusion in endovascular therapy of ischemic stroke. *Oncotarget*. 2017;8:2437-2443

130. Look DC LD. Time saving in measurement of nmr and epr relaxation times. *Rev Sci Instrum* 1970;41:250-251

131. Dai W, Shankaranarayanan A, Alsop DC. Volumetric measurement of perfusion and arterial transit delay using hadamard encoded continuous arterial spin labeling. *Magn Reson Med*. 2013;69:1014-1022

132. Wells JA, Lythgoe MF, Gadian DG, Ordidge RJ, Thomas DL. In vivo hadamard encoded continuous arterial spin labeling (h-casl). *Magn Reson Med*. 2010;63:1111-1118

133. Teeuwisse WM, Schmid S, Ghariq E, Veer IM, van Osch MJ. Time-encoded pseudocontinuous arterial spin labeling: Basic properties and timing strategies for human applications. *Magn Reson Med*. 2014;72:1712-1722

134. Nishimura DG, Macovski A, Pauly JM, Conolly SM. Mr angiography by selective inversion recovery. *Magn Reson Med*. 1987;4:193-202

135. Okell TW, Chappell MA, Woolrich MW, Gunther M, Feinberg DA, Jezzard P. Vessel-encoded dynamic magnetic resonance angiography using arterial spin labeling. *Magn Reson Med*. 2010;64:430-438

136. Sallustio F, Kern R, Gunther M, Szabo K, Griebe M, Meairs S, et al. Assessment of intracranial collateral flow by using dynamic arterial spin labeling mra and transcranial color-coded duplex ultrasound. *Stroke*. 2008;39:1894-1897

137. van Osch MJ, Hendrikse J, Golay X, Bakker CJ, van der Grond J. Non-invasive visualization of collateral blood flow patterns of the circle of willis by dynamic mr angiography. *Med Image Anal*. 2006;10:59-70

138. Kopeinigg D, Bammer R. Time-resolved angiography using inflow subtraction (trails). *Magn Reson Med*. 2014;72:669-678

139. Wu H, Block WF, Turski PA, Mistretta CA, Johnson KM. Noncontrast-enhanced three-dimensional (3d) intracranial mr angiography using pseudocontinuous arterial spin labeling and accelerated 3d radial acquisition. *Magn Reson Med*. 2013;69:708-715

140. Robson PM, Dai W, Shankaranarayanan A, Rofsky NM, Alsop DC. Time-resolved vessel-selective digital subtraction mr angiography of the cerebral vasculature with arterial spin labeling. *Radiology*. 2010;257:507-515

141. Iryo Y, Hirai T, Kai Y, Nakamura M, Shigematsu Y, Kitajima M, et al. Intracranial dural arteriovenous fistulas: Evaluation with 3-t four-dimensional mr angiography using arterial spin labeling. *Radiology*. 2014;271:193-199

142. Yan L, Wang S, Zhuo Y, Wolf RL, Stiefel MF, An J, et al. Unenhanced dynamic mr angiography: High spatial and temporal resolution by using true fisp-based spin tagging with alternating radiofrequency. *Radiology*. 2010;256:270-279

143. Le TT, Fischbein NJ, Andre JB, Wijman C, Rosenberg J, Zaharchuk G. Identification of venous signal on arterial spin labeling improves diagnosis of dural arteriovenous fistulas and small arteriovenous malformations. *AJNR Am J Neuroradiol*. 2012;33:61-68

144. Wolf RL, Wang J, Detre JA, Zager EL, Hurst RW. Arteriovenous shunt visualization in arteriovenous malformations with arterial spin-labeling mr imaging. *AJNR Am J Neuroradiol*. 2008;29:681-687

145. Gevers S, Bokkers RP, Hendrikse J, Majoie CB, Kies DA, Teeuwisse WM, et al. Robustness and reproducibility of flow territories defined by planning-

free vessel-encoded pseudocontinuous arterial spin-labeling. *AJNR Am J Neuroradiol*. 2012;33:E21-25

146. Dai W, Robson PM, Shankaranarayanan A, Alsop DC. Modified pulsed continuous arterial spin labeling for labeling of a single artery. *Magn Reson Med*. 2010;64:975-982

147. Wong EC. Vessel-encoded arterial spin-labeling using pseudocontinuous tagging. *Magn Reson Med*. 2007;58:1086-1091

148. Chappell MA, Okell TW, Payne SJ, Jezzard P, Woolrich MW. A fast analysis method for non-invasive imaging of blood flow in individual cerebral arteries using vessel-encoded arterial spin labelling angiography. *Med Image Anal*. 2012;16:831-839

149. van Laar PJ, van der Grond J, Hendrikse J. Brain perfusion territory imaging: Methods and clinical applications of selective arterial spin-labeling mr imaging. *Radiology*. 2008;246:354-364

150. Hendrikse J, van der Grond J, Lu H, van Zijl PC, Golay X. Flow territory mapping of the cerebral arteries with regional perfusion mri. *Stroke*. 2004;35:882-887

151. van der Zwan A, Hillen B, Tulleken CA, Dujovny M, Dragovic L. Variability of the territories of the major cerebral arteries. *J Neurosurg*. 1992;77:927-940

152. Hendrikse J, Petersen ET, Cheze A, Chng SM, Venketasubramanian N, Golay X. Relation between cerebral perfusion territories and location of cerebral infarcts. *Stroke*. 2009;40:1617-1622

153. Chng SM, Petersen ET, Zimine I, Sitoh YY, Lim CC, Golay X. Territorial arterial spin labeling in the assessment of collateral circulation: Comparison with digital subtraction angiography. *Stroke*. 2008;39:3248-3254

154. Davies NP, Jezzard P. Selective arterial spin labeling (sasl): Perfusion territory mapping of selected feeding arteries tagged using two-dimensional radiofrequency pulses. *Magn Reson Med*. 2003;49:1133-1142

155. Talagala SL, Ye FQ, Ledden PJ, Chesnick S. Whole-brain 3d perfusion mri at 3.0 t using casl with a separate labeling coil. *Magn Reson Med*. 2004;52:131-140

156. Gunther M. Efficient visualization of vascular territories in the human brain by cycled arterial spin labeling mri. *Magn Reson Med*. 2006;56:671-675

157. Kansagra AP, Wong EC. Mapping of vertebral artery perfusion territories using arterial spin labeling mri. *J Magn Reson Imaging*. 2008;28:762-766

158. Saver JL. Time is brain--quantified. *Stroke*. 2006;37:263-266

159. Straka M, Albers GW, Bammer R. Real-time diffusion-perfusion mismatch analysis in acute stroke. *J Magn Reson Imaging*. 2010;32:1024-1037

160. Campbell BC, Christensen S, Levi CR, Desmond PM, Donnan GA, Davis SM, et al. Comparison of computed tomography perfusion and magnetic resonance imaging perfusion-diffusion mismatch in ischemic stroke. *Stroke*. 2012;43:2648-2653

161. Dehkharghani S, Bammer R, Straka M, Albin LS, Kass-Hout O, Allen JW, et al. Performance and predictive value of a user-independent platform for ct perfusion analysis: Threshold-derived automated systems outperform examiner-driven approaches in outcome prediction of acute ischemic stroke. *AJNR Am J Neuroradiol*. 2015;36:1419-1425

162. Sillanpaa N, Saarinen JT, Rusanen H, Hakomaki J, Lahteela A, Numminen H, et al. Ct perfusion aspects in the evaluation of acute ischemic stroke: Thrombolytic therapy perspective. *Cerebrovasc Dis Extra*. 2011;1:6-16

163. Sillanpaa N, Saarinen JT, Rusanen H, Hakomaki J, Lahteela A, Numminen H, et al. The clot burden score, the boston acute stroke imaging scale, the cerebral blood volume aspects, and two novel imaging parameters in the prediction of clinical outcome of ischemic stroke patients receiving intravenous thrombolytic therapy. *Neuroradiology*. 2012;54:663-672

164. Zaharchuk G, Gong E, Wintermark M, Rubin D, Langlotz CP. Deep learning in neuroradiology. *AJNR Am J Neuroradiol*. 2018;39:1776-1784

165. Mwangi B, Soares JC, Hasan KM. Visualization and unsupervised predictive clustering of high-dimensional multimodal neuroimaging data. *J Neurosci Methods*. 2014;236:19-25

166. LeCun Y, Bengio Y, Hinton G. Deep learning. *Nature*. 2015;521:436-444

167. Lee JG, Jun S, Cho YW, Lee H, Kim GB, Seo JB, et al. Deep learning in medical imaging: General overview. *Korean J Radiol*. 2017;18:570-584

168. Wang Z, Bovik AC, Sheikh HR, Simoncelli EP. Image quality assessment: From error visibility to structural similarity. *IEEE Trans Image Process*. 2004;13:600-612

169. Chilamkurthy S, Ghosh R, Tanamala S, Biviji M, Campeau NG, Venugopal VK, et al. Deep learning algorithms for detection of critical findings in head ct scans: A retrospective study. *Lancet*. 2018;392:2388-2396

170. Arbabshirani MR, Fornwalt BK, Mongelluzzo GJ, Suever JD, Geise BD, Patel AA, et al. Advanced machine learning in action: Identification of intracranial hemorrhage on computed tomography scans of the head with clinical workflow integration. *NPJ Digit Med*. 2018;1:9

171. Ye H, Gao F, Yin Y, Guo D, Zhao P, Lu Y, et al. Precise diagnosis of intracranial hemorrhage and subtypes using a three-dimensional joint convolutional and recurrent neural network. *Eur Radiol*. 2019;29:6191-6201

172. Chang PD, Kuoy E, Grinband J, Weinberg BD, Thompson M, Homo R, et al. Hybrid 3d/2d convolutional neural network for hemorrhage evaluation on head ct. *AJNR Am J Neuroradiol*. 2018;39:1609-1616

173. Kuo W, Hne C, Mukherjee P, Malik J, Yuh EL. Expert-level detection of acute intracranial hemorrhage on head computed tomography using deep learning. *Proc Natl Acad Sci U S A*. 2019;116:22737-22745

174. Beez T, Munoz-Bendix C, Steiger HJ, Beseoglu K. Decompressive craniectomy for acute ischemic stroke. *Crit Care*. 2019;23:209

175. Chalela JA, Kidwell CS, Nentwich LM, Luby M, Butman JA, Demchuk AM, et al. Magnetic resonance imaging and computed tomography in emergency assessment of patients with suspected acute stroke: A prospective comparison. *Lancet*. 2007;369:293-298

176. Seker F, Pfaff J, Nagel S, Vollherbst D, Gerry S, Mohlenbruch MA, et al. Ct reconstruction levels affect automated and reader-based aspects ratings in acute ischemic stroke. *J Neuroimaging*. 2019;29:62-64

177. Goebel J, Stenzel E, Guberina N, Wanke I, Koehrmann M, Kleinschnitz C, et al. Automated aspect rating: Comparison between the frontier aspect score software and the brainomix software. *Neuroradiology*. 2018;60:1267-1272

178. Guberina N, Dietrich U, Radbruch A, Goebel J, Deuschl C, Ringelstein A, et al. Detection of early infarction signs with machine learning-based diagnosis by means of the alberta stroke program early ct score (aspects) in the clinical routine. *Neuroradiology*. 2018;60:889-901

179. Nagel S, Sinha D, Day D, Reith W, Chapot R, Papanagiotou P, et al. E-aspects software is non-inferior to neuroradiologists in applying the aspect

score to computed tomography scans of acute ischemic stroke patients. *Int J Stroke*. 2017;12:615-622

180. Pfaff J, Herweh C, Schieber S, Schonenberger S, Bosel J, Ringleb PA, et al. E-aspects correlates with and is predictive of outcome after mechanical thrombectomy. *AJNR Am J Neuroradiol*. 2017;38:1594-1599

181. Kuang H, Najm M, Chakraborty D, Maraj N, Sohn SI, Goyal M, et al. Automated aspects on noncontrast ct scans in patients with acute ischemic stroke using machine learning. *AJNR Am J Neuroradiol*. 2019;40:33-38

182. Murray NM, Unberath M, Hager GD, Hui FK. Artificial intelligence to diagnose ischemic stroke and identify large vessel occlusions: A systematic review. *J Neurointerv Surg*. 2019

183. Herweh C, Ringleb PA, Rauch G, Gerry S, Behrens L, Mohlenbruch M, et al. Performance of e-aspects software in comparison to that of stroke physicians on assessing ct scans of acute ischemic stroke patients. *Int J Stroke*. 2016;11:438-445

184. Maegerlein C, Fischer J, Monch S, Berndt M, Wunderlich S, Seifert CL, et al. Automated calculation of the alberta stroke program early ct score: Feasibility and reliability. *Radiology*. 2019;291:141-148

185. Lucas C, Kemmling A, Bouteldja N, Aulmann LF, Madany Mamlouk A, Heinrich MP. Learning to predict ischemic stroke growth on acute ct perfusion data by interpolating low-dimensional shape representations. *Front Neurol*. 2018;9:989

186. Chen L, Bentley P, Rueckert D. Fully automatic acute ischemic lesion segmentation in dwi using convolutional neural networks. *Neuroimage Clin*. 2017;15:633-643

187. Barreira C M. BM, Haussen DC. Abstract wp61: Automated large artery occlusion detection in stroke imaging - aladin study. *Stroke*. 2018;49, Supplement `

188. Barreira CM, Bouslama M, Lim J, et al. As10-047: Aladin study: Automated large artery occlusion detection in stroke imaging study - a multi-center experience. *European Stroke Journal*. 2018;3 (IS)

189. Oman O, Makela T, Salli E, Savolainen S, Kangasniemi M. 3d convolutional neural networks applied to ct angiography in the detection of acute ischemic stroke. *Eur Radiol Exp*. 2019;3:8

Chapter 5

Fast Automatic Detection of Large Vessel Occlusions on CT Angiography

5.1 Introduction

Large vessel occlusions (LVOs) cause approximately 10-40% of acute ischemic strokes, yet they are responsible for 90% of stroke-related mortality and severe neurological disability in survivors[1-3]. Endovascular thrombectomy has been shown to decrease disability, improve functional outcomes and reduce mortality over standard medical management, and is now the standard of care treatment in patients with anterior circulation LVOs up to 6 hours following stroke onset and can be performed in carefully selected patients up to 24 hours[4-8]. Given the availability of this highly effective treatment, and the disproportionate morbidity and mortality when left untreated, identification of LVOs in stroke patients is critically important. Non-invasive vascular imaging is used for this purpose, and is recommended by the American Heart Association guidelines in patients who "otherwise meet criteria for thrombectomy"[8]. *CT angiography* (CTA) is therefore routinely included in the multimodal stroke CT protocol that is used to evaluate patients presenting within the thrombectomy window[8, 9].

Since the time window for thrombectomy is currently limited to 24 hours, and infarct growth occurs with delay in reperfusion, identification of LVOs is time critical[10]. Even an hour's delay can result in the patient no longer being eligible for treatment. Also, there can be substantial infarct growth of up to 100 mL in an hour [11]. A meta-analysis of the early time-window randomized phase 3 thrombectomy trials showed that earlier treatment with mechanical thrombectomy was associated with better functional outcomes, with less disability at 3 months; 39 per 1000 treated patients had less disability, and 25 more patients were functionally independent, for every 15 minutes' time reduction to reperfusion with thrombectomy[12]. A more recent study found a 40% reduction in the odds of functional independence per hour's delay in treatment in patients with infarcts exceeding 50 mL in volume at baseline[13].

Unfortunately, the diagnosis of an LVO on CTA can be delayed. Acute stroke scans may not always receive the highest priority for review, especially at busy times and after-hours, when resources are limited and other time-critical scans such as trauma may be given precedence. This is likely exacerbated by the extension of the thrombectomy window to 24 hours, since it increases the number of potentially treatment eligible patients who must be screened with CTA. A recent study found that 30% of all AIS patients presented in the late (6-24 hour) time window, comparable to the number presenting in the early window, therefore potentially doubling the number of patients who must be screened[14, 15]. In turn, this increases the burden on already stretched imaging resources. Another factor that can lead to incorrect or substantially delayed diagnosis of an LVO is that CTAs are typically initially interpreted by trainees and neurologists in the acute setting. While neuroradiologists have a high accuracy for detecting LVOs on CTA, the diagnostic performance of trainees and neurologists can be considerably worse[16-18]. The diagnostic performance of general radiologists, who are required to interpret CTA in countries such as Australia that have limited subspecialist radiology services, is also likely to be poorer than that of neuroradiologists. Strategies that can improve diagnostic accuracy and efficiency are therefore required.

Clinical decision support tools that automate detection of the infarct core and ischemic penumbra are already well established and are used routinely to improve workflow in acute stroke[9, 19]. Automation has recently been applied to the task of detecting intracranial LVOs in a clinically acceptable timeframe. Such tools have the potential not only to improve the speed and accuracy of LVO detection on CTA, but also to improve intra-hospital workflow and expedite treatment; for example, by notifying the interventional neuroradiology team of a positive finding, they can be more rapidly mobilized. This is of relevance since it has been found that in-hospital patient management processes that reduce the time between brain imaging and reperfusion are associated with improved functional outcomes for patients[12]. By improving outcomes and reducing neurological disability, improved workflow efficiency may also result in health economic benefit. Although a number of automated LVO detection tools are now available for clinical use, there are no published studies that have assessed their diagnostic performance.

In this study, a new fully automated software algorithm, that uses inter-hemispheric vessel density differences to detect LVOs, was introduced and described. The algorithm was then tested in a large cohort of patients consisting of the following five subsets: 1. patients enrolled in two thrombectomy studies,

Diffusion and Perfusion Imaging Evaluation for Understanding Stroke Evolution Study (DEFUSE) 2 (n = 62) and DEFUSE 3 (n = 213), 2. who underwent CTA on presentation; 3. acute ischemic stroke patients who were imaged as potential thrombectomy candidates at a tertiary referral centre (n =82); 4. patients at the same tertiary centre who underwent CTA for indications other than ischemic stroke (n =111); and 5. consecutive patients who presented to a primary stroke centre and underwent CTA as a part of a "code stroke" workup (n = 501). Of these 969 patients, 926 patients with a technically adequate CTA were included in this analysis. The algorithm had four different relative vessel density reduction thresholds. The optimal threshold for detecting LVOs was first determined, using *receiver operating characteristic* (ROC) analysis and a pre-specified diagnostic sensitivity requirement of >95%. Subsequently, the diagnostic performance of the algorithm for detecting vessel occlusions at different anterior circulation subsites was determined for the optimal threshold. It was hypothesized that a very high sensitivity could be achieved with an acceptable number of false positives, yielding moderate specificity.

5.2 Publication

Amukotuwa SA, Straka M, Dehkharghani S, Bammer R. Fast Automatic Detection of Large Vessel Occlusions on CT Angiography. Stroke. 2019 50(12):3431-3438.

5.3 Discussion

A new software algorithm that completely automates detection of anterior circulation LVOs on CTA was introduced, described and evaluated in a large and diverse cohort of 926 patients. This is the first peer reviewed publication evaluating the diagnostic performance of an automated LVO detection tool. The work performed in this study provided validation of the algorithm and allowed it to be improved and released commercially.

The algorithm described in this study detects inter-hemispheric differences in vessel density over 3 regions of interest, *R1-R3*. The most proximal of these regions of interest, *R1*, was centred on the suprasellar cistern and proximal Sylvian fissure, where the terminal internal carotid artery and the proximal M1-segment of the MCA are located, while *R2* and *R3* included progressively more distal parts of the Sylvian fissure where the distal M1-segment and the M2- and M3-segments of the MCA are located. Four different density reduction thresholds are available: <80% to 75%, <75% to 60%, <60% to 45% and <45%, indicating progressively greater density reduction compared to the contralateral side.

The metrics that were assessed in this study were the speed of processing, which was timed, and diagnostic performance of the algorithm, which was assessed using ROC analysis with diagnostic sensitivity, specificity and area-under-the-curve determined for each of the four vessel density thresholds. ROC analysis was performed for detection of: any anterior circulation LVO; an anterior circulation LVO or M2-segment MCA occlusion; and an occlusion at the following subsites: intracranial internal carotid artery, M1-segment MCA, and M2-segment MCA.

The optimal threshold for LVO detection was found to be <75% to 60% vessel density reduction compared to contralateral. As hypothesized, an excellent diagnostic sensitivity of 97% was achieved at this threshold, with a moderate specificity of 74%. When both LVOs and M2-MCA occlusions were considered, the diagnostic sensitivity was similarly high (95%) and specificity increased to 79% at this threshold. The improvement in specificity was due to M2 occlusions detected by the algorithm being coded as “true positives” rather than “false positives”. There is evidence of improved functional outcomes with thrombectomy versus standard medical management in patients with M2-MCA occlusion[20]. M2-MCA occlusions are therefore increasingly regarded as a target for thrombectomy, particularly in patients who are ineligible for thrombolysis and to achieve rapid reperfusion in patients with severe neurological disability and ischemia of eloquent

brain regions. Since the purpose of the LVO detection algorithm is to expedite diagnosis in patients who may benefit from thrombectomy, detection of M2-MCA in addition to LVOs is therefore desirable.

The sensitivity of the algorithm for LVO detection was within the 89%-98% range reported neuroradiologists[16, 17]. There were a small number of false negatives, where an LVO was missed by the algorithm, accounting for the imperfect sensitivity. These resulted from insufficient vessel density reduction compared to the contralateral side. One cause was ICA occlusion at the skull base, proximal to *R1*, associated with only mild or no vessel density reduction downstream; relative vessel density in the regions interrogated by the algorithm, *R1-R3*, was therefore above the detection threshold. Incomplete M1-MCA occlusions and short segment occlusions associated with good collaterals also resulted in false negatives, due to opacification of vessels distal to the occlusion. The software manufacturers subsequently improved the algorithm to address these limitations that were identified. The *R1* region was extended further proximally, to include the skull base ICA, which was facilitated by implementation of a better bone subtraction mask. A vessel tracker was also added, to allow detection of short segment and incomplete occlusions. This also improved sensitivity for detecting M2-MCA occlusions. A theoretical cause of false negatives, which we did not encounter but did flag as a potential pitfall, is bilateral LVOs causing symmetrical vessel density reduction. The vessel tracker should, however, allow detection of such bilateral LVOs with the new implementation of the algorithm.

While the sensitivity of the algorithm was high, its specificity was lower than the 95%-98% reported for neuroradiologists[16, 17]. This relates to the algorithm detecting inter-hemispheric vessel density difference rather than vessel occlusion per se. A consequent limitation of the algorithm, which resulted in a number of false positives, is that it detects other causes of inter-hemispheric vessel density difference and cannot distinguish them from an LVO. These include contralateral hyperaemia and inter-hemispheric anatomical variation in ICA and MCA anatomy, such as a unilateral posterior communicating segment. Human readers, on the other hand, can easily recognize and dismiss anatomical variants and non-LVO pathologies that cause vascular asymmetry. The algorithm was also unable to differentiate between an acute LVO and chronic steno-occlusive disease; this distinction is important when triaging patients because, while chronic large vessel steno-occlusive disease can cause acute stroke, it is not amenable to mechanical thrombectomy unless there is superimposed acute thrombus. Unlike the algorithm, radiologists can localize the exact site of occlusion on CTA and assess its

morphology to determine whether it is acute and amenable to clot retrieval; they can also cross-reference the CTA with non-enhanced CT images to determine whether there is a hyperdense vessel sign to indicate acute occlusion.

Given its high but imperfect sensitivity and only moderate specificity, as well as the limitations identified above, the algorithm cannot replace the experienced human reader. A question which was therefore raised by the reviewers was: *what is the purpose of the algorithm?* The high sensitivity, exceeding 95%, and the fast processing times make it suitable for use as a screening tool in the emergent setting. It can expedite diagnosis by notifying the reporting radiologist and moving the study to the top of the reporting worklist. The tool can also be utilized to improve inter-hospital workflow, for example to notifying and mobilize the interventional neuroradiology team. These strategies to improve workflow are important, and have received emphasis recently due to the importance of decreasing time to reperfusion. Further, the algorithm can be used as a diagnostic support tool to aide less experienced readers such as trainees and general radiologists. The CTAs of stroke patients at tertiary centres are often interpreted by trainees in the emergent setting, particularly after-hours; here, a combination of the reader's inexperience and the time pressures of on-call can result in an LVO being missed. In regional and peripheral hospitals, general radiologists are required to interpret CTA. The tool can also serve as a check mechanism, since even experienced readers do occasionally miss LVOs, prompting a second look in these cases. Conversely, it is important that radiologists using the LVO detection tool remain cognizant of the occurrence and causes of false negatives, and remain vigilant when reviewing CTAs that are deemed negative for an LVO by the algorithm.

To our knowledge, this was the first peer-reviewed publication describing and assessing the diagnostic performance of a fully automated tool that detects LVOs on CTA source images. A systematic review published in October 2019 also found no previous studies that evaluated automated tools for detecting LVOs on CT or MR angiography source images[21]. Only conference abstracts have been published on the diagnostic performance of a different commercially available automated LVO detection tool, which has a reported sensitivity of 90-97% and a specificity that ranged widely from 52% to 83%[22, 23]. That LVO detection algorithm uses a machine learning approach where data was used to train a convolutional neural network (CNN) which then "learned". In contrast, our algorithm uses a deterministic rather than a machine learning approach. A limitation of the deterministic approach over machine learning is that there is no capacity for further training through input of more data. None-the-less, its diagnostic

performance was similar to that of the machine learning approach. It is likely, however, that future iterations of machine learning-based LVO detection algorithms will perform better, given the large effort invested in this field and the circumscribed nature of the task of LVO detection. "Narrow artificial intelligence" algorithms that are trained specifically for LVO detection may even outperform the human reader.

Improvement in the diagnostic performance of automated LVO detection tools using artificial intelligence algorithms is therefore an important future avenue of investigation. The use of training data that is inclusive of a wide variety of anatomical variations may help improve specificity. CTA training data could also be used to train an algorithm to differentiate between acute and chronic occlusions based on the morphology. The "hyperdense vessel sign" on non-enhanced CT is widely used by human readers to identify acute LVOs and distinguish them from chronic occlusions identified on CTA. Extrapolating from this, using non-enhanced CT in conjunction with CTA data to train an algorithm to detect this sign may help improve diagnostic performance for detecting acute occlusions.

A high clinical priority for any automated LVO detection tool, and therefore an important future avenue of investigation, detection of basilar artery occlusion. Like proximal anterior circulation LVOs, acute basilar occlusion is a time-critical emergency that can be treated safely and effectively with thrombectomy[24]. These patients have worse outcomes and higher mortality without treatment, or if treatment is delayed, than those with anterior circulation strokes[25]. Interrogation of inter-hemispheric vessel density differences cannot be used to detect occlusion, since the basilar artery is an unpaired midline artery supplying bilateral branches. Vessel tracking, which has already been incorporated into the algorithm since publication of this study to facilitate detection of incomplete and short segment occlusions, may instead be applied to this task. However, further refinements are required to adapt the algorithm to detect basilar artery occlusion. Machine learning may also be of value.

Another clinically important task that may be addressed using an automated algorithm is detection of occlusions involving the anterior cerebral artery, posterior cerebral artery and the MCA distal to the M2 segment. These distal occlusions can challenge even experienced radiologists, with a reported sensitivity as low as 33% due to the smaller calibre, large number and less opacification of these vessels compared to proximal arteries[16]. Detection of these distal occlusions is becoming more relevant to clinical practice since these patients may benefit from, and are

therefore increasingly considered for, thrombectomy[8, 26]. "Distal vessel thrombectomy" is in fact an area of active research with effort being channelled into new microcatheter development. The deterministic algorithm described in this study may be adapted to detect inter-hemispheric vessel density differences in the interpeduncular, crural and ambient cisterns and occipital sulci to enable detection of posterior cerebral artery occlusions. The specificity and sensitivity are likely to be lower than for ICA and M1 occlusions, due to the smaller size of the posterior cerebral arteries and considerable anatomical variability, in particular related to the P1 and posterior communicating segments. Vessel tracking may be used to improve sensitivity of the algorithm for detection of distal occlusions, both in the anterior and posterior circulation. Machine learning approaches could also be applied to the task of developing an accurate tool for detecting distal occlusions.

The large cohort size is a strength of this study. Another strength is the inclusion of different subgroups of patients, scanned at different hospitals, which allowed the algorithm to be tested on a representative sample of CTAs performed on CT scanners from all the major vendors and using a variety of different scan protocols. This broad testing was important to ensure the generalizability of the findings and avoid a niche solution. There were a large number of patients with LVOs in the study population (320/926, 35%), which was "enriched" for LVOs by inclusion of patients enrolled in two thrombectomy studies, DEFUSE 2 and DEFUSE 3. The large number was important for "stress testing" the algorithm and assessing is diagnostic performance for detecting LVOs at different sites and of different lengths and morphology. However, the resultant over-representation of patients with LVOs in this highly curated cohort is also a limitation of the study, since it does not allow diagnostic specificity to be tested in the real-world setting where the prevalence of LVOs is typically much lower. Field-testing is therefore required in a cohort that is representative of the population of patients with suspected ischemic stroke who are screened for LVOs with CTA, warranting a separate study.

5.4 References

1. Malhotra K, Gornbein J, Saver JL. Ischemic strokes due to large-vessel occlusions contribute disproportionately to stroke-related dependence and death: A review. *Front Neurol*. 2017;8:651

2. Rai AT, Seldon AE, Boo S, Link PS, Domico JR, Tarabishy AR, et al. A population-based incidence of acute large vessel occlusions and thrombectomy eligible patients indicates significant potential for growth of endovascular stroke therapy in the USA. *J Neurointerv Surg*. 2017;9:722-726

3. Dozois A, Hampton L, Kingston CW, Lambert G, Porcelli TJ, Sorenson D, et al. Plumber study (prevalence of large vessel occlusion strokes in mecklenburg county emergency response). *Stroke*. 2017;48:3397-3399

4. Albers GW, Marks MP, Kemp S, Christensen S, Tsai JP, Ortega-Gutierrez S, et al. Thrombectomy for stroke at 6 to 16 hours with selection by perfusion imaging. *N Engl J Med*. 2018;378:708-718

5. Goyal M, Menon BK, van Zwam WH, Dippel DW, Mitchell PJ, Demchuk AM, et al. Endovascular thrombectomy after large-vessel ischaemic stroke: A meta-analysis of individual patient data from five randomised trials. *Lancet*. 2016;387:1723-1731

6. Lin Y, Schulze V, Brockmeyer M, Parco C, Karathanos A, Heinen Y, et al. Endovascular thrombectomy as a means to improve survival in acute ischemic stroke: A meta-analysis. *JAMA Neurol*. 2019

7. Nogueira RG, Jadhav AP, Haussen DC, Bonafe A, Budzik RF, Bhuva P, et al. Thrombectomy 6 to 24 hours after stroke with a mismatch between deficit and infarct. *N Engl J Med*. 2018;378:11-21

8. Powers WJ, Rabinstein AA, Ackerson T, Adeoye OM, Bambakidis NC, Becker K, et al. 2018 guidelines for the early management of patients with acute ischemic stroke: A guideline for healthcare professionals from the american heart association/american stroke association. *Stroke*. 2018;49:e46-e110

9. Campbell BC, Yassi N, Ma H, Sharma G, Salinas S, Churilov L, et al. Imaging selection in ischemic stroke: Feasibility of automated ct-perfusion analysis. *Int J Stroke*. 2015;10:51-54

10. Saver JL. Time is brain--quantified. *Stroke*. 2006;37:263-266

11. Albers GW. Late window paradox. *Stroke*. 2018;49:768-771

12. Saver JL, Goyal M, van der Lugt A, Menon BK, Majoie CB, Dippel DW, et al. Time to treatment with endovascular thrombectomy and outcomes from ischemic stroke: A meta-analysis. *JAMA*. 2016;316:1279-1288

13. Sarraj A, Hassan AE, Savitz S, Sitton C, Grotta J, Chen P, et al. Outcomes of endovascular thrombectomy vs medical management alone in patients with large ischemic cores: A secondary analysis of the optimizing patient's selection for endovascular treatment in acute ischemic stroke (select) study. *JAMA Neurol*. 2019

14. Jadhav AP, Desai SM, Kenmuir CL, Rocha M, Starr MT, Molyneaux BJ, et al. Eligibility for endovascular trial enrollment in the 6- to 24-hour time window: Analysis of a single comprehensive stroke center. *Stroke*. 2018;49:1015-1017

15. Majersik JJ, Smith MA, Zahuranec DB, Sanchez BN, Morgenstern LB. Population-based analysis of the impact of expanding the time window for acute stroke treatment. *Stroke*. 2007;38:3213-3217

16. Becks MJ, Manniesing R, Vister J, Pegge SAH, Steens SCA, van Dijk EJ, et al. Brain ct perfusion improves intracranial vessel occlusion detection on ct angiography. *J Neuroradiol*. 2018

17. Lev MH, Farkas J, Rodriguez VR, Schwamm LH, Hunter GJ, Putman CM, et al. Ct angiography in the rapid triage of patients with hyperacute stroke to intraarterial thrombolysis: Accuracy in the detection of large vessel thrombus. *J Comput Assist Tomogr*. 2001;25:520-528

18. Wagemans BA, van Zwam WH, Nelemans PJ, van Oostenbrugge RJ, Postma AA. 4d-cta improves diagnostic certainty and accuracy in the detection of proximal intracranial anterior circulation occlusion in acute ischemic stroke. *PLoS One*. 2017;12:e0172356

19. Lansberg MG, Lee J, Christensen S, Straka M, De Silva DA, Mlynash M, et al. Rapid automated patient selection for reperfusion therapy: A pooled analysis of the echoplanar imaging thrombolytic evaluation trial (epithet) and the diffusion and perfusion imaging evaluation for understanding stroke evolution (defuse) study. *Stroke*. 2011;42:1608-1614

20. Sarraj A, Sangha N, Hussain MS, Wisco D, Vora N, Elijovich L, et al. Endovascular therapy for acute ischemic stroke with occlusion of the middle cerebral artery m2 segment. *JAMA Neurol*. 2016;73:1291-1296

21. Murray NM, Unberath M, Hager GD, Hui FK. Artificial intelligence to diagnose ischemic stroke and identify large vessel occlusions: A systematic review. *J Neurointerv Surg*. 2019

22. Barreira C M. BM, Haussen DC. Abstract wp61: Automated large artery occlusion detection in stroke imaging - aladin study. *Stroke*. 2018;49, Supplement `

23. Barreira CM, Bouslama M, Lim J, et al. As10-047: Aladin study: Automated large artery occlusion detection in stroke imaging study - a multi-center experience. *European Stroke Journal*. 2018;3 (IS)

24. Kang DH, Jung C, Yoon W, Kim SK, Baek BH, Kim JT, et al. Endovascular thrombectomy for acute basilar artery occlusion: A multicenter retrospective observational study. *J Am Heart Assoc*. 2018;7

25. Schonewille WJ, Wijman CA, Michel P, Rueckert CM, Weimar C, Mattle HP, et al. Treatment and outcomes of acute basilar artery occlusion in the basilar artery international cooperation study (basics): A prospective registry study. *Lancet Neurol*. 2009;8:724-730

26. Grossberg JA, Rebello LC, Haussen DC, Bouslama M, Bowen M, Barreira CM, et al. Beyond large vessel occlusion strokes: Distal occlusion thrombectomy. *Stroke*. 2018;49:1662-1668

Chapter 6

Detection of Large Vessel Occlusions on Computed Tomography Angiography: A Single Center Experience

6.1 Introduction

A new fully automated algorithm for detection of LVOs on CTA was introduced in the previous study. Its diagnostic performance was assessed and its optimal threshold determined in a cohort that was "enriched" for LVOs by inclusion of patients enrolled in two thrombectomy studies. The current study was motivated by the need to assess the algorithm in a cohort that is more representative of the population where LVO detection tools are likely to be used in the real-world clinical setting: patients who present with a suspected ischemic stroke and undergo emergent CTA as part of a "code stroke" workup to screen for an LVO. A separate study to determine the diagnostic performance in this population was deemed to be warranted because of the lower prevalence of LVOs than in the more selective cohort used in the first study, where 35% (320/926) of patients had an LVO.

The cohort used in this second study consisted of 501 consecutive "code stroke" patients who presented to a regional hospital (a primary stroke center) over a 24-month period and underwent multimodal stroke CT, including CTA, as part of the workup for a suspected acute ischemic stroke. Although these patients were included as a part of the previous study's larger cohort, diagnostic performance in this subgroup was not assessed separately, and the factors specific to this target population were not considered.

The rationale for using a cohort of patients from a regional hospital is that this is likely to be the target population for LVO detection tools. Patients presenting to these regional and peripheral "spoke" hospitals must be transferred to a

metropolitan "hub" where clot-retrieval services are offered. Extension of the thrombectomy window to 24 hours has placed increased demand on these primary stroke centers to perform and interpret CTA, since more stroke patients present within the treatment window and patient transfer can be undertaken even from the most remote hospitals within the treatment window. Epidemiological data from the United States and a single center study both suggest that approximately a third of patients present in the late (6-24 hour) time window, comparable to the number presenting in the early (<6 hour) window[1, 2]. This increased demand can pose a challenge for primary stroke centers, which often have limited resources and staffing, and lack around-the-clock neuroradiology expertise. This can result in the diagnosis of an LVO and patient transfer for treatment being delayed. Delay in patient transfer has been shown to be associated with worse outcomes[3]. Automated LVO detection tools may aide and expedite diagnosis, by prioritizing the study in a radiologist's worklist and drawing attention to the positive findings. Before the LVO detection tool can be deployed clinically and evaluated prospectively, to determine whether it expedites diagnosis and improves inter-hospital workflow, its diagnostic performance must be adequately assessed. The aim of this study was to assess the diagnostic performance of the algorithm at the optimal threshold in a patient cohort that is representative of the target population of LVO detection tools, and determine whether it has the high sensitivity and negative predictive value that are required of a screening tool. It was hypothesized that the algorithm could detect an LVO with a sensitivity of >90%, negative predictive value >95% and specificity >70%. The study is presented next, followed by a discussion of the findings and implications.

6.2 Publication

Amukotuwa SA, Straka M, Smith H, Chandra RV, Dehkharghani S, Fischbein NJ, Bammer R. Automated Detection of Intracranial Large Vessel Occlusions on Computed Tomography Angiography: A Single Center Experience. Stroke. 2019; 50(10):2790-2798.

6.3 Discussion

The LVO detection tool was tested in a cohort of consecutive patients presenting to a regional hospital who underwent emergent CTA for a suspected acute ischemic stroke as a part of a "code stroke" workup. 78 patients (16%) had an LVO. The diagnostic sensitivity for detection of LVOs in this cohort was 94%, negative predictive value was 97%, and specificity was 76%. When M2-segment MCA occlusions were included, sensitivity was 92% with a negative predictive value of 97% and specificity of 81%. The median processing time was 158 seconds (interquartile range 150-167 seconds). The high sensitivity and negative predictive value indicate that the algorithm can be used to screen for LVOs while the fast processing times make it suitable for use in the emergent setting.

A regional hospital cohort was selected for this study since this is the setting in which automated algorithms are most likely to be useful for improving diagnostic accuracy and efficiency of LVO detection. The population of patients who undergo CTA to screen for an LVO at such primary stroke centers is likely to be more heterogeneous, with a lower prevalence of LVOs, than at tertiary stroke centers. In an analysis of two tertiary hospitals in the United States, the prevalence of LVOs amongst acute ischaemic stroke patients screened with CTA was 51%, while it was much lower (26.5%) in a study from the Netherlands which pooled data from a number of tertiary (n=6) and primary stroke centres (n=8)[4, 5]. This is likely due to more experienced and specialized staff at tertiary hospitals allowing more refined patient triage.

Many regional and peripheral hospitals are now required to perform multimodal stroke CTs that include CTA, and provide fast and accurate interpretation of these studies so that patients with LVOs can be transferred without delay to a metropolitan hub that offers clot retrieval services. This poses a challenge for primary stroke centers, which have limited resources, especially after hours. An automated tool that draws attention to a positive finding would be value in this setting, to avoid situations where diagnosis of an LVO is delayed due to other emergent scans being prioritized ahead of the patient's CTA. The LVO detection tool may also be of value as a diagnostic aide to assist less experienced readers. Primary stroke centers in countries such as Australia are typically staffed by general radiologists; while the diagnostic sensitivity of neuroradiologists for detection of LVOs has been reported to be 94%-100%, which is comparable to that of the algorithm, the diagnostic performance of general radiologists is likely

lower[6, 7]. Diagnostic accuracy and confidence may therefore be improved by use an automated LVO detection tool for decision support.

A question which may be raised is whether the algorithm can be implemented at even smaller and more peripheral hospitals where automated LVO detection tools are likely to be of greatest value. CT technologist staff at these hospitals typically have less experience with acute stroke imaging and the CT scanners may be older and less sophisticated. Would the type of CT scanner and CTA acquisition affect the performance of the algorithm? This has in part been addressed by the previous study, where the algorithm was validated on CTAs acquired using a variety of CT scanners from different vendors. Since the algorithm was not developed using machine learning, it was already robust to scanner type and protocol variability, such as differences in scan timing and bolus size as well as duration. The two studies informed improvement of the algorithm, such as addition of a vessel tracker, that have made it even more robust. The software developers have in fact tested the algorithm and found that it performs accurately on CTAs acquired using the "Ceretom" Samsung CT scanner. This scanner is used to acquire mobile stroke CTs and has limited performance, with a rotation time of 2 seconds, limited tube output capacity, a detector width of 1 cm and just 8 detector rows. In my experience, scanner type does not lead to poor performance or failure of the algorithm.

CTA technique is, however, a cause of variability in algorithm performance. The timing of image acquisition relative to contrast injection is particularly important to ensure sufficient intracranial arterial opacification. Getting the timing right is dependent on the level of experience and skill of technologist staff, and is a potential obstacle to successful implementation of the algorithm at smaller hospitals. This can be addressed through education and training, which is routinely provided by the developers of the algorithm at the time of software installation at a hospital. The developers also help the hospital staff to set up the CTA protocol to ensure that image quality is sufficient to allow processing by the algorithm. A major strength of the algorithm that aids its implementation even in the most peripheral of hospitals is that it is fully automated, and does not require any staff input once the CTA is acquired. CTA data are automatically sent to a server for processing by the algorithm.

The limitations of the algorithm itself have already been discussed in the previous chapter. In the current study, the imperfect sensitivity resulted from five false negatives, which were encountered in cases where the inter-hemispheric difference

in vessel density was too small for the algorithm to detect at the optimal threshold. This included short segment and incomplete M1-segment MCA occlusions, where there was arterial opacification distal to the occlusion or stenosis, and ICA occlusions at the skull base where there was filling of the terminal ICA by cross flow from the contralateral side or via the posterior communicating segment. There were more false positives (n = 71) than negatives. This was mostly related to asymmetrical circle of Willis and MCA anatomy resulting from anatomical variants such as a unilateral large anterior temporal artery or unilateral posterior communicating segment. This cause of false positives may potentially be addressed using a machine learning approach where an LVO detection algorithm is trained using CTAs that have normal anatomical variants. Asymmetrical venous opacification was a remediable cause of false positives; this can be addressed by performing CTA prior to CTP to eliminate venous contamination.

The major limitation of this study is that it is retrospective. Using a retrospective cohort allowed the diagnostic performance of the algorithm to be evaluated. However, assessing the impact of the tool on workflow efficiency, which is where it is likely to be its greatest utility, requires a prospective study. Emphasis is increasingly placed on strategies and tools to improve intra- and inter-hospital workflow in order to reduce time to reperfusion, which is associated with better patient outcomes[8]. The high negative predictive value and fast processing times make the algorithm suitable for use as a screening tool for detection of LVOs. It can notify the reporting radiologist and treating stroke team or emergency physician of positive findings. Whether this enables the tool to streamline intra-hospital workflow and expedite diagnosis as well as treatment requires prospective evaluation. In the case of regional and peripheral hospitals, the tool can also be used to notify the nearest hub where thrombectomy is performed. This can potentially expedite treatment by activating transfer pathways and mobilizing the interventional neuroradiology team earlier. In order to determine whether the automated LVO detection tool can truly improve workflows both within and between hospitals, and improve patient outcomes, a multicenter prospective study that includes peripheral and regional “spoke” hospitals and a metropolitan thrombectomy hub is currently being planned. A further study is also required to evaluate the algorithm as a diagnostic support tool for less experienced readers, where the effect on diagnostic performance, confidence and speed of trainees and general radiologists is evaluated.

6.4 References

1. Jadhav AP, Desai SM, Kenmuir CL, Rocha M, Starr MT, Molyneaux BJ, et al. Eligibility for endovascular trial enrollment in the 6- to 24-hour time window: Analysis of a single comprehensive stroke center. *Stroke*. 2018;49:1015-1017

2. Majersik JJ, Smith MA, Zahuranec DB, Sanchez BN, Morgenstern LB. Population-based analysis of the impact of expanding the time window for acute stroke treatment. *Stroke*. 2007;38:3213-3217

3. Froehler MT, Saver JL, Zaidat OO, Jahan R, Aziz-Sultan MA, Klucznik RP, et al. Interhospital transfer before thrombectomy is associated with delayed treatment and worse outcome in the stratis registry (systematic evaluation of patients treated with neurothrombectomy devices for acute ischemic stroke). *Circulation*. 2017;136:2311-2321

4. Smith WS, Lev MH, English JD, Camargo EC, Chou M, Johnston SC, et al. Significance of large vessel intracranial occlusion causing acute ischemic stroke and tia. *Stroke*. 2009;40:3834-3840

5. van Seeters T, Biessels GJ, Kappelle LJ, van der Schaaf IC, Dankbaar JW, Horsch AD, et al. The prognostic value of ct angiography and ct perfusion in acute ischemic stroke. *Cerebrovasc Dis*. 2015;40:258-269

6. Becks MJ, Manniesing R, Vister J, Pegge SAH, Steens SCA, van Dijk EJ, et al. Brain ct perfusion improves intracranial vessel occlusion detection on ct angiography. *J Neuroradiol*. 2018

7. Lev MH, Farkas J, Rodriguez VR, Schwamm LH, Hunter GJ, Putman CM, et al. Ct angiography in the rapid triage of patients with hyperacute stroke to intraarterial thrombolysis: Accuracy in the detection of large vessel thrombus. *J Comput Assist Tomogr*. 2001;25:520-528

8. Saver JL, Goyal M, van der Lugt A, Menon BK, Majoie CB, Dippel DW, et al. Time to treatment with endovascular thrombectomy and outcomes from ischemic stroke: A meta-analysis. *JAMA*. 2016;316:1279-1288

Chapter 7

Cerebral Blood Flow Predicts the Infarct Core: New Insights from Contemporaneous Diffusion and Perfusion Imaging

7.1 Introduction

Once an anterior circulation large vessel occlusion has been identified in a patient presenting within the thrombectomy window, it is then important to determine whether they are likely to benefit from thrombectomy. A large infarct core reduces the likelihood of benefit from thrombectomy and increases the risk of symptomatic intracranial haemorrhage and malignant oedema[1, 2]. Patients with large infarct cores were therefore excluded from the thrombectomy trials[3-8]. In the late window, guidelines only recommend thrombectomy in patients with infarcts smaller than 50 mL (up to 24 hours) or 70 mL (up to 16 hours)[9]. Thrombectomy is also usually avoided in patients with large infarct cores in the early window. Accurate identification of patients with large infarcts is therefore important for treatment decision-making.

Magnetic resonance imaging (MRI) with DWI is regarded as the imaging gold standard for identifying infarcted brain tissue, with a reported sensitivity of up to 100%[10-13]. Since MRI is difficult to access in the emergent setting, CT is the mainstay of acute stroke imaging. Unfortunately, non-enhanced CT has a poor sensitivity for detection of early infarction and is fraught with high interrater variability due to the subjective nature of its interpretation, precluding reliable measurement of the infarct volume[14, 15].

CTP offers an alternative, objective method for measuring the size of the infarct core[16-19]. Both late window thrombectomy trials used either CTP (in the majority of cases) or MRI with DWI to exclude patients with large infarcts from treatment[3].

Guidelines therefore mandate the use of either CTP or MRI for assessment of the infarct size prior to thrombectomy in the late window[9]. In the early window, the two trials that showed the greatest magnitude of benefit from thrombectomy both used CTP to exclude patients with large infarcts (exceeding 50 mL or 70 mL) from treatment[5, 8]. Therefore, many stroke centres in Australia and the United States now perform CTP as standard-of-care in patients with a suspected acute ischemic stroke presenting within the thrombectomy window.

All four thrombectomy trials that used CTP for patient triage used a fully automated post-processing software, allowing rapid, reproducible and objective quantification of the infarct volume from CTP raw data[3, 5, 7, 8]. This eliminated the need for manual post-processing, which can introduce inter-observer variability and requires experienced staff who may not be available at peripheral "spoke" hospitals. It also avoided subjective assessment of infarct size based on visual inspection of NECT and perfusion maps, which can be fraught with large inter-observer variability and inaccuracy[20]. Automated infarct core measurement was based on reduction of *relative cerebral blood flow* (rCBF) below a preselected threshold of 0.30.

In this study, the accuracy of automated infarct volume measurement using severe rCBF reduction was evaluated against the reference standard of DWI. The purpose was to determine whether blood flow-based estimation of the infarct is sufficiently accurate for clinical triage of patients to thrombectomy: can it reliably distinguish patients with small infarct who are likely to benefit from treatment from those with large infarcts in whom reperfusion is likely to be futile and potentially harmful? The secondary aim was to determine the optimal rCBF threshold for infarct prediction.

The current study was motivated by a number of factors. Despite widespread clinical uptake, there remains controversy regarding the use of CTP for estimation of the infarct core. Some investigators have expressed concern that rCBF may not be an accurate surrogate of DWI, especially for triage decisions in individual patients[21, 22]. Further, the studies that validated rCBF reduction against DWI for measurement of the infarct core[17, 18, 23], and defined the optimal rCBF threshold, have some important methodological flaws that affect their validity. First, even in the most closely time matched analysis, there was a delay of up to 1 hour between DWI and CTP[18]. It has since been found that substantial infarct growth of up to 100 mL can occur in even this short time[24]. Second, the older CTP acquisitions that were used in these studies had limited brain coverage, precluding

analysis of the entire infarct. Third, patients with partial reperfusion, which indicates a major hemodynamic change such as distal clot migration, were included[18, 25]; blood flow at the time of imaging, even in the persistently hypoperfused area, may therefore no longer reflect the conditions that produced infarction. Due to these prior methodological limitations, and persisting doubt, there is need for further validation of automated infarct core measurement based on severe rCBF reduction.

Since publication of the two thrombectomy trials that utilized CTP for patient triage, it has been difficult to divert treatment-eligible patients to MRI for the purposes of a study. An alternative, novel approach was therefore required to assess the accuracy of blood flow-derived infarct core measurements: DWI was compared with rCBF derived from nearly perfectly temporally and volumetrically matched MR perfusion data instead of CTP. Like CTP, *dynamic susceptibility contrast perfusion weighted imaging* (DSC-PWI) is a bolus perfusion technique. The same principles of indicator dilution theory can therefore be applied to obtain CBF, and hemispheric normalization eliminates technique-related differences that apply to absolute quantification[26]. Use of MR perfusion avoided the time delays arising from patient transfer between CT and MRI. The greater brain coverage of DSC-PWI allowed the entire infarct to be imaged, hence included in analysis. The software algorithm was tuned to account for differences between CTP and DSC-PWI.

The study was performed in a cohort of 119 *acute ischemic stroke* (AIS) patients who presented within the thrombectomy window, had an anterior circulation intracranial arterial occlusion, and had undergone acute MRI with both DWI and DSC-PWI. 97 patients were from DEFUSE 2 (*Diffusion and Perfusion Imaging Evaluation for Understanding Stroke Evolution 2*), a multi-centre prospective cohort study. The other 22 patients were enrolled as a part of this PhD; these patients underwent acute MRI instead of CT with CTP due to either presentation beyond the early time window or an iodinated contrast allergy. The outcomes studied were the spatial and volumetric accuracy of infarct core measurements obtained using rCBF, and the percentage of patients who were correctly triaged to thrombectomy based on rCBF reduction. It was hypothesized that rCBF can reliably distinguish patients with large infarcts from those with small infarcts. The optimal rCBF threshold for predicting infarction was hypothesized to be lower than that previously reported, since more closely time data minimized the confounding effects of infarct growth between diffusion and perfusion imaging.

7.2 Publication

Amukotuwa S, Straka M, Aksoy D, Fischbein N, Desmond P, Albers G, Bammer R. Cerebral Blood Flow Predicts the Infarct Core: New Insights From Contemporaneous Diffusion and Perfusion Imaging. Stroke. 2019;50(10):2783-2789

7.3 Discussion

In this study, the accuracy of severely reduced rCBF as a surrogate of the infarct core was evaluated in a cohort of 119 AIS patients who were prospectively enrolled. Both spatially non-discriminative volumetric agreement and voxel-based spatial agreement between rCBF and the reference standard of DWI were assessed. Strong correlation (r >0.9) and agreement were found between infarct volume estimates obtained using rCBF reduction and DWI. Spatial agreement was better for prediction of large infarcts (>70 mL) than small infarcts (≤70 mL). The optimal rCBF threshold was found to be 0.32, which closely approximates the threshold of 0.30 used in the thrombectomy trials. At this threshold, 110/119 (92.4%) patients were correctly triaged when applying 70 mL as the volume cut-off for thrombectomy. This suggests that automated measurement of the infarct core using rCBF is reliable for identifying patients with large infarcts and can therefore be used for individual patient triage decisions in clinical practice.

Volumetric agreement between infarct core measurements obtained using rCBF and DWI was assessed using both linear correlation and Bland-Altman analyses. The latter was used since it allows detection of a fixed bias[27]. The mean volume difference was found to be small (1.9 mL), and there was no fixed bias between infarct volume measurements obtained using DWI and rCBF reduction at the optimal threshold of 0.32. However, like in previous studies, the measurement variability was high. For the optimal rCBF threshold of 0.32, the limits of agreement were +/-55.3 mL, which is similar to previously reported values of 40-56.7 mL[22, 25, 28]. This high measurement variability indicates that there is a wide range within which the infarct volume measured using rCBF can fall in an individual patient. The authors of one previous study concluded that this measurement variability is too high to allow CTP to replace MR-DWI for measurement of the infarct core, particularly if thrombectomy is deemed harmful to patients with an infarct larger than a certain threshold[22]. This concern was specifically addressed in our study. Using 70 mL as the volume cut-off for thrombectomy, the number of patients who were incorrectly categorized as having a large infarct using rCBF was determined. At the optimal threshold of 0.32, 110/119 (92.4%) of patients correctly categorized, with only 2/119 (1.7%) false negatives when applying a 70 mL as the volume limit for thrombectomy. Therefore, despite the large measurement variability, rCBF was able to reliably detect and exclude individual patients with large infarcts from thrombectomy.

Spatial agreement between DWI and rCBF for delineation of the infarct core was also assessed, using the previously described method of voxel-based receiver operating characteristic (ROC) analysis[29]. Prior studies that have assessed perfusion-derived parameters against DWI also used either this technique or a similar objective ROC method[17-19]. Analysis was confined to the region of hypoperfusion (*Tmax* >4 seconds). The status of each voxel (infarcted or non-infarcted) on DWI served as the reference standard against which its status on rCBF was assessed. A new finding that emerged from the voxel-based analysis in this study was that rCBF reduction is more accurate for predicting large infarcts (>70 mL) than small infarcts (≤70 mL), with Youden indices of 0.53 ($CI_{95\%}$ 0.49-0.56) and 0.34 ($CI_{95\%}$ 0.30-0.37) respectively. While the sensitivity for predicting DWI positive voxels was only moderate (0.54) when all patients were considered, it was higher (0.76) in patients with infarcts larger than 70 mL. Sensitivity for detecting infarcted tissue is more clinically relevant in patients with large infarcts, to avoid infarct underestimation that would lead to futile and potentially harmful reperfusion. Although there is a push to perform thrombectomy in patients with large infarcts, a recent study found that the likelihood of functional independence following treatment decreased markedly with increasing infarct size (approximately 40% for every 10 mL)[30]. Additionally, no patient with an infarct volume exceeding 100 mL had a favourable outcome[30]. Detecting large infarcts with high sensitivity and quantifying them accurately therefore remains of high clinical relevance. Conversely, in patients with small infarcts, specificity is more important to avoid overestimating the area of infarction since this can result in potentially beneficial treatment being withheld. In this group, specificity was found to be high (0.91).

On both spatial and volumetric analyses, the optimal rCBF threshold for measuring the infarct was found to be 0.32, which closely approximates the threshold of 0.30 used in the thrombectomy trials. As hypothesized, this was lower than the optimal thresholds of 0.38 and 0.40 previously reported for the same post-processing algorithm[18, 25]. This difference may be explained by the shorter latency between diffusion and perfusion imaging in our study with a median time difference of 9 minutes compared to 36 minutes and 27 minutes in these prior studies.

A difference between our analysis and prior studies was the way in which the infarct core was segmented on DWI. Instead of manual outlining of the visible DWI lesion, automated segmentation was performed applying an ADC threshold of 620×10^{-6} mm^2/sec. The infarct therefore constituted voxels with an ADC falling below this value, which has been found to be the optimal for predicting irreversible tissue injury[12, 31]. Milder ADC reduction can occur in reversibly injured tissue,

which would be misclassified as infarcted on manual segmentation because they appear bright on the DWI trace images. To avoid this pitfall, as well as subjectivity and variability related to manual outlining, automated segmentation was used. In addition to being objective and reproducible, automated segmentation is also the practical "real-world" reference standard, since this is the way in which the patient's infarct core would be measured on DWI in clinical practice.

Another point of distinction between our study and prior work is that DWI was compared with rCBF derived from DSC-PWI rather than CTP. The use of normalization minimized any discrepancy related to absolute quantification. It is conceivable that pial vessel blooming on DSC-PWI may have caused cortical blood flow underestimation secondary to partial volume effects, a potential confounder. However, this is counter-balanced by the strong spatial filtering needed for CTP, which is comparable to the far-field effects of PWI. In fact, a prior study comparing CTP-derived perfusion parameters with MR-PWI showed equivalence of volume measurements obtained using rCBV, while another study showed only a small difference in infarct volumes obtained using rCBF[32, 33].

Although this study shows that rCBF reduction at the optimal threshold can be used to reliably detect patients with large infarct cores, blood flow-based estimation of the infarct core has some important limitations that result in the measurement variability seen on Bald-Altman analysis as well as imperfect sensitivity and specificity on assessment of spatial agreement. While DWI interrogates the cellular changes resulting from tissue injury, blood flow imaging attempts to predict tissue fate by measuring the causative agent of tissue damage[11, 34]. Since irreversible tissue injury is a product of both the severity and duration of blood flow reduction, severe CBF reduction at a given time point provides only a "snapshot" of hemodynamic derangement which may not necessarily be an accurate surrogate of infarction[35]. For example, areas with infarction that have either restored or improved blood flow will not be detected using severe rCBF reduction, resulting in underestimation of the infarct volume. Conversely, the infarct core may be overestimated in patients with a short duration of severe blood flow reduction, causing them to be excluded from beneficial treatment. In one study, the absolute and relative CBF thresholds that predicted infarction were both found to be lower in patients who underwent CTP within 180 minutes of stroke onset and were reperfused within 90 minutes of the CTP[36]. The optimal CBF and rCBF threshold for predicting infarction increased with both the duration

since stroke onset and the time from imaging to reperfusion. A lower rCBF threshold is therefore likely be required to accurately predict infarcted tissue in patients who are imaged in the hyperacute time-window (within 180 minutes of stroke onset) and rapidly reperfused[36]. Unfortunately, the number of patients imaged and treated in the hyperacute time window in our study was too small to allow adequately powered analysis of the optimal rCBF threshold in this group. We are likely to see more patients in this time window, as community awareness regarding acute stroke increases and triage strategies in the emergency department and field improve. Therefore, studies that specifically address the question of the optimal threshold in different time windows are required.

There are several other potential sources of inaccuracy when measuring the infarct core using reduced rCBF. First, reduced rCBF cannot discriminate between acutely infarcted tissue and leukoaraiosis[18, 37]. The impact of leukoaraiosis can be attenuated by constraining infarct core prediction to the area of hypoperfusion using a Tmax mask. However, chronically ischaemic white matter within this area will still be included, resulting in infarct core overestimation. This was evident on post hoc analysis (presented in the supplemental material), which showed the burden of leukoaraiosis to be significantly higher in patients with infarct core overestimation using the optimal rCBF threshold. Partial volume effects related to pial vessels can cause cortical rCBF to be overestimated, in turn causing infarct core underestimation[18]. The algorithm used in this study segments out pial vessels, mitigating these partial volume effects. Use of a global rCBF threshold can also result in inaccurate estimation of the infarct, since grey and white matter have different normal rCBF values and sensitivity to blood flow reduction[38]. While a potential solution is to use tissue-specific thresholds, this is challenging to implement because it requires segmentation of grey and white matter, which can be problematic on CT, especially in patients with cerebral atrophy.

An important limitation of using rCBF to estimate the infarct core is that the optimal threshold is dependent upon the software algorithm that is used for perfusion post-processing[18, 19, 23, 25]. There is large variation between the different post-processing algorithms, with differences including the whether or not deconvolution is used, the specific type of deconvolution and filters to name a few. This leads not only to variability in the optimal threshold but also the optimal perfusion parameter for infarct prediction. The two early window trials that used CTP for patient selection, and both late-window trials, all used the same CTP post-processing software[3, 5, 7, 8]. This ensured consistency of data within each trial, and comparability between trials. The current study used the same post-processing

algorithm. There are several other post-processing software packages that are in clinical use[39]. Unfortunately, the optimal perfusion parameter and threshold has not been determined and validated for all of these packages. Applying an rCBF threshold of 0.30 or 0.32 to these other algorithms may result in incorrect calculation of the infarct size. Standardization is therefore of critical importance given that these other CTP post-processing algorithms are used for clinical patient triage. Standardization strategies include the use of data phantoms, which allow validation of post-processing algorithms, and calibration datasets [25, 40].

This study itself has some limitations. rCBF was the only parameter that was assessed, and absolute values as well as reduced relative cerebral blood volume were not considered. This was justified by previous studies that used either the same or similar software algorithms that found rCBF to be the optimal parameter for predicting infarction[17, 18, 25]. Additionally, cerebral blood volume is particularly prone to underestimation in the setting of delayed arrival of blood, as occurs within ischemic areas. Another potential limitation of this study is the use of DWI as the reference standard. The acute DWI lesion may reverse following reperfusion, particularly following thrombectomy[10, 41, 42]. Although this has been described as transient, there is some evidence that this DWI reversal may be more frequent and substantial than previously thought in patients who are reperfused within 3 hours of stroke onset and in those who undergo early thrombectomy[41, 43-45]. DWI reversal was previously evaluated in patients enrolled in DEFUSE 2, who constituted 82% of our study cohort[43]. Only 2 patients were found to have DWI reversal, therefore it is unlikely that this had a significant impacted on the findings of the current study.

7.4 References

1. Lansberg MG, Straka M, Kemp S, Mlynash M, Wechsler LR, Jovin TG, et al. Mri profile and response to endovascular reperfusion after stroke (defuse 2): A prospective cohort study. *Lancet Neurol*. 2012;11:860-867

2. Olivot JM, Mosimann PJ, Labreuche J, Inoue M, Meseguer E, Desilles JP, et al. Impact of diffusion-weighted imaging lesion volume on the success of endovascular reperfusion therapy. *Stroke*. 2013;44:2205-2211

3. Albers GW, Marks MP, Kemp S, Christensen S, Tsai JP, Ortega-Gutierrez S, et al. Thrombectomy for stroke at 6 to 16 hours with selection by perfusion imaging. *N Engl J Med*. 2018;378:708-718

4. Berkhemer OA, Fransen PS, Beumer D, van den Berg LA, Lingsma HF, Yoo AJ, et al. A randomized trial of intraarterial treatment for acute ischemic stroke. *N Engl J Med*. 2015;372:11-20

5. Campbell BC, Mitchell PJ, Kleinig TJ, Dewey HM, Churilov L, Yassi N, et al. Endovascular therapy for ischemic stroke with perfusion-imaging selection. *N Engl J Med*. 2015;372:1009-1018

6. Goyal M, Demchuk AM, Menon BK, Eesa M, Rempel JL, Thornton J, et al. Randomized assessment of rapid endovascular treatment of ischemic stroke. *N Engl J Med*. 2015;372:1019-1030

7. Nogueira RG, Jadhav AP, Haussen DC, Bonafe A, Budzik RF, Bhuva P, et al. Thrombectomy 6 to 24 hours after stroke with a mismatch between deficit and infarct. *N Engl J Med*. 2018;378:11-21

8. Saver JL, Goyal M, Bonafe A, Diener HC, Levy EI, Pereira VM, et al. Stent-retriever thrombectomy after intravenous t-pa vs. T-pa alone in stroke. *N Engl J Med*. 2015;372:2285-2295

9. Powers WJ, Rabinstein AA, Ackerson T, Adeoye OM, Bambakidis NC, Becker K, et al. 2018 guidelines for the early management of patients with acute ischemic stroke: A guideline for healthcare professionals from the american heart association/american stroke association. *Stroke*. 2018;49:e46-e110

10. Campbell BC, Purushotham A, Christensen S, Desmond PM, Nagakane Y, Parsons MW, et al. The infarct core is well represented by the acute diffusion lesion: Sustained reversal is infrequent. *J Cereb Blood Flow Metab*. 2012;32:50-56

11. Gill R, Sibson NR, Hatfield RH, Burdett NG, Carpenter TA, Hall LD, et al. A comparison of the early development of ischaemic damage following permanent middle cerebral artery occlusion in rats as assessed using magnetic resonance imaging and histology. *J Cereb Blood Flow Metab.* 1995;15:1-11

12. Wheeler HM, Mlynash M, Inoue M, Tipirneni A, Liggins J, Zaharchuk G, et al. Early diffusion-weighted imaging and perfusion-weighted imaging lesion volumes forecast final infarct size in defuse 2. *Stroke.* 2013;44:681-685

13. Gonzalez RG, Schaefer PW, Buonanno FS, Schwamm LH, Budzik RF, Rordorf G, et al. Diffusion-weighted mr imaging: Diagnostic accuracy in patients imaged within 6 hours of stroke symptom onset. *Radiology.* 1999;210:155-162

14. Chalela JA, Kidwell CS, Nentwich LM, Luby M, Butman JA, Demchuk AM, et al. Magnetic resonance imaging and computed tomography in emergency assessment of patients with suspected acute stroke: A prospective comparison. *Lancet.* 2007;369:293-298

15. Maegerlein C, Fischer J, Monch S, Berndt M, Wunderlich S, Seifert CL, et al. Automated calculation of the alberta stroke program early ct score: Feasibility and reliability. *Radiology.* 2019;291:141-148

16. Bivard A, Levi C, Spratt N, Parsons M. Perfusion ct in acute stroke: A comprehensive analysis of infarct and penumbra. *Radiology.* 2013;267:543-550

17. Bivard A, McElduff P, Spratt N, Levi C, Parsons M. Defining the extent of irreversible brain ischemia using perfusion computed tomography. *Cerebrovasc Dis.* 2011;31:238-245

18. Campbell BC, Christensen S, Levi CR, Desmond PM, Donnan GA, Davis SM, et al. Cerebral blood flow is the optimal ct perfusion parameter for assessing infarct core. *Stroke.* 2011;42:3435-3440

19. Wintermark M, Flanders AE, Velthuis B, Meuli R, van Leeuwen M, Goldsher D, et al. Perfusion-ct assessment of infarct core and penumbra: Receiver operating characteristic curve analysis in 130 patients suspected of acute hemispheric stroke. *Stroke.* 2006;37:979-985

20. Dehkharghani S, Bammer R, Straka M, Albin LS, Kass-Hout O, Allen JW, et al. Performance and predictive value of a user-independent platform for ct perfusion analysis: Threshold-derived automated systems outperform

examiner-driven approaches in outcome prediction of acute ischemic stroke. *AJNR Am J Neuroradiol*. 2015;36:1419-1425

21. Copen WA, Yoo AJ, Rost NS, Morais LT, Schaefer PW, Gonzalez RG, et al. In patients with suspected acute stroke, ct perfusion-based cerebral blood flow maps cannot substitute for dwi in measuring the ischemic core. *PLoS One*. 2017;12:e0188891

22. Schaefer PW, Souza L, Kamalian S, Hirsch JA, Yoo AJ, Kamalian S, et al. Limited reliability of computed tomographic perfusion acute infarct volume measurements compared with diffusion-weighted imaging in anterior circulation stroke. *Stroke*. 2015;46:419-424

23. Kamalian S, Kamalian S, Maas MB, Goldmacher GV, Payabvash S, Akbar A, et al. Ct cerebral blood flow maps optimally correlate with admission diffusion-weighted imaging in acute stroke but thresholds vary by postprocessing platform. *Stroke*. 2011;42:1923-1928

24. Albers GW. Late window paradox. *Stroke*. 2018;49:768-771

25. Cereda CW, Christensen S, Campbell BC, Mishra NK, Mlynash M, Levi C, et al. A benchmarking tool to evaluate computer tomography perfusion infarct core predictions against a dwi standard. *J Cereb Blood Flow Metab*. 2016;36:1780-1789

26. Meier P, Zierler KL. On the theory of the indicator-dilution method for measurement of blood flow and volume. *J Appl Physiol*. 1954;6:731-744

27. Bland JM, Altman DG. Statistical methods for assessing agreement between two methods of clinical measurement. *Lancet*. 1986;1:307-310

28. Mokin M, Levy EI, Saver JL, Siddiqui AH, Goyal M, Bonafe A, et al. Predictive value of rapid assessed perfusion thresholds on final infarct volume in swift prime (solitaire with the intention for thrombectomy as primary endovascular treatment). *Stroke*. 2017;48:932-938

29. Christensen S, Mouridsen K, Wu O, Hjort N, Karstoft H, Thomalla G, et al. Comparison of 10 perfusion mri parameters in 97 sub-6-hour stroke patients using voxel-based receiver operating characteristics analysis. *Stroke*. 2009;40:2055-2061

30. Sarraj A, Hassan AE, Savitz S, Sitton C, Grotta J, Chen P, et al. Outcomes of endovascular thrombectomy vs medical management alone in patients with large ischemic cores: A secondary analysis of the optimizing patient's

selection for endovascular treatment in acute ischemic stroke (select) study. *JAMA Neurol*. 2019

31. Purushotham A, Campbell BC, Straka M, Mlynash M, Olivot JM, Bammer R, et al. Apparent diffusion coefficient threshold for delineation of ischemic core. *Int J Stroke*. 2015;10:348-353

32. Lin L, Bivard A, Levi CR, Parsons MW. Comparison of computed tomographic and magnetic resonance perfusion measurements in acute ischemic stroke: Back-to-back quantitative analysis. *Stroke*. 2014;45:1727-1732

33. Schramm P, Schellinger PD, Klotz E, Kallenberg K, Fiebach JB, Kulkens S, et al. Comparison of perfusion computed tomography and computed tomography angiography source images with perfusion-weighted imaging and diffusion-weighted imaging in patients with acute stroke of less than 6 hours' duration. *Stroke*. 2004;35:1652-1658

34. Olsen TS. Regional cerebral blood flow after occlusion of the middle cerebral artery. *Acta Neurol Scand*. 1986;73:321-337

35. Kohno K, Hoehn-Berlage M, Mies G, Back T, Hossmann KA. Relationship between diffusion-weighted mr images, cerebral blood flow, and energy state in experimental brain infarction. *Magn Reson Imaging*. 1995;13:73-80

36. d'Esterre CD, Boesen ME, Ahn SH, Pordeli P, Najm M, Minhas P, et al. Time-dependent computed tomographic perfusion thresholds for patients with acute ischemic stroke. *Stroke*. 2015;46:3390-3397

37. Markus HS, Lythgoe DJ, Ostegaard L, O'Sullivan M, Williams SC. Reduced cerebral blood flow in white matter in ischaemic leukoaraiosis demonstrated using quantitative exogenous contrast based perfusion mri. *J Neurol Neurosurg Psychiatry*. 2000;69:48-53

38. Bristow MS, Simon JE, Brown RA, Eliasziw M, Hill MD, Coutts SB, et al. Mr perfusion and diffusion in acute ischemic stroke: Human gray and white matter have different thresholds for infarction. *J Cereb Blood Flow Metab*. 2005;25:1280-1287

39. Vagal A, Wintermark M, Nael K, Bivard A, Parsons M, Grossman AW, et al. Automated ct perfusion imaging for acute ischemic stroke: Pearls and pitfalls for real-world use. *Neurology*. 2019

40. Kudo K, Christensen S, Sasaki M, Ostergaard L, Shirato H, Ogasawara K, et al. Accuracy and reliability assessment of ct and mr perfusion analysis software using a digital phantom. *Radiology*. 2013;267:201-211

41. Chemmanam T, Campbell BC, Christensen S, Nagakane Y, Desmond PM, Bladin CF, et al. Ischemic diffusion lesion reversal is uncommon and rarely alters perfusion-diffusion mismatch. *Neurology*. 2010;75:1040-1047

42. Labeyrie MA, Turc G, Hess A, Hervo P, Mas JL, Meder JF, et al. Diffusion lesion reversal after thrombolysis: A mr correlate of early neurological improvement. *Stroke*. 2012;43:2986-2991

43. Inoue M, Mlynash M, Christensen S, Wheeler HM, Straka M, Tipirneni A, et al. Early diffusion-weighted imaging reversal after endovascular reperfusion is typically transient in patients imaged 3 to 6 hours after onset. *Stroke*. 2014;45:1024-1028

44. Soize S, Tisserand M, Charron S, Turc G, Ben Hassen W, Labeyrie MA, et al. How sustained is 24-hour diffusion-weighted imaging lesion reversal? Serial magnetic resonance imaging in a patient cohort thrombolyzed within 4.5 hours of stroke onset. *Stroke*. 2015;46:704-710

45. Yoo J, Choi JW, Lee SJ, Hong JM, Hong JH, Kim CH, et al. Ischemic diffusion lesion reversal after endovascular treatment. *Stroke*. 2019;50:1504-1509

Chapter 8

Comparison of T2*GRE and DSC-PWI for Hemorrhage Detection in Acute Ischemic Stroke Patients: Pooled Analysis of the EPITHET, DEFUSE 2 and SENSE 3 Stroke Studies

8.1 Introduction

MRI is used to guide treatment decisions in acute ischemic stroke patients in Europe, Asia and some centres in North America due to the unparalleled sensitivity and specificity of DWI for detecting infarction, and the limitations of CT perfusion identified in the previous study[1]. At the time this study was conceived, MRI was routinely used to evaluate acute ischemic patients who were being considered for thrombectomy at the centre where the study was performed. A draw-back of MRI is that it is more time-consuming than CT. Given that acute ischemic stroke is a time-critical emergency, with a limited therapeutic window, effort is made to keep the MR protocol as short as possible by performing only the sequences that are required for clinical decision making[2, 3]. A strong motivator for this study was to shorten the MRI protocol for the DEFUSE 3 study, which was in its implementation phase at the time this study was commenced.

Acute intracranial haemorrhage contraindicates thrombolytic therapies[4]. Its detection is therefore critical in acute ischemic stroke patients being considered for intravenous thrombolysis. MRI sequences such as 2D and 3D *gradient-recalled echo* (GRE) imaging and *GRE echo-planar imaging EPI* (GRE-EPI) are T_2*-weighted, allowing detection of even small amounts of paramagnetic blood product[5-8]. The mainstay of MR-based haemorrhage detection is conventional T_2*-

weighted GRE (T_2*GRE). Unfortunately, T_2*GRE is one of the slowest sequences in the acute stroke MR protocol, adding 2-3 minutes to scan duration; this potentially delays treatment and increases the likelihood of clinically significant patient motion. "Fast GRE" haemorrhage screening sequences, that use either a single-shot or multi-shot EPI readout to accelerate image acquisition and can be performed in under 1 minute, have been developed to address this limitation.

Another T_2*-weighted sequence that is included in the acute stroke MR protocol at some centres, to delineate tissue at risk of infarction, is dynamic susceptibility contrast perfusion-weighted imaging (DSC-PWI). Most clinical DSC-PWI implementations are GRE sequences that use a single-shot EPI readout. The baseline DSC-PWI images, acquired prior to arrival of contrast agent, are therefore similar to "fast GRE" sequences that use a single-shot EPI readout, with similar T_2*-weighting.

The aim of this study was to assess whether baseline DSC-PWI images can be used for haemorrhage screening in acute ischaemic stroke, based on evaluation of the baseline and follow-up MRIs of acute ischaemic stroke patients. The strength of agreement between baseline DSC-PWI and conventional T_2*GRE for detection of intracranial haemorrhage, and more specifically acute haemorrhagic transformation, was evaluated on 393 MRI scans from a large cohort of 221 patients enrolled in 3 prospective stroke studies. A cohort of acute ischemic stroke patients was selected since this is the target population for haemorrhage screening using DSC-PWI.

Excellent agreement between T_2*GRE and baseline DSC-PWI for the presence of haemorrhage was hypothesized. This hypothesis was based on the T_2*-weighting of DSC-PWI, which was anticipated to result in high conspicuity of even a small amount of paramagnetic blood product despite its lower spatial resolution. If this hypothesis is correct, conventional T_2*GRE or an alternative dedicated haemorrhage-specific sequence can be omitted from the acute MR stroke protocol when DSC-PWI is included, shortening the acquisition time and making it competitive with that of CT.

8.2 Publication

Amukotuwa SA, Fischbein NJ, Albers GW, Davis S, Donnan GA, Andre JB, Bammer R. Comparison of T2*GRE and DSC-PWI for hemorrhage detection in acute ischemic stroke patients: Pooled analysis of the EPITHET, DEFUSE 2, and SENSE 3 stroke studies. Int J Stroke. 2020;15(2):216-225

Research

International Journal of Stroke WSO

International Journal of Stroke
0(0) 1–10

DOI: 10.1177/1747493019858781
journals.sagepub.com/home/wso
SAGE

Comparison of T2*GRE and DSC-PWI for hemorrhage detection in acute ischemic stroke patients: Pooled analysis of the EPITHET, DEFUSE 2, and SENSE 3 stroke studies

Shalini A Amukotuwa[1,2], Nancy J Fischbein[3], Gregory W Albers[4], Stephen Davis[5], Geoffrey A Donnan[6], Jalal B Andre[7] and Roland Bammer[3,6]

Abstract

Aims: The objective of this study was to compare the diagnostic performance of the baseline pre-contrast images of dynamic susceptibility contrast perfusion-weighted imaging (DSC-PWI) with conventional T2*gradient recalled echo (GRE) imaging for detection of hemorrhage in acute ischemic stroke patients.

Material and methods: T2*GRE and DSC-PWI from 393 magnetic resonance imaging scans from 221 patients enrolled in three prospective stroke studies were independently evaluated by two readers blinded to clinical and other imaging data. Agreement between T2*GRE and DSC-PWI for the presence of hemorrhage, and acute hemorrhagic transformation, was assessed using the kappa statistic. Inter-reader agreement was also assessed using the kappa statistic.

Results: Agreement between the baseline images of DSC-PWI and T2*GRE regarding the presence of hemorrhage was almost perfect ($k_{reader\,1}$: 0.90, 95% confidence interval 0.86–0.95 and $k_{reader\,2}$: 0.91, 95% confidence interval 0.87–0.96). Agreement between the sequences was still higher for detection of acute hemorrhagic transformation ($k_{reader\,1}$: 0.94, 95% confidence interval 0.91–0.98 and $k_{reader\,2}$: 0.95, 95% confidence interval 0.92–0.98). Inter-reader agreement for detection of hemorrhage was also almost perfect for both T2*GRE (k: 0.95, 95% confidence interval 0.91–0.98) and DSC-PWI (k: 0.96, 95% confidence interval 0.93–0.99). Acute hemorrhagic transformation detected on T2*GRE was missed on DSC-PWI by one or both readers in 5/393 (1.3%) scans.

Conclusion: The almost perfect statistical agreement between DSC-PWI and conventional T2*GRE suggests that DSC-PWI is sufficient for hemorrhage screening prior to thrombolysis in stroke patients. T2*GRE can therefore be omitted when DSC-PWI is included, thereby shortening the acute ischemic stroke magnetic resonance imaging protocol and expediting treatment.

Trial registration: ClinicalTrials.gov Identifier: NCT02586415.

Keywords

Brain bleed, brain microbleeds, cerebral hemorrhage, cerebral infarction, magnetic resonance imaging, stroke

Received: 18 February 2019; accepted: 12 May 2019

Introduction

Acute intracranial hemorrhage is a contraindication to thrombolytic therapies in acute ischemic stroke (AIS) patients.[1] Its detection is therefore crucial but must be

[1]Department of Radiology, University of Melbourne, Melbourne, Victoria, Australia
[2]Monash Imaging, Monash Health, Clayton, Victoria, Australia
[3]Department of Radiology, Stanford University, Stanford, CA, USA
[4]Stanford Stroke Center, Stanford University School of Medicine, Stanford, CA, USA
[5]Department of Neurology, University of Melbourne, Parkville, Victoria, Australia
[6]Florey Department of Neuroscience and Mental Health, University of Melbourne, Parkville, Victoria, Australia
[7]Department of Radiology and Imaging Services, University of Washington Medical Center, Seattle, WA, USA

Corresponding author:
Shalini A Amukotuwa, Department of Radiology, University of Melbourne, Melbourne, Victoria 3052, Australia.
Email: samukotuwa@gmail.com

balanced against the need for rapid treatment in order to salvage hypoperfused brain tissue.

Although less widely accessible than computed tomography (CT), magnetic resonance imaging (MRI) is the first-line imaging modality in acute stroke at some centers because of its unparalleled sensitivity for delineation of the infarct core using diffusion-weighted imaging (DWI).[2] MRI is also more sensitive than CT for detection of intracerebral hemorrhage.[3,4] Gradient recalled echo (GRE) and echo-planar imaging (EPI) techniques are sensitive to local magnetic field inhomogeneity and produce images that are T2*-weighted, allowing detection of even small amounts of paramagnetic blood product.[3,5–7] Conventional T2*-weighted GRE (T2*GRE) is the mainstay of hemorrhage detection in AIS.

Dynamic susceptibility contrast perfusion-weighted imaging (DSC-PWI) may be included in the acute stroke MRI protocol for the identification of critically hypoperfused tissue.[8,9] Although opinion is divided on the need for penumbral imaging, a substantially higher rate of good functional outcome was observed in the early window thrombectomy trials that used perfusion imaging to identify salvageable brain tissue.[10–13] In the late time window, perfusion imaging is requisite when applying the Diffusion and Perfusion Imaging Evaluation for Understanding Stroke Evolution (DEFUSE) 3 criteria.[14]

Since stroke is a time critical emergency, effort is made to limit the MRI scan duration by including only those sequences that are necessary for clinical decision-making.[9,15] Long scan duration delays treatment and increases the likelihood of clinically significant patient motion and premature scan termination. Unfortunately, conventional T2*GRE is one of the slowest and most motion-sensitive sequences in the acute stroke protocol, adding 2 3 min to scan time. To address this, "fast GRE" hemorrhage screening sequences, which can be performed in under 60 s, have been developed.[9,14–16] These utilize a single-shot EPI (SS-EPI) readout to accelerate image acquisition, resulting in greater image distortion, blurring, and susceptibility artifacts as well as lower signal-to-noise ratio in comparison with conventional T2*GRE.[6,17,18] Despite these drawbacks, there is little validation of "fast GRE" sequences against conventional T2*GRE in patients with AIS and hemorrhage.[9,16] They are also often unavailable at peripheral and smaller hospitals that manage stroke patients.

DSC-PWI and DWI are both widely available sequences that utilize an EPI readout and are therefore inherently T2*-weighted. Diffusion-weighted spin-echo EPI sequences have been found to be inadequate for hemorrhage screening in stroke patients, with sensitivity for detection of acute hemorrhagic transformation as low as 54%.[5–7] Unlike DWI, DSC-PWI sequences typically use GRE magnetization preparation. The baseline ("snapshot") images of DSC-PWI, acquired prior to arrival of contrast agent, are therefore similar to the "fast GRE" sequences used in rapid stroke MRI protocols, with similar T2*-contrast but lower spatial resolution.[9,14,16] Whether the baseline DSC-PWI images (acquired prior to contrast agent arrival) are sufficient for hemorrhage screening in acute stroke patients has not been previously investigated.

Aim and hypothesis

The aim of this study is to determine the strength of agreement between baseline DSC-PWI images and conventional T2*GRE for detection of intracranial hemorrhage, and more specifically acute hemorrhagic transformation, in AIS patients. We hypothesize excellent agreement.

Methods

Study design and patient population

All 693 MRI scans from three large prospective stroke studies DEFUSE 2,[8] Echoplanar Imaging Thrombolytic Evaluation Trial (EPITHET),[19] and SENSitivity Encoding 3 (SENSE 3) were screened to identify scans that had both a T2*GRE sequence and a GRE-EPI-based DSC-PWI sequence. All three trials had institutional review board approval obtained at each trial site and were HIPAA compliant.

DEFUSE 2 and EPITHET study design and patient selection criteria have been previously published.[8,19] Briefly, these trials evaluated the benefit of reperfusion in AIS patients with a mismatch between DWI and DSC-PWI.[8,19] Enrollment dates were 2001 2007 (EPITHET) and 2008 2011 (DEFUSE 2).

SENSE 3 (enrollment 2014 2017) was a National Institutes of Health-sponsored randomized study performed at a single stroke referral center in the United States that evaluated MR and CT perfusion imaging techniques for predicting acute stroke evolution. All consecutively presenting patients with a clinical diagnosis of acute stroke were screened. Written informed consent was provided by enrolled patients or their surrogates. Patients were enrolled if they met the following clinical and imaging eligibility requirements: a clinical diagnosis of AIS, age over 18 years, and no contraindication to undergoing MRI or receiving gadolinium-based contrast agent.

MRI technique

Since multiple sites were involved over a span of 16 years, T2*GRE and DSC-PWI techniques were

variable. Typical scan parameters are given in Table 1. The acquisition time for T2*GRE was 2:30 5:00 min.

Image analysis

Two neuroradiologists (6 and 10 years experience, respectively) were blinded to all clinical information, the timing of the MRI relative to stroke onset, and the patient's other scans. The anonymized MRIs were presented in randomized order. T2*GRE and baseline DSC-PWI were read in separate sittings, two weeks apart, to avoid recall bias. DWI (including the b = 0 images, trace, and apparent diffusion coefficient (ADC) map) was made available at each sitting.

Baseline DSC-PWI and T2*GRE images were rated for the presence of (a) *any* hemorrhage (manifested as marked hypointensity) of *any age* and in *any compartment* (parenchymal, subarachnoid, intraventricular, subdural, or extradural); (b) acute hemorrhagic transformation, defined as an area of marked hypointensity within the area of acute infarction as seen on DWI; and specific hemorrhage location. If the readers detected an area of hypointensity, they were permitted to assess the available T2-weighted or fluid-attenuated inversion recovery (FLAIR) images to determine whether there was any perilesional edema to indicate acute hemorrhage. Acute hemorrhagic transformation was graded according to the European Cooperative Acute Stroke Study criteria (Table 2).[20]

Data analysis

Statistical analyses were performed with a software package (MedCalc Version 17.2, MedCalc Software bvba, Ostend, Belgium, 2017). Since the findings on T2*-weighted sequences are dependent on the presence

Table 1. Classification of the subtype of hemorrhagic transformation: European Cooperative Acute Stroke Study I definitions[a,20]

Grade	
HI	Petechial infarction without space-occupying effect
HI1	Small petechiae
HI2	More confluent petechiae
PH	Hemorrhage (coagulum) with mass effect
PH1	<30% of the infarcted area with mild mass effect
PH2	>30% of the infarcted area with significant mass effect, or clot remote from infarcted area

HI: hemorrhagic infarction; PH: parenchymal hematoma.

Table 2. Typical sequence parameters

Study	T2*GRE					PWI			
	Field strength	TR (ms)	TE (ms)	Slice thickness/ spacing (mm)	Acquisition matrix	TR (ms)	TE (ms)	Slice thickness/ spacing (mm)	Acquisition matrix
EPITHET	1.5T	4200–6000	50–60	5/6–7/7	128 × 128	2000–2300	30	5/6–7/8	128 × 128 or 96 × 64
DEFUSE 2	3T	600–800	10–25	5/5	244 × 194	1800	35	5/5	128 × 128
	1.5T	600–900	30	5/6.5–6/6.5	256 × 192	1800	40	5/5–6.5/5	128 × 128
SENSE 3	3T	640–800	15 or 25	5/5	256 × 128	1800	35	5/5–6/8	96 × 128 or 84 × 84
	1.5T	550–850	30	5/5–6/6.5	256 × 192	1800	40	5/5	128 × 128

GRE: gradient recalled echo; PWI: perfusion-weighted imaging; EPITHET: Echoplanar Imaging Thrombolytic Evaluation Trial; DEFUSE: Diffusion and Perfusion Imaging Evaluation for Understanding Stroke Evolution; SENSE: SENSitivity Encoding; TR: repetition time; TE: echo time.

and magnetic state of hemorrhage[21] at a given time point, scans from the same patient obtained at different time points were treated as independent. The readers were blinded to the timing of the scans, which were presented in random order to avoid recall bias.

For each reader, Cohen's kappa statistics were used to evaluate the agreement between T2*GRE and baseline DSC-PWI for the presence of *any* hemorrhage, acute hemorrhagic transformation, and hemorrhage grade. *Inter-reader* agreement was also determined for T*GRE and DSC-PWI using kappa statistics. Disagreements were adjudicated through *post hoc* review of the patient's entire imaging portfolio.

For detection of hemorrhage and acute hemorrhagic transformation, scans were subgrouped by field strength (1.5T versus 3T) and sequence implementation (the two newer studies DEFUSE 2 and SENSE 3 versus EPITHET, which used DSC-PWI and T2*GRE sequences performed on older MRI scanners with weaker gradient performance). Agreement between T2*GRE and baseline DSC-PWI for each subgroup was depicted in forest plots.

Results

A total of 393 MRI scans from 221 patients (120 males, 101 females, mean age 67.7 years, range 33 95) were included (Figure 1): 201 performed at baseline, 123 following endovascular therapy (114 within 12 h and 9 at three to five days) and 69 performed within 48 h of the baseline scan in patients who underwent medical management; 108 MRIs were performed at 3T and 285 at 1.5T. The results of statistical analyses are summarized in Table 3.

Inter-reader agreement was almost perfect for both baseline DSC-PWI ($\kappa = 0.96$ for hemorrhage detection, $\kappa = 0.98$ for acute hemorrhagic transformation, and $\kappa = 0.98$ for grade) and T2*GRE ($\kappa = 0.95$ for

Figure 1. MRI scan selection. MRI: magnetic resonance imaging; GRE: gradient recalled echo; PWI: perfusion-weighted imaging; EPITHET: Echoplanar Imaging Thrombolytic Evaluation Trial; DEFUSE: Diffusion and Perfusion Imaging Evaluation for Understanding Stroke Evolution; SENSE: SENSitivity Encoding.

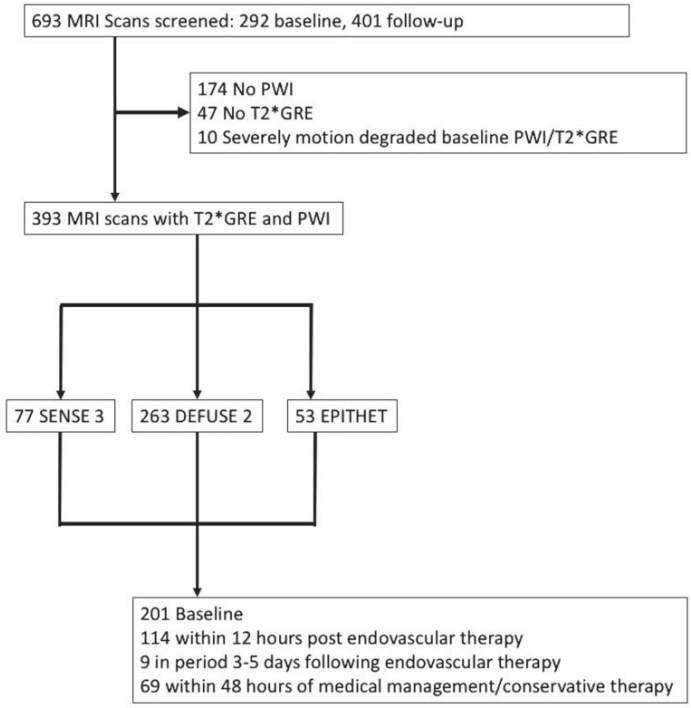

Table 3. Agreement for detection and characterization of hemorrhage

	Hemorrhage detection κ (95% CI)	Acute hemorrhagic transformation κ (95% CI)	Hemorrhage grade κ (95% CI)
Agreement between DSC-PWI and T2*GRE			
Reader 1	0.90 (0.86–0.95)	0.95 (0.91–0.98)	0.98[a] (0.96–1.00)
Reader 2	0.91 (0.87–0.96)	0.95 (0.92–0.98)	0.97[a] (0.94–1.00)
Inter-reader agreement			
T2*GRE	0.95 (0.91–0.98)	0.97 (0.94–1.00)	0.98[a] (0.96–1.00)
DSC-PWI	0.96 (0.93–0.99)	0.98 (0.95–1.00)	0.98[a] (0.96–1.00)

Note: CI: confidence interval; DSC: dynamic susceptibility contrast; GRE: gradient recalled echo; PWI: perfusion-weighted imaging.
[a]Linear weighted kappa.

Figure 2. Forest plots of agreement between T2*GRE and DSC-PWI, with kappa values (central square) and the confidence intervals (bars). (a) Field strength: agreement was similar at 1.5T versus 3T for detection of hemorrhage (blue central square) and acute hemorrhagic transformation (green central square). (b) Study: agreement was poorer for detection of hemorrhage (blue central square) in the EPITHET subgroup than the DEFUSE 2 and SENSE 3 subgroups. There was little difference between the subgroups when it came to detection of acute hemorrhagic transformation (green central square). EPITHET: Echoplanar Imaging Thrombolytic Evaluation Trial; DEFUSE: Diffusion and Perfusion Imaging Evaluation for Understanding Stroke Evolution; SENSE: SENSitivity Encoding.

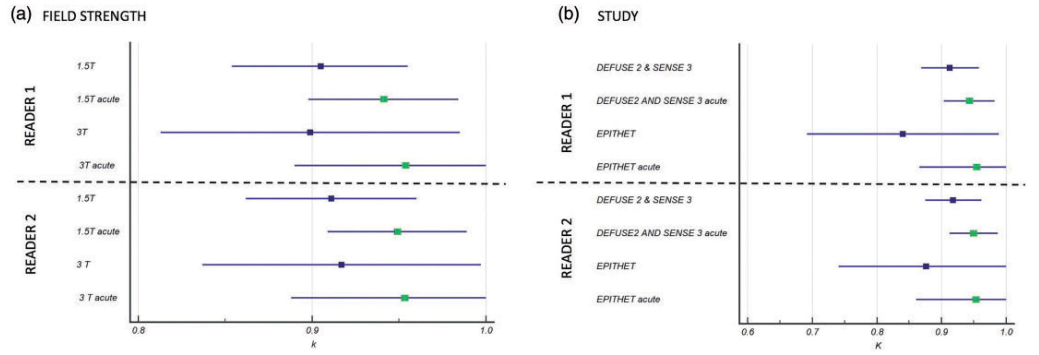

hemorrhage detection, $\kappa = 0.97$ for acute hemorrhagic transformation, and $\kappa = 0.98$ for grade).

For each reader, agreement between T2*GRE and baseline DSC-PWI for the presence of hemorrhage was almost perfect ($\kappa_{reader\,1} = 0.90$ and $\kappa_{reader\,2} = 0.91$), even greater for detection of acute hemorrhagic transformation ($\kappa_{reader\,1} = 0.94$ and $\kappa_{reader\,2} = 0.95$), and higher still for hemorrhage grade ($\kappa_{reader\,1} = 0.98$ and $\kappa_{reader\,2} = 0.97$).

Agreement between baseline DSC-PWI and T2*GRE was similar at 1.5T and 3T (Figure 2). Agreement between sequences was lower in the EPITHET ($\kappa_{reader\,1} = 0.84$ and $\kappa_{reader\,2} = 0.88$) than the DEFUSE 2/SENSE 3 ($\kappa_{reader\,1} = 0.91$ and $\kappa_{reader\,2} = 0.92$) subgroup for hemorrhage detection but not for detection of acute hemorrhagic transformation (Figure 2). Only 20% of the scans were from EPITHET, but this older study accounted for 50% (4/8) of the missed chronic microbleeds (CMBs).

Intraventricular hemorrhage (due to extension of parenchymal hemorrhagic transformation) was detected, on both DSC-PWI and T2*GRE, in 16 patients' follow-up scans; subarachnoid blood was detected in 7 of these, on both sequences. There were no patients in whom subdural or extradural hemorrhage was detected on either sequence.

Post hoc analysis

Acute hemorrhagic transformation was missed on baseline DSC-PWI in 5/393 (1.3%) scans by one or both readers; all were hemorrhagic infarction (HI) 1 petechial bleeds. In three cases, a petechial bleed in the putamen was subtle on baseline DSC-PWI due to background low signal intensity but more conspicuous on T2*GRE due to a rim of T2 hyperintensity (Figure 3(a) to (c)). In the fourth case (from EPITHET), a petechial bleed was much less conspicuous on baseline DSC-PWI than T2*GRE. A solitary petechial bleed in the insula was truly occult on review (Figure 3(d) and (e)) in the fifth case; despite the snapshot image acquisition of EPI, DSC-PWI was more motion-degraded than T2*GRE. Other contributing factors were the lower spatial resolution of DSC-PWI, blurring, and a 2-mm slice gap.

A solitary CMB was missed on DSC-PWI in 8/393 (2.0%) scans. An inferior temporal lobe CMB was completely obscured in two cases and partially obscured in one case by signal loss related to off-resonance effects from the pneumatized petrous apex (Figure 4); these scans were performed at 3T and had a longer echo time (TE) for DSC-PWI than T2*GRE, amplifying the dephasing due to susceptibility interfaces. A CMB in the cerebellum was below the DSC-PWI imaging slab and therefore missed. In the remaining four cases from EPITHET, hemorrhage was less conspicuous on DSC-PWI than T2*GRE due to image blurring.

Figure 3. (a–c) MRI performed within 12 h of endovascular therapy in a 74-year-old male. (a) Hemorrhagic transformation within the posterolateral right putamen (blue arrow) is more conspicuous on axial T2*GRE (repetition time (TR)/TE: 600 ms/30 ms), where there is a thin rim of T2 hyperintensity than (b) axial baseline DSC-PWI (TR/TE: 1800/40). (c) Day 5 follow-up axial T2*GRE (TR/TE: 900 ms/30 ms) confirms hemorrhage. (d and e) MRI performed at 3T 8 h following endovascular clot retrieval in a 45-year-old male presenting with acute left middle cerebral artery M1 segment occlusion. (d) HI1 petechial hemorrhagic transformation in the posterior left insula (white arrowhead) was visible on T2*GRE (TR/TE: 700 ms/25 ms, 5 mm/5 mm, matrix: 256 × 128) but not (e) axial baseline DSC-PWI (TR/TE: 1800/35, slice thickness and spacing: 6 mm/8 mm, matrix: 84 × 84). This was felt to be due to the slice gap, lower spatial resolution, and prominent T2*-blurring, which is less pronounced in new DSC-PWI implementations which have faster EPI readouts.

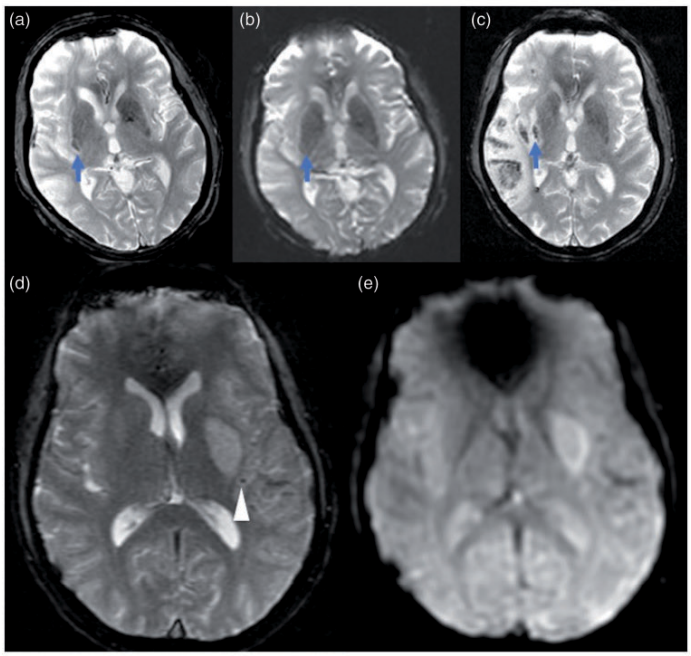

Figure 4. MRI performed at 3T in an 81-year-old woman presenting with an acute left middle cerebral artery territory stroke. (a) A solitary chronic microbleed (blue arrow) in the right temporal lobe in visible on axial T2*GRE (repetition time (TR)/TE: 617 ms/15 ms). (b) Marked signal loss (white arrowheads) in the inferior temporal lobes, related to adjacent bone-air-soft tissue interfaces, obscures the microbleed on baseline DSC-PWI (TR/TE: 1800/35).

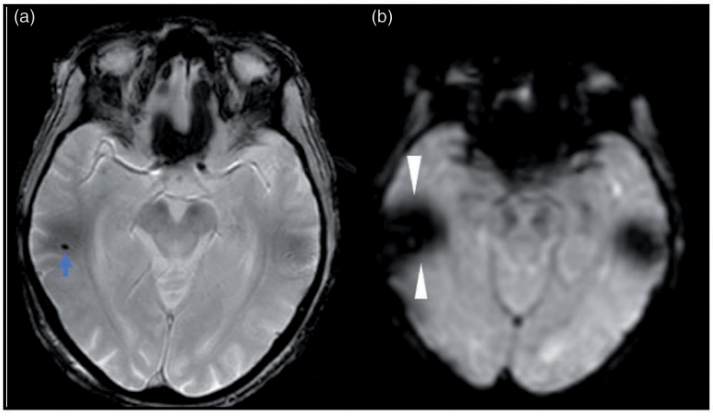

Figure 5. (a) MRI performed 12 h after endovascular therapy for left middle cerebral artery occlusion in a 79 year-old woman shows acute hemorrhagic transformation on axial T2*GRE (repetition time (TR)/TE: 967/30). (b) Hemorrhage is no longer visible on the axial T2*GRE at day 5, likely due to motion and evolution of hematoma to non-paramagnetic extracellular methemoglobin. (c) The longer TE of axial DSC-PWI (TR/TE: 1800/40) likely allowed sufficient dephasing from the small volume of residual paramagnetic intracellular methemoglobin to allow detection at this stage. (d) The ADC map shows high ADC within this area, likely reflecting transition of blood products from the intracellular compartment to extracellular.

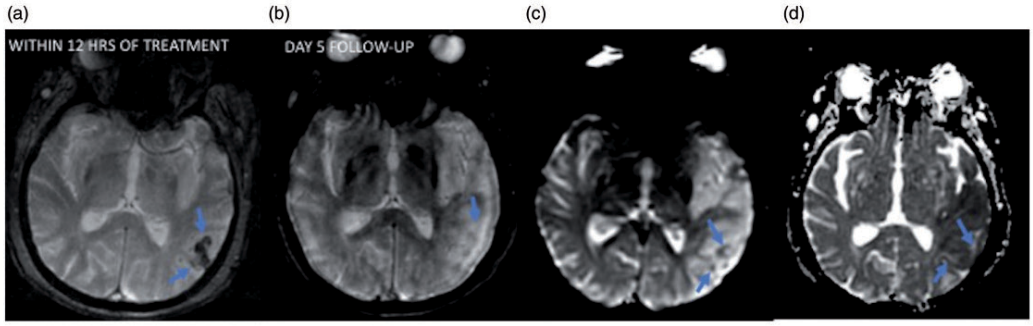

In the nine cases where hemorrhage was identified on DSC-PWI but not T2*GRE, hemorrhage was felt to be present on review of follow-up imaging. Slice gap accounted for two misses. In one case, HI1 acute hemorrhagic transformation was occult on the day 5 T2*GRE but visible on the contemporaneous DSC-PWI and both DSC-PWI and T2*GRE from the prior scan (Figure 5). Hematoma had likely evolved to predominantly extracellular methemoglobin, with little residual paramagnetic intracellular methemoglobin. In six cases, hemorrhage was visible but less conspicuous on T2*GRE than on DSC-PWI, likely due to the shorter TE.

Disparity between baseline DSC-PWI and T2*GRE for grade (two cases for *reader 1* and four for *reader 2*) were disagreement between grades 2 and 3, related to perception of mass effect.

Discussion

Acute intracranial hemorrhage contraindicates thrombolytic therapies for AIS.[1] Conventional T2*GRE is the mainstay of hemorrhage screening on MRI but is one of the slowest sequences in the acute stroke protocol. DSC-PWI, used to delineate at-risk tissue, is also typically a GRE sequence with an SS-EPI readout and is therefore inherently T2*-weighted. This study evaluated the performance of baseline DSC-PWI images, obtained prior to contrast agent arrival, against conventional T2*GRE for detection of intracranial hemorrhage in AIS patients. Almost perfect statistical agreement between baseline DSC-PWI and T2*GRE, particularly for detection of clinically relevant acute hemorrhagic transformation, suggests that DSC-PWI is adequate for hemorrhage screening.

Inclusion of two older stroke studies (EPITHET and DEFUSE 2) was justified by these being two of the largest prospectively acquired AIS studies where MRI was obtained. The newer high-profile thrombectomy studies have used mostly or exclusively CT.[11–14,22]

The need to omit T2*GRE to expedite treatment could be questioned, since new "fast GRE" sequences can be performed in under 60 s. Unfortunately, many sites that image acute stroke patients lack the software to perform these sequences, while DSC-PWI is widely available. Furthermore, the "fast GRE" sequences utilize an SS-EPI readout and therefore have the same disadvantages (compared to conventional T2*GRE) as DSC-PWI. These include greater image blurring and distortions (related to the EPI readout) and lower signal-to-noise ratio.[9,16,18] The baseline DSC-PWI images are in fact a low spatial resolution "fast GRE" sequence and can be performed in under 10 s. Given the almost perfect agreement between baseline DSC-PWI and conventional T2*GRE, there is little added yield in performing a "fast GRE" sequence when DSC-PWI is included in MR protocol. In centers that do not include perfusion imaging, and which do not have a "fast GRE" sequence available, the baseline component of DSC-PWI may be a feasible alternative for fast hemorrhage screening.

The majority of misses on DSC-PWI were solitary CMBs, which are not a contraindication to thrombolytic therapy.[1,23,24] Acute hemorrhagic transformation, which contraindicates thrombolysis, was missed on DSC-PWI in 1% (and truly occult in just one case); in comparison, hemorrhagic transformation was missed on CT in 42%.[3] A recurrent cause was the lower conspicuity of putaminal hemorrhage on DSC-PWI. The thin rim of T2-hyperintense edema on T2*GRE that allowed hemorrhage to be resolved against background hypointensity (related to iron deposition) was not seen on DSC-PWI. Obscuration of edema is likely due to the lower spatial resolution and T2-contrast of DSC-PWI and the longer TE (40 ms versus 30 ms for T2*GRE) causing more "blooming" of hemorrhage. Careful scrutiny of the putamen for hemorrhage is therefore important.

Agreement between DSC-PWI and T2*GRE was unaltered by field strength, suggesting both sequences benefit equally from increased sensitivity to off-resonance effects at 3T. Inter-sequence agreement was higher for the newer sequence implementations used in SENSE 3 and DEFUSE 2 in comparison with EPITHET. These are less motion-sensitive and have less T2*-based blurring and susceptibility distortions due to the shorter EPI readouts enabled by advances such as parallel imaging and stronger gradient performance. They also use a longer TE, increasing T2*-weighting, and therefore sensitivity for detection of hemorrhage. Blood transitions through different states, only some of which are paramagnetic.[21] Paramagnetism causes local magnetic field inhomogeneity, which in turn causes rapid dephasing and detectable signal loss on T2*-weighted sequences.[21] When only a small proportion of a hematoma is composed of paramagnetic deoxyhemoglobin or intracellular methemoglobin, signal loss may be minimal.[21] A longer TE allows greater dephasing so that even a small volume of paramagnetic blood product to be detected, likely accounting for the cases where acute hemorrhagic transformation was detected on DSC-PWI but not T2*GRE. A longer TE does, however, amplify signal loss due to off-resonance effects from skull base air- and bone-tissue interfaces, obscuring microbleeds in the inferior temporal lobes.

The T2*GRE and DSC-PWI implementations were heterogeneous, partly due to new developments in MR technology. Comparing DSC-PWI with T2*GRE from the same scan mitigated the impact of changes over time. There was large variability in sequence implementations even among contemporaneous scans, reflecting of the lack of harmonization of AIS protocols across sites and countries encountered in real life. Inclusion of a variety of implementations allows broad generalizability of the findings. To avoid missing hemorrhage on DSC-PWI, inter-slice gap should be avoided and whole-brain coverage is suggested (this is now possible with parallel imaging).

Susceptibility Weighted Imaging (SWI) was not evaluated since this sequence was not routinely included in the AIS MRI study protocol. Its long acquisition time and greater motion sensitivity discourage its use in AIS. Patients with acute primary parenchymal hemorrhage were not included in this study which draws data from three AIS studies. The signal characteristics and conspicuity of intra-axial hemorrhage are dependent on size and age of hematoma[21] and would not be expected

to differ between primary hemorrhage and hemorrhagic transformation of AIS. There were no patients with subdural or extradural hemorrhage in the study population. In the seven patients where subarachnoid hemorrhage was detected on T2*GRE, it was also detected on DSC-PWI. This number is too small to allow us to draw a meaningful conclusion regarding the sensitivity of DSC-PWI compared to T2*GRE for detection of subarachnoid blood. This is a limitation of the study but likely reflective of the low prevalence of non-parenchymal hemorrhage in AIS patients (the population from which our study sample was drawn and to which we intend to apply the findings). It is noted that acute subarachnoid hemorrhage, particularly if small volume, may not be detectable on T2*-weighted sequences since oxyhemoglobin (which can persist due to high cerebrospinal fluid oxygenation) is not paramagnetic.[25] FLAIR is highly sensitive for detection of subarachnoid hemorrhage, allows acute from chronic hemorrhage to be differentiated, and helps diagnosis of extra-axial hemorrhage, which are strong arguments for its inclusion in the AIS MRI protocol.

Conclusion

The almost perfect statistical agreement with T2*GRE for detection of intracranial hemorrhage suggests that DSC-PWI, when included in the AIS protocol, is adequate for hemorrhage screening.

Declaration of conflicting interests

The author(s) declared no potential conflicts of interest with respect to the research, authorship, and/or publication of this article.

Ethical approval

EPITHET, SENSE 3, and DEFUSE 2 all had institutional review board approval obtained at each trial site and were HIPAA compliant.

Funding

The author(s) disclosed receipt of the following financial support for the research, authorship, and/or publication of this article: Amukotuwa and Bammer are supported by the National Institutes of Health (Grants R01 EB 2711 and 5R21EB021029). The DEFUSE study was funded by National Institutes of Health (Grants RO1 NS39325, Principal Investigator, Gregory W Albers; K24 NS044848, Principal Investigator, Gregory W Albers; K23 NS051372, Principal Investigator, Maarten G Lansberg) and the RAPID software development was supported by R01 EB002711, Principal Investigator, Roland Bammer. The EPITHET study was supported by the National Health and Medical Research Council of Australia, National Stroke Foundation, and National Heart Foundation of Australia.

ORCID iD

Shalini A Amukotuwa https://orcid.org/0000-0002-1678-3930

References

1. Powers WJ, Rabinstein AA, Ackerson T, et al. 2018 guidelines for the early management of patients with acute ischemic stroke: a guideline for healthcare professionals from the American Heart Association/American Stroke Association. *Stroke* 2018; 49: e46–e110.
2. Purushotham A, Campbell BC, Straka M, et al. Apparent diffusion coefficient threshold for delineation of ischemic core. *Int J Stroke* 2015; 10: 348–353.
3. Arnould MC GC, Peeters A, Cosnard G and Duprez TP. Comparison of CT and three MR sequences for detecting and categorizing early (48 hours) hemorrhagic transformation in hyperacute ischemic stroke. *AJNR Am J Neuroradiol* 2004; 25: 939–944.
4. Kidwell CS, Chalela JA, Saver JL, et al. Comparison of MRI and CT for detection of acute intracerebral hemorrhage. *JAMA* 2004; 292: 1823–1830.
5. Lam WW, So NM, Wong KS and Rainer T. B0 images obtained from diffusion-weighted echo planar sequences for the detection of intracerebral bleeds. *J Neuroimaging* 2003; 13: 99–105.
6. Lin DD, Filippi CG, Steever AB and Zimmerman RD. Detection of intracranial hemorrhage: comparison between gradient-echo images and b(0) images obtained from diffusion-weighted echo-planar sequences. *AJNR Am J Neuroradiol* 2001; 22: 1275–1281.
7. Lu CY, Chiang IC, Lin WC, Kuo YT and Liu GC. Detection of intracranial hemorrhage: comparison between gradient-echo images and b0 images obtained from diffusion-weighted echo-planar sequences on 3.0T MRI. *Clin Imaging* 2005; 29: 155–161.
8. Lansberg MG, Straka M, Kemp S, et al. MRI profile and response to endovascular reperfusion after stroke (DEFUSE 2): a prospective cohort study. *Lancet Neurol* 2012; 11: 860–867.
9. Nael K, Khan R, Choudhary G, et al. Six-minute magnetic resonance imaging protocol for evaluation of acute ischemic stroke: pushing the boundaries. *Stroke* 2014; 45: 1985–1991.
10. Albers GW. Late window paradox. *Stroke* 2018; 49: 768–771.
11. Berkhemer OA, Fransen PS, Beumer D, et al. A randomized trial of intraarterial treatment for acute ischemic stroke. *N Engl J Med* 2015; 372: 11–20.
12. Campbell BC, Mitchell PJ, Kleinig TJ, et al. Endovascular therapy for ischemic stroke with perfusion-imaging selection. *N Engl J Med* 2015; 372: 1009–1018.
13. Saver JL, Goyal M, Bonafe A, et al. Stent-retriever thrombectomy after intravenous t-PA vs. t-PA alone in stroke. *N Engl J Med* 2015; 372: 2285–2295.
14. Albers GW, Marks MP, Kemp S, et al. Thrombectomy for stroke at 6 to 16 hours with selection by perfusion imaging. *N Engl J Med* 2018; 378: 708–718.

15. Goyal MS, Hoff BG, Williams J, et al. Streamlined hyperacute magnetic resonance imaging protocol identifies tissue-type plasminogen activator-eligible stroke patients when clinical impression is stroke mimic. *Stroke* 2016; 47: 1012–1017.
16. Prakkamakul S, Witzel T, Huang S, et al. Ultrafast brain MRI: clinical deployment and comparison to conventional brain MRI at 3T. *J Neuroimaging* 2016; 26: 503–510.
17. Farzaneh F, Riederer SJ and Pelc NJ. Analysis of T2 limitations and off-resonance effects on spatial resolution and artifacts in echo-planar imaging. *Magn Reson Med* 1990; 14: 123–139.
18. Holdsworth SJ, Skare S, Newbould RD, Guzmann R, Blevins NH and Bammer R. Readout-segmented EPI for rapid high resolution diffusion imaging at 3 T. *Eur J Radiol* 2008; 65: 36–46.
19. Davis SM, Donnan GA, Parsons MW, et al. Effects of alteplase beyond 3 h after stroke in the Echoplanar Imaging Thrombolytic Evaluation Trial (EPITHET): a placebo-controlled randomised trial. *Lancet Neurol* 2008; 7: 299–309.
20. Hacke W, Kaste M, Fieschi C, et al. Intravenous thrombolysis with recombinant tissue plasminogen activator for acute hemispheric stroke. The European Cooperative Acute Stroke Study (ECASS). *JAMA* 1995; 274: 1017–1025.
21. Bradley WG Jr. MR appearance of hemorrhage in the brain. *Radiology* 1993; 189: 15–26.
22. Nogueira RG, Jadhav AP, Haussen DC, et al. Thrombectomy 6 to 24 hours after stroke with a mismatch between deficit and infarct. *N Engl J Med* 2018; 378: 11–21.
23. Charidimou A, Shoamanesh A and International M-MI. Clinical relevance of microbleeds in acute stroke thrombolysis: comprehensive meta-analysis. *Neurology* 2016; 87: 1534–1541.
24. Fiehler J, Albers GW, Boulanger JM, et al. Bleeding risk analysis in stroke imaging before thromboLysis (BRASIL): pooled analysis of T2*-weighted magnetic resonance imaging data from 570 patients. *Stroke* 2007; 38: 2738–2744.
25. Siddiqui FM, Bekker SV and Qureshi AI. Neuroimaging of hemorrhage and vascular defects. *Neurotherapeutics* 2011; 8: 28–38.

8.3 Discussion

Acute intracranial haemorrhage is a contraindication to thrombolysis, therefore its detection is of critical importance in acute ischemic stroke patients being considered for treatment[4]. A blood-sensitive sequence must therefore be included in the acute stroke MR protocol. This study was motivated by the competing requirements of accurate detection of haemorrhage and a fast MR protocol to avoid treatment delay. Conventional T_2*GRE, the mainstay of haemorrhage screening in acute ischemic stroke, is one of the slowest sequences in the acute stroke MR protocol. DSC-PWI, which is also T_2*-weighted and therefore blood sensitive, is included in the MR protocol at some centres for delineating tissue at risk of infarction. The agreement between the baseline images of DSC-PWI and conventional T_2*GRE for detection of intracranial haemorrhage in a cohort of acute ischemic stroke patients was evaluated. Strong agreement was shown (κ = 0.90 for reader 1 and κ = 0.91 for reader 2), as hypothesized based on the T_2*-weighting of DSC-PWI. The almost perfect statistical agreement between the sequences ($\kappa = 0.94$ for reader 1 and $\kappa = 0.95$ for reader 2) for detection of clinically relevant acute haemorrhagic transformation suggests that DSC-PWI is sufficient for haemorrhage screening when it is included in the acute MR protocol, allowing T_2*GRE to be omitted.

New "fast GRE" sequences that have been developed to shorten scan duration are not universally available at all hospitals that perform MRI on acute stroke patients. They have also not been thoroughly validated against conventional T_2*GRE for haemorrhage detection in acute ischemic stroke patients. In one study which compared a 6 second "fast GRE" sequence against conventional T_2*GRE, there was poorer agreement between sequences (κ = 0.79) than in our study, with disagreement in 6/32 (19%) of cases[9].

Like these "fast GRE" sequences, DSC-PWI uses a single-shot EPI readout. The baseline DSC-PWI images are therefore similar to "fast GRE" sequences, with similar spatial resolution and T_2*-weighting. Using DSC-PWI for haemorrhage screening would avoid the requirement for a dedicated haemorrhage-specific sequence and is an alternative approach to shortening scan time. While higher spatial resolution can be achieved with "fast GRE" sequences that use a multi-shot EPI readout, this also increases motion sensitivity. Motion is a significant issue in unwell, confused AIS patients and can lead to clinically significant acute haemorrhage being missed as was seen in this study.

DWI, which is a requisite component of the acute stroke MR protocol, also uses an EPI readout. The b=0 images, which are obtained at the start of the DWI acquisition with the diffusion-encoding gradients switched off, therefore have some T_2*-weighting. However, most DWI sequences use spin-echo magnetization preparation. Given that the centre of k-space is traversed at the peak of the spin echo, the dominant contrast in the b=0 images of spin-echo DWI images is T_2- rather than T_2*-weighted. Accordingly, previous studies have found that diffusion-weighted spin-echo EPI sequences are inadequate for haemorrhage screening, with sensitivity as low as 54% for detecting acute haemorrhagic transformation[6-8].

DSC-PWI has a number of disadvantages, as do "fast GRE" sequences, compared to T2*GRE. These include greater image distortions and blurring due to the EPI readout, as well as lower signal to noise ratio (SNR) and spatial resolution[3, 9, 10]. Despite these disadvantages, haemorrhage was only missed in 13 scans. The majority of these (8/13, 62%) were chronic microbleeds, which do not contraindicate thrombolysis. There were 5/393 scan where acute haemorrhagic transformation was missed on DSC-PWI. Reader 1 detected acute haemorrhagic transformation on T_2*GRE in 115 scans and also on DSC-PWI in 111 of these (96.5%). Reader 2 detected acute haemorrhagic transformation on T_2*GRE in 111 scans, and also on DSC-PWI in 108 of these (97.3%). In comparison, in a different study, only 58% of cases of acute haemorrhagic transformation detected on MRI were also detected on CT, which is much more widely used for haemorrhage screening prior to thrombolysis[5]. There was only one case, a single petechial haemorrhage, that was truly occult on DSC-PWI even on post hoc review; this was due to a 2-mm slice gap, a remediable cause of false negatives. EPI-related blurring and the lower spatial resolution of DSC-PWI contributed to the other four false negatives.

The limitations of DSC-PWI are mitigated in newer implementations by the use of a shorter EPI readout, enabled by advances such as parallel imaging and stronger gradient performance. In turn, this decreases T_2*-based blurring and distortions as well as motion sensitivity. Accordingly, the agreement between DSC-PWI and T_2*GRE for haemorrhage was stronger in scans from DEFUSE 2 and SENSE 3, which had newer DSC-PWI implementations, than those from EPITHET. These newer DSC-PWI implementations also have a longer TE (35 ms at 3T and 40 ms at 1.5 T), which increases T_2*-weighting. While this confers greater sensitivity for detection of blood products, it also results in greater dephasing, exaggerating signal loss at air- and bone-tissue interfaces. This was apparent in the three cases where a chronic microbleed in the inferior temporal

lobe was obscured on DSC-PWI due to off-resonance effects from the pneumatized petrous apex; these microbleeds were visible on T_2*GRE due to the use of a shorter TE (10-25 ms). Off-resonance effects are increased at higher field strength, therefore while scanning at 3T increases sensitivity for blood products, it also amplifies signal loss at susceptibility interfaces. Despite this drawback, the agreement between DSC-PWI and T_2*GRE was unaltered by field strength.

A strength of this study is the use of a large dataset from acute ischemic stroke patients enrolled in 3 stroke studies, allowing validation of DSC-PWI for haemorrhage detection in the target population. The use of follow-up as well as baseline scans increased the number of MRIs with acute haemorrhagic transformation, which was important for meaningful and robust evaluation of agreement between DSC-PWI and T_2*GRE for haemorrhage detection. Random presentation of the anonymized scans, combined with the large number of MRIs assessed, avoided the scenario where two MRIs from the same patient were read in close succession, thereby minimizing potential bias related to memory.

The use of scans from multiple time points also allowed blood products of different ages to be assessed. This is important, since the appearance and conspicuity of blood product on T_2*-weighted images depends on the age of hematoma. Hematoma progressively evolves through different stages over time. The magnetic susceptibility of blood products within hematoma at a given stage depends on the conformation of the haemoglobin molecule and the number of pairs of unpaired electrons of the haeme iron related to oxidation state[11]. Deoxyhaemoglobin (acute phase), methaemoglobin (subacute phase) and hemosiderin (chronic phase) are all paramagnetic, with increasing magnetic susceptibility related to an increasing number of unpaired electrons[11]. These paramagnetic blood products cause local magnetic field inhomogeneity, which in turn causes rapid spin dephasing and signal loss on T_2*-weighted sequences. Diamagnetic blood product (oxyhaemoglobin in acute hematoma) and non-compartmentalized paramagnetic blood product (extracellular methaemoglobin, released when the red cell lyses in late subacute hematoma) do not cause magnetic field inhomogeneity. They therefore do not result in signal loss on T_2*-weighted images. Hence there may only be a small amount of blood product in a state that causes signal loss on T_2*-weighted images in hyperacute and late subacute hematomas. Inclusion of MRIs with blood of different ages, including late subacute hematoma, was therefore important when assessing the diagnostic performance of DSC-PWI against conventional T_2*GRE.

A potential limitation of the study is that patients with primary parenchymal haemorrhage were not included. However, the study included patients with acute haemorrhagic transformation. As discussed in the previous paragraph, the conspicuity of hematoma on T_2*-weighted sequences is related to the age of hematoma, as well as its size, and would not be expected to differ between primary parenchymal haemorrhage and haematoma of the same age and size resulting from haemorrhagic transformation. Another limitation is that subdural and extradural hematomas were not present in the study population, therefore were not assessed. There were also only a small number of patients with subarachnoid haemorrhage, precluding meaningful analysis of agreement between DSC-PWI and T_2*GRE. This is likely reflective of the low prevalence of extra-axial haemorrhage in the acute ischemic stroke patient population, from which the study cohort was derived and to which the findings of the study are intended to be applied.

8.4 References

1. Wintermark M, Luby M, Bornstein NM, Demchuk A, Fiehler J, Kudo K, et al. International survey of acute stroke imaging used to make revascularization treatment decisions. *Int J Stroke*. 2015;10:759-762

2. Goyal MS, Hoff BG, Williams J, Khoury N, Wiesehan R, Heitsch L, et al. Streamlined hyperacute magnetic resonance imaging protocol identifies tissue-type plasminogen activator-eligible stroke patients when clinical impression is stroke mimic. *Stroke*. 2016;47:1012-1017

3. Nael K, Khan R, Choudhary G, Meshksar A, Villablanca P, Tay J, et al. Six-minute magnetic resonance imaging protocol for evaluation of acute ischemic stroke: Pushing the boundaries. *Stroke*. 2014;45:1985-1991

4. Powers WJ, Rabinstein AA, Ackerson T, Adeoye OM, Bambakidis NC, Becker K, et al. 2018 guidelines for the early management of patients with acute ischemic stroke: A guideline for healthcare professionals from the american heart association/american stroke association. *Stroke*. 2018;49:e46-e110

5. Arnould MC GC, Peeters A, Cosnard G, Duprez TP. Comparison of ct and three mr sequences for detecting and categorizing early (48 hours) hemorrhagic transformation in hyperacute ischemic stroke. *AJNR*. 2004;25:939–944

6. Lam WW, So NM, Wong KS, Rainer T. B0 images obtained from diffusion-weighted echo planar sequences for the detection of intracerebral bleeds. *J Neuroimaging*. 2003;13:99-105

7. Lin DD, Filippi CG, Steever AB, Zimmerman RD. Detection of intracranial hemorrhage: Comparison between gradient-echo images and b(0) images obtained from diffusion-weighted echo-planar sequences. *AJNR Am J Neuroradiol*. 2001;22:1275-1281

8. Lu CY, Chiang IC, Lin WC, Kuo YT, Liu GC. Detection of intracranial hemorrhage: Comparison between gradient-echo images and b0 images obtained from diffusion-weighted echo-planar sequences on 3.0t mri. *Clin Imaging*. 2005;29:155-161

9. Prakkamakul S, Witzel T, Huang S, Boulter D, Borja MJ, Schaefer P, et al. Ultrafast brain mri: Clinical deployment and comparison to conventional brain mri at 3t. *J Neuroimaging*. 2016;26:503-510

10. Holdsworth SJ, Skare S, Newbould RD, Guzmann R, Blevins NH, Bammer R. Readout-segmented epi for rapid high resolution diffusion imaging at 3 t. *Eur J Radiol*. 2008;65:36-46

11. Bradley WG, Jr. Mr appearance of hemorrhage in the brain. *Radiology*. 1993;189:15-26

Chapter 9

Arterial Spin-Labeling Improves Detection of Intracranial Dural Arteriovenous Fistulas with MRI

9.1 INTRODUCTION

Arterial spin label (ASL) perfusion is a completely non-invasive MR imaging technique that is now widely available on clinical MRI scanners. This study was motivated by the clinical need for a non-invasive technique that can reliably detect *dural arteriovenous fistulas* (DAVFs), and our observation that intravascular ASL signal is a highly conspicuous finding which we hypothesized could be leveraged for this purpose.

A standard *pseudocontinuous ASL* (PCASL) pulse sequence was routinely included in the acute stroke MR protocol at Stanford University Medical Center, where this study was undertaken, as part of a research project investigating ASL for delineating the ischemic penumbra. Unfortunately, ASL has some inherent limitations that impede accurate quantification of blood flow in acute ischemic stroke patients. *Arterial transit time* (ATT), which is the time taken for labelled blood to reach the tissue capillary bed from the labelling plane, is delayed in the setting of arterial occlusion. This is due to the blood having to traverse collateral pathways to reach downstream tissue. ATT can be markedly prolonged in acute stroke, considering that Tmax (which is another measure of delay in arterial transport) is 6 seconds or more in critically hypoperfused ischaemic tissue. Therefore, when a standard post label delay (PLD) of 2000 ms is used, labelled blood is not given sufficient time to reach the downstream ischaemic tissue[1-3]. Tissue blood flow is therefore underestimated, due to incomplete delivery of labelled blood[4]. Instead, the labelled blood is still in arterial transit, proximal to the occlusion or within leptomeningeal collaterals, at the time of imaging and gives rise to high signal. Termed **arterial transit artifact**, this intra-arterial high signal is a highly conspicuous qualitative finding which can alert the radiologist to

the presence and location of an occlusion or stenosis[1-3]. It can also be leveraged to visualize and assess leptomeningeal collaterals[2].

The high conspicuity of arterial transit artifact can be explained by the high contrast differential between labelled blood in vessels and tissue. Theoretically, due to the use of background suppression and subtraction of control of label images, the only signal in ASL images arises from labelled blood[3, 5]. While 100% of a voxel within a blood vessel is occupied by blood, only 2-5% of a tissue voxel is comprised of blood[5]. Therefore, there is much more label (and therefore signal) within a vessel voxel than in adjacent tissue voxels, leading to the high conspicuity of vessels containing labelled blood. Observing the "light bulb" conspicuity of arterial transit artifact in acute ischemic stroke patients whose MRIs were evaluated in studies 3 and 4 led us to hypothesize that intravascular ASL signal is a qualitative finding that can be utilized to improve diagnostic performance in other conditions.

Under normal conditions, ASL signal is not observed in cerebral venous structures[6, 7]. This is due to a combination of exchange labelled blood water protons with the extravascular space and T_1 decay of label during capillary transit; the T_1 of arterial blood, which is approximately 1650 ms at 3T in patients with normal haematocrit, is shorter than the mean transit time of blood though the capillary bed[5-8]. ASL signal is, however, seen in veins in conditions where there is arteriovenous shunting, because labelled blood transits directly and rapidly from feeding arteries into draining veins, bypassing the tissue capillary bed and precluding significant T_1 decay[6, 7]. Like arterial transit artifact, and again due to the large differential between intravascular and background signal, venous ASL signal is a highly conspicuous finding. Previous studies have shown that venous ASL signal can be used to detect shunting due to arteriovenous malformations (AVMs)[6, 7].

DAVFs are less common than AVMs, constituting 10-15% of intracranial shunting lesions[9, 10]. They are characterized by direct communication between dural arteries and either a dural venous sinus or cortical vein[10, 11]. As with AVMs, the increase in blood flow and pressure in draining veins can lead to venous hypertension and complication such as cerebral oedema and hemorrhage[9]. Given the potential morbidity and mortality related to DAVFs, and the availability of an effective treatment, detection of these lesions is important.

The clinical presentation of DAVFs in non-specific, ranging from asymptomatic to aggressive neurological presentations with seizures and neurological deficits due to

haemorrhage[9]. Of the large number of patients who have a presentation potentially attributable to a DAVF, few actually have one, even when no alternative cause can be identified. The reference standard for diagnosing a DAVFs is catheter-based *digital subtraction angiography* (DSA)[9]. This invasive test carries a small but material risk of permanent neurological injury, exposes the patient to ionizing radiation, and requires access to an interventional neuroradiology service[12]. A non-invasive method with a high sensitivity for detecting DAVFs would minimize the number of patients required to undergo DSA for definitive diagnosis.

Unlike AVMs, DAVFs lack a nidus and can be challenging to detect on conventional neuroimaging techniques such as structural MR sequences and *time-of-flight MRA* (TOF MRA), due to findings being subtle or non-specific. TOF-MRA, *time-resolved contrast-enhanced-MRA* (TR-CEMRA), and *CT angiography* (CTA) do have a high reported sensitivity and specificity for detection of DAVFs in the literature[13-19]. However, this was in the context of interpretation by experienced neuroradiologists with a high index of suspicion. In real world clinical practice, the diagnostic performance for detecting DAVFs using these conventional non-invasive techniques is poorer due to the lower index of suspicion. This is particularly the case outside tertiary referral centres, and in countries such as Australia in which subspecialist radiology is not widely practiced, where the MRIs of patients with DAVFs are often interpreted by general radiologists. There is, therefore, a strong clinical need for non-invasive techniques that improve diagnostic performance and confidence for detection of DAVFs. One previous small study assessing the diagnostic performance of ASL for detecting intracranial shunting lesions included only eight patients with DAVFs[6]. A study, inclusive of a larger number of patients with DAVFs as well as controls, was therefore felt to be warranted.

The aims of this case-control study were to assess the diagnostic accuracy and the added value of 3D PCASL for detection of DAVFs. The primary outcomes that were evaluated were accuracy for detecting a DAVF, based on venous ASL signal, and whether including PCASL resulted in improvement in diagnostic performance and confidence over that on structural MR sequences and TOF-MRA. Given the high conspicuity of venous ASL signal, we hypothesized high sensitivity and specificity for detecting a DAVF using this sign, and anticipated that both diagnostic performance and confidence would therefore be improved by augmenting the MR protocol with PCASL.

The study cohort consisted of 39 patients with a DAVF and 117 (three times as many) controls. These patients had undergone DSA for either a known or potential (based on clinical presentation) DAVF. While this introduces a potential selection bias, this is the target population in which MRI with ASL would be performed to screen for a DAVF. 39 patients with a DAVF were felt to be a sufficient sample, based on power analysis, to demonstrate whether there is additive value of ASL on diagnostic performance and confidence. This calculation was based on the high conspicuity of ASL combined with the relatively large number of controls and subtlety of signs on structural MRI and TOF-MRA, which we hypothesized would result in a large effect size.

9.2 Publication

Amukotuwa SA, Marks MP, Zaharchuk G, Calamante F, Bammer R, Fischbein N. Arterial Spin-Labeling Improves Detection of Intracranial Dural Arteriovenous Fistulas with MRI. AJNR Am J Neuroradiol. 2018;39(4):669-677

ORIGINAL RESEARCH
ADULT BRAIN

Arterial Spin-Labeling Improves Detection of Intracranial Dural Arteriovenous Fistulas with MRI

S.A. Amukotuwa, M.P. Marks, G. Zaharchuk, F. Calamante, R. Bammer, and N. Fischbein

ABSTRACT

BACKGROUND AND PURPOSE: Intracranial dural arteriovenous fistulas carry a risk of substantial neurologic complications but can be difficult to detect on structural MR imaging and TOF-MRA. The purpose of this study was to assess the accuracy and added value of 3D pseudocontinuous arterial spin-labeling MR imaging for the detection of these lesions.

MATERIALS AND METHODS: This retrospective study included 39 patients with a dural arteriovenous fistula and 117 controls who had undergone both DSA and MR imaging with pseudocontinuous arterial spin-labeling. Two neuroradiologists blinded to the DSA results independently assessed MR imaging with and without pseudocontinuous arterial spin-labeling. They recorded specific signs, including venous arterial spin-labeling signal, and the likelihood of a dural arteriovenous fistula using a 5-point Likert scale. Logistic regression and receiver operating characteristic analyses were performed to determine the accuracy of specific signs and the added value of pseudocontinuous arterial spin-labeling. Interobserver agreement was determined by using κ statistics.

RESULTS: Identification of the venous arterial spin-labeling signal had a high sensitivity (94%) and specificity (88%) for the presence a dural arteriovenous fistula. Receiver operating characteristic analysis showed significant improvement in diagnostic performance with the addition of pseudocontinuous arterial spin-labeling in comparison with structural MR imaging (Δarea under the receiver operating characteristic curve = 0.179) and a trend toward significant improvement in comparison with structural MR imaging with time-of-flight MRA (Δarea under the receiver operating characteristic curve = 0.043). Interobserver agreement for the presence of a dural arteriovenous fistula improved substantially and was almost perfect with the addition of pseudocontinuous arterial spin-labeling (κ = 0.92).

CONCLUSIONS: Venous arterial spin-labeling signal has high sensitivity and specificity for the presence of a dural arteriovenous fistula, and the addition of pseudocontinuous arterial spin-labeling increases confidence in the diagnosis of this entity on MR imaging.

ABBREVIATIONS: ASL = arterial spin-labeling; AUC = area under the ROC curve; DAVF = dural arteriovenous fistula; NCH = nodular and/or curvilinear hyperintensities; NPV = negative predictive value; pCASL = pseudocontinuous ASL; PPV = positive predictive value; ROC = receiver operating characteristic; sMRI = structural MRI

Dural arteriovenous fistulas (DAVFs) are intracranial arteriovenous shunting lesions characterized by direct connection between dural arteries and either a dural sinus or cortical vein.[1,2] The consequent increase in blood flow and pressure in draining veins can lead to complications, including cerebral edema, ischemia, and hemorrhage.[2] The criterion standard for the diagnosis of a DAVF, catheter-based DSA, is invasive, uses ionizing radiation, and carries a small-but-significant risk of permanent neurologic injury.[3]

The clinical presentation of DAVFs is nonspecific and broad, ranging from asymptomatic to pulsatile tinnitus, seizures, altered mental status, and/or intracranial hemorrhage.[4] In some of these patients, an alternative etiology for the presentation is not identified by standard noninvasive imaging methods, and there remains clinical suspicion for a DAVF. A sensitive noninvasive imaging method for the detection of DAVFs would help avoid exposing such patients to the risks (and cost) of diagnostic DSA. 3D TOF-MRA, time-resolved contrast-enhanced MRA, and CTA tech-

Received April 20, 2017; accepted after revision December 26.

From the Department of Radiology (S.A.A., M.P.M., G.Z., R.B., N.F.), Stanford University, Stanford, California; and Florey Department of Neuroscience and Mental Health (S.A.A., F.C.), University of Melbourne, Melbourne, Victoria, Australia.

Drs Amukotuwa and Bammer are supported by National Institutes of Health (National Institute of Biomedical Imaging and Bioengineering) grants 3R01EB002711-06S1 and 5R21EB021029. Dr Calamante is supported by the National Health and Medical Research Council of Australia, grant APP1117724.

Please address correspondence to Shalini A. Amukotuwa, MB, BS, Stanford University, Stanford, California; and Florey Department of Neuroscience and Mental Health, University of Melbourne, Melbourne, VIC, Australia 3052; e-mail: samukotuwa@gmail.com

Indicates open access to non-subscribers at www.ajnr.org
Indicates article with supplemental on-line tables.
http://dx.doi.org/10.3174/ajnr.A5570

niques have been shown to have a high sensitivity and specificity for the identification of DAVFs.[5-10] The diagnosis of DAVFs in daily practice on these conventional imaging studies remains a challenge, however. Unlike AVMs, which often have a conspicuous nidus surrounded by brain tissue, DAVFs often manifest only subtle findings on structural imaging.[4,11] An easily applicable imaging method that increases the conspicuity of DAVFs would therefore be valuable.

Arterial spin-labeling (ASL) is a completely noninvasive MR imaging technique that is now widely available on clinical MR imaging scanners. ASL signal is not observed in cerebral veins under normal conditions due to T1 decay during capillary transit and exchange with the extravascular space of labeled blood-water protons.[11,12] In conditions with arteriovenous shunting such as DAVFs, rapid transit of labeled blood directly from feeding arteries to draining veins results in high signal in venous structures.[11,12] This venous ASL signal is a conspicuous finding that can alert the reader to the presence of shunting. Conventional sequences can then be more closely scrutinized for structural signs of a DAVF. Preliminary studies indicate that ASL improves the detection of small intracranial shunting lesions and increases the reader's diagnostic confidence.[11] These prior investigations, however, included AVMs and only a few DAVFs.[11,12]

The purpose of this case-control study was to assess the value of an MR imaging protocol augmented with 3D pseudocontinuous ASL (pCASL) for the detection of DAVFs and to determine whether reader accuracy and confidence are improved over MR imaging with conventional structural sequences and TOF-MRA.

MATERIALS AND METHODS

Patient Population

This retrospective study was approved by our institutional review board.

Thirty-nine patients (15 females, 24 males, 8–86 years of age; mean age, 55 years) with a DAVF and 117 controls (51 females, 66 males, 4 months to 80 years of age; mean age, 50 years) who underwent both DSA and MR imaging with 3D pCASL at our institution between June 1, 2009, (pCASL was used in routine brain MR imaging protocols from this date) and September 30, 2014, were included. To develop our study population, we searched reports of consecutive cerebral DSAs performed during this time for the terms "DAVF," "dural AVF," "arteriovenous fistula," "fistula," and "carotid cavernous." This search yielded 792 patients: 139 consecutive patients with a DAVF and 653 patients with no DAVF.

Patients with DAVFs. Fifty-six of 139 patients with a DAVF diagnosed on DSA also had an MR imaging with 3D pCASL. One patient was excluded due to markedly motion-degraded images; and 16, due to angiographically complete treatment of the fistula before the MR imaging. Of the 39 patients included in the study, MR imaging and DSA were performed before any treatment of the fistula in 26 patients and following partial treatment (with DSA evidence of residual shunting) in 13. Fistula Cognard grades[13] were the following: I ($n = 10$), IIa ($n = 7$), IIb ($n = 7$), II a+ b ($n = 8$), III ($n = 6$), and IV ($n = 1$). Fistula locations were the following: transverse and/or sigmoid sinus ($n = 14$), marginal sinus ($n = 2$), superior sagittal sinus ($n = 3$), torcula herophili ($n = 1$), vein of Galen ($n = 3$), sphenoparietal sinus ($n = 1$), cavernous sinus ($n = 8$), cortical vein ($n = 6$, two infratentorial), and tentorium cerebelli ($n = 1$). Clinical presentations were the following: intracranial hemorrhage ($n = 15$), pulsatile tinnitus ($n = 9$), chemosis/proptosis ($n = 6$), cranial nerve VI palsy ($n = 2$), seizures ($n = 2$), dementia ($n = 1$), and follow-up of previous dural venous sinus thrombosis ($n = 2$) and meningioma resection ($n = 2$).

Controls. Six hundred fifty-three patients who had undergone DSA due to a clinical presentation (eg, pulsatile tinnitus or intracranial hemorrhage of unclear origin) potentially attributable to an intracranial vascular malformation did not have a DAVF. Patients with an AVM (which is also associated with arteriovenous shunting) on DSA were excluded. Two hundred nineteen of these patients had an MR imaging with pCASL, and 117 of these patients (3 times the number of cases) were randomly selected as controls.

In patients with multiple imaging studies, the DSA and MR imaging examinations temporally closest to each other were selected (mean time interval, 46 days for the control group and 57 days for the DAVF group).

Imaging Methods

In 68 subjects (16 patients, 52 controls), MRIs were performed on a 3T scanner (Discovery 750w; GE Healthcare, Milwaukee, Wisconsin); and in 88 subjects (23 patients and 65 controls), on a 1.5T scanner (Signa HDx; GE Healthcare).

3D pCASL imaging (TR/TE, 4800/9.5 ms [1.5T], 5000/10.5 ms [3T]; 24-cm FOV) with background suppression was implemented using a labeling period of 1500 ms, a postlabel delay of 2000 ms, the labeling plane at the level of the foramen magnum, and a segmented 3D stack-of-spirals FSE readout (spiral arms: 6 [1.5T]; 8 [3T]). In-plane spatial resolution was 3–4 mm, and through-plane spatial resolution was 4–6 mm, yielding 24–40 slices. Scan time was 3 minutes 30 seconds–6 minutes. No vascular crusher gradients were used. This acquisition complies with the consensus recommendations of the ASL community.[14] The presence of venous ASL signal was assessed on the label-control subtraction images and required no postprocessing.

3D multislab TOF-MRA (1.5T: TR/TE, 30/2.9 ms; FOV, 22 cm; matrix, 320 × 192; 1.4-mm slice thickness; 3T: TR/TE, 22/2.5 ms; FOV = 24 cm; matrix = 512 × 288; 1.2-mm slice thickness) was performed in 147 patients (36 patients and 111 controls).

All 156 MR imaging examinations also included the following sequences: sagittal T1-weighted (1.5T: TR/TE, 600/15 ms; 3T: TR/TE/TI, 1800/6.7/920 ms) and axial T2-weighted FSE (TR/TE, 4800/84 ms [1.5T]; 4000/100 ms [3T]); T2*-weighted gradient recalled-echo (TR/TE, 600/30 ms [1.5T]; 600/15 ms [3T]); T2-weighted FLAIR (TR/TE/TI, 8802/110/2200 ms [1.5T]; 9000/143/2300 ms [3T]); and diffusion-weighted (b=1000 s/mm^2; TR/TE, 6000/70 ms [1.5T], 5000/83 ms [3T]) imaging performed with a 24-cm FOV, 5-mm slice thickness.

Catheter-based DSA for the clinical work-up of the DAVF was performed by 1 of 3 interventional neuroradiologists (with 5, 12, and >20 years' experience respectively) in a dedicated biplane neuroangiography suite (Axiom Artis; Siemens, Erlangen, Germany). Imaging included, at minimum, anteroposterior and lat-

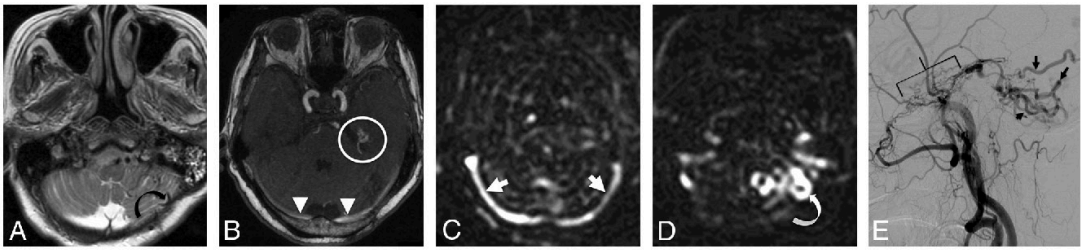

FIG 1. A 79-year-old woman presenting with ataxia. *A*, T2-weighted imaging demonstrates tortuous and ectatic pial veins (*curved black arrow*) along the inferior surface of the left cerebellar hemisphere. *B*, MIP TOF-MRA image demonstrates nodular and curvilinear hyperintensities immediately superior to the left petrous apex, representing a left tentorial fistula (*white circle*) and high signal in the transverse sinuses (*white arrowheads*). *C*, pCASL image shows venous ASL signal in the transverse sinuses (*white arrows*) due to shunting. *D*, More inferiorly, venous ASL signal is seen in draining pial veins (*white curved arrow*). *E*, DSA image following left external carotid artery injection confirms a Cognard type IV left tentorial DAVF (*bracket*) with a middle meningeal artery supply and drainage directly into ectatic cerebellar cortical veins (*black arrows*).

eral views obtained following selective injection with iodinated contrast medium (iohexol, Omnipaque 300; GE Healthcare, Piscataway, New Jersey) of the internal carotid, external carotid, and/or vertebral artery supplying the DAVF.

CTA was not included in this evaluation because it is not routinely performed for the evaluation of suspected DAVFs at our institution and it was therefore inconsistently available in the patients in the study population.

Image Interpretation

MR Imaging. MRIs were independently reviewed in random order by 2 neuroradiologists (with 20 years' and 5 years' postfellowship experience) blinded to the clinical data and DSA findings. Review of nonenhanced CT performed before MR imaging was not permitted because it was unavailable in many patients with DAVFs ($n = 31$).

The readers rated the likelihood of a DAVF on a 5-point Likert scale (1, very unlikely; 2, unlikely; 3, equally likely and unlikely; 4, likely; and 5, very likely) based on sequences presented to them. The reads were performed in 2 separate sittings, with and without pCASL, 2 months apart to negate the effects of memory and learning:

First Sitting. pCASL was omitted.

Step 1. Structural sequences (T1- and T2-weighted imaging, FLAIR, and gradient recalled-echo) were reviewed first to establish the baseline accuracy of MR imaging for identification of DAVFs. We recorded the presence or absence of each of the following signs: intracranial hemorrhage; white matter T2 hyperintensity with mass effect (edema); abnormal vessels (abnormal clusters of flow voids, serpiginous and/or dilated leptomeningeal or medullary vessels, and/or venous pouches) (Fig 1*A*); and enlarged (reader's subjective impression) dural venous sinuses. DAVFs in the cavernous sinus may produce characteristic features suggestive of this diagnosis; therefore, we specifically recorded these signs: cavernous sinus enlargement, superior ophthalmic vein enlargement, proptosis, and/or orbital edema. The overall likelihood of a DAVF was then rated on the 5-point Likert scale.

Step 2. In the 147 patients in whom TOF-MRA was performed, source images and MIPs were assessed next. The following signs were recorded as present or absent: hyperintense (signal higher than that of suppressed background tissue and similar to that within arteries) dural venous sinus (Fig 1*B*) or cortical vein; nodular and/or curvilinear hyperintense structures[5] (NCH) adjacent to a dural venous sinus, representing the fistula itself (Fig 1*B*); increased number or size of arteries near a dural venous sinus; and/or enlargement of external carotid artery branches.[5,6] The overall likelihood of a DAVF based on TOF-MRA and structural features was rated on the 5-point Likert scale.

Second Sitting. pCASL was first reviewed in conjunction with anatomic sequences. The presence or absence of venous ASL signal, defined as the presence of high signal intensity on pCASL images within a dural venous sinus (Fig 1*C*), deep venous structure, and/or cortical vein (Fig 1*D*) was recorded. TOF-MRA (source and MIP images) was subsequently reviewed, and the overall likelihood of a DAVF based on all sequences was rated.

The presence of a DAVF on angiography was considered the criterion standard. When there was discordance between the findings on MR imaging and angiography, the DSA and MR imaging were reviewed, in consensus, by the 2 neuroradiologists and an experienced neurointerventional radiologist.

Statistical Analysis

All statistical analyses were performed using SPSS (SPSS Statistics 24.0.0.1, 64 bit; IBM, Armonk, New York) and MedCalc Statistical Software, Version 17.2, 64 bit (MedCalc Software, Mariakerke, Belgium).

To test the added value of pCASL, we performed sensitivity and specificity analyses (individual reader and pooled) for the following: 1) conventional structural MR imaging (sMRI) alone; 2) structural MR imaging and TOF-MRA (sMRI/MRA); 3) structural MR imaging, TOF-MRA, and pCASL (sMRI/MRA/pCASL) using receiver operating characteristic (ROC) analyses by nonparametric estimation of the area-under-the-ROC-curve (AUC) and subsequent pair-wise comparisons using the DeLong algorithm.

Sensitivity, specificity, positive predictive value (PPV), and negative predictive value (NPV) for individual imaging features were computed using the readers' classification tables, with the reference standard being the presence or absence of a DAVF. The likelihood of a DAVF (on DSA) based on the identification of an

Table 1: Individual imaging features—univariate binary logistic regression analysis on DSA and interreader agreement

Imaging Feature	OR	SE	Wald Test	*P*	Sensitivity (95% CI) (%)	Specificity (95% CI) (%)	PPV (95% CI) (%)	NPV (95% CI) (%)	Interobserver Agreement (κ) (95% CI)
Structural MRI									
ICH	0.18	1.32	37.84	.001	37.2 (26.5–47.9)	23.1 (17.7–28.5)	13.9 (9.2–18.6)	52.4 (43.0–62.1)	0.99 (0.97–1.00)
Vasogenic edema or gliosis	0.36	1.37	10.59	.001	20.8 (11.7–58.1)	58.1 (51.8–64.4)	14.0 (7.7–20.4)	69.0 (62.6–75.5)	1.00 (1.00–1.00)
Abnormal vessels	5.57	1.32	37.24	.001	59.0 (48.1–69.9)	79.5 (74.3–84.7)	48.9 (38.8–59.0)	85.3 (80.6–90.0)	0.73 (0.67–0.79)
Enlarged sinus	2.58	1.36	9.50	.002	31.2 (20.8–41.5)	79.9 (73.9–85.8)	40.7 (28.1–53.2)	72.4 (66.1–78.7)	0.69 (0.61–0.76)
Enlarged SOV	3.68	1.62	7.36	.007	12.7 (5.3–20.0)	96.2 (93.7–98.6)	52.6 (30.2–75.1)	76.5 (71.7–81.4)	0.83 (0.74–0.93)
Cavernous sinus enlargement	34.80	2.14	21.85	.001	23.1 (13.7–32.4)	99.2 (98.0–100.3)	90.0 (76.9–103.2)	79.5 (74.8–84.1)	0.89 (0.82–0.97)
Orbital edema/proptosis	12.26	2.23	10.38	.001	10.3 (3.5–17.0)	99.2 (98.0–100.3)	80.0 (55.2–104.8)	76.8 (72.1–81.6)	1.00 (1.00–1.00)
Time-of-flight MRA									
NCH	114.70	1.88	56.75	.001	61.1 (49.9–72.4)	98.7 (97.1–100.2)	93.6 (86.6–100.6)	88.7 (84.7–92.6)	0.87 (0.82–0.93)
Abnormal vessels	6.00	1.34	37.28	.001	59.7 (48.4–71.1)	80.2 (74.9–85.4)	49.4 (38.9–59.9)	86.0 (81.3–90.7)	0.38 (0.30–0.46)
Venous signal	20.75	1.47	60.96	.001	87.5 (79.9–95.1)	74.8 (69.1–80.5)	52.9 (44.0–61.9)	94.9 (91.6–98.1)	0.87 (0.83–0.91)
Enlarged extracranial arteries	17.81	1.41	70.98	.001	62.5 (51.3–73.7)	91.4 (87.8–95.1)	70.3 (59.1–81.5)	88.3 (84.1–92.4)	0.76 (0.69–0.83)
ASL									
Venous ASL signal	103.20	1.65	84.95	.001	93.6 (88.2–99.0)	87.6 (83.4–91.8)	71.5 (62.8–80.3)	97.6 (95.6–99.7)	0.94 (0.9–0.97)

Note:—SOV indicates superior ophthalmic vein; SE, standard error; ICH, intracerebral hemorrhage.

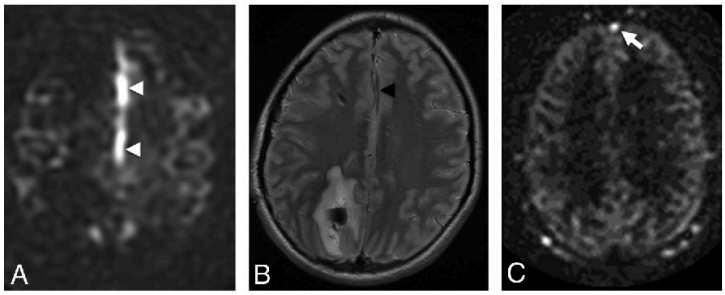

FIG 2. False-positive venous ASL signal in 2 patients. *A*, ASL signal in the A3 branches of the anterior cerebral arteries (*white arrowheads*) was mistaken for venous ASL signal in a 15-year-old male patient who presented with a right parietal parenchymal hematoma. *B*, T2-weighted images show localization of this signal to the anterior cerebral arteries (*black arrowhead*). *C*, ASL signal in the anterior aspect of the superior sagittal sinus in a 70-year-old man with subarachnoid hemorrhage (*white arrow*). This patient had no evidence of a DAVF or shunting on DSA.

individual imaging feature was determined using univariate binary logistic regression. A likelihood ratio test between multivariate binary logistic regression models was performed to determine whether the addition of the venous ASL signal feature yielded a stronger association with the presence of a DAVF than structural features alone or structural-plus-TOF-MRA features.

Interobserver agreement between readers was assessed using the Cohen κ statistic for specific imaging features and a linear weighted κ statistic for the likelihood of a DAVF. A κ of at least 0.61 (substantial agreement) was made a prerequisite to pool reader scores for subsequent analysis.

RESULTS

Individual Imaging Features

Venous ASL signal had the highest sensitivity (94%; 95%, CI 88%–99%) and NPV (98%; 95% CI, 96%–100%) for DAVFs of all the investigated specific features (Table 1).Venous ASL signal and other signs of DAVFs were not visible even on post hoc review of 2 false-negative cases. Both were low-flow DAVFs (1 incidentally detected tentorial fistula in a patient undergoing DSA for evaluation of aneurysmal subarachnoid hemorrhage and 1 low-flow cavernous sinus DAVF).

Nodular and/or curvilinear hyperintensities on TOF-MRA (Fig 1*B*) had a much lower sensitivity (61%; 95% CI, 50%–72%). Of the 36 patients with a fistula who had undergone TOF-MRA, the fistula was located above the TOF-MRA slab in 3 on post hoc analysis. Of the 33 patients whose fistula was located within the TOF-MRA slab, NCH were not identified in 9 (reader 1) and 13 (reader 2) patients, and they were absent in 7 patients (21%) on post hoc review. Three were Cognard III fistulas with a single feeding artery.

Univariate binary logistic regression analyses found extremely high odds ratios for both venous ASL signal (103) and NCH (114), reflecting their high specificity. There were a number of false-positives for venous ASL signal in our cohort; therefore, its specificity (88%; 95% CI, 83%–92%) was lower than that of NCH (99%; 95% CI, 97%–100%). On post hoc review of these 16 false-positive cases, cortical vein ASL signal was evident in 4 and dural venous sinus ASL signal was seen in 11. A definite cause for this ASL signal such as an AVM, hypervascular tumor, or subacute stroke could not be discerned on review of these patients' clinical histories and follow-up imaging, including DSAs. In 3 patients, the cortical vein ASL signal was observed immediately adjacent to a parenchymal hematoma, and we hypothesize that the hematoma may have compressed and obscured (on DSA and conventional MR imaging) a small parenchymal AVM. The other most likely explanation for venous ASL signal in these cases, as well as in 7 of the patients with dural sinus ASL signal, is seizure incited by parenchymal hematoma. In the 4 remaining patients, mild ASL signal in the anterior superior sagittal sinus (Fig 2*C*) was not associated with parenchymal hematoma, and this is likely a normal variant.

There may have been a small underlying AVM in each of these cases, obscured and compressed by hematoma, hence occult on DSA and structural MR imaging. Alternatively, subclinical seizures incited by hematoma would also account for the venous ASL signal.

Arterial transit artifact[15] was mistaken for venous ASL signal in 1 control (Fig 2*A*). Venous hyperintensity on TOF-MRA had a lower specificity (75%; 95% CI, 69%–80%) than venous ASL sig-

nal due to a greater number of false-positives (26 for reader 1 and 30 for reader 2).

Structural imaging signs of a fistula were of high specificity but low sensitivity and NPV. Although signs of a cavernous sinus DAVF had high specificity and odds ratios, fistulas in this location were too sparsely represented in our study cohort to draw meaningful conclusions related to these findings.

Agreement between the readers was almost perfect ($\kappa > 0.81$) for all individual features except 3 TOF-MRA parameters: enlarged sinus, enlarged extracranial arteries, and abnormal vessels (Table 1). Only fair agreement ($\kappa > 0.21$) was reached on the latter.

Overall Assessment

The ROC plots (Fig 3), their corresponding AUCs, and the substantial differences in the AUCs demonstrate improvement in diagnostic performance for the detection of DAVFs with the addition of pCASL (Table 2). Diagnostic performance significantly improved with the addition of TOF-MRA to sMRI (pooled ΔAUC, 0.14; $P < .01$). The addition of pCASL significantly improved diagnostic performance over sMRI (pooled ΔAUC, 0.179; $P < .01$). Improvement in diagnostic performance with the addition of pCASL to sMRI/TOF-MRA reached statistical significance for reader 2 but not reader 1 (whose excellent diagnostic performance on sMRI and TOF-MRA left little room for improvement). When reader performance was pooled, a trend toward improvement was seen (with only 11% probability that the observed improvement in the detection of DAVFs was due to chance).

These ROC analysis findings were corroborated by the multivariate binary logistic regression models indicating a significant contribution to diagnostic performance from the addition of TOF-MRA and pCASL features to sMRI (Table 3 and On-line Tables 1 and 2). If we applied a $P = .5$ classification threshold (Table 4), sensitivity was poor for sMRI (33%; 95% CI, 22%–44%), improved if TOF-MRA was added (sensitivity, 76%; 95% CI, 66%–86%), and increased further with pCASL (sensitivity, 89%; 95% CI, 81%–96%) at comparably high specificity (On-line Table 2). When used in combination, sMRI, MRA, and pCASL yielded a high NPV of 96.4% (95% CI, 93.9%–98.9%), which is crucial if MR imaging is to be used as a screening tool.

Incremental improvement in reader confidence in the presence or absence of a DAVF with the addition of pCASL is illustrated in Fig 4.

Interobserver agreement was good for structural imaging alone ($\kappa = 0.62$; 95% CI, −1.0–1.0) and improved with the addition of TOF-MRA ($\kappa = 0.72$; 95% CI, −1.0–1.0). It improved substantially and was almost perfect with the addition of pCASL ($\kappa = 0.92$; 95% CI, −0.23–1.0).

In 4 cases, a DAVF was present on DSA but was considered unlikely on MR imaging until pCASL was reviewed. In 1 case, the fistula was located outside the TOF-MRA slab. In the remaining 3 cases, the fistula was not visible on TOF-MRA despite being located within the slab, and other MRA signs were also absent. Two of these cases were partially treated fistulas with low residual flow on DSA.

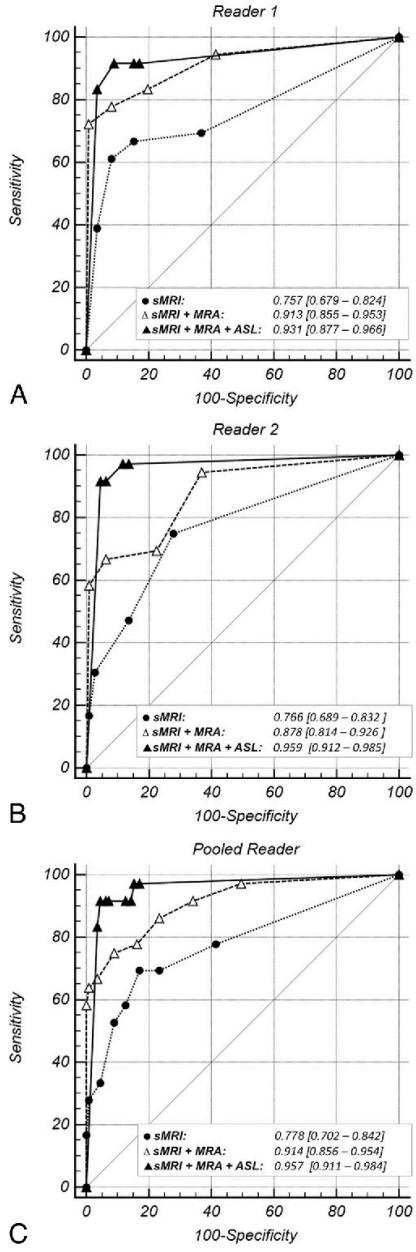

FIG 3. ROC curves for each reader's individual diagnostic performance (*A* and *B*) and their pooled diagnostic performance (*C*) with each of the following: structural MR imaging (*dotted line*), structural MR imaging and TOF-MRA (sMRI + MRA, *dashed line*), and structural MR imaging with TOF-MRA and pCASL (sMRI + MRA + pCASL, *solid line*). The *light gray diagonal* is the line of no discrimination. The triangle and dot symbols on the curve indicate true-positive rate/false-positive rate pairs computed at different discrimination thresholds. With the addition of TOF-MRA and then pCASL to structural MR imaging, the ROC curve becomes more well-rounded with an incrementally higher AUC. This indicates increased diagnostic sensitivity for detection of a DAVF at a set specificity.

Table 2: Pair-wise comparison of ROC curves

Reader, Diagnostic Instrument	ΔAUC	SE	95% CI	z	P
Reader 1					
sMRI vs sMRI + MRA	0.156	0.046	0.066–0.247	3.381	<.01
sMRI vs sMRI + MRA + pCASL	0.174	0.047	0.082–0.266	3.701	<.01
sMRI + MRA vs sMRI+MRA + pCASL	0.018	0.028	−0.036–0.072	0.644	.52
Reader 2					
sMRI vs sMRI + MRA	0.112	0.044	0.027–0.197	2.581	<.01
sMRI vs sMRI + MRA + pCASL	0.193	0.043	0.108–0.277	4.475	<.01
sMRI + MRA vs sMRI + MRA + pCASL	0.081	0.030	0.022–0.140	2.675	<.01
Pooled Readers 1 + 2					
sMRI vs sMRI + MRA	0.136	0.042	0.053–0.219	3.208	<.01
sMRI vs sMRI + MRA + pCASL	0.179	0.045	0.091–0.267	3.965	<.01
sMRI + MRA vs sMRI + MRA + pCASL	0.043	0.027	−0.009–0.100	1.615	.11

Table 3: Pair-wise likelihood ratio tests for the multivariate models

Reader, Diagnostic Instrument	-2LL	χ^2	P	Δdf
sMRI	260.18			
sMRI + MRA	117.09			
sMRI + MRA + ASL	84.23			
(sMRI) vs (sMRI + MRA)		143.09	<.001[a]	4
(sMRI + MRA) vs (sMRI + MRA + ASL)		32.86	<.001[a]	1
(sMRI) vs (sMRI + MRA + ASL)		175.95	<.001[a]	8

Note:—LL indicates log likelihood.
[a] Significance ($P < .001$)—that is, that the null hypothesis (difference in −2LLs = 0) is rejected and that the −2LLs are different.

DISCUSSION

This case-control study confirmed that venous ASL signal has a high sensitivity and specificity and an even higher NPV than previously reported[11] for detecting the presence of an intracranial DAVF. Identification of venous ASL signal improves the diagnostic accuracy and increases confidence in the presence or absence of a DAVF. We have previously shown that MR imaging with pCASL can be used to accurately determine the grade of a DAVF.[16] In this study, we investigated the clinical utility of pCASL for detection of DAVFs.

A reliable noninvasive technique for detection of DAVFs can improve patient triage, expedite referral for treatment, and decrease the number of DSAs a patient with a DAVF undergoes by allowing diagnostic and therapeutic angiography to be performed at the same session. Perfect or almost perfect sensitivity and NPV are requisite, given that failure to detect a DAVF has a greater potential for adverse consequences than a false-positive. Unfortunately, conventional structural MR imaging is unreliable for the diagnosis of DAVF as seen in this study. TOF-MRA was also less sensitive than previously reported. For example, nodular/curvilinear hyperintensities have been previously reported to be 100% sensitive,[5] but these were absent even on post hoc review in 21% of DAVFs. Three were high-grade fistulas with a single feeding artery draining directly into a nonectatic cortical vein that would not be expected to manifest as nodular/curvilinear hyperintensities.

Venous ASL signal had a higher sensitivity for the presence of a DAVF than structural or TOF-MRA signs. There were only 2 cases in which the venous ASL signal was absent. The high conspicuity of the venous ASL signal against the relatively flat background of normal ASL signal makes it easy to detect when present. Nulling of static tissue signal by background suppression and subtraction of control from label images produces a high contrast-to-noise ratio with only labeled blood giving rise to signal on pCASL images.[15,16] One hundred percent of the voxel is occupied by labeled blood in a draining vein in comparison with 2%–5% in a tissue voxel.[16] There is also greater T1 decay of signal of labeled blood by the time it reaches the tissue in comparison with labeled blood shunted directly into venous structures. Consequently, there is a large contrast differential between the draining veins of a DAVF and adjacent brain parenchyma.[16] Absence of ASL signal in arteries under normal conditions also enhances the conspicuity of the venous ASL signal. Conversely, high signal is seen in normal arteries on both TOF-MRA and contrast-enhanced MRA. A hyperintense cortical vein may therefore be dismissed or misclassified as an artery on these sequences.

pCASL is likely to be particularly beneficial to less experienced readers: The junior reader in this study had a lower sensitivity for detection of DAVFs on sMRI and TOF-MRA and demonstrated greater improvement in diagnostic performance following the addition of pCASL. The readers' confidence and agreement regarding the presence or absence of a DAVF also improved following review of pCASL. Interreader agreement for venous ASL signal was higher than for TOF-MRA signs. These findings suggest that venous ASL signal is not only easier to detect but can also be interpreted with greater certainty. Even when present, findings on structural sequences and TOF-MRA are often subtle and equivocal, requiring scrutiny of images and high diagnostic skill to identify and interpret; this has relevance in routine clinical practice, in which there is a broad range of reader experience levels and more likelihood that an unsuspected positive case will be mixed in with many negative cases. The high conspicuity of venous ASL signal may also enable detection of unsuspected DAVFs.

Venous ASL signal also had a high specificity for the presence of a DAVF. Theoretically, high signal is absent in venous structures on pCASL under normal conditions due to T1 decay of labeled blood during the time it takes to pass through the tissue capillary bed.[11,12] The shorter time that labeled blood takes to reach veins when shunted directly precludes significant T1 decay. Venous ASL signal is therefore seen in conditions with arteriovenous shunting, including hypervascular tumors, seizures, stroke, and AVMs.[11,12] False-positive cases of venous ASL signal in this study were likely due to one of these alternative causes of shunting, such as seizure or an occult AVM obscured by hematoma. Four control patients with mild ASL signal in the anterior aspect of the superior sagittal sinus lacked a plausible alternative cause of shunting. The authors have observed mild ASL signal in

Table 4: Classification tables for the multivariate binary logistic regression models[a]

MRI Sequences	Sensitivity (95% CI) (%)	Specificity (95% CI) (%)	PPV (95% CI) (%)	NPV (95% CI) (%)
Structural MRI alone	32.9 (22.3–43.5)	97.0 (94.8–99.2)	78.1 (63.8–92.5)	81.7 (77.1–86.2)
Structural MRI and TOF-MRA	75.7 (65.7–85.8)	98.7 (97.1–100.2)	94.6 (88.8–100.5)	92.8 (89.5–96.1)
Structural MRI, TOF-MRA and pCASL	88.6 (81.1–96.0)	96.4 (93.9–98.9)	88.5 (81.1–96.0)	96.4 (93.9–98.9)

[a] Classification table generated for a probability value of $P = .05$ for each of the 3 multivariate models.

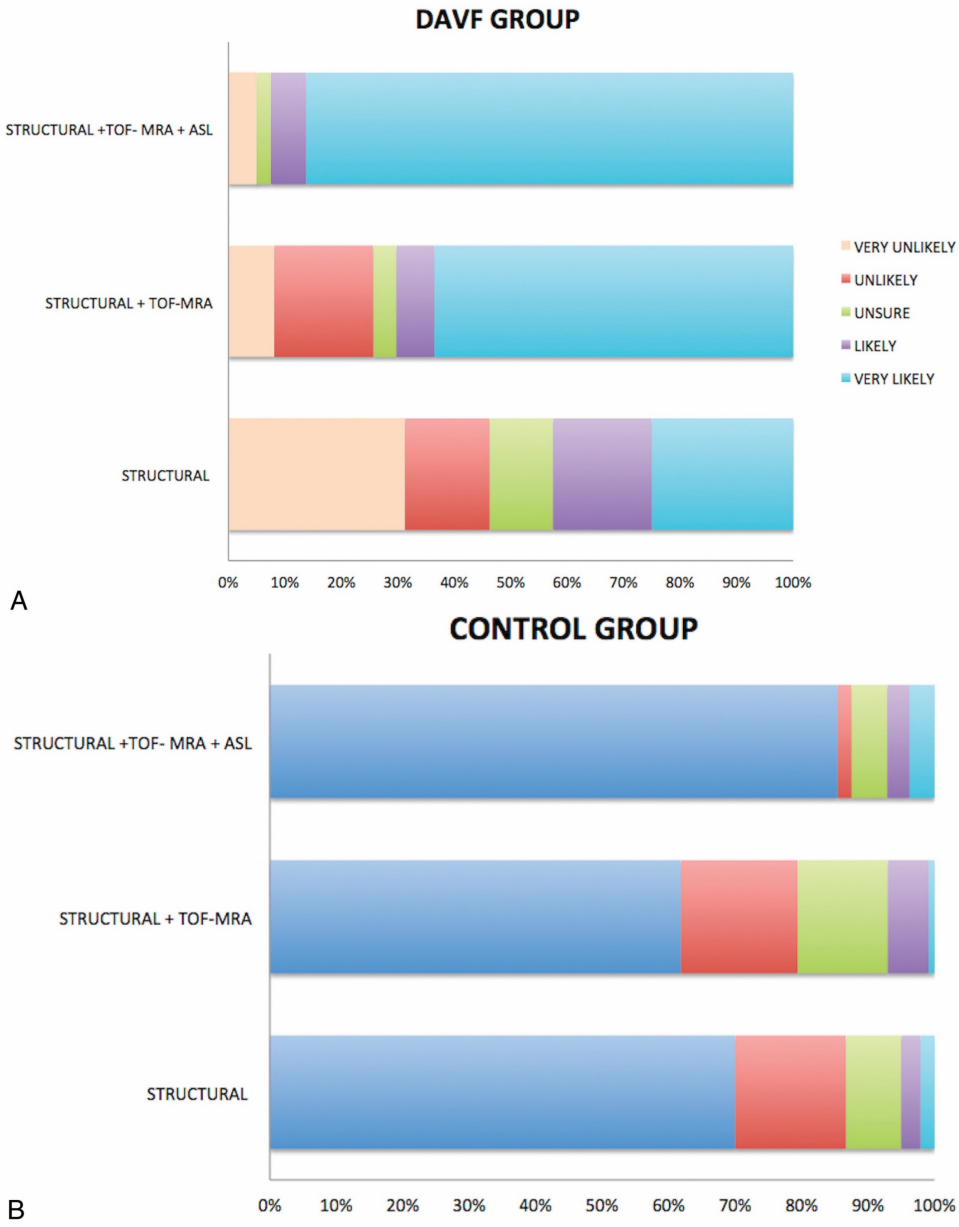

FIG 4. Distribution of Likert scale scores for patients with (*A*) and without (*B*) a DAVF on structural MR imaging alone, structural MR imaging with TOF-MRA (sMRI/MRA), and structural MR imaging with both TOF-MRA and pCASL (sMRI/MRA/pCASL). *A*, In the DAVF group, there is a marked incremental increase in reader accuracy and confidence in the presence of a DAVF—with a higher percentage considered "very likely" to have a DAVF—with the addition of pCASL. *B*, In the control group, reader accuracy and confidence in the absence of a DAVF decrease with the addition of TOF-MRA to sMRI due to a high number of false-positives for venous hyperintensity on TOF-MRA. Reader certainty as to the absence of a fistula increased (and was highest) following review of pCASL.

this location in other patients without a shunting lesion. Readers should be cognizant of this potential normal variant.

Another advantage of pCASL is whole-brain coverage in a reasonable scan time. Despite technologic advances such as 3T and parallel imaging, coverage of TOF-MRA often does not extend to the vertex due to clinical time constraints. DAVFs located superior to the imaged slabs may therefore be missed.

Venous ASL signal was absent in 2 low-flow DAVFs, likely due to an inadequate volume of shunted blood to produce perceptible signal in draining veins. Two other low-flow fistulas were detected on pCASL but missed on TOF-MRA (likely due to signal saturation). There were too few[4] low-flow DAVFs in this study to draw meaningful conclusions regarding this population. Long-label long-delay pCASL may allow detection of these low-flow fistulas, because more labeled blood would be present in draining veins at a later imaging.[15]

Another potential pitfall of pCASL is high signal in arterial structures in conditions with delayed transit of labeled blood such as steno-occlusive disease.[11,15] Cognizance of this arterial transit artifact[15] (Fig 2*A*) and careful cross-reference with other sequences are necessary to avoid false-positives.

Contrast-enhanced MRA has been reported to be accurate for the detection of DAVFs.[5,7,17] The diagnosis requires identification of early venous filling, which is likely more challenging than identification of the conspicuous venous ASL sign, given the compromise between spatial and temporal resolution required to perform clinical contrast-enhanced MRA; even with highly constrained reconstruction techniques, spatial and temporal resolution is much lower than that of DSA.[18] Contrast-enhanced MRA also requires administration of gadolinium-based contrast, adding to the cost. Gadolinium is also associated with a risk of anaphylaxis, nephrogenic systemic fibrosis, and deposition. Other advanced techniques for detection and characterization of DAVFs such as 4D ASL–based MRA[18] are still research tools not available for clinical use.

pCASL is also available on both 1.5T and 3T clinical units and is feasible within the constraints of everyday clinical practice. Given its utility for detection of intracranial shunting, we recommend its routine inclusion in the MR imaging protocol for patients with intracranial hemorrhage and pulsatile tinnitus. It should also be added to the protocol for those patients with clinical or noninvasive imaging findings raising suspicion for a DAVF.

The major limitation of this study is the small number of low-flow DAVFs, which may potentially be occult on pCASL. Its retrospective nature also limited us to reviewing routine MR images obtained at our institution. Prospective enrollment would enable inclusion and comparative assessment of CTA, contrast-enhanced MRA, and alterative ASL techniques (eg, long-label long-delay, which may be more sensitive for shunting).

CONCLUSIONS

Venous ASL signal has high sensitivity and specificity for the presence of a DAVF; hence, its identification increases confidence in the presence or absence of a DAVF on noninvasive imaging. It is also a highly conspicuous finding that is easy to detect and has the potential to increase diagnostic performance, particularly of less experienced readers. False-positives can occur and are likely due to alternative causes of intracranial shunting. False-negatives also occur, with some small and low-flow fistulas occult on MR imaging with pCASL so that sensitivity is imperfect compared with the criterion standard of DSA. We therefore do not advocate replacing DSA for the screening of DAVFs at this stage if clinical suspicion of a DAVF is high, but MR imaging with pCASL can help refine triage and expedite management by increasing confidence in the diagnosis.

ACKNOWLEDGMENTS

The authors would like to thank Dr Jarrett Rosenberg for his feedback on the statistical analyses.

Disclosures: Shalini A. Amukotuwa—*RELATED*: *Grant*: National Institute of Biomedical Imaging and Bioengineering, *Comments*: grant numbers 5R21EB021029, 3R01EB002711-06S1.* Fernando Calamante—*RELATED*: *Grant*: National Health and Medical Research Council of Australia; *UNRELATED*: *Grant*: Australian Research Council; *Payment for Lectures Including Service on Speakers Bureaus*: Siemens.* Greg Zaharchuk—*UNRELATED*: *Grants/Grants Pending*: GE Healthcare, National Institutes of Health. Roland Bammer—*RELATED*: *Grant*: National Institute of Biomedical Imaging and Bioengineering, *Comments*: grant numbers 5R21EB021029, 3R01EB002711-06S1*; *Support for Travel to Meetings for the Study or Other Purposes*: National Institutes of Health (National Institute of Biomedical Imaging and Bioengineering).* *Money paid to the institution.

REFERENCES

1. Newton TH, Cronqvist S. **Involvement of dural arteries in intracranial arteriovenous malformations.** *Radiology* 1969;93:1071–78 CrossRef Medline
2. Cognard C, Casasco A, Toevi M, et al. **Dural arteriovenous fistulas as a cause of intracranial hypertension due to impairment of cranial venous outflow.** *J Neurol Neurosurg Psychiatry* 1998;65:308–16 CrossRef Medline
3. Cloft HJ, Joseph GJ, Dion JE. **Risk of cerebral angiography in patients with subarachnoid hemorrhage, cerebral aneurysm, and arteriovenous malformation: a meta-analysis.** *Stroke* 1999;30:317–20 CrossRef Medline
4. Miller TR, Gandhi D. **Intrancranial dural arteriovenous fistulae: clinical presentation and management strategies.** *Stroke* 2015;46:2017–25 CrossRef Medline
5. Noguchi K, Melhem ER, Kanazawa T, et al. **Intracranial dural arteriovenous fistulas: evaluation with combined 3D time-of-flight MR angiography and MR digital subtraction angiography.** *AJR Am J Roentgenol* 2004;182:183–90 CrossRef Medline
6. Kwon BJ, Han MH, Kang HS, et al. **MR imaging findings of intracranial dural arteriovenous fistulas: relations with venous drainage patterns.** *AJNR Am J Neuroradiol* 2005;26:2500–07 Medline
7. Meckel S, Maier M, Ruiz DS, et al. **MR angiography of dural arteriovenous fistulas: diagnosis and follow-up after treatment using a time-resolved 3D contrast-enhanced technique.** *AJNR Am J Neuroradiol* 2007;28:877–84 Medline
8. Farb RI, Agid R, Willinsky RA, et al. **Cranial dural arteriovenous fistula: diagnosis and classification with time-resolved MR angiography at 3T.** *AJNR Am J Neuroradiol* 2009;30:1546–51 CrossRef Medline
9. Nishimura S, Hirai T, Sasao A, et al. **Evaluation of dural arteriovenous fistulas with 4D contrast-enhanced MR angiography at 3T.** *AJNR Am J Neuroradiol* 2010;31:80–85 CrossRef Medline
10. Brouwer PA, Bosman T, van Walderveen MA, et al. **Dynamic 320-section CT angiography in cranial arteriovenous shunting lesions.** *AJNR Am J Neuroradiol* 2010;31:767–70 CrossRef Medline
11. Le TT, Fischbein NJ, André JB, et al. **Identification of venous signal on arterial spin labeling improves diagnosis of dural arteriovenous fistulas and small arteriovenous malformations.** *AJNR Am J Neuroradiol* 2012;33:61–68 CrossRef Medline

12. Wolf RL, Wang J, Detre JA, et al. **Arteriovenous shunt visualization in arteriovenous malformations with arterial spin-labeling MR imaging.** *AJNR Am J Neuroradiol* 2008;29:681–87 CrossRef Medline
13. Cognard C, Gobin YP, Pierot L, et al. **Cerebral dural arteriovenous fistulas: clinical and angiographic correlation with a revised classification of venous drainage.** *Radiology* 1995;194:671–80 CrossRef Medline
14. Alsop DC, Detre JA, Golay X, et al. **Recommended implementation of arterial spin-labeled perfusion MRI for clinical applications: a consensus of the ISMRM perfusion study group and the European consortium for ASL in dementia.** *Magn Reson Med* 2015;73:102–16 CrossRef Medline
15. Amukotuwa SA, Yu C, Zaharchuk G. **3D pseudocontinuous arterial spin labeling in routine clinical practice: a review of clinically significant artifacts.** *J Magn Reson Imaging* 2016;43:11–27 CrossRef Medline
16. Amukotuwa SA, Heit JJ, Marks MP, et al. **Detection of cortical venous drainage and determination of the Borden type of dural arteriovenous fistula by means of 3D pseudocontinuous arterial spin-labeling MRI.** *AJR Am J Roentgenol* 2016;207:163–69 CrossRef Medline
17. Clark Z, Johnson KM, Wu Y, et al. **Accelerated time-resolved contrast-enhanced magnetic resonance angiography of dural arteriovenous fistulas using highly constrained reconstruction of sparse cerebrovascular data sets.** *Invest Radiol* 2016;51:365–71 CrossRef Medline
18. Iryo Y, Hirai T, Kai Y, et al. **Intracranial dural arteriovenous fistulas: evaluation with 3-T four-dimensional MR angiography using arterial spin labeling.** *Radiology* 2014;271:193–99 CrossRef Medline

On-line Table 1: Results of multivariate binary logistic regression

Assessment of Presence of DAVF	OR	SE	Wald	P[a]	95% CI of OR[b]
Structural MRI alone					
Structural MRI					
ICH	0.153	0.367	26.108	<.001	0.0747–0.3149
Vasogenic edema or gliosis	0.625	0.402	1.365	.243	0.2841–1.3749
Abnormal vessels	8.091	0.362	33.443	<.001	3.9835–16.4343
Enlarged sinus	1.085	0.389	0.0442	.833	0.5065–2.3250
Structural MRI alone plus TOF-MRA					
Structural MRI					
ICH	0.168	0.570	9.802	.002	0.0550–0.5132
Vasogenic edema or gliosis	0.562	0.651	0.782	.376	0.1571–2.0137
Abnormal vessels	7.537	0.555	13.222	<.001	2.5373–22.3870
Enlarged sinus	0.057	0.925	9.648	.002	0.0092–0.3463
Time-of-flight MRA					
Fistula	152.821	1.151	19.080	<.001	15.9993–1459.697
Abnormal vessels	0.747	0.557	0.275	.600	0.2507–2.2253
Venous signal	11.123	0.556	18.749	<.001	3.7380–33.0985
Enlarged extracranial vessels	4.919	0.630	6.386	.012	1.4297–16.9207
Structural MRI alone plus TOF-MRA plus ASL					
Structural MRI					
ICH	0.388	0.694	1.861	.173	0.0995–1.5120
Vasogenic edema or gliosis	0.357	0.781	1.738	.187	0.0772–1.6510
Abnormal vessels	2.635	0.670	2.095	.148	0.7095–9.7874
Enlarged sinus	0.083	1.133	4.842	.028	0.0090–0.7615
Time-of-flight MRA					
NCH	58.757	1.324	9.462	.002	4.3837–787.5378
Abnormal vessels	0.768	0.654	0.163	.687	0.2132–2.7670
Venous signal	8.872	0.641	11.589	<.001	2.5247–31.1798
Enlarged extracranial vessels	4.400	0.755	3.855	.050	1.0025–19.2997
ASL					
Venous ASL signal	28.888	0.676	24.748	<.001	7.6773–108.7008

Note:—ICH indicates intracerebral hemorrhage.

[a] The Wald statistic tests the null hypothesis that in the test population, there is no difference in the logarithm of the odds for detecting a DAVF on DSA for the dependent variable (ie, state variable) to be true vs false (ie, OR = 1). If the Wald test is below the standard significance level ($P < .001$), one can reject the null hypothesis.

[b] There is a 95% chance that the point estimate of the OR lies within this interval and a 5% chance that the true value is either below or above this interval.

On-line Table 2: Classification tables for the multivariate binary logistic regression models and corresponding diagnostic performance indicators

Assessment of Presence of DAVF	DSA = 0 Predicted = 0 (TN)[a]	DSA = 0 Predicted = 1 (FP)[a]	DSA = 1 Predicted = 0 (FN)[a]	DSA = 1 Predicted = 1 (TP)[a]	Sensitivity 95% CI (%)[b]	Specificity 95% CI (%)[b]	PPV 95% CI (%)[b]	NPV 95% CI (%)[b]
Structural MRI alone	227	7	51	25	32.89 (22.33–43.46)	97.01 (94.83–99.19)	78.13 (63.80–92.45)	81.65 (77.10–86.20)
Structural MRI plus TOF-MRA	219	3	17	53	75.71 (65.67–85.76)	98.65 (97.13–100.17)	94.64 (88.75–100.54)	92.80 (89.50–96.10)
Structural MRI plus TOF-MRA plus ASL	214	8	8	62	88.57 (81.12–96.02)	96.40 (93.94–98.85)	88.57 (81.12–96.02)	96.40 (93.94–98.85)

Note:—TN indicates true-negative; FP, false-positive; FN, false-negative; TP, true-positive.

[a] The classification table was generated for a probability value of $P = .5$ for each of the 3 multivariate models.

[b] There is a 95% chance that the point estimate (*z*) of the sensitivity, specificity, PPV, or NPV lies within this interval and a 5% chance that the true value is either below or above this interval. The 95% CIs were computed on the basis of $z \pm 1.96 \times$ Standard Error.

9.3 Discussion

In this study, radiologist diagnostic performance and confidence for detection of a DAVF on MRI was assessed, with and without PCASL. It was shown that venous ASL signal had a high sensitivity (94%), specificity (88%) and negative predictive value (98%) for the presence of a DAVF. Identifying this sign improved diagnostic performance, and confidence in the presence or absence of DAVF, indicating that there is added value in including PCASL in the MRI protocol.

Venous ASL signal had a higher sensitivity for a DAVF than any other sign that was assessed on structural sequences and TOF-MRA. This is likely attributable to the high conspicuity of venous ASL signal, making it easy to detect when present. There were two false negatives, however, where venous ASL signal and other signs of a DAVF were absent even on post hoc review. Both were low flow DAVFs, including one *Cognard III tentorial fistula* that required treatment.

In comparison to venous ASL signal, all the signs that were assessed on structural sequences had poor sensitivity. TOF-MRA signs had poorer sensitivity than reported in previous studies. For example, nodular and curvilinear hyperintensities (NCH) had a much lower sensitivity than reported previously (61% in comparison with 100%)[19]. This sign was not identifiable even on post hoc review in 7/33 (21%) patients whose fistula was within the TOF-MRA slab. Three of these patients had a high grade (*Cognard III*) fistulas requiring treatment. Even when present, NCH were missed by the experienced reader in two patients, indicating that this sign can be subtle and difficult to detect. In three other patients, the fistula was above the TOF-MRA field of view, precluding detection of NCH. This may seem to be an easily avoidable cause of false negatives, since all patients who are worked up for a clinical presentation that is potentially attributable to a high flow vascular lesion (such as unexplained intracranial hemorrhage) should undergo whole brain TOF-MRA. Nonetheless, this is a limitation of TOF-MRA that is encountered in real-life clinical practice, where incomplete brain coverage is often necessitated by time constraints. In contrast, whole brain coverage is routine with PCASL. Another advantage of PCASL over TOF-MRA, which enhances the conspicuity of venous ASL signal and likely contributed to the higher sensitivity, is the absence of high signal in arterial structures under normal conditions, reducing the "clutter" in the images. Conversely, high signal is present in normal arteries on TOF-MRA, which can distract the radiologist and result in an abnormal, hyperintense cortical vein being either missed or dismissed as an artery. The same limitation applies to dynamic contrast-enhanced MRA, which was not assessed in this study.

Specificity of the venous ASL sign was also high (88%) but imperfect. In theory, ASL signal is absent in venous structures under normal conditions and occurs in the presence of shunting. The false positives in this study were likely due to an alternative cause of shunting, such as seizures or an AVM obscured and compressed by hematoma at the time of DSA. Mild hyperintensity was seen in the anterior aspect of the superior sagittal sinus in four control patients in whom we could not find an alternative explanation or cause for shunting. Venous ASL signal in this location has since been observed by us in other patients who have no other evidence of a shunting lesion. This is therefore thought to be a normal variant of which radiologists should be aware when interpreting PCASL.

The findings of this study suggest that addition of PCASL to the MRI protocol may particularly benefit less experienced readers. Diagnostic accuracy increased with addition of PCASL for both readers. However, this improvement reached statistical significance only for the more junior neuroradiologist; the latter had lower sensitivity than the senior reader for detecting a DAVF on structural sequences and TOF-MRA, and demonstrated greater improvement in diagnostic performance with addition of PCASL. The senior reader, on the other hand, had good diagnostic performance already, leaving little room for improvement. The difference in performance between the readers prior to addition of PCASL reflects the subtlety and equivocal nature of findings of a DAVF on structural sequences and TOF-MRA, and the high level of skill that is therefore required to detect and interpret them. Venous ASL signal, on the other hand, has "light-bulb" conspicuity. It is therefore more easily and reliably detected, as evidenced by the high diagnostic sensitivity and almost perfect inter-reader agreement ($\kappa = 0.94$) for this sign. It is also interpreted with greater certainty, which is reflected in the readers' improvement in diagnostic confidence following review of PCASL. PCASL is therefore likely to be particularly valuable outside the tertiary hospital setting, especially in regional and peripheral hospitals, where general radiologists without subspecialist neuroradiology training and expertise are required to interpret the MRIs of patients with a presentation potentially attributable to a DAVF. To determine the added value of PCASL for readers with different levels of experience, and confirm the impression that less experienced readers are especially likely to benefit from inclusion of PCASL in the MRI protocol, a study that includes trainees, general radiologists and neuroradiologists is warranted.

Despite the smaller improvement in diagnostic performance seen in this study, addition of PCASL to the MRI protocol is also likely to benefit experienced readers.

There were four cases where signs of a DAVF were absent on TOF-MRA, and even the experienced reader considered the diagnosis to be unlikely until PCASL was reviewed. PCASL can therefore enable detection of DAVFs that are occult on structural MRI and TOF-MRA. In addition, the high conspicuity of venous ASL signal can aide detection of a DAVF when the diagnosis is not suspected, either due to it being an incidental finding or an atypical clinical presentation. In such cases, the signs on structural sequences and TOF-MRA may not be specifically sought and therefore overlooked. Another benefit of PCASL for experienced readers is the increase in diagnostic confidence.

While the high negative predictive value (98%) of MRI with PCASL makes it suitable for use as a screening tool, the occurrence of false negatives suggests that it cannot replace DSA at this stage in patients in whom there is a high index of suspicion for a DAVF. Inclusion of PCASL in the MRI protocol of patients with a presentation potentially attributable to a DAVF is, however, likely to be of utility in clinical practice as a triage tool. A positive finding, which increases confidence in the diagnosis, can expedite referral for management. It may also allow diagnostic and therapeutic catheter-based procedures to be performed in the same session, avoiding the need for a separate purely diagnostic DSA. This would especially benefit patients from regional areas, who may otherwise be required to travel twice to a tertiary centre to access interventional neuroradiology services. Additionally, in patients where the index of suspicion is low, the absence of venous ASL signal may be deemed sufficient to dismiss the diagnosis without the need for a DSA. By potentially reducing the number of DSAs performed, the risk of complication, patient radiation exposure and costs can be reduced. Routine inclusion of PCASL in the MRI protocol for patients with pulsatile tinnitus, unexplained intracranial haemorrhage or any other presentation raising suspicion for a DAVF is therefore recommended.

PCASL does have some limitations which were identified in this study. The most important was the absence of venous ASL signal in two patients with low-flow DAVFS. The volume of shunted, labelled blood was likely too small to produce a perceptible signal change in these cases. There were two other patients in the study whose low-flow DAVFs were detected on PCASL but missed on TOF-MRA. The number of patients with low-flow fistulas in this study was too small to allow meaningful conclusions to be drawn regarding the diagnostic performance of PCASL in this group, which is a limitation of the study. Another limitation of PCASL is that high signal can be present in arterial structures in patients in whom the arterial transit time exceeds the PLD, for example due to chronic steno-

occlusive disease. This, in turn, can give rise to false positives, which can be avoided by cognizance of this artifact and careful cross-reference with other sequences. Using a longer PLD of 2500 ms can also mitigate against arterial transit artifact, and is therefore recommended by guidelines in older patients and those with poor cardiac output[4]. It is emphasized that PCASL perfusion cannot be used on its own to detect DAVFs, due to its relatively low spatial resolution which results in poor resolution of anatomical detail. Instead, it should be used to augment an MRI protocol that contains standard structural sequences, which are necessary for delineation of anatomical detail and cross-reference to ensure that signal observed on ASL localizes to a venous structure, and TOF-MRA, which enables fistula localization.

This study used single-delay PCASL perfusion with a PLD of 2000 ms, in accordance with the recommended guidelines for clinical ASL[4]. A limitation of this implementation is that it only interrogates ASL signal at a single time-point, providing a "snapshot" of labelled blood. Arterial and arteriovenous transit times can vary considerably between high-flow and low-flow DAVFs, therefore the optimal timing (and therefore PLD) for detecting venous ASL signal is likely to vary between patients and cannot be determined a priori. Images acquired using a single PLD may, therefore, fail to capture the passage of the bolus of labelled blood through the fistula and draining veins.

Venous ASL signal is not exclusive to single-delay PCASL, and is also seen in other ASL implementations where vascular crusher gradients are not used[7]. Some of these alternative ASL techniques are likely to be more sensitive for detection of DAVFs. For example, with multi-delay PCASL perfusion, images are obtained at multiple time points after labelling, allowing the passage of labelled blood through the fistula into draining veins to be captured and visualized over a range of arteriovenous transit times. The later time points, obtained with PLDs exceeding 2000 ms, may improve sensitivity for detection of low-flow fistulas, since there is more time for labelled blood to accumulate in draining veins. However, multi-delay PCASL techniques are designed to assess tissue perfusion, and therefore have poor spatial resolution, necessitated by the use of large voxels to obtain sufficient SNR (due to the small signal change in tissue produced by perfusion)[4].

Since detection of DAVFs is reliant upon the identification of intra-vascular (venous) ASL signal, rather than assessment of tissue perfusion, ASL angiography (discussed in chapters 3 and 4) is likely better suited to this task and may provide higher sensitivity. It has, in fact, shown promise for the characterization of

DAVFS in one small study, although the diagnostic sensitivity for detecting these lesions was not assessed[20]. Time-resolved ASL angiographic implementations leverage the high intra-arterial signal observed in ASL techniques to provide time-resolved images of the intracranial arteries. Venous ASL signal is also seen in the presence of DAVFs, and is likely highly specific for arteriovenous shunting (since the same principles as for PCASL apply when it comes to venous outflow of label)[20]. The high temporal resolution of ASL angiography (50-300 ms) is competitive with that of DSA[20, 21]. This, in turn, allows the passage of labelled blood from feeding arteries, though the fistula into draining veins to be captured and visualized in its entirety. Much higher spatial resolution (of the order of 0.5 mm) can also be achieved than with ASL perfusion, since the high intra-vascular signal allows images to be acquired using smaller voxels[21]. The sensitivity of time-resolved ASL angiography for detecting small and low-flow DAVF is therefore anticipated to be higher, since smaller structures can be resolved and the smaller voxel size decreases partial volume effects (and may therefore allow detection of venous structures with smaller fractions of labelled blood). The absence of high signal in veins other than those draining the DAVF may also give ASL angiography a competitive advantage over other time-resolved angiographic techniques (e.g., TR-CEMRA and even DSA) for detecting small DAVFS, since the potential for obscuration by normal veins is eliminated.

A further study that assesses multi-delay ASL perfusion and time-resolved ASL angiography for detection of DAVFS, including low-flow DAVFs, is therefore warranted. We have been awarded National Institutes of Health grant funding to conduct such a study, based on the work presented here, and enrolment in this new study is currently underway.

A limitation of the study design, which also applies to previous studies that assessed ASL for detection of shunting lesions, is that the readers had a high index of suspicion for a DAVF, and were specifically seeking signs of this entity. This likely resulted in improvement of diagnostic performance both with and without PCASL. In the real-world clinical setting, not only is the index of clinical suspicion lower, DAVFs are also less prevalent, and a positive case will therefore be mixed in with many negative cases. Since venous ASL signal is a highly conspicuous finding, it is less likely to be overlooked than subtle structural MRI and TOF-MRA signs in this context. The improvement in diagnostic performance with PCASL is therefore likely to be greater in the real-world clinical setting than in a study.

The current study evaluated the diagnostic performance of PCASL for detection of DAVFs, but not for characterization or grading. The prognosis of a DAVF is dependent upon its venous drainage pattern, which in turn determines its grade[22, 23]. Treatment is indicated for high grade lesions with cortical vein drainage, due to the risk of an aggressive neurological presentation, while low grade lesions can be managed conservatively[9]. Determination of venous drainage and grade of a DAVF is therefore important for prognostication and planning management. A study that evaluates the diagnostic performance of PCASL for determining the venous drainage pattern and grade of DAVFs was therefore felt to be warranted.

9.4 References

1. Amukotuwa SA, Yu C, Zaharchuk G. 3d pseudocontinuous arterial spin labeling in routine clinical practice: A review of clinically significant artifacts. *J Magn Reson Imaging*. 2016;43:11-27

2. de Havenon A, Haynor DR, Tirschwell DL, Majersik JJ, Smith G, Cohen W, et al. Association of collateral blood vessels detected by arterial spin labeling magnetic resonance imaging with neurological outcome after ischemic stroke. *JAMA Neurol*. 2017;74:453-458

3. Wolf RL, Detre JA. Clinical neuroimaging using arterial spin-labeled perfusion magnetic resonance imaging. *Neurotherapeutics*. 2007;4:346-359

4. Alsop DC, Detre JA, Golay X, Gunther M, Hendrikse J, Hernandez-Garcia L, et al. Recommended implementation of arterial spin-labeled perfusion mri for clinical applications: A consensus of the ismrm perfusion study group and the european consortium for asl in dementia. *Magn Reson Med*. 2015;73:102-116

5. Zaharchuk G. Theoretical basis of hemodynamic mr imaging techniques to measure cerebral blood volume, cerebral blood flow, and permeability. *AJNR Am J Neuroradiol*. 2007;28:1850-1858

6. Le TT, Fischbein NJ, Andre JB, Wijman C, Rosenberg J, Zaharchuk G. Identification of venous signal on arterial spin labeling improves diagnosis of dural arteriovenous fistulas and small arteriovenous malformations. *AJNR Am J Neuroradiol*. 2012;33:61-68

7. Wolf RL, Wang J, Detre JA, Zager EL, Hurst RW. Arteriovenous shunt visualization in arteriovenous malformations with arterial spin-labeling mr imaging. *AJNR Am J Neuroradiol*. 2008;29:681-687

8. Lu H, Clingman C, Golay X, van Zijl PC. Determining the longitudinal relaxation time (t1) of blood at 3.0 tesla. *Magn Reson Med*. 2004;52:679-682

9. Gandhi D, Chen J, Pearl M, Huang J, Gemmete JJ, Kathuria S. Intracranial dural arteriovenous fistulas: Classification, imaging findings, and treatment. *AJNR Am J Neuroradiol*. 2012;33:1007-1013

10. Newton TH, Cronqvist S. Involvement of dural arteries in intracranial arteriovenous malformations. *Radiology*. 1969;93:1071-1078

11. Cognard C, Casasco A, Toevi M, Houdart E, Chiras J, Merland JJ. Dural arteriovenous fistulas as a cause of intracranial hypertension due to impairment of cranial venous outflow. *J Neurol Neurosurg Psychiatry*. 1998;65:308-316

12. Cloft HJ, Joseph GJ, Dion JE. Risk of cerebral angiography in patients with subarachnoid hemorrhage, cerebral aneurysm, and arteriovenous malformation: A meta-analysis. *Stroke*. 1999;30:317-320

13. Brouwer PA, Bosman T, van Walderveen MA, Krings T, Leroux AA, Willems PW. Dynamic 320-section ct angiography in cranial arteriovenous shunting lesions. *AJNR Am J Neuroradiol*. 2010;31:767-770

14. Farb RI, Agid R, Willinsky RA, Johnstone DM, Terbrugge KG. Cranial dural arteriovenous fistula: Diagnosis and classification with time-resolved mr angiography at 3t. *AJNR Am J Neuroradiol*. 2009;30:1546-1551

15. Kwon BJ, Han MH, Kang HS, Chang KH. Mr imaging findings of intracranial dural arteriovenous fistulas: Relations with venous drainage patterns. *AJNR Am J Neuroradiol*. 2005;26:2500-2507

16. Meckel S, Maier M, Ruiz DS, Yilmaz H, Scheffler K, Radue EW, et al. Mr angiography of dural arteriovenous fistulas: Diagnosis and follow-up after treatment using a time-resolved 3d contrast-enhanced technique. *AJNR Am J Neuroradiol*. 2007;28:877-884

17. Meckel S, Mekle R, Taschner C, Haller S, Scheffler K, Radue EW, et al. Time-resolved 3d contrast-enhanced mra with grappa on a 1.5-t system for imaging of craniocervical vascular disease: Initial experience. *Neuroradiology*. 2006;48:291-299

18. Nishimura S, Hirai T, Sasao A, Kitajima M, Morioka M, Kai Y, et al. Evaluation of dural arteriovenous fistulas with 4d contrast-enhanced mr angiography at 3t. *AJNR Am J Neuroradiol*. 2010;31:80-85

19. Noguchi K, Melhem ER, Kanazawa T, Kubo M, Kuwayama N, Seto H. Intracranial dural arteriovenous fistulas: Evaluation with combined 3d time-of-flight mr angiography and mr digital subtraction angiography. *AJR Am J Roentgenol*. 2004;182:183-190

20. Iryo Y, Hirai T, Kai Y, Nakamura M, Shigematsu Y, Kitajima M, et al. Intracranial dural arteriovenous fistulas: Evaluation with 3-t four-dimensional mr angiography using arterial spin labeling. *Radiology*. 2014;271:193-199

21. Robson PM, Dai W, Shankaranarayanan A, Rofsky NM, Alsop DC. Time-resolved vessel-selective digital subtraction mr angiography of the cerebral vasculature with arterial spin labeling. *Radiology*. 2010;257:507-515

22. Borden JA, Wu JK, Shucart WA. A proposed classification for spinal and cranial dural arteriovenous fistulous malformations and implications for treatment. *J Neurosurg*. 1995;82:166-179

23. Cognard C, Gobin YP, Pierot L, Bailly AL, Houdart E, Casasco A, et al. Cerebral dural arteriovenous fistulas: Clinical and angiographic correlation with a revised classification of venous drainage. *Radiology*. 1995;194:671-680

Chapter 10

Detection of Cortical Venous Drainage and Determination of Borden Type of Dural Arteriovenous Fistula by Means of 3D Pseudocontinuous Arterial Spin-Labeling

10.1 Introduction

The risk of neurological complication due to a DAVF is related to the pattern of venous drainage, in particular the presence of *cortical vein drainage* (CVD) of the fistula[1, 2]. CVD is therefore associated with increased morbidity and mortality. With increasing venous hypertension, retrograde cortical vein drainage can develop in a DAVFs draining primarily into a dural venous sinus[2, 3]. A fistula can also occur directly between a dural artery and cortical vein, and is associated with an even higher risk of hemorrhage since cortical veins are thinner-walled and have less capacity to deal with increased flow than dural venous sinuses[2, 3]. This is reflected in both the **Cognard** and **Borden systems** that grade DAVFs for prognostication and management planning[1, 2].

The presence of CVD, either direct or reflux, is an indication for treatment of a DAVF given the increased risk of complication[4]. Conversely, patients who have low grade fistulas that drain only into a dural venous sinus can be managed conservatively, with imaging surveillance to monitor for development of CVD. The reference standard for detecting CVD and grading DAVFs is catheter-based DSA[4]. The unparalleled spatial and temporal resolution of DSA allows accurate delineation of feeding arteries, the fistula itself and the venous drainage pattern. It is, however, invasive, carries a risk of significant complication such as stroke,

exposes the patient to ionizing radiation, and requires access to an interventional neuroradiology service[5]. A reliable non-invasive technique for detecting CVD and determining the grade of a DAVF would decrease the number of DSAs a patient requires. In turn, this would reduce the patient's exposure to procedural risk, cumulative radiation dose, and healthcare costs. Patients with low-grade DAVFs could avoid serial DSAs and instead undergo non-invasive imaging surveillance. This would particularly benefit patients from country areas who have to travel to a tertiary metropolitan center to undergo DSA. In patients with a high-grade DAVF, accurate non-invasive grading would streamline triage and allow confirmatory DSA to be performed in the same session as endovascular therapy.

A number of non-invasive MR-based techniques have previously been applied to the task of characterizing the venous drainage pattern of DAVFs, including TOF-MRA, time resolved CE-MRA and SWI. None, however, have gained wide acceptance as being sufficiently accurate for characterizing venous drainage. Flow-related hyperintensity on TOF-MRA is unreliable for detection of CVD[6-8]; false negatives can occur due to signal saturation while cortical veins that have a caudal-cranial flow direction can demonstrate false positive high signal. Detection of CVD on time resolved CE-MRA is reliant upon identification of early filling of a cortical vein, which can be challenging given the limited temporal resolution of the modality.

Venous ASL signal is a highly conspicuous qualitative finding that has been shown in the previous study to enable detection of DAVF with high sensitivity. It also has high specificity for shunting, and is typically absent in veins under normal conditions. Instead, it is seen in venous structures into which labeled arterial blood is directly shunted or subsequently flows. This lead to the idea that venous ASL signal could be used to detect CVD and grade DAVFs, which has not been previously done. The aims of this study were to evaluate the diagnostic accuracy of an MRI protocol augmented with PCASL for detection of CVD and determination of the Borden type of a DAVF. The *Borden classification* system was selected over the *Cognard* since it is simpler yet still allows clinically relevant distinctions to be made. Since the column of hyperintense blood produced by pseudocontinuous labeling is shunted directly from feeding arteries into the draining veins in a DAVF, it was hypothesized that the distribution of hyperintensity could be used to delineate the pattern of venous drainage; localization of venous ASL signal would therefore allow detection of CVD and determination of grade.

The study cohort consisted of 34 patients with a DAVF who underwent DSA for a known or clinically suspected DAVF. This is the population in which imaging is used to delineate the venous pattern for the purposes of prognostication and planning management. 22 patients had a DAVF with CVD while 12 patients had a low grade DAVF with no evidence of CVD on DSA. The study is presented in the next section, followed by a detailed discussion of the findings and implications.

10.2 Publication

Amukotuwa SA, Heit J, Marks MP, Bammer R. Detection of Cortical Venous Drainage and Determination of the Borden Type of Dural Arteriovenous Fistula by Means of 3D Pseudocontinuous Arterial Spin-Labeling MRI. AJR Am J Roentgenol. 2016; 207(1):163-9

Neuroradiology/Head and Neck Imaging • Original Research

Detection of Cortical Venous Drainage and Determination of the Borden Type of Dural Arteriovenous Fistula by Means of 3D Pseudocontinuous Arterial Spin-Labeling MRI

Shalini A. Amukotuwa[1]
Jeremy J. Heit
Michael P. Marks
Nancy Fischbein
Roland Bammer

OBJECTIVE. The risk of intracranial dural arteriovenous fistula is linked to its pattern of venous drainage (Borden type), in particular the presence of cortical venous drainage. The purpose of this study was to assetss the accuracy of 3D pseudocontinuous arterial spin-labeling (ASL) MRI for noninvasive delineation of venous drainage.

MATERIALS AND METHODS. This retrospective study included 34 patients with a dural arteriovenous fistula who had undergone both digital subtraction angiography (DSA) and 3D pseudocontinuous ASL MRI. Two neuroradiologists blinded to the DSA results independently assessed ASL images for the presence of cortical vein hyperintensity (cortical venous drainage) and the distribution of venous hyperintensity (Borden type). DSA was used as the reference standard. The sensitivity and specificity of 3D pseudocontinuous ASL MRI for the detection of cortical venous drainage were determined. Intermodality and interobserver agreement for Borden type was determined by use of the weighted kappa statistic.

RESULTS. Three-dimensional pseudocontinuous ASL MRI had high sensitivity (91%) and specificity (96%) for the detection of cortical venous drainage. Borden type was correctly identified with very good intermodality (weighted $\kappa = 0.82$) and interobserver (weighted $\kappa = 0.85$) agreement in 88% of patients.

CONCLUSION. Three-dimensional pseudocontinuous ASL MRI is highly accurate for the detection of cortical venous drainage and determination of Borden type. With this technique, high-risk fistulas requiring treatment can be reliably differentiated from low-risk lesions. Although it cannot replace DSA, incorporating 3D pseudocontinuous ASL into an MRI protocol for assessment of dural arteriovenous fistula can facilitate treatment planning.

Keywords: arterial spin labeling, cerebrovascular disease, dural arteriovenous fistula, MRI, noninvasive imaging

DOI:10.2214/AJR.15.15171

Received June 12, 2015; accepted after revision December 10, 2015.

Based on a presentation at the American Society of Neuroradiology 2015 annual meeting, Chicago, IL.

S. A. Amukotuwa was supported by NIH grant number R01EB002711.

[1]All authors: Department of Radiology, Lucas MRI Center, Stanford University, 1201 Welch Rd, Rm P271, Mail Code 5488, Stanford, CA 94305-5488. Address correspondence to S. A. Amukotuwa (samukotuwa@gmail.com).

AJR 2016; 207:163–169

0361–803X/16/2071–163

Dural arteriovenous fistula (DAVF) constitutes 10–15% of intracranial arteriovenous shunting lesions [1]. This type of fistula is characterized by direct drainage of arterial blood into a dural sinus or cortical vein without an intervening capillary bed. Increased blood flow and pressure in these draining veins can lead to cerebral edema, ischemia, and hemorrhage [2–5]. The pattern of venous drainage determines the risk of an aggressive neurologic presentation and the need for treatment [3–6]. The main risk factor for increased morbidity and mortality is cortical venous drainage (CVD) [3–6]. Because treatment itself carries risk of neurologic complications, cranial DAVFs without CVD are generally managed conservatively [6, 7]. Characterization of venous drainage is therefore critical for prognostication and treatment planning. Accordingly, the widely used Cognard and Borden (Table 1) systems are used to grade DAVF on the basis of venous drainage [3, 4].

The standard-of-care test for characterizing DAVFs is cerebral digital subtraction angiography (DSA) because its unparalleled spatiotemporal resolution allows accurate and dynamic delineation of feeding arteries, fistula sites, and draining veins. Unfortunately, DSA is invasive, requires ionizing radiation, and carries a small but important risk of severe periprocedural complications, such as stroke [8]. A reliable noninvasive test for determination of CVD and Borden type may decrease the number of DSA examinations a patient needs, decreasing exposure to procedural risk and radiation dose and decreasing costs. In patients with high-risk DAVFs, facilitation of therapeutic planning would allow performance of confirmatory DSA in the same session as endovascular therapy, and noninvasive surveillance would allow avoidance of serial follow-up DSA for patients with low-risk DAVFs.

Various MRI techniques have been evaluated for delineation of the venous drainage of DAVFs [9–14]. In 3D time-of-flight MR angiography (MRA), shunting of inflowing arterial blood is associated with flow-related hyperintensity in draining veins [9–11]. This venous hyperintensity has been found unreliable for detection of CVD [9, 10]. Despite high reported accuracy for detection of CVD, time-resolved contrast-enhanced MRA is also not widely viewed as being sufficiently reliable for noninvasive characterization of venous drainage [9–13]. Time-resolved (4D) CT angiography has been reported to be accurate for delineation of the venous drainage of DAVFs, but it has only been validated in small case series [14]. It also has the disadvantages of ionizing radiation exposure and the requirement for iodinated contrast administration.

Arterial spin labeling (ASL) is a completely noninvasive MRI technique for hemodynamic characterization that is widely available on clinical MRI systems [15]. Arterial blood water is labeled by inversion of its longitudinal magnetization in a plane proximal to the brain and acts as an endogenous flow tracer, eliminating the need for an exogenous contrast agent [15, 16]. Imaging is performed after a short time interval (postlabeling delay) that allows labeled blood to reach the brain parenchyma [15]. Although ASL signal intensity is not observed in cerebral veins under normal conditions, it is seen in the presence of arteriovenous shunting owing to rapid transit of labeled blood directly from feeding arteries to draining veins [17, 18]. This venous ASL signal intensity is a conspicuous finding and has been found to have high sensitivity for the detection of DAVF [18].

To our knowledge, the utility of ASL in characterizing the venous drainage of a DAVF has not been previously investigated. The purpose of this study was to assess the accuracy of an MRI protocol with 3D pseudocontinuous ASL for detection of CVD and for determination of the Borden type of a DAVF. We hypothesized that owing to direct shunting of labeled arterial blood into the draining veins of a DAVF, detection and localization of venous ASL signal intensity would enable accurate delineation of these features.

Materials and Methods

Patient Selection

This retrospective study was performed with an institutional ethics board–approved waiver of consent and authorization. Thirty-four patients (14 women, 20 men; age range, 19–86 years; mean age, 58 years) with a DAVF who underwent both DSA and MRI with a 3D pseudocontinuous ASL sequence (without any intervening treatment of the DAVF) at our institution between June 1, 2009, and June 30, 2014, were included. Reports of all consecutive cerebral DSA examinations performed at our institution between June 1, 2009, and June 30, 2014, were searched for the terms "DAVF," "dural AVF," "arteriovenous fistula," "fistula," and "carotid cavernous," yielding 754 studies. The reports and the images of these studies were reviewed to identify 131 consecutively registered patients with a DAVF who underwent DSA. Fifty-one patients also underwent MRI with 3D pseudocontinuous ASL. Patients were excluded if they underwent treatment between MRI and DSA (n = 16) or had pseudocontinuous ASL images that were nondiagnostic owing to severe motion (n = 1). Because pseudocontinuous ASL has been a routine component of the MRI protocol for assessment of patients with known or suspected DAVF at our

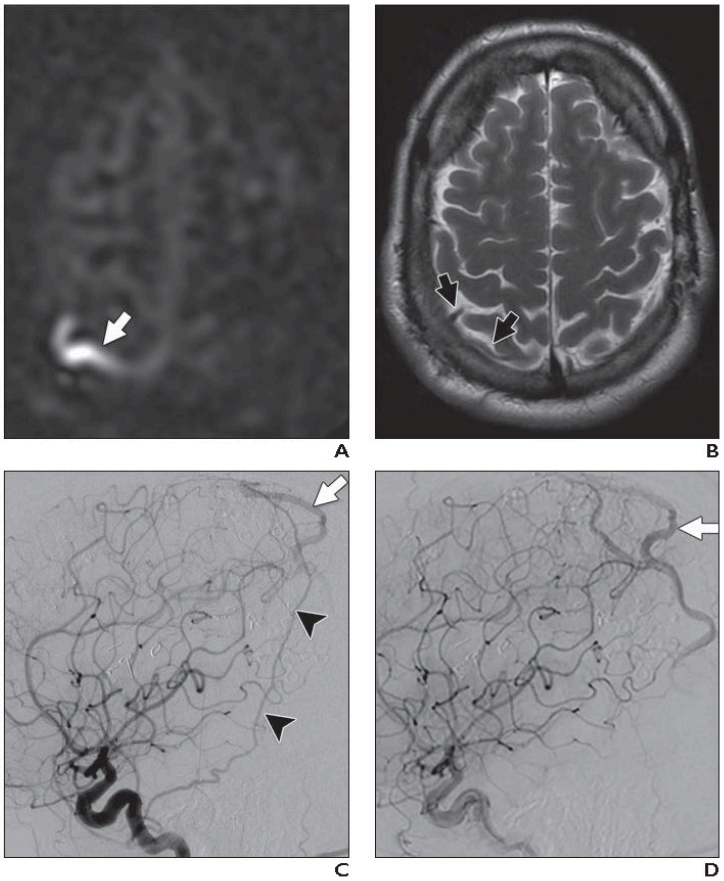

Fig. 1—51-year-old man with complex history, including previous complete resection of left temporal arteriovenous malformation, with incidental finding of Borden type III dural arteriovenous fistula during routine follow-up MRI.
A, Pseudocontinuous arterial spin-labeling MR image shows high signal intensity within enlarged right parietal cortical vein (*arrow*).
B, Axial T2-weighted MR image shows additional anatomic detail and confirms that serpentine high signal intensity in **A** is within cortical vein (*arrows*).
C and **D,** Sequential lateral projection angiograms obtained after right common carotid artery injection confirm presence of Borden type III fistula supplied by parietal branch of right superficial temporal artery (*arrowheads*, **C**) and draining directly into parasagittal cortical vein (*arrow*) that in turn drains into vein of Trolard.

TABLE 1: Venous Drainage Patterns and Risk of Complication of Intracranial Dural Arteriovenous Fistula

Pattern	Cognard System		Borden System	
	Type	Rate of Aggressive Neurologic Presentation (%)[a]	Type	Rate of Aggressive Neurologic Presentation (%)[a]
Dural sinus				
Antegrade or retrograde flow			I	2
Antegrade flow	I	0		
Retrograde flow	IIa	7		
Dural sinus and cortical vein reflux				
Antegrade or retrograde flow			II	39
Antegrade flow	IIb	38		
Retrograde flow	IIa + IIb	40		
Directly into subarachnoid veins	III	69	III	79
Directly into subarachnoid veins with ectasia of draining subarachnoid veins	IV	83		
Spinal perimedullary venous drainage	V	100		

[a]Aggressive presentation includes signs and symptoms of raised intracranial hypertension, intracranial hemorrhage, focal neurologic deficit, seizures, or altered mental status [6].

institution since 2009, there was no selection bias in the type of DAVF evaluated with pseudocontinuous ASL and included in this study. Twenty-seven patients had a primary diagnosis of DAVF, and seven were undergoing follow-up evaluation of a partially treated DAVF. DSA and pseudocontinuous ASL images of these patients were deemed of sufficient quality for classification of venous drainage. In patients with multiple studies, the DSA and MRI studies temporally closest to each other were selected (mean time interval, 46 days).

Imaging Methods

Twelve MRI examinations were performed at 3 T (Discovery 750w, GE Healthcare) and 22 at 1.5 T (Signa HDx, GE Healthcare). Three-dimensional pseudocontinuous ASL imaging (TR/TE, 5500/2.5 [1.5 T], 5500/10.5 [3 T]) with background suppression was implemented with a labeling period of 1500 milliseconds, postlabeling delay of 2000 milliseconds, and the labeling plane at the level of the foramen magnum. A segmented 3D stack-of-spirals fast spin-echo readout was used with 24-cm^3 FOV, in-plane spatial resolution of 3–4 mm, and through-plane spatial resolution of 4–6 mm, yielding 24–40 slices. The acquisition time was 4–6 minutes. No vascular crusher gradients were used. This acquisition complied with the consensus recommendations of ASL experts [19]. The presence of venous ASL signal intensity was assessed on the simple label-control subtraction images and required no postprocessing. Three-dimensional multislab time-of-flight (TOF) MRA (TR/TE, 30/2.3; FOV, 24 cm^3; matrix, 512 × 128 or 288; slice thickness, 1 mm) was performed for 31 patients.

All 34 MRI examinations included the following sequences: sagittal T1-weighted, axial T2-weighted fast spin-echo, and axial FLAIR performed with a 24-cm^2 FOV and 5-mm slice thickness.

Catheter-based DSA for clinical workup of the DAVF was performed in a biplane neuroangiography suite (Axiom Artis, Siemens Healthcare). Imaging included at minimum anteroposterior and lateral projections and was performed after selective injection of iodinated contrast medium (iohexol, Omnipaque 300, GE Healthcare) into the appropriate internal carotid, external carotid, and vertebral arteries supplying the DAVF.

Image Interpretation

MRI—MR images were independently reviewed by two neuroradiologists who were blinded to the DSA findings. Pseudocontinuous ASL images were reviewed in conjunction with the T1- and T2-weighted images. TOF MRA source images and maximum-intensity-projection images were subsequently reviewed.

Fistula location—Because of the lack of angiographic and time-resolved information for visualization of arterial feeders and determination of the venous entry point of shunted blood, fistula location could not be determined on pseudocontinuous ASL images. Visualization of the terminal portions of enlarged feeding arteries on 3D TOF MR angiograms as areas of nodular or curvilinear hyperintensity adjacent to the draining dural venous sinus and hyperintensity within draining venous structures has been reported to be up to 100% specific and sensitive for DAVF [9]. These features were specifically sought on 3D TOF MR angiograms for fistula localization.

Cortical venous drainage—Pseudocontinuous ASL images were reviewed for the presence of hyperintensity in one or more cortical veins, indicating CVD (Fig. 1).

Borden type—Determination of Borden type (Table 1) necessitates differentiation of direct CVD (type III) from dural venous sinus drainage with secondary reflux of blood into a cortical vein (type II). Because pseudocontinuous ASL is not a time-resolved technique, the sequence of drainage of shunted blood within venous structures could not be visualized to make this distinction. The distribution of venous ASL hyperintensity relative to fistula location (on TOF MR angiograms) was used instead. Direct CVD was inferred when either the fistula was immediately adjacent to a hyperintense cortical vein but remote from a dural sinus or hyperintensity was present in a cortical vein but absent in the dural sinus closest to the fistula (Fig. 2). Borden type could therefore only be assessed in the 28 patients who had undergone TOF MRA.

Digital subtraction angiography—An interventional neuroradiologist reviewed all DSA images and recorded fistula location, presence or absence of CVD, and Borden type. This was the reference standard with which MRI with pseudocontinuous ASL was compared.

Consensus review—Unblinded post hoc MRI and DSA review was performed in consensus to determine the causes of false-positive and false-negative interpretations.

Statistical Analysis

The diagnostic sensitivity and specificity of pseudocontinuous ASL for the detection of CVD

TABLE 2: Digital Subtraction Angiographic Characteristics of Intracranial Dural Arteriovenous Fistula

Characteristic	No. of Patients
Cortical venous drainage	
Present	22
Absent	12
Borden type	
I	12
II	15
III	7
Location	
Transverse or sigmoid sinus	12
Marginal sinus	2
Superior sagittal sinus	3
Sphenoparietal sinus	1
Cortical vein	6 (2 infratentorial)
Torcular herophili	1
Vein of Galen	2
Cavernous sinus	6
Tentorium cerebelli	1

for each reader were determined with 95% CIs. Linear kappa statistics were calculated to determine interreader agreement ($\kappa < 0.2$, poor agreement; $\kappa = 0.21$–0.40, fair agreement; $\kappa = 0.41$–0.60, moderate agreement; $\kappa = 0.61$–0.80, good agreement; $\kappa = 0.81$–0.90, very good agreement; and $\kappa > 0.90$, excellent agreement) [20]. Interreader and intermodality agreement between DSA and pseudocontinuous ASL ($\kappa_{DSA\text{-}ASL}$) for Borden type was determined with weighted kappa statistics. Weighting was deemed necessary to reflect the nonlinear increase in morbidity with increasing Borden type and accurately capture the clinical significance of errors. The difference in risk of an aggressive presentation between the three Borden types (Table 1) was therefore selected as the weighting element for the kappa statistics.

Results

The DSA characteristics of the DAVFs are shown in Table 2.

Fistula Location

Fistula location was assessed in the 31 patients who had undergone TOF MRA. Exclusion from the imaging slab precluded localization of three Borden type III fistulas. Both readers detected and correctly localized 27 of the 28 (96%) fistulas located within the imaging slab. One fistula could not be detected on TOF MRA images even in post hoc review. This small, low-flow tentorial fistula had superior petrosal sinus and cortical vein drainage (Borden type II).

Cortical Venous Drainage

CVD was assessed with pseudocontinuous ASL in 34 patients, 22 of whom had DSA evidence of CVD. Both readers correctly detected CVD in 20 (91%) patients. Readers 1 and 2 correctly deemed CVD to be absent in 12 (100%) and 11 (92%) patients. Average sensitivity and specificity for detection of CVD were 91% and 96%. Table 3 shows the individual reader results. Interreader agreement was very good ($\kappa = 0.82$). In the Borden type II low-flow tentorial fistula that was also occult on TOF MRA images, neither reader detected CVD. On post hoc review, venous ASL signal intensity was absent altogether in the draining superior petrosal sinus and in the draining cortical vein. The other two false-negative findings were caused by reader perceptual error. Post hoc review of these cases revealed high signal intensity in a short segment of cortical vein immediately adjacent to a hyperintense dural sinus. One false-positive finding (reader 2) resulted from high signal intensity in a cortical artery.

Borden Type

Borden type was assessed in the 28 patients with an identifiable fistula on 3D TOF MRA images and was correctly determined by readers 1 and 2 in 25 (89%) and 24 (86%) patients. Interreader agreement (weighted $\kappa = 0.85$) and intermodality agreement of pseudocontinuous ASL with DSA (average weighted $\kappa_{DSA\text{-}ASL} = 0.82$) were both very good.

For the purposes of analysis, the low-flow Borden type II fistula that had no venous ASL signal intensity was called Borden type I because of a lack of cortical venous ASL signal intensity. All other clinically significant errors, which could lead to inappropriate conservative management of a high-risk (type II or III) fistula, were also caused by failure to detect CVD. A Borden type III DAVF of the transverse sinus wall draining directly into an adjacent cortical vein was undercalled type II by both readers. Hyperintensity was present in the draining cortical vein of this high-flow fistula but also within the downstream sinus in post hoc review, preventing appreciation of initial drainage into the cortical vein (Fig. 3). The only clinically significant overcall was caused by false-positive detection of CVD, resulting in a type I fistula's being called type II.

Discussion

CVD of a DAVF is the main risk of adverse neurologic sequelae and is associated with a mortality rate of approximately 45% [3, 6]. Direct CVD presents a higher risk of complication than does reflux from a dural sinus, although this distinction is somewhat academic because both CVD patterns warrant treatment [5]. Conversely, DAVFs without CVD exhibit benign behavior and can be managed conservatively with imaging and clinical surveillance [3–7]. Cognard et al.

TABLE 3: Summary of 3D Pseudocontinuous Arterial Spin Labeling MRI Assessment of Dural Arteriovenous Fistula

Characteristic	Reader 1	Reader 2
Cortical venous drainage		
No. of patients assessed	34	34
Sensitivity (%)	91 (69–98)	91 (69–98)
Specificity (%)	100 (70–100)	92 (60–100)
Positive predictive value (%)	100 (80–100)	95 (74–100)
Negative predictive value (%)	86 (56–97)	85 (54–97)
Interreader agreement (linear κ)	0.82	0.82
Borden type		
No. of patients assessed	28	28
Correct identification	25 (89)[a]	24 (86)[a]
Agreement with digital subtraction angiography (weighted κ)	0.85	0.80
Interreader agreement (weighted κ)	0.85	0.85

Note—Unless otherwise indicated, values in parentheses are 95% CIs.
[a]Values in parentheses are percentages.

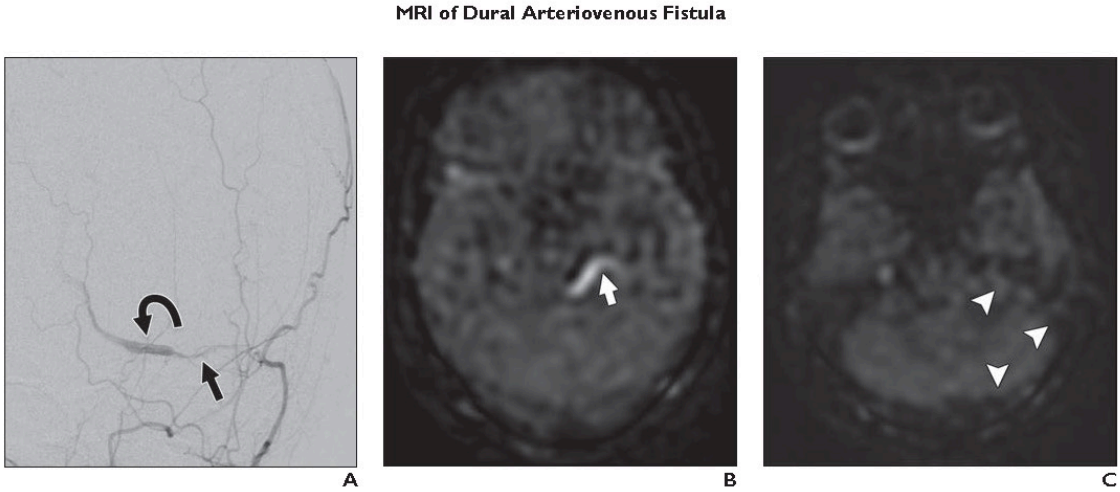

Fig. 2—36-year-old woman with dural arteriovenous fistula inferior to tentorium cerebelli with direct cortical venous drainage (Borden type III) detected incidentally during brain MRI for exclusion of traumatic brain injury after motor vehicle accident.
A, Lateral oblique projection digital subtraction angiogram obtained after selective external carotid artery injection shows dural arteriovenous fistula supplied by petrosal branch of left middle meningeal artery (*straight arrow*) and draining directly into tentorial (cortical) vein (*curved arrow*).
B and **C,** Three-dimensional pseudocontinuous arterial spin-labeling (ASL) MR images show high signal intensity in left tentorial cortical vein (*arrow*, **B**) but not adjacent left superior petrosal transverse sigmoid sinuses (*arrowheads*, **C**). Presence of venous ASL signal intensity exclusively in cortical vein indicates direct cortical vein drainage.

[3] observed no hemorrhages in this group, and Davies et al. [6] observed aggressive behavior in only 2% of patients. Delineation of venous drainage, in particular identification of CVD, is hence critical for prognostication and management planning. DSA is currently necessary for reliable detection of CVD and determination of Borden type, but it is invasive, is performed with ionizing radiation, is not always available at peripheral centers, and carries a risk (albeit small) of severe complications such as stroke [8].

Accurate, noninvasive delineation of venous drainage could facilitate treatment planning and patient counseling, allowing performance of diagnostic DSA in the same session as endovascular therapy for high-risk DAVFs. Avoiding preliminary diagnostic DSA would decrease the risk to patients and also decrease health care costs. For low-risk Borden type I DAVFs, noninvasive imaging surveillance would avoid serial DSA examinations, decreasing cumulative radiation dose to the patient. High sensitivity is necessary because missing the development of CVD would leave a high-risk DAVF untreated with potentially devastating consequences. False-positive findings are less clinically concerning because triage to DSA allows definitive delineation of venous drainage, and these patients would not be exposed to higher risk than that of the current DAVF management pathway.

ASL is a completely noninvasive MRI perfusion technique that is commercially available on the major vendors' clinical MRI systems and is being increasingly incorporated into routine brain-imaging protocols. In the technique, magnetically labeled arterial blood water is used as an endogenous flow tracer [15]. Because approximately 90% of labeled blood is exchanged at the capillary level into brain tissue, and the T1 decay of labeled water is much shorter than its mean dwell time within a voxel, ASL signal intensity is not seen in venous structures under normal conditions [17, 18]. With arteriovenous shunting, however, direct and rapid passage of labeled arterial blood into venous structures bypasses the capillary bed. High ASL signal intensity is consequently seen in the draining venous structures of shunting lesions, such as DAVFs, arteriovenous malformations, some hypervascular tumors, and subacute strokes [17, 18]. This venous signal intensity is a conspicuous qualitative finding that can be detected on ASL subtraction images. It improves sensitivity and specificity for the MRI diagnosis of DAVF, increasing reader confidence and allowing detection of even small lesions that may otherwise be missed [18].

Because a column of hyperintense blood produced by pseudocontinuous ASL labeling is shunted from feeding arteries into draining veins, we hypothesized that the distribution of venous hyperintensity could be used to delineate venous drainage. This was confirmed by the high sensitivity and specificity of pseudocontinuous ASL for detection of CVD (91% and 96%) and very good agreement ($\kappa = 0.82$) with DSA (the reference standard) for Borden type. In post hoc review, cortical venous ASL signal intensity was present in all cases of CVD except one low-flow fistula in which venous ASL signal intensity was altogether absent.

The high sensitivity of pseudocontinuous ASL for detection of CVD can be explained by the conspicuity of venous signal intensity. This is due to both the high signal intensity in draining veins and the high contrast differential between draining veins and adjacent brain parenchyma. Only labeled blood produces signal because static tissue signal is nulled by background suppression and subtraction of control from label images. A voxel comprising a draining vein, which has 100% blood volume, is entirely occupied by labeled blood and has very high signal intensity. In comparison, brain parenchyma has lower blood volume (2–5%). Therefore, a voxel occupied by brain tissue has much less labeled blood and lower signal intensity [16]. Consequently, the draining veins of a DAVF are conspicuously hyperintense despite the poor spatial resolution of ASL and T1 signal decay in the 2-second interval between labeling in the neck and imaging.

Venous hyperintensity is typically caused by direct shunting and subsequent flow of la-

beled blood into veins [15, 18]. It therefore follows that venous hyperintensity is confined to these draining veins, resulting in high specificity of pseudocontinuous ASL for CVD. Absence of high signal intensity in normal venous structures is a distinct advantage of pseudocontinuous ASL. Conversely, on images obtained with bolus contrast techniques, such as time-resolved contrast-enhanced MRA and 4D CT angiography, all patent venous structures become opacified. The relative conspicuity of signal intensity in draining veins is much less than on pseudocontinuous ASL images, and detection of draining veins requires identification of early venous filling, which in turn necessitates dynamic imaging with high temporal resolution.

High signal intensity is also not typically seen in normal arteries because a postlabeling delay of 2 seconds allows blood labeled at the skull base to reach the brain parenchyma. When blood flow is delayed, however, as in arterial stenoocclusive disease or poor cardiac output, labeled blood may be in arterial transit at the time of readout [19]. Recognition of the characteristic arterial distribution helps differentiate this serpiginous arterial transit artifact from cortical vein signal intensity, averting false-positive interpretations. Alternatively, longer postlabeling delay or multiple-delay-time pseudocontinuous ASL would address this potential confounder in patients who are anticipated to have delayed arterial blood flow.

Using a longer postlabeling delay may also improve the sensitivity of pseudocontinuous ASL for CVD by allowing the column of labeled blood to flow farther and produce a longer segment of cortical vein hyperintensity. In two cases in which CVD was missed, only a short segment of cortical vein hyperintensity was evident at post hoc review. Resolving a short segment of cortical vein hyperintensity from an adjacent hyperintense dural sinus can be difficult because of the low spatial resolution of pseudocontinuous ASL MRI. Given the 100% blood volume and high contrast relative to adjacent parenchyma, we postulate that draining veins will remain conspicuous even at longer postlabeling delays despite signal loss caused by T1-relaxation of labeled blood.

Delineation of venous drainage by use of pseudocontinuous ASL may be problematic when only a small volume of labeled blood is shunted. Inclusion of only two low-flow fistulas is therefore a limitation of this study, given that flow rate and volume may affect the sensitivity of pseudocontinuous ASL for detection of CVD. Although venous ASL signal intensity was absent in one low-flow fistula with CVD in this study, cortical venous hyperintensity was evident in the other. Therefore, further investigation of low-flow fistulas is necessary.

Another limitation of pseudocontinuous ASL is the lack of time-resolved information. Inability to visualize the entry point of labeled blood into draining veins precludes fistula localization with pseudocontinuous ASL MRI. Without dynamic information, it also is not possible to differentiate direct CVD from cortical vein reflux in cases in which hyperintense shunted blood has already reached the downstream dural sinus at the time of imaging, as shown in Figure 3. Although hemorrhage risk is higher with direct CVD, this distinction is less important because both drainage patterns usually warrant treatment [3, 5–7].

Time-resolved (4D) ASL implementations are available. In a 2014 study of nine patients with DAVFs evaluated with the 4D ASL technique with 300-millisecond spatial resolution [20], all four cases of CVD were cor-

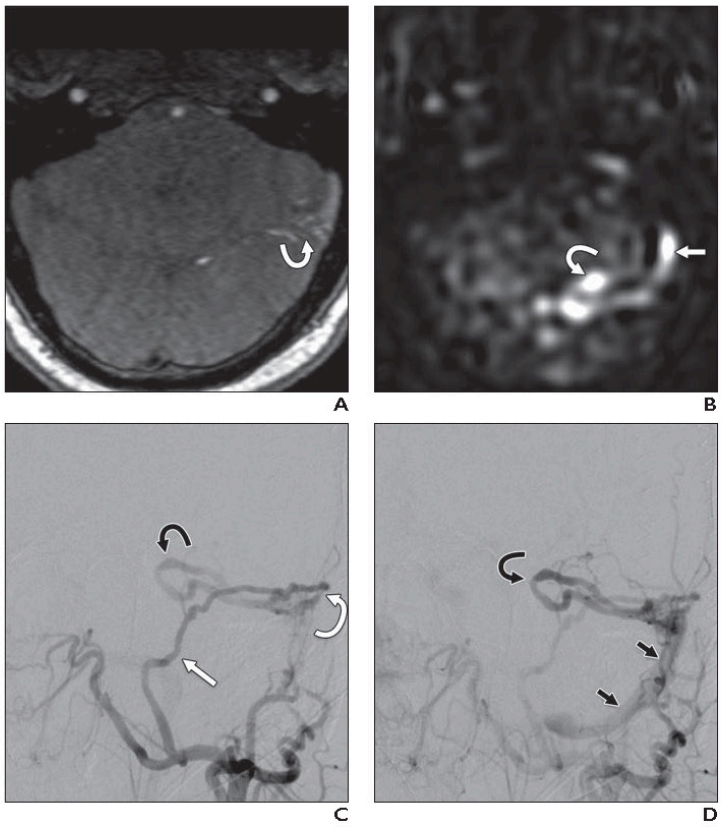

Fig. 3—65-year-old man with Borden type III dural arteriovenous fistula (DAVF) who presented with altered mental status and seizures.
A, Three-dimensional time-of-flight MR angiographic source image shows nodular and curvilinear hyperintensities (*arrow*), indicative of DAVF adjacent to lateral aspect of left transverse sinus.
B, Pseudocontinuous arterial spin-labeling MR image shows conspicuous area of high signal intensity (*curved arrow*) in draining cortical vein, indicating cortical venous drainage. High signal intensity (*straight arrow*) is also evident in downstream left transverse and sigmoid sinuses, preventing appreciation of direct cortical venous drainage.
C and **D,** Digital subtraction angiograms show fistula (*white curved arrow*, **C**) adjacent to left transverse sinus and supplied by left middle meningeal artery (*straight arrow*, **C**). Time-resolved nature of digital subtraction angiography allows appreciation of drainage directly into cortical vein (*black curved arrow*) with subsequent flow into left transverse and sigmoid sinuses (*straight arrows*, **D**).

rectly identified. However, such techniques are not widely available and have a number of disadvantages, including an acquisition time in excess of 8 minutes, which is unrealistic in the clinical setting, and applicability only at 3 T [20]. Pseudocontinuous ASL techniques similar to that which we used, conversely, are widely clinically available, require no complex postprocessing, can be performed in less than 5 minutes, and have high accuracy even at 1.5 T, as found in this study.

Although this study was performed with pseudocontinuous ASL, in accordance with the recommendations for clinical ASL, venous signal intensity is also seen in shunting with other ASL implementations provided that vascular crusher gradients are not used [17, 19]. Pulsed ASL is anticipated to have lower sensitivity for detection of CVD than pseudocontinuous ASL does because the column of labeled blood is shorter, background suppression is not routinely used, and the echo-planar readout is much more susceptible to off-resonance and T2* effects than is the fast spin-echo readout used in our pseudocontinuous ASL implementation. The use of a fast spin-echo readout is particularly valuable in the evaluation of patients who have surgical or embolization material from previous treatment and gives pseudocontinuous ASL a further advantage over time-resolved contrast-enhanced MRA, which is performed with a more off-resonance sensitive spoiled gradient-echo readout.

Conclusion

Three-dimensional pseudocontinuous ASL is accurate and reliable in the detection of CVD. After fistula localization on TOF MRA images, pseudocontinuous ASL MRI can be used for accurate and reliable determination of Borden type. Because this study was small and the sensitivity was imperfect, we do not advocate replacement of DSA with pseudocontinuous ASL MRI. Instead, we suggest that pseudocontinuous ASL be incorporated into the MRI protocol for assessment of patients with DAVF to facilitate triage, treatment planning, and patient counseling.

References

1. Newton TH, Cronqvist S. Involvement of dural arteries in intracranial arteriovenous malformations. *Radiology* 1969; 93:1071–1078
2. Cognard C, Casasco A, Toevi M, et al. Dural arteriovenous fistulas as a cause of intracranial hypertension due to impairment of cranial venous outflow. *J Neurol Neurosurg Psychiatry* 1998; 65:308–316
3. Cognard C, Gobin YP, Pierot L, et al. Cerebral dural arteriovenous fistulas: clinical and angiographic correlation with a revised classification of venous drainage. *Radiology* 1995; 194:671–680
4. Borden JA, Wu JK, Shucart WA. A proposed classification for spinal and cranial dural arteriovenous fistulous malformations and implications for treatment. *J Neurosurg* 1995; 82:166–179
5. van Dijk JM, terBrugge KG, Willinsky RA, et al. Clinical course of cranial dural arteriovenous fistulas with long-term persistent cortical venous reflux. *Stroke* 2002; 33:1233–1236
6. Davies MA, terBrugge K, Willinsky R, et al. The validity of classification for the clinical presentation of intracranial dural arteriovenous fistulas. *J Neurosurg* 1996; 85:830–837
7. Gandhi D, Chen J, Pearl M, Huang J, Gemmete JJ, Kathuria S. Intracranial dural arteriovenous fistulas: classification, imaging findings, and treatment. *AJNR* 2012; 33:1007–1013
8. Cloft HJ, Joseph GJ, Dion JE. Risk of cerebral angiography in patients with subarachnoid hemorrhage, cerebral aneurysm, and arteriovenous malformation: a meta-analysis. *Stroke* 1999; 30:317–320
9. Noguchi K, Melhem ER, Kanazawa T, Kubo M, Kuwayama N, Seto H. Intracranial dural arteriovenous fistulas: evaluation with combined 3D time-of-flight MR angiography and MR digital subtraction angiography. *AJR* 2004; 182:183–190
10. Kwon BJ, Han MH, Kang HS, et al. MR imaging findings of intracranial dural arteriovenous fistulas: relations with venous drainage patterns. *AJNR* 2005; 26:2500–2507
11. Meckel S, Maier M, Ruiz DS, et al. MR angiography of dural arteriovenous fistulas: diagnosis and follow-up after treatment using a time-resolved 3D contrast-enhanced technique. *AJNR* 2007; 28:877–884
12. Farb RI, Agid R, Willinsky RA, et al. Cranial dural arteriovenous fistula: diagnosis and classification with time-resolved MR angiography at 3T. *AJNR* 2009; 30:1546–1551
13. Nishimura S, Hirai T, Sasao A, et al. Evaluation of dural arteriovenous fistulas with 4D contrast-enhanced MR angiography at 3T. *AJNR* 2010; 31:80–85
14. Brouwer PA, Bosman T, van Walderveen MA, Krings T, Leroux AA, Willems PW. Dynamic 320-section CT angiography in cranial arteriovenous shunting lesions. *AJNR* 2010; 31:767–770
15. Alsop DC, Detre JA. Multisection cerebral blood flow MR imaging with continuous arterial spin labeling. *Radiology* 1998; 208:410–416
16. Zaharchuk G. Theoretical basis of hemodynamic MR imaging techniques to measure cerebral blood volume, cerebral blood flow, and permeability. *AJNR* 2007; 28:1850–1858
17. Wolf RL, Wang J, Detre JA, Zager EL, Hurst RW. Arteriovenous shunt visualization in arteriovenous malformations with arterial spin-labeling MR imaging. *AJNR* 2008; 29:681–687
18. Le TT, Fischbein NJ, André JB, Wijman C, Rosenberg J, Zaharchuk G. Identification of venous signal on arterial spin labeling improves diagnosis of dural arteriovenous fistulas and small arteriovenous malformations. *AJNR* 2012; 33:61–68
19. Alsop DC, Detre JA, Golay X, et al. Recommended implementation of arterial spin-labeled perfusion MRI for clinical applications: a consensus of the ISMRM perfusion study group and the European consortium for ASL in dementia. *Magn Reson Med* 2015; 73:102–116
20. Iryo Y, Hirai T, Kai Y, et al. Intracranial dural arteriovenous fistulas: evaluation with 3-T four-dimensional MR angiography using arterial spin labeling. *Radiology* 2014; 271:193–199

10.3 Discussion

Cortical vein drainage was detected with high sensitivity and specificity, greater than 90%, by both readers, with very good inter-reader agreement ($\kappa = 0.82$) for cortical vein ASL signal. When PCASL was interpreted in conjunction with TOF-MRA, there was very good agreement with DSA ($\kappa = 0.85$ for reader 1 and $\kappa = 0.80$ for reader 2) and between readers ($\kappa = 0.85$) for the Borden type of a fistula. These findings indicate that CVD, the main risk factor for complication of a DAVF, can be reliably and accurately detected using on PCASL. An MRI protocol with TOF-MRA and PCASL also allows accurate grading of a DAVF for risk stratification.

An accurate technique for non-invasive detection of CVD and delineation of venous drainage can reduce the number of DSAs a patient with a DAVF is required to undergo, decreasing procedural risk, radiation exposure, and healthcare costs. Patients with low-risk *Borden type I* DAVFs could be monitored non-invasively for progression to a higher grade using serial MRI instead of DSA. For a non-invasive test to be able to replace DSA for definitive characterization of a DAVF, it requires perfect sensitivity. This is because the clinical implications of missing CVD are that a high-risk fistula is left untreated, with potentially devastating consequences, which would not be acceptable. A lower diagnostic specificity is tolerated, since a false positive would not result in the patient being exposed to a greater risk than they are in the current DAVF management pathway, since it would simply result in triage to DSA for definitive delineation of venous drainage. Unfortunately, the sensitivity of MRI with PCASL was imperfect, with CVD missed in 2/22 (9%) DAVFs where it was identified on DSA; venous ASL signal was not visible in a cortical vein even on post hoc review in one of these cases. Therefore, MRI with PCASL cannot replace DSA for characterization of venous drainage and identification of CVD at this stage. It can, however, facilitate treatment planning and triage; for example, it can trigger expedited referral of patients identified as being at high risk of complication for management, and allow better-informed patient counselling. Diagnostic DSA could be performed in the same session as endovascular therapy in patients requiring treatment, avoiding the additional risks, healthcare costs and inconvenience of a separate purely diagnostic DSA.

The high conspicuity of venous ASL signal, the cause of which was explained in the previous chapter, resulted in high sensitivity for detection of CVD. Another factor which likely contributed to the high sensitivity for detection of ASL signal

in cortical veins is the absence of high signal in arteries on PCASL images under normal conditions. In comparison, arteries are normally hyperintense on both TOF-MRA and time resolved CE-MRA, which can distract the radiologist and cause high signal within a cortical vein to be dismissed as arterial. High signal is also present in normal cortical veins on time resolved CE-MRA, since all patent venous structures are opacified in the venous phase. Detection of CVD is therefore reliant upon identification of early filling of a cortical vein in the arterial phase, which may be impaired by the limited temporal resolution of the technique when shunting is slow. Additionally, due to the limited spatial resolution (which must often be sacrificed in order to achieve the desired higher temporal resolution), opacification of normal veins and arteries can obscure cortical vein drainage on time-resolved CE-MRA. Conversely, venous ASL signal is highly specific for shunting, as was seen in the previous study. Since it results from direct shunting or subsequent flow of a column of labeled arterial blood into veins, venous ASL signal is confined to the draining veins of a DAVF. These factors allowed CVD to be detected with high sensitivity and specificity on PCASL, despite the lack of temporal information regarding venous filling.

Perceptual errors are infrequent on PCASL as seen in this study and the previous, because of the high conspicuity of venous ASL signal. Each reader had one false negative that was related to perceptual error, the other reader detected CVD. On post hoc review, high signal was only evident within a short segment of cortical vein, immediately adjacent to a dural venous sinus, in both of these cases. This was likely missed due to the low spatial resolution of PCASL, which makes it difficult to resolve a short segment of high signal in a cortical vein separate to an adjacent hyperintense dural venous sinus. The other false negative, where both readers failed to detect CVD, was a low-flow DAVF. Venous ASL signal was truly absent even on post hoc review in this case. This may be due to the volume of labeled blood being too small to allow a perceptible change in venous ASL signal, precluding detection of the fistula and delineation of the venous drainage pattern. PCASL may, therefore, have limited sensitivity for detection of low-flow DAVFs. Unfortunately, there were too few low-flow DAVFs in this study to permit meaningful conclusions to be drawn regarding the effect of reduced flow rate and volume on diagnostic performance of PCASL in these group.

This study used single-delay PCASL perfusion with a PLD of 2000 ms, in accordance with the recommended guidelines for clinical ASL[9]. A limitation of this implementation, as discussed in the previous chapter, is that it only interrogates ASL signal at a single time-point, providing a “snapshot” of labelled blood.

Therefore, no temporal information regarding venous drainage is obtained. Consequently, the entry point of labeled blood into draining veins cannot be visualized, precluding localization of the fistula. Temporal information is important for grading DAVF, in particular for differentiating direct CVD (*Borden type III*) from cortical vein reflux (*Borden type II*). In this study, there was one *Borden type III* fistula within the wall of the transverse sinus that drained directly into an adjacent cortical vein which was misclassified as Borden type II, due to the presence of ASL signal in both the cortical vein and the downstream transverse sinus. It was incorrectly assumed that blood had refluxed into the cortical vein from the transverse sinus, when in fact the cortical vein was the primary draining structure. A time-resolved sequence would help avoid this error by providing information about the sequence of signal changes in venous structures. Although CVD is an indication for treatment regardless of whether it is due to reflux or direct drainage of the fistula, the distinction is important for prognostication and treatment planning; for example, the higher risk posed by a *Borden type III* fistula may warrant earlier intervention.

It is emphasized that single-delay PCASL perfusion cannot be used on its own to detect CVD and delineate the venous drainage pattern, due to its limited spatial resolution, hence the paucity of anatomical detail it provides. Instead, it must be interpreted in conjunction with standard anatomical sequences, with cross-reference to ensure that extra-parenchymal high ASL signal does localize to a cortical vein; careful correlation with structural sequences and TOF-MRA is important to avoid false positives due to arterial transit artifact being mistaken for venous ASL signal. TOF-MRA is also critical for grading the DAVF, since it allows visualization and anatomical delineation of the fistula itself, so that the relative distribution of venous ASL signal can be assessed.

As discussed in the previous chapter, arterial and arteriovenous transit times can vary considerably between high-flow and low-flow DAVFs, therefore the optimal timing for detecting ASL signal in the draining veins of a DAVF is likely to vary considerably between patients. Images acquired using a single PLD may, therefore, fail to capture the passage of the bolus of labelled blood through the fistula and draining veins. For example, we have observed that label is usually already in venous structures downstream from high-flow fistulas when images are obtained with a PLD of 2000 ms, precluding localization of the fistula and differentiation of direct cortical vein drainage from cortical vein reflux.

With multi-delay PCASL perfusion and time-resolved (4D) ASL angiography, images are obtained at multiple time points after labelling, allowing visualization of the passage of labelled blood from arteries though the fistula into draining veins. These alternative ASL techniques are therefore likely to be more accurate for delineating the pattern of venous drainage of DAVFs. Time-resolved ASL angiography in particular is promising for the characterization and grading of DAVFs, as shown in a study with 9 patients[10]; in this study, there was perfect agreement between time-resolved ASL angiography and DSA for venous drainage, and CVD was detected in all 4 patients in whom it was present[10]. ASL angiography leverages the high conspicuity of intravascular ASL signal to produce dynamic time-resolved angiographic images [10, 11]. As in other ASL techniques, high signal is seen in veins into which there is direct shunting or subsequently flow of labeled arterial blood. This venous ASL signal is likely highly specific for the draining veins of an arteriovenous shunt, and absent in normal venous structures (since the same principles as for PCASL apply when it comes to venous outflow of label)[10]. Time-resolved ASL angiography has very high temporal resolution (50-300 ms), comparable to DSA. The passage of labelled from feeding arteries, though the fistula and into draining veins can therefore be captured accurately and visualized. This, in turn, allows accurate localization of the fistula and assessment of venous drainage; for example, direct CVD can be distinguished from cortical vein reflux. Much higher spatial resolution that can be achieved than with ASL perfusion (of the order of 0.5 mm), since the high intra-vascular signal allows images to be acquired using smaller voxels[10, 11]. At least the main feeding arteries of the DAVF can therefore be delineated[10]. The higher spatial resolution than ASL perfusion is also likely to benefit detection of cortical vein drainage, since smaller draining veins and short segment reflux can be visualized. Another advantage of the technique is the absence of high signal in veins other than those draining the DAVF, reducing the potential for obscuration of small feeding draining veins.

Time-resolved ASL angiography is therefore likely to enable accurate characterization of DAVFs. A study that assesses this technique as well as multi-delay ASL for the detection and characterization of DAVFS, including low-flow DAVFs, is therefore warranted. We have been awarded a National institutes of Health grant funding to conduct such a study, based on the work presented in Chapters 9 and 10. Enrolment in this new prospective study is currently underway.

10.4 References

1. Borden JA, Wu JK, Shucart WA. A proposed classification for spinal and cranial dural arteriovenous fistulous malformations and implications for treatment. *J Neurosurg*. 1995;82:166-179

2. Cognard C, Gobin YP, Pierot L, Bailly AL, Houdart E, Casasco A, et al. Cerebral dural arteriovenous fistulas: Clinical and angiographic correlation with a revised classification of venous drainage. *Radiology*. 1995;194:671-680

3. Cognard C, Houdart E, Casasco A, Gabrillargues J, Chiras J, Merland JJ. Long-term changes in intracranial dural arteriovenous fistulae leading to worsening in the type of venous drainage. *Neuroradiology*. 1997;39:59-66

4. Gandhi D, Chen J, Pearl M, Huang J, Gemmete JJ, Kathuria S. Intracranial dural arteriovenous fistulas: Classification, imaging findings, and treatment. *AJNR Am J Neuroradiol*. 2012;33:1007-1013

5. Cloft HJ, Joseph GJ, Dion JE. Risk of cerebral angiography in patients with subarachnoid hemorrhage, cerebral aneurysm, and arteriovenous malformation: A meta-analysis. *Stroke*. 1999;30:317-320

6. Kwon BJ, Han MH, Kang HS, Chang KH. Mr imaging findings of intracranial dural arteriovenous fistulas: Relations with venous drainage patterns. *AJNR Am J Neuroradiol*. 2005;26:2500-2507

7. Meckel S, Maier M, Ruiz DS, Yilmaz H, Scheffler K, Radue EW, et al. Mr angiography of dural arteriovenous fistulas: Diagnosis and follow-up after treatment using a time-resolved 3d contrast-enhanced technique. *AJNR Am J Neuroradiol*. 2007;28:877-884

8. Noguchi K, Melhem ER, Kanazawa T, Kubo M, Kuwayama N, Seto H. Intracranial dural arteriovenous fistulas: Evaluation with combined 3d time-of-flight mr angiography and mr digital subtraction angiography. *AJR Am J Roentgenol*. 2004;182:183-190

9. Alsop DC, Detre JA, Golay X, Gunther M, Hendrikse J, Hernandez-Garcia L, et al. Recommended implementation of arterial spin-labeled perfusion mri for clinical applications: A consensus of the ismrm perfusion study group and the european consortium for asl in dementia. *Magn Reson Med*. 2015;73:102-116

10. Iryo Y, Hirai T, Kai Y, Nakamura M, Shigematsu Y, Kitajima M, et al. Intracranial dural arteriovenous fistulas: Evaluation with 3-t four-

dimensional mr angiography using arterial spin labeling. *Radiology.* 2014;271:193-199

11. Robson PM, Dai W, Shankaranarayanan A, Rofsky NM, Alsop DC. Time-resolved vessel-selective digital subtraction mr angiography of the cerebral vasculature with arterial spin labeling. *Radiology.* 2010;257:507-515

Chapter 11

General Discussion of Findings, Contributions, Limitations, and Future Directions

In this dissertation, the clinical utility of perfusion imaging and automated software algorithms was evaluated in the setting of two specific cerebrovascular diseases: *acute ischaemic stroke* (AIS) and *dural arteriovenous fistulas* (DAVFs). These diseases have in common the availability of a highly effective treatment that can decrease morbidity and improve patient outcomes, but carries a risk of complication[1, 2]. Additionally, treatment requires access to a centre with interventional neuroradiology services and is costly. Therefore, it is important to identify patients who require and are likely to benefit from treatment, while excluding those in whom treatment is either futile or unwarranted. Unfortunately, standard neuroimaging techniques have some key shortcomings when it comes to diagnosing and triaging patients to treatment. This dissertation showed that perfusion imaging and automated software algorithms can be used to address these limitations, in order to improve diagnostic accuracy and efficiency and ensure appropriate and timely patient triage to treatment so that the best outcomes can be achieved. The working hypothesis that perfusion and automated software algorithms are of clinical utility in AIS and DAVF patients was therefore confirmed.

11.1 Summary of Findings, Contributions, and Limitations

11.1.1 Automated Software Algorithms in Acute Ischemic Stroke

Acute ischemic stroke is a time-critical emergency. Interpretation of imaging in AIS patients must therefore be accurate, fast and efficient in order to achieve reperfusion as quickly as possible. It has been found that in-hospital patient management processes that reduce the time between brain imaging and reperfusion

are associated with improved functional outcomes for patients[3]. This poses an increasing challenge for hospitals, since expansion of the thrombectomy window to 24 hours means that more patients are potentially eligible for treatment and must be screened. Further, an increasing number of small regional hospitals are required to perform and interpret *CT angiography* (CTA), since transfer of patients from even the most remote sites is possible within this extended treatment window. This can be a considerable burden for these small hospitals which often have limited resources and lack around-the-clock neuroradiology expertise. There is, therefore, a strong clinical need for strategies that provide decision support for such centres and streamline imaging interpretation and workflow.

Automated software tools can be used to provide decision support, improve workflow and expedite treatment in AIS. Fully automated algorithms that process perfusion data are already well established, and are used routinely in clinical practice to detect and quantify the infarct core and ischemic penumbra[4, 5]. They provide rapid and objective information regarding the presence and volume of salvageable tissue that facilitates identification of patients who are likely to benefit from reperfusion, in turn expediting triage of these patients to treatment. Automation has recently been applied to the task of *large vessel occlusion* (LVO) detection on CTA.

The first two studies evaluated the diagnostic performance of a new fully-automated deterministic software algorithm that can detect LVOs on CTA. These are the first published studies on an automated LVO detection tool. This tool has the potential to improve diagnostic accuracy and workflow in acute ischemic stroke patients, so that reperfusion can be expedited. In the first study, the algorithm was introduced, described and validated in a large cohort of AIS patients. It was shown to have sufficiently high sensitivity, exceeding 95%, and moderate specificity. Combined with the fast processing times, this diagnostic performance makes it suitable for use as a screening tool. In the second study, the algorithm was field tested for screening of consecutive code stroke patients presenting to a regional centre who underwent CTA. The sensitivity remained high in this population, with moderate specificity. This confirms that the algorithm can be applied to the task of screening for LVOs in the population of patients who present with a suspected ischemic stroke and undergo emergent CTA. The findings of the two studies enabled us to alert the software manufacturers to the causes of false negatives, where LVOs were missed by the algorithm: *internal carotid artery* (ICA) occlusions at the skull base and short segment *middle cerebral artery* (MCA) occlusions. These limitations were addressed and the algorithm improved by:

addition of a vessel tracker, to allow detection of short segment occlusions; and extension of the region in which vessel density is interrogated to include the skull base ICA. An improved bone subtraction mask was developed to enable the latter. The causes of impaired specificity that were identified, and the ideas that were proposed solutions, have also prompted further work by the manufacturers: machine learning approaches are being explored as a way of reducing false negatives related to normal anatomical variants; and the use of non-enhanced CT data for differentiation of acute LVOs from chronic steno-occlusive disease is also being investigated.

The work performed to validate the LVO detection algorithm led to its commercial release and United States Food and Drug Administration approval. The major clinical impact of these studies, therefore, was to provide the clinical community access to the LVO detection tool, so that it can be used for LVO detection in clinical practice. The tool is now incorporated into a software platform that also automates estimation of the infarct core and tissue at-risk on *CT perfusion* (CTP). This platform is used at regional spoke hospitals, however the impact on diagnostic performance and speed for detecting LVOs and workflow remain to be assessed. The major limitation of these first two studies was that they were retrospective. The utility of the LVO detection algorithm as a diagnostic support tool, and its impact on workflow efficiency, could therefore not be assessed. Whether the LVO detection tool adds value by improving intra- and inter-hospital workflow efficiency, in turn expediting treatment, requires prospective evaluation.

11.1.2 Perfusion-Based Infarct Core Estimation

Given the unparalleled sensitivity and specificity of DWI for detecting infarcted tissue, all suspected acute ischaemic stroke patients who are eligible for thombectomy and have no contraindication would undergo emergent MRI in an ideal world. Unfortunately, access to MRI is limited at most hospitals around the world, and safety screening is an obstacle that may delay treatment at best and be insurmountable in obtunded patients. It is therefore practical in the real-world clinical setting to use multi-modal CT with CTA and CTP to work-up acute ischaemic stroke patients and determine whether they should be triaged to thrombectomy. When there remains doubt following CT, and MRI can be accessed rapidly, it is reasonable to perform a limited acute MRI with DWI and FLAIR sequences for problem-solving, in particular to more accurately assess the volume and extend of the infarct core. In patients with uncertain onset time, MRI is of

added value to determine eligibility for intravenous thrombolysis, based on the DWI-FLAIR mismatch.

Automated detection and quantification of the infarct core on CTP, based on severely reduced *relative cerebral blood flow* (rCBF), is well established and widely used for patient triage to thrombectomy. However, prior studies that validated CTP for measurement of the infarct core against the reference standard of *diffusion-weighted imaging* (DWI) had a number of methodological flaws that may have affected their validity[6-8]. Additionally, some investigators have expressed concern that perfusion-derived blood flow reduction may not be an accurate surrogate of DWI, especially for triage decisions in individual patients, due to large measurement variability in the infarct core volumes obtained[9, 10]. These factors were the motivation for the third study that was undertaken as a part of this dissertation, which assessed the spatial and volumetric accuracy of infarct core measurements obtained using rCBF. A novel approach was adopted, where MR perfusion data was used, allowing comparison of rCBF-derived infarct core measurements with almost perfectly volumetrically and temporally matched DWI (the reference standard). The close temporal match ensured that there was no substantial infarct growth between DWI and perfusion imaging. 94% of patients were correctly categorized when 70 mL was applied as the volume limit for thrombectomy. The findings of this study support the use of automated estimation of the infarct core using reduced rCBF for the purposes of individual patient triage to thrombectomy. The study also found the optimal rCBF threshold to be 0.32; this confirms that the threshold of 0.30 that was used in the thrombectomy studies, and has since been adopted clinically for the same algorithm, was appropriate for making treatment decisions.

The main limitation of the study was that only a small number of patients who presented in the hyperacute time window were included. There is some evidence that a lower rCBF threshold may be required to predict infarction in these patients, since infarction is a product of both the severity and duration of blood flow reduction[11]. Therefore, further work is required to determine how well rCBF performs for predicting infarction, and to determine the optimal rCBF threshold in patients presenting in the hyperacute time window.

11.1.3 Added Value of Perfusion MRI

The last three studies showed that MR perfusion techniques can be of value beyond quantification of tissue blood flow; ancillary *qualitative* findings on DSC-PWI and ASL can be leveraged to detect pathology and guide treatment, increasing the clinical utility of these techniques and expanding their clinical applications.

While CTP is the first-line imaging modality for AIS in the United States and Australia, MRI is still preferred in Europe and in some centres in Asia due to the unparalleled sensitivity and specificity of DWI for detecting infarction[12]. Since stroke is a time-critical emergency, and MRI takes longer to perform than multimodal CT, strategies have been sought to shorten the acute stroke MR protocol. *T_2*-weighted gradient recalled imaging* (T_2*GRE), which is included in the protocol for haemorrhage detection, is one of the longest and time-consuming sequences in the acute stroke MR protocol. *Dynamic susceptibility-contrast perfusion-weighted imaging* (DSC-PWI), which is included at some centres for detecting penumbral tissue, is also T_2*-weighted. The fourth study compared the agreement between the baseline pre-contrast DSC-PWI images and conventional T_2*GRE for haemorrhage detection. Almost perfect agreement was found, indicating that DSC-PWI can be used for haemorrhage screening in addition to detecting tissue at-risk. The clinical implications are that the acute stroke MRI protocol inclusive of DSC-PWI can be shortened by omission of conventional T_2*GRE sequence, potentially expediting treatment. A limitation of the study is that the diagnostic performance of DSC-PWI for detecting subdural and extradural haemorrhage was not assessed, however these are uncommon in AIS patients.

Arterial spin labelling (ASL) is an alternative MR perfusion technique to DSC-PWI which does not require an exogenous contrast agent. Instead, it uses magnetically labelled arterial blood water as an endogenous flow tracer[13]. 3D *pseudo-continuous ASL* (PCASL) sequences are now widely available on clinical MRI scanners from the major vendors. While its use in AIS is largely confined to the research arena, it was shown in the fifth and sixth studies that ASL is of utility in routine clinical practice for detecting and risk stratifying DAVFs.

In the fifth study, venous ASL signal was shown to be a highly conspicuous sign that had high sensitivity, specificity and negative predictive value for the presence of a DAVF; it had a higher sensitivity and negative predictive value than any feature on structural sequences or TOF-MRA. Neuroradiologists' diagnostic performance for detection of DAVFs and their confidence improved when PCASL

was added to the MRI protocol. The improvement in diagnostic performance was greater for the more junior reader. The findings of the study indicate that addition of a PCASL perfusion sequence to the MR protocol increases radiologists' diagnostic performance and confidence for detecting DAVFs and is especially beneficial for less experienced readers. High inter-reader agreement is reflective of the high conspicuity of the sign, making it easy to detect and interpret with confidence.

The idea of using PCASL to identify cortical vein drainage and grade a DAVF arose from the observed high specificity of venous ASL signal for shunting, and our hypothesis that this signal localizes to the veins into which labelled arterial blood is either directly shunted or subsequently flows into the draining veins of the DAVF. As hypothesized, it was shown in the sixth study that venous ASL signal could be leveraged for grading and risk stratification of DAVFs. Cortical vein drainage, the main risk factor for complication of a DAVF, was detected with high sensitivity and specificity based on identification of venous ASL signal. MRI with PCASL also had very good agreement with DSA for the *Borden type* of a DAVF. The lack of time-resolved information in PCASL resulted in imperfect accuracy for distinguishing between direct cortical vein drainage and cortical vein reflux, hence imperfect agreement with DSA for Borden grade.

In both studies, low-flow DAVFs were found to be a cause of false negatives. There were, however, two other patients with low-flow DAVFs in whom venous ASL signal was present, allowing detection and grading. A limitation of the work presented is that the accuracy of PCASL for detection and grading of low-flow DAVFs was not assessed, due to there being too few patients with low-flow fistulas in the study cohort. The ASL technique that was used in both studies was single-delay PCASL perfusion, with a *post-label delay* (PLD) of 2000 ms; this is the ASL implementation that is recommended for clinical applications and therefore most commonly available on clinical MRI scanners[14]. A limitation of this implementation is that it only interrogates ASL signal at a single time-point, providing a "snapshot" of labelled blood. Arterial and arterio-venous transit times can vary considerably between high-flow and low-flow DAVFs, therefore the optimal timing for detecting venous ASL signal is likely to vary between patients and cannot be determined a priori. Images acquired using a single PLD may, therefore, fail to capture the passage of the bolus of labelled blood through the fistula and draining veins. For example, the author has observed that label is usually already in venous structures downstream from high-flow fistulas when images are obtained with a PLD of 2000 ms, precluding localization of the fistula.

The clinical implications of an accurate and reliable non-invasive technique for detecting and grading DAVFs include that it can decrease the number of patients who are required to undergo DSA for definitive diagnosis, and it can also decrease the number of DSAs performed in an individual patient. This, in turn, would decrease the procedural risk and cumulative radiation dose that patients are exposed to, and reduce health care costs. The high negative predictive value of MRI with PCASL suggests that it can be used as a screening tool in patients with a presentation potentially attributable to a DAVF. Unfortunately, the imperfect sensitivity for detecting DAVFs means that DSA is still required for definitive exclusion of the diagnosis in patients where there remains a strong index of suspicion for the diagnosis despite absence of venous ASL signal. When the index of suspicion is lower, a negative MRI with PCASL may be sufficient to dismiss a DAVF, without requirement for a DSA. In patients in whom a DAVF is detected, the accurate and confident diagnosis enabled by MRI with PCASL may allow diagnostic and therapeutic DSA procedures to be performed in the same session, avoiding the need for a purely diagnostic procedure. The high sensitivity for detecting cortical vein drainage can improve workflow by allowing expedited referral of patients at high risk of complication. It may also allow non-invasive surveillance of patients with low-grade fistulas. However, since the sensitivity of MRI with PCASL for detecting cortical vein drainage is imperfect, it is emphasized that DSA would still be required for definitive characterization in patients with low grade DAVFs in whom there is clinical concern for progression, for example a change in symptoms.

These two studies provide strong justification for inclusion of PCASL in routine MRI protocols that are used to screen patients with a presentation potentially attributable to a DAVF, e.g. pulsatile tinnitus and unexplained intracranial haemorrhage. The major impact of this work on DAVFs is that PCASL has been added to MRI protocols at a number of hospitals where the author of this dissertation works or has worked, beyond the institution where the studies were performed. At one institution, PCASL is now used for non-invasive risk stratification and monitoring of patients with DAVFs.

The challenge, now, is broader implementation of these techniques, inclusive of regional centres. These hospitals are often staffed by general radiologists rather than subspecialist neuroradiologists. Given that the high conspicuity of venous ASL signal was shown to especially benefit readers who have less experience in diagnosing DAVFs on MRI, including PCASL in the MRI protocol is likely to improve diagnostic performance and confidence in this setting. These regional and

peripheral hospitals also rarely have an in-house interventional neuroradiology service. Accurate non-invasive diagnosis and characterization of DAVFs would facilitate patient counselling and referral to a tertiary centre for treatment. It may allow local monitoring of patients with low-grade DAVFs, who would otherwise have to travel to a tertiary metropolitan centre for serial DSA. Augmenting the MRI protocol with PCASL is therefore likely to be of particular value in regional settings.

11.2 Future Directions

The use of advanced imaging techniques to improve diagnostic accuracy and patient triage in regional and peripheral hospitals has been an important theme throughout in this dissertation. Both LVO detection tools and PCASL are likely to be of greatest utility in this setting. Work is therefore required to deploy these tools broadly, and prospectively assess their impact on diagnostic accuracy, speed and overall workflow efficiency. A prospective multicentre study involving a metropolitan tertiary stroke centre, where thrombectomy is performed, and multiple regional and peripheral spoke hospitals is required to assess whether the LVO detection tool can be used to streamline intra and inter-hospital workflows and achieve faster times to reperfusion as well as better patient outcomes. Such a study is being planned.

Future work is also required to deploy PCASL more widely, including at regional hospitals. This would allow prospective assessment of diagnostic performance for detecting and characterizing DAVFs. The work performed as a part of this dissertation provided the preliminary evidence and motivation necessary to obtain National Institutes of Health grant funding (National Institutes of Health (NIH) grant R21EB021029 RPPR: **PCASL Methods for Detection and Characterization of Intracranial High-Flow Vascular Malformations**). This funding is for a prospective study to investigate the potential benefits, in terms of diagnostic accuracy, workflow and health economic impact, of non-invasive screening, characterization and surveillance of DAVFs. The author of this dissertation is a chief investigator on this grant, and is currently in the process of rolling out PCASL at multiple sites as a part of this study.

As a part of this prospective NIH-funded study, ideas that arose from the current work will also be explored further. In particular, alternative ASL techniques, which we hypothesized would improve diagnostic performance for detection and

characterization of DAVFs, will be further developed and evaluated, thereby addressing a major limitation of the work presented. The techniques which will be used are multi-delay PCASL perfusion and time-resolved ASL angiography. These techniques have been discussed in the literature review (chapters 3, section 3.5.6 and 4, section 4.5.7 and 4.5.8) as well as in the discussion following the two DAVF studies (chapters 9 and 10). Time-resolved (4D) ASL angiography in particular shows promise for detection and characterization DAVFs[15]. It leverages the high intravascular ASL signal to produce high spatial- and temporal-resolution dynamic angiographic images analogous to DSA and *time-resolved contrast-enhanced MRA* (TR-CEMRA). The temporal resolution of time-resolved ASL angiography is of the order of 50 - 300 ms, which is competitive with that that of DSA (150 ms - 500 ms) and superior to that of TR CEMRA (1200 - 1300 ms)[15, 16]. The spatial resolution of time-resolved ASL angiography (0.5 mm - 0.6 mm) is intermediate between DSA and TR CEMRA, and much higher than that of ASL perfusion. Therefore, this technique is likely to allow accurate detection of DAVFs, as well as localization of the fistula site, determination of feeding arteries and characterization of the venous drainage pattern; the high temporal resolution would allow direct CVD to be differentiated from cortical vein reflux, which was a limitation of PCASL perfusion. A major advantage of an ASL-based technique over bolus contrast techniques is that high signal is not seen in venous structures under normal conditions; instead, venous ASL signal is specifically seen in venous structures into which labelled arterial blood is directly shunted and subsequently flows. The high specificity of venous ASL signal for the draining veins of am arteriovenous shunt, and the lack of "contamination" of images by high signal in normal venous structures, may give ASL angiography a competitive advantage over other time-resolved angiographic techniques. While detection of shunting requires identification of early venous drainage on DSA and TR-CEMRA, venous ASL signal *per se* would enable detection of a DAVF and its draining veins on ASL angiography. This may potentially allow detection of small and low-flow DAVFs which may be otherwise obscured by overlapping venous structures on DSA and TR-CEMRA.

The clinical utility of time-resolved ASL is currently limited by the long acquisition times, in excess of 8 minutes. Further work is currently being undertaken as part of the NIH-funded grant to develop a time-resolved ASL sequence that can both be performed in a clinically acceptable time frame and deliver the high diagnostic performance that is required of a test for detecting and characterizing DAVFs. Prospective evaluation will allow comparative and additive assessment with other non-invasive techniques, including TR CEMRA, which is widely used to detect

and characterize DAVFs and AVMs on MRI. In addition, the impact of including these ASL sequences in the MRI protocol on diagnostic performance of radiologists at peripheral and region hospitals, and the workflow and the health economic impact of non-invasive diagnosis and surveillance of DAVFs will be assessed.

Another important future avenue of investigation is the use of machine learning for improving diagnostic performance and workflow in acute ischemic stroke. It has already been shown that a machine learning tool outperforms individual neuroradiologists for identifying signs of acute infarction on non-enhanced CT[17]. The use of deep learning algorithms may improve the diagnostic performance of automated tools for detecting LVOs. The deterministic algorithm that was investigated in this dissertation had only moderate specificity. Training deep learning algorithms with both CTA and NECT data may help improve both sensitivity and specificity for detection of acute arterial occlusion. The use of CTA training datasets with normal variants may also improve specificity for LVO detection.

Detection of distal vessel occlusions and arterial occlusions in the posterior circulation remains a challenge for inexperienced radiologists and neurologists but is becoming increasingly relevant to clinical practise. These patients may benefit from, and are therefore increasingly considered for, thrombectomy[18, 19]. "Distal vessel thrombectomy" is in fact an area of active research with effort being channelled into new microcatheter development. Tools to aid detection of these occlusions are therefore required. As such, further work is warranted to adapt the deterministic algorithm described in this study and also to develop new machine learning algorithms that can detect these occlusions. Other future investigations that are warranted include radiation dose reduction, image quality improvement and accelerating MR image acquisition using deep learning. Given the important of workflow efficiency in AIS, further studies are warranted to develop and validate machine learning algorithms that can both identify the imaging findings of patients who are likely to benefit from reperfusion and move these patients' scans to the top of the reporting worklist. The field of machine learning is rapidly transforming neuroimaging, and is likely to provide new automated tools to help the radiologist and neurologist improve diagnostic accuracy and patient outcomes.

11.3 References

1. Gandhi D, Chen J, Pearl M, Huang J, Gemmete JJ, Kathuria S. Intracranial dural arteriovenous fistulas: Classification, imaging findings, and treatment. *AJNR Am J Neuroradiol*. 2012;33:1007-1013
2. Goyal M, Menon BK, van Zwam WH, Dippel DW, Mitchell PJ, Demchuk AM, et al. Endovascular thrombectomy after large-vessel ischaemic stroke: A meta-analysis of individual patient data from five randomised trials. *Lancet*. 2016;387:1723-1731
3. Saver JL, Goyal M, van der Lugt A, Menon BK, Majoie CB, Dippel DW, et al. Time to treatment with endovascular thrombectomy and outcomes from ischemic stroke: A meta-analysis. *JAMA*. 2016;316:1279-1288
4. Campbell BC, Yassi N, Ma H, Sharma G, Salinas S, Churilov L, et al. Imaging selection in ischemic stroke: Feasibility of automated ct-perfusion analysis. *Int J Stroke*. 2015;10:51-54
5. Lansberg MG, Lee J, Christensen S, Straka M, De Silva DA, Mlynash M, et al. Rapid automated patient selection for reperfusion therapy: A pooled analysis of the echoplanar imaging thrombolytic evaluation trial (epithet) and the diffusion and perfusion imaging evaluation for understanding stroke evolution (defuse) study. *Stroke*. 2011;42:1608-1614
6. Bivard A, McElduff P, Spratt N, Levi C, Parsons M. Defining the extent of irreversible brain ischemia using perfusion computed tomography. *Cerebrovasc Dis*. 2011;31:238-245
7. Campbell BC, Christensen S, Levi CR, Desmond PM, Donnan GA, Davis SM, et al. Cerebral blood flow is the optimal ct perfusion parameter for assessing infarct core. *Stroke*. 2011;42:3435-3440
8. Kamalian S, Kamalian S, Maas MB, Goldmacher GV, Payabvash S, Akbar A, et al. Ct cerebral blood flow maps optimally correlate with admission diffusion-weighted imaging in acute stroke but thresholds vary by postprocessing platform. *Stroke*. 2011;42:1923-1928
9. Copen WA, Yoo AJ, Rost NS, Morais LT, Schaefer PW, Gonzalez RG, et al. In patients with suspected acute stroke, ct perfusion-based cerebral blood flow maps cannot substitute for dwi in measuring the ischemic core. *PLoS One*. 2017;12:e0188891
10. Schaefer PW, Souza L, Kamalian S, Hirsch JA, Yoo AJ, Kamalian S, et al. Limited reliability of computed tomographic perfusion acute infarct volume

measurements compared with diffusion-weighted imaging in anterior circulation stroke. *Stroke*. 2015;46:419-424

11. d'Esterre CD, Boesen ME, Ahn SH, Pordeli P, Najm M, Minhas P, et al. Time-dependent computed tomographic perfusion thresholds for patients with acute ischemic stroke. *Stroke*. 2015;46:3390-3397

12. Wintermark M, Luby M, Bornstein NM, Demchuk A, Fiehler J, Kudo K, et al. International survey of acute stroke imaging used to make revascularization treatment decisions. *Int J Stroke*. 2015;10:759-762

13. Alsop DC, Detre JA. Multisection cerebral blood flow mr imaging with continuous arterial spin labeling. *Radiology*. 1998;208:410-416

14. Alsop DC, Detre JA, Golay X, Gunther M, Hendrikse J, Hernandez-Garcia L, et al. Recommended implementation of arterial spin-labeled perfusion mri for clinical applications: A consensus of the ismrm perfusion study group and the european consortium for asl in dementia. *Magn Reson Med*. 2015;73:102-116

15. Iryo Y, Hirai T, Kai Y, Nakamura M, Shigematsu Y, Kitajima M, et al. Intracranial dural arteriovenous fistulas: Evaluation with 3-t four-dimensional mr angiography using arterial spin labeling. *Radiology*. 2014;271:193-199

16. Robson PM, Dai W, Shankaranarayanan A, Rofsky NM, Alsop DC. Time-resolved vessel-selective digital subtraction mr angiography of the cerebral vasculature with arterial spin labeling. *Radiology*. 2010;257:507-515

17. Maegerlein C, Fischer J, Monch S, Berndt M, Wunderlich S, Seifert CL, et al. Automated calculation of the alberta stroke program early ct score: Feasibility and reliability. *Radiology*. 2019;291:141-148

18. Grossberg JA, Rebello LC, Haussen DC, Bouslama M, Bowen M, Barreira CM, et al. Beyond large vessel occlusion strokes: Distal occlusion thrombectomy. *Stroke*. 2018;49:1662-1668

19. Powers WJ, Rabinstein AA, Ackerson T, Adeoye OM, Bambakidis NC, Becker K, et al. 2018 guidelines for the early management of patients with acute ischemic stroke: A guideline for healthcare professionals from the american heart association/american stroke association. *Stroke*. 2018;49:e46-e110

Chapter 12

Summary and Concluding Remarks

Acute ischaemic stroke (AIS) and *dural arteriovenous fistulas* (DAVFs) are cerebrovascular diseases which have in common the availability of a highly effective treatment, triage to which is heavily reliant upon neuroimaging. Standard non-invasive neuroimaging techniques are limited when it comes to accurately and efficiently identifying those patients who are likely to require and benefit from treatment. In this dissertation, the use of advanced neuroimaging tools to address these limitations was investigated. Specifically, the six studies presented in this dissertation explored how perfusion imaging and automated software algorithms can be used to either improve diagnostic accuracy or efficiency in order to ensure appropriate and timely patient triage to treatment.

The interpretation of imaging in AIS must be accurate, fast and efficient to ensure that patients who are likely to benefit from reperfusion are treated as soon as possible and the best outcomes are achieved. Automated software tools can be used to expedite diagnosis and triage by providing decision support and improving workflow. Automated detection and quantification of the infarct core and ischaemic penumbra on *CT perfusion* (CTP) allow rapid and objective assessment of the benefit and risks of reperfusion therapies in individual AIS patients. Despite being widely used, there are concerns that infarct core predictions obtained using CTP are not sufficiently accurate for guiding treatment decisions. It was shown in this thesis that severely reduced *relative cerebral blood flow* (rCBF) can reliably distinguish patients with small infarct, who are likely to benefit from treatment, from those with large infarcts, who may be harmed by reperfusion, confirming that it can be used for triage decisions in individual patients.

This dissertation also introduced, validated and field-tested a new fully automated software tool for detecting intracranial *large vessel occlusions* (LVOs) on *CT angiography* (CTA). The tool was shown to have the high diagnostic sensitivity and negative predictive value, exceeding 95%, that are required of a screening tool. It was also able to rapidly process the CTAs, making it ideally suited for use in the emergent clinical setting to screen the CTAs of stroke patients. Given its

imperfect sensitivity and only specificity, this tool cannot replace the experienced human reader however it can provide diagnostic support for less experienced readers, which may, in turn, improve diagnostic speed and accuracy. It is also likely to add value by improving intra- and inter-hospital workflow efficiency, in turn expediting treatment, however this requires prospective validation.

The other three studies showed that perfusion techniques are of clinical utility beyond quantification of tissue blood flow. Ancillary qualitative findings on MR perfusion can be leveraged to detect pathology and guide treatment. It was shown that *dynamic susceptibility contrast perfusion-weighted imaging* (DSC-PWI), which is used at some centres for detecting penumbral tissue in AIS, can also be used to reliably detect acute haemorrhage in AIS patients. *Arterial spin labelling* (ASL), an alternative perfusion technique, was shown to be able to detect as well as risk stratify DAVFs with high sensitivity and negative predictive value. The addition of a *pseudo-continous ASL* (PCASL) perfusion sequence improved both diagnostic performance and confidence for detection of DAVFs on MRI. However, the sensitivity of MRI with PCASL was imperfect when compared to the reference standard of catheter-based digital subtraction angiography (DSA). It cannot, therefore, replace DSA for definitive diagnosis at this stage, but can be used to screen patients. More advanced ASL sequences, in particular time-resolved ASL angiography, show promise for further improving diagnostic performance. These techniques have much higher spatial resolution than PCASL perfusion, and temporal resolution which is comparable or superior to DSA. Further work is currently underway to determine whether can detect and characterize DAVFs with sufficient accuracy to allow confident non-invasive exclusion of the diagnosis and pre-treatment work-up of patients, without the requirement for DSA.

The findings of the studies presented in this thesis confirm the working hypothesis that perfusion and automated software algorithms are of clinical utility in AIS and DAVF patients. The challenge, now, is broader implementation of these techniques to benefit more patients, including at regional centres. The use of advanced imaging techniques to improve diagnostic accuracy and patient triage in regional and peripheral hospitals has been an important theme throughout in this body of work. Both LVO detection tools and PCASL are likely to be of greatest utility at these centres, which are staffed by general radiologists rather than subspecialist neuroradiologists. These hospitals also rarely have an in-house interventional neuroradiology service. Accurate identification of AIS patients who are likely to benefit from thrombectomy and DAVF patients who require treatment is therefore important to ensure that the right patients are referred or transferred

to a tertiary centre for treatment. Work is therefore required to deploy these tools broadly, and prospectively assess their impact on diagnostic accuracy, speed and overall workflow efficiency.

The studies presented in this thesis show some of the important limitations of both automation and the experienced human reader, indicating that they are complementary rather than alternatives. As shown, automation is well suited to narrow tasks such as LVO detection and infarct core segmentation. They provide objective results rapidly, which is important in the emergent setting, and help avoid variability related to subjective interpretation. However, the use of a narrow set of decision criteria leads to both false positives and false negatives, such as incorrect diagnosis of an anatomical variant as an LVO. Radiologists are able to avoid many of these pitfalls and, as such, cannot yet be replaced by automated tools. We are, however, prone to perceptual errors, as was seen in the studies on haemorrhage and DAVF detection presented in this thesis. Our performance is heavily dependent on our level of experience, as was evidenced by the difference in diagnostic performance between the experienced and junior neuroradiologist for detecting DAVFs, and factors such as fatigue and distraction. In turn, these lead to error and variability. We are also limited in how many tasks we can perform at a time and slower than powerful computers at analysing imaging data. Automation can help address these human limitations by rendering diagnoses and providing decision support and workflow tools. Much work is currently being done on automation in neuroimaging using machine learning, in particular deep learning, algorithms. Continuing advances in this field promise to yield more accurate and sophisticated automated tools to improve diagnostic accuracy, efficiency, and ultimately the outcomes of AIS and DAVF patients.

Chapter 13

Other Contributions

13.1. Peer Reviewed Articles

1. **Amukotuwa S**, Straka M, Aksoy D, Fischbein NJ, Albers GW, Bammer R. Relative Cerebral Blood Flow Can Reliably Predict Large Infarcts That Contraindicate Thrombectomy: Validation Using Contemporaneous Perfusion and Diffusion Imaging. Magnetic Resonance in Medicine, under review.
2. Christensen S, **Amukotuwa S**, Lansberg M, Kemp S, Heit JJ, Mlynash M, Marks MP, Albers GW, Bammer R. Comparison of Tmax values between full and half dose gadolinium perfusion studies. *Journal of Cerebral Blood Flow & Metabolism,* 2020, accepted for publication (in press).
3. Peters J, Ding C, **Amukotuwa S**, Kempster P. Cerebellar atrophy with Chiari malformation: An example of trans-synaptic degeneration? *J Clin Neurosci,* 2019. 69: 279-280.
4. **Amukotuwa SA**, Yu C, Zaharchuk G. 3D Pseudocontinuous arterial spin labeling in routine clinical practice: A review of clinically significant artifacts. *Journal of Magnetic Resonance in Medicine*, 2016. 43: 11-27. (peer-reviewed Review Article)

13.2 Book Chapters

5. **Amukotuwa S**, Bammer R. Perfusion in dAVFs. In: *MR and CT Perfusion and Pharmacokinetic Imaging – Theory, Clinical Applications, and Protocols*. R. Bammer (Ed). Lippincott Williams & Wilkins, Philadelphia, PA, 2016.
6. Youngkyoo J, Maldjian JA, Whitlow CT, Zaharchuk G, **Amukotuwa S**, Hendrikse J. Arterial Spin Labeling Acquisition Protocols. In: *MR and CT Perfusion and Pharmacokinetic Imaging – Theory, Clinical Applications,*

and Protocols. R. Bammer (Ed). Lippincott Williams & Wilkins, Philadelphia, PA, 2016.

7. Peterson E, Samsonov A, van den Brink J, Glover G, **Amukotuwa S**, Schmiedeskamp H, Newbould R, Bammer R. In: *MR and CT Perfusion and Pharmacokinetic Imaging – Theory, Clinical Applications, and Protocols*. R. Bammer (Ed). Lippincott Williams & Wilkins, Philadelphia, PA, 2016.
8. Molvin L, Wilson T, Zorich C, Bammer R and **Amukotuwa S**. General patient dressing for CT and MR studies. In: *MR and CT Perfusion and Pharmacokinetic Imaging – Theory, Clinical Applications, and Protocols*. R. Bammer (Ed). Lippincott Williams & Wilkins, Philadelphia, PA.
9. **Amukotuwa SA**, Aksoy D and Bammer R. Normal blood flow values in organs. In: *MR and CT Perfusion and Pharmacokinetic Imaging – Theory, Clinical Applications, and Protocols*. R. Bammer (Ed). Lippincott Williams & Wilkins, Philadelphia, PA, 2016.
10. E. Peterson, **S.A. Amukotuwa**, and R. Bammer. S. Sunaert, W. Acquisition Methods. In: *Practical Handbook of DTI.* Springer, Berlin, Germany. Van Hecke, L Emsell (Eds); 2014
11. **Amukotuwa S.** Applications of perfusion in the brain. In: *Quantitative Magnetic Resonance Imaging*. Seiberlich N and Gulani V (Eds.). Elsevier, in press.

13.3. Invited and Oral Presentations

1. **Amukotuwa SA.** Perfusion Imaging in Cerebrovascular Disease *(RC721C)*. In: *Innovations in CT and MR Perfusion.*, 2019 Annual Meeting of the Radiological Society of North America (RSNA), Chicago, IL, Dec 5th, 2019.
2. **Amukotuwa SA.** Motion in clinical MRI. *ISMRM Motion Correction in MRI & MRS* workshop, Cape Town, South Africa September 2017.
3. Industry sponsored and hospital-based talks and workshops on **CT perfusion in acute stroke** eg GE CTP workshop, Melbourne, March 2016
4. Amukotuwa SA, Heit J, Marks MP, Bammer R. 3D Pseudocontinuous ASL for detection of cortical vein drainage and determination of Cognard grade

in patients with dural arteriovenous fistulae. Presented at the Annual Meeting of the American Society of Neuroradiology, Chicago, Ill, USA 2015.

5. S.A. Amukotuwa, M. Aksoy, J.R. Maclaren, J.B. Andre, R. Bammer. *A Comprehensive Motion-Corrected Neuroimaging Protocol*. Presented at the Annual Meeting of the American Society of Neuroradiology, Montreal, CAN 2014.

13.4. Conference Abstracts

1. Amukotuwa SA, Calamante F, Bammer R. Comparative Assessment of SAGE and GRE DSC Perfusion: Initial Assessment in a Stroke Cohort. *23rd Annual Meeting of the ISMRM. Toronto, Ontario, Canada, 2015.* p. 2329.

Chapter 14

Copyright Permissions

14.1. American Journal of Neuroradiology

1. **Amukotuwa** SA, Marks MP, Zaharchuk G, Calamante F, Bammer R, Fischbein N. Arterial Spin-Labeling Improves Detection of Intracranial Dural Arteriovenous Fistulas with MRI. AJNR Am J Neuroradiol. 2018;39(4):669-677.

600004247	AJNR, American journal of neuroradiology	Accepted	Arterial Spin-Labeling Improves Detection of Intracranial Dural Arteriovenous Fistulas with MRI.	Shalini Amukotuwa	Monash Health	26-Dec-2019	22-Jan-2020	Karen Halm	0.00 USD

14.2. International Journal of Stroke

1. **Amukotuwa SA**, Fischbein NJ, Albers GW, Davis S, Donnan GA, Andre JB, Bammer R. Comparison of T2*GRE and DSC-PWI for hemorrhage detection in acute ischemic stroke patients: Pooled analysis of the EPITHET, DEFUSE 2, and SENSE 3 stroke studies. Int J Stroke. 2020;15(2):216-225.

PERMISSIONS GRE

PermissionsUK Fri, Dec 27, 2019, 2:26 AM

to me

Dear Shalini Amukotuwa,

Thank you for your email. I am pleased to report we can grant your request without a fee as part of your thesis.

Please accept this email as permission for your request as detailed below. Permission is granted for the life of the edition on a non-exclusive basis, in the English language, throughout the world in all formats provided full citation is made to the original SAGE publication.
The permission is subject to approval from any co-authors on the original project. Please note approval excludes any graphs, photos, excerpts, etc. which required permission from a separate copyright holder at the time of publication. If your material includes anything which was not your original work, please contact the rights holder for permission to reuse those items.

If you have any questions, or if we may be of further assistance, please let us know.

Best Wishes,

Craig Myles
Rights Coordinator
on behalf of **SAGE Ltd. Permissions Team**

SAGE Publishing
1 Oliver's Yard
London, EC1Y 1SP
UK

14.3. American Journal of Radiology

1. **Amukotuwa SA**, Heit J, Marks MP, Bammer R. Detection of Cortical Venous Drainage and Determination of the Borden Type of Dural Arteriovenous Fistula by Means of 3D Pseudocontinuous Arterial Spin-Labeling MRI. AJR Am J Roentgenol. 2016; 207(1):163-9.

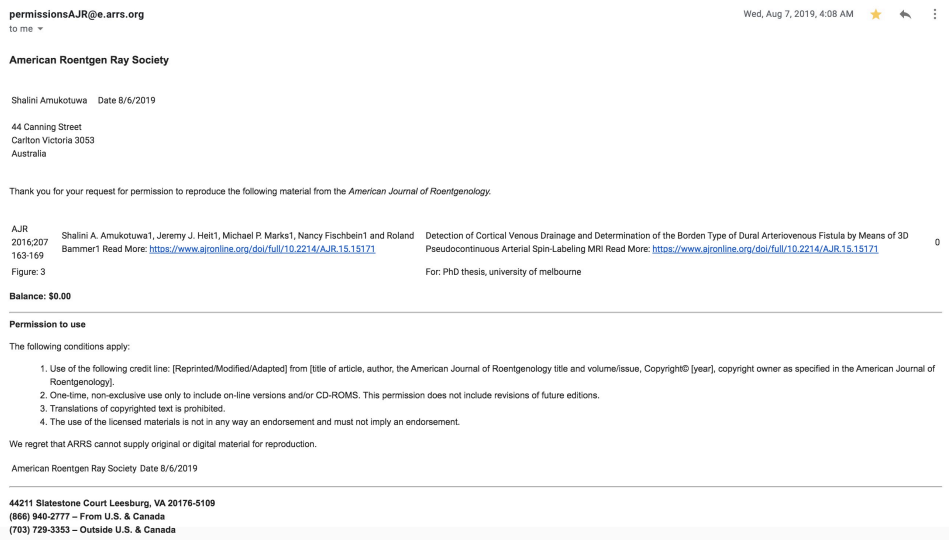

permissionsAJR@e.arrs.org Wed, Aug 7, 2019, 4:08 AM

to me

American Roentgen Ray Society

Shalini Amukotuwa Date 8/6/2019

44 Canning Street
Carlton Victoria 3053
Australia

Thank you for your request for permission to reproduce the following material from the *American Journal of Roentgenology.*

AJR 2016;207 163-169	Shalini A. Amukotuwa1, Jeremy J. Heit1, Michael P. Marks1, Nancy Fischbein1 and Roland Bammer1 Read More: https://www.ajronline.org/doi/full/10.2214/AJR.15.15171	Detection of Cortical Venous Drainage and Determination of the Borden Type of Dural Arteriovenous Fistula by Means of 3D Pseudocontinuous Arterial Spin-Labeling MRI Read More: https://www.ajronline.org/doi/full/10.2214/AJR.15.15171	0
Figure: 3		For: PhD thesis, university of melbourne	

Balance: $0.00

Permission to use

The following conditions apply:

1. Use of the following credit line: [Reprinted/Modified/Adapted] from [title of article, author, the American Journal of Roentgenology title and volume/issue, Copyright© [year], copyright owner as specified in the American Journal of Roentgenology].
2. One-time, non-exclusive use only to include on-line versions and/or CD-ROMS. This permission does not include revisions of future editions.
3. Translations of copyrighted text is prohibited.
4. The use of the licensed materials is not in any way an endorsement and must not imply an endorsement.

We regret that ARRS cannot supply original or digital material for reproduction.

American Roentgen Ray Society Date 8/6/2019

44211 Slatestone Court Leesburg, VA 20176-5109
(866) 940-2777 – From U.S. & Canada
(703) 729-3353 – Outside U.S. & Canada

14.4. Stroke

1. **Amukotuwa SA**, Straka M, Dehkharghani S, Bammer R. Fast Automatic Detection of Large Vessel Occlusions on CT Angiography. Stroke. 2019 50(12):3431-3438.

2. **Amukotuwa** SA, Straka M, Smith H, Chandra RV, Dehkharghani S, Fischbein NJ, Bammer R. Automated Detection of Intracranial Large Vessel Occlusions on Computed Tomography Angiography: A Single Center Experience. Stroke. 2019; 50(10):2790-2798.

3. **Amukotuwa S**, Straka M, Aksoy D, Fischbein N, Desmond P, Albers G, Bammer R. Cerebral Blood Flow Predicts the Infarct Core: New Insights From Contemporaneous Diffusion and Perfusion Imaging. Stroke. 2019;50(10):2783-2789.

See next page for copyright permission from Wolters Kluwer

This permission letter is issued as of 5 February 2020 by Wolters Kluwer Health, Inc., a Delaware corporation having as its principal place of business at Two Commerce Square 2001 Market Street Philadelphia, PA 19103 USA (referred to in this Agreement as "LICENSOR") for (Referred to in this agreement as "LICENSEE") listed below:

LICENSEE
Shalini Amukotuwa
Monash Health
University of Melbourne
samukotuwa@gmail.com

Wolters Kluwer Health, Inc. Content:	Shalini A. Amukotuwa , Matus Straka, Seena Dehkharghani, Roland Bammer, "Fast Automatic Detection of Large Vessel Occlusions on CT Angiography," Nov 2019 *Stroke*. 2019;50:3431–3438
Wolters Kluwer Health, Inc. Content:	Shalini A. Amukotuwa , Matus Straka, Heather Smith, Ronil V. Chandra, Seena Dehkharghani, Nancy J. Fischbein, Roland Bammer, "Automated Detection of Intracranial Large Vessel Occlusions on Computed Tomography Angiography: A Single Center Experience," Sep 2019 *Stroke*. 2019;50:2790–2798
Wolters Kluwer Health, Inc. Content:	Shalini Amukotuwa , Matus Straka, Didem Aksoy, Nancy Fischbein, Patricia Desmond, Gregory Albers, Roland Bammer, "Cerebral Blood Flow Predicts the Infarct Core: New Insights From Contemporaneous Diffusion and Perfusion Imaging," Aug 2019 *Stroke*. 2019;50:2783–2789
Material Used:	Full Article
Request Number:	Marketplace 600004250
Purpose of the reuse:	Reuse in a thesis
Format:	Print only
New Reuse:	For thesis submission to University of Melbourne. Secure electronic submission to 3 examiners only. Archive in print format in institution's library repository.
Not for Profit or Commercial Reuse:	Non-profit
Additional Permissions:	Online posting is not permitted.

TERMS AND CONDITIONS

1. Duration of License: Permission is granted for a one time use only. Rights herein do not apply to future reproductions, editions, revisions, or other derivative works. This permission shall be effective as of the date of execution by the parties for the maximum period of 12 months which will end on 5 February 2021 and should be renewed after the term expires.
    i. When content is to be republished in a book or journal the validity of this agreement should be the life of the book edition or journal issue.
    ii. When content is licensed for use on a website, internet, intranet, or any publicly accessible site (not including a journal or book), you agree to remove the material from such site after 12 months, or request to renew your permission license.

2. Credit Line: A credit line must be prominently placed and include:
    i. For book content: the author(s), title of book, edition, copyright holder, year of publication;
    ii. For journal content: the author(s), titles of article, title of journal, volume number, issue number, inclusive pages and website URL to the journal page;
    iii. If a journal is published by a learned society the credit line must include the details of that society.

3. Warranties: The requestor warrants that the material shall not be used in any manner which may be considered derogatory to the title, content, authors of the material, or to Wolters Kluwer Health, Inc.

4. Indemnity: You hereby indemnify and hold harmless Wolters Kluwer Health, Inc. and its respective officers, directors, employees and agents, from and against any and all claims, costs, proceeding or demands arising out of your unauthorized use of the Licensed Material.

5. Geographical Scope: Permission granted is non-exclusive and is valid throughout the world in the English language and the languages specified in the license.

6. Copy of Content: Wolters Kluwer Health, Inc. cannot supply the requestor with the original artwork, high-resolution images, electronic files or a clean copy of content.

7. Validity: Permission is valid if the borrowed material is original to a Wolters Kluwer Health, Inc. imprint (J.B Lippincott, Lippincott-Raven Publishers, Williams & Wilkins, Lea & Febiger, Harwal, Rapid Science, Little Brown & Company, Harper & Row Medical, American Journal of Nursing Co, and Urban & Schwarzenberg - English Language, Raven Press, Paul Hoeber, Springhouse, Ovid), and the Anatomical Chart Company.

8. Third Party Material: This permission does not apply to content that is credited to publications other than Wolters Kluwer Health, Inc. or its Societies. For images credited to non-Wolters Kluwer Health, Inc. books or journals, you must obtain permission from the source referenced in the figure or table legend or credit line before making any use of the image(s), table(s) or other content.

9. Adaptations: Adaptations are protected by copyright. For images that have been adapted, permission must be sought from the rightsholder of the original material and the rightsholder of the adapted material.

10. Modifications: Wolters Kluwer Health, Inc. material is not permitted to be modified or adapted without written approval from Wolters Kluwer Health, Inc. with the exception of text size or color. The adaptation should be credited as follows: Adapted with permission from Wolters Kluwer Health, Inc.: [the author(s), title of book, edition, copyright holder, year of publication] or [the author(s), titles of article, title of journal, volume

number, issue number, inclusive pages and website URL to the journal page].

11. Full Text Articles: Rights granted to republish a journal article as a book chapter do not include rights for the book publisher to grant any further permission for that content, reuse that chapter in any other way, or permit the article to be sold as an individual chapter.

    i. A credit line must be prominently placed on the opening page of the chapter crediting the Wolters Kluwer article and journal.

12. Branding and Marketing: No drug name, trade name, drug logo, or trade logo can be included on the same page as material borrowed from *Diseases of the Colon & Rectum, Plastic Reconstructive Surgery, Obstetrics & Gynecology (The Green Journal), Critical Care Medicine, Pediatric Critical Care Medicine, the American Heart Association publications and the American Academy of Neurology publications.*

13. Open Access: Unless you are publishing content under the same Creative Commons license, the following statement must be added when reprinting material in Open Access journals: "The Creative Commons license does not apply to this content. Use of the material in any format is prohibited without written permission from the publisher, Wolters Kluwer Health, Inc. Please contact permissions@lww.com for further information."

14. Translations: The following disclaimer must appear on all translated copies: Wolters Kluwer Health, Inc. and its Societies take no responsibility for the accuracy of the translation from the published English original and are not liable for any errors which may occur.

15. Published Ahead of Print (PAP): Articles in the PAP stage of publication can be cited using the online publication date and the unique DOI number.
    i. Disclaimer: Articles appearing in the PAP section have been peer-reviewed and accepted for publication in the relevant journal and posted online before print publication. Articles appearing as PAP may contain statements, opinions, and information that have errors in facts, figures, or interpretation. Any final changes in manuscripts will be made at the time of print publication and will be reflected in the final electronic version of the issue. Accordingly, Wolters Kluwer Health, Inc., the editors, authors and their respective employees are not responsible or liable for the use of any such inaccurate or misleading data, opinion or information contained in the articles in this section.

16. Termination of Contract: Wolters Kluwer Health, Inc. must be notified within 90 days of the original license date if you opt not to use the requested material.

17. Waived Permission Fee: Permission fees that have been waived are not subject to future waivers, including similar requests or renewing a license.

18. Contingent on Payment: You may exercise these rights licensed immediately upon issuance of the license, however until full payment is received by the publisher, this license is not valid. If full payment is not received on a timely basis, then any license preliminarily granted shall be deemed automatically revoked and shall be void as if never granted. Further, in the event that you breach any of these terms and conditions or any of Wolters Kluwer Health, Inc.'s other billing and payment terms and conditions, the license is automatically revoked and shall be void as if never granted. Use of materials as described in a revoked license, as well as any use of the materials beyond the scope of an unrevoked license, may constitute copyright infringement and publisher reserves the right to take any and all action to protect its copyright in the materials.

19. STM Signatories Only: Any permission granted for a particular edition will apply to subsequent editions and for editions in other languages, provided such editions are for the work as a whole in situ and do not involve the separate exploitation of the permitted illustrations or excerpts. Please view: STM Permissions Guidelines

20. Warranties and Obligations: LICENSOR further represents and warrants that, to the best of its knowledge and belief, LICENSEE's contemplated use of the Content as represented to LICENSOR does not infringe any valid rights to any third party.

21. Breach: If LICENSEE fails to comply with any provisions of this agreement, LICENSOR may serve written notice of breach of LICENSEE and, unless such breach is fully cured within fifteen (15) days from the receipt of notice by LICENSEE, LICENSOR may thereupon, at its option, serve notice of cancellation on LICENSEE, whereupon this Agreement shall immediately terminate.

22. Assignment: License conveyed hereunder by the LICENSOR shall not be assigned or granted in any manner conveyed to any third party by the LICENSEE without the consent in writing to the LICENSOR.

23. Governing Law: The laws of The State of New York shall govern interpretation of this Agreement and all rights and liabilities arising hereunder.

24. Unlawful: If any provision of this Agreement shall be found unlawful or otherwise legally unenforceable, all other conditions and provisions of this Agreement shall remain in full force and effect.

Royalties

The LICENSEE shall pay to the LICENSOR the following for this permission request: **$0.00**
Any monies due from the LICENSEE to the LICENSOR shall be paid as follows: **N/A**

AS WITNESS THE HAND AND SEALS OF THE PARTIES HERETO:

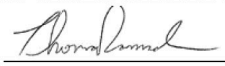

5 February 2020

Thomas Ramsden
Director of Licensing, Rights, and Permissions Operations
Wolters Kluwer Health, Inc. Health Learning Research & Practice Division